AD-772 718

THE LOW-G ACCELEROMETER CALIBRATION SYSTEM ORBITAL ACCELEROMETER EXPERIMENT. VOLUME II. EXPERIMENT ANALYSES AND RESULTS

J. A. Pearson, et al

Aerospace Corporation

Prepared for:

Space and Missile Systems Organization

1 July 1973

DISTRIBUTED BY:

NTIS

National Technical Information Service
U. S. DEPARTMENT OF COMMERCE
5285 Port Royal Road, Springfield Va. 22151

LABORATORY OPERATIONS

The Laboratory Operations of The Aerospace Corporation is conducting experimental and theoretical investigations necessary for the evaluation and application of scientific advances to new military concepts and systems. Versatility and flexibility have been developed to a high degree by the laboratory personnel in dealing with the many problems encountered in the nation's rapidly developing space and missile systems. Expertise in the latest scientific developments is vital to the accomplishment of tasks related to these problems. The laboratories that contribute to this research are:

Aerophysics Laboratory: Launch and reentry aerodynamics, heat transfer, reentry physics, chemical kinetics, structural mechanics, flight dynamics, atmospheric pollution, and high-power gas lasers.

Chemistry and Physics Laboratory: Atmospheric reactions and atmospheric optics, chemical reactions in polluted atmospheres, chemical reactions of excited species in rocket plumes, chemical thermodynamics, plasma and laser-induced reactions, laser chemistry, propulsion chemistry, space vacuum and radiation effects on materials, lubrication and surface phenomena, photosensitive materials and sensors, high precision laser ranging, and the application of physics and chemistry to problems of law enforcement and biomedicine.

Electronics Research Laboratory: Electromagnetic theory, devices, and propagation phenomena, including plasma electromagnetics; quantum electronics, lasers, and electro-optics; communication sciences, applied electronics, semiconducting, superconducting, and crystal device physics, optical and acoustical imaging; atmospheric pollution; millimeter wave and far-infrared technology.

Materials Sciences Laboratory: Development of new materials; metal matrix composites and new forms of carbon; test and evaluation of graphite and ceramics in reentry; spacecraft materials and electronic components in nuclear weapons environment; application of fracture mechanics to stress corrosion and fatigue-induced fractures in structural metals.

Space Physics Laboratory: Atmospheric and ionospheric physics, radiation from the atmosphere, density and composition of the atmosphere, aurorae and airglow; magnetospheric physics, cosmic rays, generation and propagation of plasma waves in the magnetosphere; solar physics, studies of solar magnetic fields; space astronomy, x-ray astronomy; the effects of nuclear explosions, magnetic storms, and solar activity on the earth's atmosphere, ionosphere, and magnetosphere; the effects of optical, electromagnetic, and particulate radiations in space on space systems.

THE AEROSPACE CORPORATION
El Segundo, California

ib

UNCLASSIFIED
Security Classification

AD-772 718

DOCUMENT CONTROL DATA - R & D

(Security classification of title, body of abstract and indexing annotation must be entered when the overall report is classified)

1. ORIGINATING ACTIVITY (Corporate author) The Aerospace Corporation El Segundo, California	2a. REPORT SECURITY CLASSIFICATION Unclassified 2b. GROUP

3. REPORT TITLE

THE LOW-G ACCELEROMETER CALIBRATION SYSTEM ORBITAL ACCELEROMETER EXPERIMENT, Volume II: Experiment Analyses and Results

4. DESCRIPTIVE NOTES (Type of report and inclusive dates)

5. AUTHOR(S) (First name, middle initial, last name)

J. A. Pearson, Editor, and R. W. Bruce, Y. T. Chiu, W. A. Feess, E. G. Fotou, J. A. Pearson, A. B. Prag, and K. R. Young, Authors

6. REPORT DATE	7a. TOTAL NO. OF PAGES	7b. NO. OF REFS
1 July 1973	~~407~~ 425	50

8a. CONTRACT OR GRANT NO. F04701-73-C-0074 b. PROJECT NO.	9a. ORIGINATOR'S REPORT NUMBER(S) TR-0074(4260-10)-1, Vol II
c d	9b. OTHER REPORT NO(S) (Any other numbers that may be assigned this report) SAMSO-TR-73-355, Vol II

10. DISTRIBUTION STATEMENT

Approved for public release; distribution unlimited

11. SUPPLEMENTARY NOTES	12. SPONSORING MILITARY ACTIVITY Space and Missile Systems Organization Air Force Systems Command Los Angeles, California

13. ABSTRACT

THE LOGACS (Low-G Accelerometer Calibration System) experiment, which contained a miniature electrostatic accelerometer (MESA), was placed in a low-altitude polar orbit on 22 May 1967. The experiment provided approximately 100 hours of acceleration data from which the accelerometer scale factor, accelerometer null bias, and atmospheric drag on the satellite were calculated.

Extensive comparisons of the data to various model atmospheres are made. These analyses are the more interesting because of the intense solar and geomagnetic activity during the latter part of the LOGACS flight. From the data, both midlatitude and polar models of atmospheric density have been developed over altitudes for which LOGACS data were available.

An analysis was also performed to determine wind characteristics normal to the LOGACS' orbit plane. The results confirm that the atmosphere (up to 100 nmi) has high-velocity winds in the high-latitude regions as a result of the great magnetic storm. Theoretical analysis shows these winds can be described as convective motion due to excessive heating of the polar thermosphere.

14

KEY WORDS

Accelerometers

Thermodynamic Density

Atmosphere Models

Distribution Statement (Continued)

Abstract (Continued)

Air Force Report No.
SAMSO-TR-73-355, Vol II

Aerospace Report No.
TR-0074(4260-10)-1, Vol II

THE LOW-G ACCELEROMETER CALIBRATION SYSTEM ORBITAL ACCELEROMETER EXPERIMENT

Volume II

Experiment Analyses and Results

Prepared by

J. A. Pearson
Electronics and Optics Division
Engineering Science Operations

73 JUL Ø1

Laboratory Operations
THE AEROSPACE CORPORATION

Prepared for

SPACE AND MISSILE SYSTEMS ORGANIZATION
AIR FORCE SYSTEMS COMMAND
LOS ANGELES AIR FORCE STATION
Los Angeles, California

Approved for public release;
distribution unlimited.

i c

FOREWORD

This report is published by The Aerospace Corporation, El Segundo, California, under Air Force Contract No. F04701-73-C-0074. The document was compiled and edited by J. A. Pearson; the authors include R. W. Bruce, W. A. Feess, E. G. Fotou, J. A. Pearson, and K. R. Young, Engineering Science Operations, and Y. T. Chiu and A. B. Prag, Laboratory Operations.

This report documents experimental work carried out from June 1966 through June 1970. The present compilation, published in the interests of wider dissemination of this technical information, was completed in March 1973 and submitted on 1 July 1973 to Lt. E. L. Lockwood, SAMSO (DYAE) for review and approval.

This work gathers together under one cover a complete description of the LOGACS orbital accelerometer experiment and the results obtained from that experiment. The editor gratefully acknowledges the assistance and support of members of both the Upper Atmosphere Physics Department of the Space Physics Laboratory, Laboratory Operations, and the Satellite Navigation Department of the Electronics and Optics Division, Engineering Science Operations, in the preparation of this document. The editor also thanks the authors of the individual papers included in these volumes for permitting their work to be included and for their valuable technical assistance. A list of the LOGACS documents is included in the bibliography of this volume.

Approved by

A J Boardman

A. J. Boardman, Director
Navigation and Sensor Subdivision
Electronics and Optics Division
Engineering Science Operations

G A Paulikas

G. A. Paulikas, Director
Space Physics Laboratory
Laboratory Operations

Publication of this report does not constitute Air Force approval of the report's findings or conclusions. It is published only for the exchange and stimulation of ideas.

Ernest L Lockwood

E. L. Lockwood, 1st Lt., USAF
Technology Development Division
Deputy for Technology

ABSTRACT

The LOGACS (LOw-G Accelerometer Calibration System) experiment, which contained a miniature electrostatic accelerometer (MESA), was placed in a low-altitude polar orbit on 22 May 1967. The experiment provided approximately 100 hr of acceleration data from which the accelerometer scale factor, accelerometer null bias, and atmospheric drag on the satellite were calculated.

Many reports were written during 1967 and 1968 on the LOGACS experiment and on the analyses that were performed on the data. These reports have been combined into this document, which will be the definitive report on the LOGACS experiment by The Aerospace Corporation.

The mission description, the characteristics of the accelerometer, the instrumentation used in the experiment, and a summary of the results of the inflight accelerometer calibration are presented in Volume I. The accelerometer's sensing environment is discussed, as are the data reduction methods used to extract the scale factor and bias of the accelerometer and the methods of determining the acceleration due to aerodynamic drag.

Volume II contains data plots of the reduced accelerometer time histories and of the deduced atmospheric densities over the flight. Peculiarities of the density data are examined in some detail and extensive comparisons of the data to various model atmospheres are made. These analyses are the more interesting because of the intense solar and geomagnetic activity during the latter part of the LOGACS flight, which enormously affected the atmosphere.

Models of atmospheric density have been developed over the altitudes for which LOGACS data were available. Both midlatitude models and polar and auroral models are formulated and presented.

An analysis was also performed on the LOGACS data to determine the wind magnitude and characteristics normal to the orbit plane of the

experiment. The results confirm that the earth's atmosphere (up to the altitude of 100 nmi) rotates with the earth and find that high-velocity winds are present in high-latitude regions as a result of the great magnetic storm. An analysis of these wind data shows they can be described as convective motion due to excessive heating of the polar thermosphere.

VOLUME I

CONTENTS

FOREWORD ii

ABSTRACT iii

I. LOGACS EXPERIMENT .... (E. G. Fotou) 1-1

A. Historical Background 1-1
B. Experiment Design 1-2
C. Description of MESA 1-6
D. Equipment Design 1-13
E. Preflight Checkout 1-21
F. Flight Operations 1-25
G. Equipment Problems During Flight 1-26
H. Data Acquisition 1-27
I. Data Processing 1-28
J. Discussion of Results 1-30
1. Instrument Results 1-30

II. LOGACS DATA REDUCTION .... (W. A. Feess) 2-1

A. LOGACS Sensing Environment 2-1
1. Agena Configuration 2-1
2. Acceleration Algorithms 2-4
3. Agena Rigid Body Equations of Motion 2-6
4. Agena Control System Response Characteristics .. 2-9
5. Aerodynamic Forces and Moments 2-17
6. Order of Magnitude Estimates 2-18
7. Time Average Responses 2-21
B. LOGACS Data Processing Methods 2-23
1. Accelerometer Calibrations - Apogee 2-25
2. Accelerometer Rotating Modes - Perigee 2-26
3. Fixed Mode Data Processing 2-27
4. Control System Functions 2-28
C. Data Processing Results 2-30
D. Response Anomalies 2-32

VOLUME I

CONTENTS (continued)

REFERENCES 3-1

BIBLIOGRAPHY 4-1

APPENDIXES

A. EXPERIMENTAL CLOCK ERROR A-1

B. LOGACS DRAWINGS AND DOCUMENTS B-1

C. SPECIFICATION FOR LOGACS DATA ANALYSIS PROGRAM C-1

D. LOGACS DATA ANALYSIS PROGRAM D-1

E. LOGACS SENSED ACCELERATION ALGORITHM E-1

F. SAMPLE RAW DATA PLOTS F-1

G. REDUCED DATA PLOTS G-1

VOLUME II

CONTENTS

FOREWORD ii

ABSTRACT iii

I. UPPER ATMOSPHERE DENSITY DETERMINATION FROM LOGACS . . . . (R.W. Bruce) 1-1

A. The Orbit 1-1

1. Orbital Parameters 1-1

2. Tracking and Orbit Determination 1-2

B. Aerodynamic Coefficients 1-2

C. Solar Activity 1-4

D. Atmosphere Density Data 1-7

1. Atmosphere Density Between 75 and 120 nmi Before Great Magnetic Storm 1-9

2. Atmosphere Density Between 75 and 120 nmi During Great Magnetic Storm 1-21

3. Variation in Density at 90 nmi During Intense 25 May Proton Shower 1-32

4. Relative Density vs Time for Specific Altitudes 1-33

5. Atmosphere Density Amplitude and Phase Reponse Due to Great Magnetic Storm 1-35

6. Comparison of LOGACS Measured Density with Density Obtained from Orbital Decay of LOGACS Spacecraft, Satellite 1967 50B 1-39

7. Comparison of LOGACS Measured Density with Prevalent Model Atmospheres 1-42

II. ANALYSIS OF UPPER ATMOSPHERE DENSITY (J.A. Pearson) 2-1

A. Comparisons of LOGACS Densities with Models 2-1

B. Internal Comparisons of LOGACS Densities 2-7

1. Sorting by Time 2-7

2. Sorting by Altitude 2-19

III. ATMOSPHERIC PREDICTABILITY . . . . (J.A. Pearson) 3-1

A. Density Prediction 3-1

B. Discussion 3-1

C. Conclusion 3-2

VOLUME II

CONTENTS (continued)

IV. MIDLATITUDE DENSITY MODEL ATMOSPHERE BETWEEN 120 AND 175 km . . . . (A. B. Prag) 4-1

A. Introduction 4-1

B. Data Reduction 4-1

C. Results 4-3

1. Forms of g and Z 4-3

2. Density Coefficients 4-4

D. Discussion 4-8

1. Limitations of Model 4-9

2. Extensions of Model 4-10

3. Examples of Model 4-11

V. ALTERNATE FORMULATION OF MIDLATITUDE MODEL . . . . (A. B. Prag) 5-1

A. Introduction 5-1

B. Temperature/Density Profile 5-1

C. Method of Analysis 5-3

D. Results 5-4

1. Discussion 5-10

2. Energy Considerations 5-27

VI. AURORAL AND POLAR ATMOSPHERE DENSITY MODEL BETWEEN 120 AND 175 km . . . . (A. B. Prag) 6-1

A. Introduction 6-1

B. Data Reduction 6-1

C. Polar Model 6-4

1. Symbols List 6-4

2. Region of Validity 6-4

VOLUME II

CONTENTS (continued)

3. Bulge Model 6-5

4. Bulgeless Model 6-7

D. Discussion 6-8

VII. LOGACS WIND ANALYSIS . . . . (W.A. Feess) 7-1

A. Introduction 7-1

B. Force and Moment Algorithms 7-1

C. Aerodynamic Coefficients 7-5

D. LOGACS Side Force Processing 7-10

E. Parameter Calibration 7-14

F. Mission Pitch and Yaw Angle-of-Attack Time Histories 7-27

G. Yaw Winds in Geographical Coordination 7-28

H. Wind Analysis Conclusions 7-39

VIII. THERMOSPHERIC CONVECTIVE INSTABILITY (Y.T. Chiu) 8-1

A. Introduction 8-1

B. Observation 8-1

C. Convective Instability 8-3

D. Thermohydrodynamic Instability in Rotating Thermosphere 8-22

E. Characteristic Features and Observation 8-28

F. Fully Developed Convective Instability 8-30

REFERENCES 9-1

BIBLIOGRAPHY 10-1

APPENDIXES

A. ACCELEROMETER DATA A-1

B. DENSITY DATA B-1

C. LOGACS WIND DATA C-1

VOLUME I

FIGURES

1. Bias and Scale Factor Calibration Concept 1-4

2. Exterior View of MESA Accelerometer 1-7

3. MESA Without Insulating Cover 1-8

4. Exploded View of MESA 1-9

5. Cross Section of MESA 1-10

6. Characteristic Accelerometer Output (Constant Drag Case) 1-14

7. LOGACS Centrifuge 1-15

8. Block and Signal Flow Diagram for LOGACS Experiment 1-18

9. Relay Closure Logic Pulse 1-21

10. Location of LOGACS Equipment on Agena 1-22

11. LOGACS Side Panel 1-23

12. LOGACS Bottom Panel 1-24

13. Data Analysis with No Thruster Edit 1-35

14. Data Analysis with Thruster Edit 1-36

15. Alternate Data Analysis 1-39

16. Nonsymmetrical Proof Mass 1-42

17. Relationship of Scale Factor to Pickoff Null 1-47

18. Typical Curve from MESA Saturation Tests 1-51

19. Configuration of Vehicle and LOGACS 2-2

20. Static Performance Characteristics 2-10

21. Idealized Time History 2-12

VOLUME I

FIGURES (continued)

22.	Time History Assuming a Small Constant Torque	2-13
23.	Density and Drag Accelerations	2-20
A-1.	Experiment Clock Error	A-3
A-2.	Experiment Clock Error as a Function of Temperature	A-4
E-1.	Force Vector Diagram	E-1
F-1.	Sample Raw Data (revolution 52.7 to 53.8)	F-2
F-2.	Acceleration Profile from Revolution 52 Apogee Calibration	F-3
F-3.	Corrected Raw Accelerometer Data (revolution 52.7 to 53.8)	F-4
F-4.	Corrected Raw Accelerometer Data (modes 1 and 2, revolution 54 perigee)	F-5
G-1(a)	Acceleration Profile and Ephemeris Data (23 May)	G-2
G-1(b)	Acceleration Profile and Ephemeris Data (24 May)	G-3
G-1(c)	Acceleration Profile and Ephemeris Data (25 May)	G-4
G-1(d)	Acceleration Profile and Ephemeris Data (26 May)	G-5
G-2(a)	Agena Control System Functions (23 May)	G-6
G-2(b)	Agena Control System Functions (24 May)	G-7
G-2(c)	Agena Control System Functions (25 May)	G-8
G-2(d)	Agena Control System Functions (26 May)	G-9

VOLUME II

FIGURES

1. Apogee and Perigee, and Latitude of Perigee vs Time 1-3

2. Agena Configuration Used to Determine Aerodynamic Coefficients 1-5

3. Drag Coefficient at Zero Angle of Attack vs Altitude for Agena 1-6

4. Solar Indices Observed During LOGACS Experiment 1-8

5. LOGACS Satellite Ground Traces for Revs. 26, 27, 28, and 31 1-10

6. Density vs Altitude for Rev. 26 1-11

7. Density vs Altitude for Rev. 27 1-12

8. Density vs Altitude for Rev. 28 1-13

9. Density vs Altitude for Rev. 31 1-15

10. Normalized Density vs Latitude for Rev. 26 1-16

11. Normalized Density vs Latitude for Rev. 27 1-17

12. Normalized Density vs Latitude for Rev. 28 1-18

13. Normalized Density vs Latitude for Rev. 31 1-19

14. Reference Model Density vs Altitude 1-20

15. LOGACS Satellite Ground Traces for Revs. 46, 47, 48, and 57 1-22

16. Density vs Altitude for Rev. 46 1-23

17. Density vs Altitude for Rev. 47 1-24

18. Density vs Altitude for Rev. 47 (Toward Perigee) 1-25

19. Density vs Altitude for Rev. 47 (Away from Perigee) 1-26

20. Density vs Altitude for Rev. 48 1-27

VOLUME II

FIGURES (continued)

21. Density vs Altitude for Rev. 57 1-28

22. Normalized Density vs Latitude for Rev. 46 1-29

23. Normalized Density vs Latitude for Rev. 47 1-30

24. Normalized Density vs Latitude for Rev. 48 1-31

25. Normalized Density vs Latitude for Rev. 57 1-33

26. Density vs Altitude During Proton Shower 1-34

27. Normalized Density vs Time (Toward Perigee) 1-36

28. Normalized Density vs Time (Away from Perigee) 1-37

29. Phase Response of Atmosphere Density to Great Magnetic Storm vs Altitude and Latitude 1-38

30. Amplitude Response of Atmosphere Density to Great Magnetic Storm vs Altitude and Latitude 1-40

31. Density Comparison: Orbital Decay vs LOGACS 1-41

32. Comparison of LOGACS Data (Rev. 5, Leaving Perigee) with Jacchia Static Diffusion Model 2-2

33. Comparison of LOGACS Data (Rev. 59, Leaving Perigee) with Jacchia Static Diffusion Model 2-4

34. Ratio of LOGACS-Derived Density to Walker-Bruce Model Density for a Portion of 23 May 1967; Vehicle Altitude Included for Reference 2-5

35. Ratio of LOGACS-Derived Density to Walker-Bruce Model Density for a Portion of 25 May 1967; Vehicle Altitude Included for Reference 2-6

36. Ratio of LOGACS-Derived Density to 1962 U.S. Standard Atmosphere Density for a Portion of 23 May 1967; Vehicle Altitude Included for Reference 2-8

37. Ratio of LOGACS-Derived Density to 1962 U.S. Standard Atmosphere Density for a Portion of 25 May 1967; Vehicle Altitude Included for Reference 2-9

VOLUME II

FIGURES (continued)

38. The Density Ratio LOGACS/Jacchia-Walker-Bruce Model for High Latitude (Toward Perigee) Data at Various Altitudes 2-10

39. The Density Ratio LOGACS/Jacchia-Walker-Bruce Model for High Latitude (Away from Perigee) Data at Various Altitudes 2-11

40. Density vs Altitude for Vector 1 2-12

41. Density vs Altitude for Vector 2 2-13

42. Density vs Altitude for Vector 3 2-14

43. Density vs Altitude for Vector 4 2-15

44. Density vs Altitude for Vector 5 2-16

45. Density vs Altitude for Vector 6 2-17

46. Density vs Altitude for Vector 7 2-18

47. Mean and RMS of Density Values at 148 km (80 nmi) During LOGACS Flight 2-20

48. Mean and RMS of Density Values at 150 km (81 nmi) During LOGACS Flight 2-21

49. Mean and RMS of Density Values at 166 km (90 nmi) During LOGACS Flight 2-22

50. Mean and RMS of Density Values at 185 km (100 nmi) During LOGACS Flight 2-23

51. Mean and RMS of Density Values at 200 km (108 nmi) During LOGACS Flight 2-24

52. Mean and RMS of Density Values at 203 km (110 nmi) During LOGACS Flight 2-25

53. Mean and RMS of Density Values at 222 km (120 nmi) During LOGACS Flight 2-26

VOLUME II

FIGURES (continued)

54. Mean and RMS of Density Values at 250 km (135 nmi) During LOGACS Flight 2-27

55. Ratio of Measured Densities to Those Predicted by Present Model for Entire Flight at Low Latitudes 4-6

56. Comparison Between Steady-State Density Prediction of Present Model and That of CIRA 1965 4-12

57. Variation of Present Model with $\overline{F}$ 4-13

58. Response of Present Model to a 30 min Impulsive Disturbance with Maximum Amplitude $a_p = 100$ 4-14

59. Response of Present Model to Realistic Moderate Magnetic Storm 4-16

60. Mass Density vs Altitude for $a_p = 0$, 5, 10, and 20 5-5

61. Mass Density vs Altitude for $a_p = 40$, 59, 60, and 100 5-6

62. Mass Density vs Altitude for $a_p = 200$, 300, and 400 5-7

63. Temperature Distribution Parameters H_T, T_0, and a 5-8

64. Mass Densities of N_2, O_2, and O at 120 km 5-9

65. Temperature Profiles for $a_p = 0$, 10, 40, 60, and 400 5-12

66. Number Density Profiles of Atomic Oxygen for $a_p = 0$, 10, 40, 60, and 400 5-13

67. Number Density Profiles of Molecular Nitrogen for $a_p = 0$, 10, 40, 60, and 400 5-14

68. Number Density Profiles of Molecular Oxygen for $a_p = 0$, 10, 40, 60, and 400 5-15

69. Left Ordinate: Energy Content of Atmosphere Above 120 km. Right Ordinate: Minimum Energy Deposition Rate Above 120 km 5-28

70. Average Density of Polar Atmosphere 6-11

VOLUME II

FIGURES (continued)

54. Mean and RMS of Density Values at 250 km (135 nmi) During LOGACS Flight 2-27

55. Ratio of Measured Densities to Those Predicted by Present Model for Entire Flight at Low Latitudes 4-6

56. Comparison Between Steady-State Density Prediction of Present Model and That of CIRA 1965 4-12

57. Variation of Present Model with $\overline{F}$ 4-13

58. Response of Present Model to a 30 min Impulsive Disturbance with Maximum Amplitude $a_p = 100$ 4-14

59. Response of Present Model to Realistic Moderate Magnetic Storm 4-16

60. Mass Density vs Altitude for $a_p = 0$, 5, 10, and 20 5-5

61. Mass Density vs Altitude for $a_p = 40$, 59, 60, and 100 5-6

62. Mass Density vs Altitude for $a_p = 200$, 300, and 400 5-7

63. Temperature Distribution Parameters H_T, T_0, and a 5-8

64. Mass Densities of N_2, O_2, and O at 120 km 5-9

65. Temperature Profiles for $a_p = 0$, 10, 40, 60, and 400 5-12

66. Number Density Profiles of Atomic Oxygen for $a_p = 0$, 10, 40, 60, and 400 5-13

67. Number Density Profiles of Molecular Nitrogen for $a_p = 0$, 10, 40, 60, and 400 5-14

68. Number Density Profiles of Molecular Oxygen for $a_p = 0$, 10, 40, 60, and 400 5-15

69. Left Ordinate: Energy Content of Atmosphere Above 120 km. Right Ordinate: Minimum Energy Deposition Rate Above 120 km 5-28

70. Average Density of Polar Atmosphere 6-11

FIGURES (continued)

71. Fractional Density Between 270° and 30°E, 50° to 90°N 6-13

72. Force/Moment Diagram (Yaw Plane) 7-2

73. Aerodynamic Coefficients as a Function of Molecular Speed 7-7

74. Molecular Speed Ratio vs Altitude and Temperature 7-8

75. Aerodynamic Coefficients as a Function of Altitude 7-9

76. LOGACS Side Force Processing 7-13

77. Revolution 38 (TRGO = 202490) 7-15

78. Revolution 39 (TRGO = 208640) 7-16

79. Revolution 41 (TRGO = 218880) 7-17

80. Revolution 43 (TRGO = 229120) 7-18

81. Revolution 53 (TRGO = 282240) 7-19

82. Revolution 54 (TRGO = 288384) 7-20

83. Revolution 56 (TRGO = 298624) 7-21

84. Parameter Calibration Results (Revs. 38, 39, 41, 43) 7-25

85. Parameter Calibration Results (Revs. 53, 54, 56) 7-26

86. Orbit Geometry 7-29

87. Wind Components in Geographical Coordinates (Revs. 38, 39, 41, 43) 7-31

88. Wind Components in Geographical Coordinates (Revs. 53, 54, 56) 7-32

89. Wind Components in Geographical Coordinates for 23 May 1968 7-33

90. Wind Components in Geographical Coordinates for 24 May 1968 7-34

FIGURES (continued)

91.	Wind Components in Geographical Coordinates for 25 May 1968	7-35
92.	Wind Components in Geographical Coordinates for 26 May 1968	7-36
93.	Expanded View of Fig. 92 (Trajectory Toward Pole)	7-37
94.	Expanded View of Fig. 92 (Trajectory Away from Pole)	7-38
95.	Thomas-Ching Model Temperature Profile of CIRA 2 Atmosphere Heated by Sheet Source at 150 km Depositing 3×10^5 erg/cm^2 Spread over Polar Caps, Equivalent to 7×10^{18} erg/sec Energy Deposition Rate over 8 hr	8-5
96.	Ring Current Energy Dissipation Rate of 26 May 1967 Storm	8-6
97.	Thomas-Ching Model Temperature Profile of CIRA 2 Atmosphere Heated by Sheet Source at 150 km depositing 3×10^4 erg/cm^2 Spread over Polar Caps, Equivalent to 1.17×10^{18} erg/sec Energy Deposition Rate over 8 hr	8-8
98.	Thomas-Ching Model Temperature Profile of CIRA 2 Atmosphere Heated by Sheet Source at 150 km Depositing 1×10^5 erg/cm^2 Spread over Polar Caps, Equivalent to 2.34×10^{18} erg/sec Energy Deposition Rate over 8 hr	8-9
99.	Thomas-Ching Model Temperature Profile of CIRA 2 Atmosphere Heated by Sheet Source at 150 km Depositing 2×10^5 erg/cm^2 Spread over Polar Caps, Equivalent to 4.67×10^{18} erg/sec Energy Deposition Rate over 8 hr	8-10
100.	Effect of Increasing Heat Source Thickness	8-11
101.	Relation Between Rayleigh Number R and Horizontal Characteristic Length η in Units of Layer Depth h	8-18
102.	Solution of $G(\lambda) = 0$ for λ Near Zero and $m = 1$	8-21

VOLUME II

FIGURES (continued)

103. Relation Between Rayleigh Number R and Characteristic Length η Showing Effects of Coriolis Force in Case of Vanishing Growth Rate 8-27

A-1. LOGACS Accelerometer Data for Rev. 5 . . . . A-3

A-2. LOGACS Accelerometer Data for Rev. 6 . . . . A-4

A-3. LOGACS Accelerometer Data for Rev. 7 . . . . A-5

A-4. LOGACS Accelerometer Data for Rev. 8 . . . . A-6

A-5. LOGACS Accelerometer Data for Rev. 9 . . . . A-7

A-6. LOGACS Accelerometer Data for Rev. 10 . . . . A-8

A-7. LOGACS Accelerometer Data for Rev. 11 . . . . A-9

A-8. LOGACS Accelerometer Data for Rev. 12 . . . . A-10

A-9. LOGACS Accelerometer Data for Rev. 13 . . . . A-11

A-10. LOGACS Accelerometer Data for Rev. 14 . . . . A-12

A-11. LOGACS Accelerometer Data for Rev. 15 . . . . A-13

A-12. LOGACS Accelerometer Data for Rev. 16 . . . . A-14

A-13. LOGACS Accelerometer Data for Rev. 17 . . . . A-15

A-14. LOGACS Accelerometer Data for Rev. 18 . . . . A-16

A-15. LOGACS Accelerometer Data for Rev. 19 . . . . A-17

A-16. LOGACS Accelerometer Data for Rev. 20 . . . . A-18

A-17. LOGACS Accelerometer Data for Rev. 21 . . . . A-19

A-18. LOGACS Accelerometer Data for Rev. 22 . . . . A-20

A-19. LOGACS Accelerometer Data for Rev. 23 . . . . A-21

A-20. LOGACS Accelerometer Data for Rev. 24 . . . . A-22

VOLUME II

FIGURES (continued)

A-21. LOGACS Accelerometer Data for Rev. 25 .... A-23

A-22. LOGACS Accelerometer Data for Rev. 26 .... A-24

A-23. LOGACS Accelerometer Data for Rev. 27 .... A-25

A-24. LOGACS Accelerometer Data for Rev. 28 .... A-26

A-25. LOGACS Accelerometer Data for Rev. 29 .... A-27

A-26. LOGACS Accelerometer Data for Rev. 30 .... A-28

A-27. LOGACS Accelerometer Data for Rev. 31 .... A-29

A-28. LOGACS Accelerometer Data for Rev. 32 .... A-30

A-29. LOGACS Accelerometer Data for Rev. 33 .... A-31

A-30. LOGACS Accelerometer Data for Rev. 34 .... A-32

A-31. LOGACS Accelerometer Data for Rev. 35 .... A-33

A-32. LOGACS Accelerometer Data for Rev. 36 .... A-34

A-33. LOGACS Accelerometer Data for Rev. 37 .... A-35

A-34. LOGACS Accelerometer Data for Rev. 38 .... A-36

A-35. LOGACS Accelerometer Data for Rev. 39 .... A-37

A-36. LOGACS Accelerometer Data for Rev. 40 .... A-38

A-37. LOGACS Accelerometer Data for Rev. 41 .... A-39

A-38. LOGACS Accelerometer Data for Rev. 42 .... A-40

A-39. LOGACS Accelerometer Data for Rev. 43 .... A-41

A-40. LOGACS Accelerometer Data for Rev. 44 .... A-42

A-41. LOGACS Accelerometer Data for Rev. 45 .... A-43

A-42. LOGACS Accelerometer Data for Rev. 46 .... A-44

VOLUME II

FIGURES (continued)

A-43. LOGACS Accelerometer Data for Rev. 47 . . . . A-45

A-44. LOGACS Accelerometer Data for Rev. 48 . . . . A-46

A-45. LOGACS Accelerometer Data for Rev. 49 . . . . A-47

A-46. LOGACS Accelerometer Data for Rev. 50 . . . . A-48

A-47. LOGACS Accelerometer Data for Rev. 51 . . . . A-49

A-48. LOGACS Accelerometer Data for Rev. 52 . . . . A-50

A-49. LOGACS Accelerometer Data for Rev. 53 . . . . A-51

A-50. LOGACS Accelerometer Data for Rev. 54 . . . . A-52

A-51. LOGACS Accelerometer Data for Rev. 55 . . . . A-53

A-52. LOGACS Accelerometer Data for Rev. 56 . . . . A-54

A-53. LOGACS Accelerometer Data for Rev. 57 . . . . A-55

A-54. LOGACS Accelerometer Data for Rev. 58 . . . . A-56

A-55. LOGACS Accelerometer Data for Rev. 59 . . . . A-57

A-56. LOGACS Accelerometer Data for Rev. 60 . . . . A-58

A-57. LOGACS Accelerometer Data for Rev. 61 . . . . A-59

A-58. LOGACS Accelerometer Data for Rev. 62 . . . . A-60

A-59. LOGACS Accelerometer Data for Rev. 63 . . . . A-61

A-60. LOGACS Accelerometer Data for Rev. 64 . . . . A-62

A-61. LOGACS Accelerometer Data for Rev. 65 . . . . A-63

A-62. LOGACS Accelerometer Data for Rev. 66 . . . . A-64

A-63. LOGACS Accelerometer Data for Rev. 67 . . . . A-65

B-1. LOGACS Density Data for Rev. 5, Toward Perigee B-2

VOLUME II

FIGURES (continued)

B-2. LOGACS Density Data for Rev. 5, Away from Perigee B-3

B-3. LOGACS Density Data for Rev. 6, Toward Perigee B-4

B-4. LOGACS Density Data for Rev. 6, Away from Perigee B-5

B-5. LOGACS Density Data for Rev. 7, Toward Perigee B-6

B-6. LOGACS Density Data for Rev. 7, Away from Perigee B-7

B-7. LOGACS Density Data for Rev. 9, Toward Perigee B-8

B-8. LOGACS Density Data for Rev. 9, Away from Perigee B-9

B-9. LOGACS Density Data for Rev. 10, Toward Perigee B-10

B-10. LOGACS Density Data for Rev. 10, Away from Perigee B-11

B-11. LOGACS Density Data for Rev. 11, Toward Perigee B-12

B-12. LOGACS Density Data for Rev. 11, Away from Perigee B-13

B-13. LOGACS Density Data for Rev. 12, Toward Perigee B-14

B-14. LOGACS Density Data for Rev. 12, Away from Perigee B-15

B-15. LOGACS Density Data for Rev. 13, Toward Perigee B-16

B-16. LOGACS Density Data for Rev. 13, Away from Perigee B-17

B-17. LOGACS Density Data for Rev. 14, Away from Perigee B-18

B-18. LOGACS Density Data for Rev. 18, Toward Perigee B-19

B-19. LOGACS Density Data for Rev. 18, Away from Perigee B-20

B-20. LOGACS Density Data for Rev. 20, Away from Perigee B-21

B-21. LOGACS Density Data for Rev. 21, Toward Perigee B-22

B-22. LOGACS Density Data for Rev. 21, Away from Perigee B-23

B-23. LOGACS Density Data for Rev. 22, Toward Perigee B-24

VOLUME II

FIGURES (continued)

B-24. LOGACS Density Data for Rev. 24, Toward Perigee B-25

B-25. LOGACS Density Data for Rev. 24, Away from Perigee B-26

B-26. LOGACS Density Data for Rev. 25, Toward Perigee B-27

B-27. LOGACS Density Data for Rev. 25, Away from Perigee B-28

B-28. LOGACS Density Data for Rev. 26, Toward Perigee B-29

B-29. LOGACS Density Data for Rev. 26, Away from Perigee B-30

B-30. LOGACS Density Data for Rev. 27, Toward Perigee B-31

B-31. LOGACS Density Data for Rev. 27, Away from Perigee B-32

B-32. LOGACS Density Data for Rev. 28, Toward Perigee B-33

B-33. LOGACS Density Data for Rev. 29, Toward Perigee B-34

B-34. LOGACS Density Data for Rev. 29, Away from Perigee B-35

B-35. LOGACS Density Data for Rev. 30, Toward Perigee B-36

B-36. LOGACS Density Data for Rev. 30, Away from Perigee B-37

B-37. LOGACS Density Data for Rev. 31, Toward Perigee B-38

B-38. LOGACS Density Data for Rev. 31, Away from Perigee B-39

B-39. LOGACS Density Data for Rev. 32, Toward Perigee B-40

B-40. LOGACS Density Data for Rev. 32, Away from Perigee B-41

B-41. LOGACS Density Data for Rev. 33, Toward Perigee B-42

B-42. LOGACS Density Data for Rev. 33, Away from Perigee B-43

B-43. LOGACS Density Data for Rev. 34, Toward Perigee B-44

B-44. LOGACS Density Data for Rev. 34, Away from Perigee B-45

B-45. LOGACS Density Data for Rev. 35, Toward Perigee B-46

VOLUME II

FIGURES (continued)

B-46. LOGACS Density Data for Rev. 35, Away from Perigee B-47

B-47. LOGACS Density Data for Rev. 36, Away from Perigee B-48

B-48. LOGACS Density Data for Rev. 37, Toward Perigee B-49

B-49. LOGACS Density Data for Rev. 37, Away from Perigee B-50

B-50. LOGACS Density Data for Rev. 38, Toward Perigee B-51

B-51. LOGACS Density Data for Rev. 38, Away from Perigee B-52

B-52. LOGACS Density Data for Rev. 39, Toward Perigee B-53

B-53. LOGACS Density Data for Rev. 39, Away from Perigee B-54

B-54. LOGACS Density Data for Rev. 40, Toward Perigee B-55

B-55. LOGACS Density Data for Rev. 40, Away from Perigee B-56

B-56. LOGACS Density Data for Rev. 41, Toward Perigee B-57

B-57. LOGACS Density Data for Rev. 41, Away from Perigee B-58

B-58. LOGACS Density Data for Rev. 43, Toward Perigee B-59

B-59. LOGACS Density Data for Rev. 43, Away from Perigee B-60

B-60. LOGACS Density Data for Rev. 44, Toward Perigee B-61

B-61. LOGACS Density Data for Rev. 45, Toward Perigee B-62

B-62. LOGACS Density Data for Rev. 45, Away from Perigee B-63

B-63. LOGACS Density Data for Rev. 46, Toward Perigee B-64

B-64. LOGACS Density Data for Rev. 46, Away from Perigee B-65

B-65. LOGACS Density Data for Rev. 47, Toward Perigee B-66

B-66. LOGACS Density Data for Rev. 47, Away from Perigee B-67

B-67. LOGACS Density Data for Rev. 48, Toward Perigee B-68

VOLUME II

FIGURES (continued)

B-68. LOGACS Density Data for Rev. 48, Away from Perigee B-69

B-69. LOGACS Density Data for Rev. 49, Toward Perigee B-70

B-70. LOGACS Density Data for Rev. 50, Away from Perigee B-71

B-71. LOGACS Density Data for Rev. 51, Toward Perigee B-72

B-72. LOGACS Density Data for Rev. 51, Away from Perigee B-73

B-73. LOGACS Density Data for Rev. 52, Toward Perigee B-74

B-74. LOGACS Density Data for Rev. 52, Away from Perigee B-75

B-75. LOGACS Density Data for Rev. 53, Toward Perigee B-76

B-76. LOGACS Density Data for Rev. 53, Away from Perigee B-77

B-77. LOGACS Density Data for Rev. 54, Toward Perigee B-78

B-78. LOGACS Density Data for Rev. 54, Away from Perigee B-79

B-79. LOGACS Density Data for Rev. 55, Toward Perigee B-80

B-80. LOGACS Density Data for Rev. 55, Away from Perigee B-81

B-81. LOGACS Density Data for Rev. 56, Toward Perigee B-82

B-82. LOGACS Density Data for Rev. 56, Away from Perigee B-83

B-83. LOGACS Density Data for Rev. 57, Toward Perigee B-84

B-84. LOGACS Density Data for Rev. 57, Away from Perigee B-85

B-85. LOGACS Density Data for Rev. 58, Away from Perigee B-86

B-86. LOGACS Density Data for Rev. 59, Toward Perigee B-87

B-87. LOGACS Density Data for Rev. 59, Away from Perigee B-88

B-88. LOGACS Density Data for Rev. 61, Away from Perigee B-89

B-89. LOGACS Density Data for Rev. 62, Toward Perigee B-90

VOLUME II

FIGURES (continued)

B-90. LOGACS Density Data for Rev. 62, Away from Perigee B-91

B-91. LOGACS Density Data for Rev. 63, Toward Perigee B-92

B-92. LOGACS Density Data for Rev. 63, Away from Perigee B-93

B-93. LOGACS Density Data for Rev. 64, Toward Perigee B-94

B-94. LOGACS Density Data for Rev. 64, Away from Perigee B-95

B-95. LOGACS Density Data for Rev. 65, Toward Perigee B-96

B-96. LOGACS Density Data for Rev. 65, Away from Perigee B-97

B-97. LOGACS Density Data for Rev. 66, Toward Perigee B-98

B-98. LOGACS Density Data for Rev. 66, Away from Perigee B-99

C-1. Revolution 56, Corrected Data C-3

C-2. Revolution 56, Residuals C-5

C-3. Pitch and Yaw Angle-of-Attack Time Histories C-7

VOLUME I

TABLES

1.	LOGACS Centrifuge Modes	1-13
2.	Typical Data Page from LOGACS Flight	1-29
3.	MESA Instrument Bias and Scale Factor (No edit of data acquired during thrust valve firings)	1-31
4.	MESA Instrument Bias and Scale Factor (Edit of all data acquired during thrust valve firings)	1-33
5.	MESA Instrument Bias and Scale Factor (Data reduced by means of alternate analysis program)	1-37
6.	Bias and Scale Factor	1-40
7.	Expected Relationship of Bias and Scale Factor	1-41
8.	Bias Determination at Bell Aerosystems Company	1-41
9.	Configuration Data	2-3
10.	Accelerations During Gas Valve Firing	2-16
11.	Aerodynamic Coefficients	2-17
12.	Aerodynamic Forces and Accelerations	2-19
13.	Order of Magnitude Estimates	2-22

VOLUME II

TABLES

1. Orbital Parameters for LOGACS 1-1

2. Representative LOGACS Density Measurements 1-43

3. Comparison of LOGACS Data with Density Models 1-43

4. Mean and RMS Density for All 12-Rev. Groups 3-2

5. First Rev. After 12-Rev. Mean, Relative Difference 3-3

6. Second Rev. After 12-Rev. Mean, Relative Difference 3-3

7. Third Rev. After 12-Rev. Mean, Relative Difference 3-3

8. Fourth Rev. After 12-Rev. Mean, Relative Difference 3-4

9. Values of Adopted Parameters for Present Model 4-5

10. Comparison of Present Model with Four Others During LOGACS Flight 4-7

11. Atmospheric Parameters for $\bar{F} = 183$, $a_p = 0$ 5-16

12. Atmospheric Parameters for $\bar{F} = 183$, $a_p = 5$ 5-17

13. Atmospheric Parameters for $\bar{F} = 183$, $a_p = 10$ 5-18

14. Atmospheric Parameters for $\bar{F} = 183$, $a_p = 20$ 5-19

15. Atmospheric Parameters for $\bar{F} = 183$, $a_p = 40$ 5-20

16. Atmospheric Parameters for $\bar{F} = 183$, $a_p = 59$ 5-21

17. Atmospheric Parameters for $\bar{F} = 183$, $a_p = 60$ 5-22

18. Atmospheric Parameters for $\bar{F} = 183$, $a_p = 100$ 5-23

19. Atmospheric Parameters for $\bar{F} = 183$, $a_p = 200$ 5-24

20. Atmospheric Parameters for $\bar{F} = 183$, $a_p = 300$ 5-25

21. Atmospheric Parameters for $\bar{F} = 183$, $a_p = 400$ 5-26

22. Comparison of Density Models 6-9

SECTION I

UPPER ATMOSPHERE DENSITY DETERMINATION FROM LOGACS

A. THE ORBIT

1. ORBITAL PARAMETERS

The LOGACS experiment was placed into a nearly polar orbit on an Atlas-Agena vehicle from the Western Test Range at approximately 1830 GMT on 22 May 1967. The perigee altitude was 80 nmi initially, apogee was 193 nmi, and the orbital period was very nearly 90 min, resulting in about 16 orbital revs. per day. During the eighteenth rev. one day later, two small solid propellant rockets on the Agena were fired near perigee and the orbit was adjusted such that its apogee altitude was raised to about 218 nmi to increase the orbital lifetime. The orbital parameters for LOGACS at injection and after the orbit adjustment are summarized in Table 1.

Table 1. Orbital Parameters for LOGACS

		Injection	After Orbit Adjust at Rev. 18.4
	Date	22 May 1967	23 May 1967
	Time	1839 GMT	2124 GMT
Perigee Altitude	h_p	80.0 nmi	79.4 nmi
Apogee Altitude	h_a	193.0 nmi	217.8 nmi
Inclination	i	91.5°	91.5°
Eccentricity	e	0.015	0.018
Period	P	89.4 min	89.8 min
Longitude of Asc Node	ϕ_p	43.3° N	40.7° N
Argument Perigee	ω_p	136.7°	139.3°

During the course of the flight, due to atmospheric drag and gravitational anomalies, apogee and perigee decayed to about 160 and 76 nmi, respectively, and the latitude of perigee moved northward from about 41° N to 59° N as shown in Fig. 1.

2. TRACKING AND ORBIT DETERMINATION

The LOGACS vehicle, which had an S-band transponder on board, was tracked by the pulse radar network of the U.S. Air Force Satellite Control Facility. Approximately eight tracking passes per day were obtained and the orbit was determined from the data by two independent programs (Refs. 1 and 2).

The quantity (and quality) of the tracking data used permitted solution of an ephemeris which was, in most instances, within 450 ft rms of the radar range observations. This degree of accuracy, of course, is more than adequate for effective merging of the ephemeris with the accelerations measured by LOGACS.

Any ephemeris determined from tracking data, however, is always more accurate in the vicinity of the tracking stations and less accurate at points far removed from tracking stations. In this case, it is felt that an accuracy of 2500 ft was achieved corresponding to regions in the southern hemisphere where there was no tracking coverage, and, in a few instances in the northern hemisphere when the spacecraft was adequately tracked but the data were of poor quality. For the atmosphere density data presented herein, the accuracy limitations imposed by the ephemeris are not significant.

B. AERODYNAMIC COEFFICIENTS

To deduce density values from the LOGACS acceleration measurements, a detailed study of the aerodynamic coefficients of the Agena was performed (Ref. 3). The coefficients were obtained, in the free molecule flow regime, from the analysis of Sentman (Ref. 4), using molecular speed ratios determined from the Jacchia 1965 model atmosphere (Ref. 5) modified by Bruce (Ref. 6).

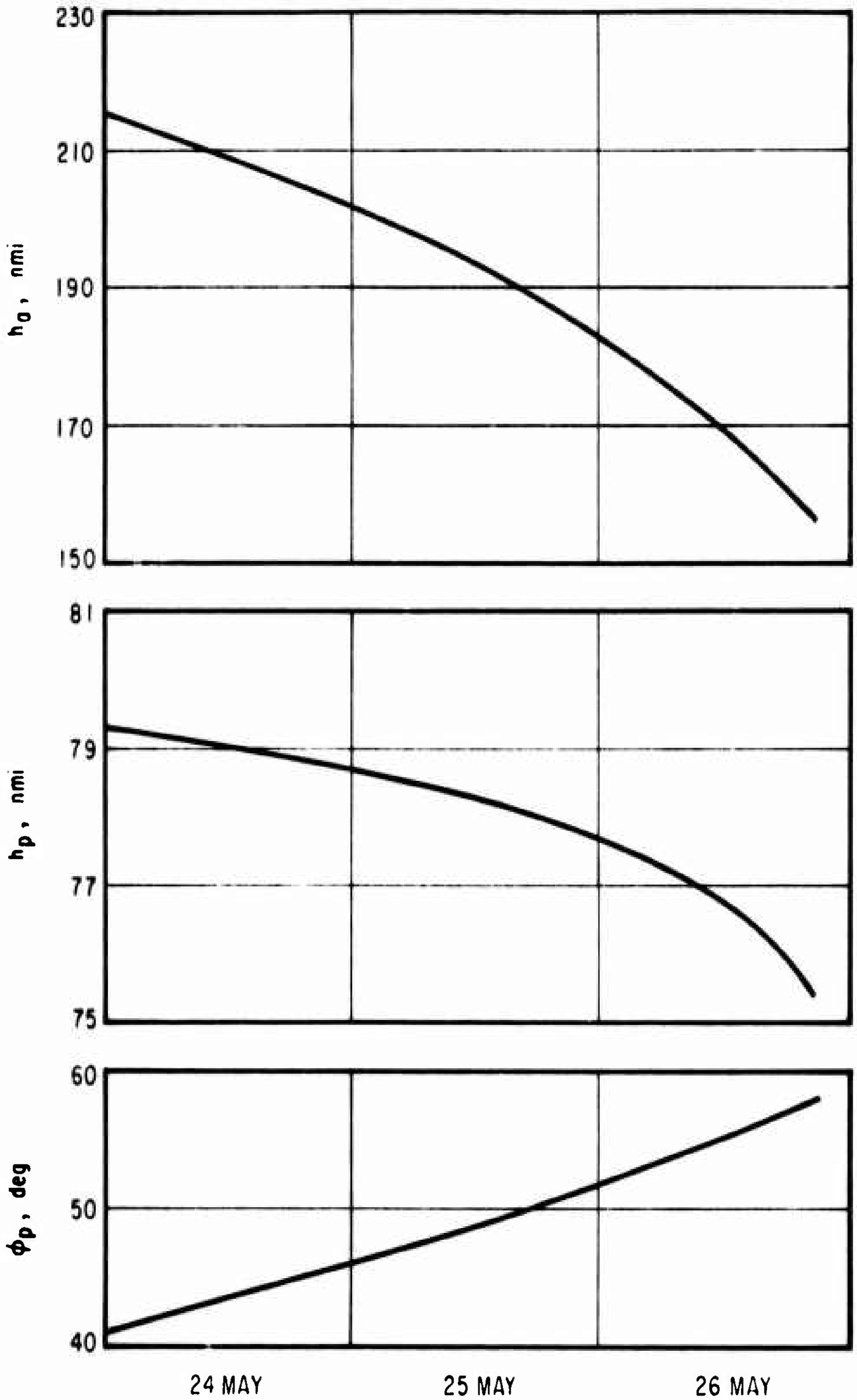

Fig. 1. Apogee and Perigee, and Latitude of Perigee vs Time

For purposes of computing the aerodynamic coefficients, the Agena configuration geometry shown in Fig. 2 was used. The frontal section was assumed to be a flat plate, whereas in actuality it is composed of a number of instrument components having shapes like spheres, boxes, an open section, and some truss members. The assumption that this surface is flat instead of being composed of complex concavities is not considered to significantly affect the estimate of the overall drag coefficient (Ref. 7). The aft portion of the Agena, in the region of the structural elements near the rocket nozzle, was assumed to be a closed cylinder for aerodynamic purposes. The surface of the Agena is considered to be rough on the molecular scale; therefore, diffuse molecular reflection was assumed.

In Fig. 3 the drag coefficient at zero angle of attack is shown for a representative value of exospheric temperature to illustrate its variation with altitude. Free molecule flow is prevalent above 75 nmi. Similar curves exist for other values of exospheric temperature and angle of attack. During the LOGACS flight the vehicle angle of attack ranged between about ±2°. This resulted in no appreciable effect on drag coefficient variation, although the variation in exospheric temperature and altitude which occurred during the flight did affect the drag coefficient by a measurable amount. However, to avoid any possible confusion in the interpretation of the density data contained in this report, a constant value of the drag coefficient (equal to 2.6) has been purposely adopted throughout. This corresponds to a ballistic coefficient C_DA/W equal to 0.0265 ft^2/lb. For the density data contained in this report, the effect of not accounting for a variable C_D is considered to fall within the uncertainty associated with the C_D itself, which, under the assumption of diffuse reflection, amounts to about ±10 percent.

C. SOLAR ACTIVITY

During the latter part of the LOGACS flight the atmosphere was strongly perturbed by extreme solar activity. The accelerometer measurements that paralleled the several solar phenomena have revealed enormous variations in atmosphere density never before observed.

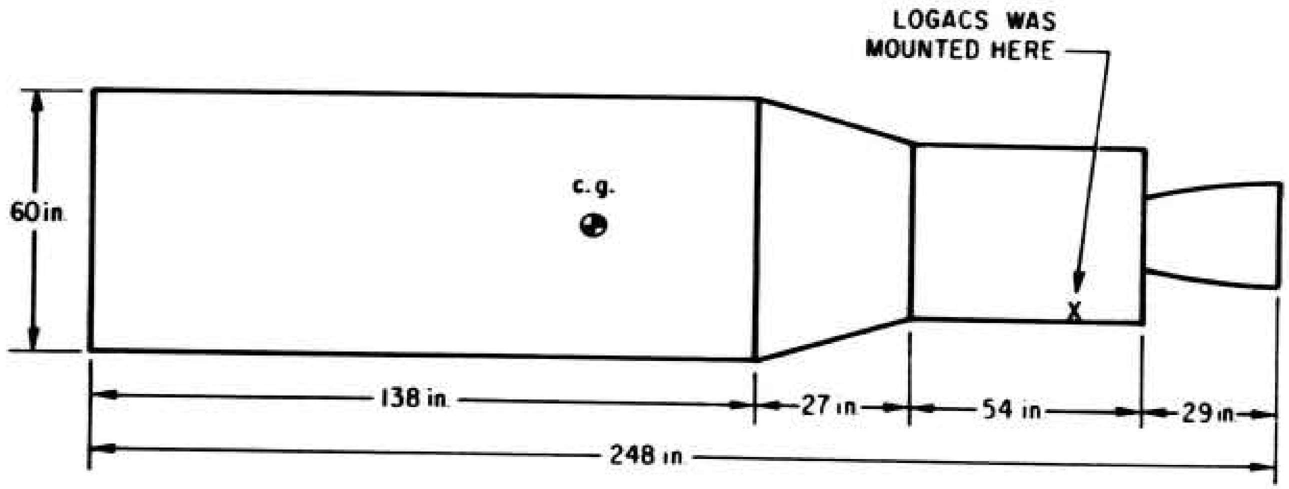

Fig. 2. Agena Configuration Used to Determine Aerodynamic Coefficients

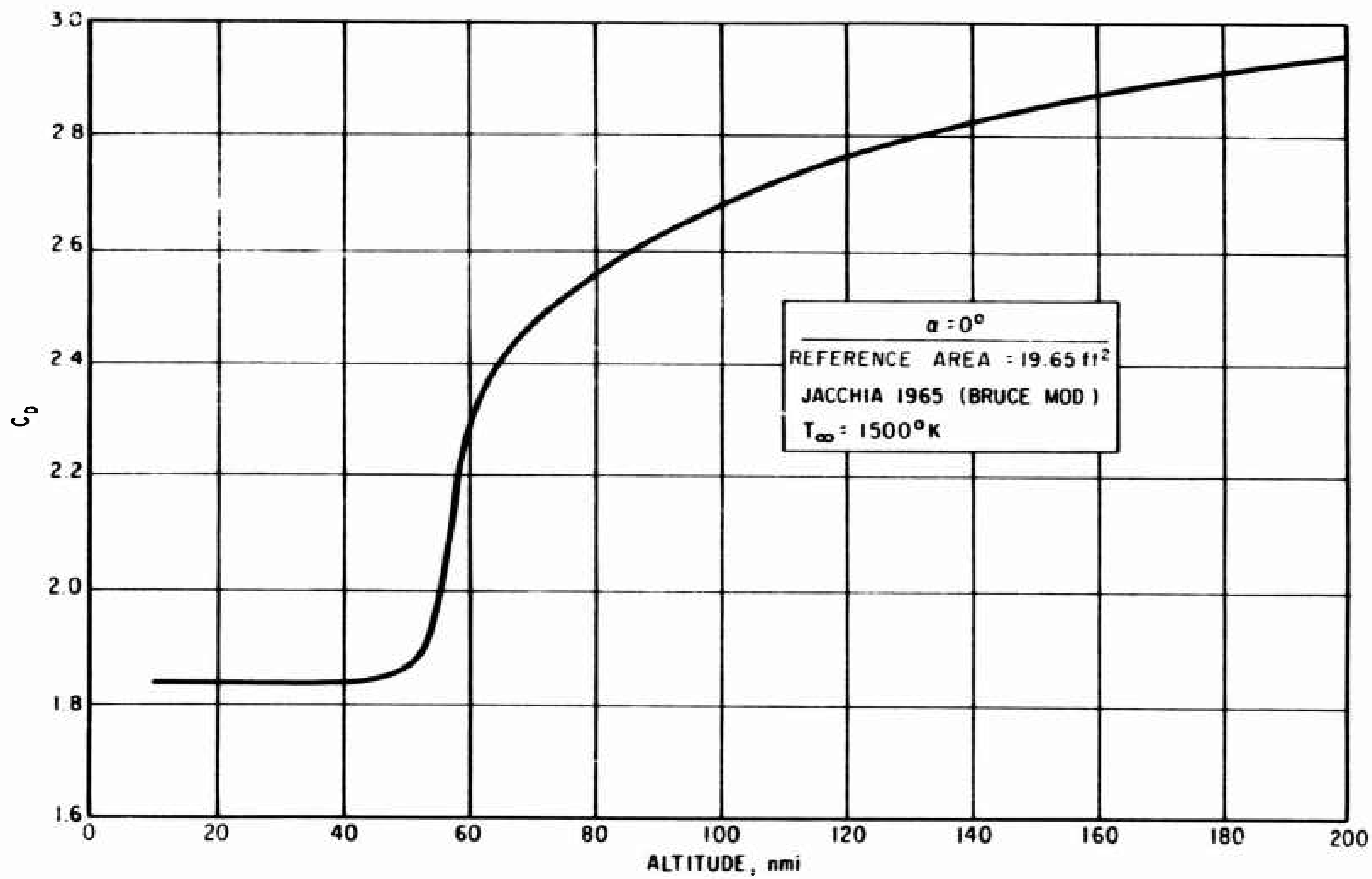

Fig. 3. Drag Coefficient at Zero Angle of Attack vs Altitude for Agena

Two commonly used indices of solar activity are shown in Fig. 4 for the period of the LOGACS experiment. Geomagnetic activity, as shown by the planetary range index K_p, was fairly quiet for the first 40 revs. of the satellite. At about Rev. 42 a great geomagnetic storm commenced, and near the end of 25 May the K_p index reached its maximum value of 9 for two successive 3-hr reporting periods -- a similar event having occurred only once before in the last 30 years. The great storm, which was accompanied by auroral activity as far south as New Mexico, resulted from two class 2B flares and one class 3B flare on 23 May, during which time solar X rays were also detected. The 10.7-cm flux, usually associated with solar EUV, increased rapidly during this period from 170 ($W/m^2/Hz \times 10^{-22}$) to 220. These levels were also well above the average value of 144 which prevailed over the previous 90 days.

Solar protons with energies of 0.5 to 2 MeV were detected frequently during this period, with intensities two to six times the normal background level. On 25 May at 1335 GMT, an extremely intense proton shower nearly 20 times higher than the normal level was recorded. At 1600 GMT, the protons began to fall off and within 0.5 hr had reduced by a factor of 5 from the peak level.

Various types of ionospheric disturbances were also prevalent during the entire period of the LOGACS flight.

D. ATMOSPHERE DENSITY DATA

The atmosphere density data contained herein have been obtained from hand-reduced drag acceleration measurements from several selected orbital revs. which span the LOGACS flight. The drag measurements were obtained directly from the Bell MESA accelerometer data during the fixed modes of operation. In the rotating modes, the drag data were obtained by linear interpolation with time of the acceleration measured at each instant the accelerometer was pointing along the drag vector.

Appendix A contains plots of the drag accelerations, while Appendix B contains plots of computer reduced densities. Section II of this volume deals with some analyses of these computer-reduced densities.

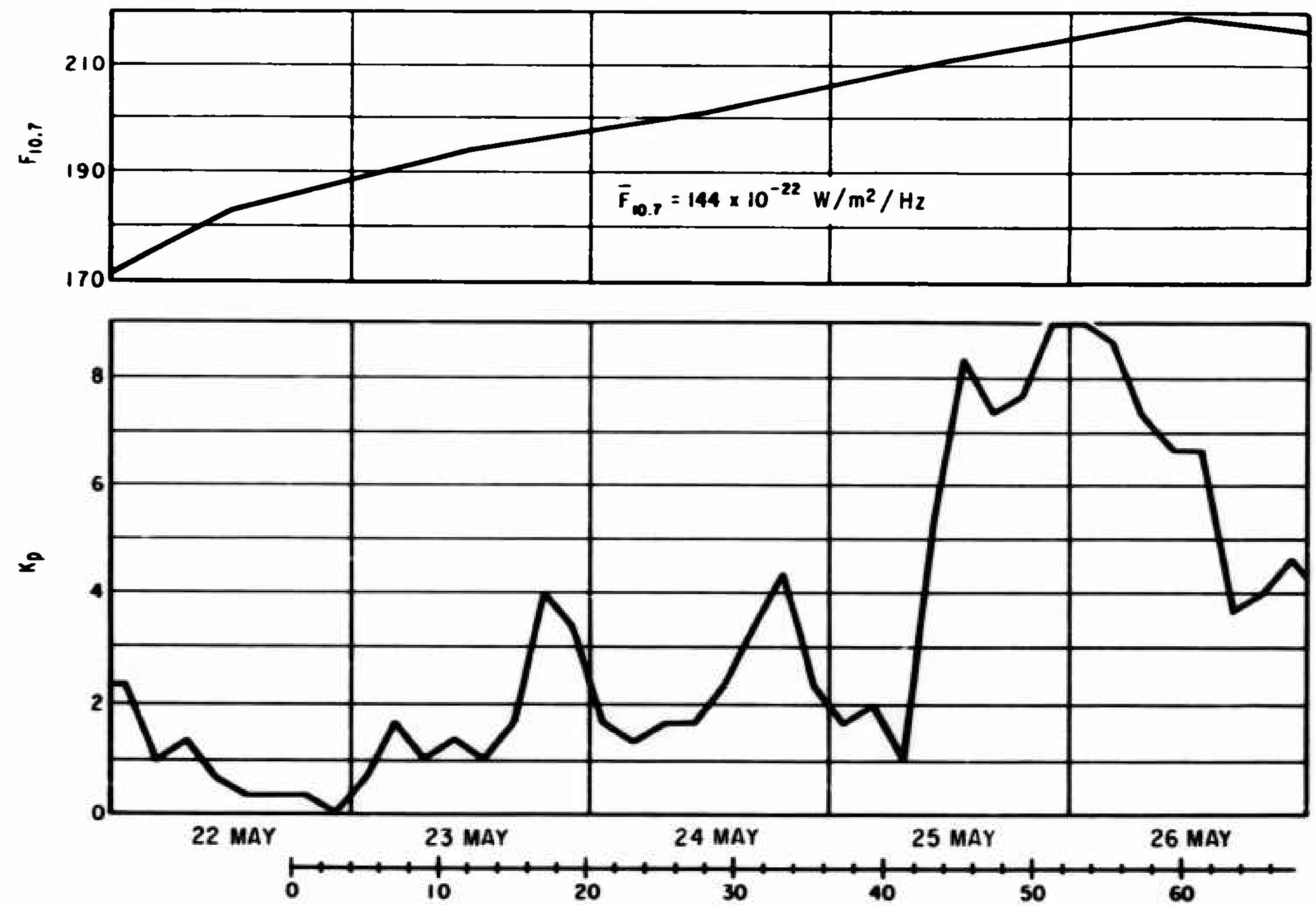

Fig. 4. Solar Indices Observed During LOGACS Experiment

The drag acceleration values are considered to be accurate to less than 1 percent based upon the stable performance of the Bell MESA accelerometer which was demonstrated throughout the experiment. The density values deduced from the acceleration measurements are considered accurate to within ±10 percent, due primarily to the uncertainty associated with the drag coefficient.

Variation of the density data with altitude, latitude, and time is shown, and a number of interesting comparisons are presented.

1. ATMOSPHERE DENSITY BETWEEN 75 AND 120 NMI BEFORE GREAT MAGNETIC STORM

Atmosphere density values obtained from satellite Revs. 26, 27, 28, and 31 have been selected to illustrate conditions prior to the great magnetic storm. These revolutions occurred during 24 May 1967 (see Fig. 4), when the K_p level was less than 4. These revs. are also particularly interesting because they pass through the high latitude atmosphere density bulge found and later modeled by Jacobs (Refs. 8 and 9). The size and location of this density bulge is shown in Fig. 5 together with the ground traces of the LOGACS satellite for Revs. 26, 27, 28, 31. Note that the points of minimum altitude of the orbit are near the vicinity of the bulge and that Rev. 28 passes directly through the center, and most dense part, of the distribution.

The LOGACS densities versus altitude obtained during these revs. are shown in Figs. 6, 7, and 8. As indicated, the solid circles represent data obtained as the satellite was approaching perigee and the open circles the data leaving perigee. For the most part, the data are shown at 1-min intervals, although some gaps exist. During the "toward-perigee" portion of the trace, the satellite was moving through the high latitudes of the northern hemisphere, and going south. For the "away-from-perigee" portion, the satellite was in the midlatitudes and approaching the equator. This is the situation for all the data presented in this report. Therefore, for every case, the toward-perigee data represent high latitude measurements and the away-from-perigee data represent mid and equatorial latitudes.

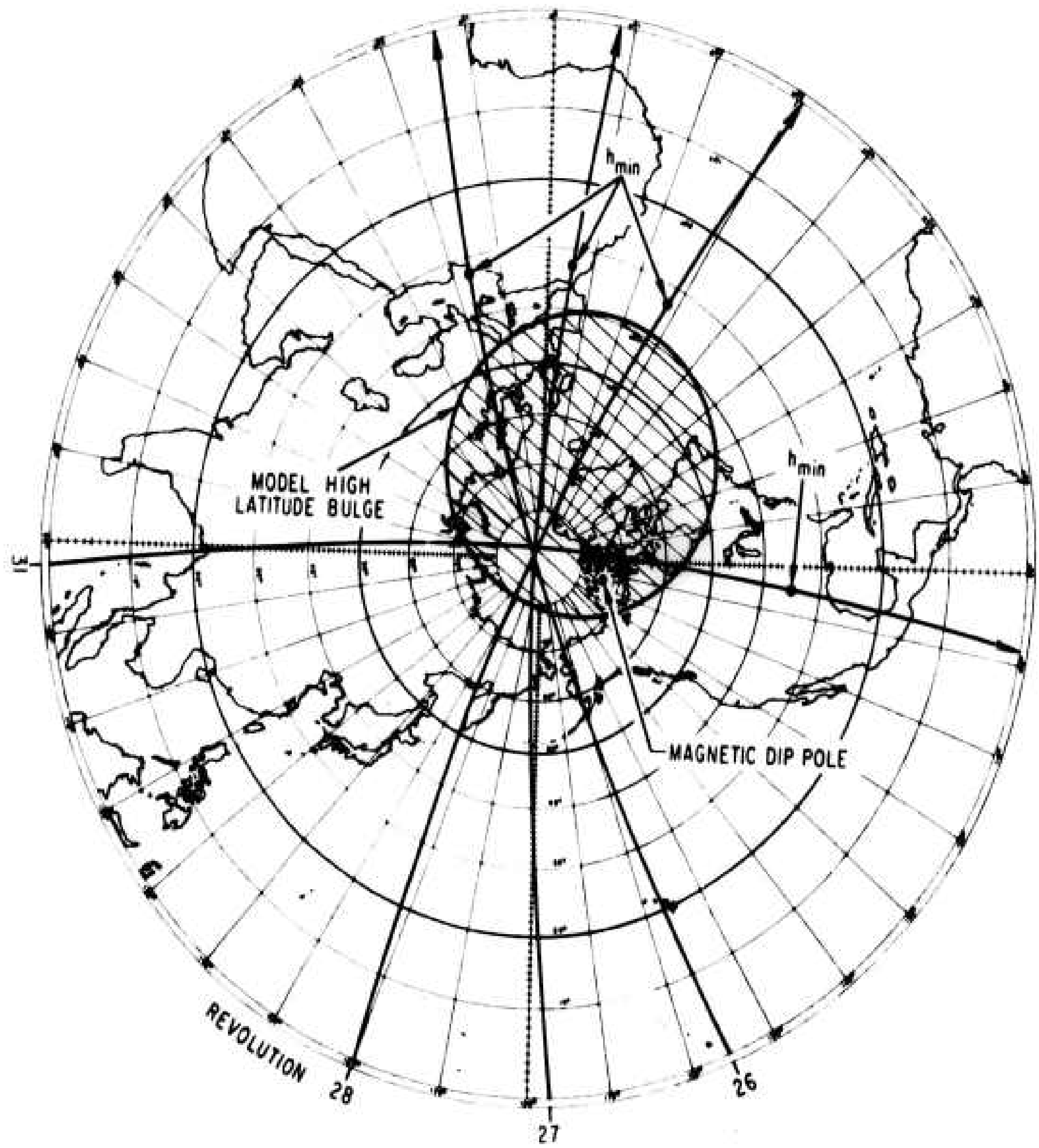

Fig. 5. LOGACS Satellite Ground Traces for Revs. 26, 27, 28, and 31

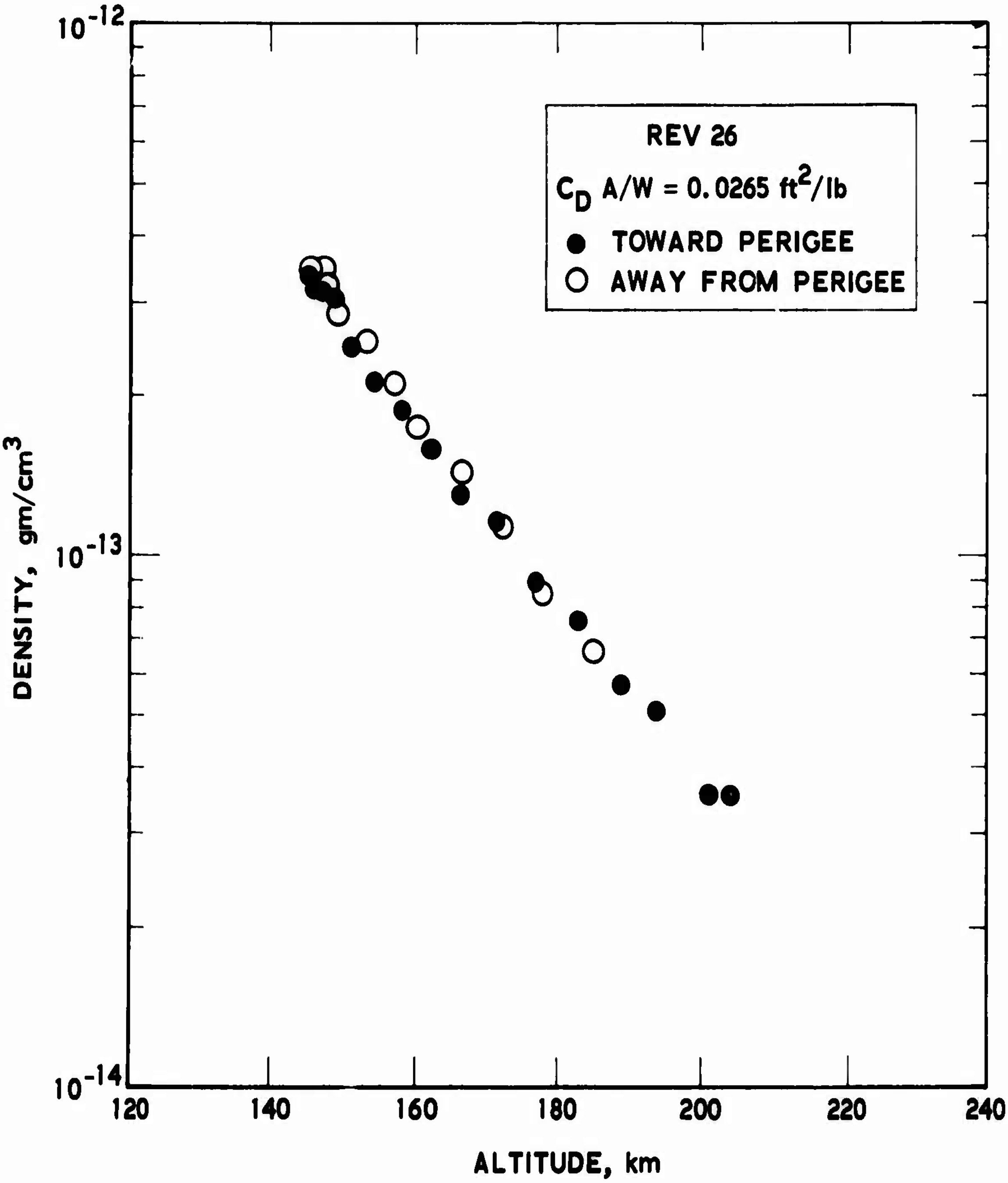

Fig. 6. Density vs Altitude for Rev. 26

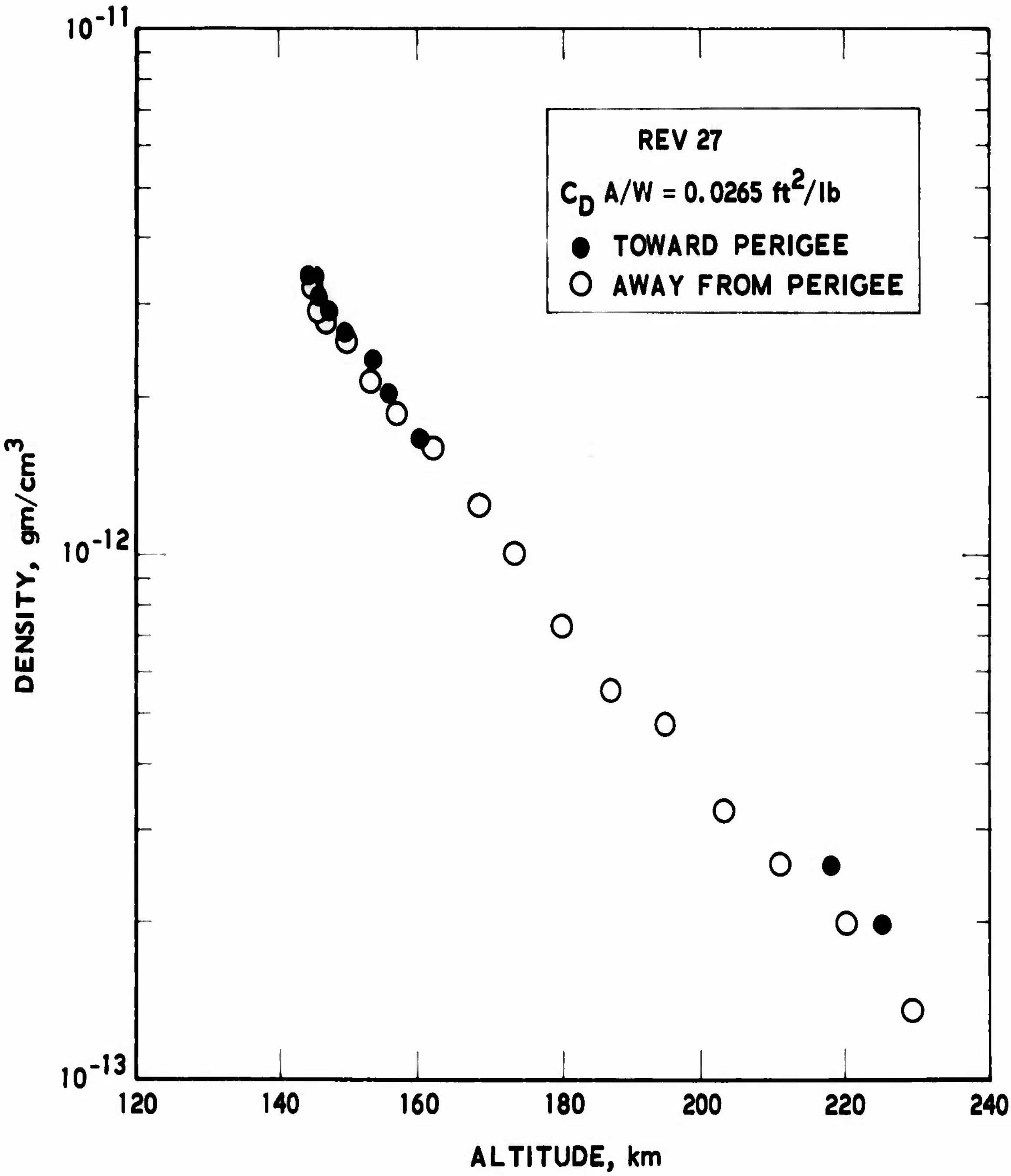

Fig. 7. Density vs Altitude for Rev. 27

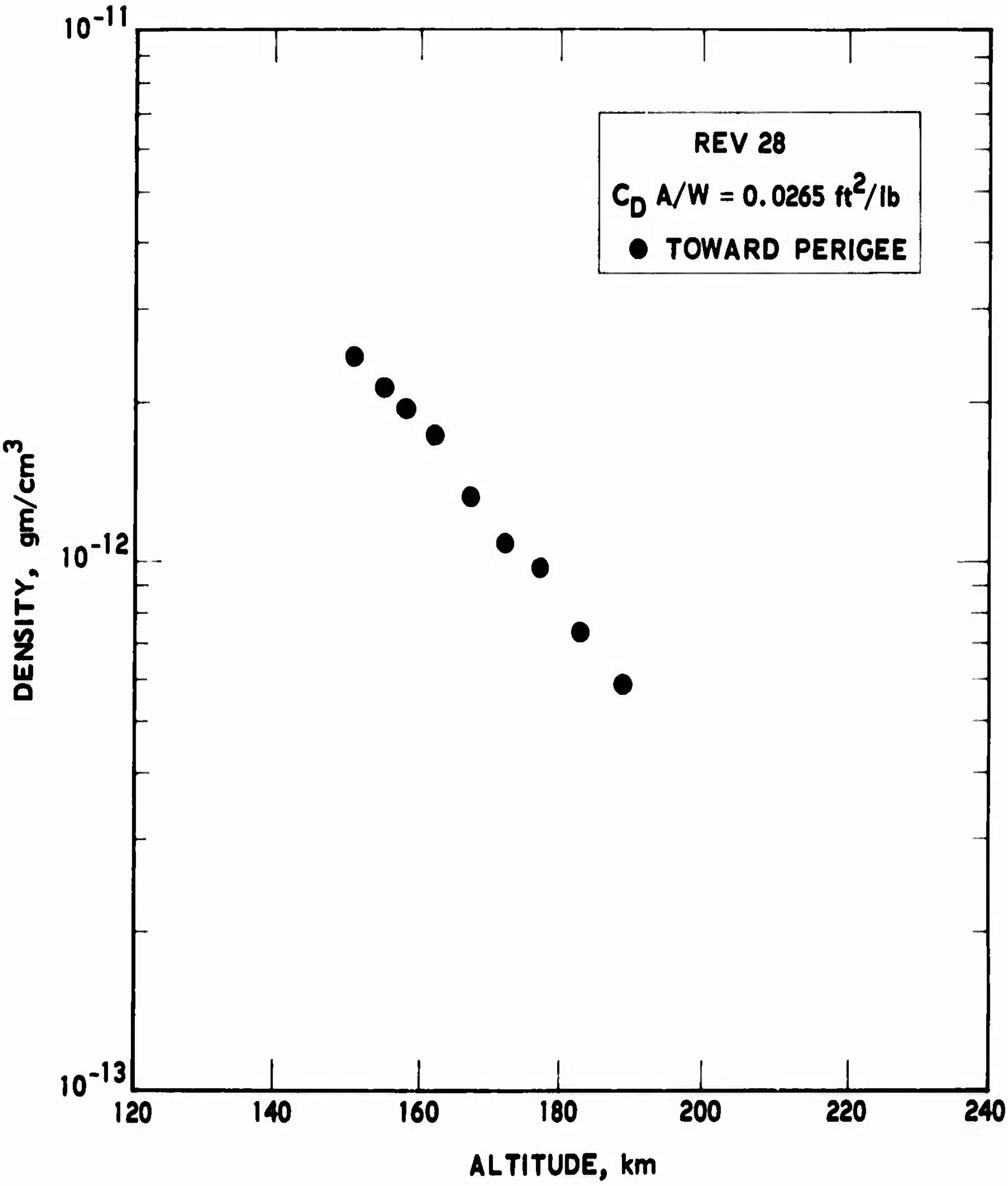

Fig. 8. Density vs Altitude for Rev. 28

Upon close comparison of the data from Revs. 26, 27, and 28, little evidence can be found to support the existence of the high latitude density bulge modeled by Jacobs. If it did exist at this location, the densities obtained toward perigee in Rev. 28 would be significantly higher (~30 percent) than those obtained in Rev. 27, which in turn would be higher than the density toward perigee in Rev. 26. This is not the case.

It cannot be concluded, however, that such a bulge does not exist at some other location on the earth or under different conditions of solar activity. Nor can it be concluded, as did Jacchia and Slowey (Ref. 10), that the bulge-attributed phenomena are entirely of nonatmospheric origin, as will be evident shortly. In fact, in the light of unpublished density data recently obtained from satellite tracking data, Jacobs now contends that there is clearly a bulge due to atmospheric causes but that it sporadically changes position from time to time or even disappears completely (Ref. 11).

Figure 9 shows the LOGACS density data for Rev. 31, which passes over the north magnetic dip pole. The Rev. 31 data, contrary to the earlier data, do suggest increased density at the high latitudes. This is best illustrated by comparison of Figs. 10 to 13, which show normalized density for these revs. versus latitude. The normalization eliminates the dominant altitude variation and was accomplished by dividing the LOGACS density values by the reference density model shown in Fig. 14 (Refs. 5 and 6). Note, in particular, that the density between 50°N and 70°N during Rev. 31 is 20 percent greater than the earlier revs., which clearly indicates the possibility of a bulge over the region of the magnetic dip pole even during conditions of quiet geomagnetic activity.

Further analysis of the data in the region of the dip pole may provide better definition of this effect.

It is also evident in Figs. 10, 11, and 13 that there is a systematic increase in density in the region of the sub-solar point at about 10° N to 20° N latitude. This is very likely a diurnal bulge effect, in part, since the orbital plane was about 26° west of the noon meridian.

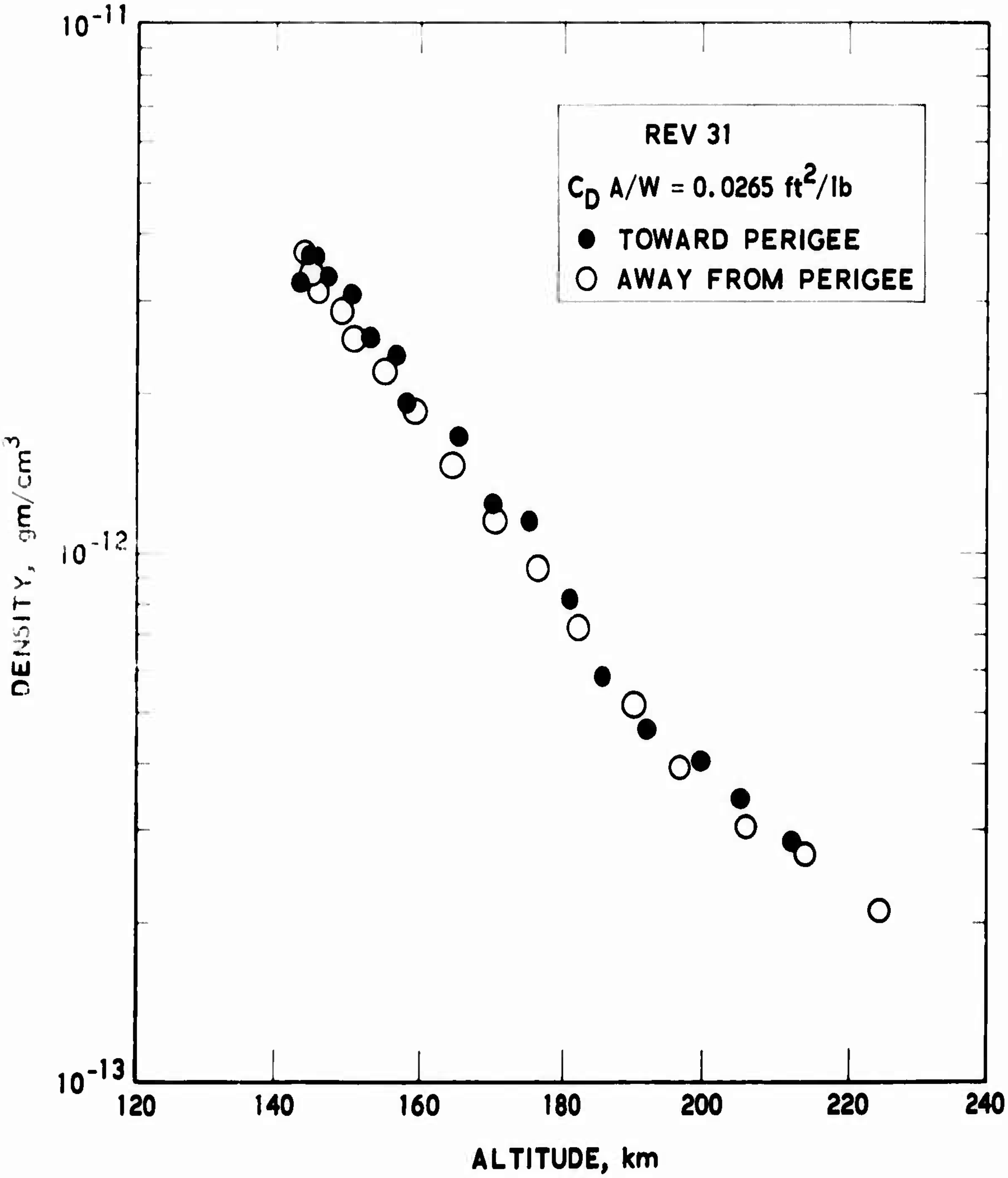

Fig. 9. Density vs Altitude for Rev. 31

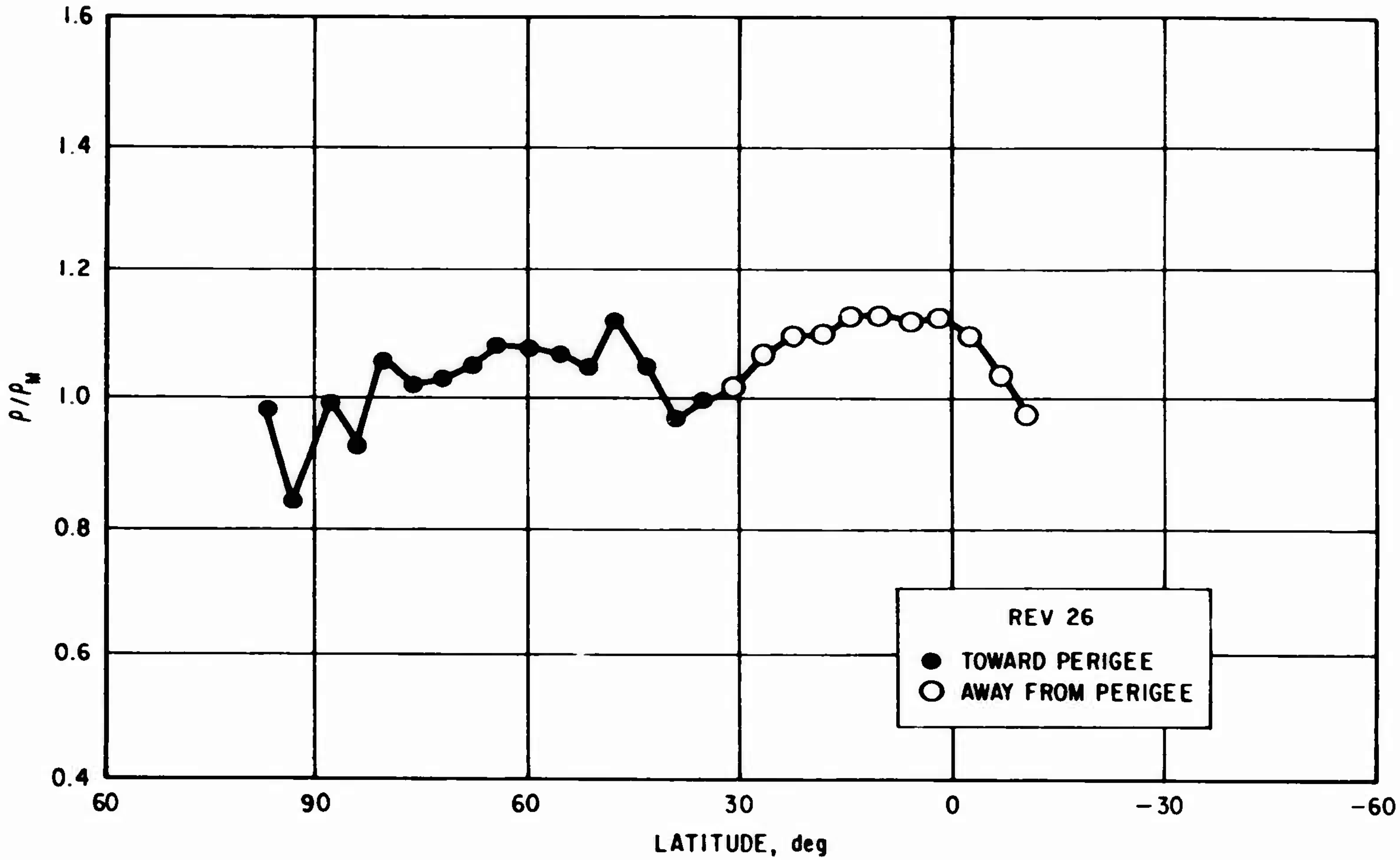

Fig. 10. Normalized Density vs Latitude for Rev. 26

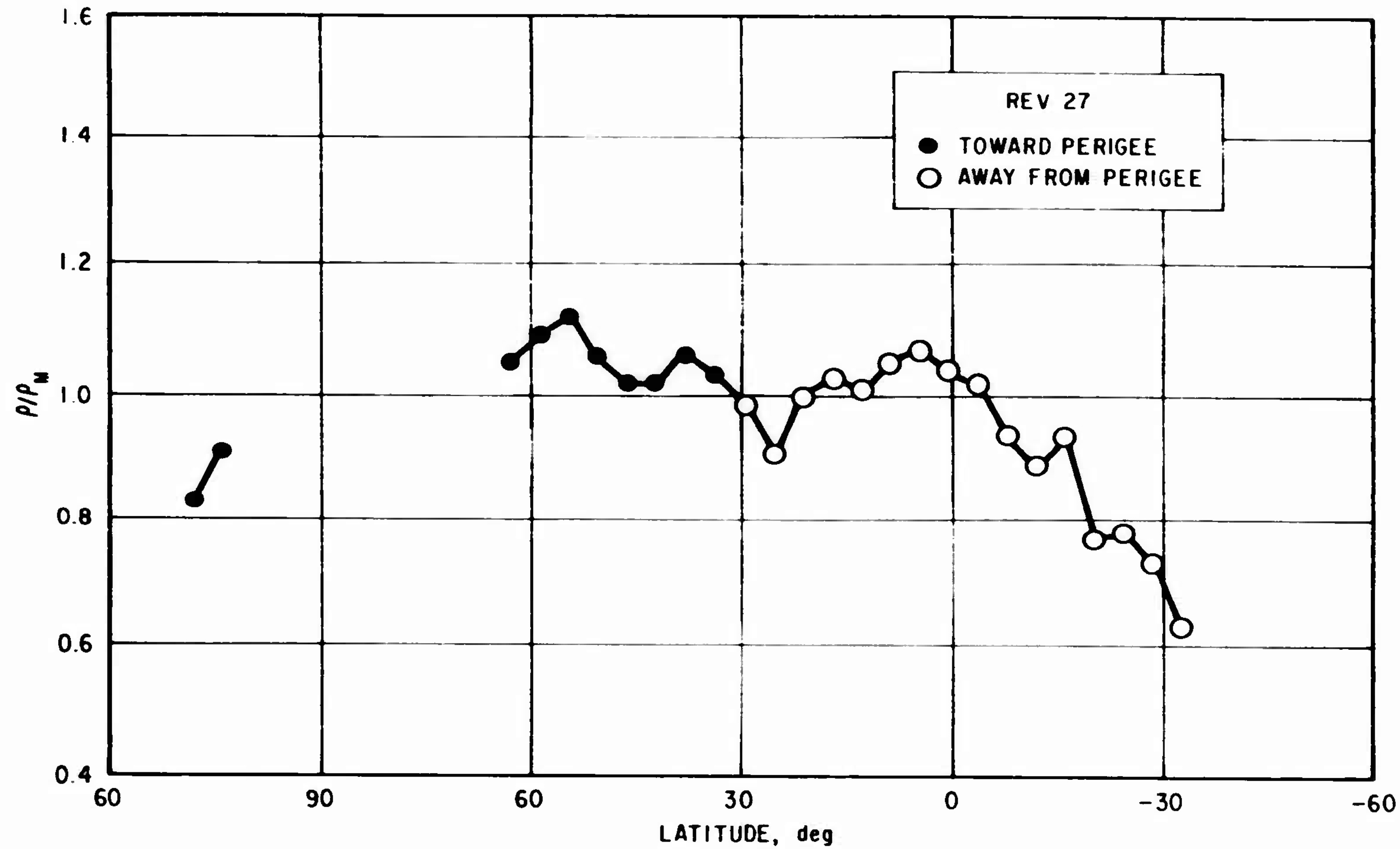

Fig. 11. Normalized Density vs Latitude for Rev. 27

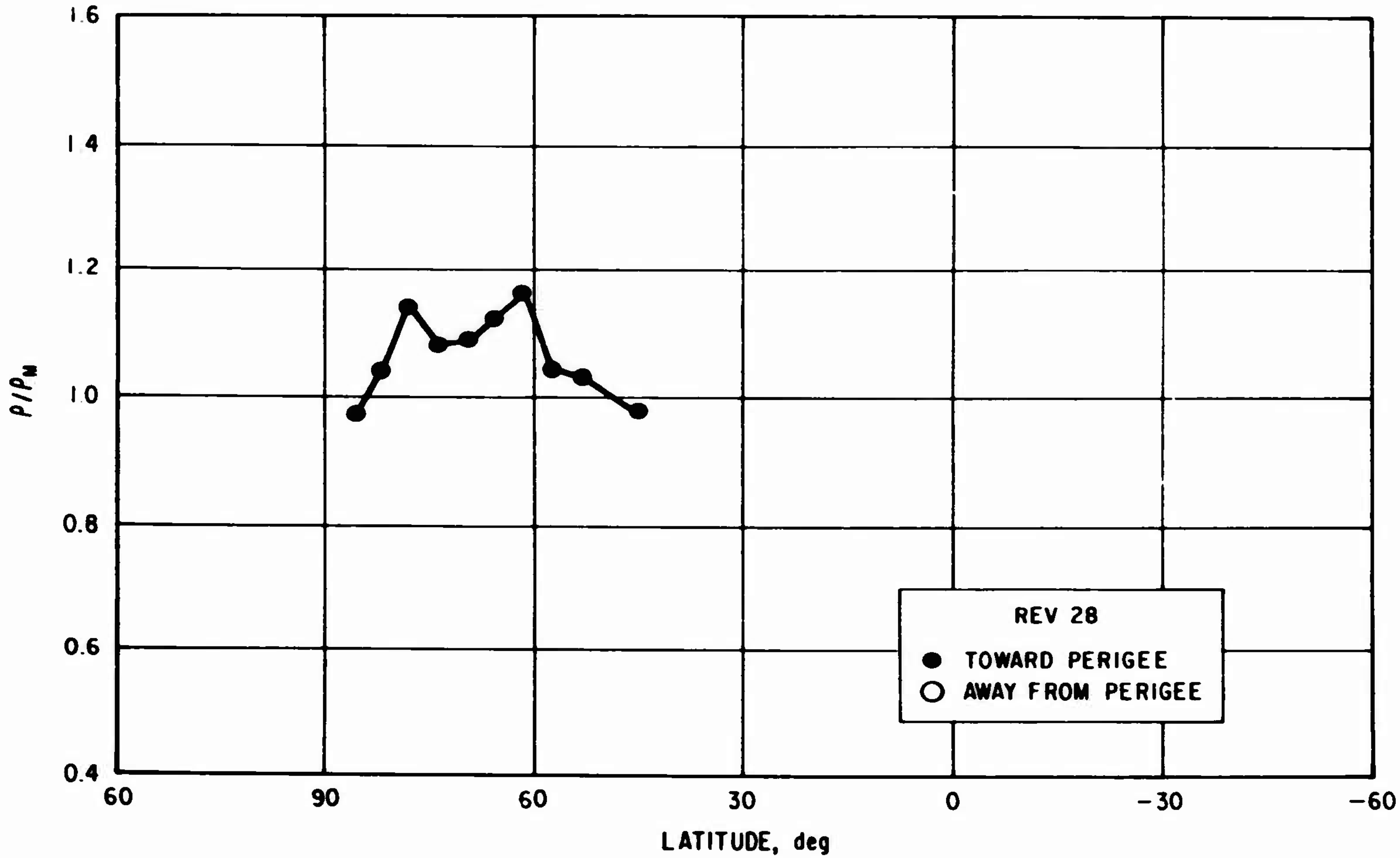

Fig. 12. Normalized Density vs Latitude for Rev. 28

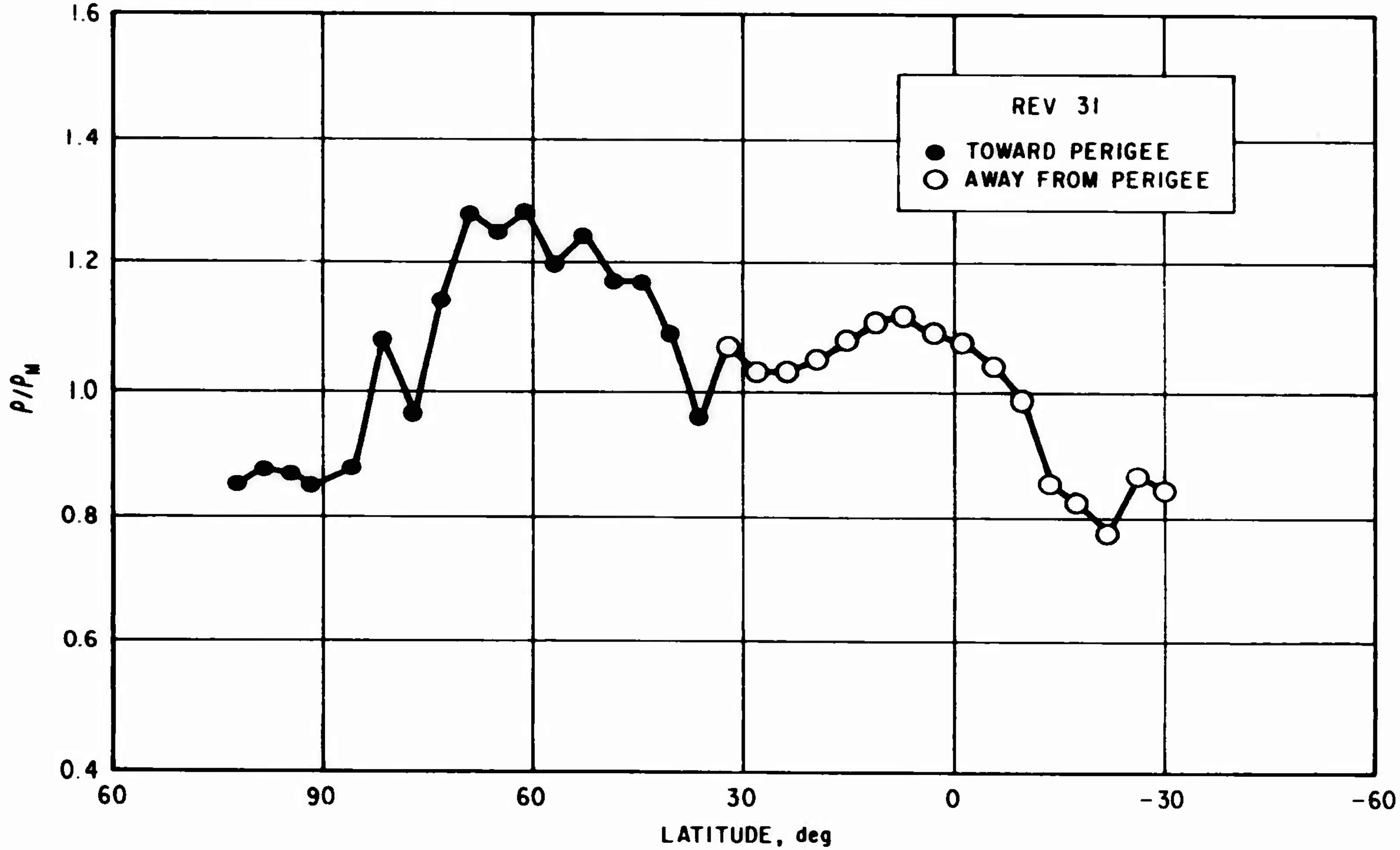

Fig. 13. Normalized Density vs Latitude for Rev. 31

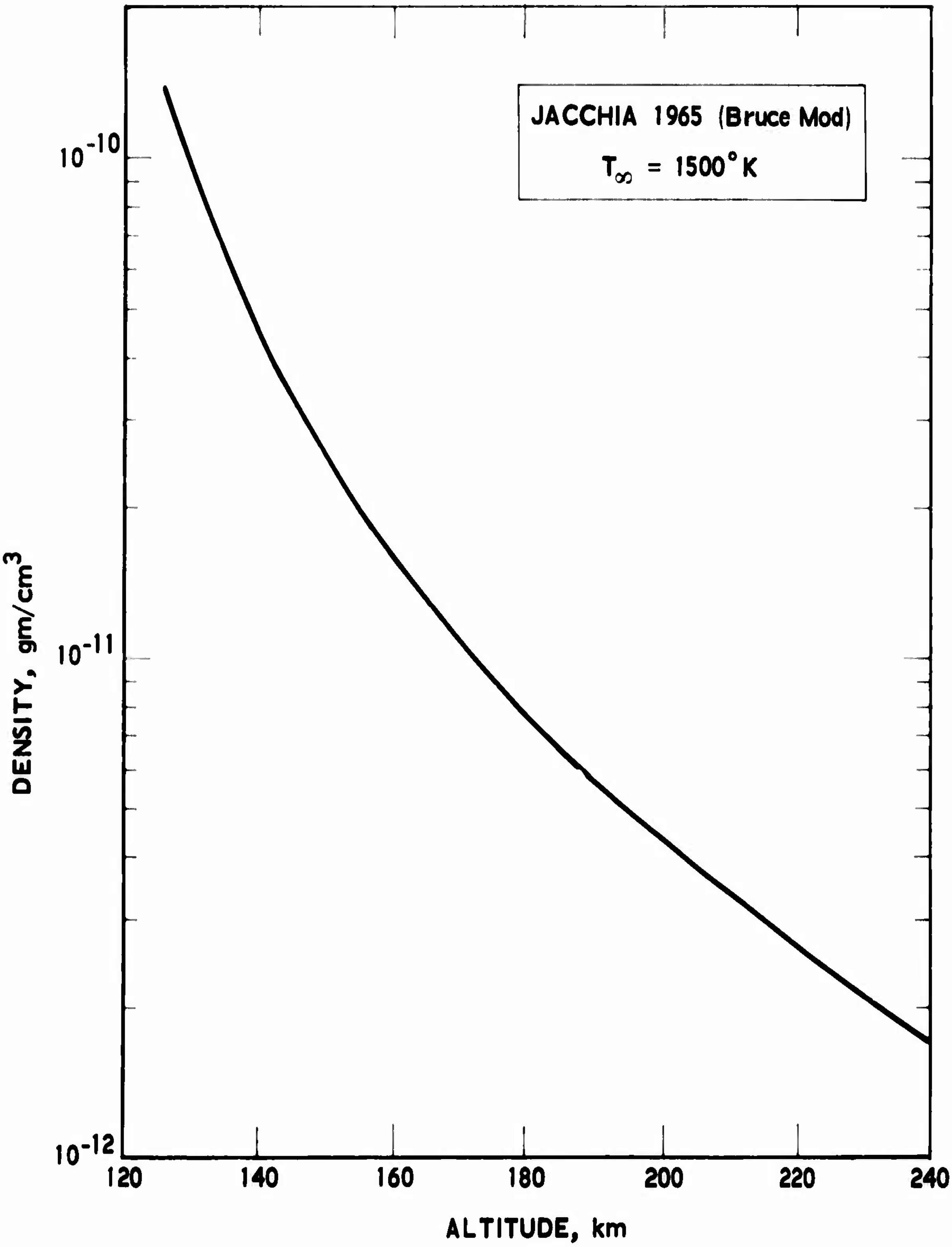

Fig. 14. Reference Model Density vs Altitude

2. ATMOSPHERE DENSITY BETWEEN 75 AND 120 NMI DURING GREAT MAGNETIC STORM

To illustrate conditions in the atmosphere during the great magnetic storm, density values obtained from satellite Revs. 46, 47, 48, and 57 were selected. The ground traces for these revs. are shown in Fig. 15.

The density data exhibit enormous variations in response to the extreme solar and geomagnetic activity that was prevalent on 25 and 26 May (see Fig. 4) as shown in Figs. 16 to 21. In general, the toward-perigee (high latitude) data are more oscillatory than the away-from-perigee (low latitude) data, although regular patterns exist. Density variations of 50 percent at the same altitude, but different latitudes, which occur within the same rev., are not uncommon, as shown in Fig. 16. In Rev. 47, Fig. 17, a 50 percent spatial change in density is seen to occur at 81 nmi (150 km). A regular pattern of behavior, not evident in Fig. 17, is clearly seen when the same data are separated as shown in Figs. 18 and 19.

Rev. 48 data, shown in Fig. 20, indicate the same tendency for density to begin decreasing with decreasing height at about 85 nmi as was evident in Rev. 47.

Rev. 57 data, shown in Fig. 21, have been included to show a factor of 2 increase in density which was measured near 79 nmi at two points over the earth separated by only 4° along the orbital path.

The density values for these revs., normalized and plotted versus latitude in Figs. 22 to 25, clearly reveal the large fluctuating spatial and temporal behavior that was characteristic during the storm.

In Fig. 22, during Rev. 46, an immense two-pronged high latitude bulge almost 70 percent greater than the reference density was measured. The diurnal bulge, although small in comparison, was still evident between 10° N and 20° N. By Rev. 47, 1.5 hr later, shown in Fig. 23, the high latitude bulge, still two-pronged, had diminished somewhat, but the "diurnal" bulge increased (the quotes signifying that this effect may have been influenced by other phenomena, e.g., the equatorial electrojet, Refs. 12 and 13). Finally, by Rev. 48, Fig. 24, the high latitude bulge had essentially

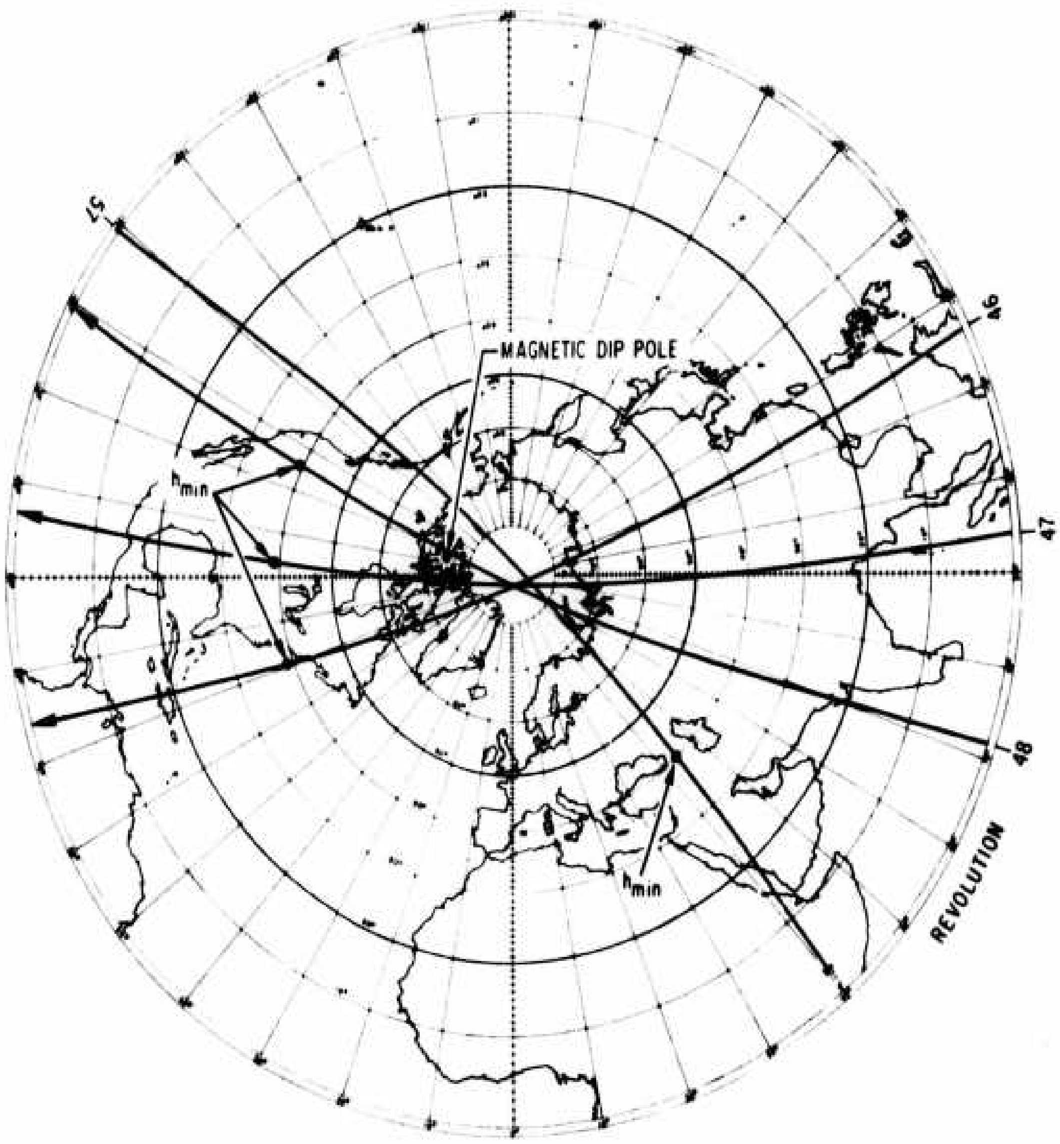

Fig. 15. LOGACS Satellite Ground Traces for Revs. 46, 47, 48, and 57

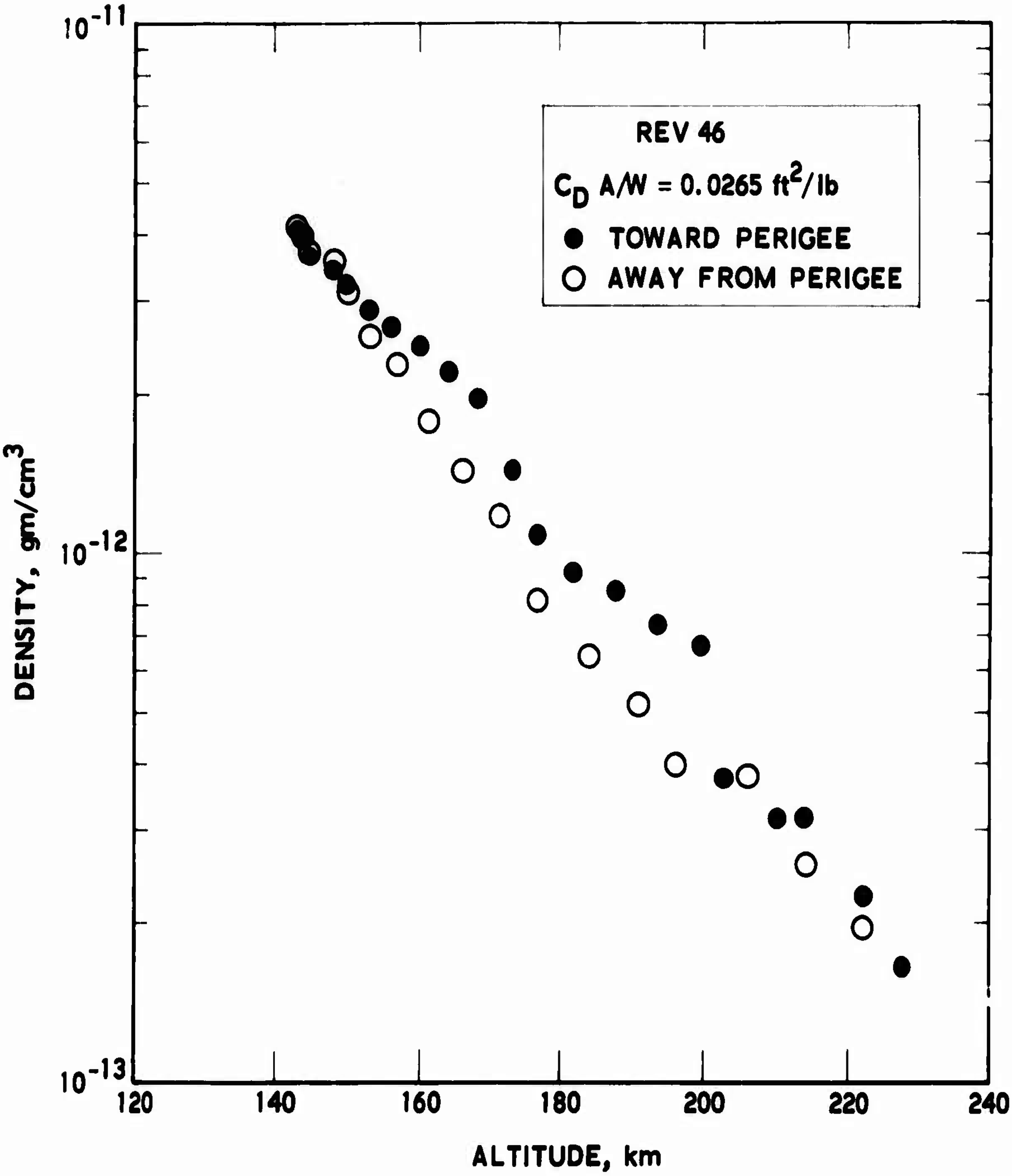

Fig. 16. Density vs Altitude for Rev. 46

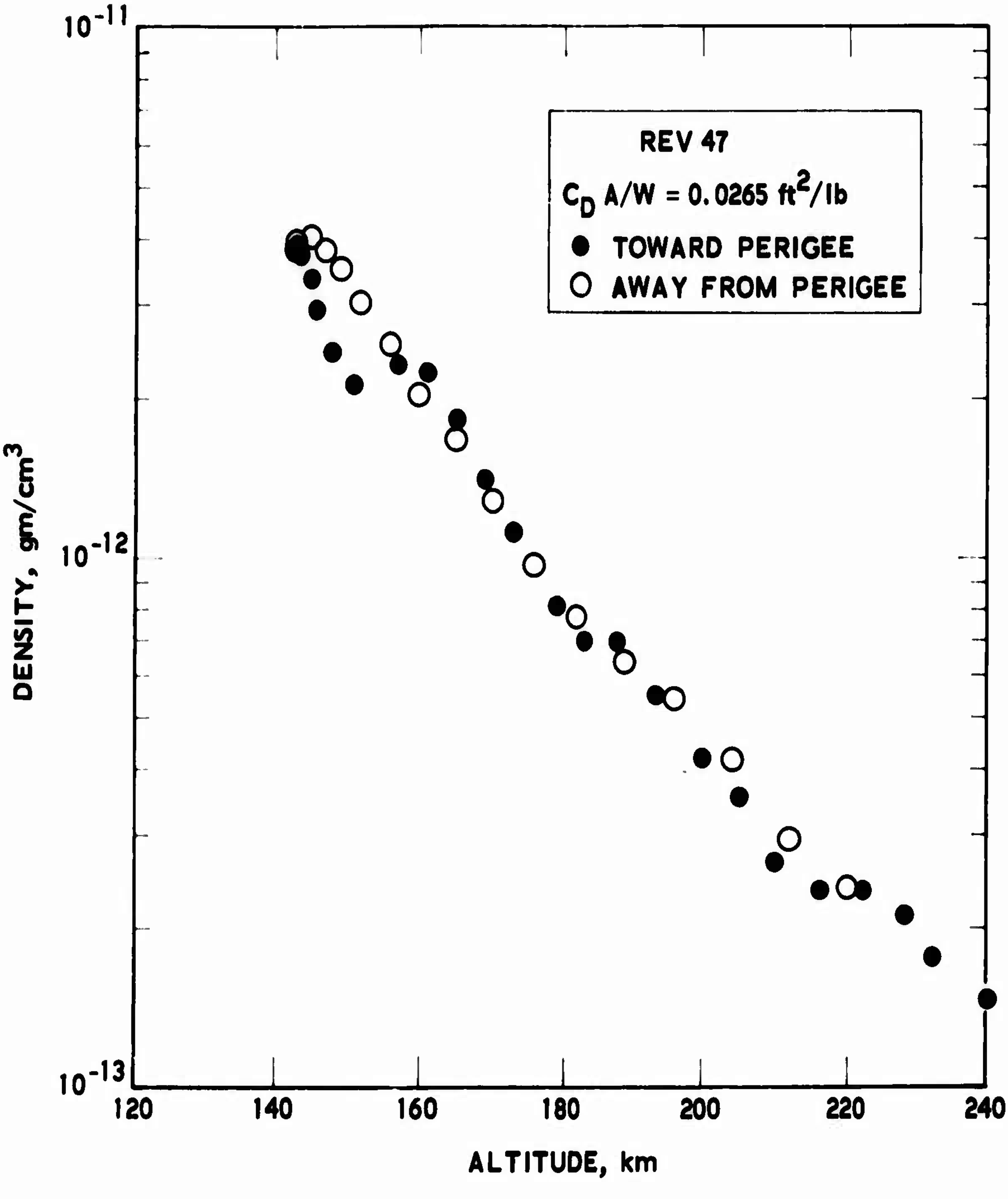

Fig. 17. Density vs Altitude for Rev. 47

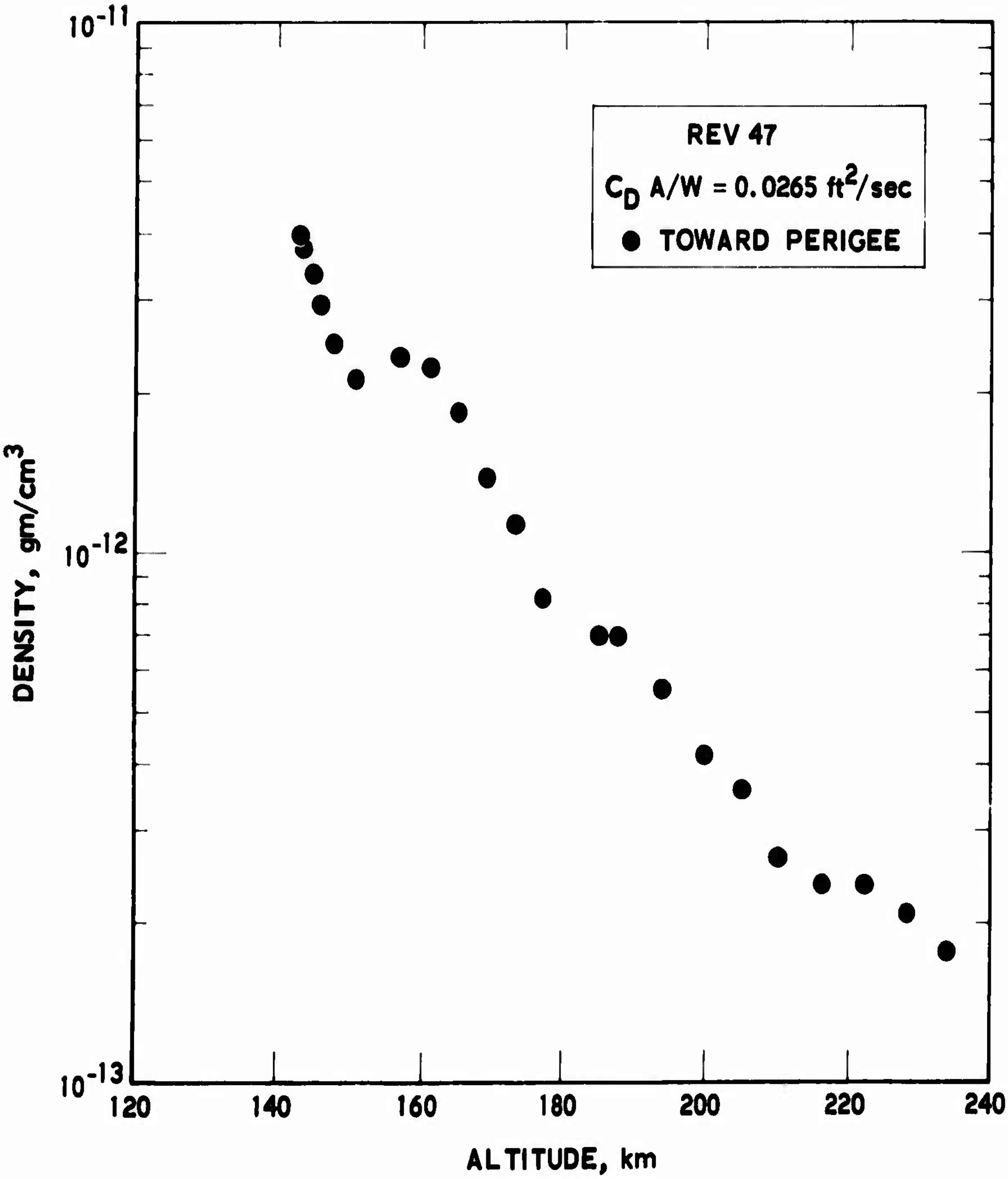

Fig. 18. Density vs Altitude for Rev. 47 (Toward Perigee)

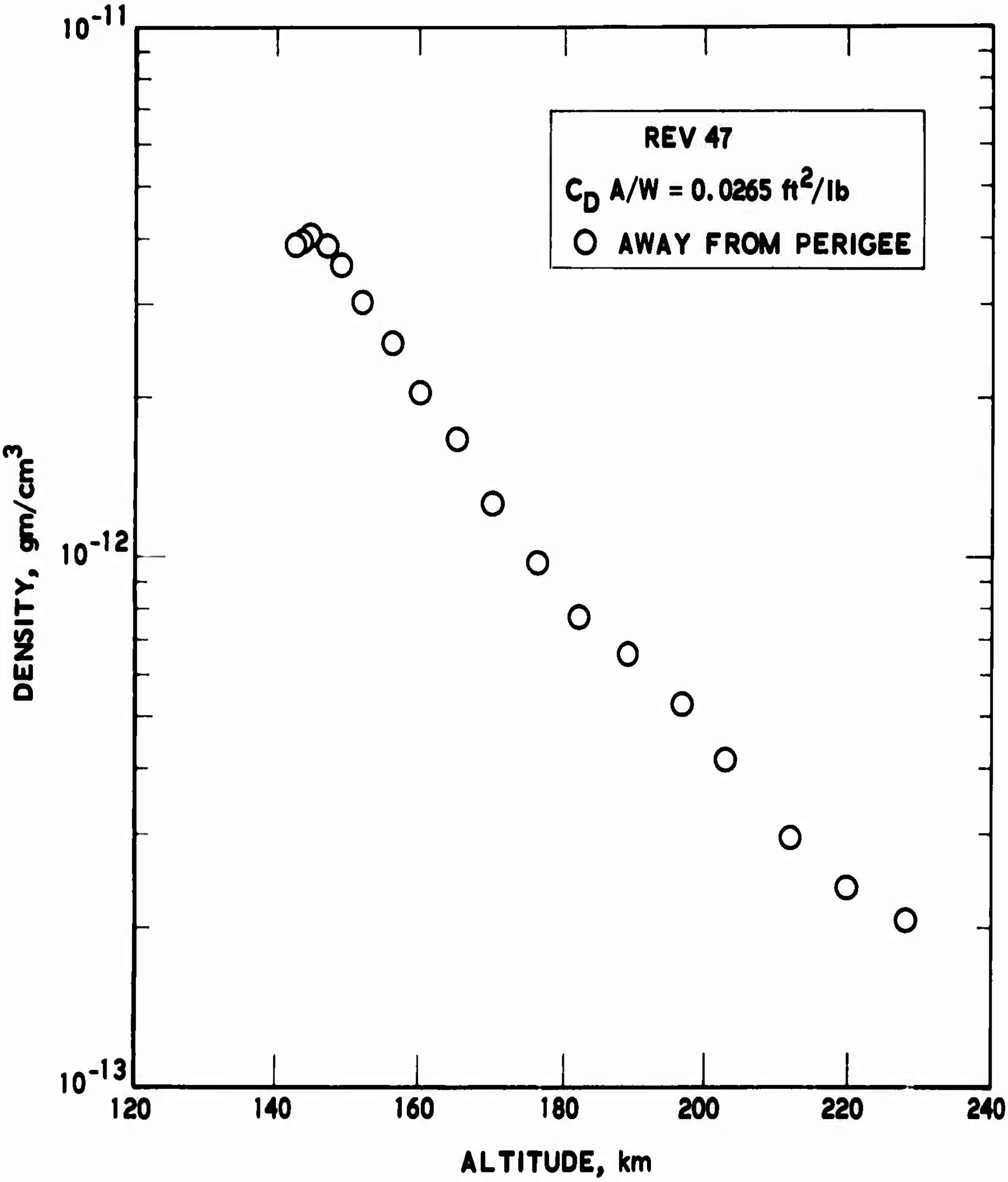

Fig. 19. Density vs Altitude for Rev. 47
(Away from Perigee)

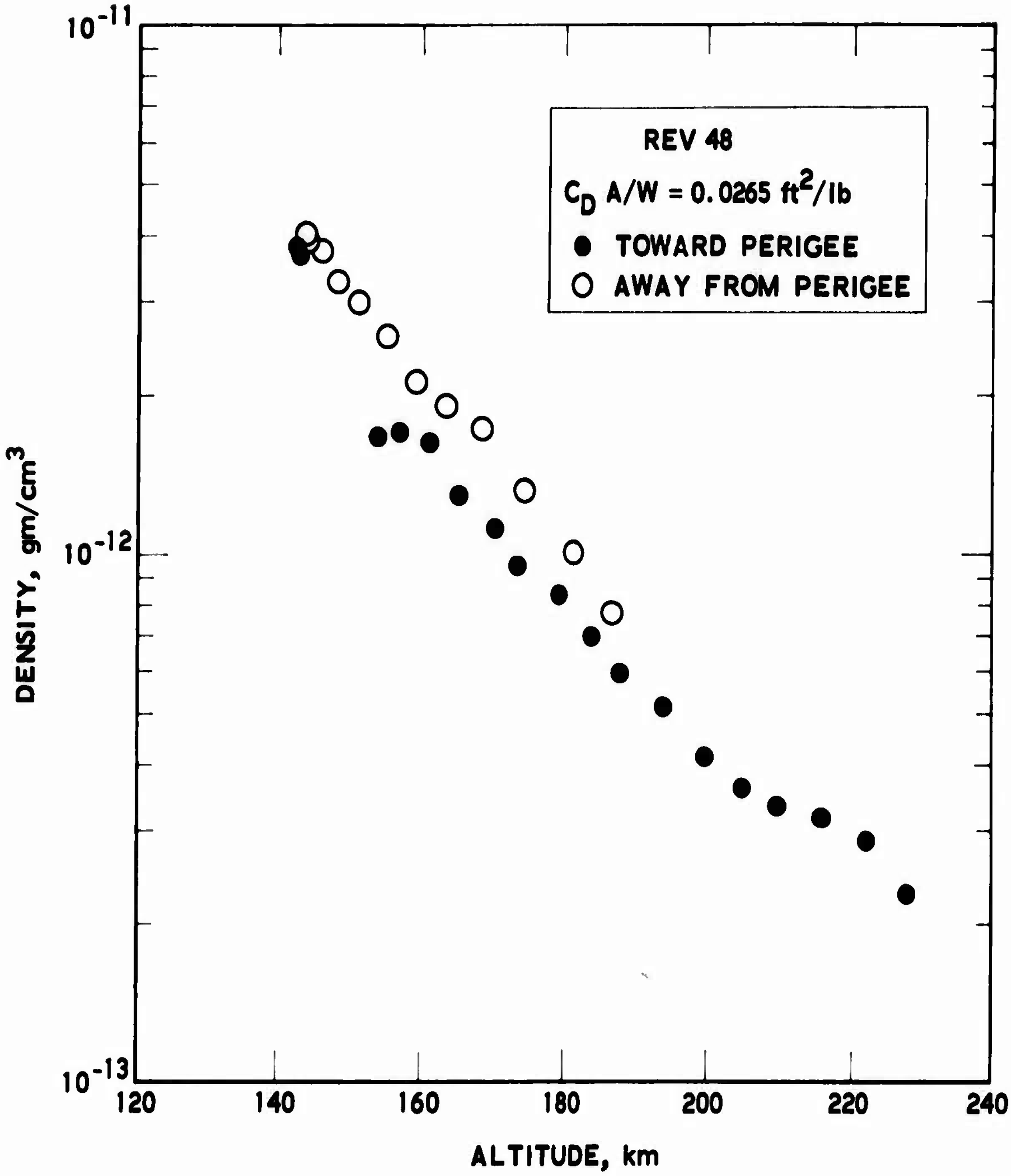

Fig. 20. Density vs Altitude for Rev. 48

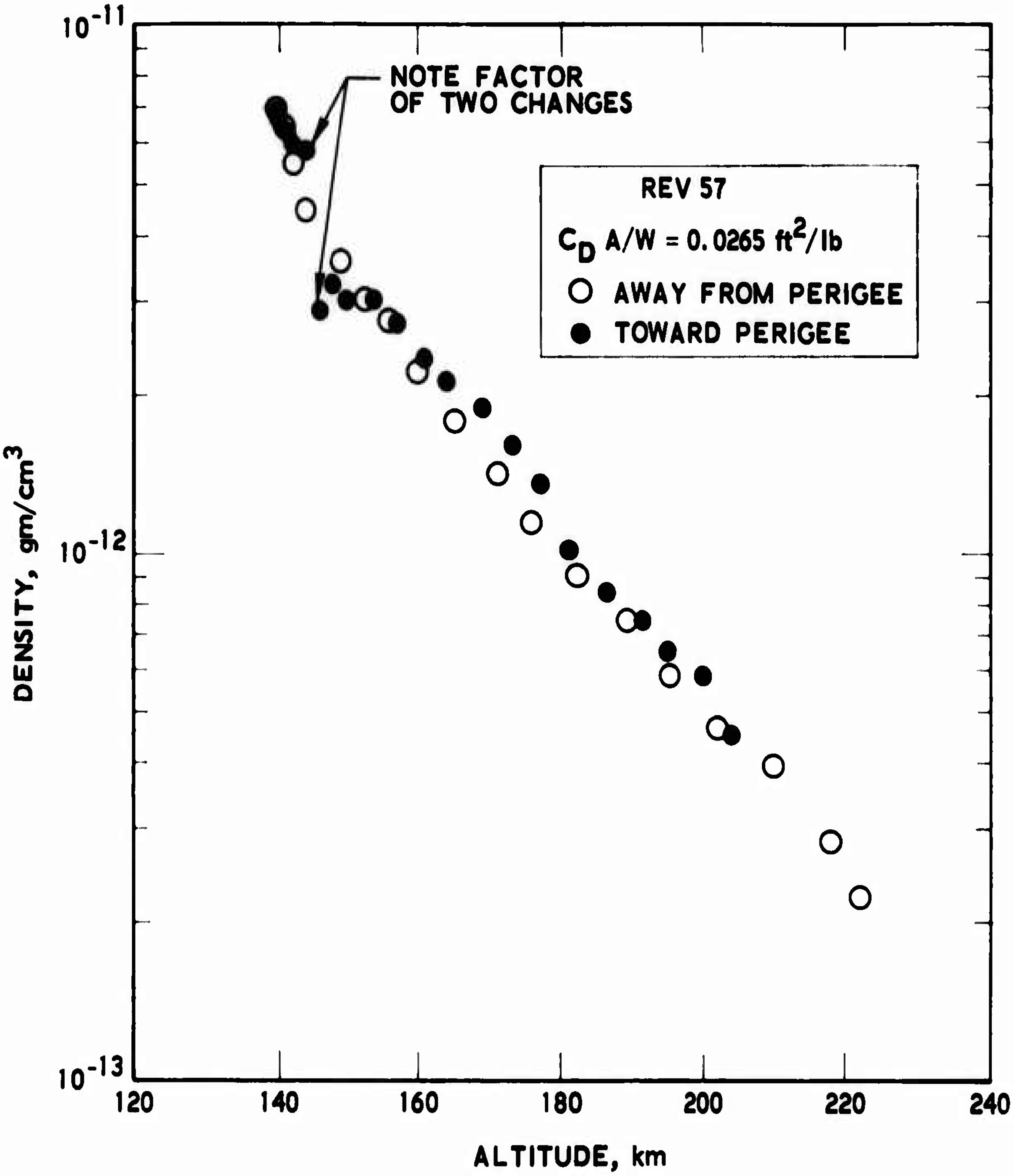

Fig. 21. Density vs Altitude for Rev. 57

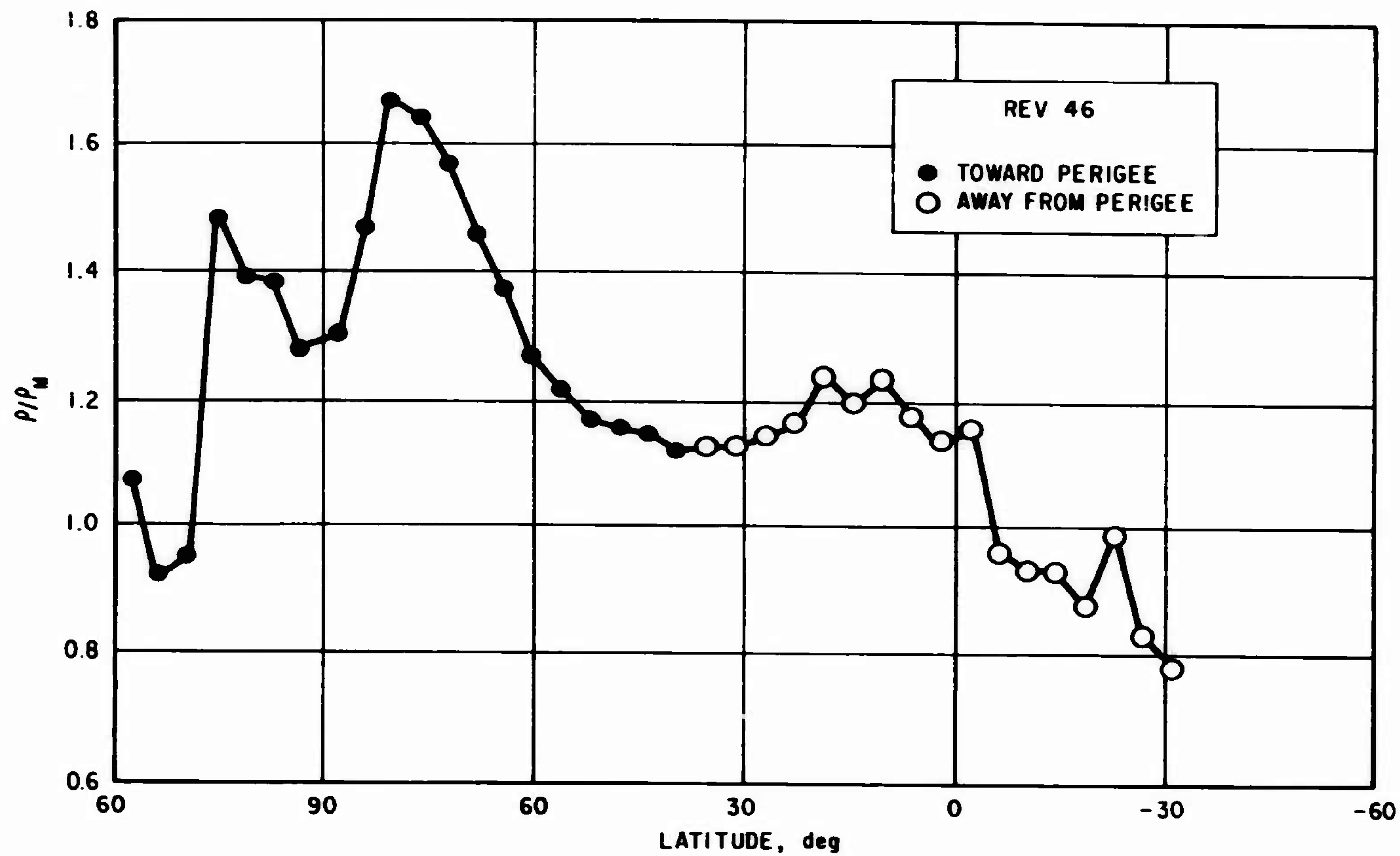

Fig. 22. Normalized Density vs Latitude for Rev. 46

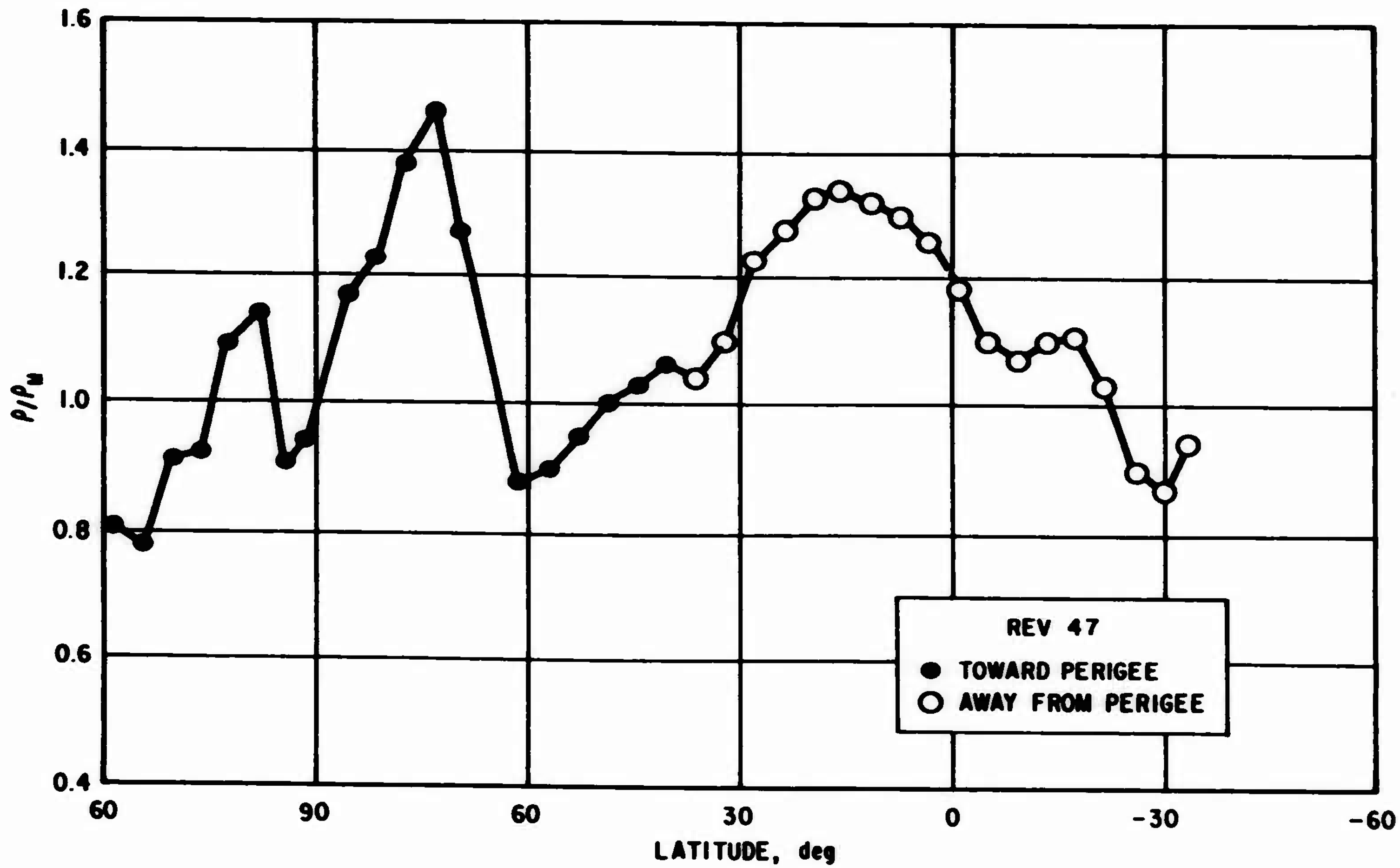

Fig. 23. Normalized Density vs Latitude for Rev. 47

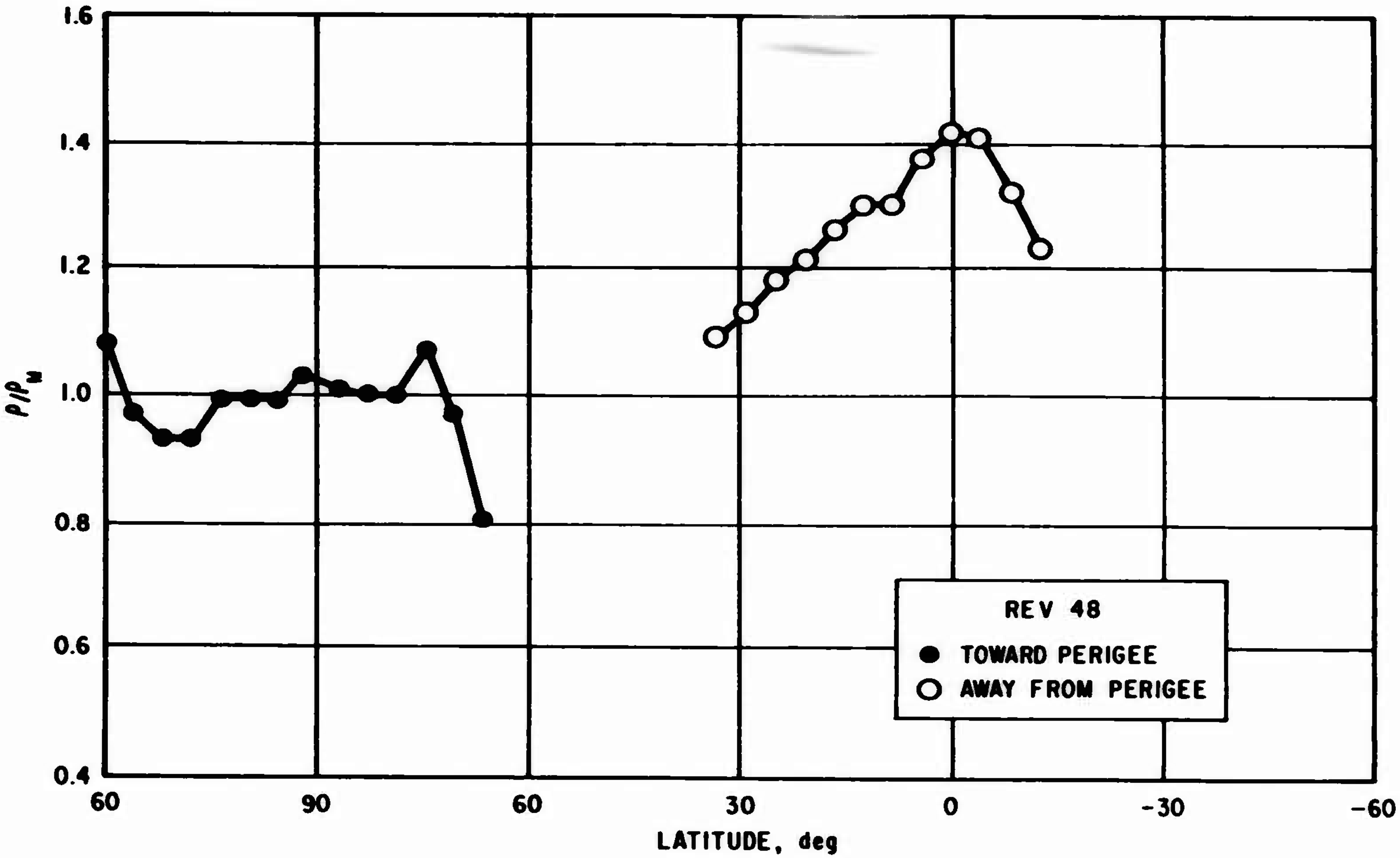

Fig. 24. Normalized Density vs Latitude for Rev. 48

disappeared, but the diurnal bulge had doubled in amplitude. Then, by Rev. 57, half a day later, shown in Fig. 25, the high latitude bulge had reappeared, and the diurnal bulge was even more intense than before.

These results suggest the existence of a high latitude density bulge that is dependent upon the level of geomagnetic activity, and contradict the high latitude bulge model of Jacobs (Ref. 9), which is not dependent upon magnetic activity. Also, the pronounced diurnal bulge that is evident conflicts with most atmosphere models (Refs. 5, 9, 14 and 15), which often show decreases in density in the region of the sub-solar point at low altitudes.

3. VARIATION IN DENSITY AT 90 NMI DURING INTENSE 25 MAY PROTON SHOWER

As mentioned previously, an intense proton shower nearly 20 times greater than normal levels was recorded on 25 May 1967, reaching its peak at 1335 GMT. At 1600 GMT, the proton intensity began to decrease, and within 0.5 hr it had been reduced by a factor of 5 from its peak level.

The LOGACS data corresponding to that time period were examined to determine the effects, if any, that might be correlated with the proton shower. A marked density response was found, at about 90 nmi and 80° N latitude, that may be the result of highly localized particle precipitation related to the proton event (Ref. 16). This is illustrated in Fig. 26 where the density values for this time period are shown. As time progressed, it can be seen that the density at about 90 nmi increased by 35 percent shortly after the recorded peak of the proton shower. Then, by 1630 GMT, the density returned to its prestorm levels with a rapidity totally unexpected according to present one-dimensional theory (Ref. 17).

4. RELATIVE DENSITY VS TIME FOR SPECIFIC ALTITUDES

With the LOGACS data, it has been possible for the first time to observe atmosphere density as a function of time at specific altitudes. Examples are shown here for 100, 90, and 80 nmi, and the minimum altitude experienced. During each rev., each of the selected altitudes (except the minimum) was reached twice by the satellite. Therefore, the density

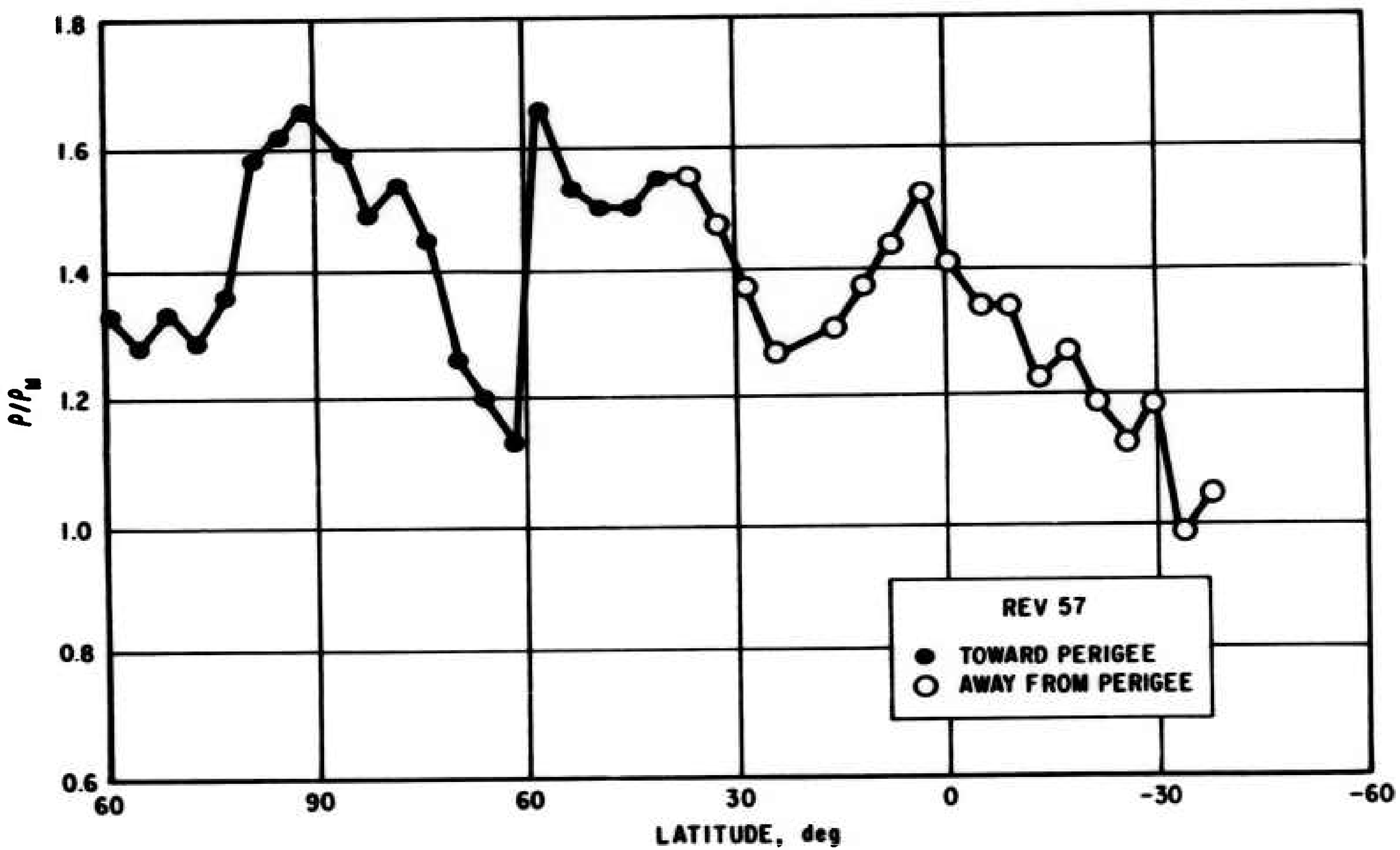

Fig. 25. Normalized Density vs Latitude for Rev. 57

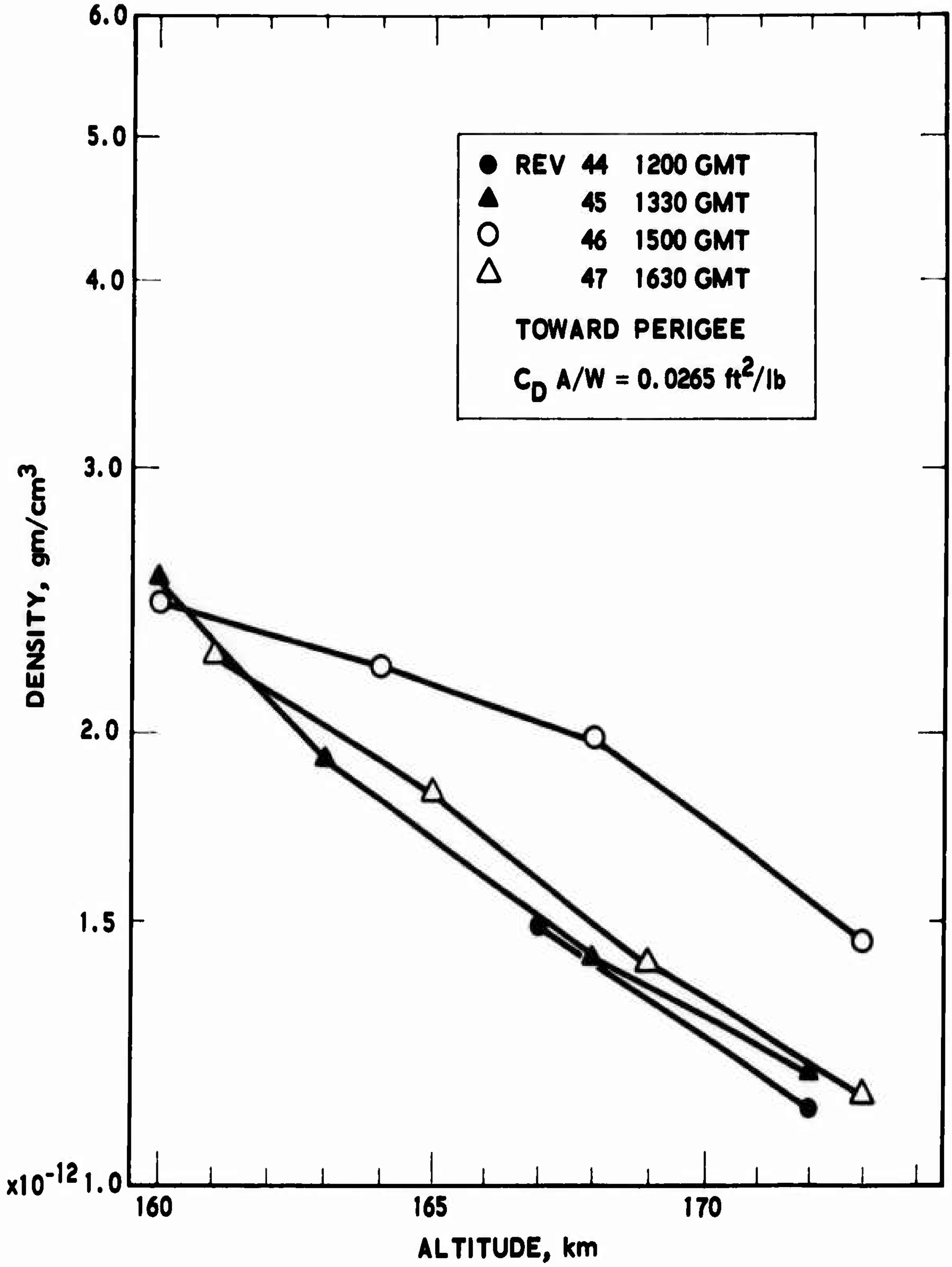

Fig. 26. Density vs Altitude During Proton Shower

values presented have been separated according to whether they were measured going toward perigee (actually minimum altitude) or measured going away from perigee. To aid in the interpretation, the density data were normalized in the same manner as was done previously.

In Fig. 27, normalized density toward perigee is shown versus time for the altitudes indicated. The geomagnetic planetary amplitudes a_p is also shown for comparison. The maximum relative density, shown at the bottom of the figure, corresponds to the minimum altitudes reached by the satellite, which varied, for the time period shown, between 78.1 and 75.6 nmi.

Several extremely striking features are immediately evident, namely, the remarkable correlation with magnetic activity and the varying response with altitude, both in amplitude and in phase. Also, there are some instances when the densities are increasing with time at one altitude and decreasing at another. This is clear, for example, on 24 May at 90 and 100 nmi and suggests that the energy responsible for this response may be deposited between these two altitudes.

In Fig. 28, the corresponding normalized density away from perigee is shown. Here it is evident that the variations, although complex, are much less so than those seen toward perigee. However, it is interesting to note that the increase in density due to the great magnetic storm is greater in this case than it was in the toward-perigee portion of the orbit.

5. ATMOSPHERE DENSITY AMPLITUDE AND PHASE RESPONSE DUE TO GREAT MAGNETIC STORM

When the relative density data shown in Figs. 27 and 28 are examined in detail, it can be seen that the amplitude and phase of the response to the great magnetic storm vary with altitude. The amplitude and phase are also dependent on latitude in that the response is markedly different toward perigee (high latitude) than it is away from perigee (low latitude).

The results of a preliminary analysis of the phase response are shown in Fig. 29. The phase (or time lag) is shown versus altitude for the toward-perigee and away-from-perigee cases, and was determined by comparing the onset of the storm with the onset of the response. There is

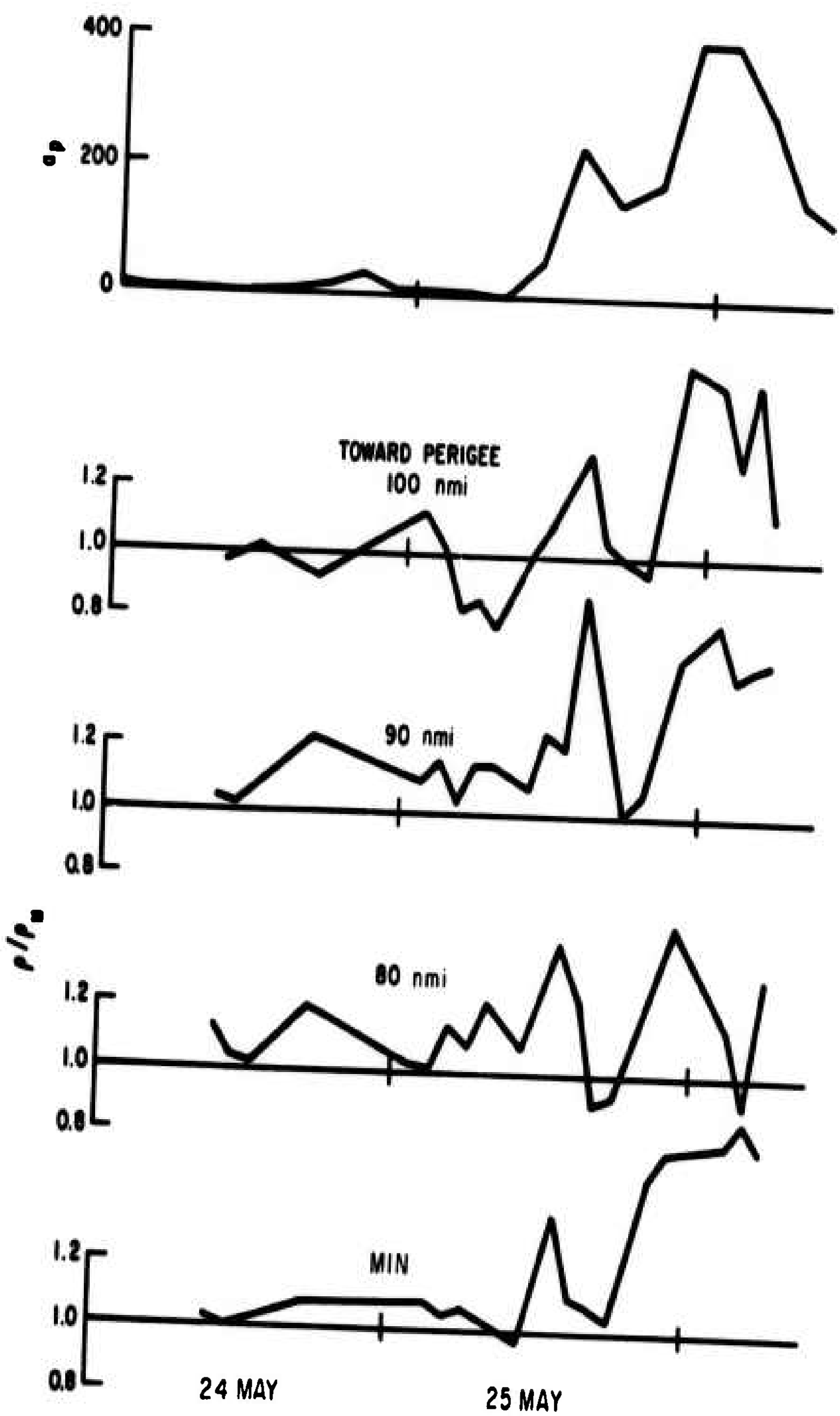

Fig. 27. Normalized Density vs Time (Toward Perigee)

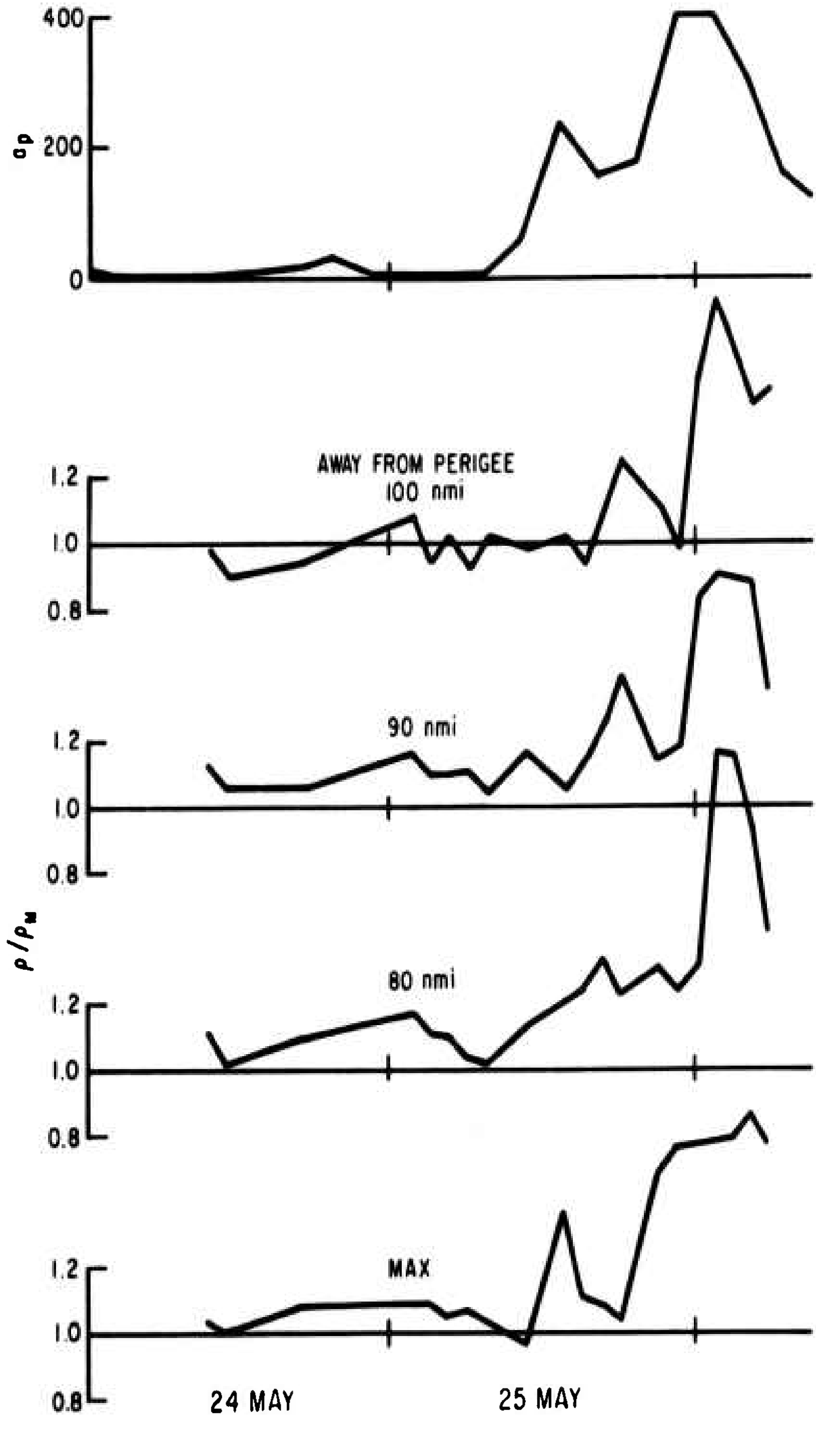

Fig. 28. Normalized Density vs Time (Away from Perigee)

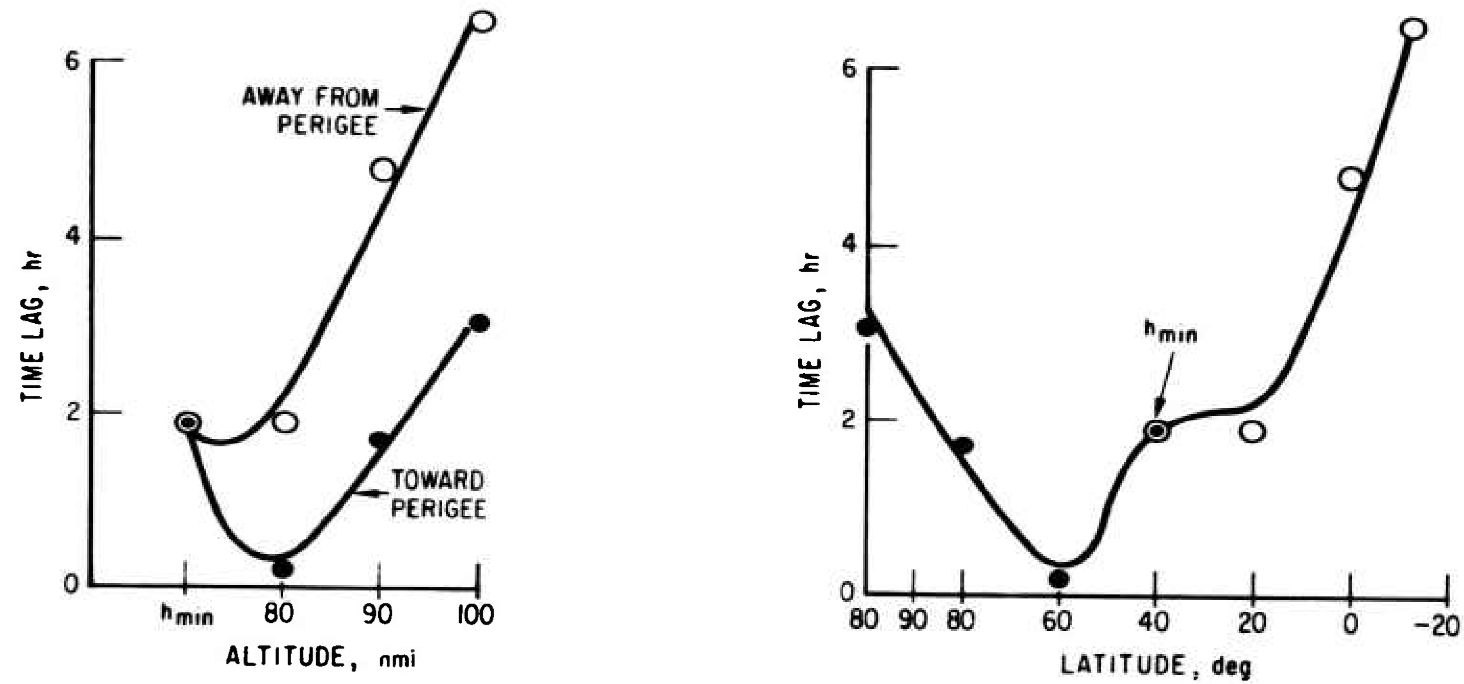

Fig. 29. Phase Response of Atmosphere Density to Great Magnetic Storm vs Altitude and Latitude

considerable variation with altitude and latitude, ranging between almost no time lag to a lag of greater than 6 hr. Therefore, these results support in a general sense the variable time lags found by DeVries, Friday, and Jones (Ref. 18), but conflict somewhat with the results of Jacchia, Slowey, and Verniani (Ref. 19), who found only slight variation in time lag with latitude from the drag data on four high inclination satellites.

The amplitude of the density response to the magnetic storm, shown in Fig. 30, has considerable variation with altitude and latitude also. Here, it is easy to see, as mentioned previously, that the density increase at low latitudes (away from perigee) is greater than at high latitudes (toward perigee)--a most interesting result.

6. COMPARISON OF LOGACS MEASURED DENSITY WITH DENSITY OBTAINED FROM ORBITAL DECAY OF LOGACS SPACECRAFT, SATELLITE 1967 50B

The tracking data from the LOGACS spacecraft, Satellite 1967 50B, have been reduced by Schusterman (Ref. 2) to obtain perigee density as a function of time based upon observed orbital decay rates. We have been provided, therefore, with a unique opportunity to compare the density values determined in this manner with the actual density measurements obtained by a sensor on the same vehicle. This comparison is shown in Fig. 31. In Ref. 2 a value of the ballistic coefficient $C_D A/W$ equal to 0.0311 ft^2/lb was assumed. We believe that this value was based upon an erroneous estimate of the spacecraft weight and have therefore adjusted the density values derived by Schusterman to correspond to the ballistic coefficient used throughout this report.

The trend of the orbital decay density, as can be seen in Fig. 31, parallels the LOGACS data, but there are discrepancies considered to be extremely significant. Note, in particular, that the sharp peak in the orbital decay density which occurs during 25 May lags the corresponding peak in the measured density by 0.15 day (3.6 hr). It would appear, in fact, that much closer agreement would be accomplished if the entire orbital decay density curve was shifted in time by the above amount. Since precise knowledge of

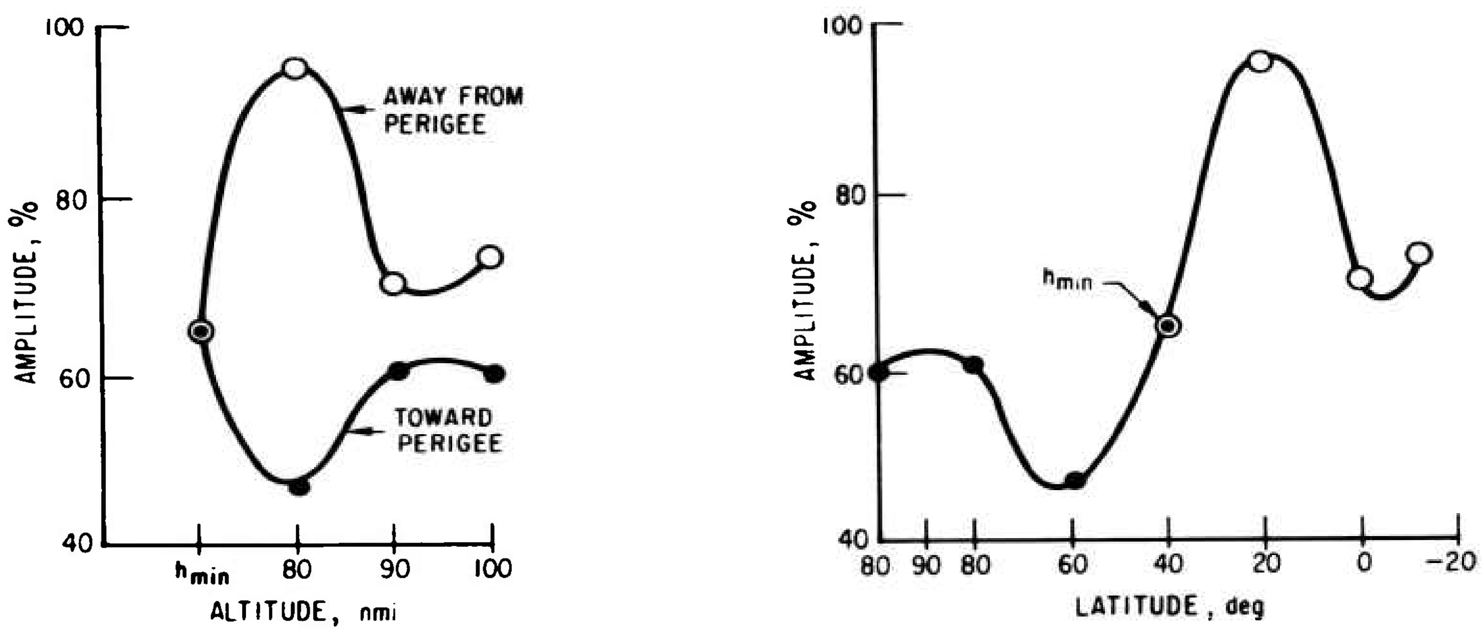

Fig. 30. Amplitude Response of Atmosphere Density to Great Magnetic Storm vs Altitude and Latitude

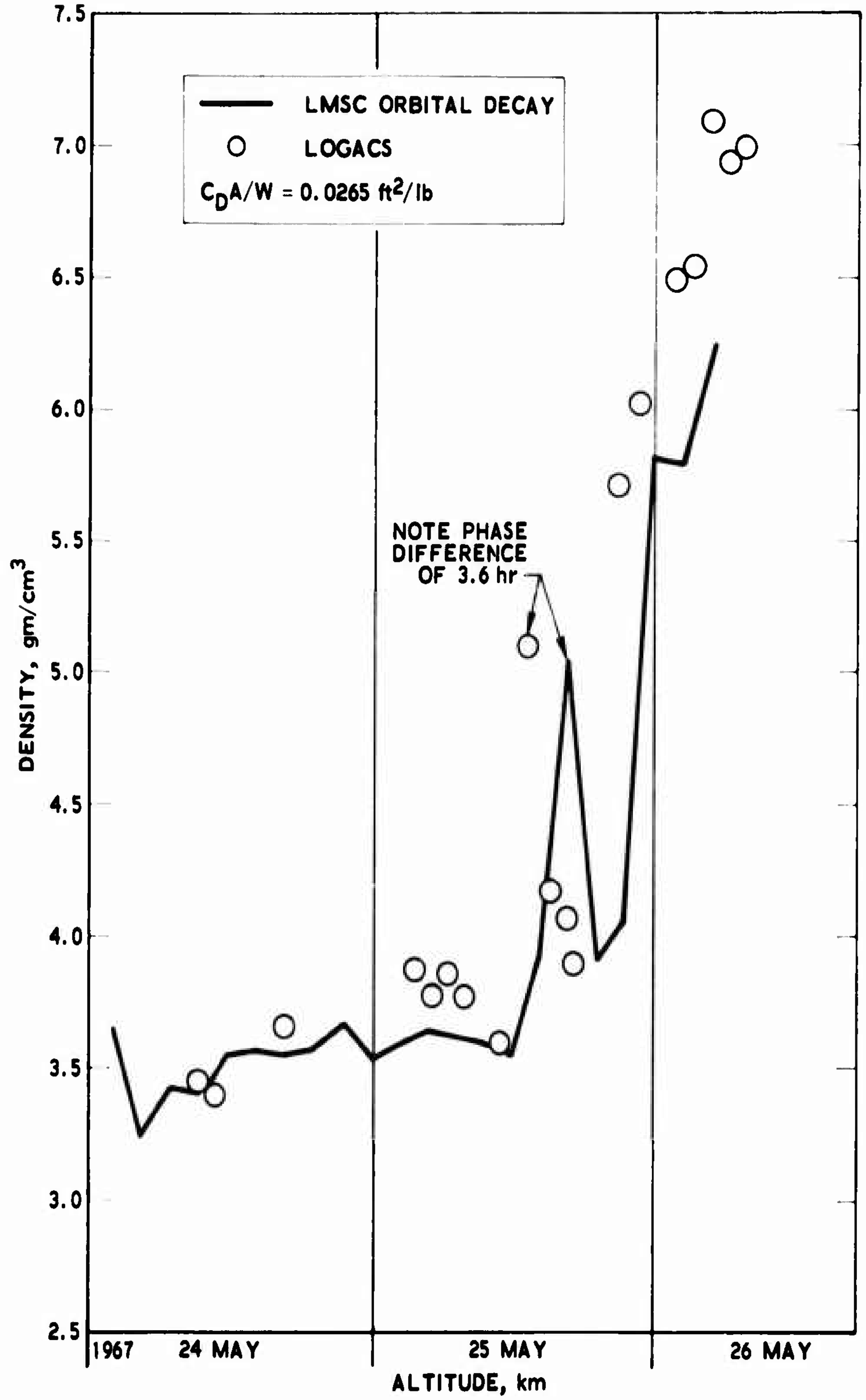

Fig. 31. Density Comparison: Orbital Decay vs LOGACS

the phasing of short term phenomena in the atmosphere is required to successfully construct short term density models, it is clear that great care is required when determining density values from orbital decay.

7. COMPARISON OF LOGACS MEASURED DENSITY WITH PREVALENT MODEL ATMOSPHERES

The LOGACS data obtained throughout the flight were scanned to obtain representative density values that could be compared with currently used model atmospheres. This was done for two altitudes and two levels of magnetic activity. The density values selected as representative of these conditions are shown in Table 2.

Values of density that would be predicted by several prevalent model atmospheres (Refs. 5, 6, 9, 14, and 15) for these altitudes and levels of magnetic activity were then compared with the selected LOGACS densities. This comparison is shown in Table 3. As can be seen, there is an enormous spread in the results, indicating how unsuccessful recent modeling attempts have been. In general, the best agreement is at the higher altitude, 108 nmi, which is probably due to the fact that density data at this altitude have been more abundant. The agreement at the lower altitude, 81 nmi, is extremely poor--the most serious contradiction occurring with the U.S. 1966 summer model. Curiously, much better agreement would have been obtained, in this case, if the U.S. 1966 winter model had been used instead. The LOGACS data seem, therefore, to be in considerable conflict with the seasonal results found by Champion (Ref. 20), which were extended to form the bases of the U.S. 1966 seasonal models (Ref. 21).

Table 2. Representative LOGACS Density Measurements

	Quiet Kp (K_p = 0-4)		Active Kp (K_p = 7-8)	
	81 nmi (150 km)	108 nmi (200 km)	81 nmi (150 km)	108 nmi (200 km)
LOGACS ρ, gm/cm^3	2.8×10^{-12}	3.9×10^{-13}	3.4×10^{-12}	a

[a]Not shown because of extreme temporal and spatial variability.

Table 3. Comparison of LOGACS Data with Density Models

	ρ/ρ_M -1, percent			
	Quiet Kp $T_\infty \approx 1500°K$		Active Kp $T_\infty \approx 1800°K$	
	81 nmi (150 km)	108 nmi (200 km)	81 nmi (150 km)	108 nmi (200 km)
LMSC 67[a]	-13 percent[b]	-12[b]	- 2[c]	d
Jacchia 65 (Bruce mod.)	+13 percent	-11	+31	d
Jacchia 65	+31 percent	- 3	+60	d
Cira 65	+34 percent[e]	+26[e]	+60[f]	d
U.S. 66 summer	+51 percent	+ 1	+84	d

[a]Version used here is an unpublished modification of Ref. 9 submitted by Lockheed Missiles and Space Company (LMSC).

[b]S = 200, diurnal maximum.

[c]S = 250, diurnal maximum.

[d]Not shown because of extreme temporal and spatial variability.

[e]Model 5, Hour 14.

[f]Model 8, Hour 14.

SECTION II

ANALYSIS OF UPPER ATMOSPHERE DENSITY

A. COMPARISONS OF LOGACS DENSITIES WITH MODELS

One of the most striking features of the LOGACS density data is the extreme variability. This has been commented upon with regard to the hand-reduced data reported in the previous section. These hand-reduced cases are not atypical, as a glance at Appendix B will confirm. In many places (for examples see Rev. 48, approaching perigee, and Rev. 53, approaching perigee), density decreases with decreasing altitude. Further, in many places pronounced density differences can be seen at the same altitude but different latitudes by comparing the two plots for each rev.

A quick comparison of the LOGACS densities with model atmospheres deserves mention. Extrapolation of the plots in Appendix B to 120 km will confirm that the invariant boundary conditions assumed at this altitude for most model atmospheres are incorrect. As a result, these plots differ markedly from plots of model atmospheres derived from similar conditions, and show one reason why model atmospheres have great difficulty in "fitting" the LOGACS data.

Comparison of the LOGACS densities with models having the same values of exospheric temperature reveals pronounced differences in slope and in other characteristics. The LOGACS data for Rev. 5, leaving perigee, are displayed as Curve 1 in Fig. 32. This rev. was characterized by a computed exospheric temperature T_∞ of 1164°K. Curve 2 in Fig. 32 is the Jacchia static diffusion model for $T_\infty = 1150$°K; while representing the density very well near perigee, it is inadequate beyond 170 km. However, a Jacchia static diffusion model with $T_\infty = 1000$°K (Curve 3) represents the data much better. These Jacchia models are obtained from Ref. 5.

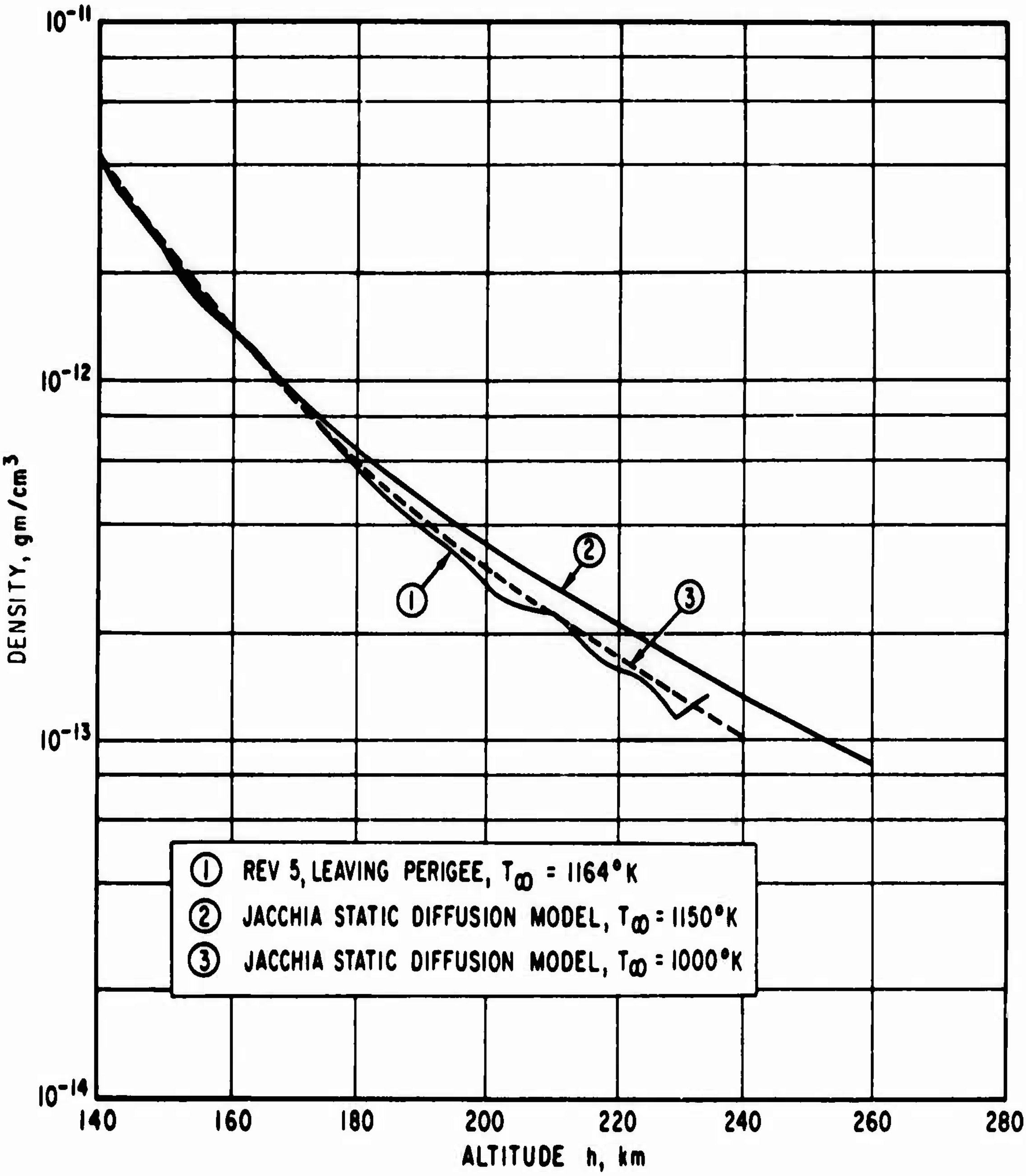

Fig. 32. Comparison of LOGACS Data (Rev. 5, Leaving Perigee) with Jacchia Static Diffusion Model

The problem is not one of a simple difference, however. Curve 1 of Fig. 33 shows the LOGACS data for Rev. 59, leaving perigee. A much higher value of $T_\infty = 1408°K$ is associated with this revolution. Curve 2 in this figure shows the data from Jacchia's static diffusion model for $T_\infty = 1400°K$. It is readily apparent that this curve in no way represents the data; it is consistently lower than the data. A drastic increase in the model temperature, to $T_\infty = 2100°K$ (Curve 3), does not improve the agreement to a significant degree. These two examples serve to show clearly that the Jacchia model dependence on temperature is not correct.

The behavior of model atmospheres in predicting LOGACS densities is consistently poor for all models. The Jacchia model, used above for comparison, was chosen because it is considered to be representative of the state of the art. In fact, comparisons shows that the Jacchia model is, if anything, slightly better than the others considered.

Ratios of LOGACS density to model atmosphere density can be computed by the Computer Printout of Densities (CPD) program mentioned earlier. Figures 34 and 35 present portions of a plot of such ratios against time, using the Walker-Bruce modification of Jacchia's model atmosphere (Ref. 6). Also plotted against time is vehicle altitude, for visual reference. These graphs show a clear correlation of the density ratio with altitude. They further show that this model does a better job, relatively speaking, of predicting densities near perigee than near apogee. In fact, the ratio becomes very poor near apogee. In some cases near apogee, large "spikes" occur (see 1870 min on Fig. 34, for example); these are as yet unexplained. The larger ones occur at intervals with periods that are near integral multiples of 6 hr; smaller peaks of this sort occur on nearly every orbit (period 1.5 hr). These spikes, which occur near apogee where the data quality was poor, may be a result of the data reduction process, and may not represent actual behavior. In general, all data obtained near apogee are suspect; however, the data obtained below 250 km are of excellent quality. Figure 35 shows the portion of the ratio data in which the effects of the storm were most pronounced; the failure of the model to adequately respond is very evident in this region.

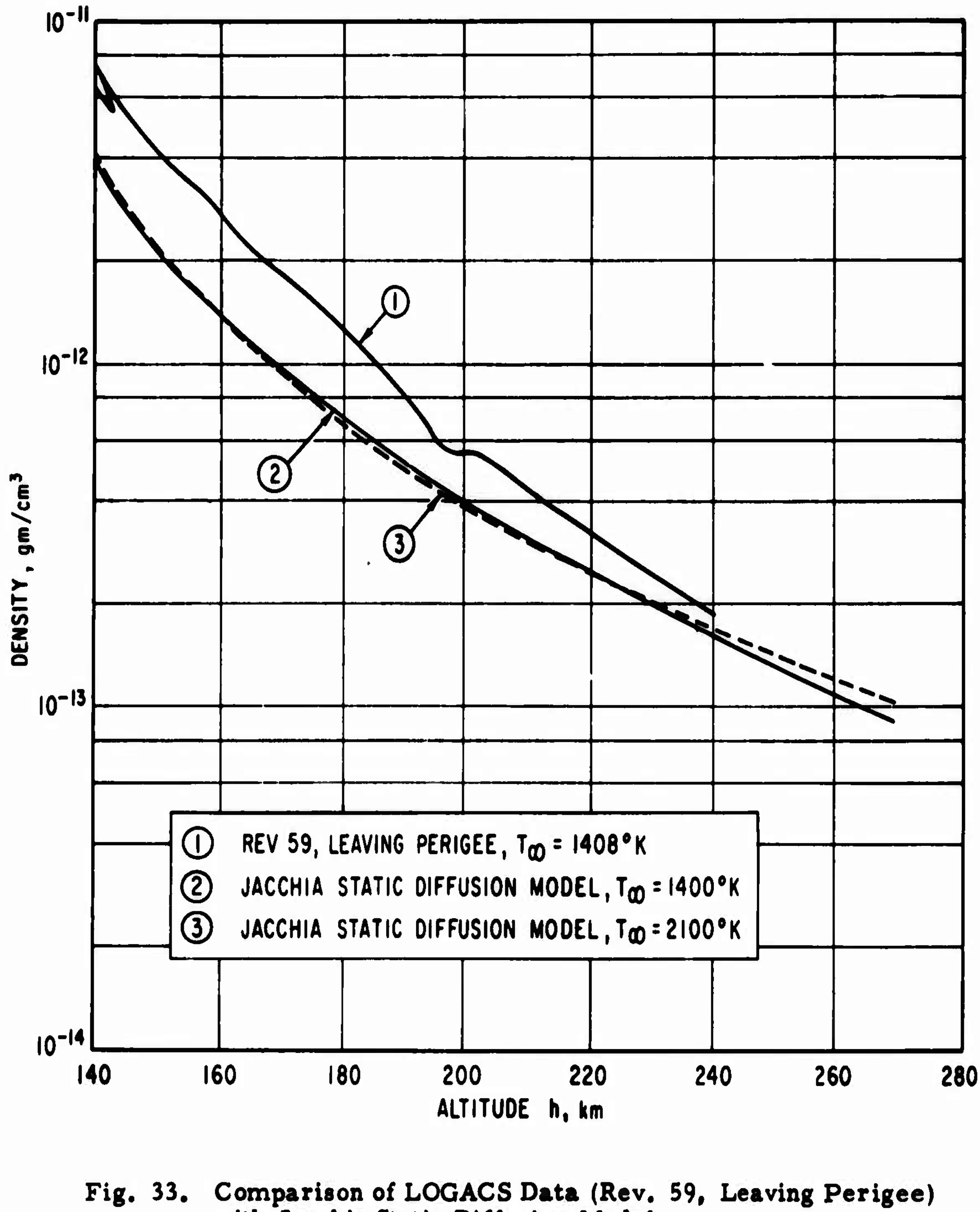

Fig. 33. Comparison of LOGACS Data (Rev. 59, Leaving Perigee) with Jacchia Static Diffusion Model

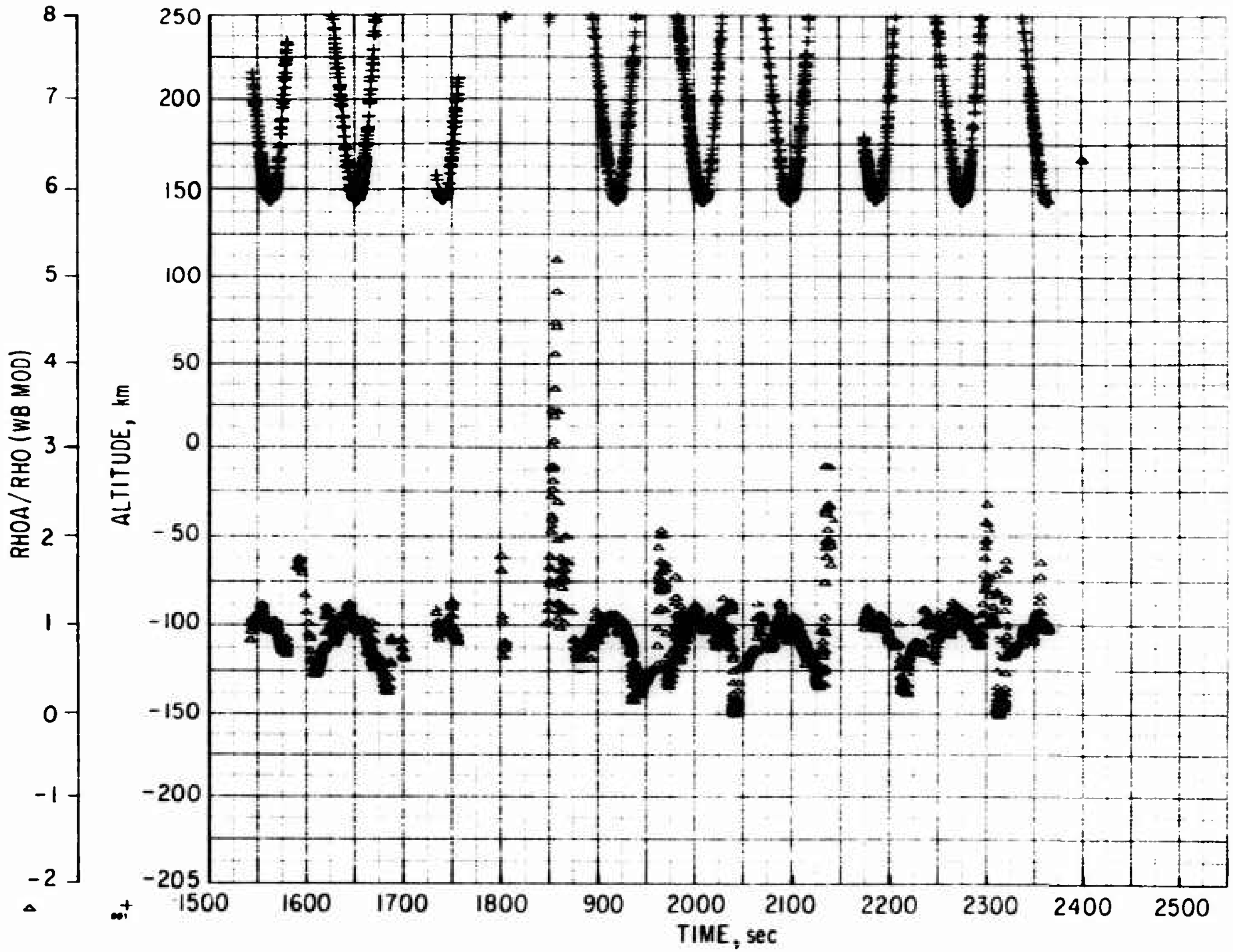

Fig. 34. Ratio of LOGACS-Derived Density to Walker-Bruce Model Density for a Portion of 23 May 1967; Vehicle Altitude Included for Reference

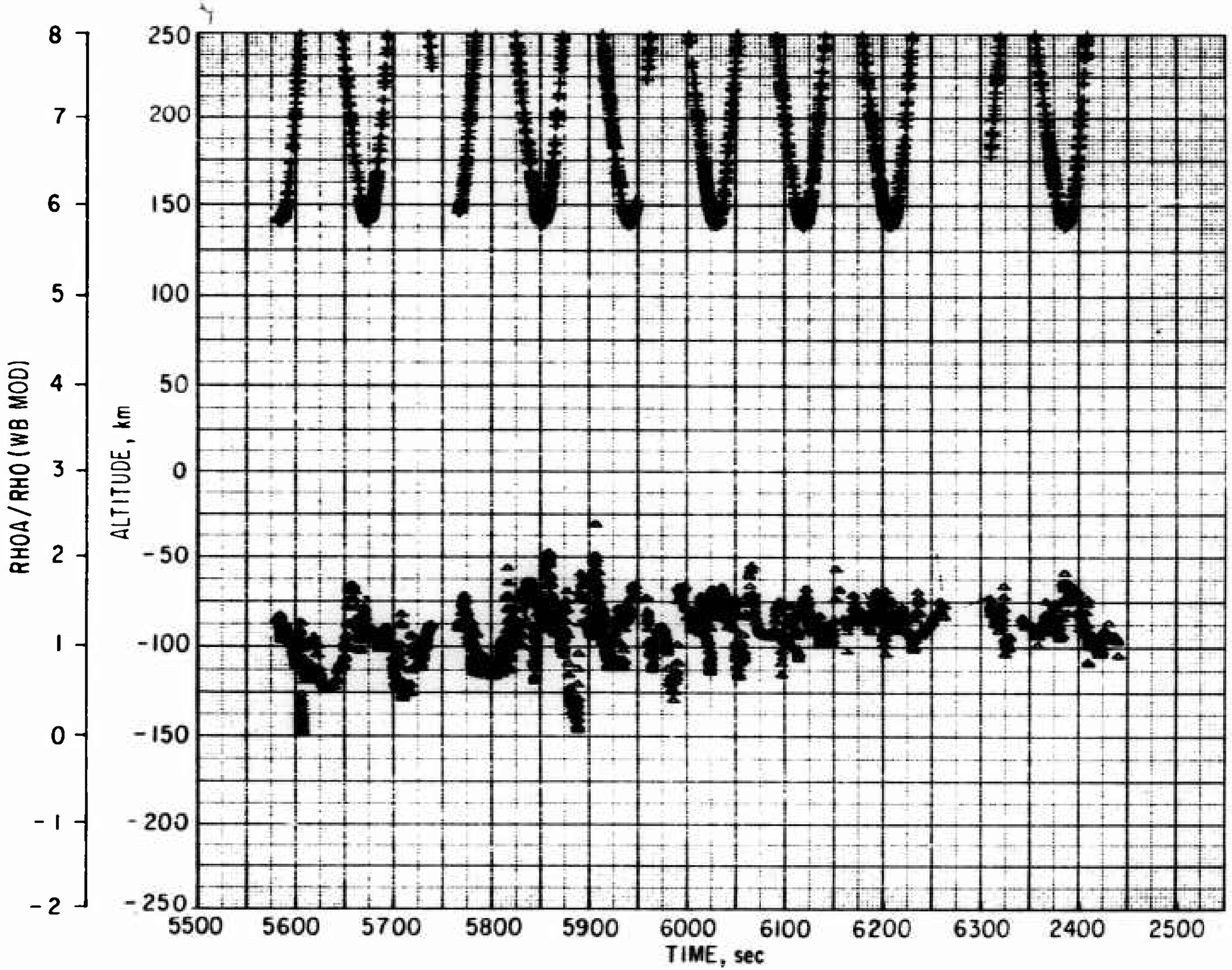

Figure 35. Ratio of LOGACS-Derived Density to Walker-Bruce Model Density for a Portion of 25 May 1967; Vehicle Altitude Included for Reference

For comparison, Figs. 36 and 37 present the ratio of the LOGACS density to the 1962 U.S. Standard Atmosphere density (Ref. 22). This atmosphere, being a table lookup model, incorporates no response to varying solar and geomagnetic parameters. Its behavior is much worse than the Jacchia model in predicting LOGACS densities. Figure 37, which contains the time interval of the storm's effects, shows the complete failure of this model under these conditions.

The two models discussed above are the best and worst cases, respectively, of all models considered in attempting to predict LOGACS densities. Clearly the comparisons show that the models are fundamentally in error in the lower altitude region (140 to 200 km) in particular and that the behavior of the models under conditions characterized by high solar and geomagnetic indices at all altitudes is inadequate.

The ratios of LOGACS density to the density of the Jacchia-Walker-Bruce model were examined then at fixed altitudes. Figures 38 and 39 show the approaching-perigee and away from perigee data, respectively.

It is obvious that, especially during the storm, the model represents the data rather poorly. The minimum altitude case shows a single large peak on 26 May which lags the peak in the planetary range index K_p (see Fig. 28) by some 10 hr.

The data at all altitudes both toward and away from perigee show a number of large peaks during 25 and 26 May. The relative size and separation of these peaks vary with altitude and latitude in a manner as yet not understood.

B. INTERNAL COMPARISONS OF LOGACS DENSITIES

1. SORTING BY TIME

The LOGACS data is broken into seven groupings, called vectors, as a result of the postflight ephemeris computation (Ref. 1). These vectors are of differing lengths, but serve as convenient, albeit arbitrary, data spans for analysis purposes. Figures 40 through 46 present linear plots of density versus altitude for each of the seven vectors; these plots have been annotated

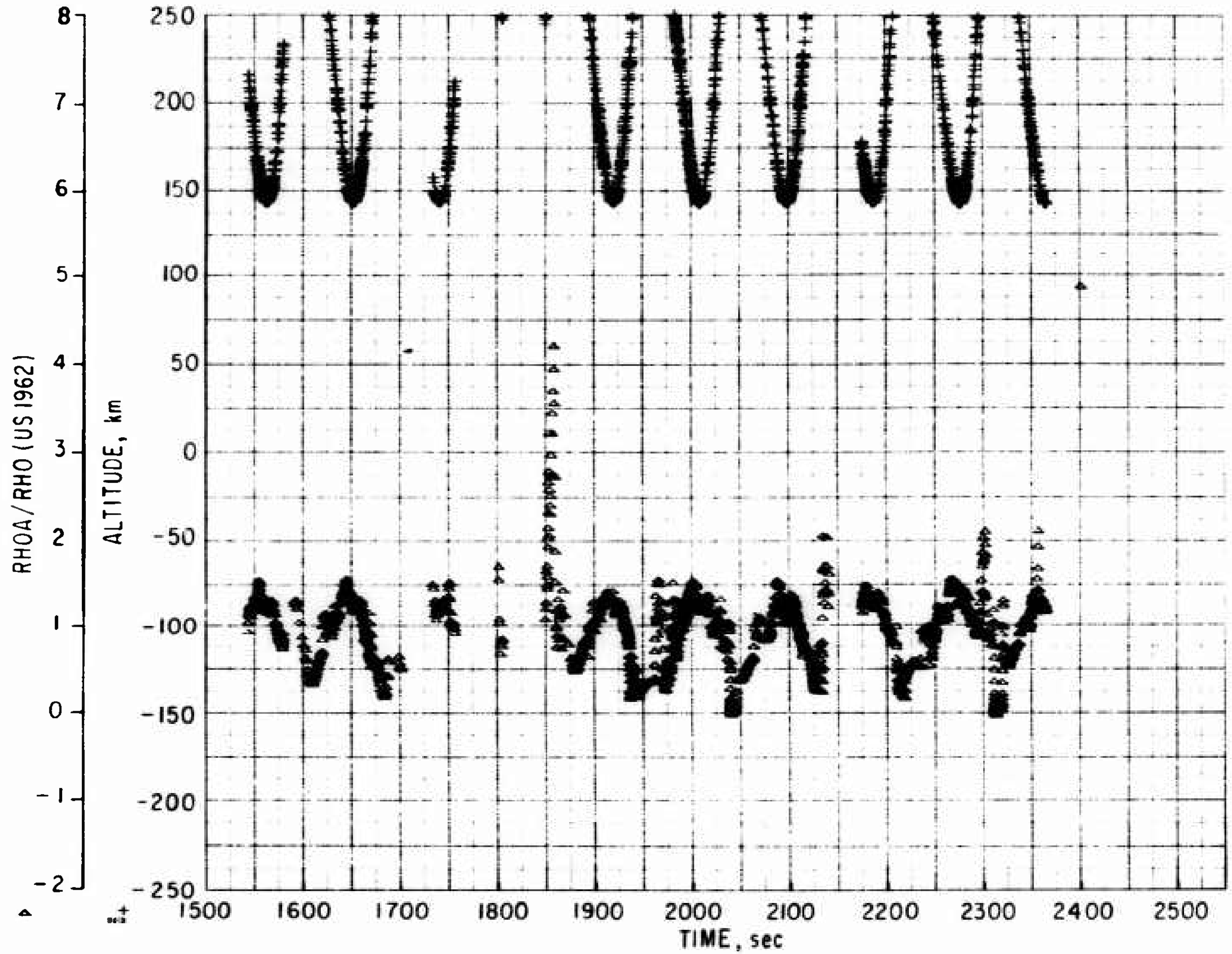

Fig. 36. Ratio of LOGACS-Derived Density to 1962 U.S. Standard Atmosphere Density for a Portion of 23 May 1967; Vehicle Altitude Included for Reference

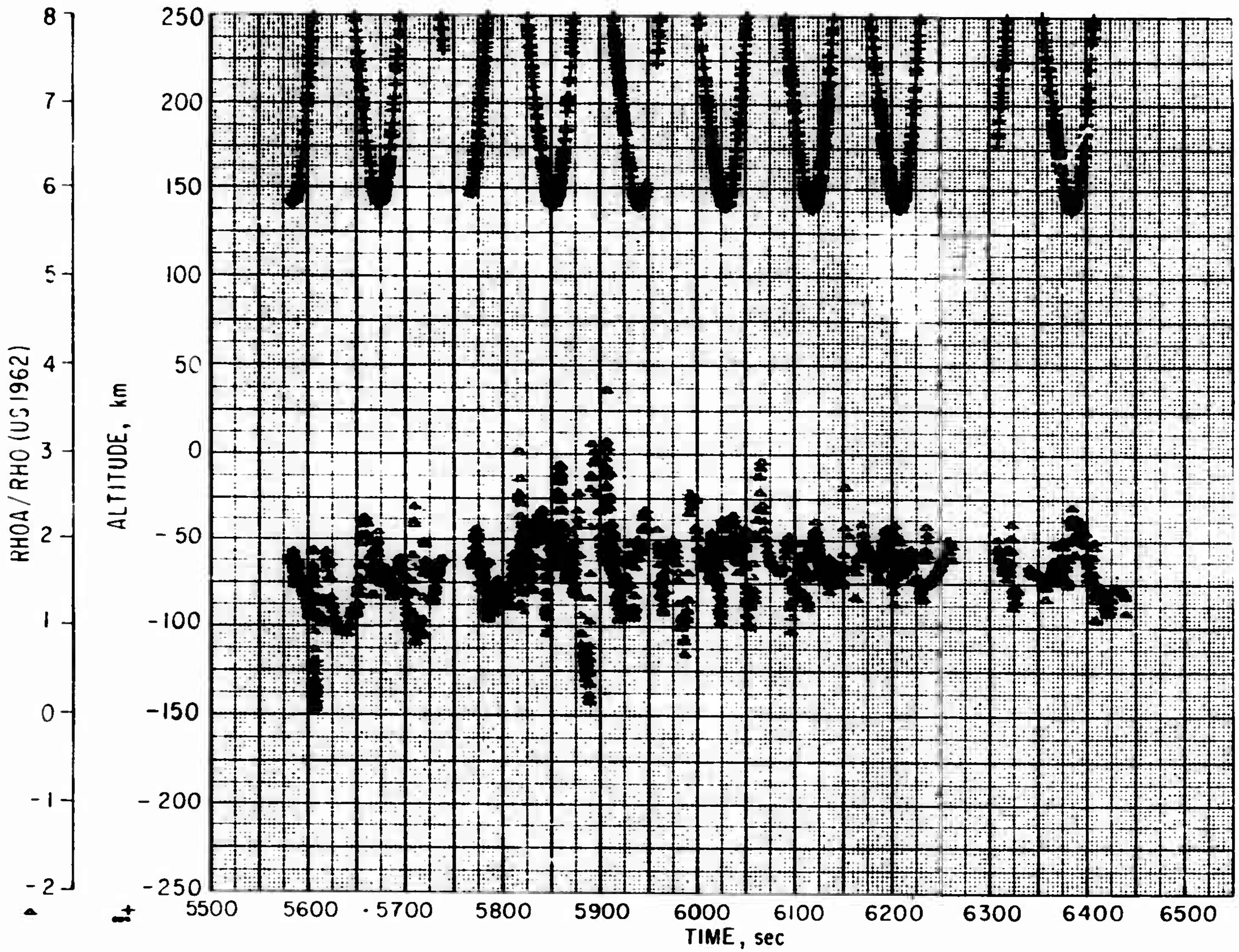

Fig. 37. Ratio of LOGACS-Derived Density to 1962 U.S. Standard Atmosphere Density for a Portion of 25 May 1967; Vehicle Altitude Included for Reference

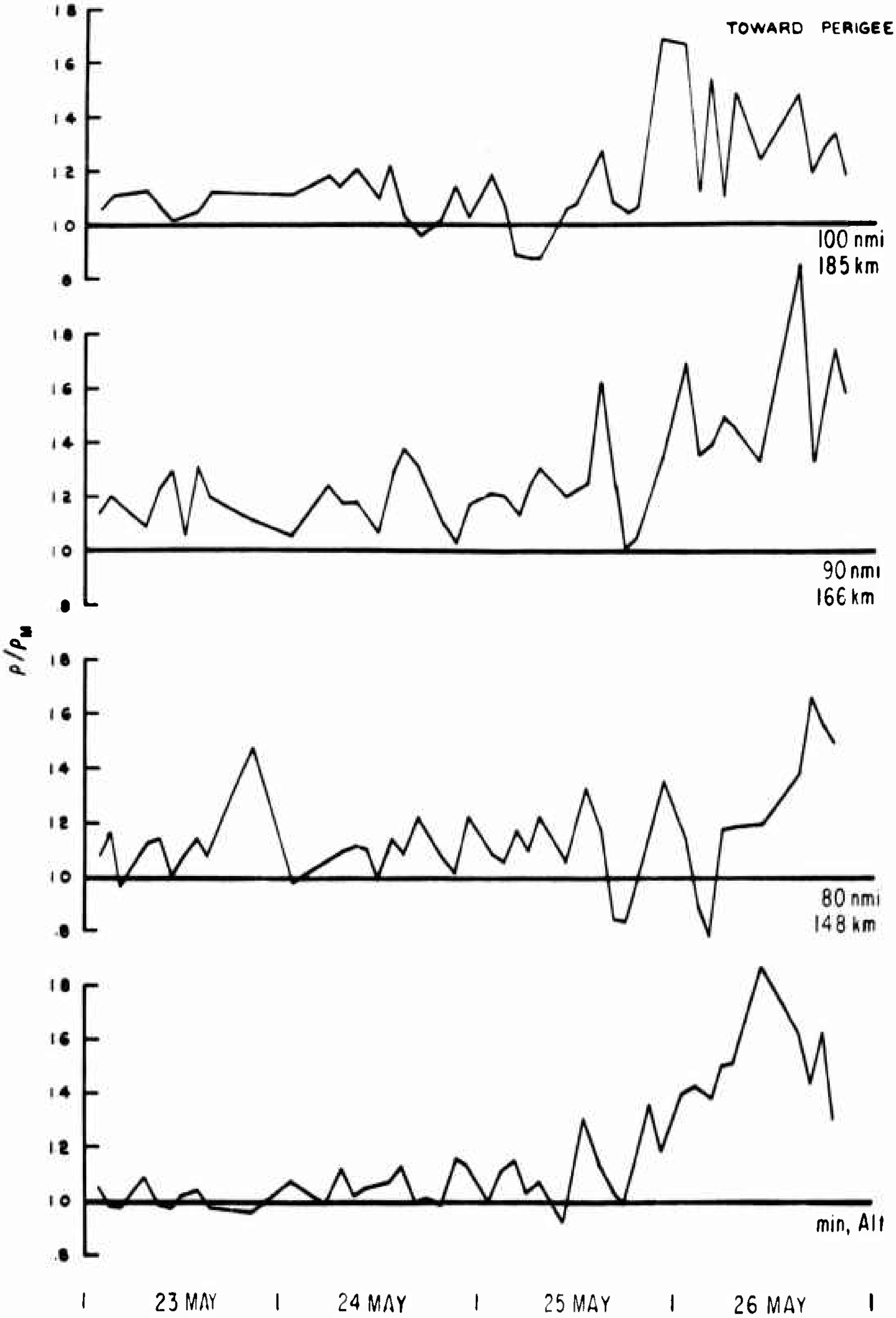

Fig. 38. The Density Ratio LOGACS/Jacchia-Walker-Bruce Model for High Latitude (Toward Perigee) Data at Various Altitudes

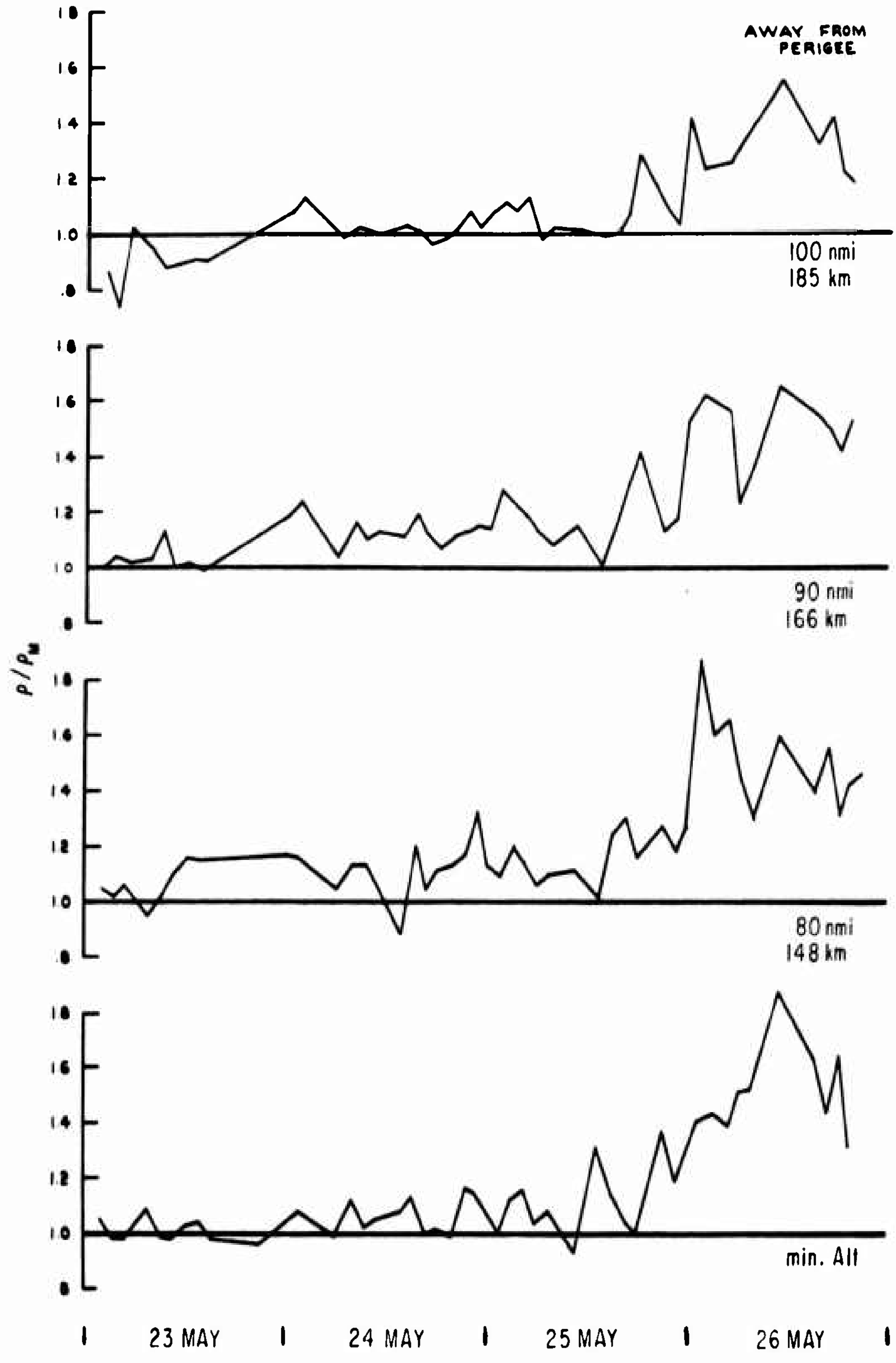

Fig. 39. The Density Ratio LOGACS/Jacchia-Walker-Bruce Model for Low Latitude (Away from Perigee) Data at Various Altitudes

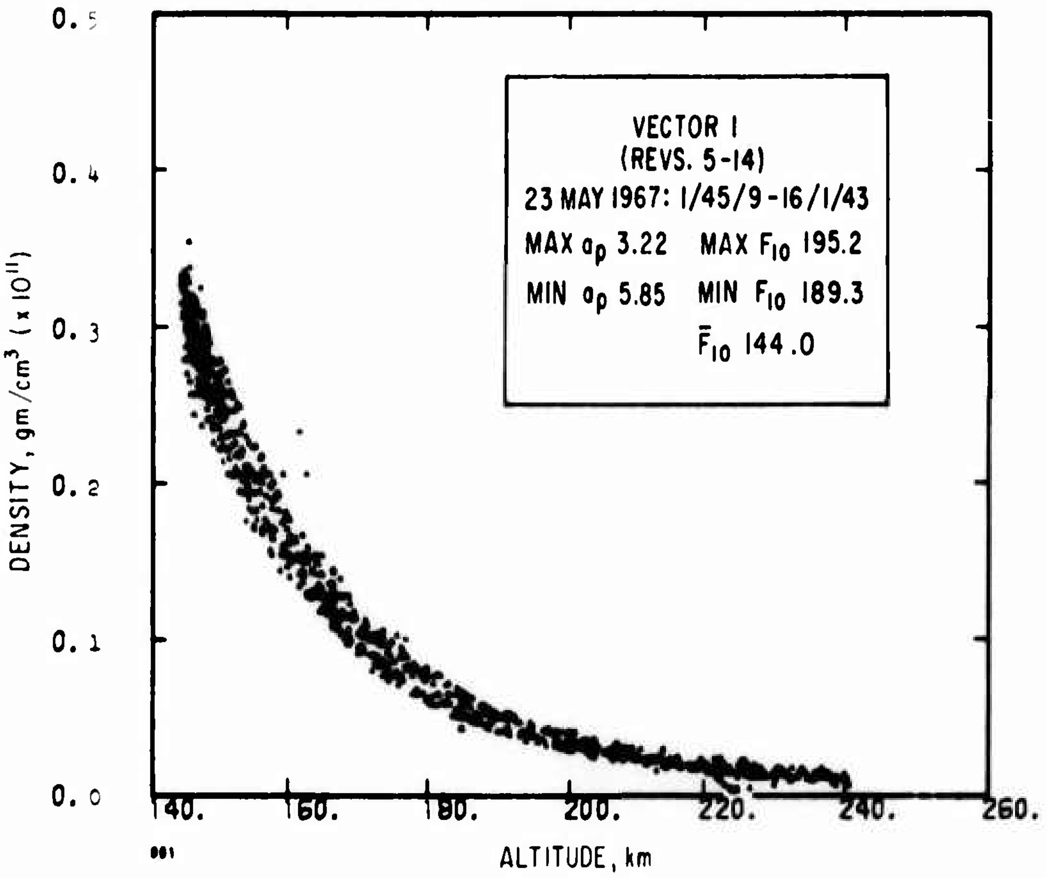

Fig. 40. Density vs Altitude for Vector 1

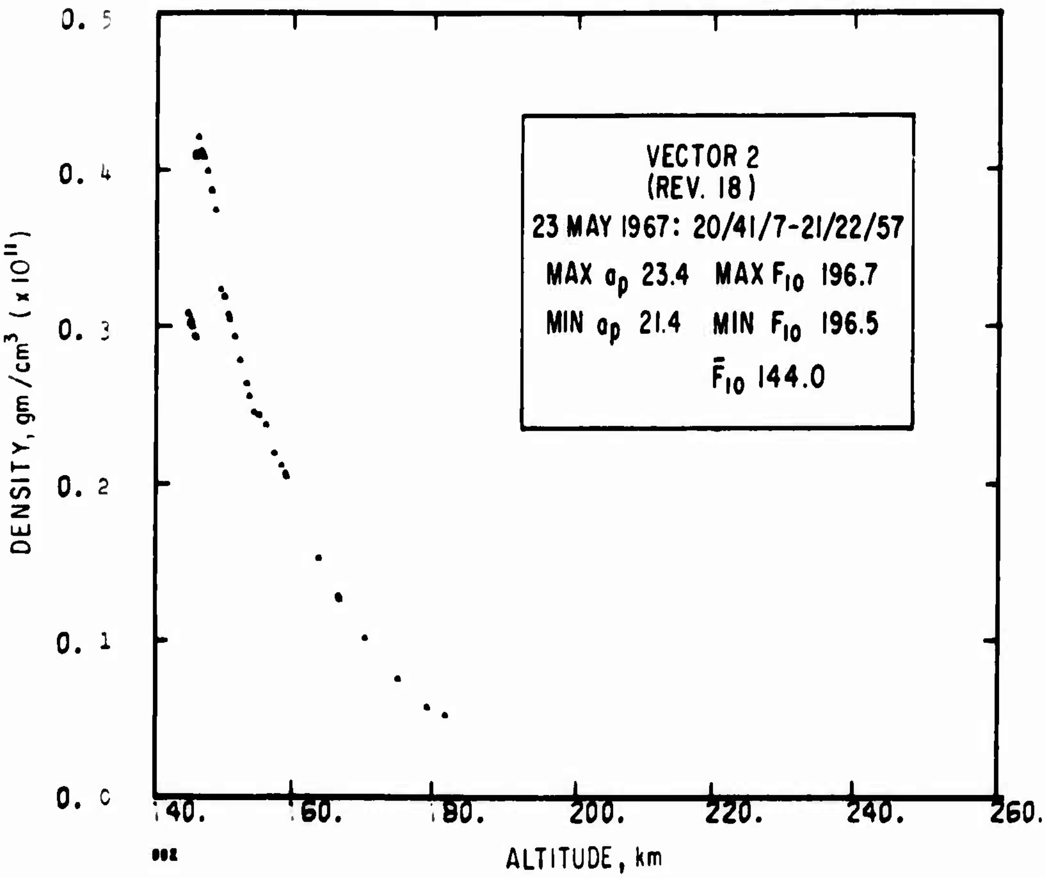

Fig. 41. Density vs Altitude for Vector 2

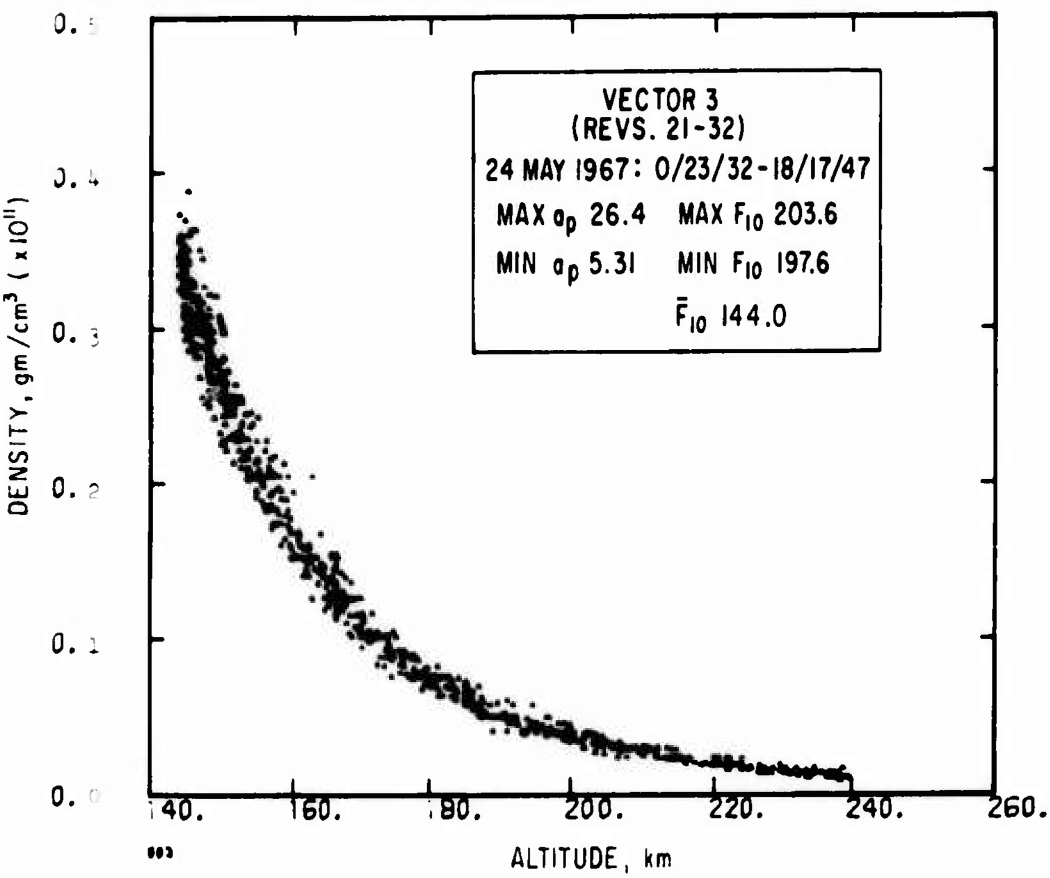

Fig. 42. Density vs Altitude for Vector 3

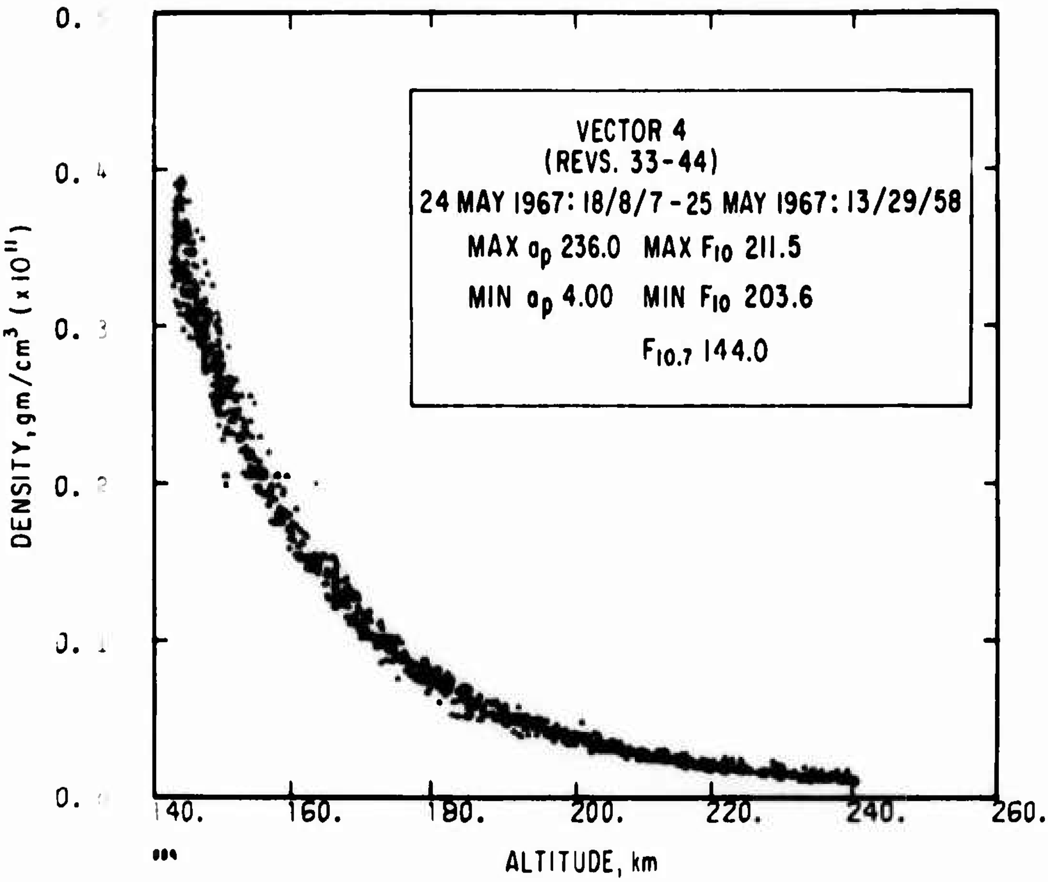

Fig. 43. Density vs Altitude for Vector 4

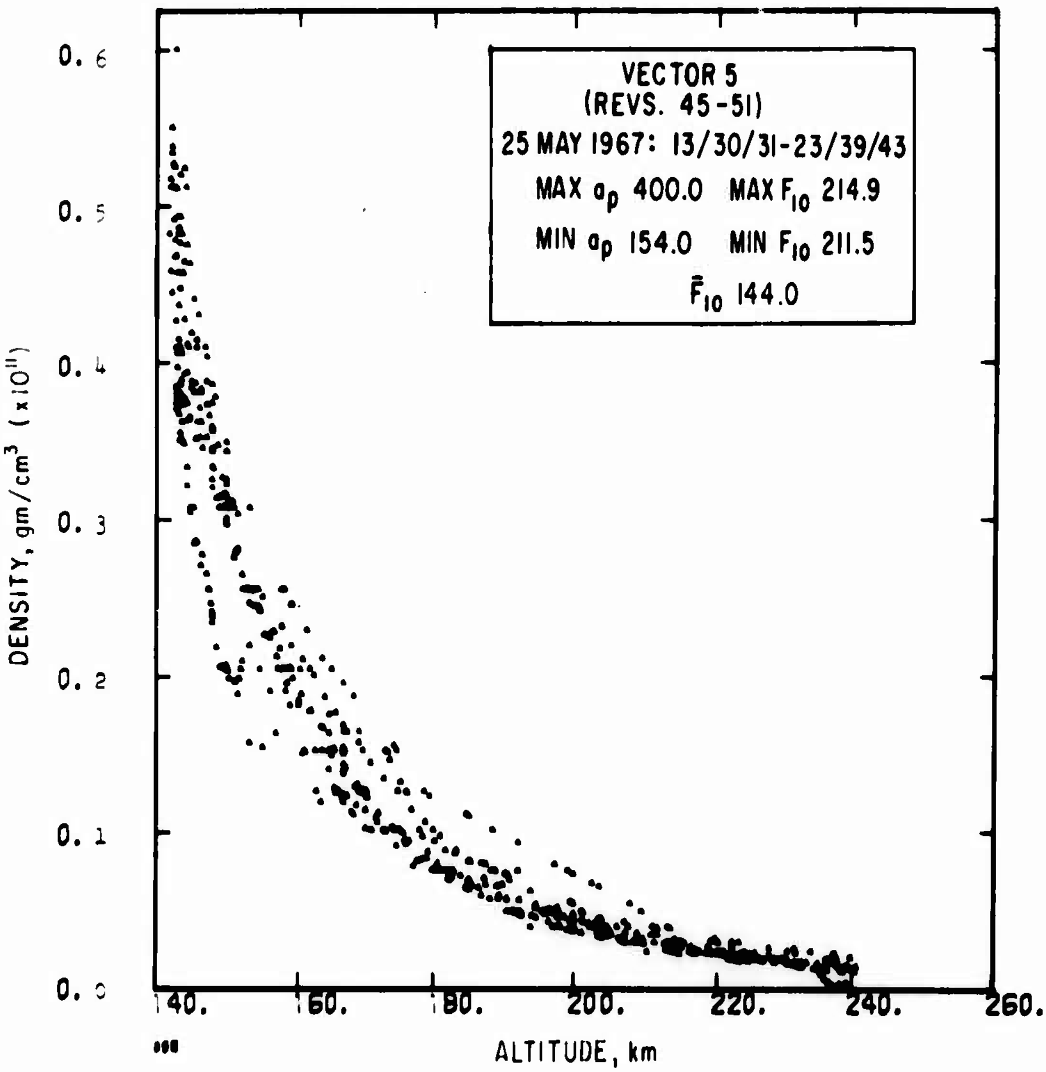

Fig. 44. Density vs Altitude for Vector 5

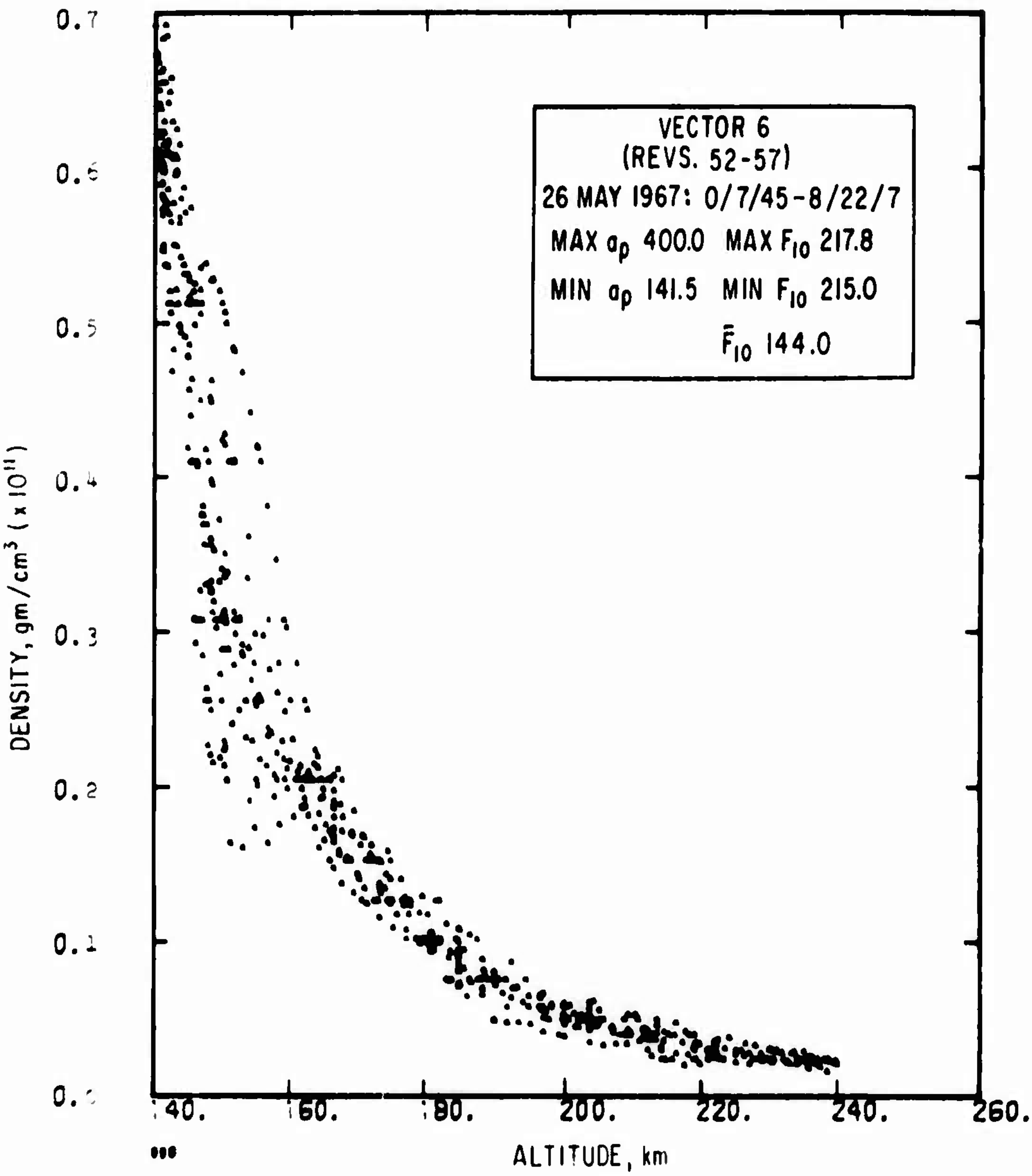

Fig. 45. Density vs Altitude for Vector 6

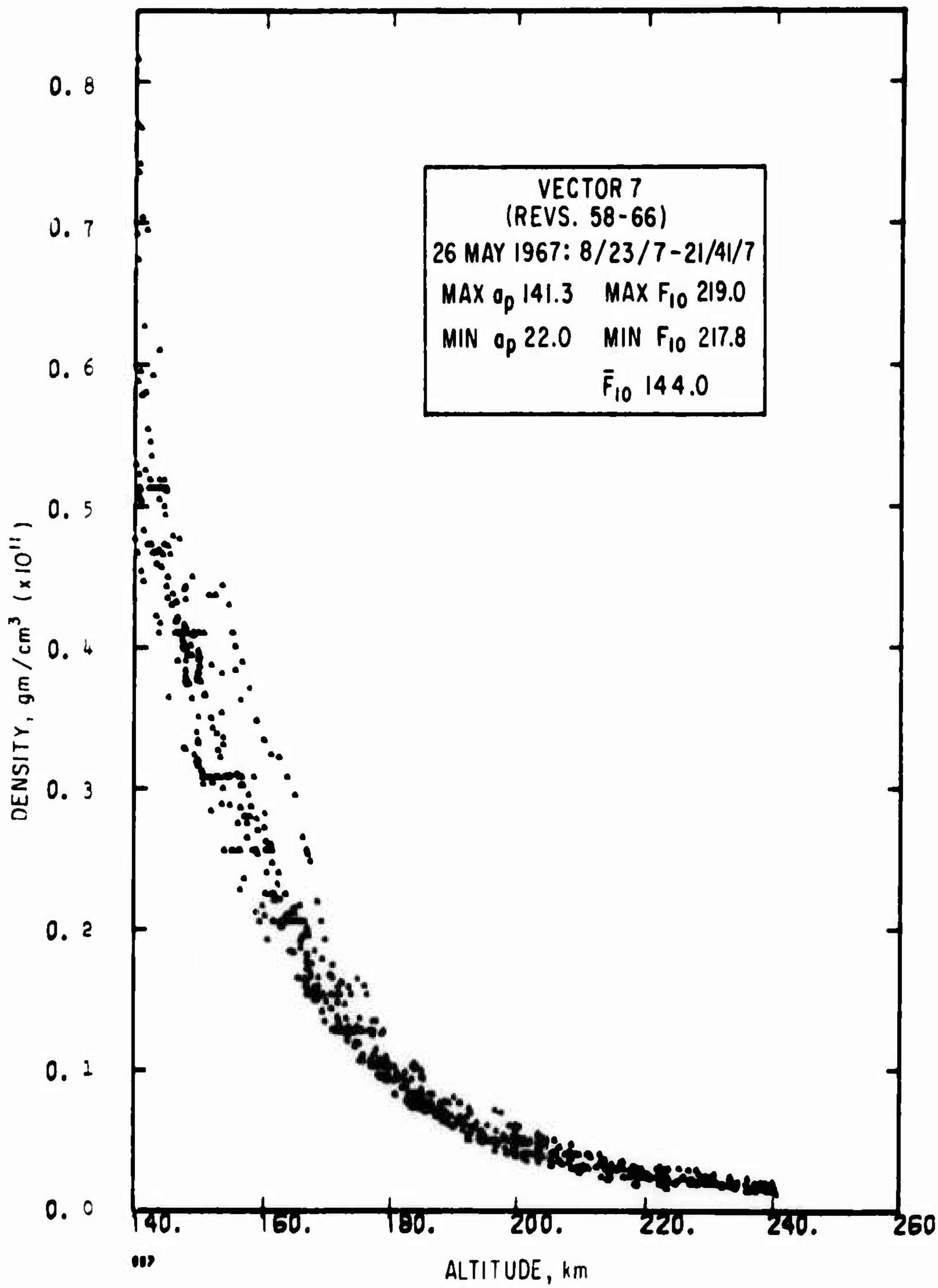

Fig. 46. Density vs Altitude for Vector 7

to reflect the time span, and the solar and geomagnetic conditions which existed during the time span, of each vector.

In Fig. 40 (Vector 1), there is a spread in density values of 33 percent at 150 km. This vector is characterized by relatively constant solar and geomagnetic activity and is well before the disturbances. A part of this spread is attributable to latitudinal effects, but a good portion of it is due to local temporal perturbations of the density. The effects of the storm are most clearly seen in Figs. 43 and 44 (Vectors 5 and 6). Corresponding to the above, the spread in density values at 150 km is 55 percent in Fig. 43.

2. SORTING BY ALTITUDE

The interpolative features of the CPD program were utilized to determine density and other parameters at reference altitudes throughout the flight. To make the variation discussed in the previous section more quantitative, some simple statistics were performed on the densities at the reference altitudes. A mean and rms of the density for each vector were computed at each altitude. These results are graphically displayed in Figs. 47 through 54. The mean was plotted at the time midpoint of its vector, and error bars are used to denote a $\pm 1\sigma$ variation. Vector 2 was extremely short and therefore is not a valid sample.

Readily apparent from these plots is the increase in the spread of density values caused by the storm, as well as the increase in the average density caused by the storm. Apparently the storm caused different phenomena at various levels in the atmosphere. For example, at 148 km and 150 km the average density was still increasing with time in Vector 7 (although the 1σ spread was somewhat reduced). This can be compared with the data beyond 185 km, where an apparent return to unperturbed conditions commenced.

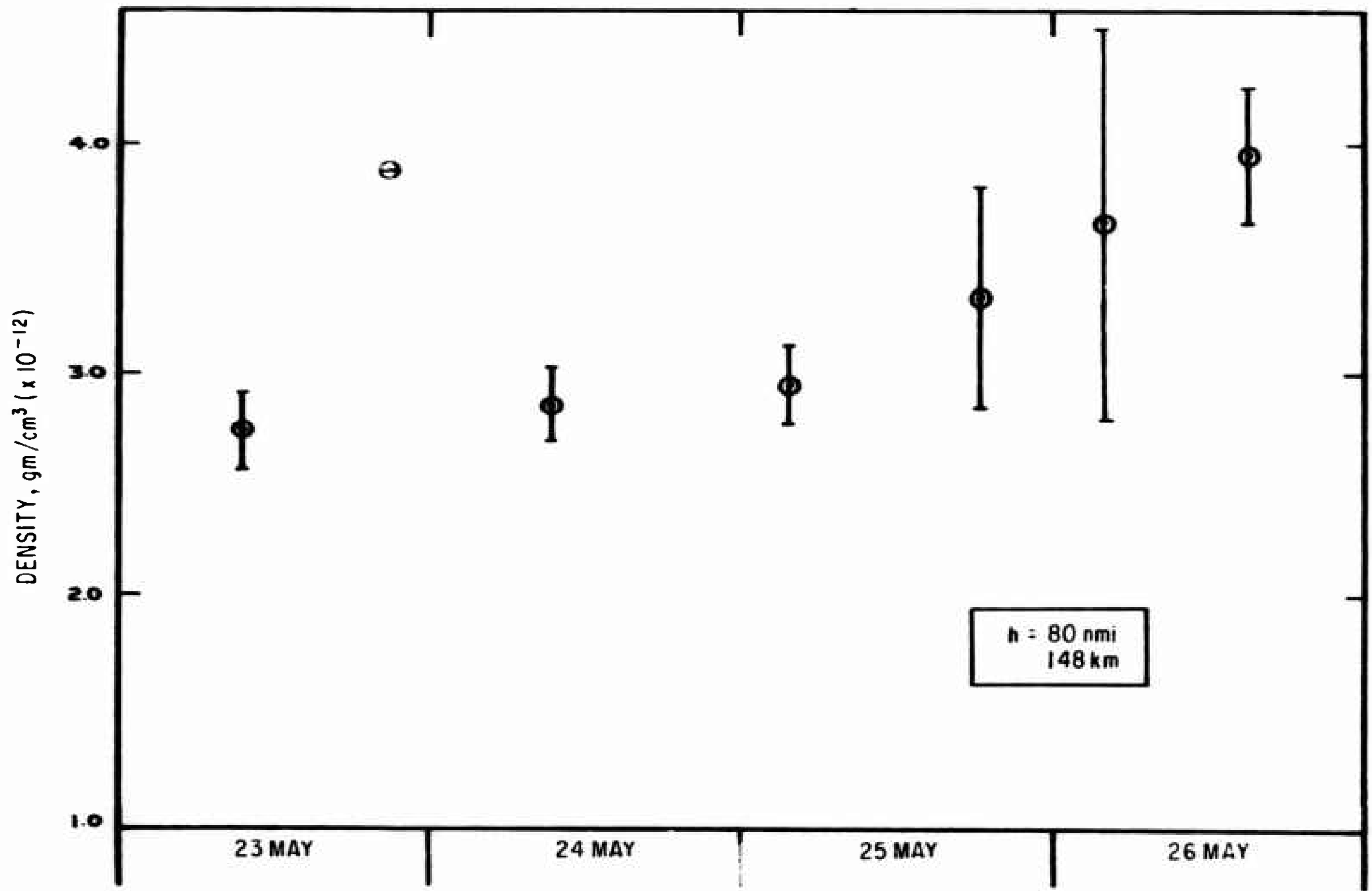

Fig. 47. Mean and RMS of Densi[illegible]ues at 148 km (80 nmi)
During LOGACS Flight

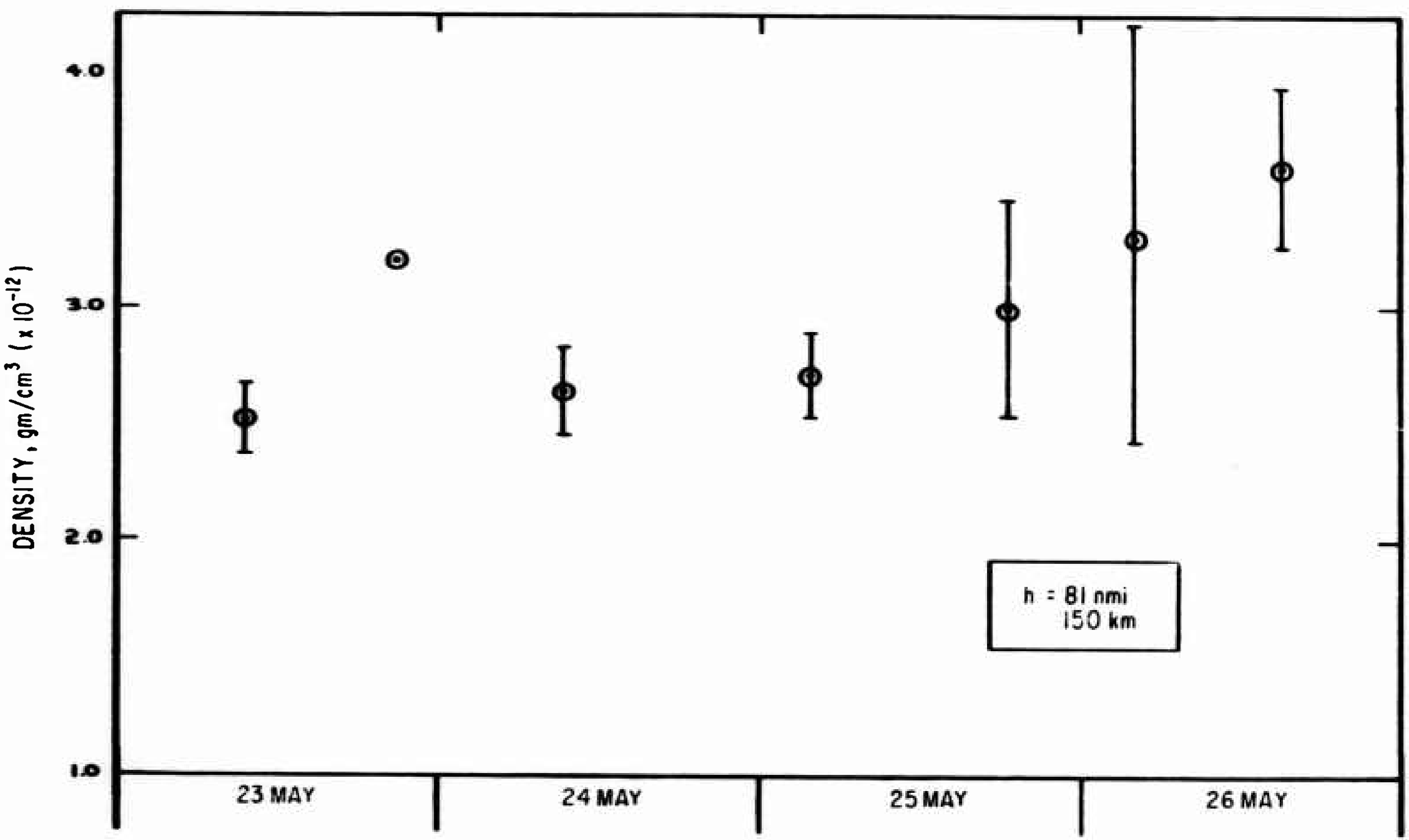

Fig. 48. Mean and RMS of Density Values at 150 km (81 nmi) During LOGACS Flight

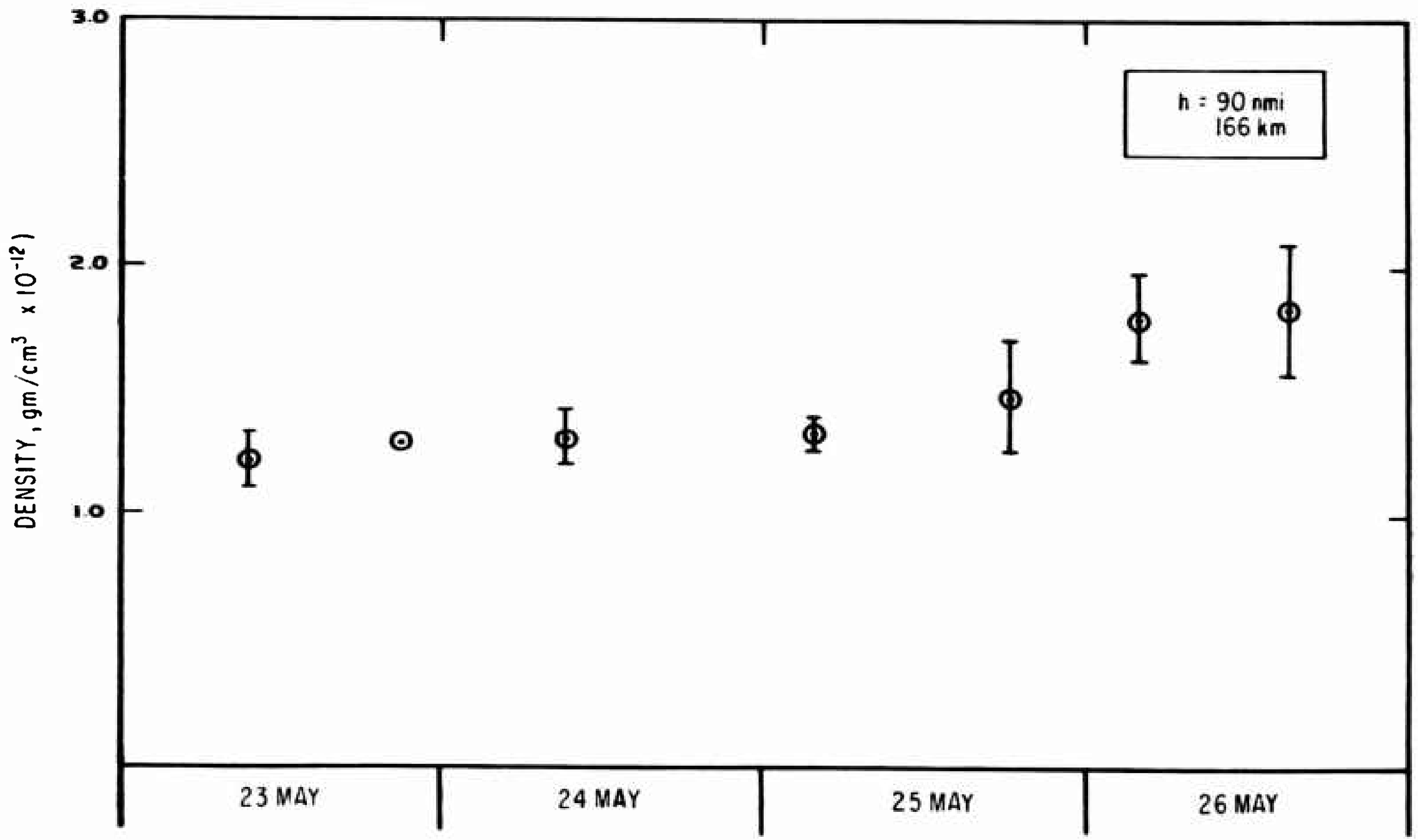

Fig. 49. Mean and RMS of Density Values at 166 km (90 nmi) During LOGACS Flight

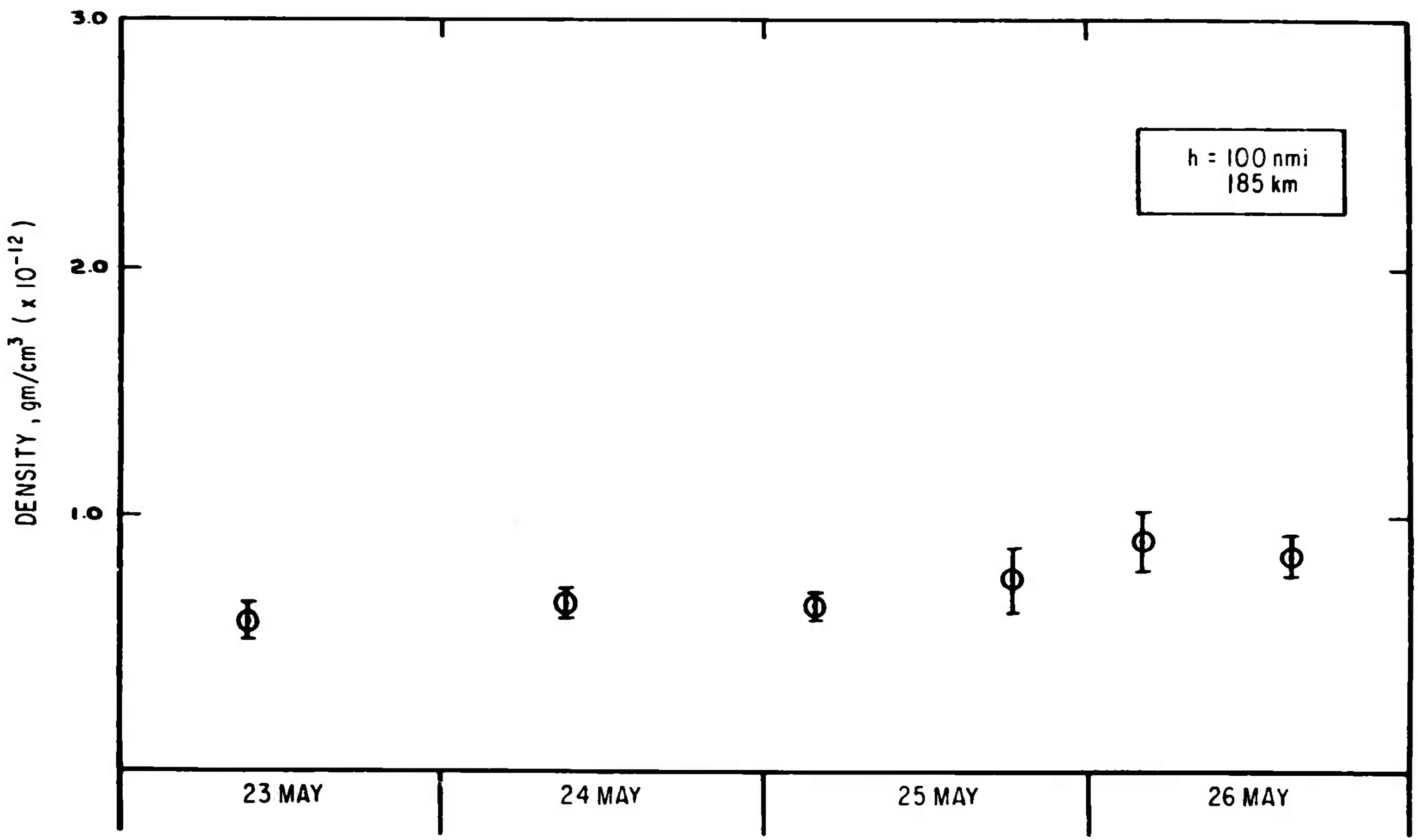

Fig. 50. Mean and RMS of Density Values at 185 km (100 nmi) During LOGACS Flight

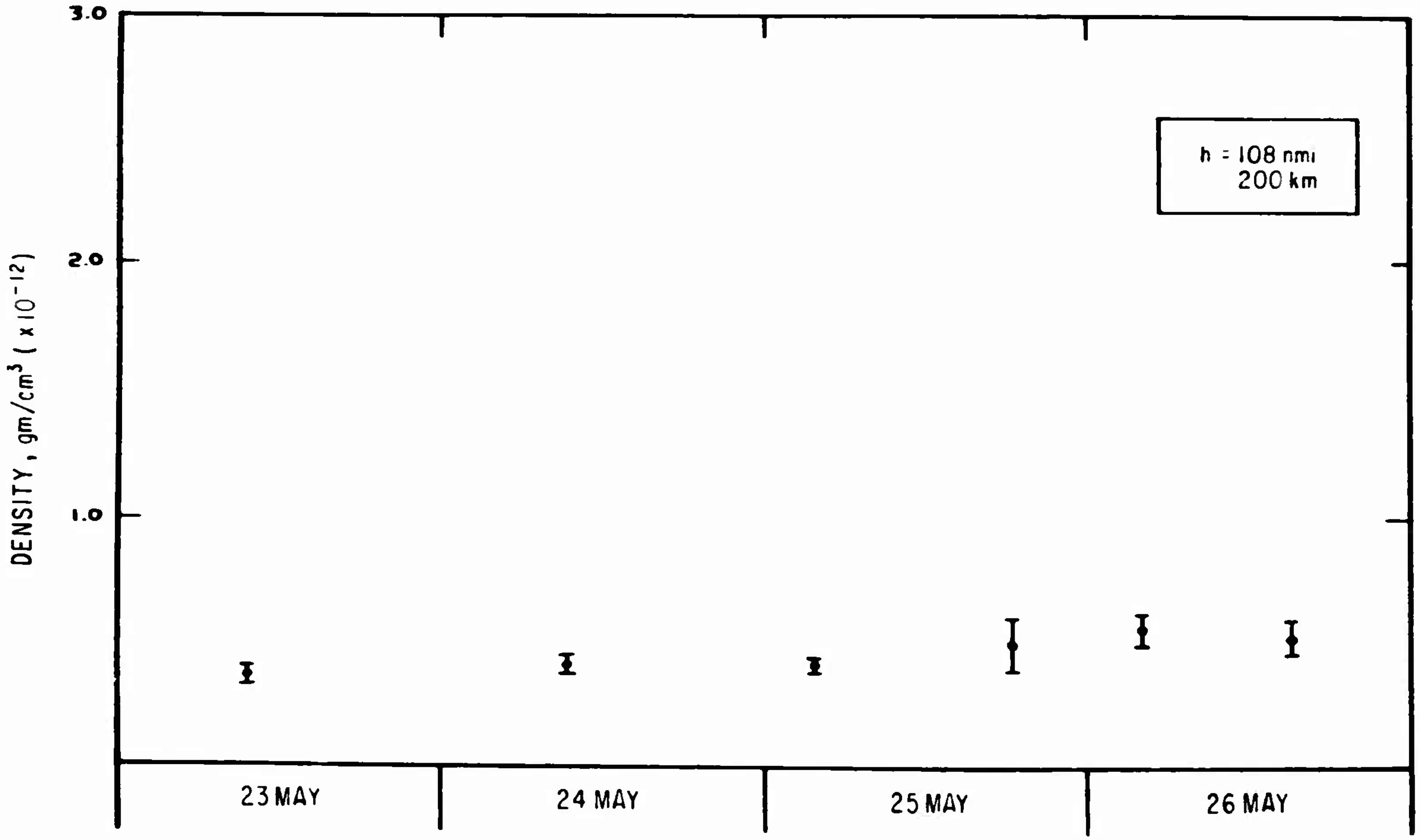

Fig. 51. Mean and RMS of Density Values at 200 km (108 nmi) During LOGACS Flight

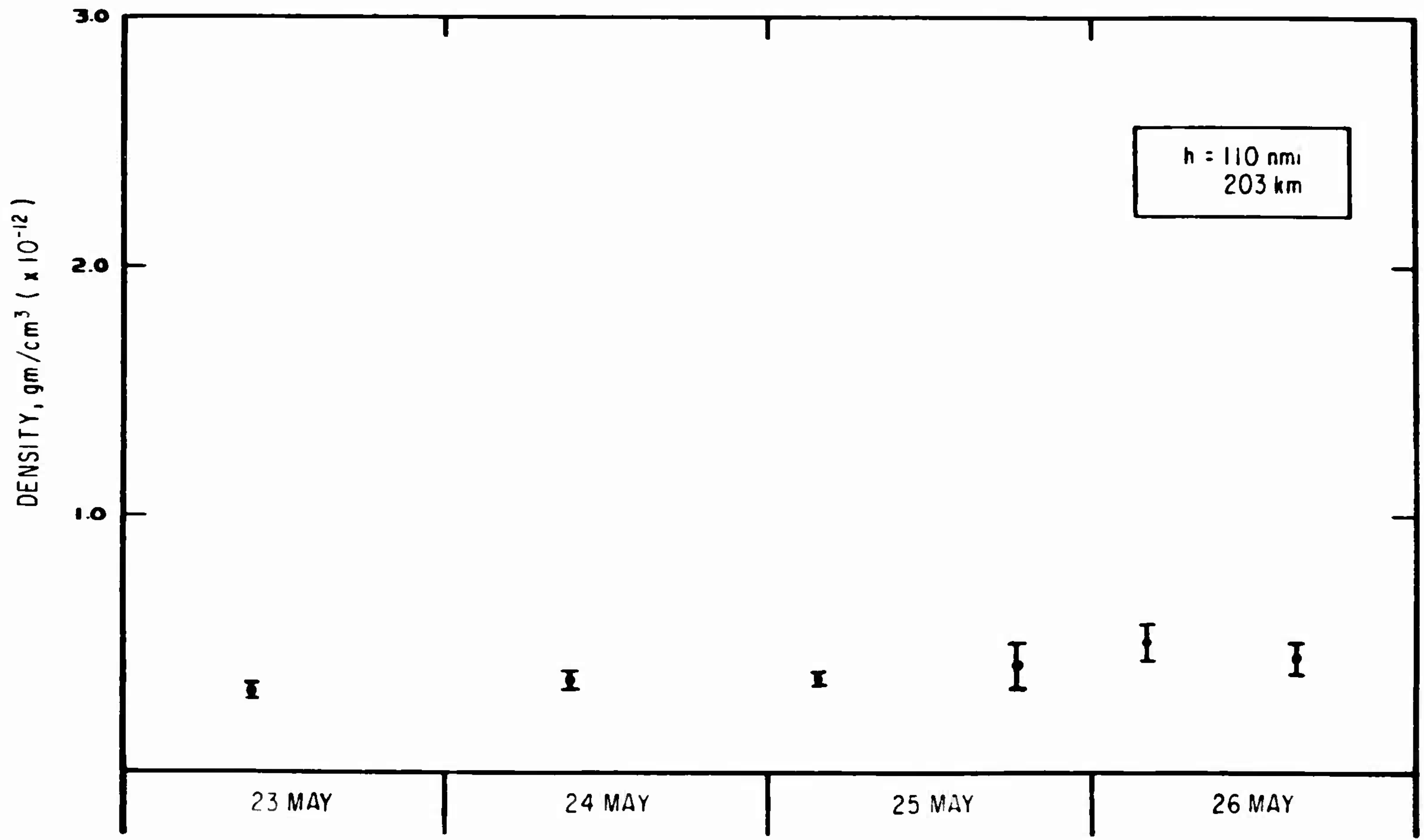

Fig. 52. Mean and RMS of Density Values at 203 km (110 nmi) During LOGACS Flight

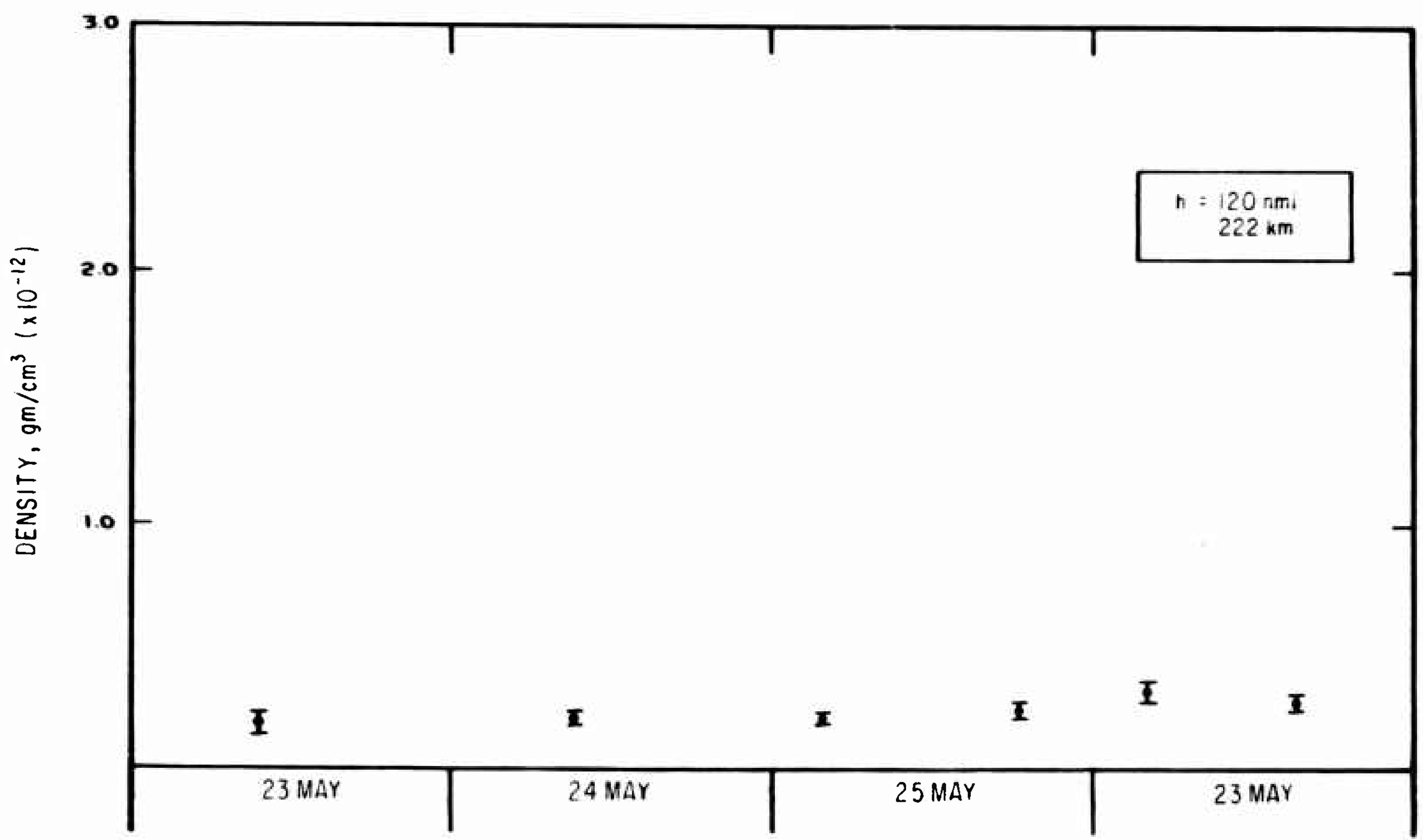

Fig. 53. Mean and RMS of Density Values at 222 km (120 nmi) During LOGACS Flight

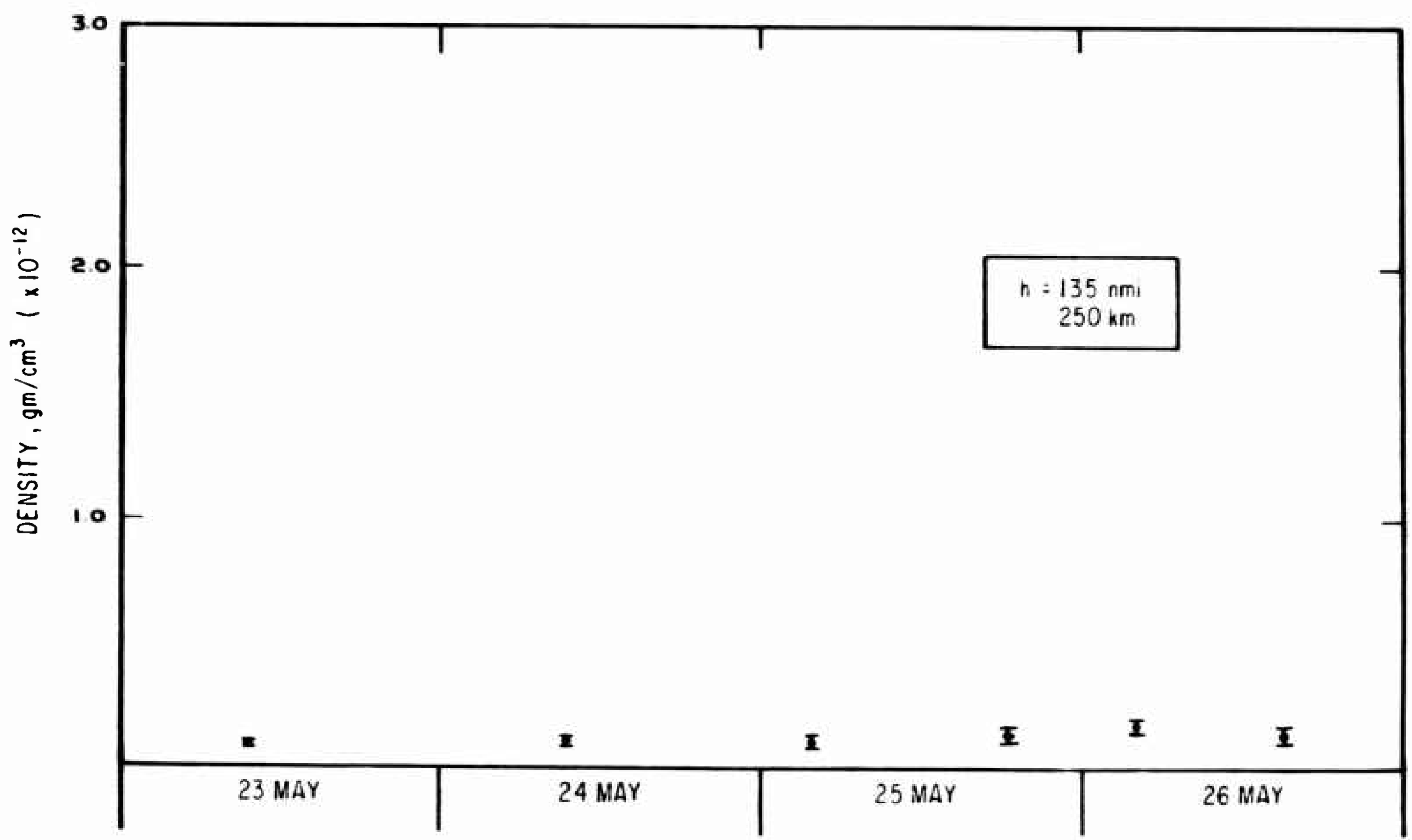

Fig. 54. Mean and RMS of Density Values at 250 km (135 nmi) During LOGACS Flight

SECTION III

ATMOSPHERIC PREDICTABILITY

A. DENSITY PREDICTION

The LOGACS experiment provided several days of near-continuous data about the forces the Agena experienced. From these data, it was possible to extract density along the orbit, based on theoretical aerodynamic considerations of the Agena. The LOGACS density data have made it possible to determine some idea of the predictability of atmospheric density at various altitudes. Along these lines, the following analysis was performed. In order to simulate the average drag in a manner analogous to what is done in a seven-parameter orbit determination, LOGACS densities were averaged at selected altitudes over suitable rev. spans. Twelve-rev. averaging was chosen for this study. The average values determined in this way were considered to correspond to the average drag determined from a fit to tracking data. The "predicted" density values were obtained from the LOGACS data for revs. immediately following the spans used for averaging. Each of the four revs. adjacent to the averaged spans was examined at the selected altitudes. The differences between each of the density values in the "predict" interval and those obtained by averaging were considered to represent a measure of drag predictability. The results of this analysis are contained in this section.

B. DISCUSSION

The LOGACS flight covered a period of four days, totaling some 66 orbits. The data from 49 of these orbits were sufficiently complete for inclusion in this analysis. Four altitudes, 110, 100, 90, and 80 nmi, were chosen as representative altitudes for study. The density data for these altitudes were collated by rev.; those revs. having two data points or less were rejected.

The density data for a given altitude contained in all 12-rev. spans were collated and examined. The mean density value and the rms of the data (expressed as a percentage of the mean value) were computed for each 12-rev. group at each altitude, as shown in Table 4.

Table 4. Mean and RMS Density for All 12-Rev. Groups

Altitude, nmi	Mean, gm/cm^3	Rms (Percent of Mean)
110	3.876×10^{-13}	11.91
100	6.971×10^{-13}	11.52
90	1.432×10^{-12}	10.96
80	3.094×10^{-12}	11.09
Overall	--	11.37

Data from each of four revs. following each 12-rev. group were then compared with the mean for the 12-rev. groups. The difference of this value from the mean was computed and expressed as a percentage of the mean. These percentage values were averaged for each altitude and for all the data; as a measure of the dispersion of the data, the rms about the average was computed for each case. These results are shown for the first, second, third, and fourth rev. after the 12-rev. groups in Tables 5, 6, 7, and 8, respectively.

C. CONCLUSION

As can be easily seen from the following tables, the average predicted dispersions varied between approximately 6 and 10 percent, with an rms of approximately 14 percent. The most obvious feature of the table is the expected; that the prediction grows worse as time increases. Another expected feature is the increase in dispersions with altitude.

Table 5. First Rev. after 12-Rev. Mean, Relative Difference

Altitude, nmi	Average of Difference, Percent of Mean	Rms about Average of Difference, Percent of Mean
110	7.125	±19.534
100	5.421	±12.738
90	5.426	±11.558
80	5.740	± 8.975
Overall	5.987	±13.655

Table 6. Second Rev. after 12-Rev. Mean, Relative Difference

Altitude, nmi	Average of Difference, Percent of Mean	Rms about Average of Difference, Percent of Mean
110	8.679	±20.727
100	6.328	±13.936
90	6.945	±11.625
80	6.921	± 9.437
Overall	7.207	±14.516

Table 7. Third Rev. after 12-Rev. Mean, Relative Difference

Altitude, nmi	Average of Difference, Percent of Mean	Rms about Average of Difference, Percent of Mean
110	9.707	±21.428
100	7.485	±14.370
90	8.094	±12.108
80	8.001	± 9.607
Overall	8.303	±14.977

Table 8. Fourth Rev. after 12-Rev. Mean, Relative Difference

Altitude, nmi	Average of Difference, Percent of Mean	Rms about Average of Difference, Percent of Mean
110	11.390	±21.903
100	8.994	±15.293
90	9.434	±12.364
80	9.081	± 9.503
Overall	9.705	±15.415

The data in Tables 5 through 8 present the difference of the predicted rev. from the base rev. as a measure of prediction accuracy. The rms about this difference is sufficiently large to allow the predicted value to be either larger or smaller than the base case. The analysis here implicitly assumes that the data are random, when in fact they are not. The LOGACS flight was characterized by extreme values of solar and geomagnetic parameters; see, for example, Ref. 23. These parameters were increasing over most of the flight. Since density responds to changes in these parameters, all or part of the worsening prediction with time can be attributed to this change.

SECTION IV

MIDLATITUDE DENSITY MODEL ATMOSPHERE BETWEEN 120 AND 175 km

A. INTRODUCTION

Examination of the LOGACS density data revealed three separate geographic regions having an apparently very different behavior. For purposes of discussion these regions are referred to as "low latitude," "polar," and "high altitude" regimes. The low latitude region lies between +40 and -30° geocentric latitude, at altitudes up to about 220 km; the polar region lies between +40° latitude and the North Pole up to 220 km; the high altitude region includes the whole atmosphere above this altitude. These limits were delineated by the availability of the density data, not necessarily by physical boundaries.

Perigee (or, more accurately, the minimum altitude point) occurred within the low latitude regime, and varied from about +30° to +43° latitude (Ref. 1), with most of the data being obtained when the minimum altitude point was near +35° latitude.

B. DATA REDUCTION

In the low latitude regime, the density data were sorted according to geocentric latitude. Previous models suggested that a "bulge" would be seen either near the latitude of the subsolar point, or near the equator; therefore, the density data were examined at 5° increments. When no measurements were available at an exact latitude increment, the density was interpolated between the nearest two measurements on either side, provided neither measurement was more than 2.5° from the desired position. Orbital characteristics were such that the altitude was nearly constant at each latitude throughout the flight.

The following form was fitted to the data at each latitude

$$\rho(z,t,\phi) = A(\phi) + B(\phi)g(z,t - \tau,a_p) \tag{1}$$

where

ρ = mass density

z = altitude

ϕ = latitude

t = time of measurement

τ = time delay between changes in the planetary magnetic index a_p and changes in ρ.

All time variations in ρ were absorbed into g, and the form of both g and τ were determined. A and B were assumed to be constant, and several forms of g were tried; the form that gave the largest correlation coefficient between g and ρ was considered "best." After selecting the best form of g, it was found that to first order, ρ had no significant latitudinal dependence; the apparent latitudinal changes in A and B could be more accurately ascribed to changes in altitude. Equation (1) was then rewritten as

$$\rho(z,t) = A(z) + B(z)g(z,t - \tau,a_p) \tag{2}$$

To proceed further, an analytic form was established for A and B by making the following physically reasonable assumptions:

1. If there were no disturbances (g = 0), the atmosphere would obey hydrostatic constraints
2. If g = 0, the atmosphere is in diffusive equilibrium above some reference level (arbitrarily chosen to be 120 km)
3. If g = 0, mean free paths are sufficiently long that the temperature of any one constituent is constant above the reference level

4. Atoms are warmer than molecules since they are created with excess kinetic energy. (Detailed theoretical calculations of the temperature difference have been made.)

5. To a first approximation, the quiet-time atmosphere between 120 and 220 km can be considered to be composed of only oxygen atoms and molecules with a mass of about 29 amu

6. During disturbed times ($g \neq 0$), several forms of atmospheric heating may be operative; joule heating and dumping of high energy (2 to 10 keV) particles from the exospheric ring current (Refs. 24, 25) are examples.

These six conditions impose the following form on A and suggest the form of B that will be used

$$A(z) = a_1 \exp\left[-\alpha_1(z - 120)\right] + a_2 \exp\left[-\alpha_2(z - 120)\right] \tag{3}$$

$$B(z) = b_1 \exp\left[-\beta_1(z - 120)\right] + b_2 \exp\left[-\beta_2(z - 120)\right] \tag{4}$$

It was expected that the values of a_i and b_i would change when a_p exceeded some critical value, indicating that the ring current had become unstable and was dumping particles into the atmosphere (Ref. 6).

C. RESULTS

The numerical results reported in this section were derived from low latitude data obtained during the entire LOGACS flight. Discussions of extensions of the model and applications to future flights are presented in Section D below.

1. FORMS OF g AND τ

The change in density at midlatitudes correlates well with changes in a_p, evaluated at a time τ earlier. In particular, the correlation coefficient is greater than 0.9 when g is of the form

$$g(\tau, a_p) = \ln[a_p(t - \tau) + 1] \tag{5}$$

and τ is represented by

$$\tau = \begin{cases} 42.759 - 1.406\,(z - 120) & 130.0 \le z < 146.5 \\ 5.5 & 146.5 \le z < 157.5 \\ 0.0625 + 0.145(z - 120) & 157.5 \le z < 174.0 \\ 7.9 & 174.0 \le z \end{cases} \tag{6}$$

where τ is measured in hours, and z in kilometers; the decimal places have been carried only to ensure continuity.

The altitude-dependent time delay is of a form consistent with localized heating near 140 km (Ref. 17), and, when averaged over the entire flight, is accurate to about 10 percent, which does not justify an expression more complicated than this linear form.

2. DENSITY COEFFICIENTS

Equation (2), using the functional forms given by Eqs. (3) through (6), was used to fit the atmospheric density measured on all orbits available (about 40 were useful in the low altitude regime). The residuals showed a sudden, apparently discontinuous, increase when $g(\tau, a_p)$ become greater than about 4.0; therefore, the data were divided into two groups. One group included the densities measured during moderately disturbed times $[a_p(t - \tau) \le 59]$; the other group included densities measured during more severely disturbed times $[a_p(t - \tau) > 59]$. The numeral 59 is accurate to about 20 percent. The free parameters implicit in Eq. (2) were then fitted independently in each group. The results are shown in Table 9.

A measure of the goodness of fit can be obtained by forming the quantity

$$\sigma = \left[\frac{1}{N - M} \sum_{i=1}^{N} (1 - \rho_i / \rho_M)^2 \right]^{1/2} \tag{7}$$

Table 9. Values of Adopted Parameters for Present Model

$$\rho(z,t) = a_1 e^{-\alpha_1(z-120)} + a_2 e^{-\alpha_2(z-120)}$$

$$+ \left[b_1 e^{-\beta_1(z-120)} + b_2 e^{-\beta_2(z-120)}\right] g(z, a_p)$$

	$a_p(t - \tau) \le 59$, gm/cm^3	$a_p(t - \tau) > 59$, gm/cm^3
a_1	103.05×10^{-13}	115.53×10^{-13}
a_2	12.45×10^{-13}	9.18×10^{-13}
b_1	6.49×10^{-13}	13.56×10^{-13}
b_2	1.79×10^{-13}	2.66×10^{-13}
α_1	0.06064 km^{-1}	
α_2	0.02145	
β_1	0.08410	
β_2	0.02005	

where ρ_i is the i^{th} measured density and ρ_M is the density calculated from the model; N - M is the number of degrees of freedom. The ratios ρ_i/ρ_M are plotted in Fig. 55. The density ratios and standard deviations derived from this model for the period of the LOGACS flight can be compared with those obtained using other model atmospheres that have been proposed. The comparison, both in an overall sense and as a function of altitude, is shown in Table 10.

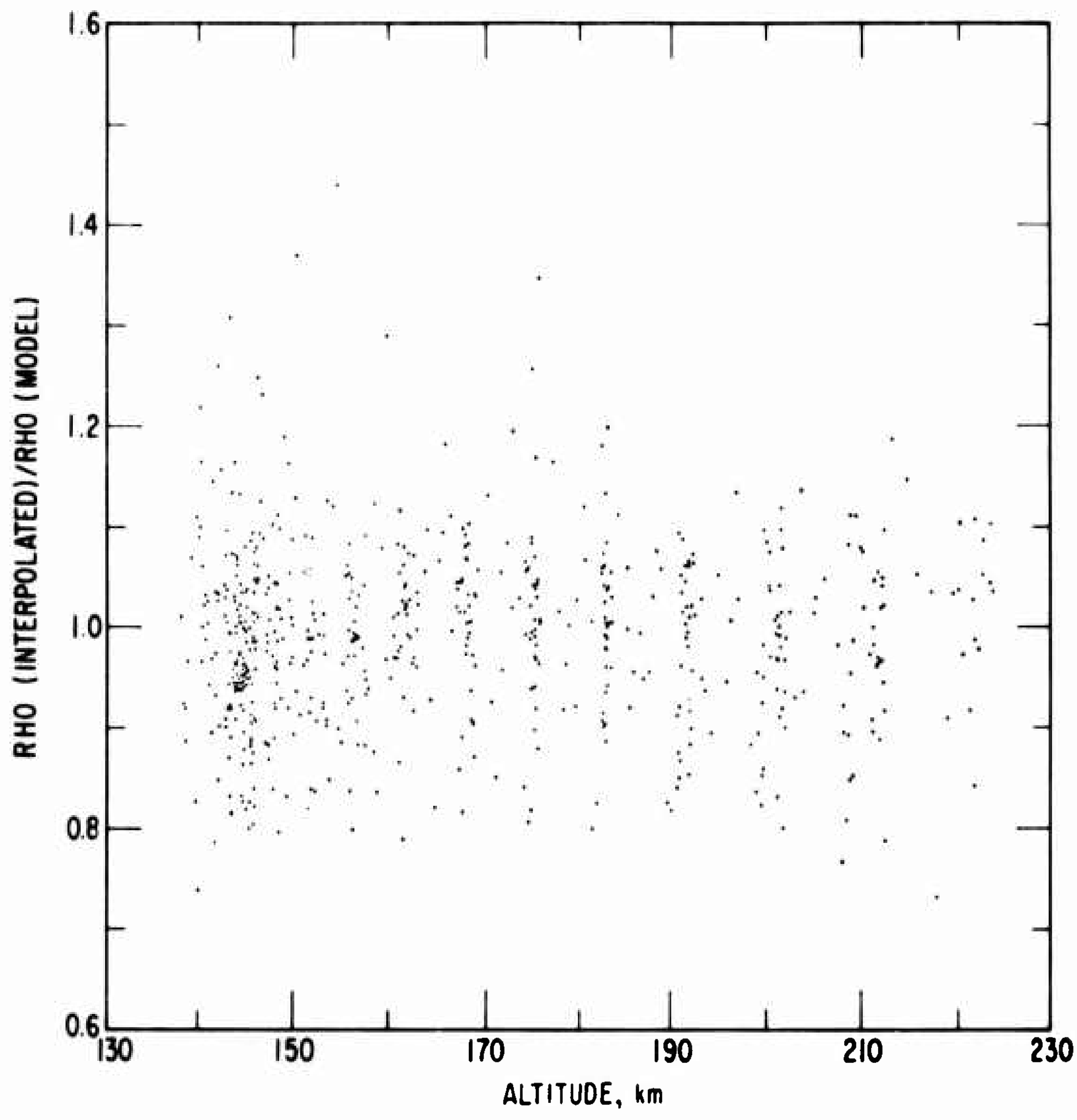

Fig. 55. Ratio of Measured Densities to Those Predicted by Present Model for Entire Flight at Low Latitudes

Table 10. Comparison of Present Model with Four Others During LOGACS Flight

Model Nominal Altitude, km	US62		L-Density[c]		J-W-B[d]		Champion[e]		Prag[f]	
	R[a]	σ[b]	R	σ	R	σ	R	σ	R	σ
144	1.50	0.29	1.62	0.34	1.15	0.20	1.11	0.14	0.98	0.09
149	1.65	0.33	1.65	0.35	1.25	0.21	1.16	0.15	0.99	0.10
153	1.62	0.34	1.56	0.34	1.24	0.22	1.14	0.15	0.99	0.11
158	1.59	0.30	1.48	0.28	1.22	0.20	1.12	0.12	0.99	0.09
163	1.56	0.28	1.41	0.25	1.21	0.18	1.11	0.10	1.01	0.08
169	1.48	0.30	1.30	0.27	1.17	0.20	1.07	0.11	1.01	0.09
177	1.41	0.27	1.21	0.24	1.13	0.18	1.04	0.11	1.01	0.09
184	1.34	0.27	1.12	0.24	1.08	0.18	1.00	0.10	0.99	0.08
192	1.28	0.27	1.03	0.22	1.03	0.18	0.97	0.10	0.97	0.08
201	1.25	0.29	1.00	0.23	1.02	0.19	0.97	0.12	0.97	0.09
211	1.30	0.31	1.05	0.25	1.05	0.21	1.00	0.13	1.00	0.10
Average:	1.47	0.29	1.39	0.30	1.14	0.20	1.08	0.13	0.99	0.09

[a] $R = 1/N \Sigma_{i=1}^{N} \rho_i/\rho_M$

[b] $\sigma = [1/N - 1 \Sigma_{i=1}^{N} (1 - \rho_1/\rho_M)^2]^{1/2}$

[c] Current operational model, essentially Jacchia 1960

[d] The Bruce modification to Walker's analytical Jacchia model (Ref. 6)

[e] See Ref. 27. Fractional density changes and time delay at 150 km have been applied at all altitudes

[f] The present model

D. DISCUSSION

The U.S. Standard 1962 atmosphere is completely static, but the "L-DENSITY" model has a variation due to change in $F_{10.7}$. From results shown in Table 10, for these two models alone, it would appear that some type of $F_{10.7}$ variation is useful above, but not below, about 170 km. The present model has no short-term radio flux variation designed into it, yet it has a standard deviation of the residuals considerably less than that of L-DENSITY; thus, the apparent short-term $F_{10.7}$ dependence in previous models is not sufficient to completely reflect actual changes in density.

The J-W-B model eliminates the density inversion near 150 km that troubles the more recent Jacchia models, but retains the exospheric temperature variations with $F_{10.7}$, local time, magnetic activity, and other characteristics of the Walker-Jacchia formulation (Ref. 6). A dramatic improvement at low altitudes is the result.

The Champion model (Ref. 27), as used here, introduces a constant time delay between geomagnetic variations and the resulting density changes. The magnetic disturbance not only increases the exospheric temperature, but also increases the calculated density by an empirically derived, disturbance-dependent fraction at all altitudes. The improvement of σ results primarily from the time delay.

The present model differs in several ways from the other four models of Table 10. It is not simply a modification to an existing model, but, rather, is an attempt to "start from scratch," incorporating the relevant physical processes that we believe dominate the upper atmosphere. The two most significant results of this approach are (1) incorporation of an altitude-dependent time delay, and (2) recognition that the atomic and molecular constituents of the atmosphere do not necessarily share a common temperature. The latter makes the reasoning behind the present one-parameter models, i.e., T_∞, somewhat suspect at low altitudes where the number density of molecules becomes significant relative to that of the atoms.

The present model is not restricted by the artificial constraint that the boundary conditions at 120 km remain constant; in fact, the density at 120 km can vary by as much as a factor of 2 during a severe magnetic storm. Krankowsky, et al. (Ref. 28) observe similarly large variations near 120 km on a day-to-day or day-to-night basis, even in the absence of exceptionally great magnetic activity. Density variations are minimal in this model near 150 km, and even there the variations can be as much as 80 percent.

1. LIMITATIONS OF MODEL

The form of the present model is believed adequate to describe and predict density changes in the atmosphere at midlatitudes between 140 and 200 km. It must be emphasized, however, that the numerical values of the coefficients apply to conditions during the LOGACS flight. In particular, long-term variations in $F_{10.7}$ and diurnal variations were not considered.

From an operational viewpoint, this model, alone, is not adequate to describe the drag history of any satellite that is at low altitudes above about 50° latitude for a significant time period. From a physical viewpoint, the model is incomplete because temporal relaxation effects and the horizontal transfer of energy from the polar and auroral regions have not been included, but will be incorporated later.

The quiet-time temperatures derived from the model are near 810° and 320°K for the atomic and molecular constituents, respectively (a mass of 29 was used for the molecules to correct for the oxygen actually present). Even for extremely undisturbed times, a 300°K temperature difference is surprisingly large, and brings into question the original functional form. If assumption 3 (Section B), that the temperature of any one constituent is constant above the reference level, is replaced by the assumption that all constituents have the same temperature at a given altitude but that the temperature profile is altitude dependent, another plausible form for the model can be generated. In particular, a temperature profile of the form shown in Eq. (8) is being used to fit the data

$$T = T_{\infty} \left| 1 - a \exp\left[-(z - z_o)/b \right] \right| \tag{8}$$

where T_{∞}, a, and b are constants, and z_o is the reference altitude. The results of this fitting procedure will be discussed in Section V.

2. EXTENSIONS OF MODEL

The correlation between changes in density and changes in solar radio flux is well known. Presumably, a change in radio flux is accompanied by a change in solar EUV flux; therefore, the heat input to the atmosphere should be similar to that due to particle dumping. Equation (5) can be rewritten as

$$g(\tau, a_p, \bar{F}) = \ln[a_p(t - \tau) + 1] + 0.027(\bar{F} - 183) \tag{9}$$

where $\bar{F}$ is the five-day average of the Ottawa 10.7 cm solar flux ending on the day for which ρ is to be calculated; $\bar{F}$ is measured in solar flux units of 10^{-22} W-m^{-2}-Hz^{-1}. The numerical factors were chosen to agree with the average $\bar{F}$ observed during the LOGACS flight, and to match the density variations of CIRA 1965 (Ref. 28) near 220 km.

Diurnal effects must eventually be included. Several investigators have measured these changes (Refs. 29 and 30), but the large discrepancies make more complete sampling necessary before they can be included quantitatively. Other effects, such as horizontal energy transport and the latitude dependence of the solar "bulge," will be included when a more sophisticated model becomes necessary.

An independent model applicable to the polar and auroral regions is being developed. It will be joined to this midlatitude model in a future report.

3. EXAMPLES OF MODEL

If the altitude-dependent time delay is ignored (or, alternatively, if the value of a_p has been constant for about 24 hr), the present model can be compared with other models currently in use. Figure 56 shows the total mass density plotted against altitude for $a_p = 0$, 20, 59, and 200, calculated from the present model for $\bar{F} = 175$ flux units; and the density plotted from the CIRA 1965 model for $a_p = 5$ and 200. When compared with the CIRA model, the major characteristics of this new model are immediately apparent: variable density at 120 km, generally higher densities between 140 and 220 km, and much larger variability with a_p.

Figure 57 shows how ρ, calculated from the extended model, depends on $\bar{F}$, when $\bar{F}$ varies from 125 to 200 flux units for $a_p = 5$.

Figure 58 shows the response of the atmosphere to an impulsive change in a_p, as reflected by the present model. An increase of a_p from zero to 100 is made to occur from time $t = 0$ to $t = 0.5$. The density of the atmosphere is unaffected until $t = 5.5$ hr, when a "bump" appears between 147 and 157 km. The bump then splits into two. The high-altitude bump moves to successively higher altitudes, and becomes increasingly broad until, by $t = 8$ hr, the whole atmosphere above 172 km is disturbed. Between 146 and 171 km, however, the density has already returned to its quiet-time value; by $t = 8.5$ hr, the density above 171 km has also returned to its prestorm value. The low-altitude bump moves very slowly toward lower altitudes, and becomes somewhat narrower; by $t = 8.5$ hr, this bump is the only indication that a storm has occurred.

The traveling density bulges are the result of a slowly moving disturbance, accompanied by mass flow, propagating away from the 150 km region where the initial heating occurred. The existence of density bulges considerably complicates the interpretation of any measurements of atmospheric density. For example, in the extreme case shown in Fig. 58, a measurement of density scale height made vertically upward at $t = 7.5$ hr would show the scale height to be reasonable up to about 145 km, then vary

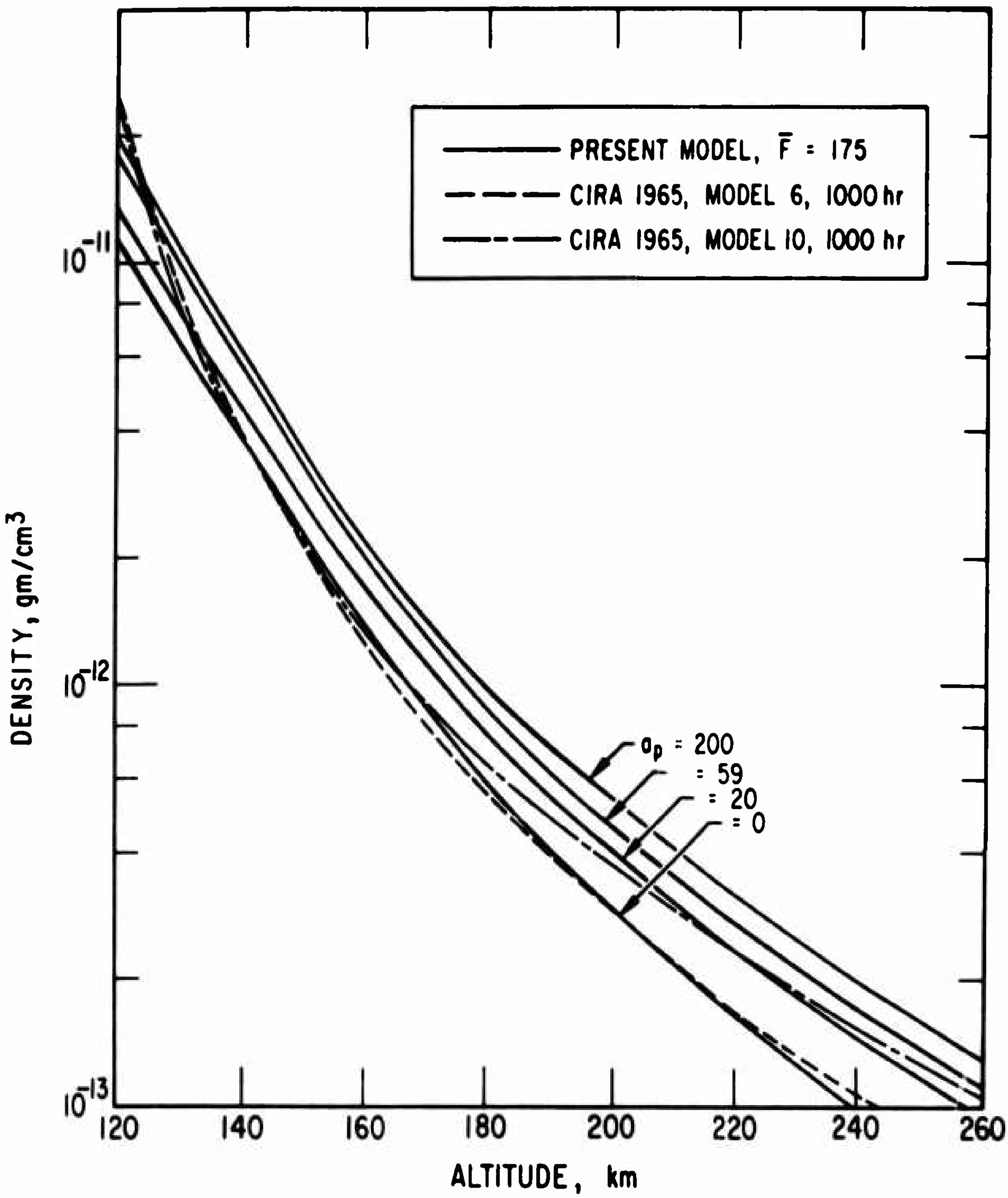

Fig. 56. Comparison Between Steady-State Density Prediction of Present Model and That of CIRA 1965

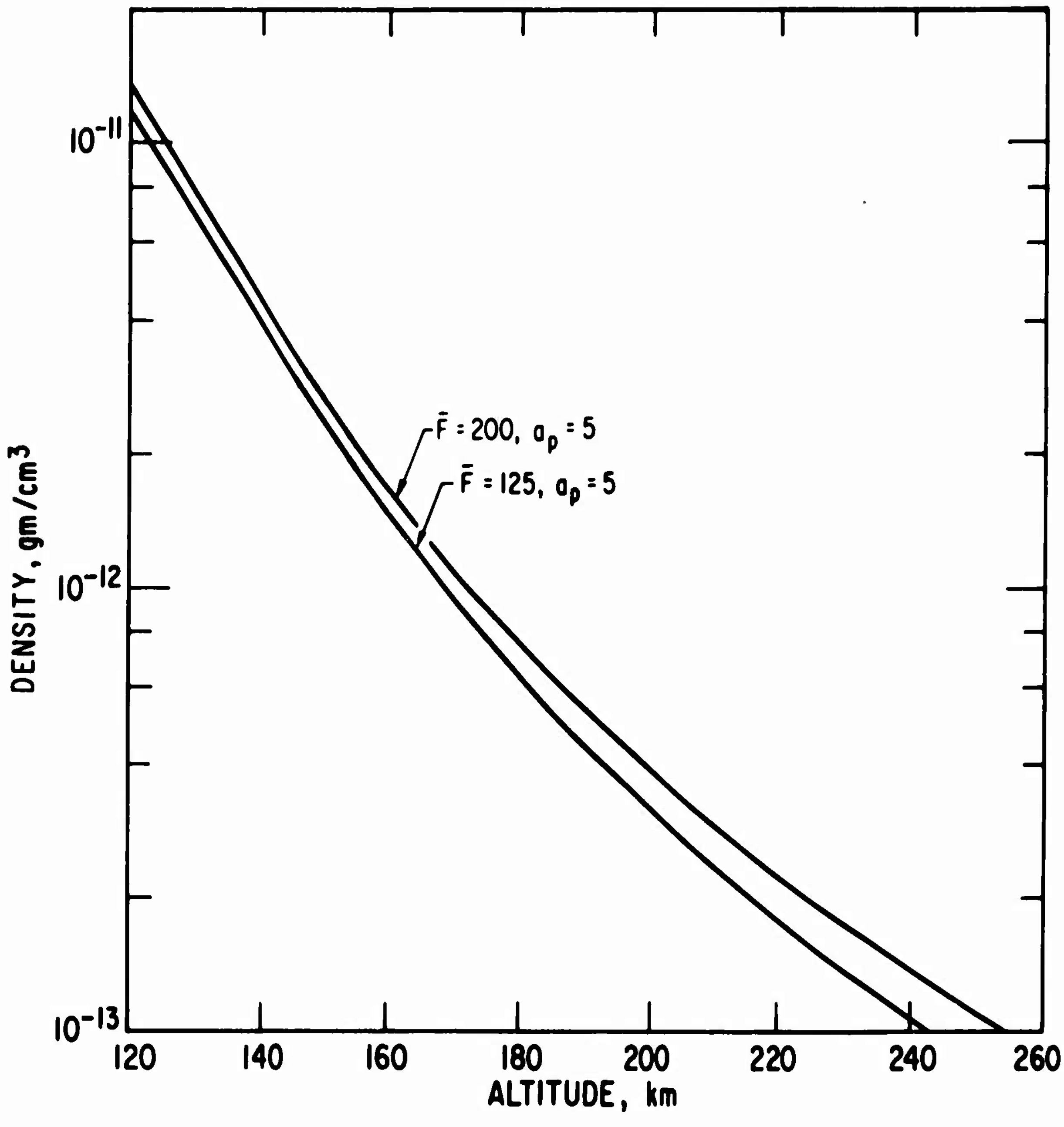

Fig. 57. Variation of Present Model with $\overline{F}$

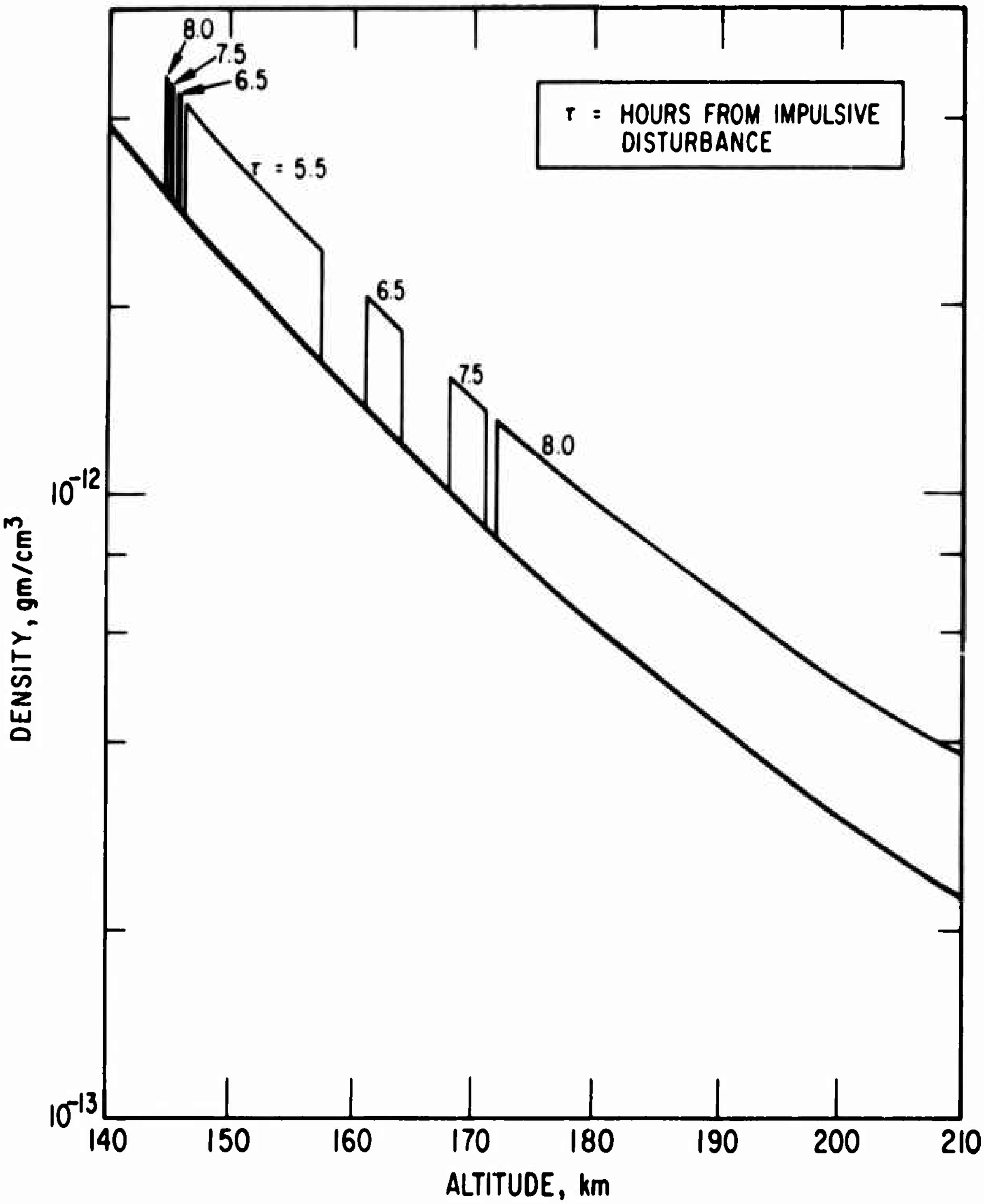

Fig. 58. Response of Present Model to a 30 min Impulsive Disturbance with Maximum Amplitude a_p = 100

wildly from positive to negative through minus infinity and back to positive, all in the space of a few kilometers; it would then settle down until an altitude of about 168 km was reached, then repeat the same gyrations, although somewhat less violently. The model predicts that negative scale heights rarely occur in the absence of particle dumping; therefore, for small disturbances ($a_p < 40$), density measurements would indicate only that there were regions where the deduced scale height became very large, then suddenly small before returning to a more normal value.

An example of the density response to a very moderate magnetic storm is shown in Fig. 59. It is assumed that a_p was zero until time $t = 0$ when it linearly increased to 100 in a period of 3 hr, remained stable for another 3 hr, then linearly decayed to zero in the succeeding 15 hr. The density is shown as a function of altitude for $t = 5$ to 20 hr. Again, the effect of the traveling disturbances is evident. Since previous model atmospheres cannot reproduce this very complicated response of the atmosphere to even moderate storms, it is to be expected that this new model will allow much more accurate and detailed prediction of the drag force experienced by low-altitude satellites.

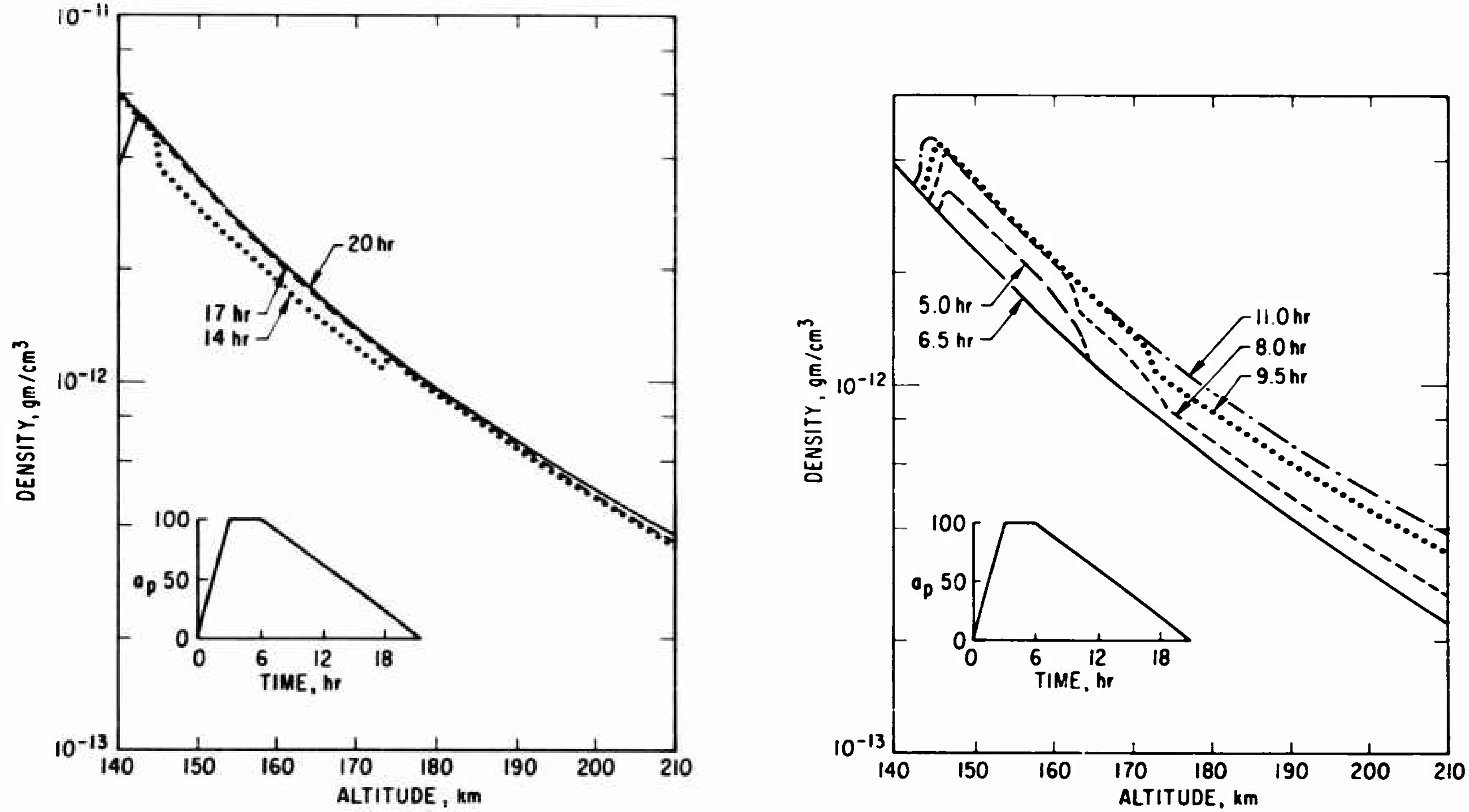

a. 5-11 hr after Onset

b. 14-20 hr after Onset

Fig. 59. Response of Present Model to Realistic Moderate Magnetic Storm

SECTION V

ALTERNATE FORMULATION OF MIDLATITUDE MODEL

A. INTRODUCTION

Section IV proposed a novel physical explanation for the midlatitude results of the LOGACS experiment, namely, that during magnetically quiet times each individual constituent of the atmosphere has its own characteristic temperature. It was found that atomic species were several hundred degrees warmer than molecular species. Since atomic oxygen is created with a considerable excess of kinetic energy, it must be somewhat hotter than either molecular oxygen or nitrogen, but the temperature difference necessary to fit the data was surprisingly large.

Accordingly, the exact opposite assumption, that all constituents share a common altitude-dependent temperature, is made in this section. The other characteristics of the previous model are retained; most importantly, the altitude-dependent time delay between variations in the magnetic field and the corresponding variations in atmospheric density has been left unchanged.

B. TEMPERATURE/DENSITY PROFILE

The following temperature profile was assumed

$$T = T_\infty \{1 - a \exp[-(z - z_0)/H_T]\} \tag{10}$$

where T is the temperature at any altitude z, T_∞ is the exospheric temperature, a and H_T are positive constants, and z_0 is the reference altitude. At z_0, one finds

$$T = T_0 \equiv (1 - a)T_\infty \tag{11}$$

Assuming diffusive equilibrium, it can be shown that the number density of any one constituent is given by

$$n = n_0(T_0/T)^{1+H_T/H_M} \exp\left[-(z - z_0)/H_M\right] \tag{12}$$

where n_0 is the number density at z_0 and H_M is the exospheric scale height. We have defined

$$H_M \equiv kT_\infty/mg \tag{13}$$

where k is Boltzmann's constant, m is the mass of the constituent, and g is the acceleration due to gravity (assumed constant between 120 and 250 km where the model applies).

This temperature profile can be made to fit that used by CIRA by adjusting the values of a, H_T, and T_0, and is of the same form as that which Jacchia assumes. It has several properties which are very useful in a wide variety of atmospheric problems. The temperatures gradient, given by

$$\frac{\partial T}{\partial z} = T_\infty \frac{a}{H_T} \exp\left[-(z - z_0)/H_T\right] \tag{14}$$

is everywhere positive, and both its magnitude and curvature are adjustable by varying a and H_T. The temperature profile makes the transition to the isothermal case smoothly as $a \rightarrow 0$, and there is no discontinuous change of form in the number density profile. The number density of any one constituent in a vertical column above some height z is simply given by

$$N = nH \tag{15}$$

where n is evaluated at z and

$$H = H(z) \equiv kT(z)/mg \tag{16}$$

Similarly, the pressure due to that constituent is

$$p = nkT = p_0 \left[\frac{(1 - a)\exp[-(z - z_0)/H_T]}{1 - a\exp[-(z - z_0)/H_T]}\right]^{H_T/H_M} \tag{17}$$

which is useful in employing the analytical isobaric models of Thomas and Ching (Refs. 7 and 31), for instance.

The total mass density is given by

$$\rho = \sum_i M_i n_i \tag{18}$$

$$\rho = (T_0/T)\left[\rho_{0,O}q + \rho_{0,N_2}q^{1.75} + \rho_{0,O_2}q^2\right] \tag{19}$$

where $\rho_{0,O}$, ρ_{0,N_2}, and ρ_{0,O_2} are the mass densities of the three major constituents at the 120 km reference level, and

$$q = (T_0/T)^{H_T/H_{16}} \exp[-(z - z_0)/H_{16}] \tag{20}$$

where H_{16} is the exospheric scale height of atomic oxygen.

C. METHOD OF ANALYSIS

The model derived in the earlier section represented the density at any altitude by a sum of four exponentials with scale heights independent of the level of magnetic activity; the preexponential factors were functions of the magnetic index a_p and altitude only.

In deriving the present model, the time-independent densities from the previous model were used as inputs to a least-squares routine which sought the best values of T_0, a, H_T, and the individual mass densities at the reference level $\rho_{0,O}$, ρ_{0,O_2}, and ρ_{0,N_2} for eleven values of a_p between zero and 400. The fits in each case showed standard deviations of less than 2 percent in the logarithmic density ratios, which were well within the experimental uncertainties. Several runs were then made allowing z_0 to vary from its arbitrarily assigned value of 120 km. The results gave a least-squares fit to the data that always yielded a value of z_0 within a few kilometers of 120 km, and the standard deviation was not significantly changed. Consequently, z_0 was held fixed at 120 km for the computations reported here.

D. RESULTS

Figures 60 through 62 show the quality of the least-squares fits. The points are the density values calculated from the previous model; the solid curves represent the best-fit densities of this new formulation.

Figures 63 and 64 show how each of the six fitted parameters mentioned above vary as a function of $\ln(a_p + 1)$. The sharp break at 4.1 ($a_p = 59$) reflects the discontinuous nature of the prior model, which we have attributed to the onset of significant particle dumping.

The variations in the temperature parameters can be approximated analytically, as follows

$$x \equiv \ln(a_p + 1) \tag{21}$$

$$a = 0.6719 + 0.027x \tag{22}$$

$$T_0(°K) = \begin{cases} 536.3 - 2.31x & a_p \le 59 \quad (23a) \\ 505.5 - 2.03x & a_p > 59 \quad (23b) \end{cases}$$

$$H_T(km) = \begin{cases} 305.6 - 2.87x & a_p \le 59 \quad (24a) \\ 308.0 - 2.98x & a_p > 59 \quad (24b) \end{cases}$$

$$T_\infty(°K) = \begin{cases} 1612 + 175.4x & a_p \le 59 \quad (25a) \\ 1658 + 204.6x & a_p > 59 \quad (25b) \end{cases}$$

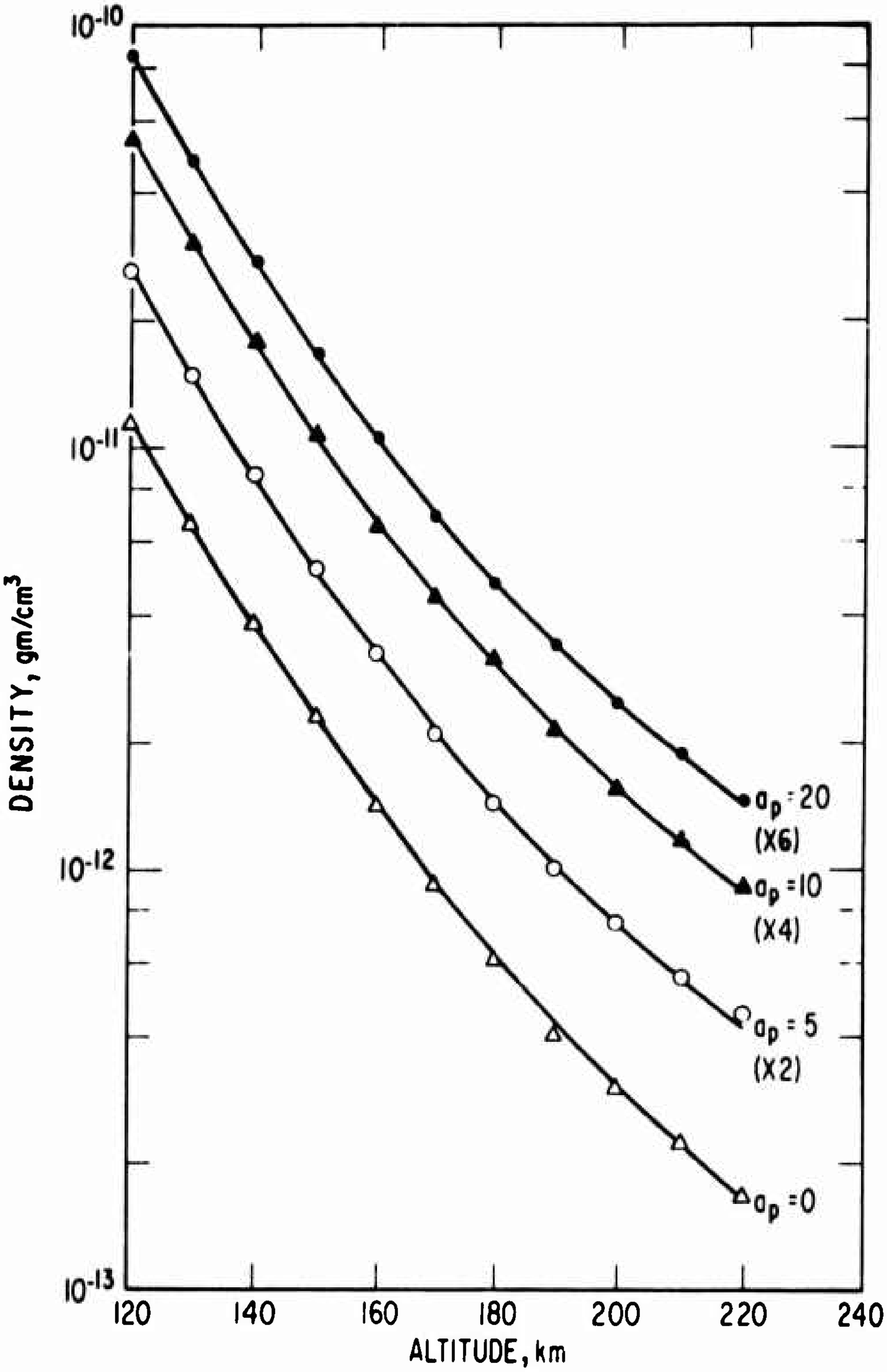

Fig. 60. Mass Density vs Altitude for a_p = 0, 5, 10, and 20. (Points taken from Section IV; solid curves are best-fit solutions reported here.)

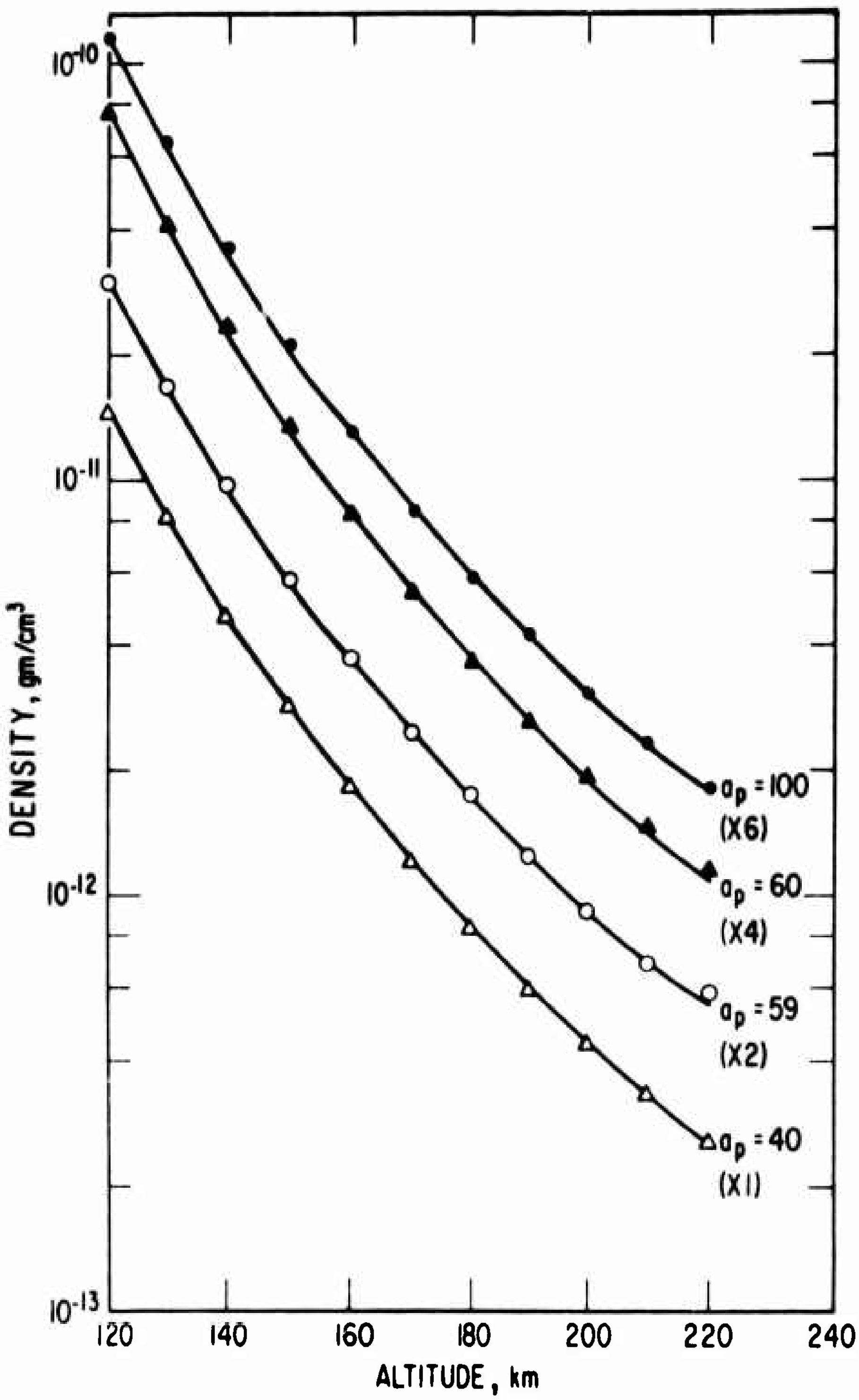

Fig. 61. Mass Density vs Altitude for a_p = 40, 59, 60, and 100. (Points taken from Section IV; solid curves are best-fit solutions reported here.)

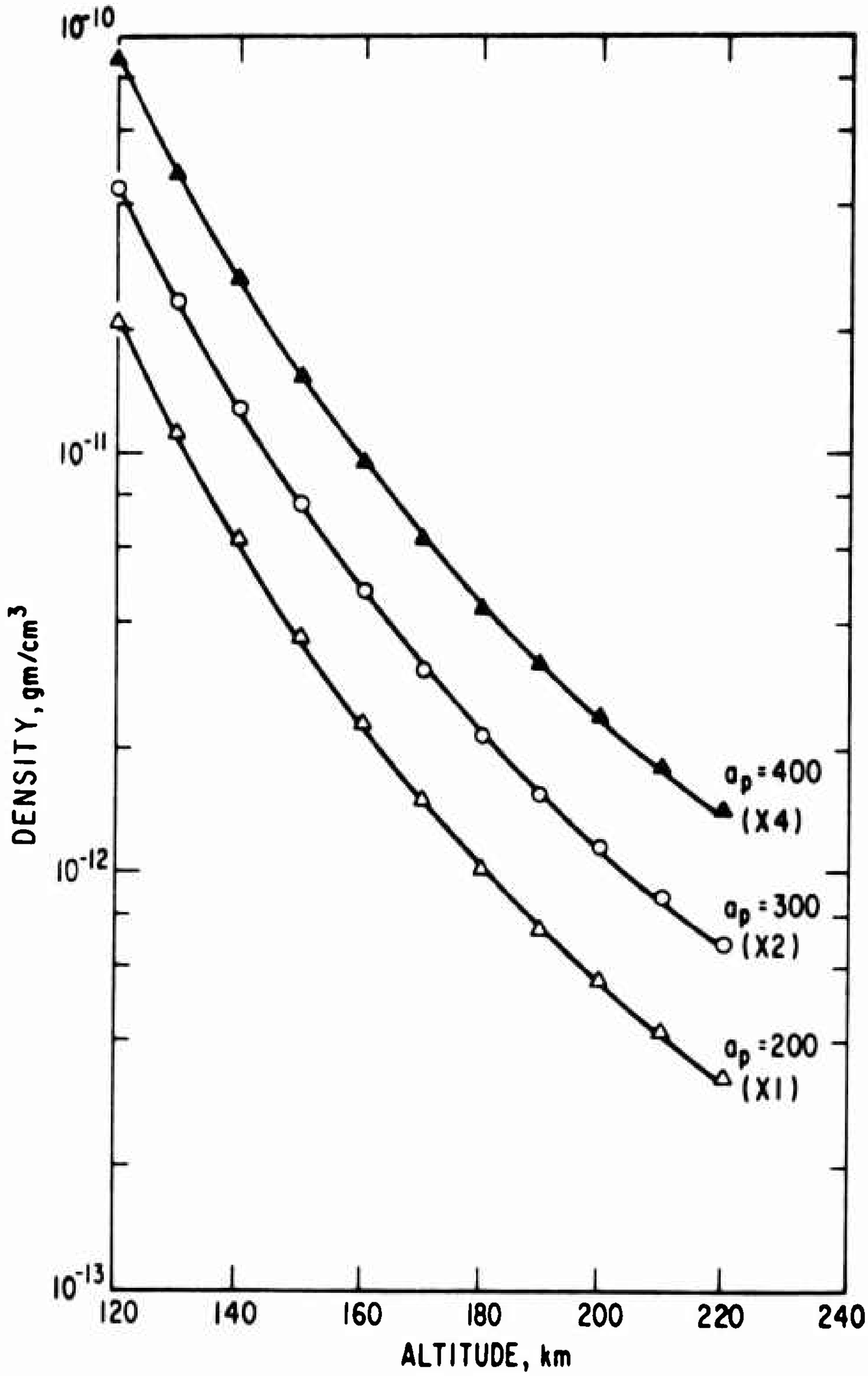

Fig. 62. Mass Density vs Altitude for a_p = 200, 300, and 400. (Points taken from Section IV; solid curves are best-fit solutions reported here.)

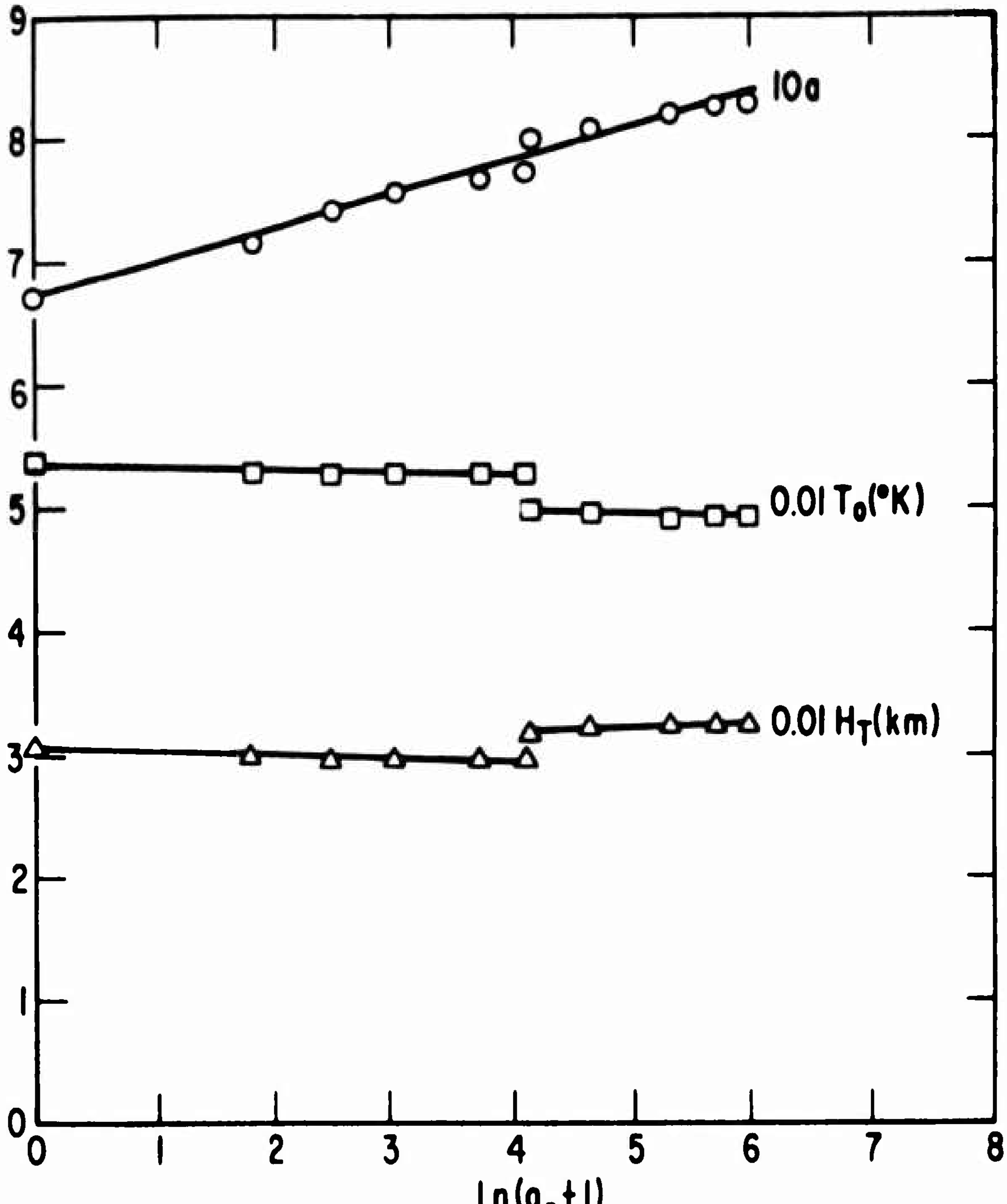

Fig. 63. Temperature Distribution Parameters H_T, T_0, and a. [Solid lines represent Eqs. (22), (23), and (24).]

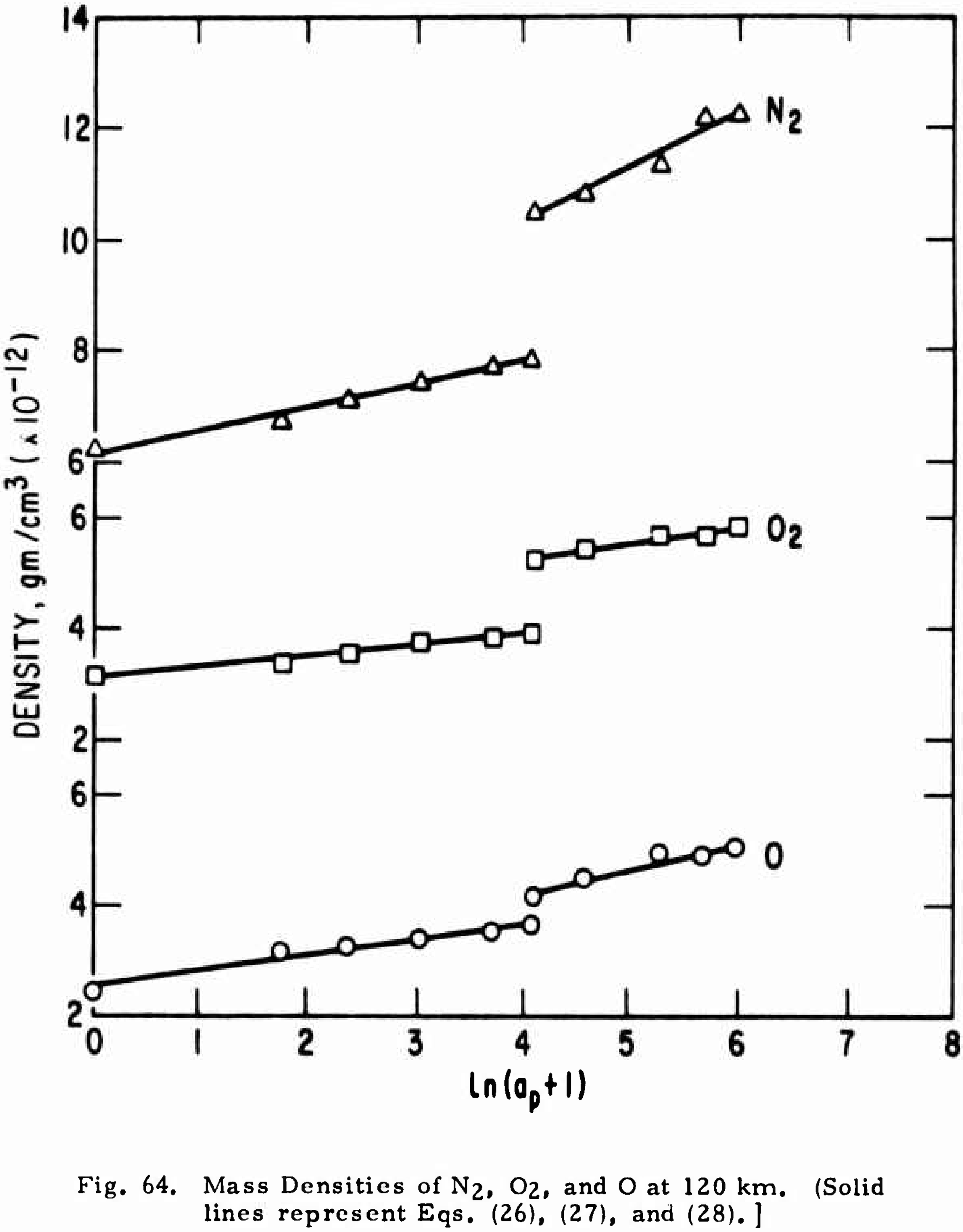

Fig. 64. Mass Densities of N_2, O_2, and O at 120 km. (Solid lines represent Eqs. (26), (27), and (28).]

The densities of the three individual constituents O, O_2, and N_2 at the 120 km reference level vary in much the same way

$$\rho_{0,O}(10^{-12}\mathrm{gm/cm}^3) = \begin{cases} 2.537 + 0.286x & a_p \le 59 \quad (26a) \\ 2.405 + 0.449x & a_p > 59 \quad (26b) \end{cases}$$

$$\rho_{0,N_2}(10^{-12}\mathrm{gm/cm}^3) = \begin{cases} 6.173 + 0.413x & a_p \le 59 \quad (27a) \\ 6.447 + 0.972x & a_p > 59 \quad (27b) \end{cases}$$

$$\rho_{0,O_2}(10^{-12}\mathrm{gm/cm}^3) = \begin{cases} 3.103 + 0.201x & a_p \ge 59 \quad (28a) \\ 4.160 + 0.273x & a_p > 59 \quad (28b) \end{cases}$$

Equations (22) through (28) were derived using a linear least-squares fit. Equations (22), (23), and (24) are shown as solid lines in Fig. 63; Eqs. (26), (27), and (28) are similarly shown in Fig. 64.

1. DISCUSSION

It is much more convenient to use the model form given in Section IV (a sum of four exponentials) to calculate the total density at any given altitude than it is to use the present formulation. However, the sum of exponentials cannot easily be used to obtain any information on the detailed behavior of the individual components of the atmosphere, nor is it adequate to calculate the pressure, which is necessary to determine the dynamical response of the atmosphere to changes in the heating rate.

The present form of the midlatitude model is constructed so that it reproduces the same densities and density variations as the previous one, and in addition, makes explicit the relationships among all the temperatures and composition parameters.

Figure 65 shows the steady-state temperature profile for five values of a_p, as calculated by the present model. A quiet and a disturbed profile taken from CIRA are shown for comparison. At the 120 km reference level the present model indicates that the temperature is 150 to 200° hotter than CIRAs fixed 355°K, and decreases with increasing magnetic activity. Above approximately 150 km, the temperatures indicated by this model increase monotonically with a_p, but at a much slower rate than CIRA predicts. The temperature gradient is about half that of CIRAs: for $a_p = 0$ and 400 we have $(\partial T/\partial z)$ 150 km $\sim$3.2 and 6.7°/km, respectively, while for the two extreme CIRA models the gradients are 6.1 and 13.7°/km. The exospheric temperatures predicted by the present model are considerably higher than CIRAs; since this model was derived from data below 220 km only, not much credence should be placed on extrapolated values, including T_∞, far above about 250 km.

Figures 66 through 68 show the steady-state altitude profiles of the number densities of atomic oxygen, molecular nitrogen, and molecular oxygen, respectively, for the same five values of a_p. The altitude dependence of all three constituents in this model is much closer to being exponential than is the CIRA's dependence, which is a consequent of the smaller temperature gradient in this model. The number density of molecular nitrogen is fairly close to that predicted by CIRA, although below 140 km it is somewhat less. Both atomic and molecular oxygen have densities that are considerably larger than the CIRA densities. None of the constituents in the present model exhibit the inversion below about 180 km that is a characteristic of fixing the total mass above a reference level, as is the practice in most other models.

Tables 11 through 21 list the temperature (°K), mean molecular mass (amu), number densities of O, N_2, and O_2 (cm^{-3}), and pressure scale height (km) every 5 km between 120 and 220 km for a_p = 0, 5, 10, 20, 40, 59, 60, 100, 200, 300, and 400. The discontinuous change in the model between a_p = 59 and 60 is an artifact representing the onset of particle dumping; LOGACS saw a large change in density near a_p = 60, but the data were not

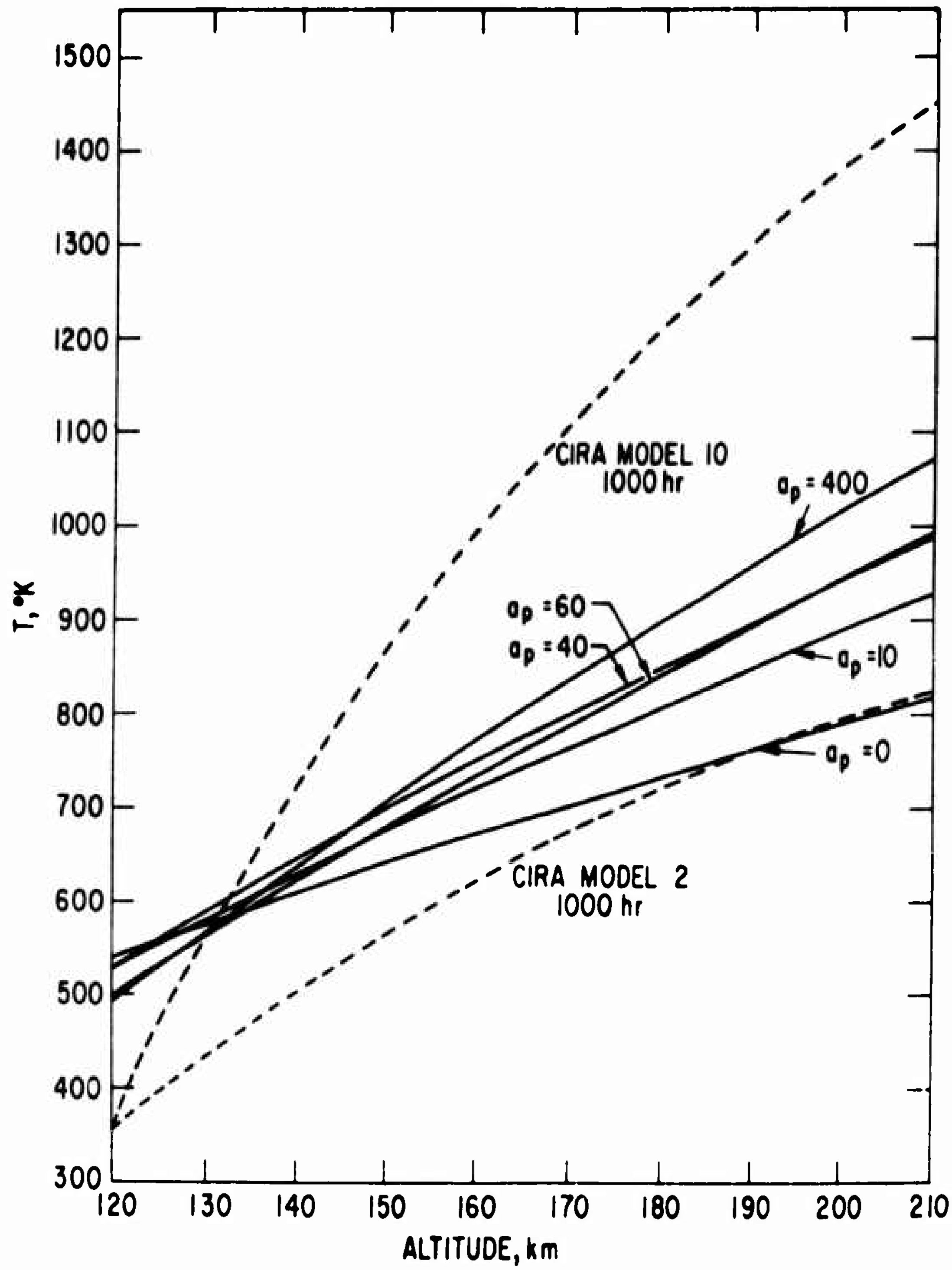

Fig. 65. Temperature Profiles for a_p = 0, 10, 40, 60, and 400. (Dashed curves are extreme CIRA temperatures.)

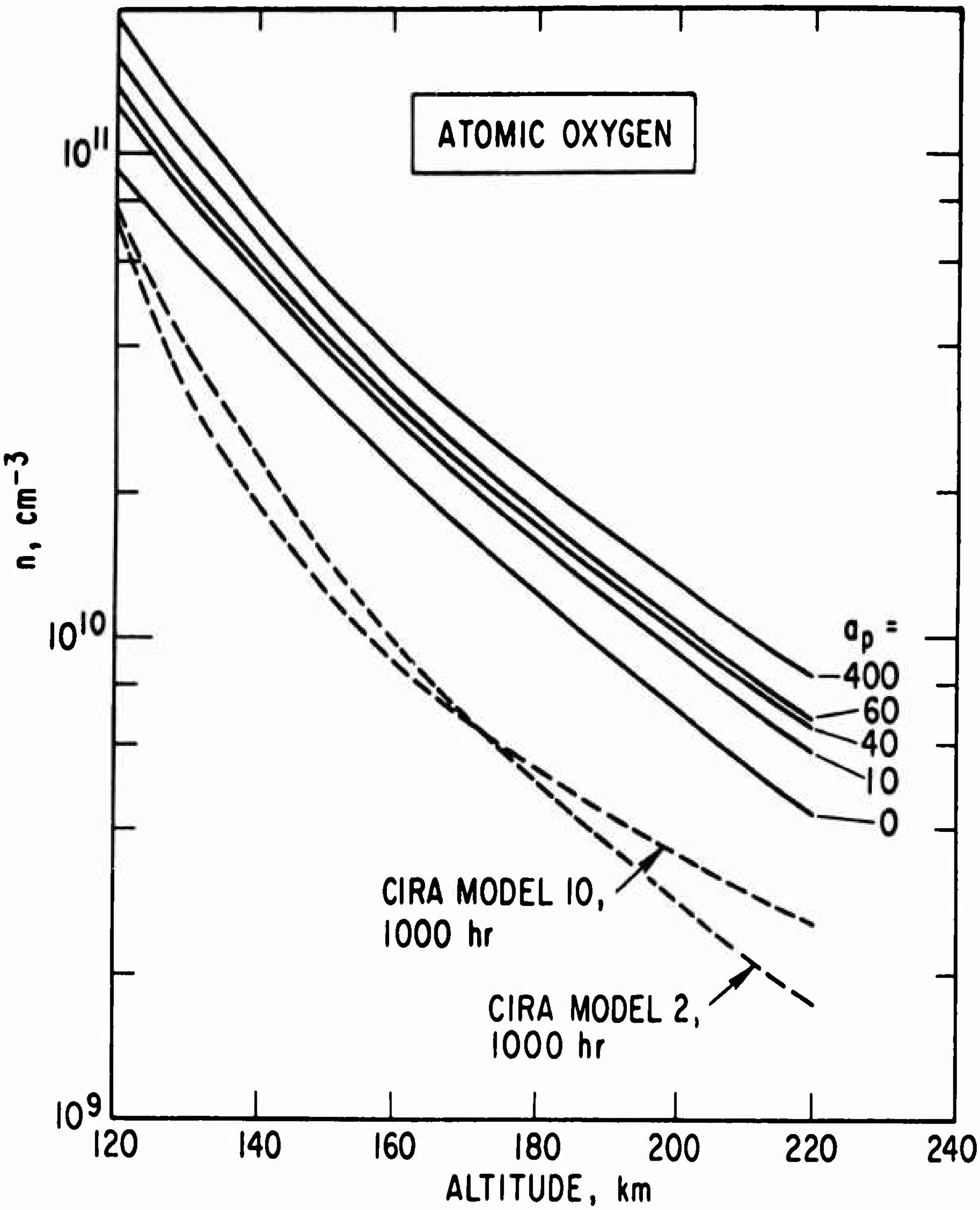

Fig. 66. Number Density Profiles, n, of Atomic Oxygen for a_p = 0, 10, 40, 60, and 400. (Dashed curves are extreme CIRA number densities.)

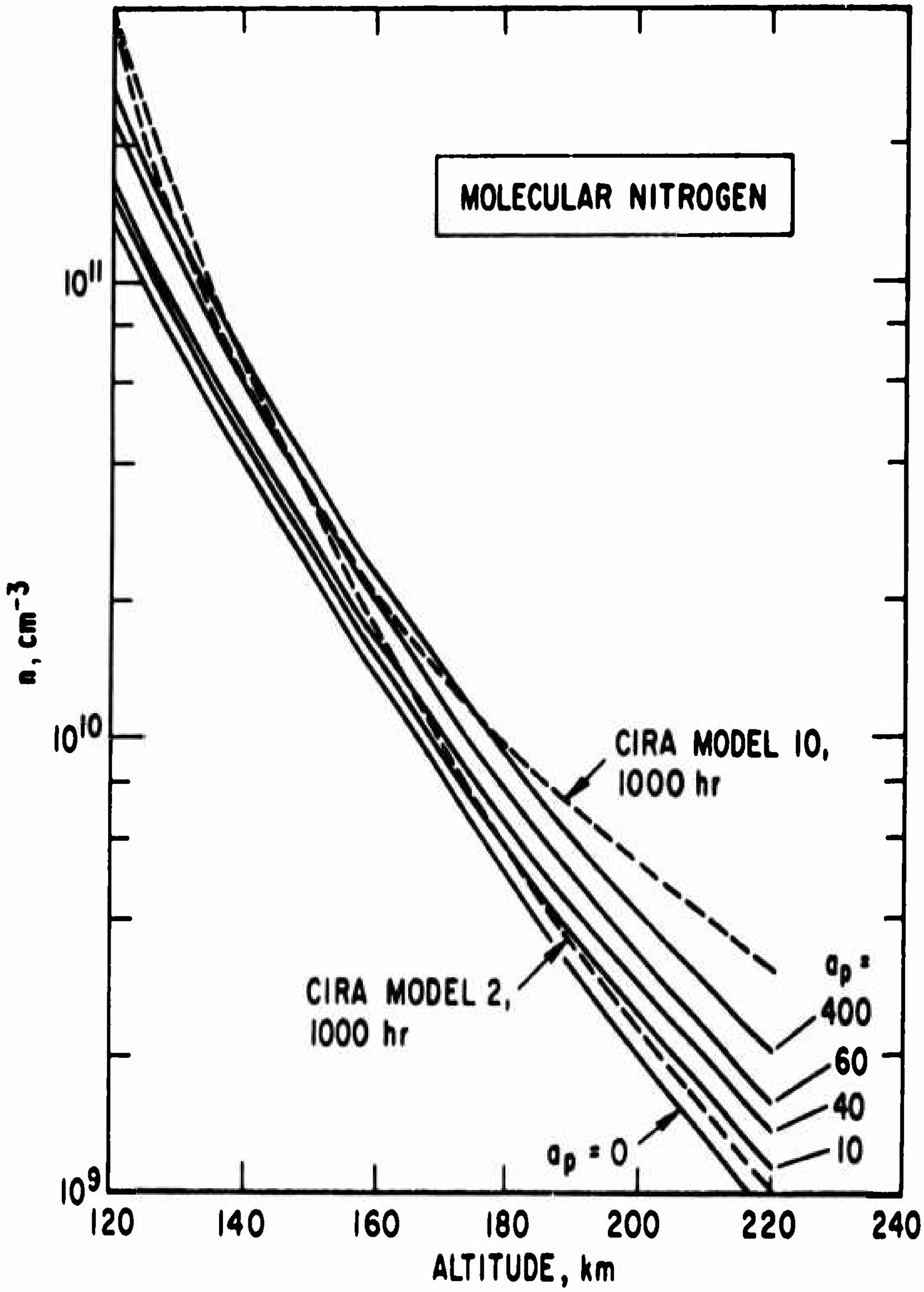

Fig. 67. Number Density Profiles, n, of Molecular Nitrogen for ap = 0, 10, 40, 60, and 400. (Dashed curves are extreme CIRA number densities.)

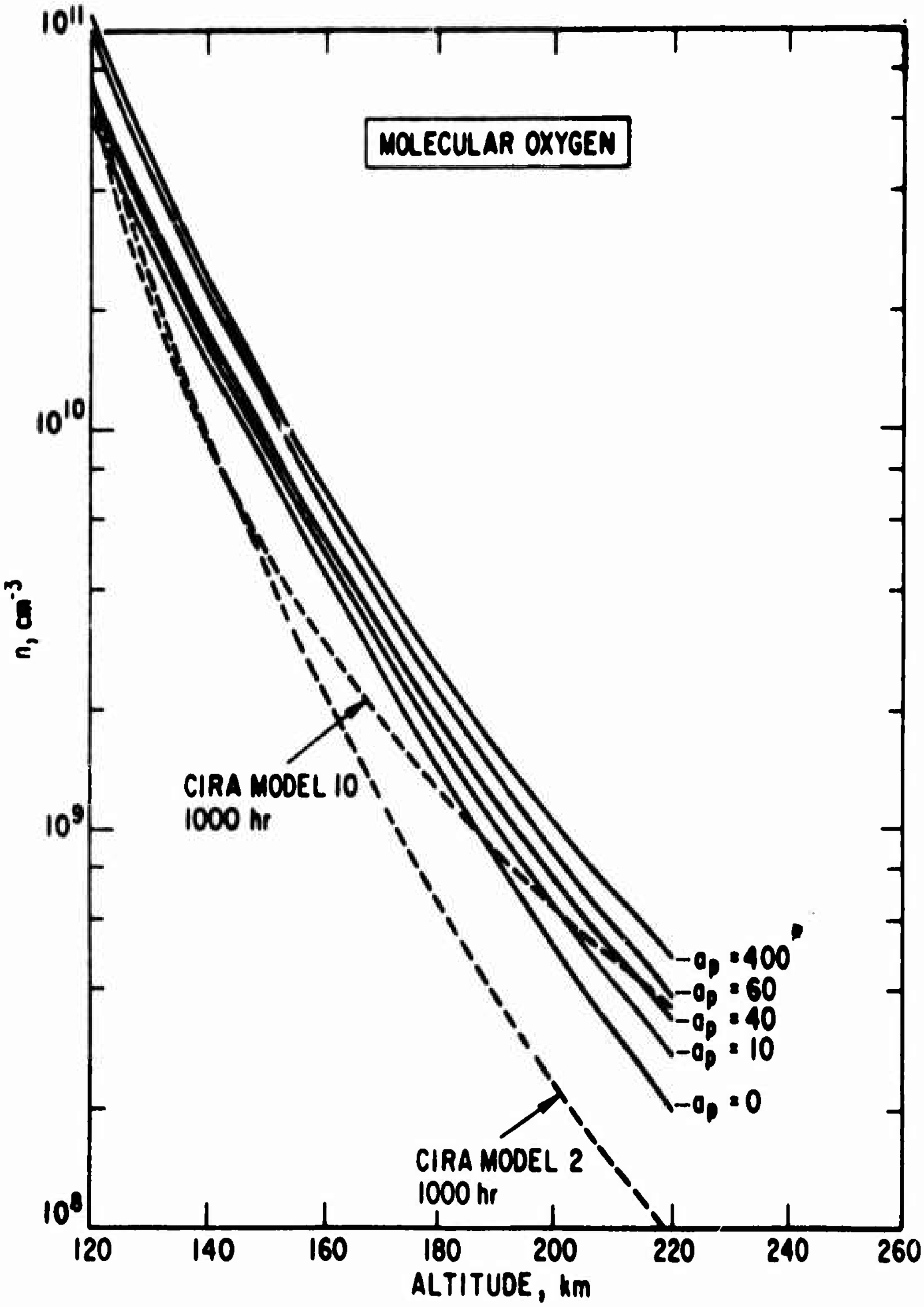

Fig. 68. Number Density Profiles, n, of Molecular Oxygen for a_p = 0, 10, 40, 60, and 400. (Dashed curves are extreme CIRA number densities.)

Table 11. Atmospheric Parameters for $\overline{F}$ = 183, a_p = 0

$\overline{F}$ = 183, a_p = 0

Z	T	MBAR	NO	NN2	NO2	H
120	5.387E+02	2.497E+01	9.211E+10	1.351E+11	5.913E+10	1.908E+01
125	5.563E+02	2.454E+01	7.559E+10	9.794E+10	4.114E+10	2.005E+01
130	5.738E+02	2.412E+01	6.246E+10	7.176E+10	2.896E+10	2.104E+01
135	5.904E+02	2.370E+01	5.192E+10	5.309E+10	2.061E+10	2.205E+01
140	6.077E+02	2.328E+01	4.340E+10	3.963E+10	1.481E+10	2.308E+01
145	6.243E+02	2.288E+01	3.648E+10	2.984E+10	1.075E+10	2.413E+01
150	6.406E+02	2.248E+01	3.081E+10	2.264E+10	7.869E+09	2.520E+01
155	6.567E+02	2.210E+01	2.615E+10	1.730E+10	5.808E+09	2.627E+01
160	6.724E+02	2.174E+01	2.228E+10	1.331E+10	4.320E+09	2.736E+01
165	6.880E+02	2.138E+01	1.907E+10	1.031E+10	3.236E+09	2.846E+01
170	7.033E+02	2.105E+01	1.638E+10	8.032E+09	2.441E+09	2.955E+01
175	7.183E+02	2.072E+01	1.412E+10	6.294E+09	1.852E+09	3.065E+01
180	7.331E+02	2.042E+01	1.221E+10	4.958E+09	1.414E+09	3.175E+01
185	7.476E+02	2.013E+01	1.060E+10	3.925E+09	1.086E+09	3.284E+01
190	7.620E+02	1.986E+01	9.223E+09	3.123E+09	8.386E+08	3.393E+01
195	7.761E+02	1.961E+01	8.050E+09	2.496E+09	6.507E+08	3.501E+01
200	7.899E+02	1.937E+01	7.046E+09	2.003E+09	5.074E+08	3.607E+01
205	8.036E+02	1.914E+01	6.183E+09	1.614E+09	3.974E+08	3.713E+01
210	8.170E+02	1.893E+01	5.439E+09	1.306E+09	3.127E+08	3.817E+01
215	8.302E+02	1.873E+01	4.795E+09	1.060E+09	2.470E+08	3.919E+01
220	8.432E+02	1.855E+01	4.238E+09	8.639E+08	1.959E+08	4.020E+01

Table 12. Atmospheric Parameters for $\overline{F}$ = 183, a_p = 5

$\overline{F}$ = 183, a_p = 5

Z	T	MBAR	NO	NN2	NO2	H
120	5.299E+02	2.441E+01	1.197E+11	1.457E+11	6.379E+10	1.920E+01
125	5.520E+02	2.396E+01	9.724E+10	1.044E+11	4.382E+10	2.038E+01
130	5.738E+02	2.352E+01	7.967E+10	7.581E+10	3.057E+10	2.157E+01
135	5.951E+02	2.309E+01	6.579E+10	5.574E+10	2.163E+10	2.279E+01
140	6.161E+02	2.268E+01	5.473E+10	4.145E+10	1.549E+10	2.403E+01
145	6.368E+02	2.228E+01	4.583E+10	3.115E+10	1.123E+10	2.528E+01
150	6.571E+02	2.189E+01	3.862E+10	2.363E+10	8.227E+09	2.655E+01
155	6.771E+02	2.153E+01	3.272E+10	1.809E+10	6.087E+09	2.782E+01
160	6.968E+02	2.118E+01	2.788E+10	1.396E+10	4.545E+09	2.909E+01
165	7.161E+02	2.085E+01	2.386E+10	1.086E+10	3.423E+09	3.037E+01
170	7.351E+02	2.054E+01	2.052E+10	8.502E+09	2.599E+09	3.165E+01
175	7.538E+02	2.025E+01	1.772E+10	6.702E+09	1.987E+09	3.292E+01
180	7.722E+02	1.998E+01	1.537E+10	5.317E+09	1.530E+09	3.419E+01
185	7.903E+02	1.972E+01	1.337E+10	4.242E+09	1.186E+09	3.544E+01
190	8.080E+02	1.948E+01	1.168E+10	3.403E+09	9.250E+08	3.669E+01
195	8.255E+02	1.925E+01	1.023E+10	2.744E+09	7.255E+08	3.792E+01
200	8.427E+02	1.904E+01	8.993E+09	2.223E+09	5.721E+08	3.914E+01
205	8.596E+02	1.884E+01	7.927E+09	1.810E+09	4.534E+08	4.035E+01
210	8.763E+02	1.866E+01	7.006E+09	1.479E+09	3.611E+08	4.153E+01
215	8.926E+02	1.849E+01	6.209E+09	1.214E+09	2.889E+08	4.270E+01
220	9.087E+02	1.833E+01	5.516E+09	1.000E+09	2.321E+08	4.385E+01

Table 13. Atmospheric Parameters for $\overline{F} = 183$, $a_p = 10$

$\bar{F} = 183$, $a_p = 10$

Z	T	MBAR	NO	NN2	NO2	H
120	5.280E+02	2.449E+01	1.232E+11	1.540E+11	6.742E+10	1.906E+01
125	5.534E+02	2.404E+01	9.945E+10	1.096E+11	4.602E+10	2.035E+01
130	5.785E+02	2.361E+01	8.109E+10	7.929E+10	3.198E+10	2.167E+01
135	6.031E+02	2.318E+01	6.673E+10	5.817E+10	2.258E+10	2.301E+01
140	6.273E+02	2.278E+01	5.538E+10	4.324E+10	1.618E+10	2.436E+01
145	6.510E+02	2.238E+01	4.632E+10	3.251E+10	1.174E+10	2.572E+01
150	6.744E+02	2.201E+01	3.900E+10	2.472E+10	8.627E+09	2.710E+01
155	6.974E+02	2.165E+01	3.306E+10	1.897E+10	6.408E+09	2.849E+01
160	7.200E+02	2.131E+01	2.818E+10	1.470E+10	4.808E+09	2.988E+01
165	7.423E+02	2.099E+01	2.415E+10	1.148E+10	3.642E+09	3.127E+01
170	7.641E+02	2.069E+01	2.081E+10	9.039E+09	2.782E+09	3.266E+01
175	7.856E+02	2.040E+01	1.801E+10	7.167E+09	2.142E+09	3.405E+01
180	8.068E+02	2.014E+01	1.565E+10	5.720E+09	1.662E+09	3.543E+01
185	8.275E+02	1.988E+01	1.366E+10	4.594E+09	1.298E+09	3.681E+01
190	8.490E+02	1.965E+01	1.197E+10	3.712E+09	1.021E+09	3.817E+01
195	8.681E+02	1.942E+01	1.052E+10	3.015E+09	8.077E+08	3.952E+01
200	8.878E+02	1.922E+01	9.278E+09	2.461E+09	6.426E+08	4.086E+01
205	9.072E+02	1.902E+01	8.209E+09	2.019E+09	5.141E+08	4.218E+01
210	9.263E+02	1.884E+01	7.284E+09	1.664E+09	4.133E+08	4.348E+01
215	9.451E+02	1.867E+01	6.481E+09	1.377E+09	3.338E+08	4.477E+01
220	9.636E+02	1.851E+01	5.782E+09	1.144E+09	2.709E+08	4.604E+01

Table 14. Atmospheric Parameters for $\overline{F}$ = 183, a_p = 20

$\overline{F}$ = 183, a_p = 20

Z	T	MBAR	NO	NN2	NO2	H
120	5.296E+02	2.450E+01	1.280E+11	1.603E+11	7.015E+10	1.908E+01
125	5.561E+02	2.405E+01	1.030E+11	1.138E+11	4.777E+10	2.045E+01
130	5.831E+02	2.362E+01	8.381E+10	8.217E+10	3.316E+10	2.183E+01
135	6.096E+02	2.320E+01	6.888E+10	6.026E+10	2.341E+10	2.324E+01
140	6.357E+02	2.279E+01	5.712E+10	4.481E+10	1.679E+10	2.466E+01
145	6.613E+02	2.241E+01	4.775E+10	3.374E+10	1.221E+10	2.610E+01
150	6.865E+02	2.204E+01	4.022E+10	2.570E+10	8.990E+09	2.755E+01
155	7.113E+02	2.169E+01	3.410E+10	1.977E+10	6.698E+09	2.901E+01
160	7.357E+02	2.135E+01	2.910E+10	1.536E+10	5.043E+09	3.047E+01
165	7.597E+02	2.104E+01	2.497E+10	1.204E+10	3.834E+09	3.193E+01
170	7.832E+02	2.074E+01	2.154E+10	9.509E+09	2.941E+09	3.339E+01
175	8.064E+02	2.046E+01	1.867E+10	7.567E+09	2.275E+09	3.485E+01
180	8.292E+02	2.020E+01	1.625E+10	6.064E+09	1.773E+09	3.630E+01
185	8.516E+02	1.995E+01	1.421E+10	4.890E+09	1.392E+09	3.775E+01
190	8.736E+02	1.972E+01	1.247E+10	3.968E+09	1.100E+09	3.918E+01
195	8.953E+02	1.950E+01	1.099E+10	3.237E+09	8.749E+08	4.060E+01
200	9.165E+02	1.930E+01	9.712E+09	2.655E+09	6.998E+08	4.201E+01
205	9.375E+02	1.910E+01	8.612E+09	2.188E+09	5.629E+08	4.340E+01
210	9.581E+02	1.892E+01	7.660E+09	1.812E+09	4.550E+08	4.477E+01
215	9.783E+02	1.876E+01	6.832E+09	1.506E+09	3.697E+08	4.613E+01
220	9.982E+02	1.860E+01	6.110E+09	1.258E+09	3.017E+08	4.747E+01

Table 15. Atmospheric Parameters for $\overline{F} = 183$, $a_p = 40$

$\overline{F} = 183$, $a_p = 40$

Z	T	MBAR	NO	NN2	NO2	H
120	5.290E+02	2.447E+01	1.339E+11	1.662E+11	7.277E+10	1.912E+01
125	5.582E+02	2.403E+01	1.074E+11	1.177E+11	4.943E+10	2.055E+01
130	5.869E+02	2.359E+01	8.721E+10	8.490E+10	3.427E+10	2.200E+01
135	6.152E+02	2.318E+01	7.157E+10	6.224E+10	2.420E+10	2.347E+01
140	6.429E+02	2.278E+01	5.931E+10	4.630E+10	1.736E+10	2.496E+01
145	6.703E+02	2.240E+01	4.957E+10	3.490E+10	1.264E+10	2.647E+01
150	6.971E+02	2.203E+01	4.175E+10	2.662E+10	9.329E+09	2.798E+01
155	7.235E+02	2.169E+01	3.541E+10	2.052E+10	6.967E+09	2.950E+01
160	7.495E+02	2.136E+01	3.024E+10	1.598E+10	5.260E+09	3.103E+01
165	7.750E+02	2.105E+01	2.597E+10	1.255E+10	4.012E+09	3.256E+01
170	8.001E+02	2.076E+01	2.242E+10	9.944E+09	3.088E+09	3.408E+01
175	8.248E+02	2.049E+01	1.946E+10	7.938E+09	2.398E+09	3.561E+01
180	8.491E+02	2.023E+01	1.697E+10	6.382E+09	1.876E+09	3.712E+01
185	8.729E+02	1.998E+01	1.486E+10	5.165E+09	1.479E+09	3.863E+01
190	8.964E+02	1.976E+01	1.306E+10	4.206E+09	1.174E+09	4.013E+01
195	9.194E+02	1.954E+01	1.153E+10	3.444E+09	9.376E+08	4.161E+01
200	9.421E+02	1.934E+01	1.021E+10	2.835E+09	7.534E+08	4.308E+01
205	9.644E+02	1.915E+01	9.067E+09	2.346E+09	6.087E+08	4.453E+01
210	9.863E+02	1.898E+01	8.080E+09	1.950E+09	4.944E+08	4.597E+01
215	1.008E+03	1.881E+01	7.221E+09	1.628E+09	4.035E+08	4.739E+01
220	1.029E+03	1.865E+01	6.471E+09	1.365E+09	3.309E+08	4.879E+01

Table 16. Atmospheric Parameters for $\overline{F}$ - 183, a_p = 59

$\overline{F}$ = 183, a_p = 59

Z	T	MBAR	NO	NN2	NO2	W
120	5.287E+02	2.444E+01	1.380E+11	1.693E+11	7.412E+10	1.913E+01
125	5.588E+02	2.399E+01	1.105E+11	1.197E+11	5.027E+10	2.060E+01
130	5.884E+02	2.356E+01	8.963E+10	8.627E+10	3.482E+10	2.209E+01
135	6.175E+02	2.314E+01	7.351E+10	6.321E+10	2.458E+10	2.360E+01
140	6.461E+02	2.274E+01	6.088E+10	4.702E+10	1.764E+10	2.512E+01
145	6.743E+02	2.236E+01	5.086E+10	3.545E+10	1.285E+10	2.666E+01
150	7.020E+02	2.200E+01	4.284E+10	2.705E+10	9.489E+09	2.821E+01
155	7.292E+02	2.166E+01	3.634E+10	2.087E+10	7.094E+09	2.977E+01
160	7.559E+02	2.134E+01	3.103E+10	1.627E+10	5.363E+09	3.133E+01
165	7.822E+02	2.103E+01	2.666E+10	1.280E+10	4.096E+09	3.289E+01
170	8.081E+02	2.074E+01	2.303E+10	1.015E+10	3.158E+09	3.445E+01
175	8.335E+02	2.047E+01	2.000E+10	8.113E+09	2.456E+09	3.601E+01
180	8.585E+02	2.022E+01	1.745E+10	6.532E+09	1.925E+09	3.756E+01
185	8.831E+02	1.998E+01	1.529E+10	5.295E+09	1.520E+09	3.910E+01
190	9.073E+02	1.975E+01	1.345E+10	4.318E+09	1.209E+09	4.063E+01
195	9.311E+02	1.954E+01	1.188E+10	3.542E+09	9.675E+08	4.214E+01
200	9.544E+02	1.934E+01	1.053E+10	2.921E+09	7.790E+08	4.364E+01
205	9.774E+02	1.915E+01	9.359E+09	2.421E+09	6.307E+08	4.513E+01
210	1.000E+03	1.898E+01	8.348E+09	2.016E+09	5.134E+08	4.660E+01
215	1.022E+03	1.882E+01	7.467E+09	1.687E+09	4.199E+08	4.805E+01
220	1.044E+03	1.866E+01	6.698E+09	1.417E+09	3.451E+08	4.948E+01

Table 17. Atmospheric Parameters for $\overline{F}$ = 183, a_p = 60

$\overline{F}$ = 183, a_p = 60

Z	T	MBAR	NO	NN2	NO2	H
120	4.985E+02	2.492E+01	1.572E+11	2.264E+11	9.911E+10	1.769E+01
125	5.296E+02	2.446E+01	1.240E+11	1.566E+11	6.560E+10	1.915E+01
130	5.602E+02	2.402E+01	9.931E+10	1.107E+11	4.448E+10	2.063E+01
135	5.904E+02	2.359E+01	8.052E+10	7.977E+10	3.082E+10	2.213E+01
140	6.201E+02	2.318E+01	6.602E+10	5.846E+10	2.176E+10	2.366E+01
145	6.494E+02	2.279E+01	5.467E+10	4.350E+10	1.562E+10	2.520E+01
150	6.781E+02	2.241E+01	4.568E+10	3.282E+10	1.139E+10	2.676E+01
155	7.065E+02	2.205E+01	3.847E+10	2.506E+10	8.419E+09	2.833E+01
160	7.344E+02	2.171E+01	3.264E+10	1.935E+10	6.300E+09	2.991E+01
165	7.619E+02	2.139E+01	2.788E+10	1.509E+10	4.768E+09	3.150E+01
170	7.889E+02	2.109E+01	2.396E+10	1.188E+10	3.646E+09	3.308E+01
175	8.155E+02	2.080E+01	2.071E+10	9.437E+09	2.815E+09	3.467E+01
180	8.417E+02	2.053E+01	1.799E+10	7.553E+09	2.192E+09	3.625E+01
185	8.675E+02	2.028E+01	1.570E+10	6.089E+09	1.721E+09	3.783E+01
190	8.929E+02	2.004E+01	1.376E+10	4.942E+09	1.361E+09	3.940E+01
195	9.179E+02	1.982E+01	1.211E+10	4.036E+09	1.084E+09	4.096E+01
200	9.426E+02	1.961E+01	1.070E+10	3.315E+09	8.693E+08	4.251E+01
205	9.668E+02	1.941E+01	9.492E+09	2.738E+09	7.012E+08	4.405E+01
210	9.906E+02	1.922E+01	8.445E+09	2.273E+09	5.688E+08	4.557E+01
215	1.014E+03	1.905E+01	7.537E+09	1.896E+09	4.638E+08	4.708E+01
220	1.037E+03	1.889E+01	6.747E+09	1.589E+09	3.802E+08	4.857E+01

Table 18. Atmospheric Parameters for $\overline{F} = 183$, $a_p = 100$

$\overline{F} = 183$, $a_p = 100$

Z	T	MBAR	NO	NN2	NO2	H
120	4.956E+02	2.479E+01	1.697E+11	2.340E+11	1.024E+11	1.768E+01
125	5.280E+02	2.432E+01	1.335E+11	1.612E+11	6.749E+10	1.920E+01
130	5.599E+02	2.388E+01	1.066E+11	1.136E+11	4.563E+10	2.074E+01
135	5.913E+02	2.345E+01	8.623E+10	8.168E+10	3.155E+10	2.230E+01
140	6.222E+02	2.303E+01	7.059E+10	5.979E+10	2.225E+10	2.389E+01
145	6.527E+02	2.264E+01	5.839E+10	4.446E+10	1.597E+10	2.549E+01
150	6.827E+02	2.227E+01	4.875E+10	3.353E+10	1.164E+10	2.711E+01
155	7.122E+02	2.192E+01	4.104E+10	2.561E+10	8.609E+09	2.874E+01
160	7.413E+02	2.158E+01	3.482E+10	1.979E+10	6.448E+09	3.038E+01
165	7.699E+02	2.127E+01	2.974E+10	1.545E+10	4.886E+09	3.202E+01
170	7.981E+02	2.097E+01	2.556E+10	1.218E+10	3.742E+09	3.366E+01
175	8.258E+02	2.069E+01	2.210E+10	9.686E+09	2.894E+09	3.530E+01
180	8.532E+02	2.043E+01	1.920E+10	7.764E+09	2.258E+09	3.694E+01
185	8.801E+02	2.018E+01	1.677E+10	6.270E+09	1.776E+09	3.857E+01
190	9.065E+02	1.995E+01	1.471E+10	5.098E+09	1.408E+09	4.020E+01
195	9.326E+02	1.973E+01	1.296E+10	4.172E+09	1.124E+09	4.181E+01
200	9.583E+02	1.952E+01	1.146E+10	3.434E+09	9.036E+08	4.341E+01
205	9.836E+02	1.933E+01	1.018E+10	2.842E+09	7.307E+08	4.500E+01
210	1.008E+03	1.915E+01	9.062E+09	2.365E+09	5.943E+08	4.657E+01
215	1.033E+03	1.898E+01	8.097E+09	1.977E+09	4.859E+08	4.812E+01
220	1.057E+03	1.883E+01	7.256E+09	1.660E+09	3.993E+08	4.966E+01

Table 19. Atmospheric Parameters for $\overline{F}$ = 183, a_p = 200

$\bar{F}$ = 183, a_p = 200

Z	T	MBAR	NO	NN2	NO2	H
120	4.920E+02	2.463E+01	1.867E+11	2.449E+11	1.065E+11	1.767E+01
125	5.261E+02	2.416E+01	1.461E+11	1.678E+11	6.980E+10	1.926E+01
130	5.597E+02	2.371E+01	1.163E+11	1.178E+11	4.701E+10	2.088E+01
135	5.927E+02	2.327E+01	9.384E+10	8.453E+10	3.243E+10	2.252E+01
140	6.252E+02	2.286E+01	7.667E+10	6.178E+10	2.283E+10	2.419E+01
145	6.573E+02	2.247E+01	6.334E+10	4.591E+10	1.638E+10	2.587E+01
150	6.888E+02	2.210E+01	5.283E+10	3.462E+10	1.194E+10	2.756E+01
155	7.199E+02	2.176E+01	4.446E+10	2.646E+10	8.840E+09	2.927E+01
160	7.505E+02	2.143E+01	3.771E+10	2.046E+10	6.629E+09	3.098E+01
165	7.806E+02	2.112E+01	3.221E+10	1.600E+10	5.031E+09	3.269E+01
170	8.103E+02	2.083E+01	2.770E+10	1.263E+10	3.861E+09	3.440E+01
175	8.395E+02	2.056E+01	2.395E+10	1.006E+10	2.992E+09	3.612E+01
180	8.683E+02	2.030E+01	2.083E+10	8.081E+09	2.341E+09	3.782E+01
185	8.966E+02	2.006E+01	1.821E+10	6.540E+09	1.847E+09	3.952E+01
190	9.245E+02	1.984E+01	1.599E+10	5.330E+09	1.468E+09	4.121E+01
195	9.520E+02	1.963E+01	1.410E+10	4.372E+09	1.176E+09	4.289E+01
200	9.790E+02	1.943E+01	1.248E+10	3.609E+09	9.477E+08	4.456E+01
205	1.006E+03	1.925E+01	1.109E+10	2.995E+09	7.688E+08	4.621E+01
210	1.032E+03	1.908E+01	9.893E+09	2.499E+09	6.273E+08	4.784E+01
215	1.058E+03	1.891E+01	8.850E+09	2.095E+09	5.147E+08	4.946E+01
220	1.083E+03	1.876E+01	7.942E+09	1.764E+09	4.244E+08	5.106E+01

Table 20. Atmospheric Parameters for $\overline{F} = 183$, $a_p = 300$

$\overline{F} = 183$, $a_p = 300$

Z	T	MBAR	NO	NN2	NO2	H
120	4.943E+02	2.476E+01	1.844E+11	2.622E+11	1.059E+11	1.765E+01
125	5.302E+02	2.431E+01	1.440E+11	1.794E+11	6.932E+10	1.929E+01
130	5.657E+02	2.387E+01	1.144E+11	1.260E+11	4.670E+10	2.096E+01
135	6.006E+02	2.345E+01	9.230E+10	9.043E+10	3.225E+10	2.265E+01
140	6.349E+02	2.305E+01	7.541E+10	6.619E+10	2.276E+10	2.436E+01
145	6.688E+02	2.267E+01	6.231E+10	4.929E+10	1.637E+10	2.609E+01
150	7.021E+02	2.231E+01	5.202E+10	3.727E+10	1.197E+10	2.783E+01
155	7.349E+02	2.197E+01	4.381E+10	2.856E+10	8.892E+09	2.958E+01
160	7.672E+02	2.165E+01	3.720E+10	2.216E+10	6.694E+09	3.134E+01
165	7.990E+02	2.134E+01	3.182E+10	1.738E+10	5.101E+09	3.311E+01
170	8.304E+02	2.106E+01	2.740E+10	1.377E+10	3.931E+09	3.487E+01
175	8.612E+02	2.079E+01	2.374E+10	1.101E+10	3.060E+09	3.664E+01
180	8.916E+02	2.054E+01	2.068E+10	8.877E+09	2.404E+09	3.840E+01
185	9.215E+02	2.030E+01	1.811E+10	7.212E+09	1.905E+09	4.015E+01
190	9.510E+02	2.004E+01	1.593E+10	5.901E+09	1.522E+09	4.189E+01
195	9.800E+02	1.987E+01	1.408E+10	4.860E+09	1.224E+09	4.363E+01
200	1.009E+03	1.967E+01	1.249E+10	4.027E+09	9.917E+08	4.535E+01
205	1.037E+03	1.948E+01	1.112E+10	3.356E+09	8.083E+08	4.706E+01
210	1.064E+03	1.931E+01	9.938E+09	2.811E+09	6.627E+08	4.876E+01
215	1.092E+03	1.914E+01	8.910E+09	2.367E+09	5.463E+08	5.044E+01
220	1.119E+03	1.899E+01	8.012E+09	2.001E+09	4.526E+08	5.210E+01

Table 21. Atmospheric Parameters for $\overline{F}$ = 183, a_p = 400

$\overline{F}$ = 183, a_p = [redacted]

Z	T	MBAR	NO	NN2	NO2	H
120	4.949E+02	2.474E+01	1.896E+11	2.634E+11	1.100E+11	1.769E+01
125	5.312E+02	2.428E+01	1.481E+11	1.802E+11	7.198E+10	1.935E+01
130	5.670E+02	2.384E+01	1.177E+11	1.265E+11	4.850E+10	2.103E+01
135	6.022E+02	2.342E+01	9.489E+10	9.085E+10	3.350E+10	2.274E+01
140	6.369E+02	2.302E+01	7.753E+10	6.653E+10	2.365E+10	2.447E+01
145	6.711E+02	2.264E+01	6.407E+10	4.956E+10	1.702E+10	2.622E+01
150	7.047E+02	2.228E+01	5.349E+10	3.749E+10	1.246E+10	2.798E+01
155	7.379E+02	2.194E+01	4.507E+10	2.875E+10	9.260E+09	2.975E+01
160	7.705E+02	2.162E+01	3.828E+10	2.232E+10	6.976E+09	3.152E+01
165	8.026E+02	2.131E+01	3.275E+10	1.752E+10	5.321E+09	3.330E+01
170	8.343E+02	2.103E+01	2.821E+10	1.389E+10	4.103E+09	3.509E+01
175	8.654E+02	2.076E+01	2.445E+10	1.111E+10	3.197E+09	3.687E+01
180	8.961E+02	2.051E+01	2.131E+10	8.967E+09	2.514E+09	3.864E+01
185	9.263E+02	2.027E+01	1.867E+10	7.291E+09	1.994E+09	4.041E+01
190	9.561E+02	2.005E+01	1.643E+10	5.970E+09	1.594E+09	4.217E+01
195	9.853E+02	1.984E+01	1.452E+10	4.921E+09	1.284E+09	4.392E+01
200	1.014E+03	1.964E+01	1.289E+10	4.080E+09	1.041E+09	4.566E+01
205	1.043E+03	1.946E+01	1.148E+10	3.403E+09	8.489E+08	4.738E+01
210	1.071E+03	1.929E+01	1.026E+10	2.853E+09	6.966E+08	4.909E+01
215	1.098E+03	1.912E+01	9.204E+09	2.403E+09	5.748E+08	5.078E+01
220	1.125E+03	1.897E+01	8.290E+09	2.034E+09	4.766E+08	5.246E+01

sufficient to allow a more realistic (i.e., smoother) representation than has been used here.

2. ENERGY CONSIDERATIONS

A considerable quantity of energy is required to change the atmosphere from its quiet-time distribution to one which corresponds to values of a_p greater than zero. The total energy content per cm^2 above 120 km is given approximately by

$$E(a_p) \simeq \sum_{i=1}^{3} \int_{120}^{\infty} [m_i gz + 1.5\, kT(a_p)]n_i(a_p)\, dz \tag{29}$$

where the index runs over the three major atmospheric constituents. Figure 69 shows the quantity $E(a_p) - E(0)$ plotted against a_p; the dashed line represents a best-fit curve

$$E(a_p) - E(0) = 1.425 + 0.658\sqrt{a_p} \tag{30}$$

and the solid line represents a best-fit curve to the next higher order

$$E(a_p) - E(0) = 0.015 + 1.142\sqrt{a_p} - 0.024\, a_p \tag{31}$$

where E is measured in units of 10^4 erg/cm^2.

Thomas and Ching (Ref. 17) find that the total heat input at 150 km in Jacchia's models (Ref. 5) is proportional to $\sqrt{a_p}$, although there is some scatter. We find that in this model the total energy change in the upper atmosphere can be represented as being proportional to $\sqrt{a_p}$ [Eq. (30)], but the representation is roughly three times better when the expansion is carried to the next higher order, as in Eq. (31).

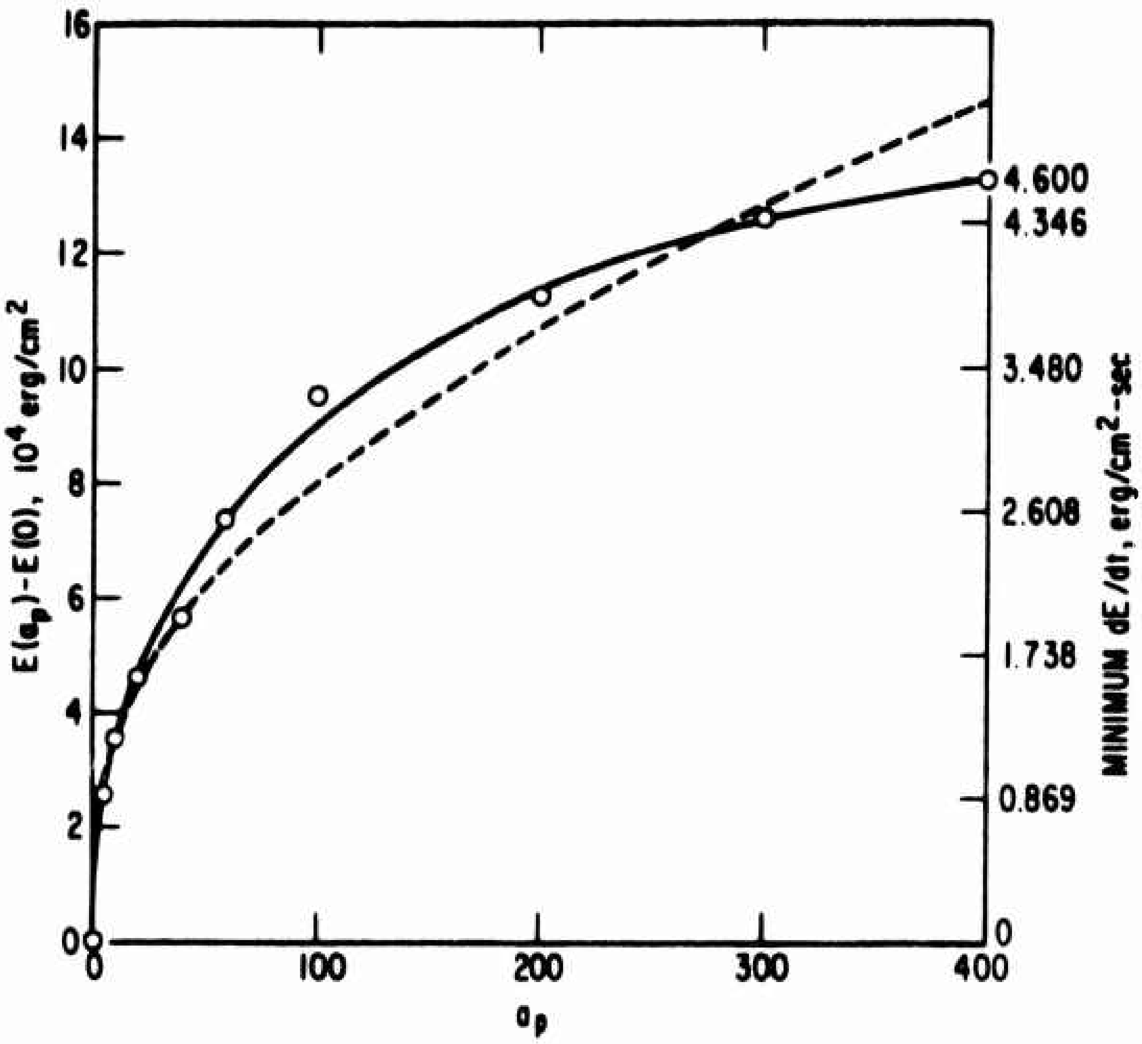

Fig. 69. Left Ordinate: Energy Content of Atmosphere Above 120 km. Right Ordinate: Minimum Energy Deposition Rate Above 120 km. [Points calculated from model; dashed and solid curves represent Eqs. (30) and (31), respectively.]

The rate of energy deposition cannot be obtained directly, since loss processes have not been included. It is possible, however, to find a lower limit to this rate. According to the time delays built into the model (Section IV), it takes 7.9 hr for the upper atmosphere to become completely accommodated to a step change in the value of a_p. Assuming that the energy deposition were constant over this entire time and that a_p changed from zero to $a_{p,max}$ and then remained constant, the average energy deposition rate is

$$\overline{\frac{dE}{dt}} \geq 0.396\sqrt{a_{p,max}} - 0.0083\, a_{p,max}\ \mathrm{erg/cm^2\text{-}sec} \tag{32}$$

This is the same form, up to a constant term, as in Eq. (31); the scale on the right side of Fig. 69 refers to this minimum average energy deposition rate.

The change in upper atmospheric energy with changes in a_p applies specifically to this particular model, which is valid for $\overline{F}_{10.7}$ = 183 flux units (10^{-22} erg/m^2-Hz) at about 1030 local time. It was suggested in Section IV that the response of the atmosphere to a variation of $\overline{F}_{10.7}$ from 183 could be treated as being similar to its response to a variation in $\ln(a_p + 1)$

$$\Delta\overline{F}_{10.7} \simeq 37 \times \Delta[\ln(a_p + 1)] \tag{33}$$

This relationship is a consequence of requiring that the densities predicted by this model vary with $\overline{F}_{10.7}$ in the same way as do the CIRA densities at about 220 km.

If Eq. (33) holds, we can obtain some knowledge of the variation in solar EUV flux with changes in $\overline{F}_{10.7}$, since by assuming the equality in Eq. (32) and combining it with Eq. (33) we find

$$\frac{\Delta Q}{\Delta \overline{F}} = [2.18 - 0.230Q - (4.723 - Q)^{1/2}]/[-8.51 + 18.5(4.723 - Q)^{1/2}] \tag{34}$$

where Q is the energy input in erg/cm^2-sec. The value $\Delta Q/\Delta F$ varies from 0.014 for Q = 1.0 to a maximum of 0.032 at Q = 3.5, then decreases with increasing energy input. During solar quiet times, Hinteregger and Hall (Ref. 32) find that the solar flux is about 3.0 erg/cm^2-sec between 100 and 1027 Å; this is the wavelength region that is thought to be most effective in heating the atmosphere above 120 km. Examination of Eq. (34) shows that Q can be no larger than ~4.7 erg/cm^2-sec. If this value is adopted for times of maximum solar radio flux ($\overline{F} \simeq 225$) and Eq. (34) is used to determine Q at $\overline{F} = 100$, we find $Q_{100} \simeq 1.45$ erg/cm^2-sec. Comparing this with the 3.0 erg/cm^2-sec incident, the heating efficiency is ~50 percent. The ratio of active-to-quiet-time Q is about 3.2. Since even during solar quiet times the atmosphere is optically thick in this wavelength region, if we assume that eddy diffusion is constant or small, then the heating efficiency should be nearly constant. This strongly suggests that the solar EUV flux itself varies by more than a factor of three when $\overline{F}_{10.7}$ varies from 100 to 225 flux units.

This conclusion is supported by some results from OSO-1, reported by Bourdeau, et al. (Ref. 34). They found that over a solar rotation, when $\overline{F}_{10.7}$ changed from about 80 to 125, the solar emission intensity between 170 and 370 Å changed from 0.37 to 0.55 erg/cm^2-sec, yielding $(1/Q)\Delta Q/\Delta F \simeq 0.009$. Over the wavelength range included in Eq. (34), we find that for $\overline{F}_{10.7} = 100$, $(1/Q)\Delta Q/\Delta F \simeq 0.014$ is in remarkably good agreement.

Hinteregger and Hall (Ref. 34) have reported some measurements of the variations with $\overline{F}_{10.7}$ of the intensities of six solar lines between 304 and 1025 Å. The measurements were made between the middle of April and the middle of June 1967, a period which included the time of LOGACS flight when $\overline{F}_{10.7}$ reached a maximum of 209. The maximum value of the previous solar rotation was 135; on the following rotation it was 132. The minimum value of $\overline{F}_{10.7}$ during the period reported was 105 in June and 108 in early May. The energy average of the ratio of the maximum EUV intensity near the 26 May maximum to the average of the minima before and after was about 1.5, and $(1/Q)\Delta Q/\Delta F = 0.004$. This is less than was observed by

Bourdeau, et al., in 1962, and considerably less than would have been predicted by the present model. The differences may be due to the differing wavelength intervals used in the three calculations, or it may be that the anomalously high values of $\overline{F}_{10.7}$ in the middle of May were not related to changes in the EUV flux in the same way as the more normal changes in $\overline{F}_{10.7}$ during most solar rotations. It is interesting to note that if the maximum $\overline{F}_{10.7}$ during the rotations preceding and following the 26 May event were used, $(1/Q)\Delta Q/\Delta F = 0.017$ is in much better agreement with the other two determinations. Since the maximum solar EUV was measured on 26 May, however, this apparent agreement may be fortuitous.

SECTION VI

AURORAL AND POLAR ATMOSPHERE DENSITY MODEL BETWEEN 120 AND 175 km

A. INTRODUCTION

The previous two sections described a density and composition model of the upper atmosphere that was valid between 120 and 220 km, and that applied only to midlatitude regions. This section presents a new density model that is designed to represent the polar atmosphere. Since both of these models have been developed using the LOGACS density data exclusively, the inputs have been limited to a single 4-day period. The actual use of these models under a variety of other conditions will probably lead to some modification of the values of the parameters quoted, but it is hoped that the analytical form will remain an accurate representation of the density, and density variations, in the upper atmosphere.

B. DATA REDUCTION

The only LOGACS-derived density data used in this model were those obtained on the "day" side of the orbit between ~87 and 35°N geocentric latitude. The data were first used in an interpolation routine to estimate the atmospheric density every 5° of geomagnetic latitude between 75° and 40°N; no estimate was made unless there was at least one measured density value on either side, and within 2.5°, of the desired latitude. There were 311 interpolated densities so generated; these were used in the initial model calculations.

The parameters of an analytic density model similar to that used in the midlatitude case (a sum of exponentials) were adjusted to fit the data in a least-squares sense at each latitude independently. The temporal variation in the densities was assumed to be correlated with magnetic activity, and various indices (a_p, $\Delta\gamma_{Eielson}$, $\Delta\gamma_{Thule}$) and time delays were used to find the combination that best fit the interpolated densities. No combination gave a very convincing fit.

The original density data were again used in the interpolation routine, this time generating densities at each 5° increment of geocentric latitude. There were 321 such points between 85° and 50°N. The fits were much improved; in particular, the use of $(\Delta\gamma_{Eielson}/20 + \Delta\gamma_{Thule}/8)$ as the magnetic index and a time delay of 8 hr gave the best overall fit.

The coefficients at each latitude were very different, however, and it was not possible to find a single set of coefficients that adequately fit the data. A detailed examination of the residuals indicated two reasons for this. During disturbed times there was a marked latitudinal variation in the density, with some longitudinal asymmetry; and during both quiet and disturbed times there was a local and very large increase in density over the region near Baffin Island. This will be called a "bulge" for convenience in discussion.

Both of these variations had to be modeled to obtain a good fit, but this meant the introduction of several more free parameters; to minimize the total number of parameters, the basic sum-of-exponentials model was recast into a slightly different form. Equation (35) is the sum-of-exponentials model

$$\rho = a_1 \exp(-\alpha_1 Z) + a_2 \exp(-\alpha_2 Z) + [b_1 \exp(-\beta_1 Z) + b_2 \exp(-\beta_2 Z)] \ln(M + 1) \tag{35}$$

The a_i, b_i, α_i, and β_i are free parameters, ρ is the density at time t, Z is the altitude, and M is the magnetic index evaluated at some time, τ, earlier. Excluding τ, there are eight parameters. This form was replaced by

$$\rho = a_1 \exp\left[(\alpha_1 Z - \alpha_2)^2\right] + b_1 \exp\left[(\beta_1 Z - \beta_2)^2\right] \ln(M + 1) \tag{36}$$

The number of parameters has been reduced to six, but at some loss of generality. Above some altitude, roughly α_2/α_1, this would predict that the density increases without limit as Z approaches infinity, so the model must be restricted to altitudes below what in practice turns out to be β_2/β_1.

All the interpolated data were fit using Eq. (36), with the magnetic index M being the weighted average of the Eielson and Thule $\Delta\gamma$ ranges, and using an altitude-independent time delay of 8 hr. As in the midlatitude model, two sets of coefficients were required: one for quiet and moderately active times and one for extremely disturbed times.

The influence of the bulge had to be removed before the latitudinal variations could be studied. The bulge seemed to be localized and symmetric during quiet times, centered at about 67°N and 290°E. During more disturbed times it moved northward and eastward, becoming an elongated, somewhat ridge-like structure. The easy way to model such movement and shape change is to transform to a coordinate system whose origin moves with the center of the bulge along one cartesian axis, make a symmetric, magnetic-activity-dependent bulge in that system, then transform back.

When this was done a deep density trough appeared in the residuals at about 68°N over Asia and the western Pacific, and at about 60°N over Canada and Europe. This suggests that geomagnetic coordinates would be the appropriate system to use, but the trough in any one section seemed to follow a line of constant geocentric latitude, with a fairly abrupt transition between the sections. This is consistent with the results of the initial fits, where the use of geocentric coordinates gave a far better overall fit than did the use of geomagnetic coordinates. This trough was then modeled with a simple cosine function.

C. POLAR MODEL

1. SYMBOLS LIST

The symbols applicable to the polar model are:

B	correction to the model due to the bulge
$\overline{F}$	5-day average of $F_{10.7}$, ending on the day of interest
M	magnetic index, evaluated 8 hr prior to the time of interest
TR	correction to the model due to the trough
Z	altitude, km
$\Delta\gamma_E$	Eielson $\Delta\gamma$ range
$\Delta\gamma_T$	Thule $\Delta\gamma$ range
$\Delta\theta'$	effective width of the bulge, deg
θ	geocentric colatitude
θ_o	geocentric colatitude of center of bulge
θ'	colatitude in bulge system
ρ	density, gm/cm^3
ϕ	geocentric east longitude
ϕ_0	geocentric east longitude of center of bulge
ϕ'	east longitude in bulge system

2. REGION OF VALIDITY

Because of the variability of the polar atmosphere, this model applies only when conditions are similar to those when the LOGACS flight was made. Some extensions of the model are suggested, but these must be validated in practice before too much confidence can be placed in them.

Altitude: $135 \le Z \le 175$	Lower limit imposed by available data, but can probably be extrapolated to 120 km; upper limit imposed by the form of the model; for higher altitudes use the midlatitude model with a_p replaced by M.
Latitude: $\ge 50°N$ $(0 \le \theta \le 40°)$	For lower latitudes, to 50°S, use the midlatitude model.
Local time: ~1030	The model presumably can be extended to about 3 hr on either side fairly safely; no information is available at other times.
$\overline{F}$: ~180	For difference values of $\overline{F}$, replace M by $\{M + \exp[0.027(\overline{F}-183)] - 1\}$; this is in analogy to the midlatitude model.
Season: ~summer solstice	

There are two models. One includes the bulge and is more accurate in reproducing the LOGACS-derived densities. Because the bulge is so variable in both position and extent, and because a badly modeled bulge is worse than none at all, a second model, which averages the effects of the bulge, is also presented.

3. BULGE MODEL

Parameters for the bulge model are evaluated as follows:

a. Magnetic Index

$$M = \Delta\gamma_E/20 + \Delta\gamma_T/8 \tag{37}$$

b. Evaluation of B

If ϕ is not between 280 and 340°, B = 0.

If ϕ is between 280 and 340°

$$\theta_o = 23° - 0.18M \tag{38}$$

$$\phi_o = 290° + 0.18M \tag{39}$$

$$\phi' = \tan^{-1}\left[\frac{\theta \sin(\phi - 115°) - \theta_o \sin(\phi_o - 115°)}{\theta \cos(\phi - 115°) - \theta_o \cos(\phi_o - 115°)}\right]$$

$$\theta' = [\theta \cos(\phi - 115°) - \theta_o \cos(\phi_o - 115°)]/\cos\phi' \tag{40}$$

If $M \le 16.33$

$$\Delta\theta' = \exp(0.177M) \tag{41a}$$

$M > 16.33$

$$\Delta\theta' = 18° \tag{41b}$$

If $|\theta'| > \Delta\theta'$

$$B = 0 \tag{42a}$$

If $|\theta'| \le \Delta\theta'$ and $M \le 59$

$$B = 0.276 \cos[(\theta'/\Delta\theta')(45°)] \tag{42b}$$

If $|\theta'| \le \Delta\theta'$ and $M > 59$

$$B = 0.222 \cos[(\theta'/\Delta\theta')(45°)] \tag{42c}$$

c. <u>Evaluation of TR</u>

If $M \le 59$, $TR = 0$.
If $M > 59$, and $50° < \phi \le 230°$

$$TR = \cos[7.9(\theta - 22.5°)] \tag{43a}$$

If $M > 59$, $230° < \phi \leq [(360°) + 50°]$, and $\theta < 13°$

$$TR = -0.743 \tag{43b}$$

If $M > 59$, $230° < \phi \leq [(360°) + 50°]$, and $\theta \geq 13°$

$$TR = \cos [8.1(\theta - 30°)] \tag{43c}$$

d. Evaluation of ρ

If $M \leq 59$

$$\rho = 3.89 \times 10^{-14} \left\{ \exp\left[\left(\frac{Z - 324.5}{87.08}\right)^2\right] + 1.635 \exp\left[\left(\frac{Z - 215.0}{53.11}\right)^2\right] \ln(M + 1) \right\}$$

$$\times (1 - 0.0047\, M) \times (1 + B) \tag{44a}$$

If $M > 59$

$$\rho = 5.605 \times 10^{-14} \exp\left[\left(\frac{Z - 241.7}{59.3}\right)^2\right]$$

$$\times [1 + \ln(M + 1)](1 + B)[1 + 0.0396\, TR\, (1 - 0.0515\, M)] \tag{44b}$$

4. BULGELESS MODEL

The correction B is not calculated; TR is evaluated in the same way as for the bulge model, and the coefficients in the ρ calculation are changed slightly.

If $M \leq 59$

$$\rho = 3.96 \times 10^{-14} \left\{ \exp\left[\left(\frac{Z - 324.5}{87.08}\right)^2\right] + 1.635 \exp\left[\left(\frac{Z - 215.0}{53.11}\right)^2\right] \ln(M + 1) \right\} \times (1 - 0.0047M) \qquad (45a)$$

If $M > 59$

$$\rho = 5.75 \times 10^{-14} \exp\left[\left(\frac{Z - 241.7}{59.3}\right)^2\right] \times [1 + \ln(M + 1)] \times [1 + 0.0442\ TR(1 - 0.0515M)] \qquad (45b)$$

D. DISCUSSION

Since only LOGACS data were used in the development of this polar model, it is difficult to estimate its accuracy when applied to other flights. If attention is restricted to the LOGACS vehicle only, however, one may compare the rms density residuals obtained by using this model with those from several other model atmospheres. Such a comparison is given in Table 22.

The first three models, L-DENSITY, ARDC-59, and US-62, were derived from midlatitude data near the peak of the previous solar cycle. Even so, they underestimate the average polar density below 200 km by about 30 percent. (A similar situation occurred when the midlatitude LOGACS data were compared with these models; see Section IV.) Evidently, either the density boundary conditions at 120 km or the vertical temperature gradient, or both, are in error. The J-W-B atmosphere maintains constant

Table 22. Comparison of Density Models

Model	R[a]	σ[b]	100 σ/R
L-DENSITY[c]	1.50	0.32	21.5
ARDC-59	1.62	0.31	19.2
US-62	1.56	0.28	18.0
J-W-B[d]	1.21	0.20	16.2
Champion[e]	1.11	1.17	15.0
Prag (no bulge)[f]	1.00	0.12	11.7
Prag (bulge)[f]	1.00	0.10	9.9

[a] $R = (1/N)\Sigma_i \rho_i/\rho_M$

[b] $\sigma = \left\{[1/(N - 1)]\Sigma_i(1 - \rho_i/\rho_M)^2\right\}^{1/2}$

[c] Essentially Jacchia 1960.

[d] Bruce's modification to Walker's analytical Jacchia model (Ref. 6).

[e] See Ref. 7. Fractional density changes and the time delay at 150 km have been applied at all altitudes.

[f] The models proposed here.

boundary conditions, but has a considerably smaller temperature gradient than the three previous models; the Champion model modifies both the boundary conditions and, to a lesser extent, the temperature distribution.

The Prag models proposed here were adjusted to fit the measured densities; in particular, it was required that the average ratio of the measured density to the model density be unity. As a consequence, the average model density is considerably higher over the polar regions than the earlier models had predicted.

The last column in Table 22 gives the overall rms percentage error of the various models when compared with the observations. The major portion of the error in all seven models occurred in the last day and a half of the flight, during the magnetic storm. The average overall percentage error of the first three models was 19.6 percent; these models have no provision for including magnetic activity. The J-W-B model uses the planetary magnetic index (derived from midlatitude observations) to modify its predicted density, and the Champion model uses the College, Alaska, K index, which is a measure of auroral activity. There is a 17 and a 25 percent improvement, respectively, over the no-index models. The Prag models use the weighted average of the Eielson and Thule $\Delta\gamma$ ranges. The Eielson range is essentially equivalent to the College K index, and is also a measure of auroral activity. The Thule range is a measure of polar cap activity, which is often quite different than that in the auroral regions. There is a 40 percent (no bulge) and a 49 percent (with bulge) improvement over the no-index models.

Additionally, the Prag models introduce a considerable amount of structure in the atmosphere during disturbed times. (During reasonably quiet times the density of the atmosphere below 200 km had little or no dependence on either latitude or longitude, except for the very localized bulge.) A "trough" appears in the region of the auroral oval, which reduces the density thereby as much as 30 percent ($M = 150$) at all altitudes ($135 \leq Z \leq 200$ km). A possible explanation for this is the explosive heating due to a very large influx of high energy particles in this region. This heating is presumably the source of high-velocity winds in the polar regions, as reported in Section VII, so some care must be taken in interpreting the trough as a true density minimum; about 20 percent of the apparent decrease in density could be due to the winds "pushing" the vehicle, thereby reducing the measured deceleration. Since the effect on drag measurements is the same whether there are tailwinds or a true density decrease, it was decided to include the trough in the density model and not bring in the added complication of dynamic mass motion.

Figure 70 shows the average density of the polar atmosphere between 120 and 190 km according to the models presented here. The dashed lines represent two extreme CIRA models. For low to moderate magnetic activity the new models are lower than CIRA below 140 km and roughly comparable at higher altitudes; during highly active times CIRA everywhere underestimates

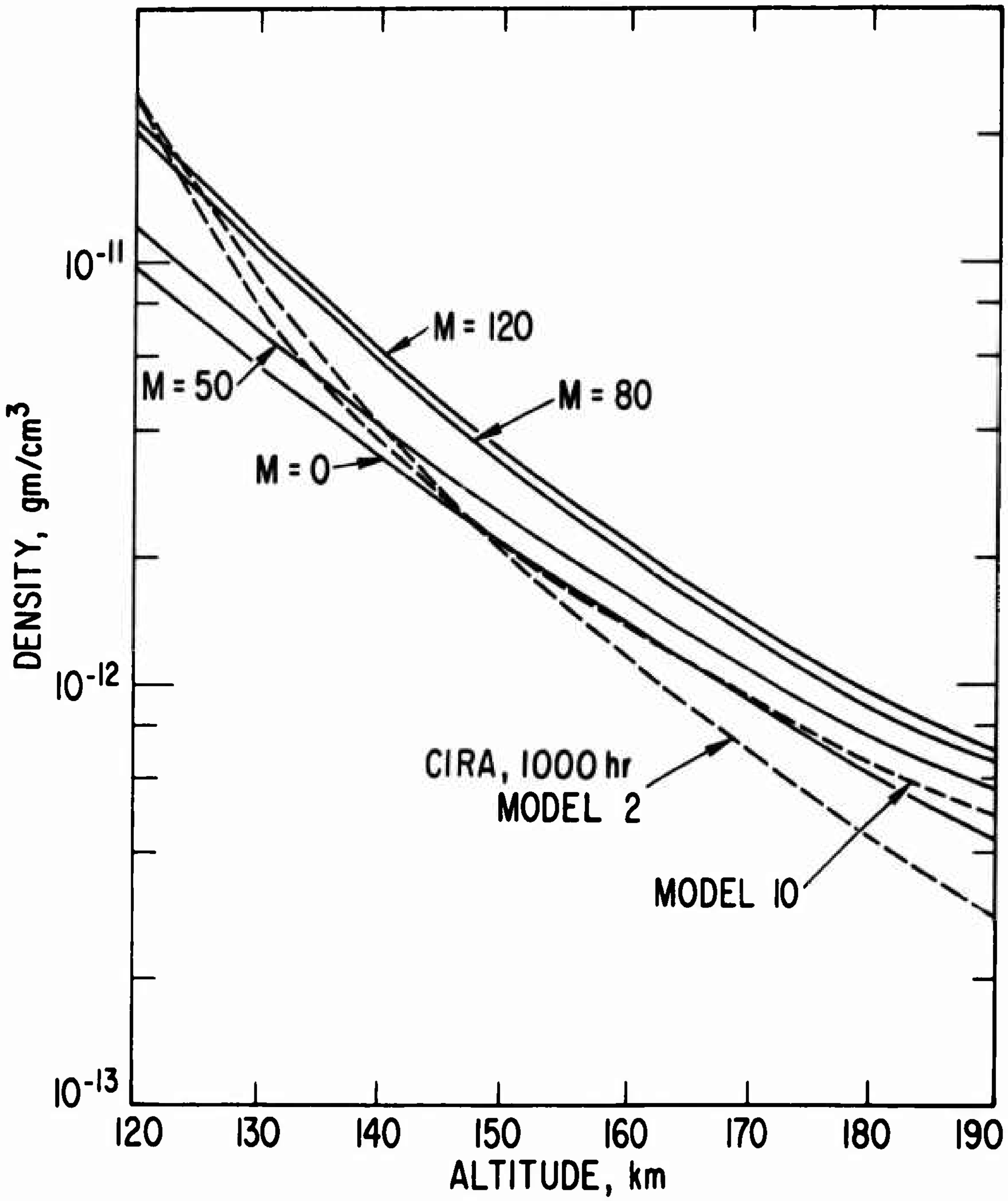

Fig. 70. Average Density of Polar Atmosphere

the density above 125 km. As with the midlatitude model (Section IV), the low-altitude scale height is much larger than previous model atmospheres have predicted.

Figure 71 is a three-dimensional projection of the atmosphere near the bulge. The "fractional density" is the ratio of the model density to the average density; the figure has been drawn for M = 60 and applies to all altitudes between 120 and 175 km. The density trough between 350° and 30°E longitude, and again at 270°, emphasizes the highly localized nature of the bulge even for the fairly active time under consideration.

No altitude-dependent time delay, such as was found in the mid-latitude regime, is included here. Such a delay is undoubtedly present, but the data were not extensive enough to adequately determine its nature. As more information becomes available, it will be included and will probably significantly improve the performance of these polar models.

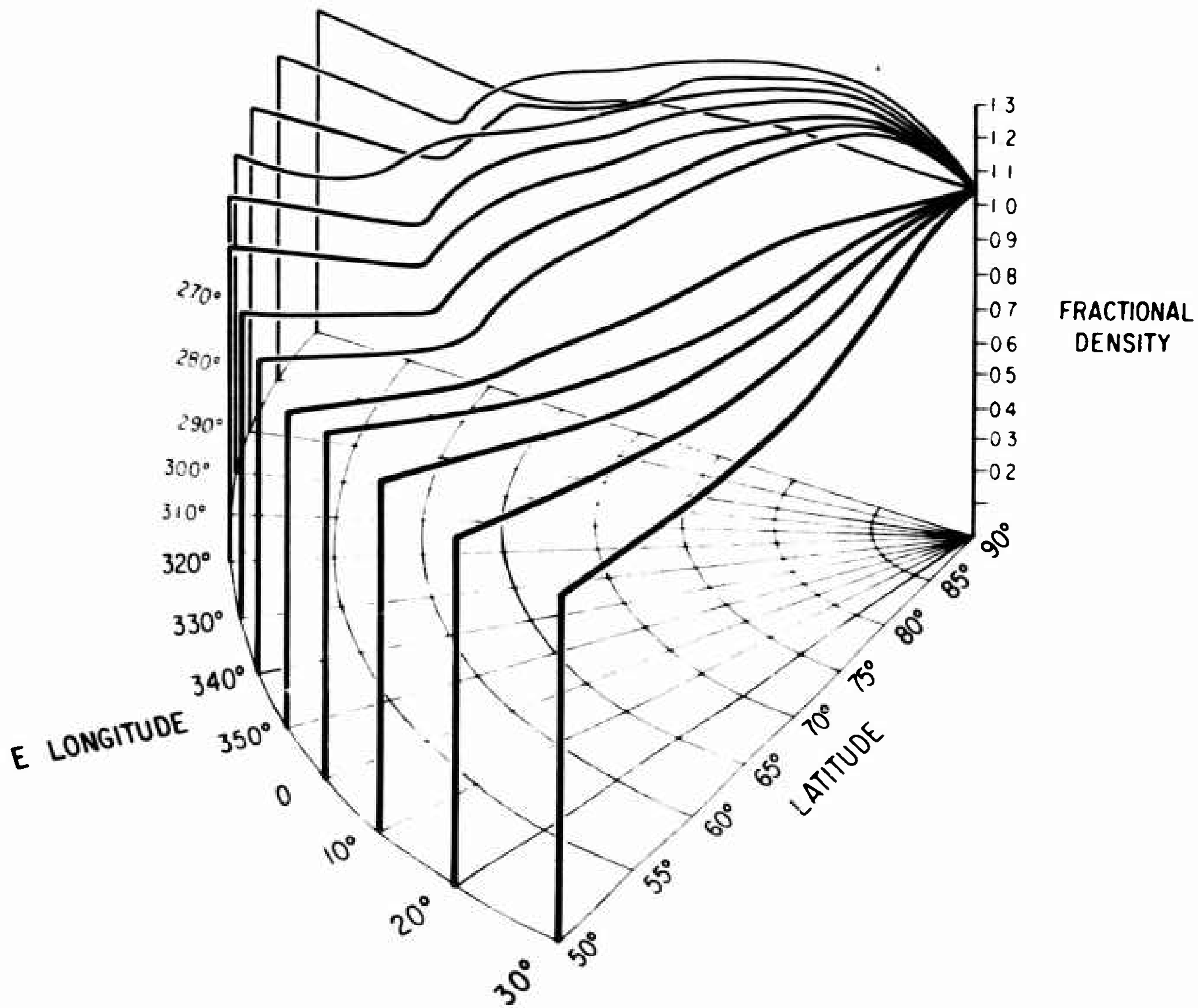

Figure 71. Fractional Density Between 370° and 30°E, 50° to 90°N

SECTION VII

LOGACS WIND ANALYSIS

A. INTRODUCTION

The processing of LOGACS data (Volume I, Section II) revealed large anomalies in drag acceleration following the occurrence of the large magnetic storm. Correlated with this phenomenon was a change in polarity of the yaw control force and consequently a corresponding polarity change of the yaw control moment. From this response characteristic and the assumption it is externally caused, it follows that during this interval the yaw aerodynamic moment changed polarity. This in turn leads to the conclusion that there occurred a large change in the yaw angle of attack and the corresponding hypothesis of large horizontal wind components normal to the orbit plane.

Wind calculations could not have been performed had the LOGACS experiment not been instrumented for control gas firing data. Also, the rotating accelerometer mode provided data necessary to calibrate the control force scale factor (see Section E). The attitude data, although not explicitly used in the wind calculation, provided required information for evaluating the control system performance.

B. FORCE AND MOMENT ALGORITHMS

Figure 72 presents a force/moment diagram of the Agena configuration and defines the symbols used in the analysis. The force and moment equations can be written by inspection as

Force

$$mA_y = -F_y = -(F_{ay} + F_{cy}) \tag{46}$$

Moment

$$M_z = I\dot{\omega}_z = F_{cy}X_{gv} - F_{ay}X_{cp} - F_{ax}(Y_{cg} - Y_{cp}) \tag{47}$$

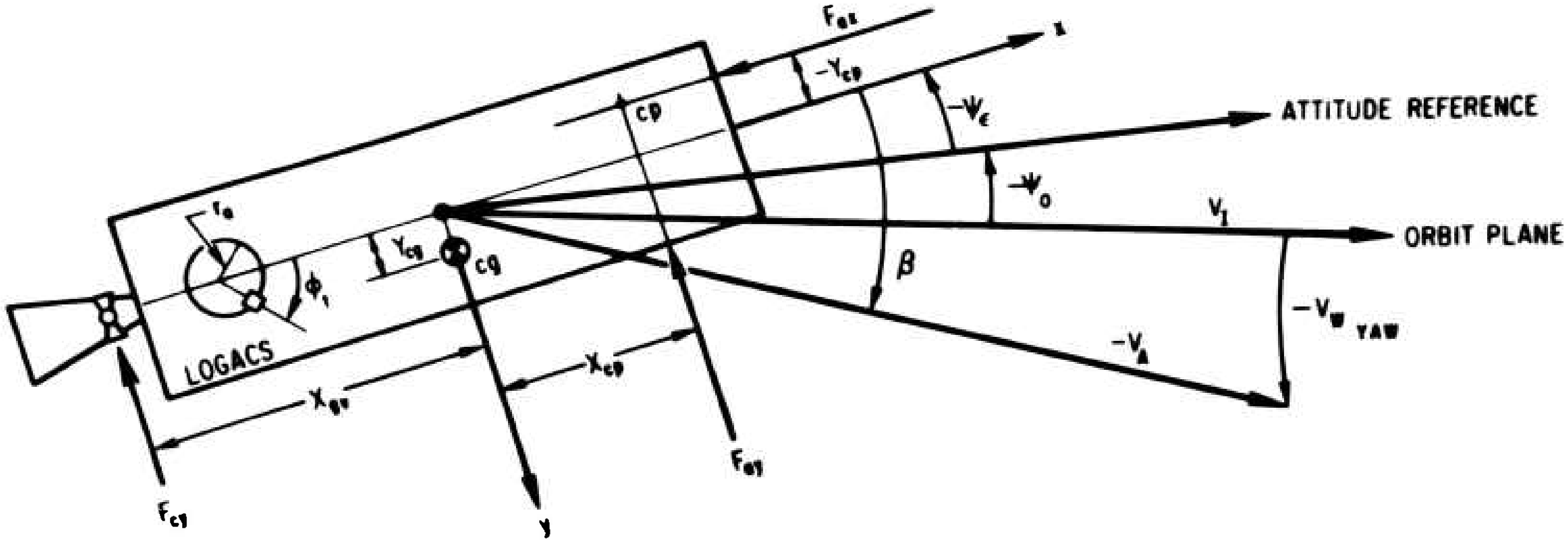

ψ_0 : YAW REFERENCE ERROR

ψ_ϵ : YAW GYRO ERROR

β : YAW ANGLE OF ATTACK

F_{ax} : AERODYNAMIC AXIAL FORCE

F_{ay} : AERODYNAMIC SIDE FORCE

F_{cy} : YAW CONTROL FORCE

X_{cp} AERODYNAMIC SIDE FORCE LEVER ARM

X_{gv} CONTROL FORCE LEVER ARM

Y_{cp} AERODYNAMIC CENTER OF PRESSURE ALONG y

Y_{cg} y COORDINATE OF cg

V_I INERTIAL VELOCITY

V_A RELATIVE VELOCITY OF VEHICLE WITH RESPECT TO THE ATMOSPHERE

$V_{w_{YAW}}$ ATMOSPHERIC VELOCITY NORMAL TO ORBIT PLANE

Fig. 72. Force/Moment Diagram (Yaw Plane)

where the individual terms on the right-hand side are defined in Fig. 72. When the side acceleration is measured, Eq. (46) can be used to calculate the yaw angle of attack* as follows

$$F_{ay} = C_{N\beta} QS\beta$$

$$F_{ax} = C_A QS \rightarrow QS = F_{ax}/C_A \qquad \text{(product of dynamic pressure Q and reference area S)}$$

$$F_{ay} = (C_{N\beta}/C_A) F_{ax}\beta = F_y - F_{cy}$$

from which β is calculated as

$$\beta = \left(\frac{C_A}{C_{N\beta}}\right) \frac{F_y - F_{cy}}{F_{ax}} \tag{48}$$

where

$C_A/C_{N\beta}$ = ratio of aerodynamic axial to normal force slope coefficients

F_y = total side force determined from processing LOGACS accelerometer data in the rotating modes

F_{cy} = control force determined from processing LOGACS control valve firing data

F_{ax} = axial force determined from the LOGACS accelerometer data

When the accelerometer is in the fixed fore or aft mode, Eq. (47) can be used to calculate the yaw angle of attack. In the perigee region the control system is operating on the control deadband so that the time average

---

*When it is assumed there is no wind component in the in-track coordinate, the yaw wind velocity is calculated as $V_I \tan \beta \approx V_I \beta$.

of angular acceleration is zero (see Volume I, Section II). Therefore, Eq. (47) relates a moment balance condition as follows

$$F_{cy}X_{gv} = F_{ay}X_{cp} + F_{ax}(Y_{cg} - Y_{cp})$$

When it is assumed that Y_{cp} is a linear function of β, i.e.,

$$Y_{cp} = K\beta$$

where K may be zero, the above equation reduces to

$$F_{cy}X_{gv} = (C_{N\beta}X_{cp} - C_A K)QS\beta + C_A QSY_{cg}$$

We define the coefficient of β as

$$C_N X_{cp} - C_A K \triangleq C_{N\beta}X_{cpe} \triangleq C_{m\beta}$$

where X_{cpe} is defined as the effective center of pressure and $C_{m\beta}$ is the moment coefficient about the vehicle center of gravity. Using this relationship and solving the β results in

$$\beta = \left(\frac{C_A}{C_{m\beta}}\right)\left(\frac{F_{cy}}{F_{ax}} X_{gv} - Y_{cg}\right) \tag{49}$$

Also, assuming vehicle symmetry,* the pitch angle of attack can be calculated as

$$\alpha = \left(\frac{C_A}{C_{m\beta}}\right)\left(\frac{F_{cz}}{F_{ax}} X_{gv} - Z_{cg}\right) \tag{50}$$

---

*With the assumption of symmetry, $C_{m\beta} = C_{m\alpha}$ and $C_{N\beta} = C_{N\alpha}$. The subscript symbols α and β are used interchangeably throughout the report.

During the period when Eq. (48) can be used to solve for β, a consistency check can be made between the results obtained by Eqs. (48) and (49). If they do not agree (as was the case initially, see Section E), then the following relationship is used to determine the source of inconsistency

$$\left(\frac{C_A}{C_{N\beta} X_{cpe}}\right)\left(\frac{F_{cy}}{F_{ax}} X_{gv} - Y_{cg}\right) = \left(\frac{C_A}{C_{N\beta}}\right)\frac{F_y - F_{cy}}{F_{ax}}$$

$$\therefore X_{cpe} = \frac{F_{cy} X_{gv} - F_{ax} Y_{cg}}{F_y - F_{cy}} \qquad (51)$$

The terms on the right-hand side of Eq. (51) can be adjusted to produce an expected (predicted) value of X_{cpe}. Since the acceleration data errors are small, the terms most suspect are a scale factor on the control force level and the value of Y_{cg}.

C. AERODYNAMIC COEFFICIENTS

The data of Ref. 3 were used to determine the aerodynamic coefficients required in this analysis. Since force coefficients were presented in terms of wind axis (lift and drag), they were transformed to body axis coefficients using the following transformation

$$\begin{bmatrix} C_A \\ C_N \end{bmatrix} = \begin{bmatrix} \cos\alpha & -\sin\alpha \\ \sin\alpha & \cos\alpha \end{bmatrix} \begin{bmatrix} C_D \\ C_L \end{bmatrix}$$

The ratio of C_A to $C_{N\beta}$ was calculated as

$$\frac{C_A}{C_{N\beta}} = \left(\frac{C_A}{C_N}\right)\beta$$

The effective center of pressure was determined from

$$X_{cpe} = L_{ref}(C_m/C_N) + L_{cg}$$

where

L_{ref} = reference length (5 ft)

C_m = moment coefficient referenced to Agena Station 247

L_{cg} = distance from Station 247 to the vehicle cg (8.7 ft)

Since the coefficients depend on the molecular speed ratio, which in turn depends on exospheric temperature, T_∞, and altitude, and required coefficients were first calculated as a function of molecular speed ratio for the angle of attack range considered in Refs. 3 (2° and 4°). These are plotted in Fig. 73. The molecular speed ratio as a function of altitude and exospheric temperature is presented in Fig. 74.* From the data of Figs. 73 and 74, plots of predicted aerodynamic coefficients are presented in Fig. 75 as a function of altitude for angles of attack of 2° and 4° and exospheric temperature of 1000° and 1500°K. Since the predicted variation of $C_A/C_{N\alpha}$ is ±1.5 about a mean value of 52.5 (±3 percent), a constant value was used for this coefficient.† The predicted characteristics of X_{cpe} were not explicitly used in the wind calculations, but were used as a guide in evaluating Eq. (51) (Section B).

---

*Reproduction of curve presented in Ref. 3.

†When $T_\infty \rightarrow 0$, the molecular speed ratio goes to ∞ and the coefficients $C_A/C_{N\alpha}$ can be calculated by an area rule which results in a value of 1 rad = 57.2958°.

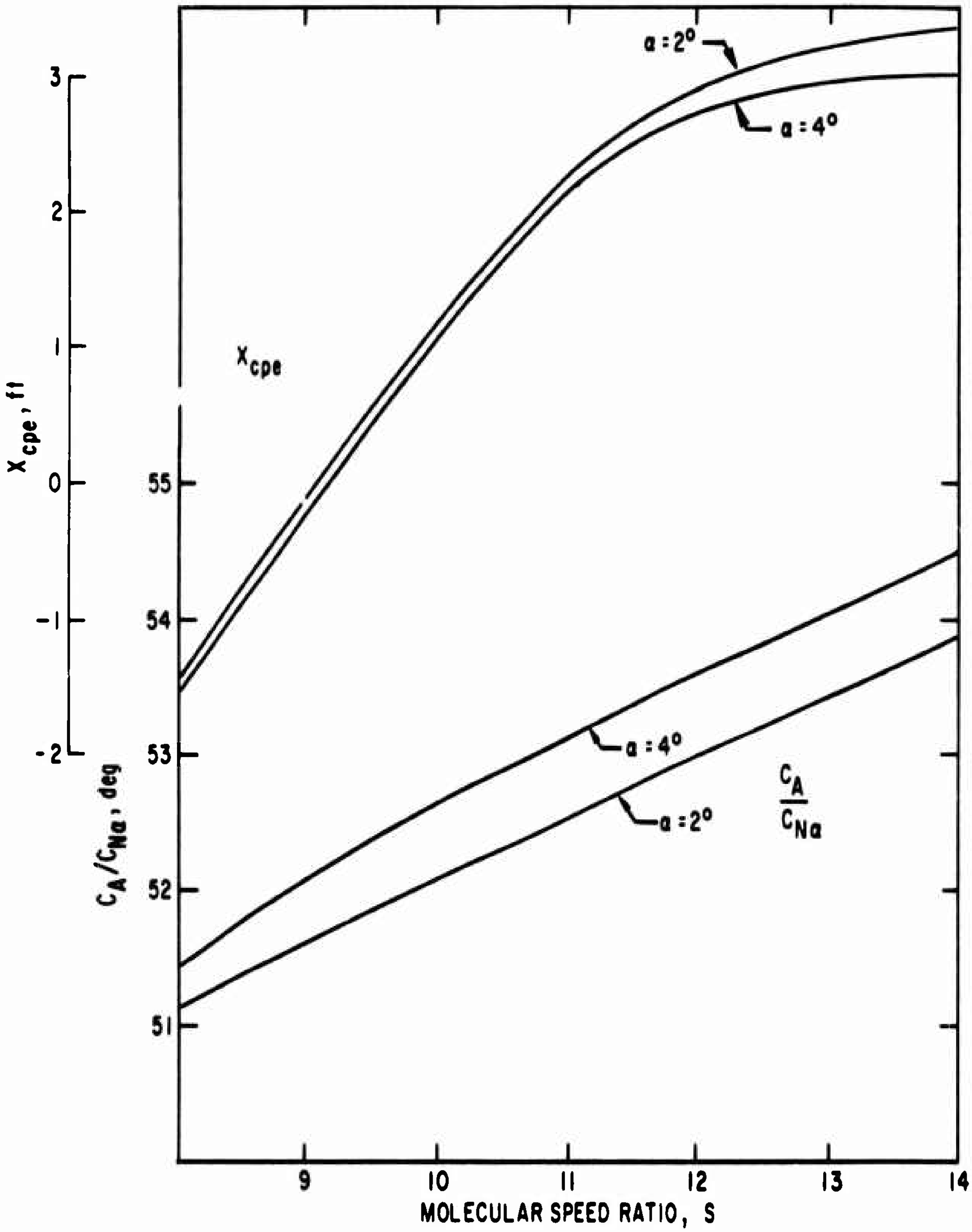

Fig. 73. Aerodynamic Coefficients as a Function of Molecular Speed

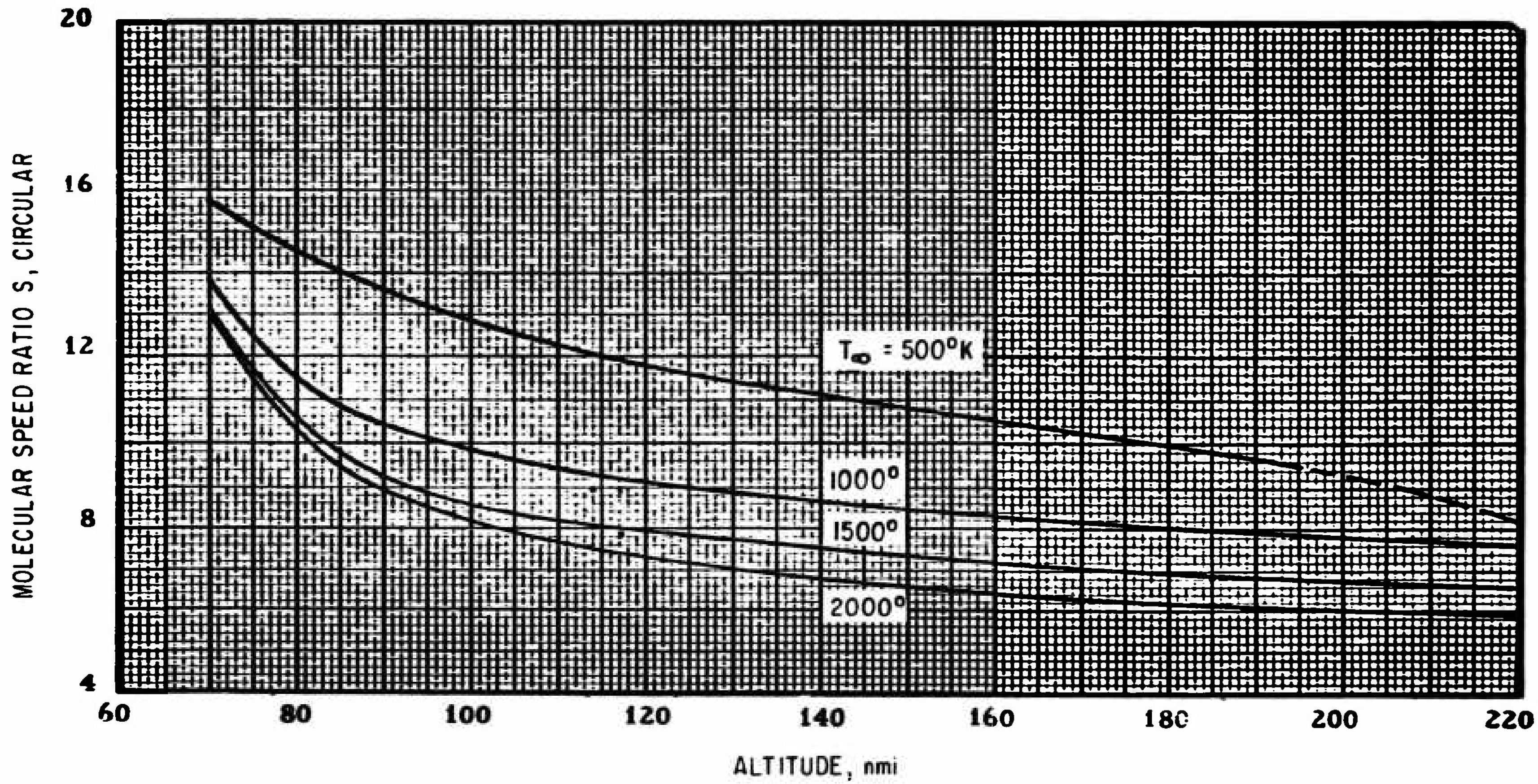

Fig. 74. Molecular Speed Ratio vs Altitude and Temperature (Based on Walker-Jacchia 1964 atmosphere model as modified by Bruce.)

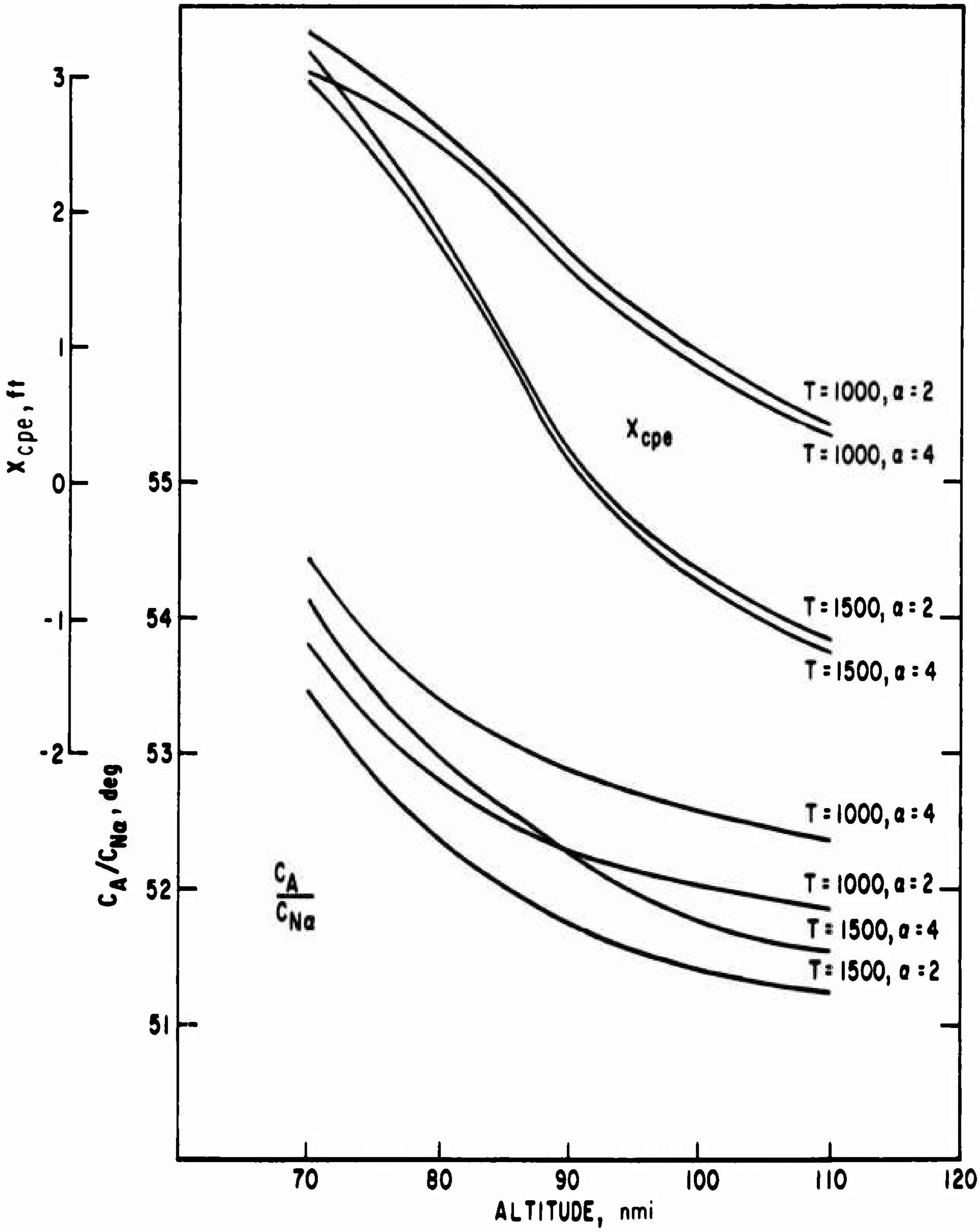

Fig. 75. Aerodynamic Coefficients as a Function of Altitude

D. LOGACS SIDE FORCE PROCESSING

The equation for LOGACS accelerometer counts is (see Volume I, Section II)

$$N_i = K \int_{t_i - 1}^{t_i} \left(r_a \dot{\Phi}_t^2 + A_x \cos \Phi_t + A_y \sin \Phi_t \right) dt + E + B \qquad (52)$$

where

N_i = incremental accelerometer counts recorded each second

r_a = turntable radius arm

$\dot{\Phi}_t$ = angular rate of turntable

A_x = acceleration along the -x axis due to aerodynamic drag

A_y = acceleration along the -y axis due to aerodynamic side force and control valve firings

E = error term due to angular rate and acceleration induced by control firings and aerodynamic torques; the mean value of E is zero with a variance proportional to sin Φ_t and the number of control firings

K = instrument scale factor

B = instrument bias

The instrument scale factor and bias were determined from the rotating mode data at apogee. Since the expected (average) value of E is zero, it is dropped from further consideration. Since the recording interval is 1 sec, the integration can be dropped assuming the variables are constant over the interval. The term $r_a \dot{\Phi}_t^2$ is a known constant for a given accelerometer mode. Applying these considerations, Eq. (52) can be rearranged as

$$A_x \cos \Phi_t + A_y \sin \Phi_t = \frac{N - B}{K} - r_a \dot{\Phi}_t^2 \qquad (53)$$

Since Φ_t and the mode event times are known, Φ_t is known except for the initial condition errors due to turntable mode transients. Included with the LOGACS data were event times when the turntable passed the 0° and 180° positions (identified as Switch A and Switch B data). The complete data set of event times was processed to determine the mean and variance of the time difference between predicted and measured event times (fore and aft positions). The angular error was determined as

$$\Delta\Phi_t = \dot{\Phi}_t \Delta t$$

The angular means obtained are tabulated as follows:

	Switch A	Switch B
Mode 1	2.99°	3.22°
Mode 2	3.19°	3.45°

The standard deviation about the mean was less than 0.1° and was probably due to telemetering errors rather than any deviation of event times. It is seen that the data indicate an angular error between Switch A and B of ≈0.2°. The Mode 1 startup transient resulted in a 3.1° phase error during Mode 1 and an additional 0.2° during Mode 2, which was caused by the motor speed change transient. For the analysis presented here, a constant 3.2° phase error was used.

An undetermined phase angle error, Φ_e, would result in an error in the estimated forces as follows:

$$\begin{bmatrix} \hat{F}_{ax} \\ \hat{F}_{ay} \end{bmatrix} = \begin{bmatrix} \cos \Phi_e & \sin \Phi_e \\ -\sin \Phi_e & \cos \Phi_e \end{bmatrix} \begin{bmatrix} F_{ax} \\ F_{ay} \end{bmatrix}$$

For small angles this reduces to

$$\hat{F}_{ax} = F_{ax} + F_{ay} \sin \Phi_e$$

$$\hat{F}_{ay} = -F_{ax} \sin \Phi_e + F_{ay}$$

Since F_{ax} is approximately an order of magnitude larger than F_{ay}, little error results in the estimated value of F_{ax}. However, the estimation error for F_{ay} is not negligible. If the above expression for $\hat{F}_{ay}$ is used in Eq. (48), it is seen that there is a nearly one-to-one relationship between Φ_e and the resulting β calculated.

The method used to determine A_x and A_y of Eq. (53) was to assume a model of each function as depicted in Fig. 76. A_x was assumed to vary linearly between estimated values for A_x at the fore and aft phase angles. A_y was assumed to be constant over the same phase angle interval. This results in a linear model with time-varying coefficients where the right-hand side of Eq. (53) is the corrected data set. The parameters to be estimated are the table points of $\hat{A}_x$ and $\hat{A}_y$. This model was mechanized in Post Flight Reconstruction Program (PFRP), which is part of Modularized Vehicle Simulation Program (MVS), and is described in Ref. 35. The PFRP estimation model chosen was the least-squares version.

Seven sets of Mode 1 and 2 perigee data were chosen for processing. Three were before and four followed the magnetic storm activity. The specific revolutions were: Rev. 38, which included the time interval going toward perigee; Rev. 39, coming from perigee; Rev. 41, which bracketed perigee; and Revs. 43, 53, 54, and 56, which all included data of time intervals when anomalies in drag acceleration and yaw control response were observed.

In the course of processing the data sets, it was observed that the estimated values of side acceleration had a consistent oscillation, producing a result greater in magnitude for phase angles from $-\pi$ to zero than for phase angles between zero and π. The source of this characteristic has not been identified, but could be the result of a phase angle error, or equivalently an

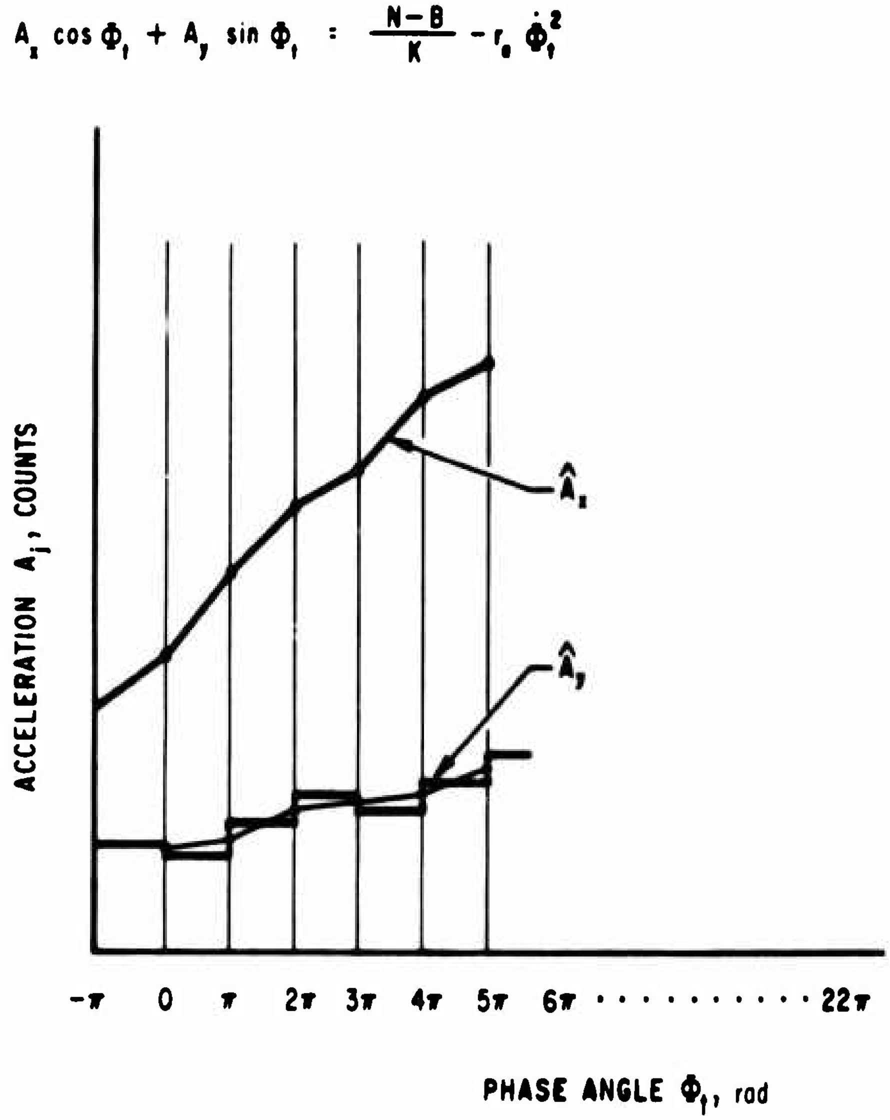

Fig. 76. LOGACS Side Force Processing

instrument misalignment error, and/or an accelerometer sensitivity to cross-axis acceleration. The order of magnitude of the oscillation indicates the error magnitude is about 0.5° angle or 1 percent accelerometer cross-axis sensitivity. To compensate for the oscillation effects, adjacent values of $\hat{A}_y$ estimates were averaged and tagged with the midpoint phase angle argument (zero or π). To construct time histories, a linear interpolation of the average $\hat{A}_y$ values between arguments was used.

The results of the processings of the seven revolutions are presented in Figs. 77 through 83. The time axis is referenced to the Mode 1 start time, which is listed also as TRGO. These can be directly correlated with data presented in Section II, Volume I. The units for the x and y axis accelerations are in terms of accelerometer counts and are normalized so that one count equals 10^{-7} g. To convert to force, the acceleration is scaled by the vehicle weight (1912 lb), or the counts should be scaled by 1.912×10^{-4}. Included in these plots are the pitch and yaw control force data, also in units of accelerometer counts. These are directly from the data of Volume I, Section II, scaled by 0.5 to reflect the calibration results discussed in Section E.

Appendix C presents the Rev. 56 data set used to produce the results presented in Fig. 83. This is typical of all the data sets. Figure C-1 presents the corrected raw data [right-hand side of Eq. (53)] and Fig. C-2 presents the residuals of the fit (right-hand side minus the left-hand side after estimating $\hat{A}_x$ and $\hat{A}_y$). The large noise level is primarily caused by the effects of control valve firings.

E. PARAMETER CALIBRATION

The initial attempt to process the force data of Section D to arrive at angle-of-attack histories was to use Eq. (48) to calculate β, use Eq. (51) to calculate X_{cpe}, and use X_{cpe} in Eq. (50) to calculate α. This led to extremely erratic results for X_{cpe} [some calculated values were ahead and some were behind the vehicle, dependent upon polarity of the denominator of Eq. (51)] and corresponding erroneous calculations of α.

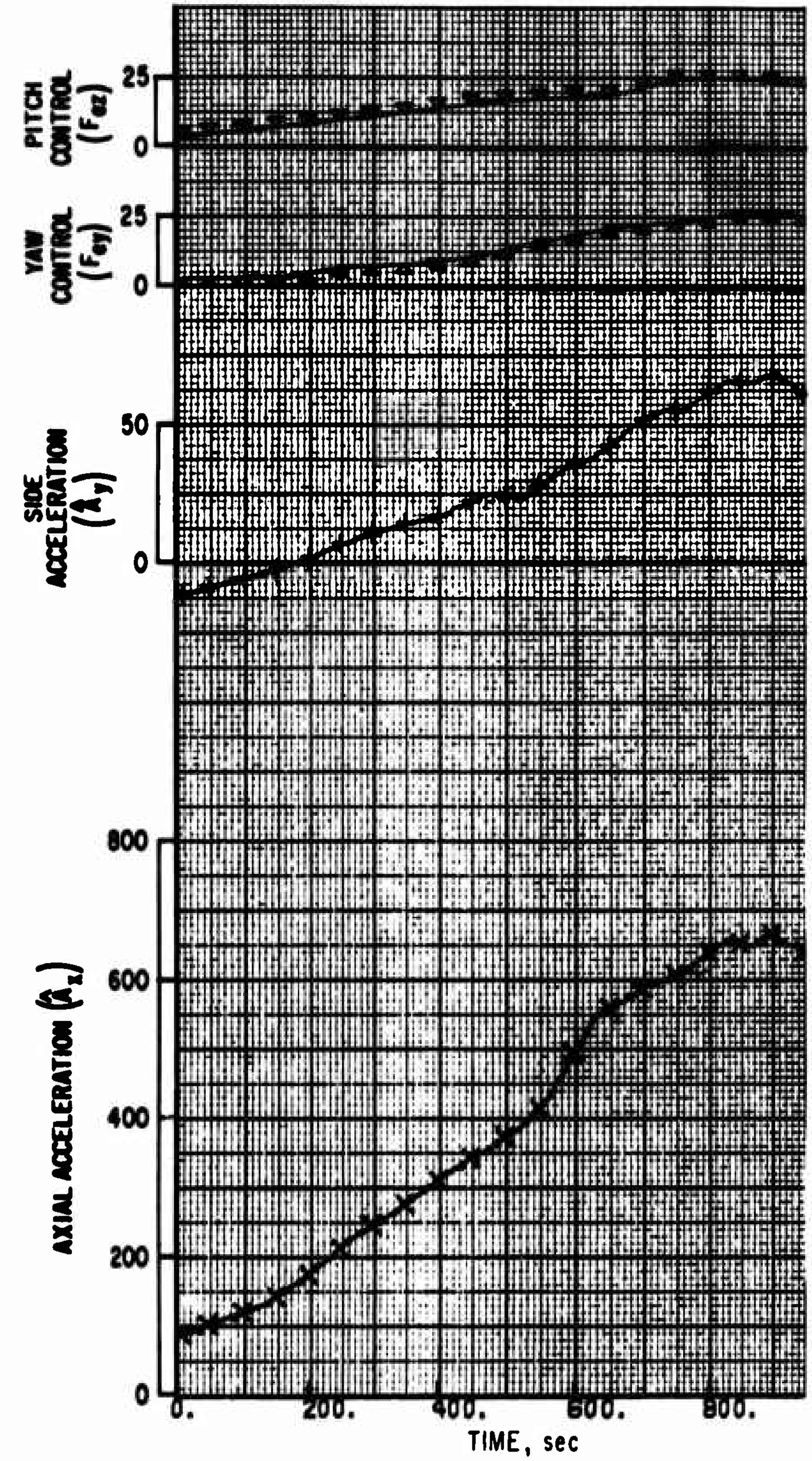

Fig. 77. Revolution 38 (TRGO = 202490)

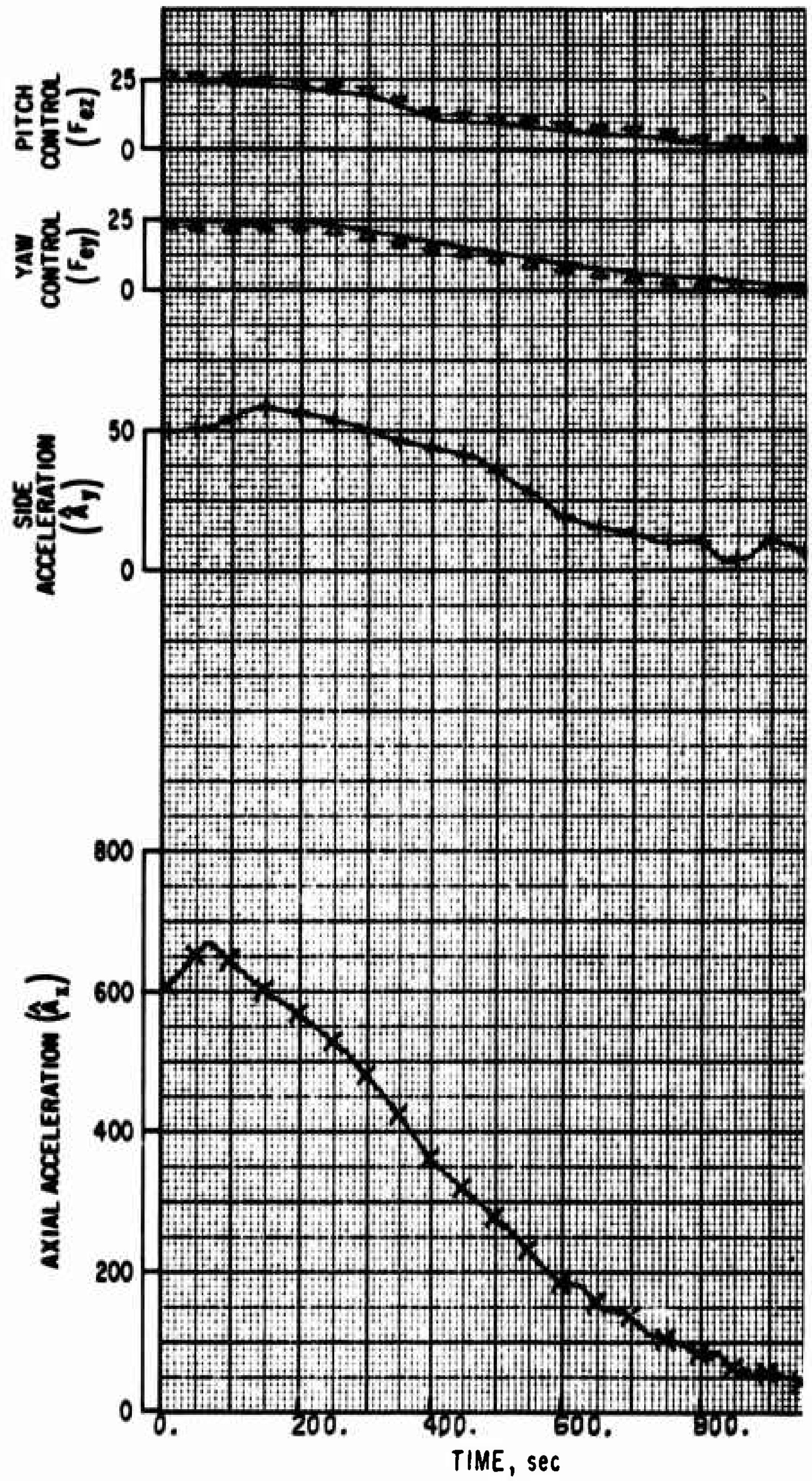

Fig. 78. Revolution 39 (TRGO = 208640)

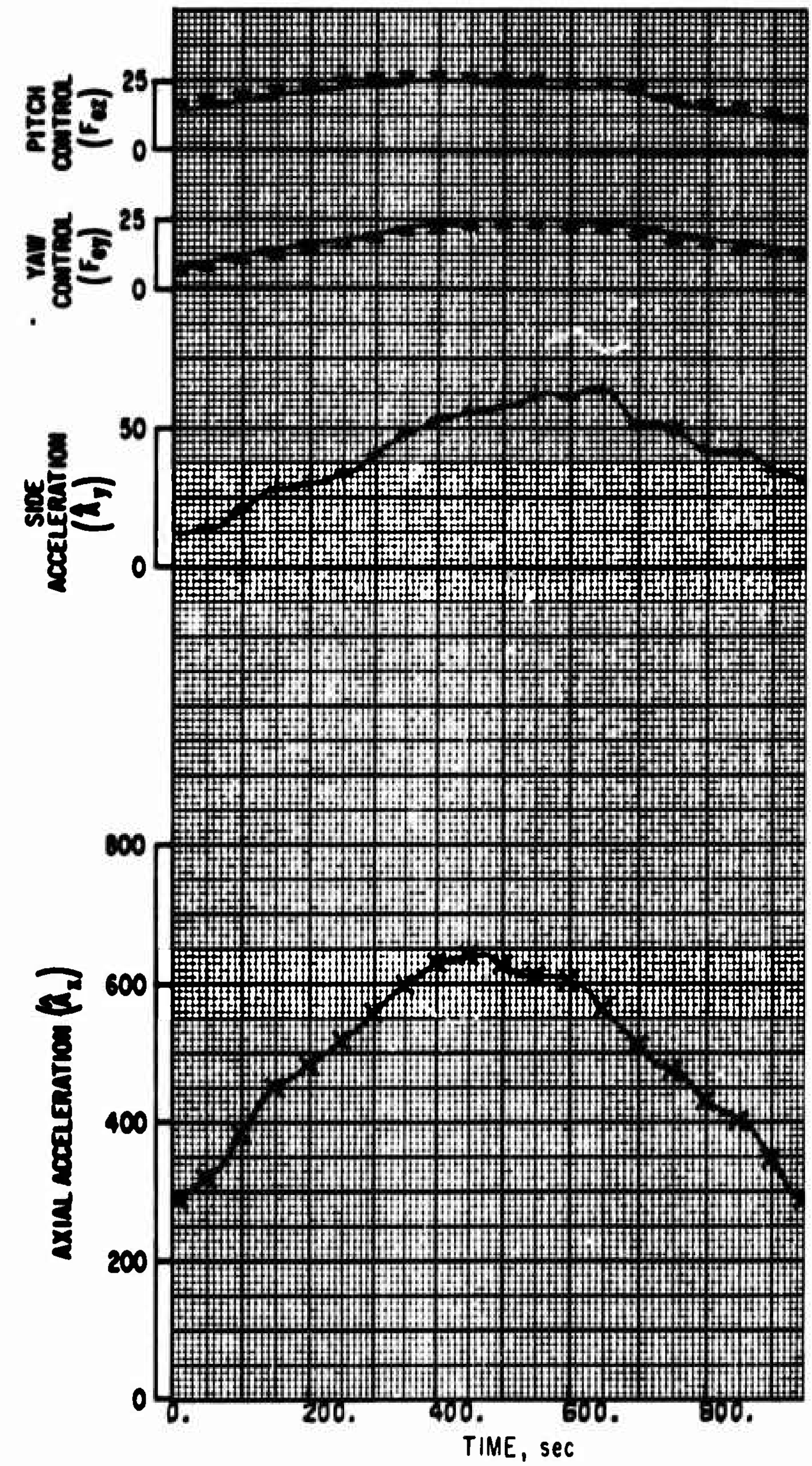

Fig. 79. Revolution 41 (TRGO = 218880)

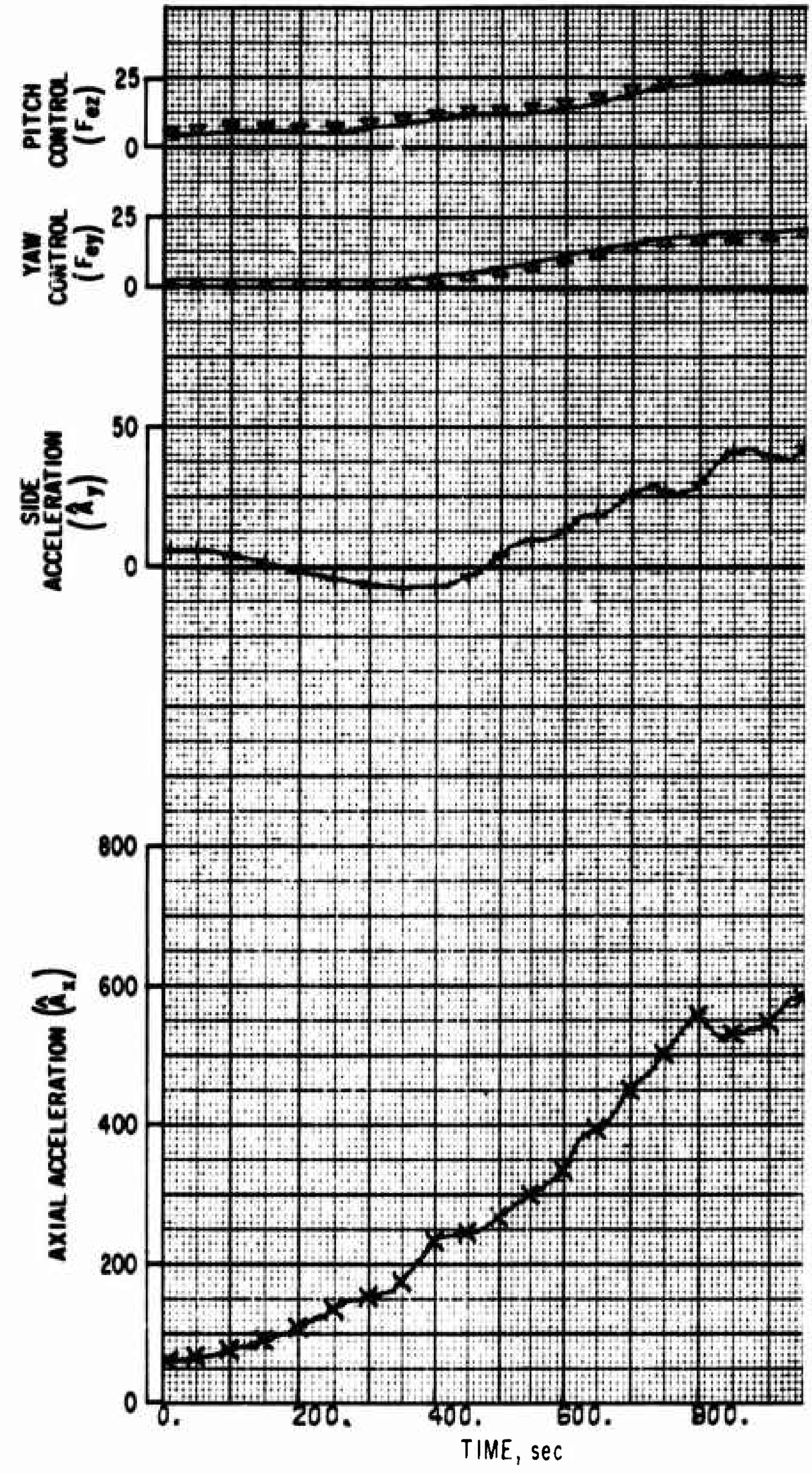

Fig. 80. Revolution 43 (TRGO - 229120)

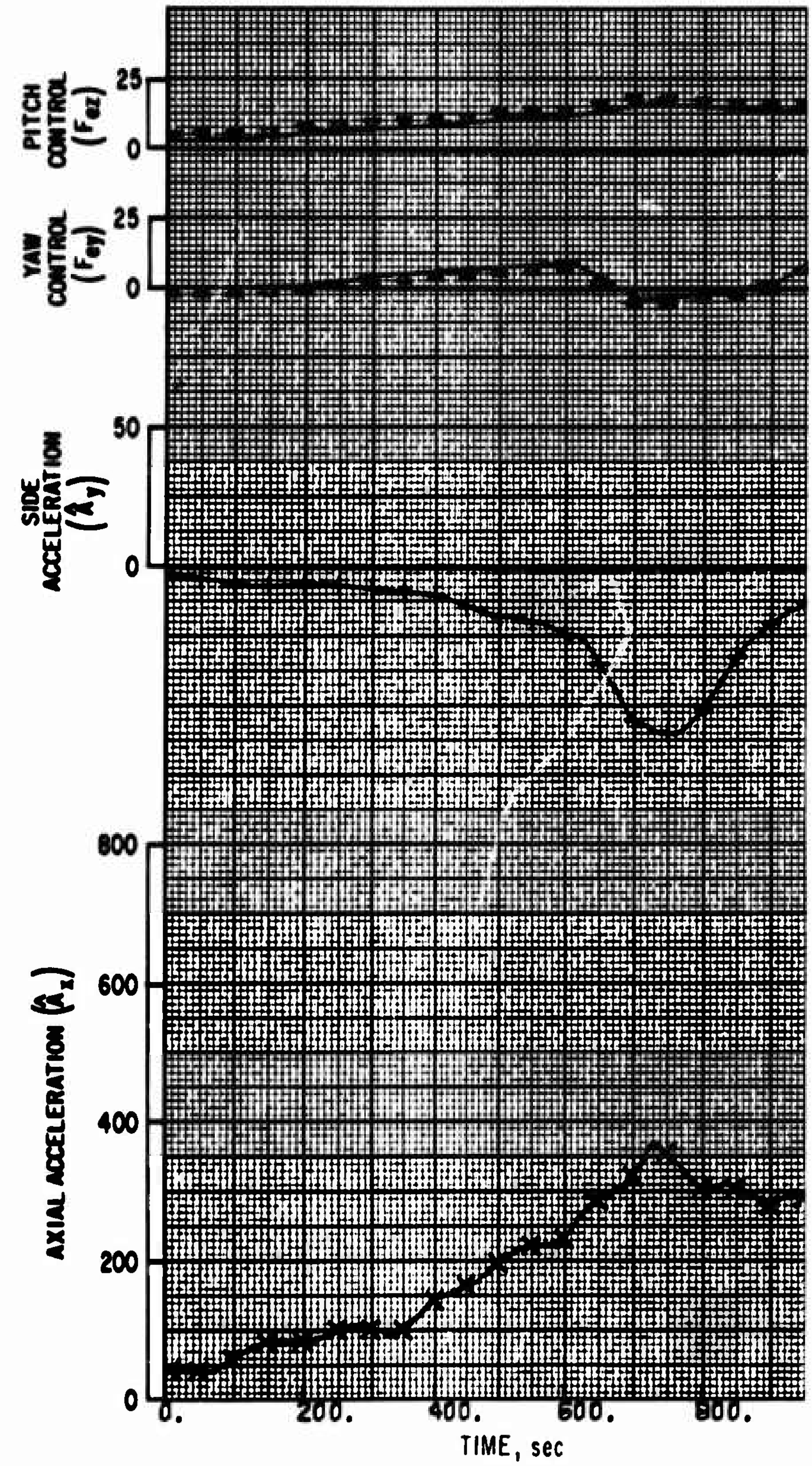

Fig. 81. Revolution 53 (TRGO = 282240)

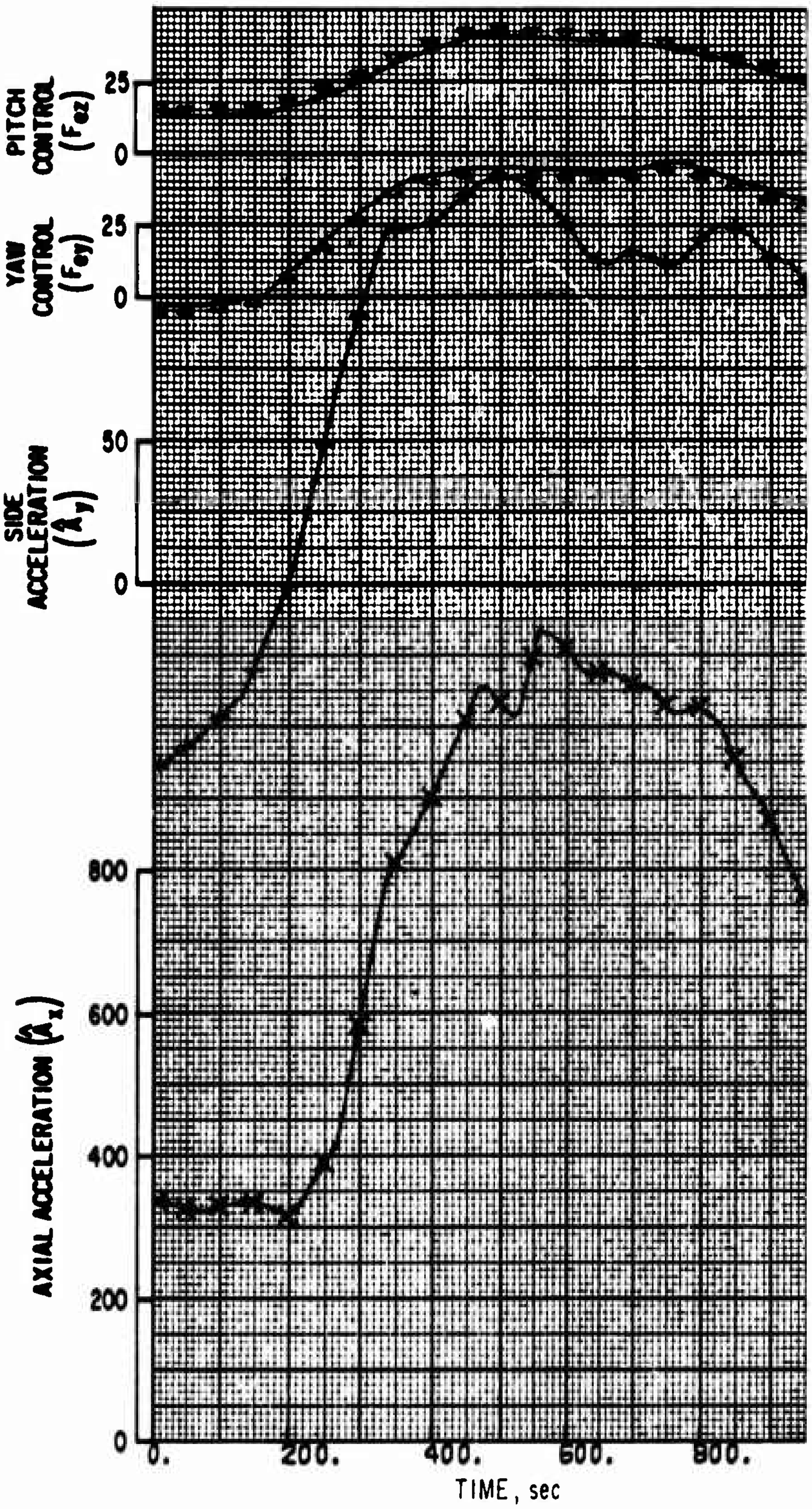

Fig. 82. Revolution 54 (TRGO = 288384)

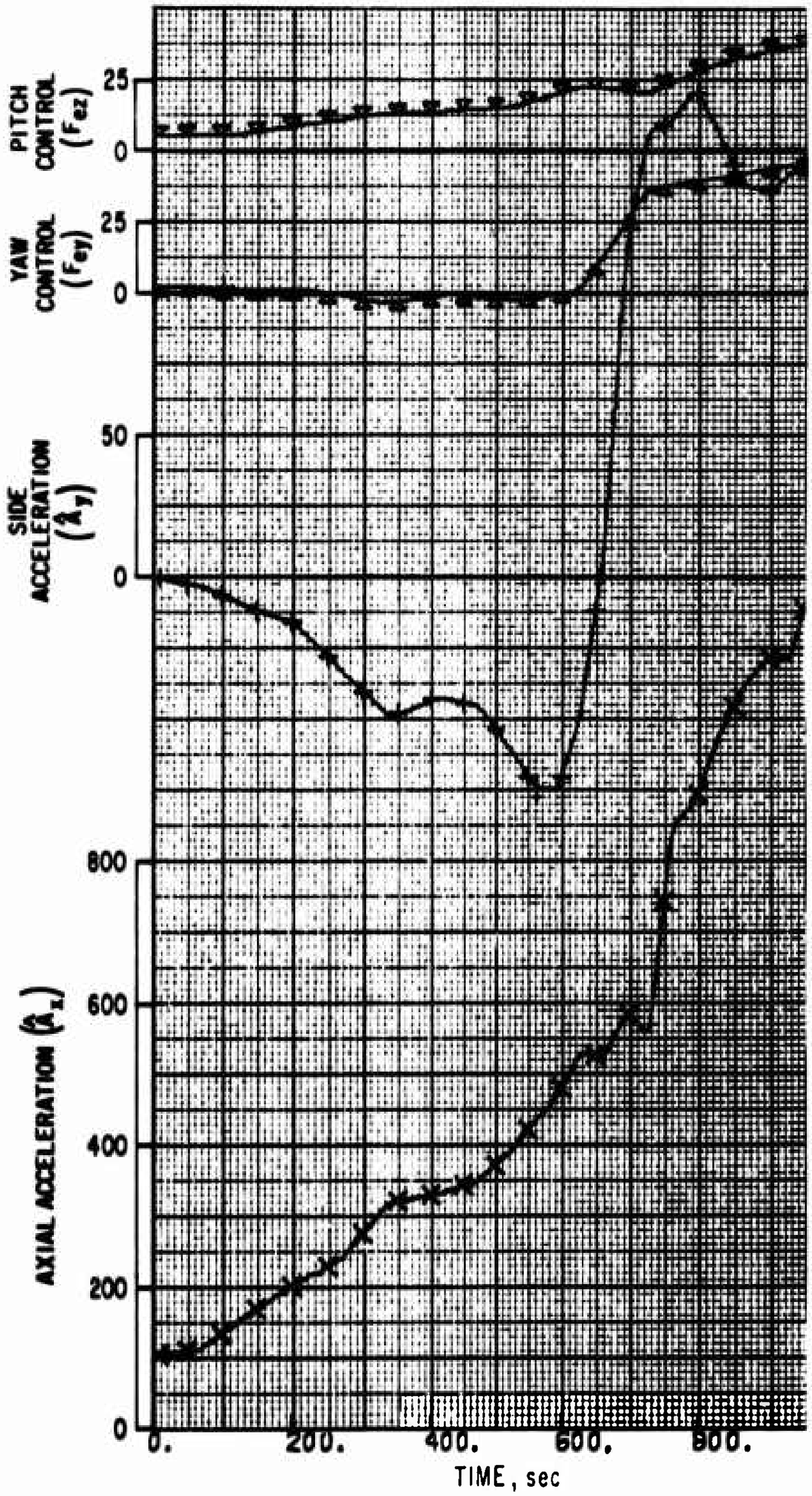

Fig. 83. Revolution 56 (TRGO = 298624)

The next approach was to use several different scale factors on the control force, F_{cy}, and several different values of Y_{cg} in Eq. (51) to observe the resulting time histories of X_{cpe}, α, and β for the data sets of each of the seven revolutions. The best results were obtained when a scale factor of 0.5 was used on control force and the predicted value of Y_{cg} was used. Except for Rev. 53, the resulting time history of X_{cpe} was near constant and did not reflect the altitude dependence predicted by the curves of Fig. 75. There does appear to be a possible temperature (T_{∞}) sensitivity in that the results for Revs. 38, 39, 41, and 43 imply a constant value of 2 ft for X_{cpe}, while Revs. 54 and 56 appear to show a somewhat lower value for X_{cpe}. The above numbers are approximate, based on an eyeball estimate. The principal characteristic from this evaluation is that to first order X_{cpe} is a constant and does not depend on altitude for the range of altitude (75 to 110 nmi) considered here. This result implies that either the moment coefficients and resulting aerodynamic center of pressure as a function of molecular speed ratio are in error (Fig. 73), or the molecular speed ratio versus altitude (Fig. 74) is in error for the altitude regions considered.

With a constant value for X_{cpe}, the calculation of angles of attack using the moment relationship [Eqs. (49) and (50)] is in error by a possible scale factor, depending on the value of X_{cpe} chosen. To further investigate the proper choice of numerical values to use, we made a consistency check by comparing the results obtained for β from Eq. (48) to those obtained from Eq. (49). For this test, a value of 2 ft was used for X_{cpe}. As before, the value of 0.5 for control force scaling and the predicted value for Y_{cg} produced the most consistent results. The comparison of Rev. 54 and Rev. 56 also showed that a slightly smaller value for X_{cpe} would have produced a closer comparison; i.e., for these revolutions the force equation produced a slightly larger calculated β.

Some characteristics of equation sensitivities to data errors can be explained by the following comments. The sensitivity of the calculated angle of attack to lateral cg is determined from Eq. (49) as

$$\frac{\partial \beta}{\partial Y_{cg}} = -\frac{C_A}{C_{m\alpha}} \doteq -26°/\text{ft} = -2.16°/\text{in.}$$

An error in predicted cg thus acts as a bias of calculated angle of attack. Comparing Eqs. (48) and (49) with respect to control force scaling, one sees that the control force is scaled by a factor of X_{gv}/X_{cpe} in Eq. (49) (≈ 4.5). Also, the polarity of the control force term is different in each equation. Therefore, if a control scale factor error exists, one equation will give a greater value and the other a smaller value than the true value in the absence of other errors. Additionally, the control force is generally a factor of 2 or more smaller than total side force so that Eq. (48) is relatively insensitive to a scale factor error of the control force. The coefficient $C_A/C_{N\alpha}$ is common to both expressions.

With respect to the control force scale factor, it had been determined (Volume I, Section II) that the control firings were a pulse of minimum duration (20 msec). Also, the nominal control force level was assumed to be 0.5 lb. Therefore, the processing for this earlier work was based on an impulse of 0.01 lb-sec per gas valve firing. The pulse referred to here was the minimum electrical current pulse. Since the valve does not respond instantaneously to the current pulse, the full impulse is not realized. Test results at LMSC had indicated that only 63 percent of the ideal impulse is achieved when valves are pulsed at the minimum duration for force levels of 10 lb. No tests have been run for the 0.5-lb force level. With these considerations, a 0.5 scale factor is within expected tolerances of the control system.

It is of interest to compare the time histories of α and β derived from the data with those predicted from the orbit characteristics. The pitch angle of attack α is related to the flight path angle and attitude as

$$\alpha = \theta - \gamma \tag{54}$$

where

θ = pitch attitude determined from horizon sensor data

γ = flight path angle determined from the Best-Fit Ephemeris (BFE)

Therefore, when the vehicle is going toward perigee, $\alpha > \theta$; when coming from perigee, $\alpha < \theta$. For the yaw angle of attack β, the predicted model chosen is one which assumes the atmosphere rotates with the earth. For a polar orbit and the yaw attitude reference of Agena, the following relationship for predicted β results

$$\beta = -(\psi + R\omega_e \cos \lambda [\mathrm{sgn}\ \dot{\lambda}]) \tag{55}$$

where

ψ = yaw attitude with respect to the orbit plane (sum of $\psi_\epsilon + \psi_0$, see Fig. 72)

R = radius from center of earth

ω_e = rotation rate of the earth

λ = latitude

$[\mathrm{sgn}\ \dot{\lambda}]$ = sign of latitude rate

Therefore, when the vehicle is going south, $\beta > \psi$; when going north, $\beta < \psi$.

The data processing results of the seven revolutions are shown in Figs. 84 and 85. Presented are the predicted and processed data points, where the predicted curves are smooth lines and the processed data are identified with a symbol. For β, both the results from the force equation

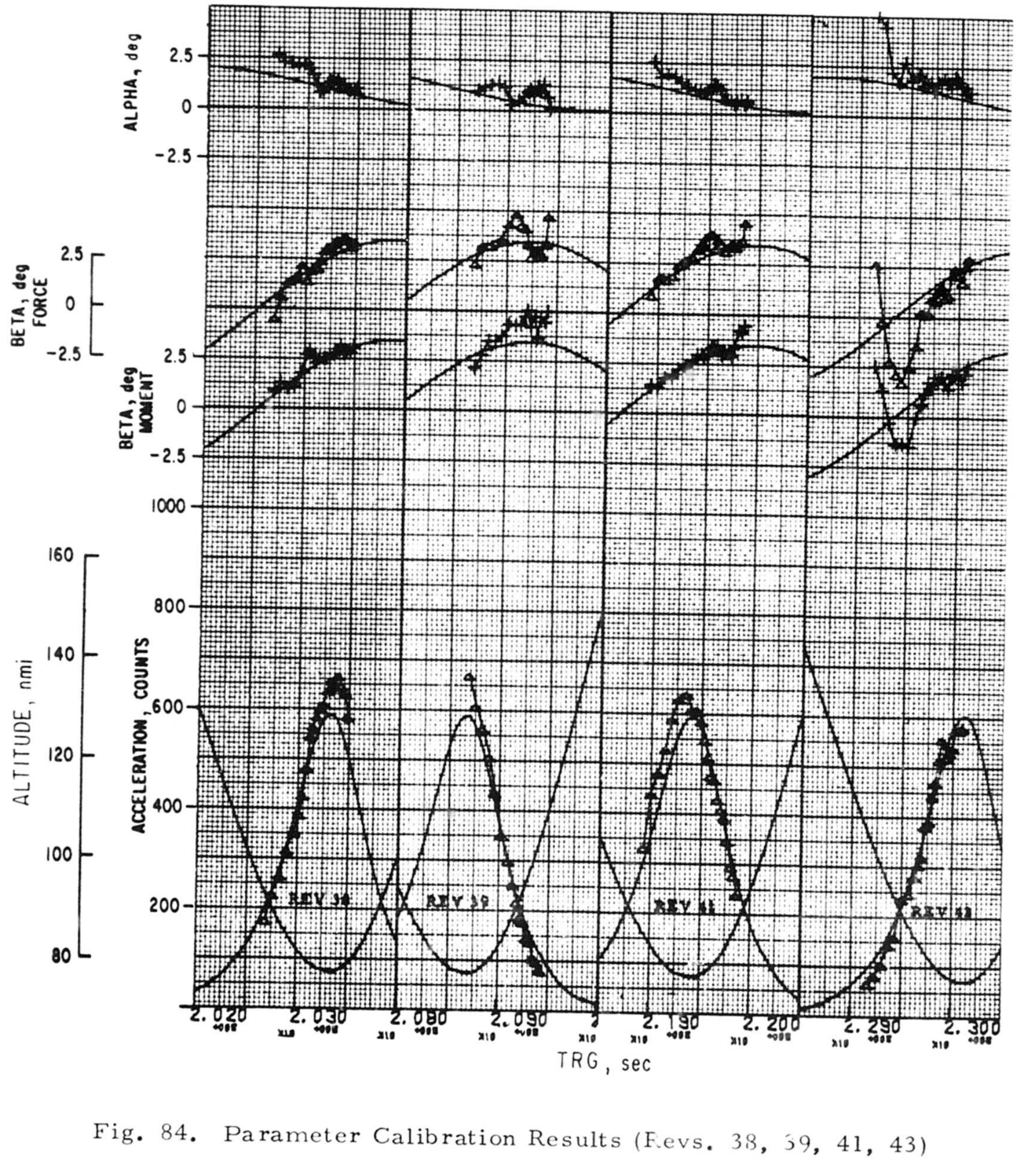

Fig. 84. Parameter Calibration Results (Revs. 38, 39, 41, 43)

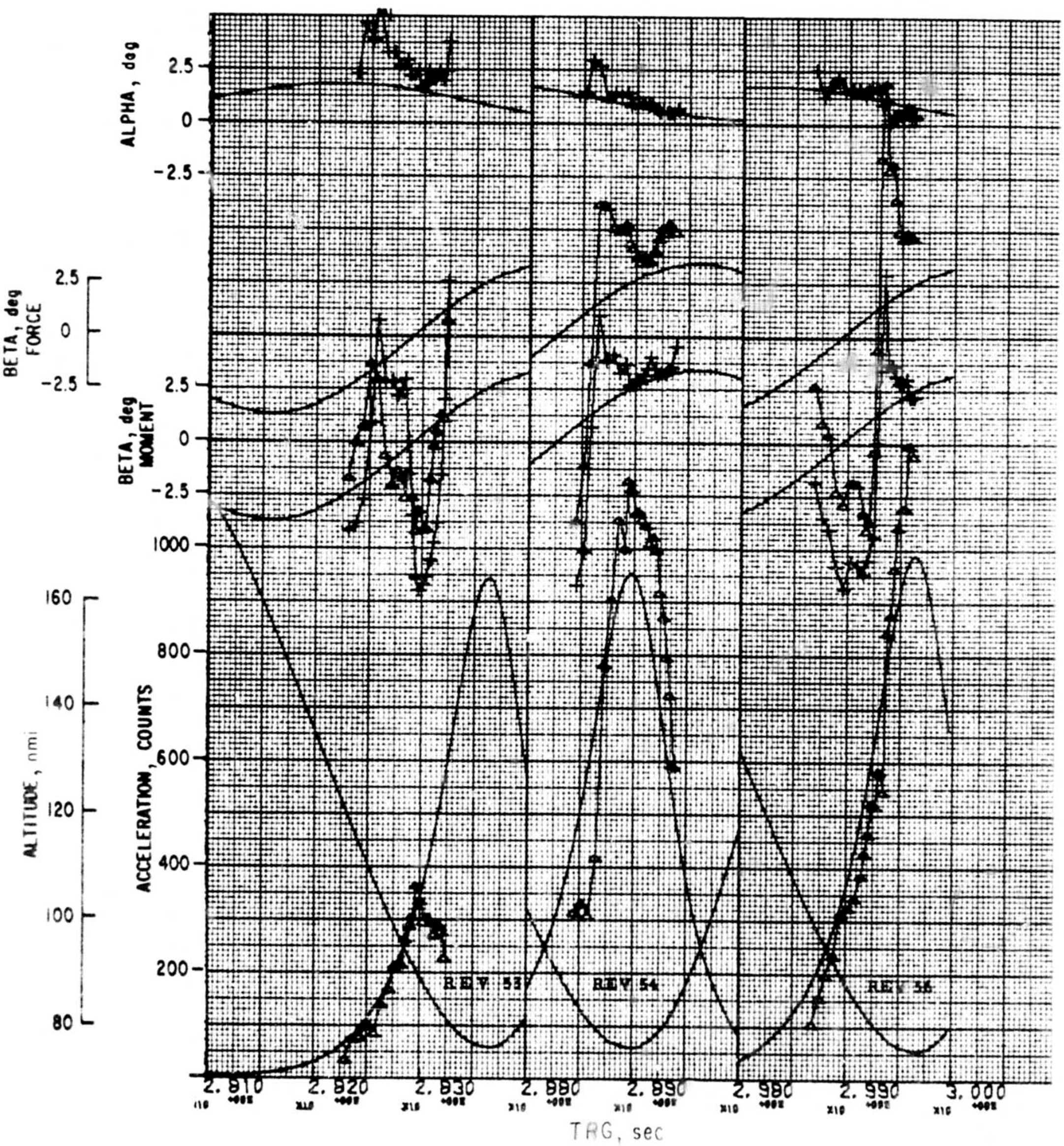

Fig. 85. Parameter Calibration Results (Refs. 53, 54, 56)

[Eq. (48)] and the moment equation [Eq. (49)] are plotted. The high degree of correlation between predicted and processed data for Revs. 38, 39, and 41 is apparent. Also apparent is the good correlation of results (except for part of Rev. 53) obtained by the two separate β algorithms on all seven revolutions. Finally, it is observed that the differences of the β angles from those predicted, which are of magnitudes greater than 7° and of both polarities, are contained in the data, and that the transitions from one polarity to the other occur in very short time intervals.

F. MISSION PITCH AND YAW ANGLE-OF-ATTACK TIME HISTORIES

Equations (49) and (50) require time history data of control force and axial force only to calculate angles of attack. Therefore, these equations can also be used for the modes when the accelerometer orientation was fixed, provided the control system was on its deadband ($I\dot{\omega} = 0$). Since the time history data were available from Volume I, Section II, no further data reduction was necessary. To provide consistent time arguments on the control force and the axial force data, we filtered the latter to produce data at the 100-sec data rate of the control data processing. In general, the attitude was on the control deadband when the drag acceleration level reached a 100-count level. Therefore, for this analysis all acceleration data below the 100-count level were deleted from further consideration (in general this limits the analysis to altitudes below 110 nmi). When the data duty cycle* is low, the confidence level of the processed control force data is also low (see Volume I, Section II). Therefore, control force values which were processed for duty cycles less than 90 percent were deleted from consideration here. With the above data editing, the remaining data were processed for angle-of-attack histories using Eqs. (48) and (49). In this processing, a control force scale factor of 0.5, a X_{cpe} of 2 ft, and the predicted cg values were used.

---

*Duty cycle is defined as the ratio of the number of raw data points contained in a filter span to the number of points of a filter span.

The results of this processing are plotted and presented in Fig. C-3 of Appendix C. Included in this plot are the predicted angle-of-attack histories, the processed angle-of-attack histories, the 100-sec filtered axial acceleration, and the best-fit ephemeris values of altitude and axial acceleration.

It can be observed from these plots that there exists good correlation of predicted and processed angle-of-attack histories before the magnetic storm. There are some observed points in the early portion of each rev. (going toward perigee) that seem to be erroneous. Two problems exist for this region. The first is that the control system may not have settled on the control deadband; therefore, F_{cy} is zero until the attitude reaches the deadband, and then F_{cy} is large when it first reaches the deadband to stop the vehicle angular rate. The second problem is associated with force levels. When the average forces are small, the induced noise on accelerometer data due to control firings is greater in proportion; consequently, less accuracy can be expected for these calculated angles of attack. Nevertheless, good correlation exists before the storm, and large yaw angles of attack are observed after the storm. The pitch angle of attack (sensitive to vertical winds) seems relatively unaffected by the magnetic storm activity.

For these plots the value of θ[Eq. (54)] used was 1° and the value of ω[Eq. (55)] used as 0°. This implies that there existed a yaw reference error of 1° or a Y_{cg} error of 0.46 in. Either are within expected tolerances and cannot be separated by this analysis. Also, control force scaling and the coefficient C_A/C_{mo} can influence the results to some extent.

G. YAW WINDS IN GEOGRAPHICAL COORDINATION

In order to determine the source of the large winds, we decided to first display the wind components in geographical coordinates. Figure 86 presents a plan view of the general orbit characteristics for this mission (the orbit inclination was essentially 90°). Perigee occurred in the general latitude region of 45° N. The altitude below 110 nmi was generally contained in the sector from the North Pole to the equator. It therefore was convenient to

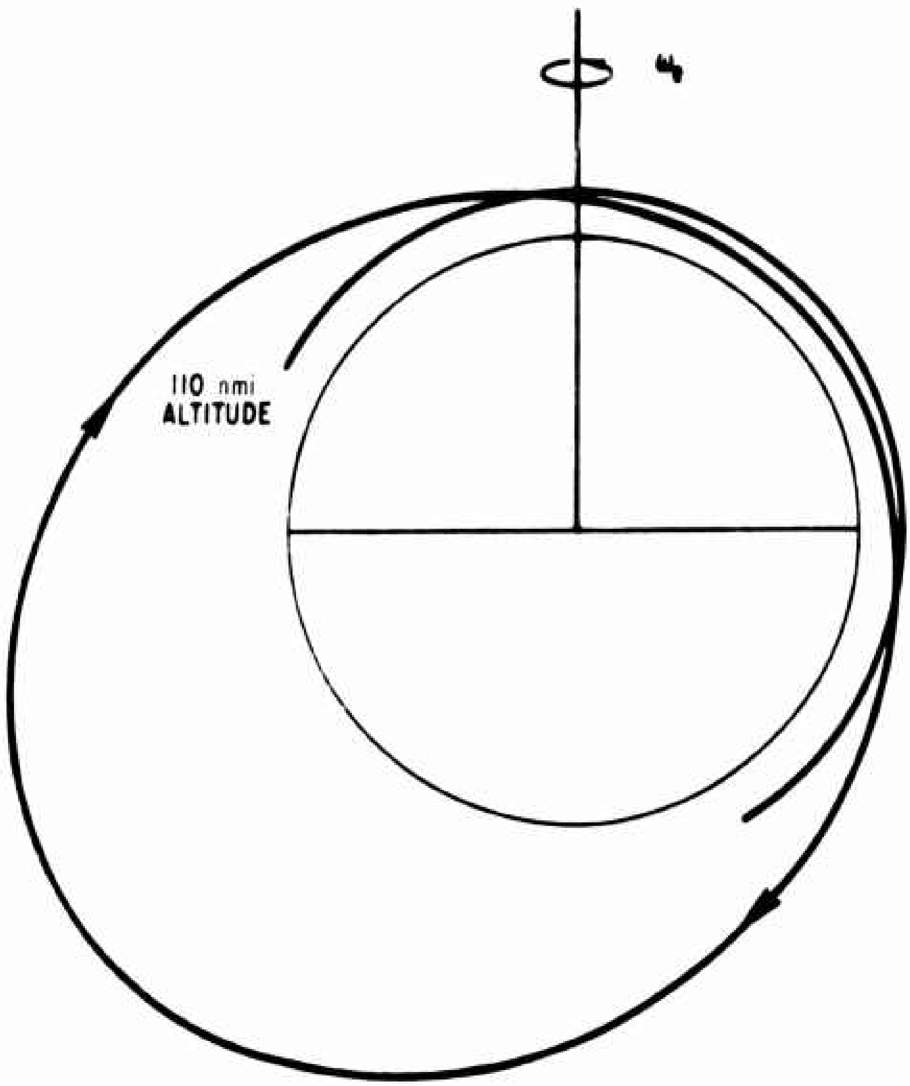

Fig. 86. Orbit Geometry

present the orbit trajectory (geographical coordinates) looking down from the North Pole in terms of colatitude and longitude. For each calculated wind component, a line normal to the trajectory was constructed whose magnitude was proportional to the difference between calculated and predicted β, and the direction is based on the polarity of the difference. An arrow was placed at the end of the line to indicate the wind direction.

Figure 87 presents the results from the parameter calibration of Revs. 38, 39, 41, and 43 (Fig. 84 time histories) in the described geographical coordinates. Similarly, Fig. 88 presents the results of Revs. 53, 54, and 56 (Fig. 85 time histories). The rev. number associated with each is also indicated on the figures; an arrow displays the trajectory direction. The scale used for β is indicated, where one major division is equal to $10° \beta$ ($\approx$4500 fps wind magnitude).

Similarly, the time history of Fig. C-3 is presented in geographical coordinates in Figs. 89 through 92.* To avoid trajectory overlap, the data are presented by mission day (from 23 May to 26 May). It is readily observed that very little deviation from predicted wind components existed prior to the magnetic storm activity (Rev. 5 through Rev. 41). Following the storm, large wind magnitudes of both polarities are evident in the northern latitudes, particularly for the data of 26 May.

The 26 May data (Fig. 92) are of greatest interest. The overlap observed is due to the orbit altitude decay with time, so that the 110-nmi altitude occurred before reaching the North Pole. Some of this overlap is also due to the northerly rotation of perigee during the mission. Figures 93 and 94 amplify the data presented in Fig. 92. The colatitude was reduced to 45° and the β plot scale was extended so that two major divisions equals 10°. Figure 93 plots the data for the trajectory going toward the pole while Fig. 94 plots the data from the pole to a colatitude of 45°. Also included are lines of

*The method of plotting these data was to plot the first observed wind component for a particular revolution and then to continue the trajectory plot to a colatitude of 95°. If no points were observed, then the corresponding trajectories were not plotted.

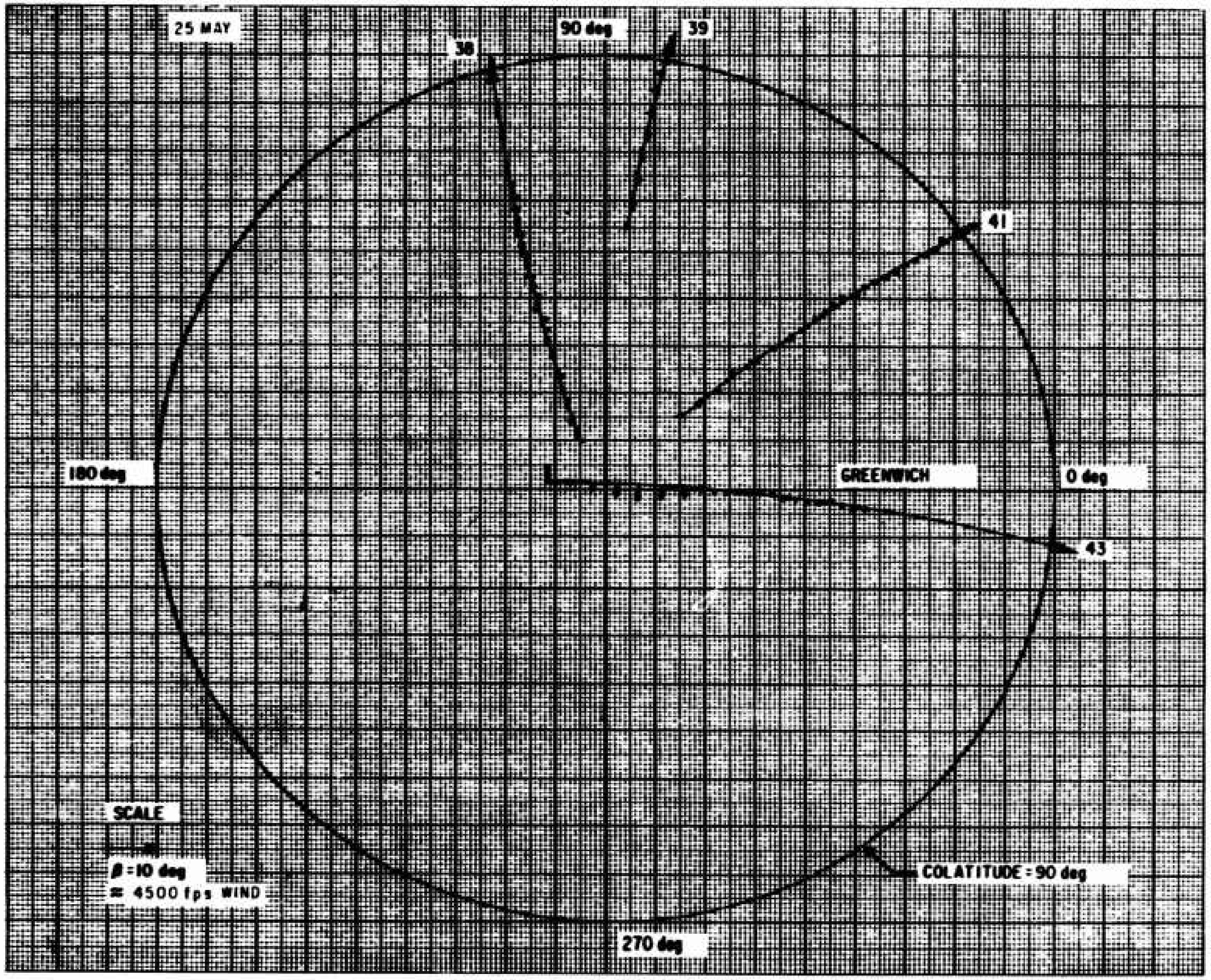

Fig. 87. Wind Components in Geographical Coordinates (Revs. 38, 39, 41, 43)

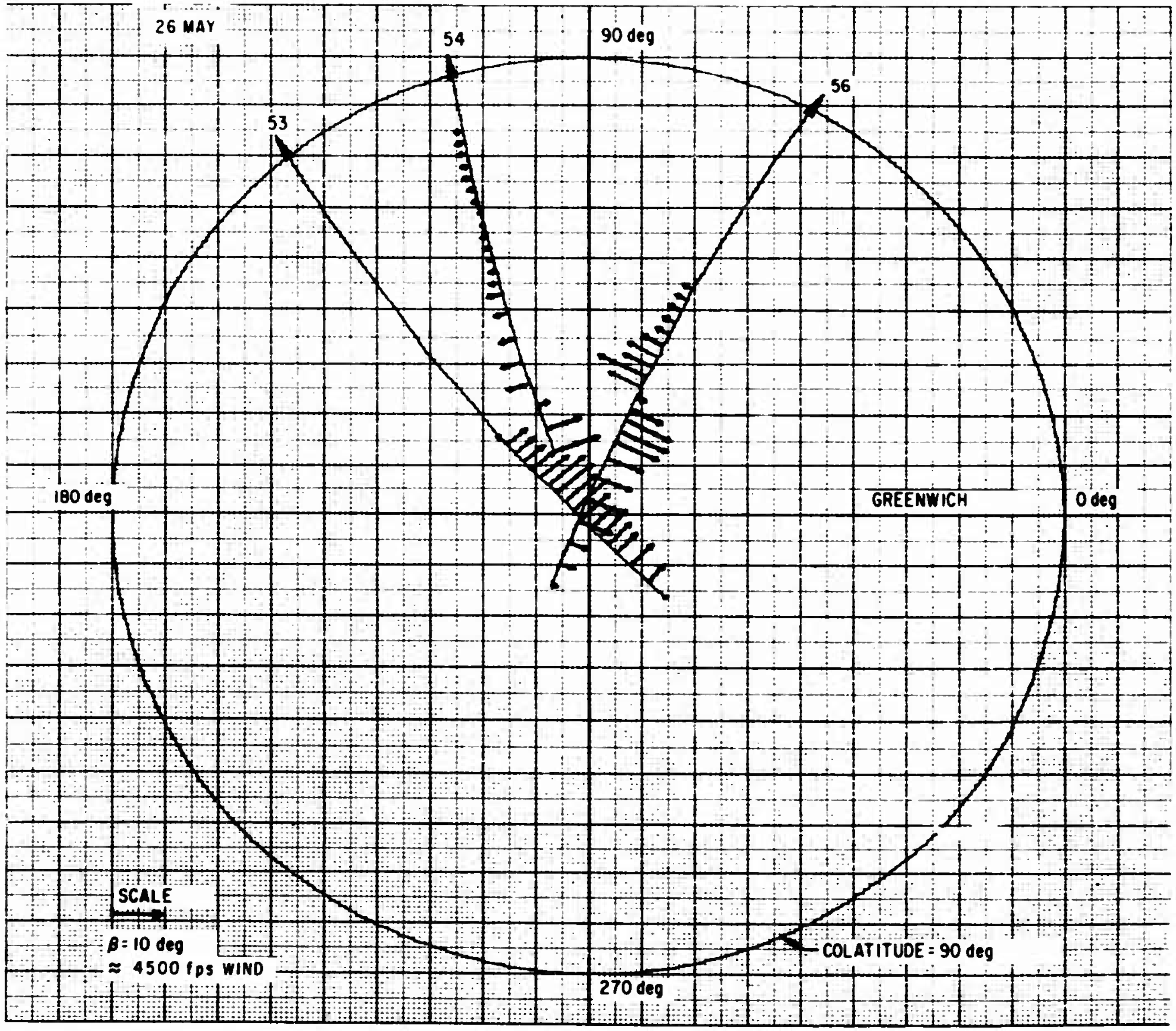

Fig. 88. Wind Components in Geographical Coordinates (Revs. 53, 54, 56)

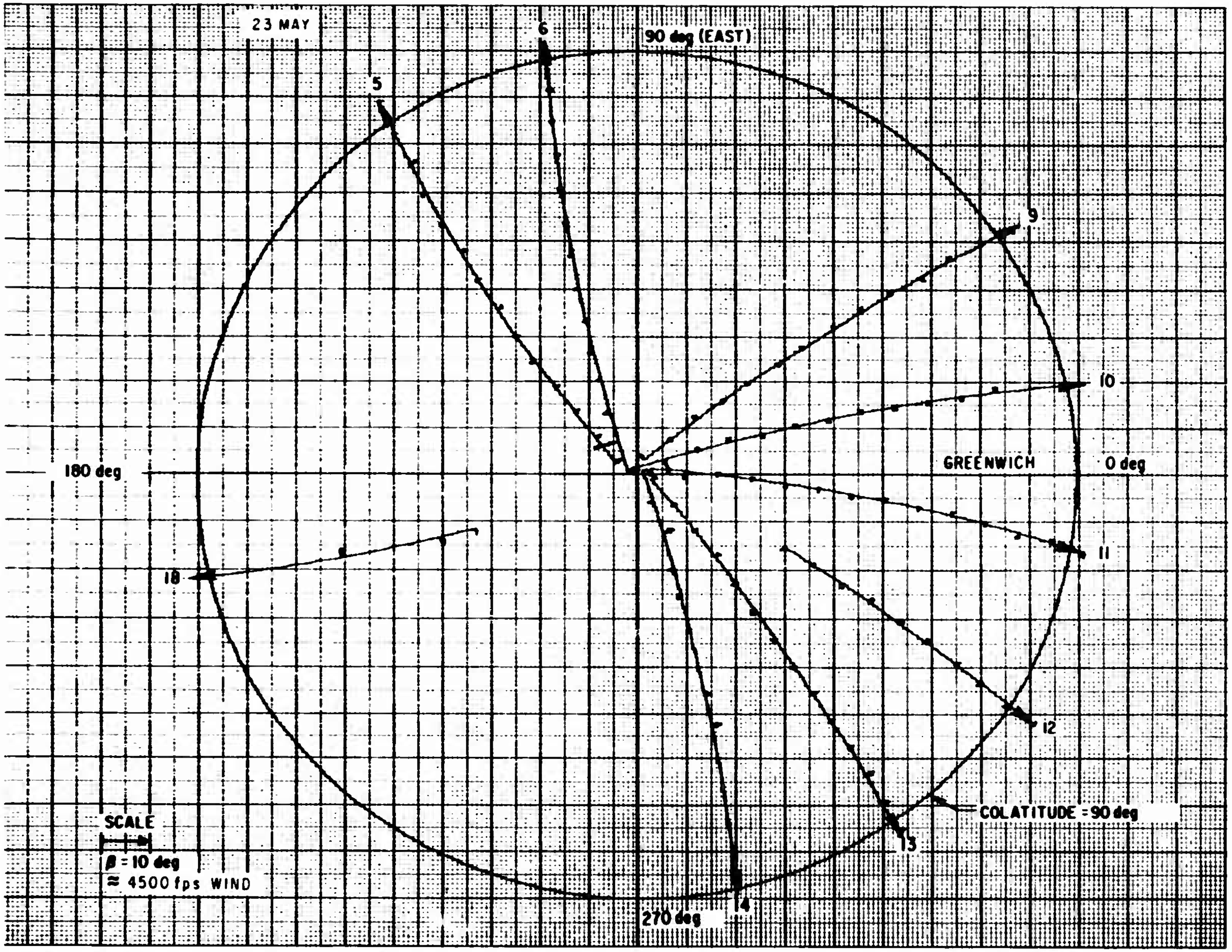

Fig. 89. Wind Components in Geographical Coordinates for 23 May 1968

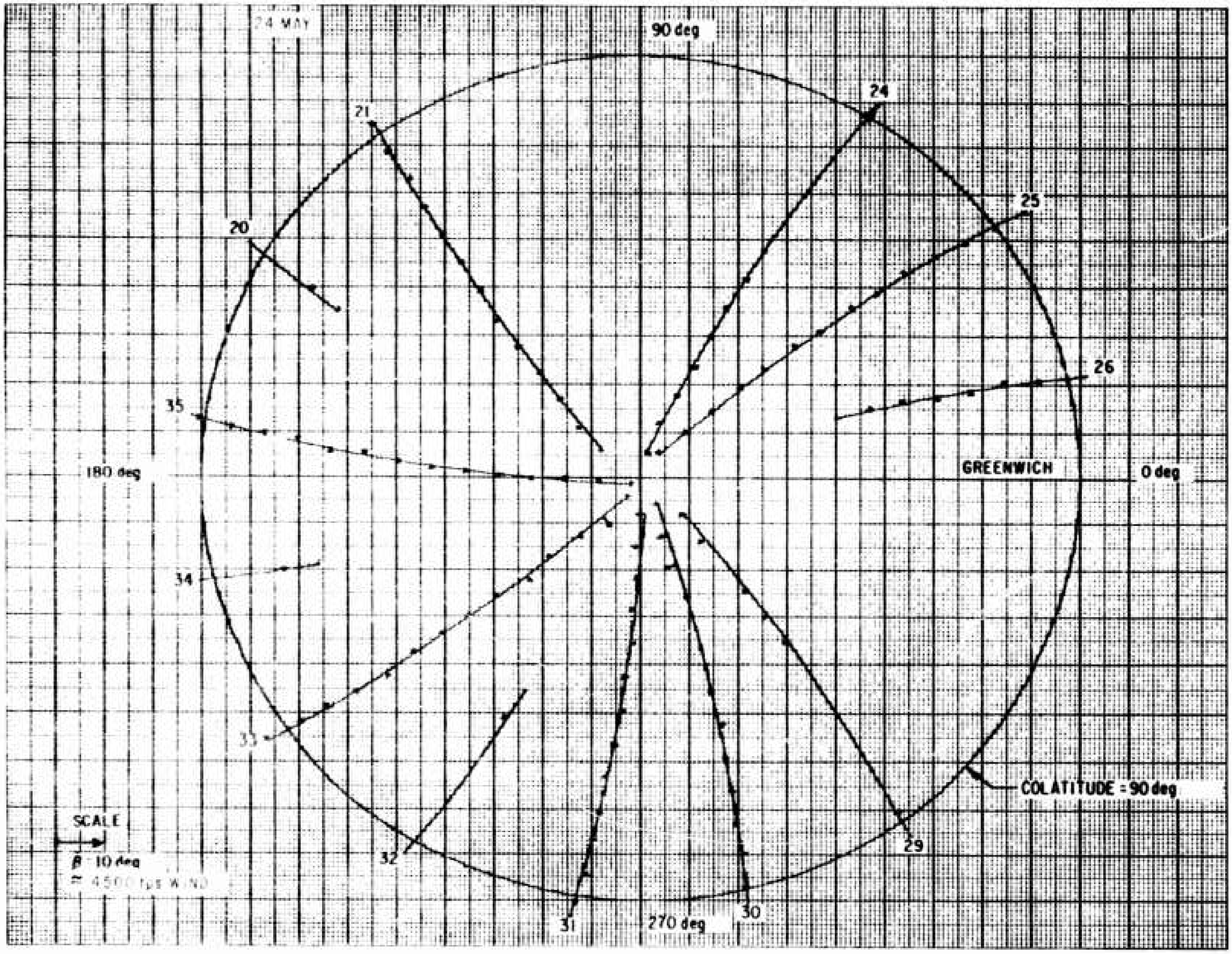

Fig. 90. Wind Components in Geographical Coordinates for 24 May 1968

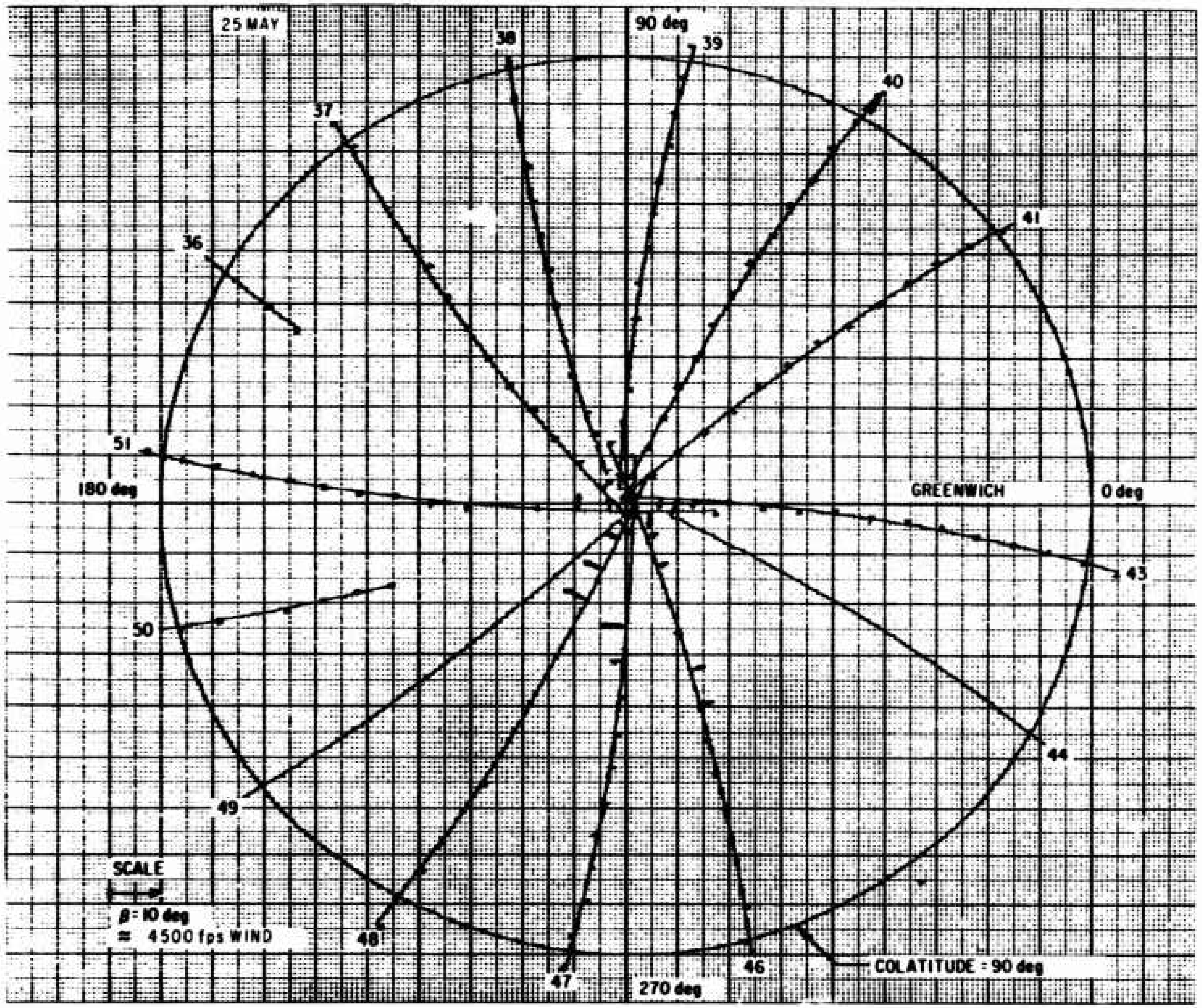

Fig. 91. Wind Components in Geographical Coordinates

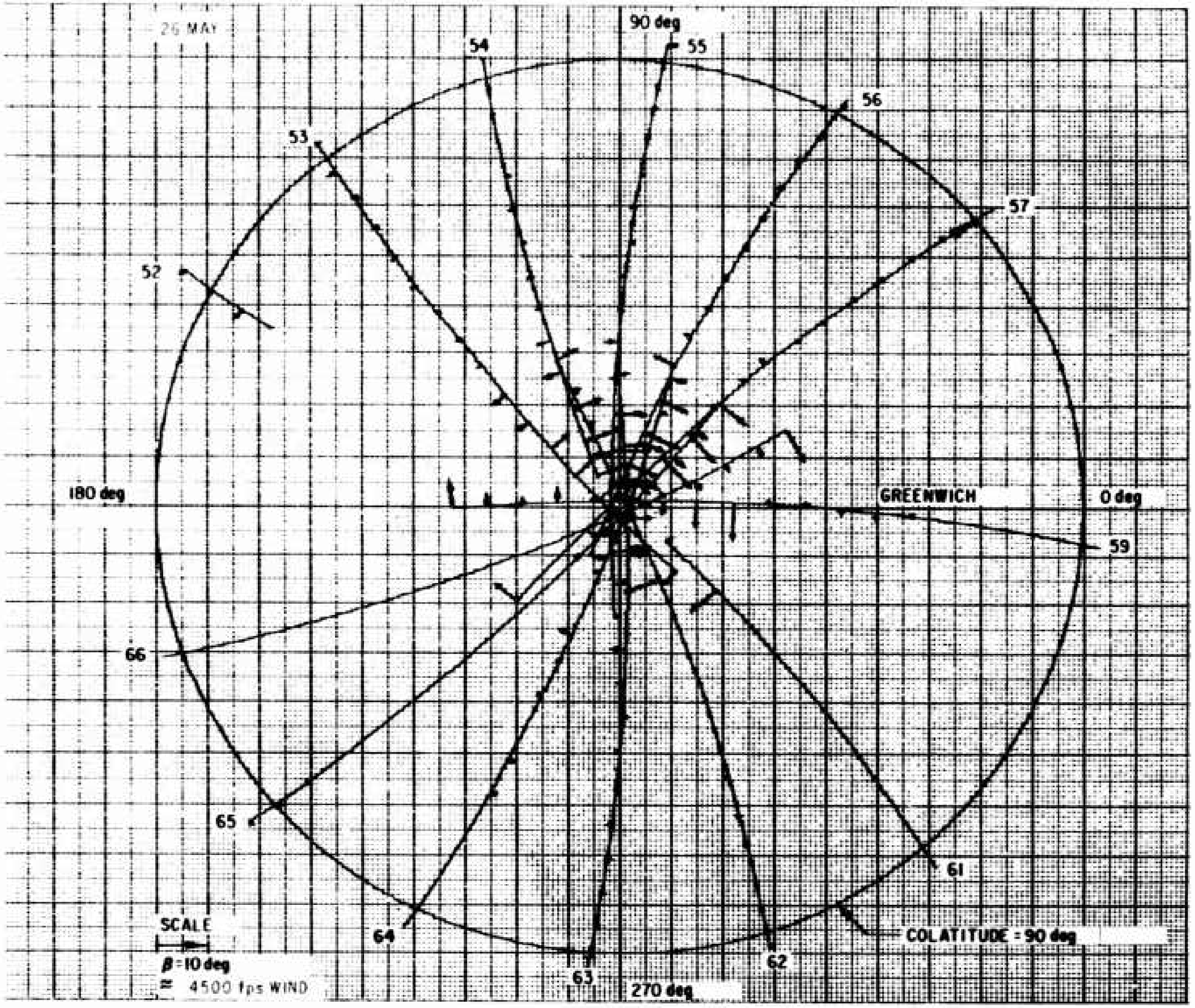

Fig. 92. Wind Components in Geographical Coordinates for 26 May 1968

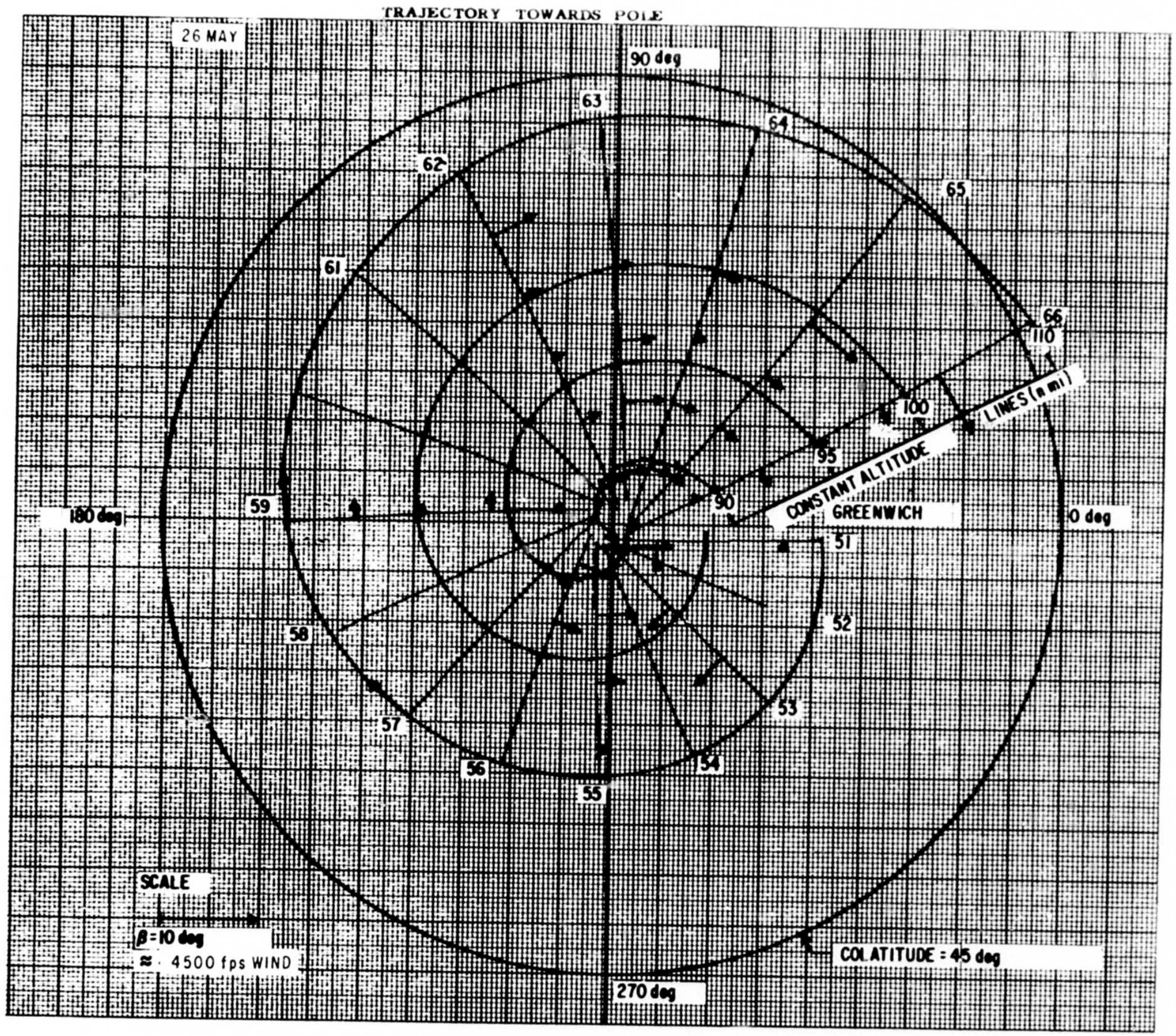

Fig. 93. Expanded View of Fig. 92 (Trajectory Toward Pole)

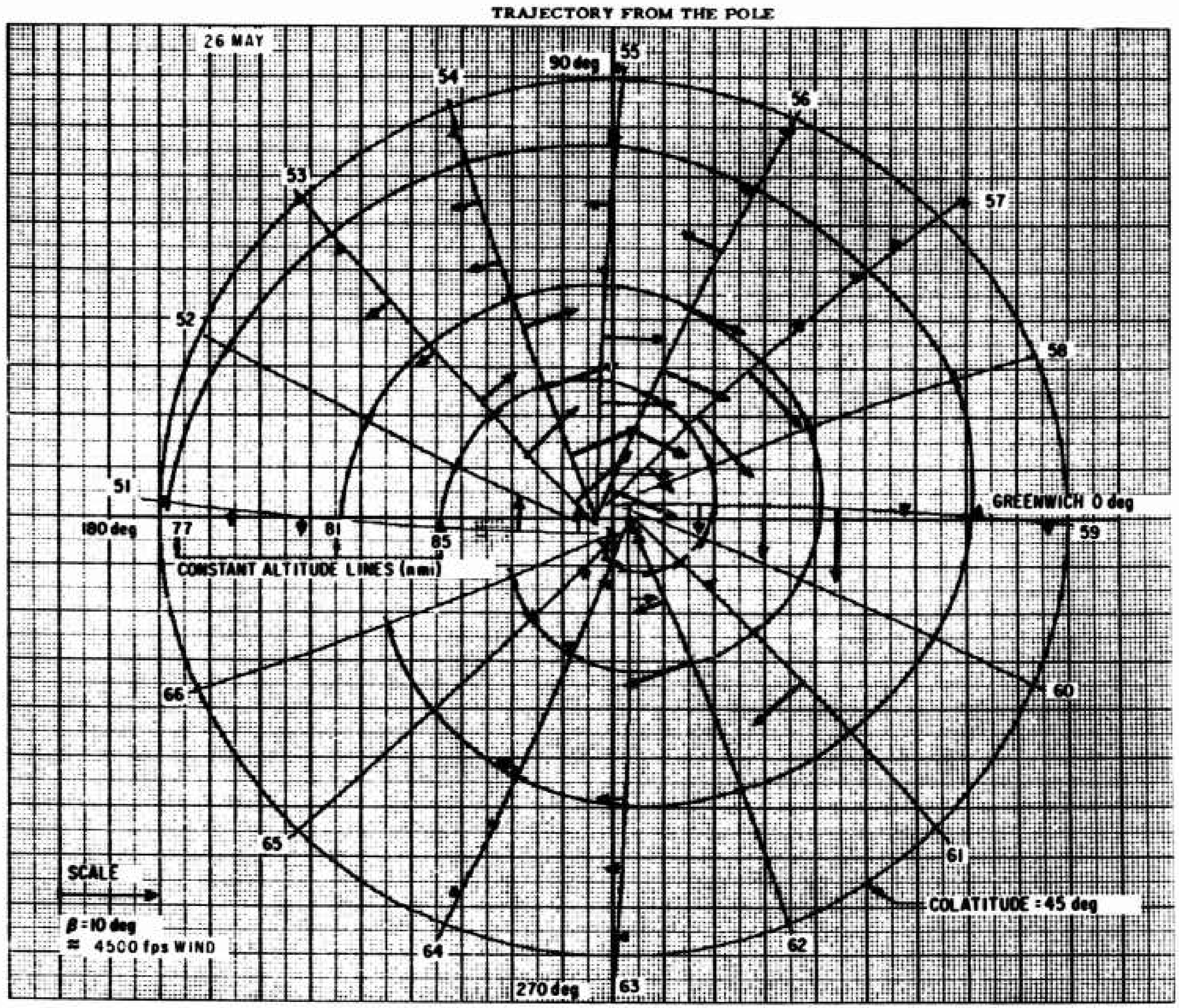

Fig. 94. Expanded View of Fig. 92 (Trajectory Away from Pole)

constant altitude of 110, 100, 95, and 90 nmi in Fig. 93, and lines of 85, 81, and 77 nmi in Fig. 94.

H. WIND ANALYSIS CONCLUSIONS

The results clearly confirm the theory that the atmosphere normally rotates with the earth up to and including 110 nmi altitude. However, the vehicle forces produced by responding to this wind component are highly dependent on the location of the vehicle center of gravity and the type of vehicle control system. In low altitude regions (below 80 nmi), the magnitude of the lateral forces generated can exceed the magnitude of geopotential harmonic terms. With the configuration of this experiment, lateral accelerations of 5 to 15 μg were experienced due to aerodynamic and control forces.

Following the magnetic storm, the results of the data analysis confirm the hypothesis of large velocity wind components normal to the orbit plane (apparently restricted to the polar regions). It therefore can be concluded that wind components exist in the in-track coordinate as well. Consequently, the analysis of drag acceleration, and its variation, must include the effect of wind as well as the effect of density variation. For example, a 5000-fps wind velocity in the in-track coordinate could result in a 40-percent variation in drag acceleration.

The aerodynamic coefficients are dependent on the predicted molecular speed ratio, which in turn is dependent on the model of temperature versus altitude (Fig. 74). In the processing of the moment equations, as noted in Section F, the variation with altitude of the aerodynamic moment coefficient was not demonstrated. This suggests that the predicted molecular speed ratio versus altitude is in error. If the predicted molecular speed ratio is in error, then the predicted aerodynamic drag coefficient versus altitude is also in error. This in turn affects the accuracy of the derived densities from drag acceleration data. Additional analysis will be required to support this conclusion.

SECTION VIII

THERMOSPHERIC CONVECTIVE INSTABILITY

A. INTRODUCTION

It has been known for some time that local winds up to 100 m/sec exist in the thermosphere even during magnetically quiet times. Some of these disturbances are undoubtedly related to the traveling gravity-heat conduction type of wave phenomena (Refs. 36 and 37). Recently, vapor trail measurements at low latitudes during geomagnetically active times reveal strong wind components of approximately 200 m/sec at 180-km altitude (Ref. 38). The direction and speed of these winds seem to agree quite well with the hypothesis that they are generated by the existence of polar high pressure regions during geomagnetic activity (Ref. 39). Despite the lack of direct proof of the existence of such polar high pressure regions in the thermosphere, it has been conjectured that they are generated by particle and/or magnetic energy absorption below 160 km (Refs. 40 and 41). Monte Carlo calculations have shown that particle energy deposition occurs essentially in a limited layer of the thermosphere (Ref. 25). Although the low latitude winds are good indirect evidence of thermospheric heating in the polar regions during magnetic storms, direct evidence is as yet not available. Theoretically, if such heating exists and is strong enough a direct consequence would be the production of strong atmospheric motion since, under suitable conditions, a fluid layer heated from below is convectively unstable.

B. OBSERVATION

Polar anomalous winds were observed on 26 May 1967 by the 1967-50B satellite. The measurements were recorded when the satellite passed, in near circular orbit, within approximately 30° of the North Pole. Since the satellite has a perigee of 145 km at approximately 40°N latitude, the observations were recorded in a thermospheric layer of approximately 60 km, i.e., from 220 to 160 km. This particular satellite ephemeris is rather important because it establishes the polar character of the anomalous winds, for if it were global in character they would have been observed in the low latitude regions where the satellite passed through a layer of similar altitude.

Approximately 8 hr after the peak of the magnetic storm at the polar regions, wind patterns were seen to persist for 15 hr with very little change. The horizontal components of wind velocity exhibit well-organized direction changes with a characteristic length of 2000 to 4000 km. Since the horizontal component changes very smoothly within one horizontal characteristic length, the altitude change of the satellite within that horizontal length allows us to determine the minimal vertical characteristic length, which turns out to be 15 to 30 km. The maximal horizontal speed observed was approximately 1 km/sec, while the maximal vertical speed was 100 ± 100 m/sec. There seems to be an increase of maximal horizontal speed with altitude of less than one e-fold. The full wind pattern unfortunately, cannot be mapped because of the lack of information on the in-track wind component. Finally, the growth phase of the wind pattern seems to last one or two satellite orbits.

From the physical point of view, there are several significant features which must be considered if one attempts to understand the meaning of the measurements.

The anomalously high horizontal wind speeds (~1 km/sec) at a typical altitude of 200 km, where the sound speed is approximately 0.8 km/sec, would exclude the interpretation of such wind phenomenon as gravity waves, which are essentially stable small amplitude oscillations akin to sound. Although large wavelength gravity waves may conceivably have a phase velocity of order of 1 km/sec, it must be emphasized that the observation is on the molecular flow speed and not the phase velocity of the disturbance. Hence, it is eminently clear that we cannot explain the observation on the basis of small amplitude stable oscillations. On the other hand, the necessity of small amplitude disturbances (~50 m/sec) to grow to anomalously large speeds finds a rather natural explanation if we are to interpret the observations in terms of some hydrodynamic instability of the thermosphere that allows such growth to occur.

The close association between the wind observations and the magnetic storm as well as evidences of atmospheric heating during magnetic disturbances point rather directly at the cause of such a thermospheric instability, namely, excessive heating of the thermosphere at a particular level. If one adopts such a hypothesis, the polar character of the anomalous winds immediately finds a rather natural explanation since the polar caps are directly accessible to energetic particles, which can deposit their energy in the thermosphere.

C. CONVECTIVE INSTABILITY

The observational evidence of the previous sections strongly suggests that the anomalous winds can be interpreted as convective motion due to stationary heating. Since it is likely that energy is deposited in the thermosphere below 160 km during a magnetic storm (Refs. 40 and 41), we envisage a layer of atmosphere heated from below 160 km as the basis of our model. Convective instabilities in a fluid heated from below have been studied extensively in the astrophysical and meteorological regime. Detailed studies of convective instability have been made by Lord Rayleigh (Ref. 42), Pellew and Southwell (Ref. 43), and Chandrasekhar (Ref. 44) for incompressible fluids. More recently, convective instability in a polytropic gas has been studied by a number of authors [see, for example, Ref. 45)]. Most of these are considered for conditions appropriate to the granulation phenomenon in the solar photosphere, where convective heating is a dominant feature. In the earth's thermosphere, where the density is essentially exponential, the conditions are somewhat different. Unlike the solar photosphere, the earth's thermosphere is only occasionally heated strongly from below, if at all; hence, we expect unstable situations to occur only rarely in the thermosphere. Furthermore, it is not clear that a temperature inversion can be set up in the thermosphere to generate convective instability.

To study the generation of an unstable temperature inversion, we first recall that steady heat conduction with only vertical motion is clearly possible in the thermosphere. Indeed, one-dimensional models with very slow vertical motion have been considered (Ref. 46) in order to account for observed time delays between atmospheric heating and the density response of the thermosphere. For moderate energy deposition, these models show no tendency to form unstable inverse temperature gradients. The reason for this occurrence is rather clear because the vertical motion due to the expansion of the heated air quickly spreads the heat, so that after a few hours only a general rise of the temperature profile is evident. On the other hand, if a larger amount of energy is deposited over a long period, say 8 hr, the situation becomes quite different. The temperature increase near the level of steady heating now overtakes the tendency to spread the temperature by mass motion, and a local temperature inversion in the temperature profile may result in the model. Figure 95 shows the temperature profile calculated from a Thomas-Ching model in which a total energy of 3×10^5 erg/cm^2 is deposited over 8 hr as a sheet source at 150 km. The above amount of energy deposited over an area within 30° of the poles is equivalent to a ring current energy dissipation rate of 7×10^{18} erg/sec over 8 hr. Figure 96 shows the ring current energy dissipation rate of the same 26 May 1967 magnetic storm. Note that 7×10^{18} erg/sec over 8 hr is only a small fraction of the total ring current loss. From Fig. 95 we see that a temperature inversion occurs in a layer of approximately 60 km for several hours.

In order to gain a proper interpretation to the temperature inversion shown on Fig. 95, as well as subsequent figures, several points should be considered. First of all, the Thomas-Ching one-dimensional model calculates essentially the response of the atmosphere to heating; i.e., it predicts increments of temperature profile as a result of energy input. The total temperature profile is a superposition of some arbitrary static profile and the increment profile. In order to show that the temperature increment profile immediately above the heating layer is sufficiently large to produce a temperature inversion against a steep static temperature profile, we have chosen to superimpose the increment profile and the CIRA 2 (Ref. 14) profile, which has the steepest temperature gradient. Since there is no clean separation between the heat sources maintaining the two profiles, the temperatures shown on the figures may be too high. However, the point is that our increment profile is

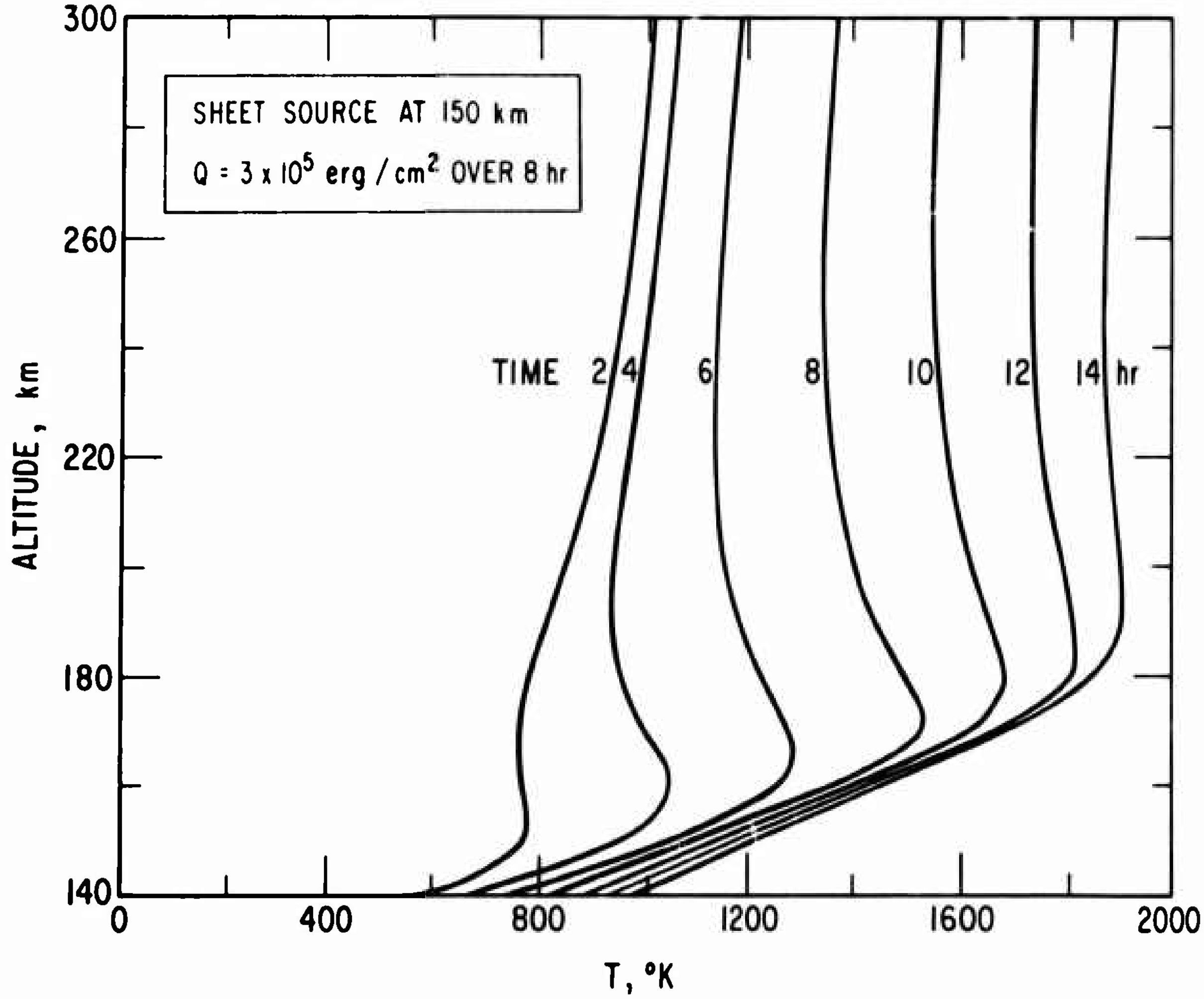

Fig. 95. Thomas-Ching Model Temperature Profile of CIRA 2 Atmosphere Heated by Sheet Source at 150 km Depositing 3×10^5 erg/cm^2 Spread over Polar Caps, equivalent to 7×10^{18} erg/sec Energy Deposition Rate over 8 hr

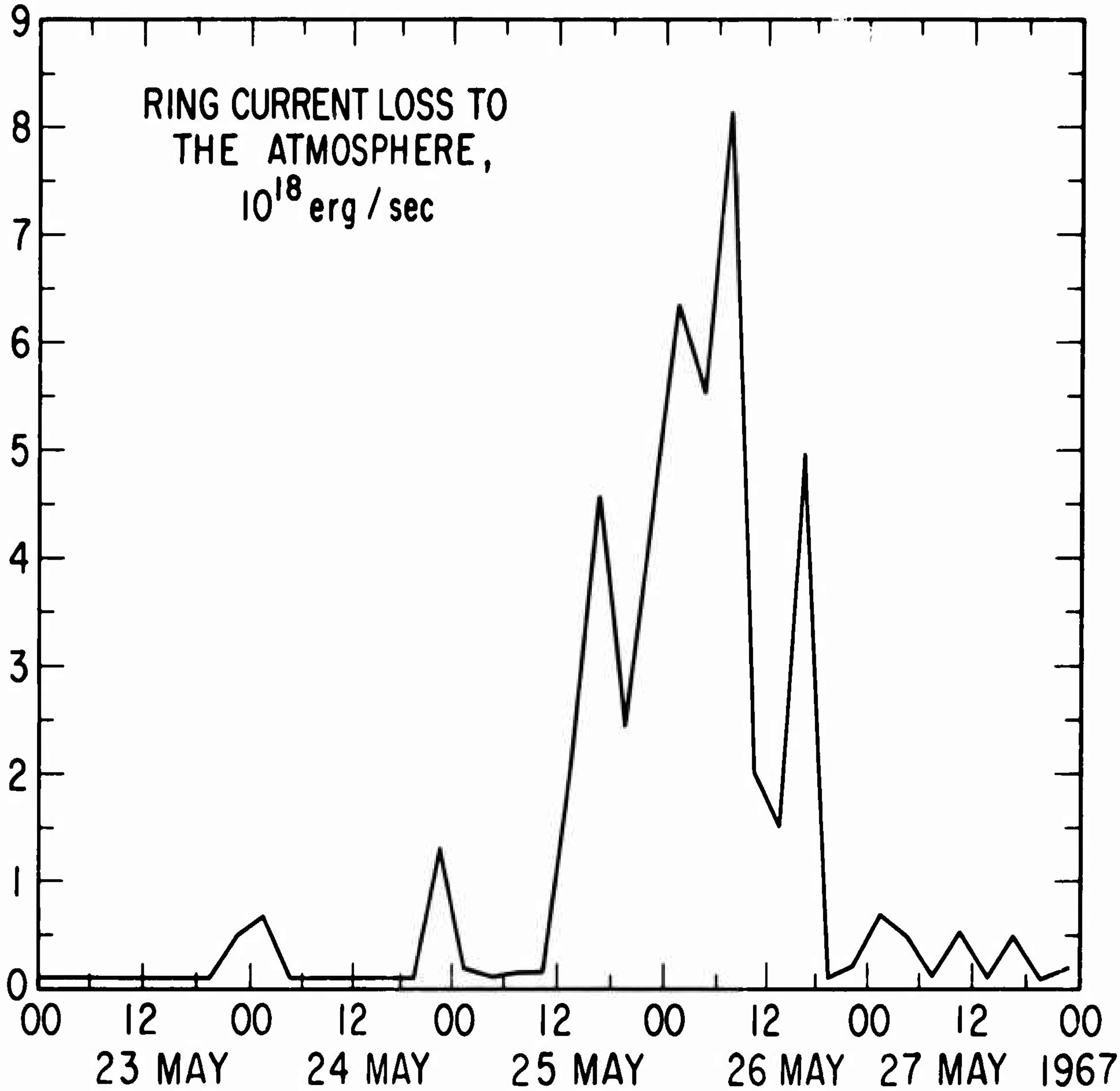

Fig. 96. Ring Current Energy Dissipation Rate of 26 May 1967 Storm

sufficiently strong to maintain an inversion against the steepest static CIRA model temperature profile. Second, the total amounts of energy input used in the model calculations represent upper limits to the energy input in the production of temperature inversion since we spread the total energy input over areas within 30° of both polar caps. In reality, it is only necessary to produce a temperature inversion over an area whose linear dimension is a couple of the observed characteristic lengths. Thus, temperature inversion can be generated by an energy input much less than 7×10^{18} erg/sec over 8 hr. A more appropriate quantity is energy deposition per unit area, which is shown on the figures as the quantity Q. Finally, it should be emphasized that a temperature inversion is necessarily unstable so that an instability occurs to destroy the temperature inversion. Thus, the occurrence of an inverse temperature profile in a one-dimensional model does not mean that such an inversion exists in nature but simply that a three-dimensional model is required to describe the motion of the atmosphere adequately in such a case.

Since the generation of our convective instability is predicated on the production of a temperature inversion in a given atmospheric layer, we could vary the energy deposition rate to obtain a qualitative criterion between the magnitude of the storm ring current loss rate and the likelihood of observing the anomalous wind. Figures 97 through 99 show the temperature profile predicted by the Thomas-Ching one-dimensional model corresponding to ring current loss rate of 1.17×10^{18}, 2.34×10^{18}, and 4.67×10^{18} erg/sec over 8 hr and within 30° of the polar caps, respectively. It is seen that we are unlikely to observe anomalous winds unless the above ring current loss rate is larger than 2.34×10^{18} erg/sec. Such a loss rate is to be compared with 7×10^{18} erg/sec of the historic 26 May 1967 storm, which generated the observed winds. Finally, Fig. 100 shows that the heating source thickness can be increased up to 10 km if we increase the heat input slightly.

To investigate the possible mechanism for the generation of instability, we shall henceforth assume that an unstable temperature profile with a layer of inverse temperature gradient as shown in Fig. 95 exists. The

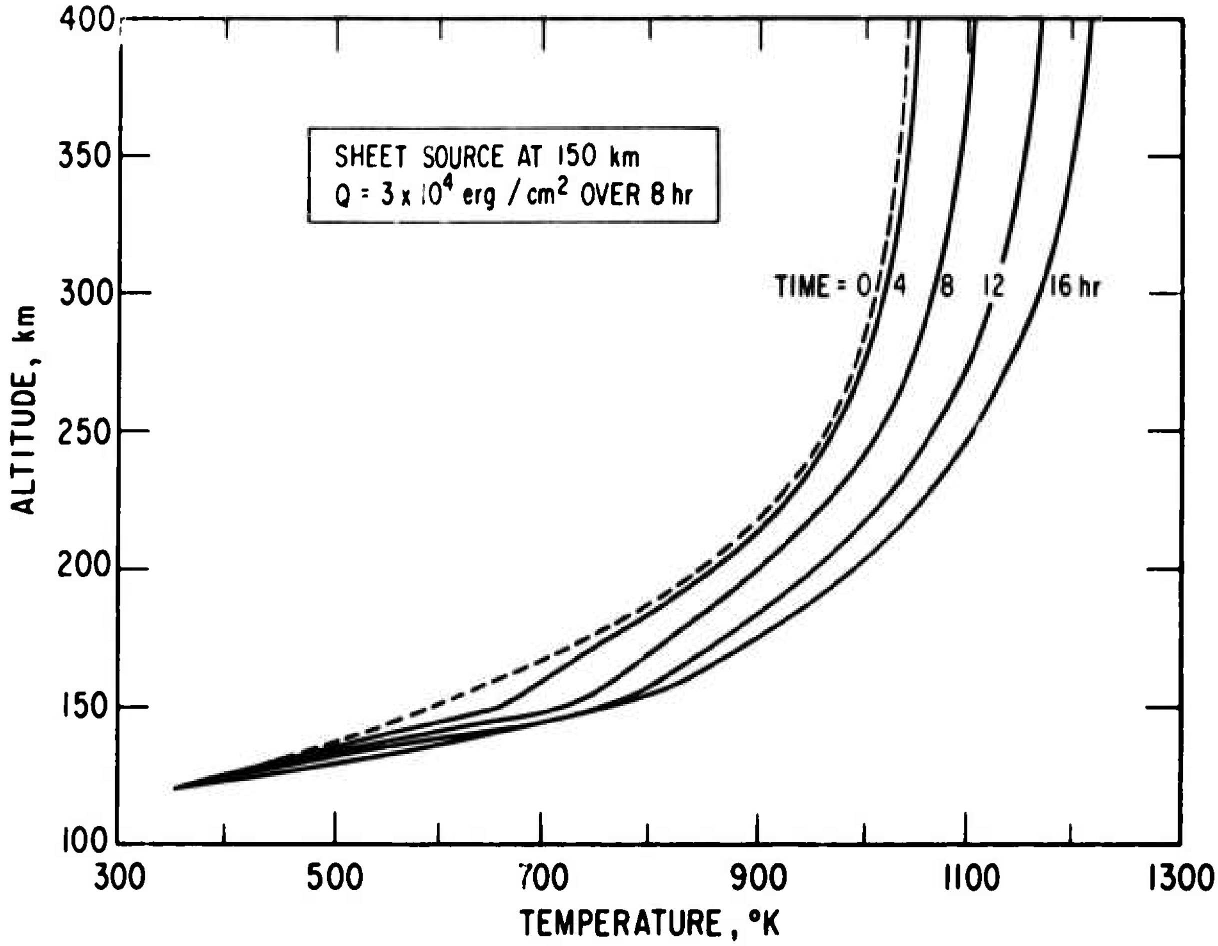

Fig. 97. Thomas-Ching Model Temperature Profile of CIRA 2 Atmosphere Heated by Sheet Source at 150 km Depositing 3×10^4 erg/cm^2 Spread over Polar Caps, Equivalent to 1.17×10^{18} erg/sec Energy Deposition Rate over 8 hr

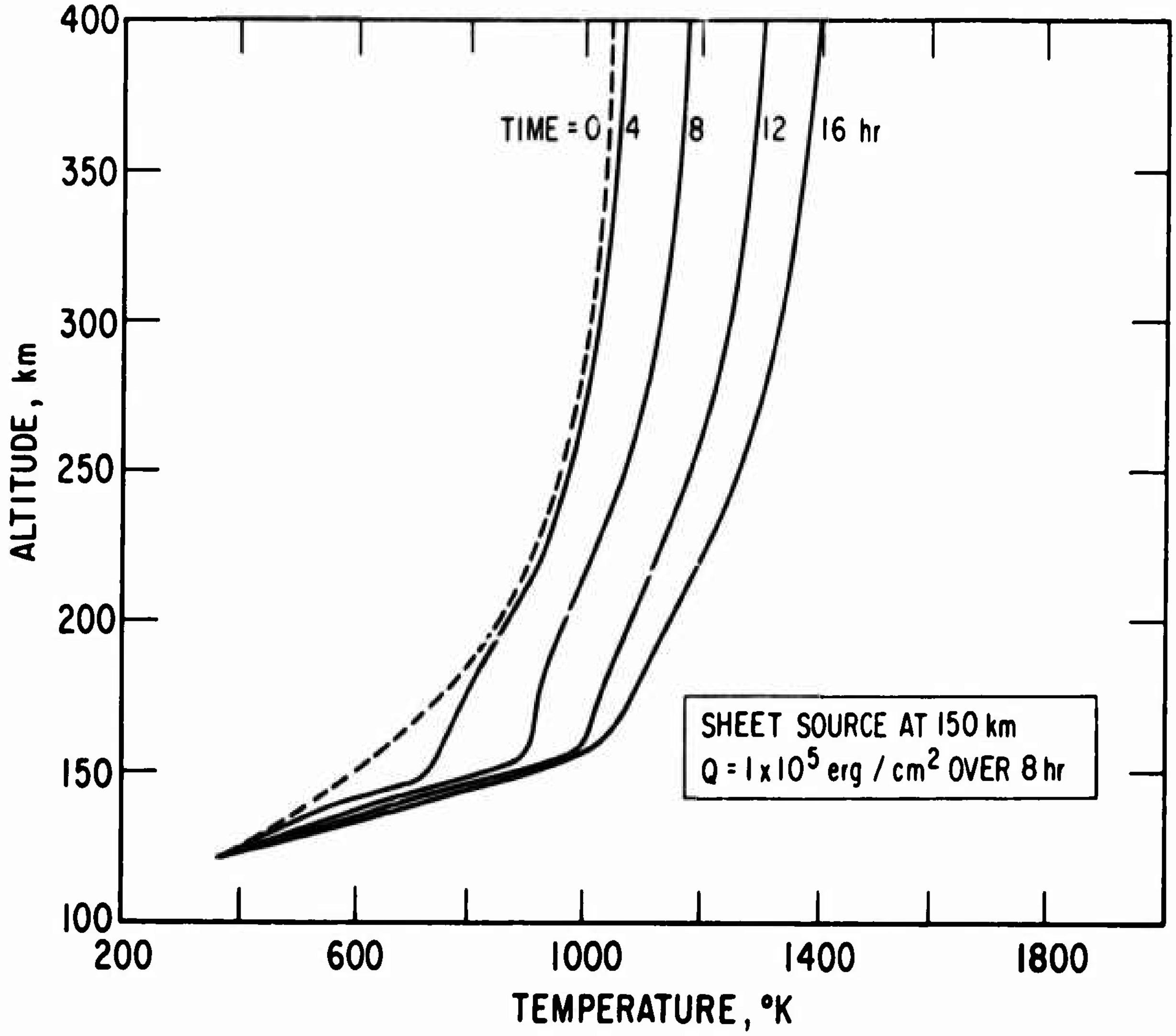

Fig. 98. Thomas-Ching Model Temperature Profile of CIRA 2 Atmosphere Heated by Sheet Source at 150 km Depositing 1×10^5 erg/cm^2 Spread over Polar Caps, Equivalent to 2.34×10^{18} erg/sec Energy Deposition Rate over 8 hr

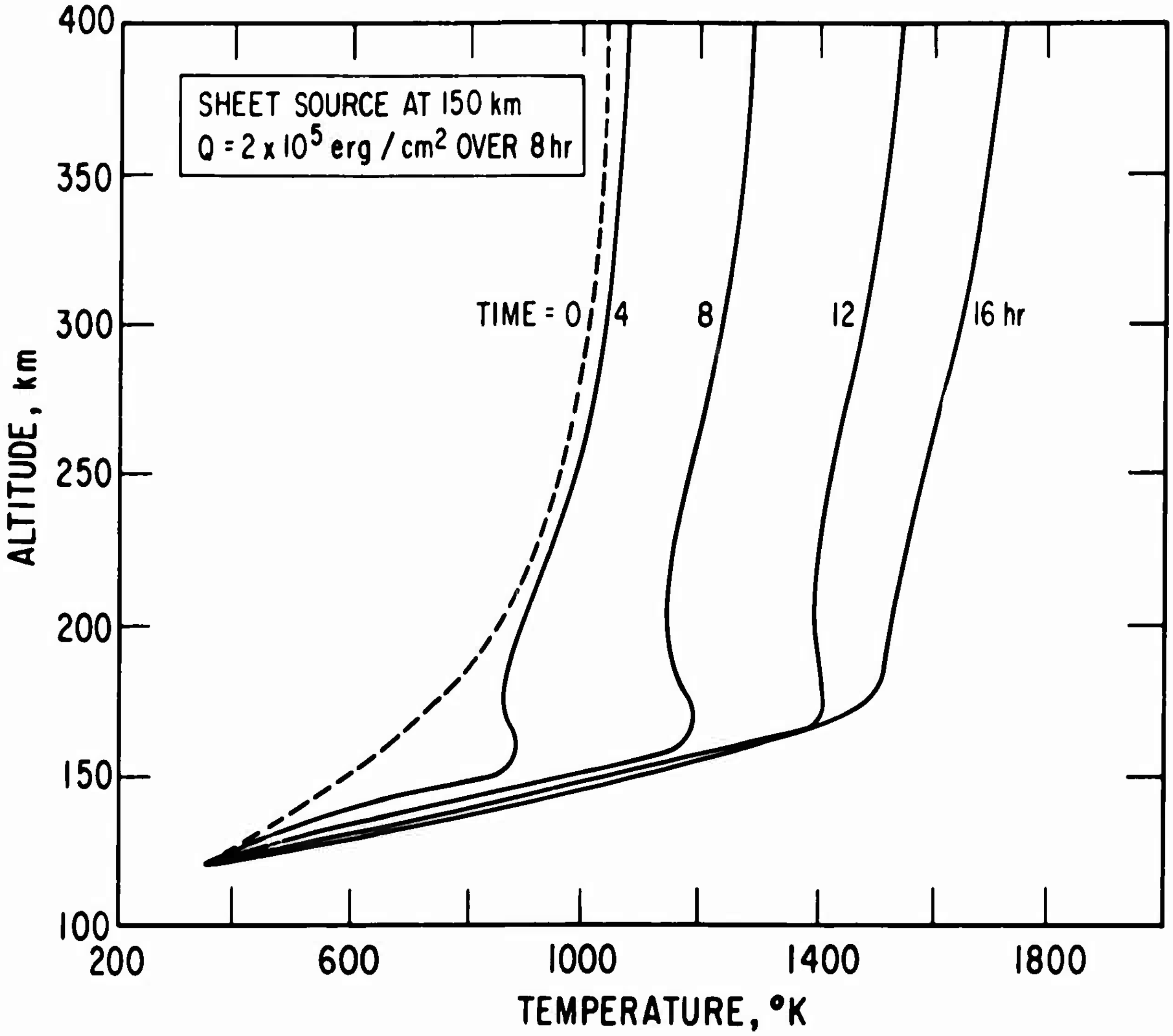

Fig. 99. Thomas-Ching Model Temperature Profile of CIRA 2 Atmosphere Heated by Sheet Source at 150 km Depositing 2×10^5 erg/cm^2 Spread over Polar Caps, Equivalent to 4.67×10^{18} erg/sec Energy Deposition Rate over 8 hr

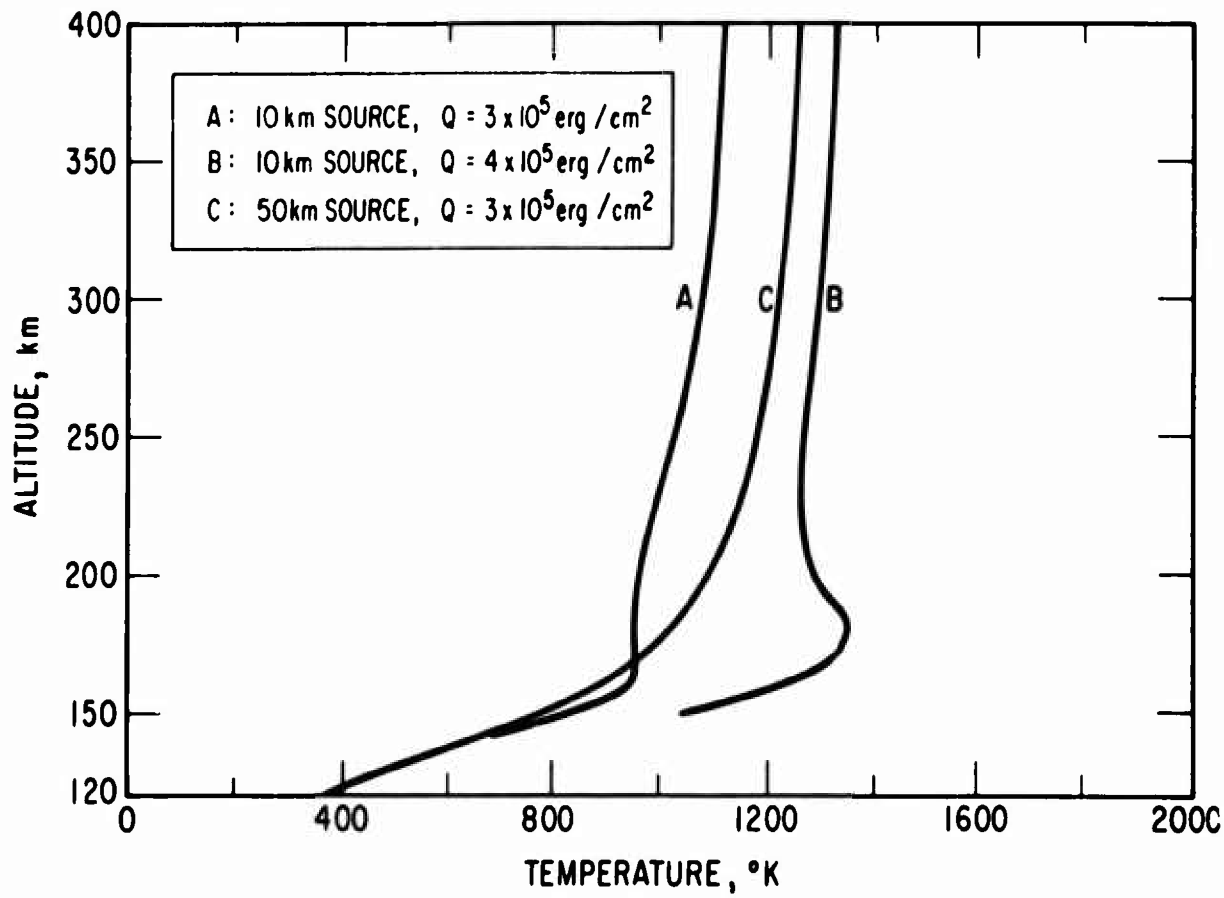

Fig. 100. Effect of Increasing Heat Source Thickness

characteristics of the instability can then be described by the equations of continuity, motion, and heat flow for the realistic case of a rotating exponential atmosphere. The full formalism and solutions shall be exhibited in the next section. Since a number of the features turn out to be not significantly different from that of the simpler stationary convection, we shall, for illustration purposes, first develop the description of thermospheric convection in a nonrotating exponential atmosphere.

The general set of equations governing atmospheric motion of a layer without heat sources are as follows:

Continuity: $$\text{div}\,(\rho\vec{v}) = -\partial\rho/\partial t \tag{56}$$

Motion: $$\vec{v}\cdot\nabla\vec{v} + (1/\rho)\nabla p - \vec{g} = \gamma\nabla^2\vec{v} - \partial\vec{v}/\partial t \tag{57}$$

Heat Flow: $$\vec{v}\cdot\nabla T - (1/\rho c_p)\,\text{div}\,(K\nabla T) = -\partial T/\partial t \tag{58}$$

In the above, ρ is the density (gm/cm^3), $\vec{v}$ is the velocity (cm/sec), p is the pressure (dyne/cm^2), and T is the temperature (°K). The parameters are the kinematic viscosity γ (cm^2/sec), heat capacity as constant pressure c_p (erg/gm-°K), and heat conductivity K (erg/cm/sec-°K). Throughout the analysis, γ, c_p, and K shall be assumed constant, equal to their values evaluated at 200-km altitude. A more sophisticated treatment would include altitude dependence of these parameters as well as a tensor form for the kinematic viscosity.

At the onset of the instability we assume that the velocity is small so that the above equations can be linearized by dropping all second-order terms in the perturbations of density, pressure, temperature, and velocity. The perturbed quantities shall be denoted by the subscript 1, and the unperturbed quantities shall be denoted by the subscript 0. Assuming that the zeroeth-order quantities obey the equation of state

$$p_0 = (k/m)\,\rho_0 T_0 \tag{59}$$

the zeroeth-order solutions are simply

$$T_0 = \overline{T}_0 - z\Delta T/h \tag{60}$$

$$\begin{pmatrix} p_0 \\ \rho_0 \end{pmatrix} = \begin{pmatrix} \overline{p}_0 \\ \overline{\rho}_0 \end{pmatrix} e^{-z/H_0} \quad ; \quad H_0 = \frac{k\overline{T}_0}{mg} \tag{61}$$

where $\overline{T}_0$, $\overline{p}_0$, and $\overline{\rho}_0$ are constants given by an appropriate CIRA model. In Eq. (60), we have specified our solution to one appropriate to our inversion region of thickness h and maximum inversion ΔT. The coordinate z is measured from the lower surface, i.e., $0 \le z \le h$. Since $\Delta T/\overline{T}_0$ is usually small, e.g., Fig. 95, we have ignored the $z\Delta T/h$ term in Eq. (61). H_0 in Eq. (61) is the scale height and is approximately 53 km for our conditions.

For the perturbed quantities, we note that the density and temperature are related by the law of thermal expansion

$$\rho_1 = \left(\frac{\partial \rho_0}{\partial T}\right)_p T_1 = -\rho_0 \beta T_1 \simeq -\rho_0 \frac{T_1}{T_0} \tag{62}$$

With the use of Eqs. (59) through (62), the first-order equations become, after disregard of $\partial \rho_1/\partial t$ (Refs. 42 and 44)

$$\frac{\partial v_x}{\partial x} + \frac{\partial v_y}{\partial y} + \frac{1}{\rho_0}\frac{\partial}{\partial z}(\rho_0 v_z) = 0 \tag{63}$$

$$\frac{1}{\rho_0}\nabla p_1 + \vec{g}\beta T_1 = \gamma \nabla^2 \vec{v} - \frac{\partial \vec{v}}{\partial t} \tag{64}$$

$$K\nabla^2 T_1 = -\rho_0 c_p \frac{\Delta T}{h} v_z + \rho_0 c_p \frac{\partial T_1}{\partial t} \tag{65}$$

where ∇^2 is the Laplacian operator. Equations (62) through (65) now give a complete perturbative approach to instability. The procedure is to look for solutions that represent a spatial disturbance, i.e., exp $(i\vec{k} \cdot \vec{x})$, but have an exponentially increasing time dependence e^{wt}(Re$w \geq 0$). Such solutions are unstable because the amplitude of the disturbance will grow with time until the state of the system becomes quite different. These unstable solutions, however, can be separated into two classes depending on whether Im$w = 0$ or Im$w \neq 0$. Those with Im$w = 0$ are convective instabilities because the fluid motion, though growing in time, is confined to a volume in space. Those with Im$w \neq 0$ are traveling wave-type instabilities (overstability). For the incompressible case, Pellew and Southwell (Ref. 43) have shown that only the convective mode exists. Chandrasekhar (Ref. 44) has shown, however, that the overstable mode is also allowed in the constant density case if we include the effects of a rotating atmosphere. In the following, we shall show that these results are essentially unchanged in the case of the more realistic exponential atmosphere.

Since the measured wind pattern seems to be stationary, in this section we shall study, for illustrative purposes, the simpler convective instability in a nonrotating atmosphere. Furthermore, the stable and unstable states are separated by a marginal state of stationary convection, i.e., Re$w = 0$. If the growth rate is small, the characteristics of the marginal state are essentially the same as the unstable state; hence, for the sake of simplicity we shall first study the solutions of Eqs. (63) through (65) with $\partial/\partial t = 0$. The complete case is considered in the next section.

With $\partial/\partial t = 0$, we decouple Eqs. (62) through (65) to obtain

$$v_x = -\partial\Phi/\partial x - \partial\psi/\partial y \qquad (66)$$

and

$$v_y = -\partial\Phi/\partial y + \partial\psi/\partial x \qquad (67)$$

where

$$\nabla^2 \nabla_1^2 \psi = 0 \tag{68}$$

$$\nabla_1^2 \Phi = \partial v_z/\partial z - v_z/H_0 \tag{69}$$

$$\nabla_1^2 p_1 = -\rho_0 \gamma \nabla^2 (1/\rho_0)\left(\frac{\partial}{\partial z} \rho_0 v_z\right) \tag{70}$$

and

$$-\nabla^2 \frac{1}{\rho_0} \frac{\partial}{\partial z} \rho_0 \nabla^2 \frac{1}{\rho_0} \frac{\partial}{\partial z} \rho_0 v_z + \frac{g\beta \Delta T cp}{\gamma K h} \cdot \rho_0 \nabla_1^2 v_z = \nabla^2 \nabla^2 \nabla_1^2 v_z \tag{71}$$

In these equations, $\nabla_1^2 = \partial^2/\partial x^2 + \partial^2/\partial y^2$. Thus, if we solve Eq. (71) for v_z, all the other unknowns could be obtained by solving Eqs. (65) through (70). The boundary conditions are

$$v_z(z = 0) = v_z(z = h) = 0 \tag{72}$$

If our inversion layer were bounded by free surfaces then we would require, in addition, $\partial^2 v_z/\partial z^2$ to vanish there because $\partial v_x/\partial z$ and $\partial v_y/\partial z$ must vanish at the surfaces. However, there are no surfaces in our problem and because of viscous drag, our solution for v_x and v_y must be joined to a boundary layer type of solution outside of $0 \le z \le h$. The boundary condition in the x and y coordinates are, of course, not determined by our problem unless a particular convection pattern is postulated. Whatever the convection pattern, the operator ∇_1^2 in Eq. (71) indicates quite clearly that the solution is a linear combination of exp $(i\vec{K} \cdot \vec{r})$, where r is a vector in the x-y plane. Thus the boundary condition (72) determines the dominant horizontal wave number k, which in turn is related to the size of the convection cells. It should be pointed out, however, that a complete solution of the convection pattern cannot be obtained unless we know more about the horizontal boundary conditions and the boundary layers in the vertical direction.

Transforming to the dimensionless variable $\xi = z/h$, we seek v_z in the form

$$v_z = e^{i\vec{k}\cdot\vec{r}} f(\xi) \tag{73}$$

where $f(\xi)$ is determined by

$$\left(\frac{d^2}{d\xi^2} - k^2h^2\right)^2 \left[\left(\frac{d}{d\xi} - \frac{h}{H_0}\right)^2 - k^2h^2\right] f(\xi) = -k^2h^2Rf(\xi) \tag{74}$$

R, the Rayleigh number, is defined by

$$R = \frac{g\beta c_p \rho_0 h^4}{K\gamma}\left(\frac{\Delta T}{h}\right) \tag{75}$$

It is customary in the treatment of convection in compressible fluids (Refs. 45 and 47) to treat R as a constant although, strictly speaking, this is incorrect since ρ_0 changes with ξ. We shall show that large changes in R induce only small changes in kh.

Before we consider the solution of Eq. (74), it may be instructive to repeat the solution of the incompressible case, which corresponds to the infinite H_0 limit, i.e.,

$$\left(\frac{d^2}{d\xi^2} - k^2h^2\right)^3 f(\xi) = -k^2h^2Rf(\xi) \tag{76}$$

The general solution to Eq. (76) is a linear combination of cosh $\mu\xi$ and sinh $\mu\xi$, where μ is determined by the algebraic equation

$$(\mu^2 - k^2h^2)^3 = -k^2h^2R \tag{77}$$

Since the various cosh and sinh solutions are linearly independent, the solution satisfying the boundary condition is

$$f(\xi) = C \sin m\pi\xi \qquad , \qquad m \neq 0 \tag{78}$$

i.e., $\mu = \pm im\pi$. Thus, in terms of the wave length in units of h, one finds

$$\eta = 2\pi/kh$$

Equation (77) becomes a relation between the convection cell size ηh and the Rayleigh number R, which depends on the local properties of the atmosphere

$$R = 16\pi^4 \frac{1}{\eta^4}\left(1 + \frac{m^2\eta^2}{4}\right)^3 \tag{79}$$

The case for m = 1 is plotted as Curve C on Fig. 101. Note that no instability can occur unless R is greater than R critical where

$$R \text{ critical} = 27\, m^4\pi^4/4 \tag{80}$$

The critical Rayleigh numbers for m = 1 and 2 are also shown on Fig. 101.

The case of an exponential atmosphere is considerably more complex. We can seek a solution $f(\xi)$ to Eq. (74) in the form

$$f(\xi) = C\, e^{\lambda\xi} \sin m\pi\xi \tag{81}$$

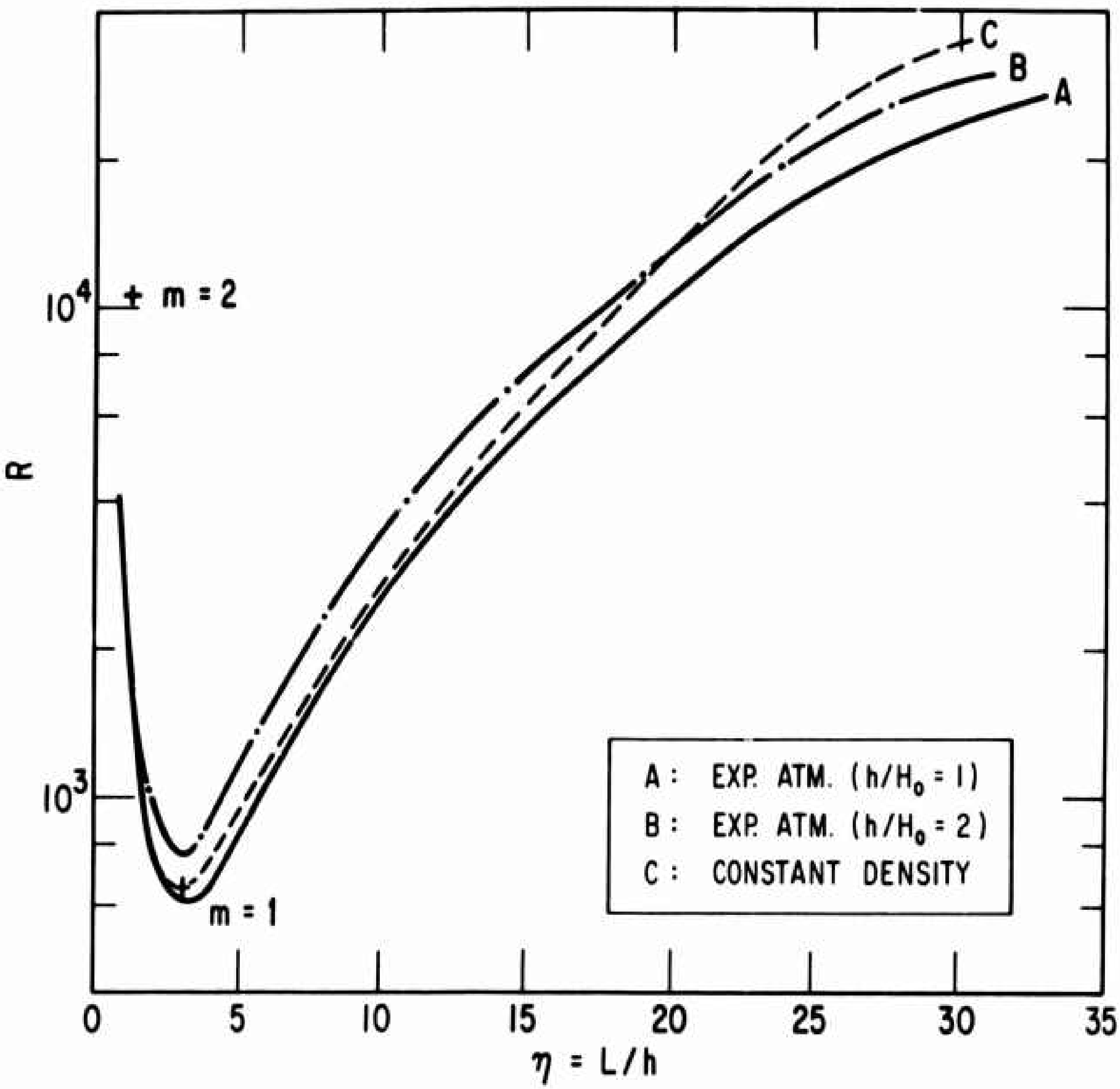

Fig. 101. Relation Between Rayleigh Number R and Horizontal Characteristic Length η in Units of Layer Depth h

which satisfies the boundary conditions (72). Substitution of Eq. (81) into Eq. (74) yields two equations from which λ and kh can be determined. These are

$$\left(\lambda - \frac{h}{H_0}\right)[(\lambda^2 - m^2\pi^2 - k^2h^2)^2 - 4m^2\pi^2\lambda^2]$$

$$+ 2\lambda(\lambda^2 - m^2\pi^2 - k^2h^2)\left[\left(\lambda - \frac{h}{H_0}\right)^2 - m^2\pi^2 - k^2h^2\right] = G(\lambda) = 0 \qquad (82)$$

$$[(\lambda^2 - m^2\pi^2 - a^2)^2 - 4m^2\pi^2\lambda^2]\left[\left(\lambda - \frac{h}{H_0}\right)^2 - m^2\pi^2 - k^2h^2\right]$$

$$- 8m^2\pi^2\lambda\left(\lambda - \frac{h}{H_0}\right)(\lambda^2 - m^2\pi^2 - k^2h^2) = -Rk^2h^2 \qquad (83)$$

Equation (82) determines λ as a function of k, and Eq. (83) determines the relation between cell size and the Rayleight number. It is a simple matter to show that Eq. (82) has five real roots for λ. The bounds for these roots are given by

$$+ (m^2\pi^2 + k^2h^2)^{1/2} \leq \lambda 1 \leq \infty$$

$$h/H_0 \leq \lambda_2 \leq + (m^2\pi^2 + k^2h^2)^{1/2}$$

$$0 \leq \lambda_3 \leq h/H_0$$

$$- (m^2\pi^2 + k^2h^2)^{1/2} \leq \lambda_4 \leq -h/H_0$$

$$-\infty \leq \lambda_5 \leq - (m^2\pi^2 + k^2h^2)^{1/2}$$

These inequalities are derived under the assumption $h/H_0 \le (m^2\pi^2 + k^2h^2)^{1/2}$, which is quite well satisfied because $1 \le h/H_0 \le 2$ in our case. Since the observations do not show a strong dependence of maximum wind speed with altitude, solutions λ_1, λ_2, λ_4, and λ_5 can be excluded. Solution λ_3, on the other hand, seems to be a good candidate for the physical situation, since it gives an increase of maximum wind speed of less than one e-fold. Under the approximation

$$h/H_0 \ll (m^2\pi^2 + k^2h^2)^{1/2} \tag{84}$$

we obtain

$$\lambda_3 \simeq \frac{(h/H_0)(m^2\pi^2 + k^2h^2)}{3(m^2\pi^2 + k^2h^2) - 2(h/H_0)^2} \tag{85}$$

$$\approx 1/3\left(\frac{h}{H_0}\right)$$

Figure 102 shows the rigorous solution for $G(\lambda) = 0$ for the case $m = 1$ and $k^2h^2 \ll \pi^2$. It is seen that Eq. (85) is a good representation of λ_3 even if $h/H_0 = 2$. We shall see presently that $k^2h^2 \ll \pi^2$ is an exceedingly good approximation for realistic values of R in our case.

Using the definition of η and the representation of λ_3 given by Eq. (85), we obtain the relation between η and R from Eq. (83). Curves A and B in Fig. 101 show this relationship for h/H_0 equal to 1 and 2 in the $m = 1$ mode, respectively. Comparison with the constant density case (Curve C) shows that the exponential atmosphere case for solution λ_3 differs little from it. For other solutions (λ_1, λ_2, λ_4, and λ_5), the differences between compressible and incompressible atmospheres are, however, quite drastic. The existence of the λ_3 solution is not surprising for it is well known that compressible hydrodynamics often has a mode of motion approximating incompressible hydrodynamics.

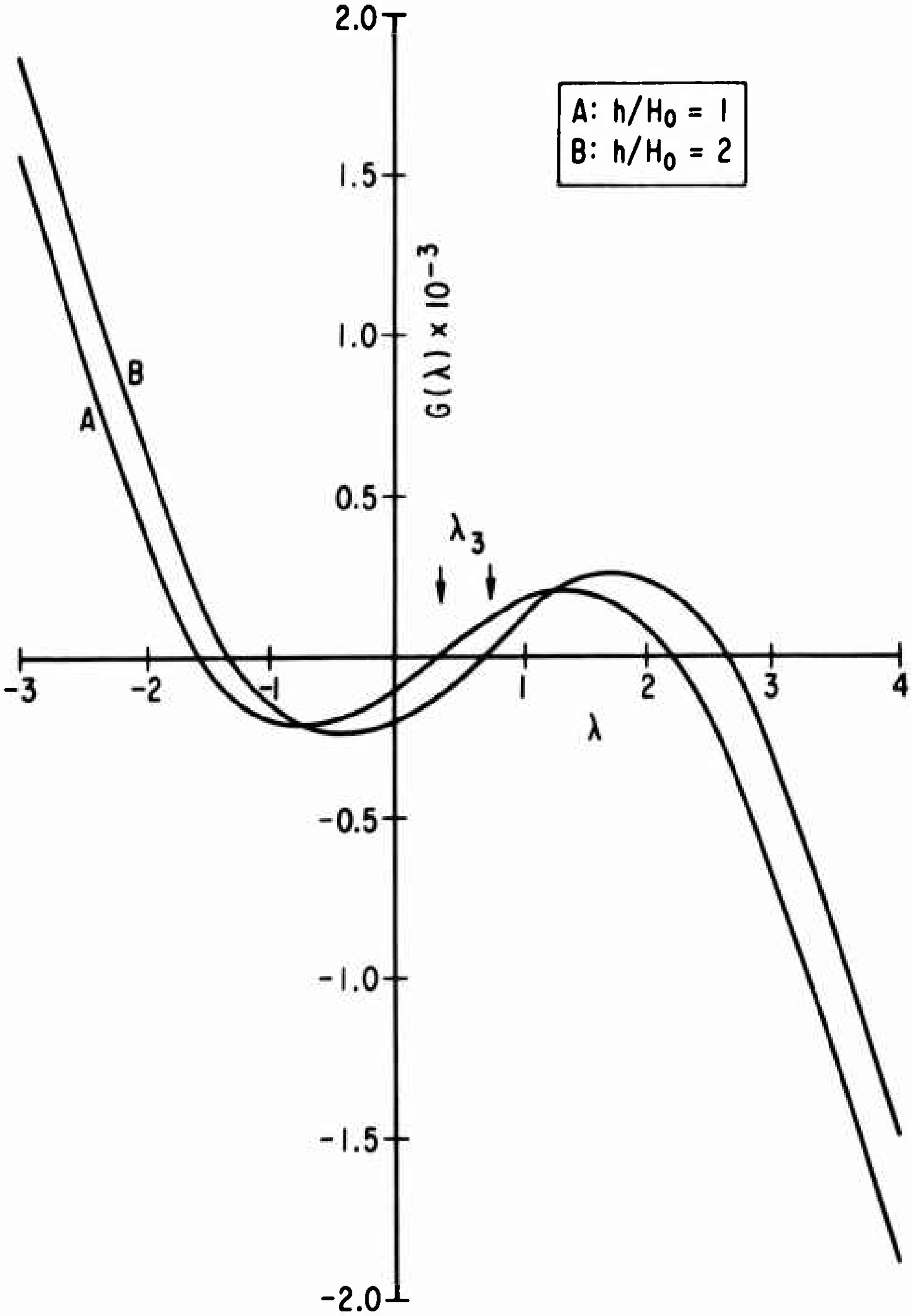

Fig. 102. Solution of $G(\lambda) = 0$ for λ Near Zero and $m = 1$

D. THERMOHYDRODYNAMIC INSTABILITY IN ROTATING THERMOSPHERE

In the previous section, we have examined the features of steady convection in a stationary exponential atmosphere. In this section, we shall examine the more realistic case of a rotating exponential atmosphere. Further, the question of growth rate and the existence of growing solutions will be studied in more detail.

The first-order perturbation equations corresponding to a rotating exponential atmosphere within a layer of inverse temperature profile are given by Eqs. (63) to (65) with the slight modification that a Coriolis force term $2\vec{v} \times \vec{\Omega}$ is added to the right-hand side of Eq. (64) corresponding to the effects of an atmosphere rotating with angular velocity vector $\vec{\Omega}$. Since we are interested in local winds in the polar regions, $\vec{\Omega}$ shall be assumed parallel to the z axis, and effects due to curvature of the earth shall be ignored. Linear dependence on $\partial/\partial t$ of the variables v, T_1, and p_1 introduces the common time factor e^{wt} (w complex) in our equations. The resultant set is

$$\frac{\partial v_x}{\partial x} + \frac{\partial v_y}{\partial y} + \frac{1}{\rho_0}\frac{\partial}{\partial z}(\rho_0 v_z) = 0 \tag{86}$$

$$\frac{1}{\rho_0}\frac{\partial p_1}{\partial x} = (\gamma\nabla^2 - w)v_x + 2\Omega v_y \tag{87}$$

$$\frac{1}{\rho_0}\frac{\partial p_1}{\partial y} = (\gamma\nabla^2 - w)v_y - 2\Omega v_x \tag{88}$$

$$\frac{1}{\rho_0}\frac{\partial p_1}{\partial z} = (\gamma\nabla^2 - w)v_z + g\beta T_1 \tag{89}$$

$$K\nabla^2 T_1 - w\rho_0 c_p T_1 = -\rho_0 c_p \frac{\Delta T}{h} v_z \tag{90}$$

With $\rho_0 \propto e^{-z/H_0}$ and the usual assumption of constant Rayleigh number, a tedious reduction gives an equation for v_z

$$\left(\nabla^2 - \frac{w\rho_0 c_p}{k}\right)\left\{\left[\left(\nabla^2 - \frac{w}{\gamma}\right)^2 + \frac{4\Omega^2}{\gamma^2}\right]\left(\frac{\partial}{\partial z} - \frac{1}{H_0}\right)^2 + \left(\nabla^2 - \frac{w}{\gamma}\right)^2 \nabla_1^2\right\} v_z = \frac{R}{h^4}\left(\nabla^2 - \frac{w}{\gamma}\right)\nabla_1^2 v_z \tag{91}$$

Proceeding as before, we consider solutions of the form

$$v_z = e^{wt} e^{ik\cdot r} f(\xi) \quad , \quad \xi = z/h \quad , \quad r = (x, y)$$

and obtain the dimensionless equation for $f(\xi)$

$$\left(\frac{d^2}{d\xi^2} - a^2 - pw\right)\left\{\left[\left(\frac{d^2}{d\xi^2} - a^2 - qw\right)^2 + 4\Omega^2 q^2\right]\left(\frac{d}{d\xi} - s\right)^2 - a^2\left(\frac{d^2}{d\xi^2} - a^2 - qw\right)^2\right\} f(\xi)$$

$$= -R\left(\frac{d^2}{d\xi^2} - a^2 - qw\right) a^2 f(\xi) \tag{92}$$

where the parameters are defined by $p = h^2\rho_0 c_p/K$, $q = h^2/\gamma$, $s = h/H_0$, and $a = hk$. It is a simple but tedious matter to show that Eq. (92) has a solution of the form

$$f(\xi) = e^{\lambda\xi} \sin m\pi\xi \tag{93}$$

One then obtains two conditions relating the unknowns a, λ, and w. These relations are not particularly enlightening because of their complexity; thus we shall consider the various limit situations in order to study the effect of various terms.

First, we consider the question of the existence of the overstable mode. In the case of a nonrotating atmosphere, i.e., Ω vanishes, then Eqs. (92) and (93) yield two conditions

$$(\lambda^2 - m^2\pi^2 - a^2 - wp)\{(\lambda^2 - m^2\pi^2 - a^2 - wq)[(\lambda - s)^2 - m^2\pi^2 - a^2] - 4m^2\pi^2\lambda(\lambda - s)\}$$

$$- 4m^2\pi^2\lambda\{\lambda[(\lambda - s)^2 - m^2\pi^2 - a^2] + (\lambda - s)(\lambda^2 - m^2\pi^2 - a^2 - wq)\} = -Ra^2 \qquad (94)$$

and

$$\lambda[(\lambda - s)^2 - m^2\pi^2 - a^2][2(\lambda^2 - m^2\pi^2 - a^2) + w(-p - q)]$$

$$+ (\lambda - s)[(\lambda^2 - m^2\pi^2 - a^2 - wq)(\lambda^2 - m^2\pi^2 - a^2 - wp) - 4m^2\pi^2\lambda^2] = 0 \qquad (95)$$

From Eqs. (94) and (95), we obtain

$$\lambda[w(-p - q) + 2(\lambda^2 - m^2\pi^2 - a^2)]\{[(\lambda - s)^2 - m^2\pi^2 - a^2]^2 + 4m^2\pi^2(\lambda - s)^2 = Ra^2(\lambda - s)$$

(96)

Since all parameters are real in Eq. (96), w cannot be complex when Eq. (96) is considered as an equation for w. This implies that no overstable modes are allowed in an exponential atmosphere without rotation because an overstability necessarily requires that $\mathrm{Re}w > 0$ and $\mathrm{Im}w \neq 0$. On the other hand, if $\Omega \neq 0$, the conditions on w would be quartic in w so that complex solutions with $\mathrm{Re}w > 0$ and $\mathrm{Im}w \neq 0$ are possible. While the actual case involves coupled quartic equations for w, the $\lambda \rightarrow 0$ limit leads to simpler equations which indeed have a solution $\mathrm{Re}w > 0$ and $\mathrm{Im}w \neq 0$. Similar results were obtained by Chandrasekhar and Pellew and Southwell by a somewhat different analysis.

Next, we note that the existence of solutions with $\mathrm{Re}w > 0$ has been tacitly assumed in the previous section. In order to prove the existence of such growing solutions in the nonrotating case, we consider Eq. (96) together with the physical solution $\lambda \simeq 1/3s$. Since the expression in braces is positive and $m^2\pi^2 + a^2 > \lambda^2$, it is easy to see that growing solutions can be obtained in either of two cases

$$\text{Case 1:} \quad -p - q < 0 \quad \text{and} \quad \left|Ra^2(\lambda - s)\right| > \left|2\lambda(\lambda^2 - m^2\pi^2 - a^2)\{\cdots\}\right|$$

$$\text{Case 2:} \quad -p - q > 0 \quad \text{and} \quad \left|Ra^2(\lambda - s)\right| < \left|2\lambda(\lambda^2 - m^2\pi^2 - a^2)\{\cdots\}\right|$$

In the case of the thermosphere at 160 to 220 km, $-p - q < 0$ holds, hence condition 1 must be satisfied. Using the observed value of $\eta \cong 18$, i.e., $a \simeq 1/3$ and values of parameters given in the next section, we obtain the growth time

$$t = 1.1 \left(\frac{2}{9} R - 2.115\right)^{-1} \text{hr}$$

where R is measured in units of 1000. Hence, if $R \gtrsim 9500$ is contained in our range of estimated R values, the observed 1 to 2 hr growth time can be accounted for.

Next, we shall consider the effects of atmospheric rotation on the relation between the horizontal characteristic length, a, and the Rayleigh number. For this purpose, we study two limits of Eq. (92), namely the case of small growth rate, i.e., $w \to 0$ and the case of large growth rate, i.e., $w \gg a^2$.

The $w \to 0$ case yields the conditions

$$2\lambda(\lambda^2 - m^2\pi^2 - a^2)[(\lambda - s)^2 - m^2\pi^2 - a^2] + (\lambda - s)[(\lambda^2 - m^2\pi^2 - a^2)^2 - 4\lambda^2 m^2\pi^2 + Q^2] = 0$$

and

$$[(\lambda^2 - m^2\pi^2 - a^2)^2 - 4\lambda^2 m^2\pi^2][(\lambda - s)^2 - m^2\pi^2 - a^2]$$
$$-8m^2\pi^2\lambda(\lambda - s)(\lambda^2 - m^2\pi^2 - a^2) + Q^2[(\lambda - s)^2 - m^2\pi^2] = -Ra^2 \qquad (98)$$

where the dimensionless parameter Q is $2\Omega h^2/\lambda \simeq 5$ for $\lambda = 10^9$ cm^2/sec at 200-km altitude. Equations (97) and (98) are to be compared to Eqs. (82) and (83) for the $\Omega \to 0$ limit. Since $Q^2 \ll (m\pi)^4$, the solution λ_3 for Eq. (97) is essentially unchanged, i.e., $\lambda \approx 1/3s$. The relation between R and η, Eq. (98), is shown on Fig. 103. Thus, for very small growth rate, the characteristic length of the convective instability is not essentially changed even if we include the effects of atmospheric rotation.

For the case of large growth rate, the situation becomes much more complicated. The essential features, however, can be studied in the constant density limit. Letting s vanish in Eq. (92), we obtain the solution

$$f(\xi) = \sin m\pi\xi$$

and the condition

$$(m^2\pi^2 + a^2 + pw)[(m^2\pi^2 + a^2 + qw)^2(m^2\pi^2 + a^2) + Q^2m^2\pi^2] = Ra^2(m^2\pi^2 + a^2 + qw) \tag{99}$$

For values of Ω and q appropriate to the thermosphere near 200-km altitude, $Q^2 \ll m^4\pi^4$ is very well satisfied; hence, we lose no generality in simplifying Eq. (99) by dropping the Q^2 term. In terms of the dimensionless characteristic length $\eta = 2\pi/a$, one finds

$$R = \frac{16\pi^4}{4}\left(1 + \frac{m^2\pi^2 + pw}{4\pi^2}\eta^2\right)\left(1 + \frac{m^2\pi^2 + qw}{4\pi^2}\eta^2\right)\left(1 + \frac{m^2\eta^2}{4}\right) \tag{100}$$

This is to be compared to Eq. (79), which is a special case of Eq. (100) with $w = 0$.

Since pw and qw are both positive, Eq. (100) indicates that for a given R the cell size η obtained is smaller than that given by Eq. (79). For the observed growth rate of approximately 1.5 to 3 hr, the reduction of η due

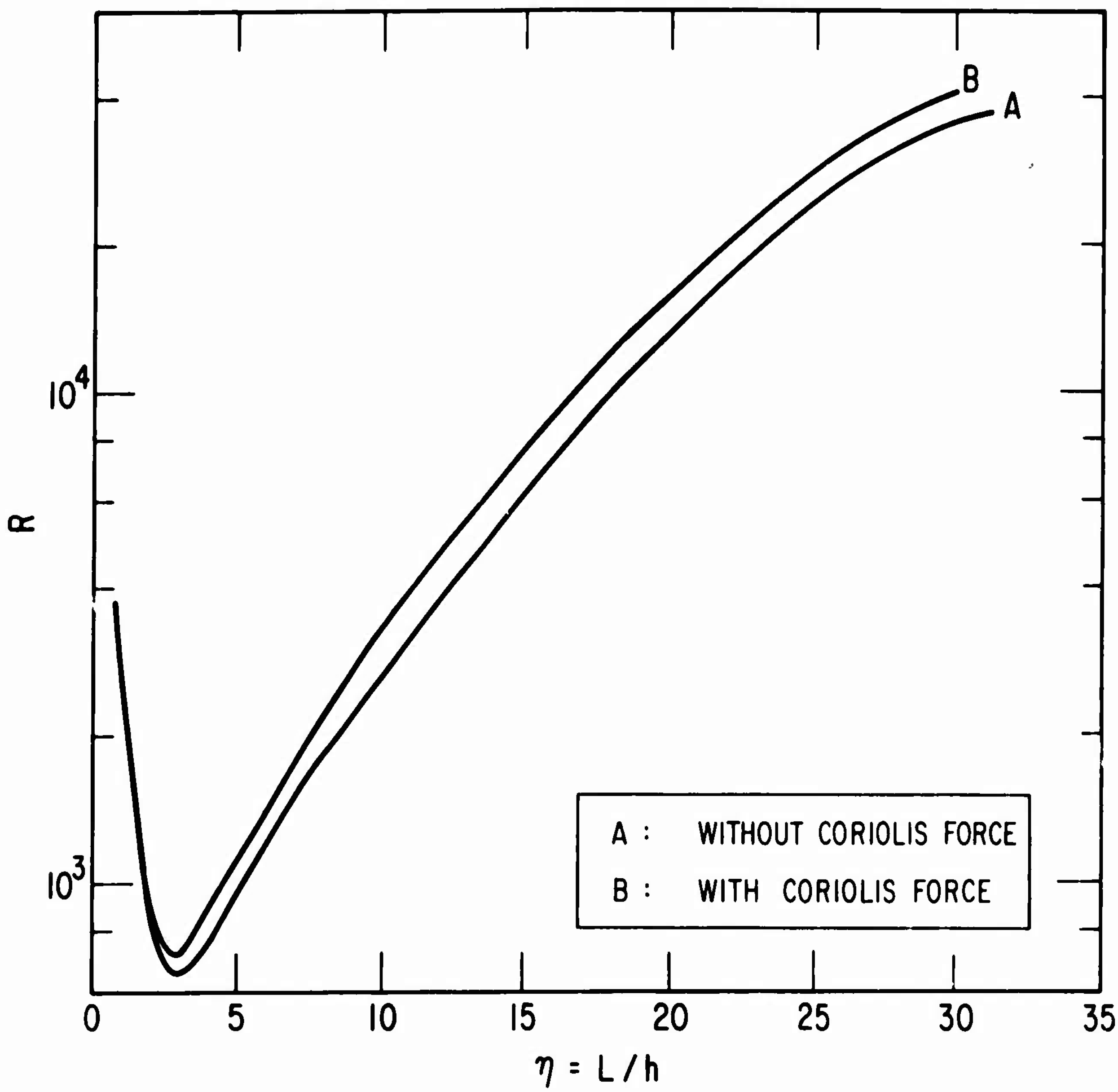

Fig. 103. Relation Between Rayleigh Number R and Characteristic Length η Showing Effects of Coriolis Force in Case of Vanishing Growth Rate

to this effect is quite small since pw and qw are both smaller than π^2. On the other hand, if $\lambda \neq 0$, this tendency can be compensated for in the opposite direction, depending on the value of h/H_0. Large uncertainties in the parameters making up R do not make a determination of growth rate and cell size profitable, although the previous consideration does show that 1.5 to 3 hr growth time is quite consistent with $\eta \sim 20$ as is observed.

E. CHARACTERISTIC FEATURES AND OBSERVATION

At the end of the previous section, we show that the instability growth time can be accounted for. In this section, we shall compare other characteristic features of our theory with the observations. The first and crucial question that has to be answered is, of course, whether a convectively unstable solution can be maintained by a reasonable amount of energy deposition. Part of the answer lies in the production of a temperature inversion, which is model-dependent. Figure 96 shows that an inversion can be maintained in at least one atmospheric model by an energy deposition roughly equal to one third the energy loss from the ring current. Given the existence of a temperature inversion, the criterion of instability is given in the incompressible case by

$$R \simeq \frac{g c_p \rho_0 h^4}{K h \gamma} \left(\frac{\Delta T}{T_0}\right) > \frac{27 m^4 \pi^4}{4} \tag{101}$$

The small difference between the incompressible case and the λ_3 solution of the exponential atmosphere can be ignored. From Fig. 96 it is seen that the first mode is excited at R > 657 and the second mode is excited at R > 10600. On the other hand, our range of R values must encompass R ≃ 9500 in order to account for the observed growth time.

To see if instability can be excited, we shall use the atmospheric parameters appropriate to 200-km altitude during extremely high geomagnetic activity (CIRA 10). c_p, K are given in terms of ρ_0 and H_0 (Ref. 48). The kinematic viscosity γ is given by Kohl and King (Ref. 49). We have

$$c_p = 10^7 \text{ erg/gm-°K}$$

$$K = 1.06 \times 10^4 \text{ erg/cm-sec-°K}$$

$$\gamma = 10^9 \text{ cm}^2\text{/sec}$$

From Fig. 95, $\Delta T/T_0 \approx 1/10$. If we let ρ_0 vary over the range of altitudes from 160 to 220 km, the Rayleigh number is bounded by

$$4250 \leq R \leq 22,000$$

with a typical value at 190 km of R = 9500. Thus, the parameters favor the generation of the first mode of the instability. The existence of the second mode of instability is possible, but the characteristic lengths are much smaller.

If we are to interpret the observations in terms of the excitation of convection in the first mode, we find that the large horizontal characteristic length can be explained. From the curves on Fig. 101, we determine the horizontal characteristic length to be between 960 and 2000 km for the above variation of R. If the second mode is excited the characteristic length is of the order 150 km. On the other hand, if we include the effect of growth rate a decrease of 10 percent in the above figures is possible for w slightly above 2 hr. As is evidenced in Fig. 103 and Eq. (99), the decrease in horizontal characteristic length due to the effects of atmospheric rotation is very small.

Next, without constructing the full set of solutions, we can also find the magnitude ratio between horizontal and vertical velocity components. This is easily obtained by substitution of the solution for v_z

$$v_z = v_{z0}\, e^{\lambda\xi} \sin \pi\xi \; e^{i\vec{k}\cdot\vec{r}} \tag{102}$$

into the equation of continuity (63). Then it is evident that

$$\frac{v_{x0}}{v_{z0}} \approx \frac{v_{y0}}{v_{z0}} \approx \frac{\pi}{kh} = \frac{\eta}{2} \tag{103}$$

From Fig. 96 again, η is bounded by $16 \le \eta \le 30$, so we have

$$v_{x0}/v_{z0} \approx 10 \tag{104}$$

Equation (104) agrees quite well with observation. Thus, we see that the most significant features of the observations are quite consistent with the interpretation of lowest mode steady convection generated by local heating.

Finally, one must examine the validity of comparing convection characteristics of a low velocity perturbation theory with observed characteristics of an extremely high speed wind pattern. To this end, we note that our predicted features originate from solution for λ_3 from Eqs. (82) and (83), which as we recall, also hold if the growth rate of the instability is small. This immediately means that the characteristic length L is essentially time-independent. Further, the time dependence, e^{wt} ($\mathrm{Im}\,w = 0$), in v_{x0} and v_{z0} cancel in Eq. (103), so the speed ratio Eq. (104) remains unchanged. On the other hand, if the growth rate is large, the effect is to decrease the characteristic length.

F. FULLY DEVELOPED CONVECTIVE INSTABILITY

In previous sections we have attempted to interpret features of the observed wind in terms of theoretically predicted features of a convective instability analysis valid during the onset phase when the velocities are small. Although many of the features show good agreement between theory and experiment, we still must be cautious about the validity of the comparison since the observed wind speed components are so large that the nonlinear $\vec{v} \cdot \nabla\vec{v}$ dominate. Thus, in order for our interpretation to be valid, it is necessary to show that solutions of the type given by Eq. (102) exist in the case

$\gamma\nabla^2 v \ll \vec{v} \cdot \nabla\vec{v}$, so that the characteristic features of such solutions can be maintained when the amplitude of a disturbance grows to large values.

In compressible hydrodynamic flow, if the velocity is close to the velocity of sound, compressibility becomes important, and the number of degrees of freedom rapidly increases until turbulence sets in. Qualitatively, the onset of a turbulent state as distinguished from a well-organized state of motion is determined by a critical Reynolds number $N = lv/\gamma$ where l is the dimension of the problem, v is the observed velocity, and γ is the viscosity. For our maximum speeds $N \approx 1000$. If incompressible flow between two planes a distance h apart is any guide, the critical Reynolds number for onset of turbulence is $N \approx 7700$ (Ref. 50). Thus, a steady, organized motion is quite possible even for wind speeds of the order of 1 km/sec, although the sonic speed

$$c = (\nu g H_0)^{1/2} \tag{105}$$

with $3/2 \le \nu \le 5/3$ near 200 km, is approximately 800 m/sec.

Assuming the existence of organized motion, we can obtain an approximate set of equations valid for the high speed case. We shall assume that pressure, density, and temperature changes are still small. Ignoring $\gamma\nabla^2 v$ and $(K/\rho_0 c_p)$ div (∇T) terms in Eqs. (56) through (58), we have

$$\frac{\partial v_x}{\partial x} + \frac{\partial v_y}{\partial y} + \frac{1}{\rho_0}\frac{\partial}{\partial z}(\rho_0 v_z) = 0 \tag{106}$$

$$\vec{v} \cdot \nabla\vec{v} + \frac{1}{\rho_0}\nabla p_1 + \vec{g}\beta T_1 = 0 \tag{107}$$

$$\vec{v} \cdot \nabla T_1 = 0 \tag{108}$$

In Eq. (107), we shall, in addition, ignore $v_z(dv_z/dz)$ in accordance with the observations.

Although there is little resemblance between Eqs. (107) and (63) or between Eqs. (108) and (64), the above set of equations have the following partial solutions which are akin to Eq. (73)

$$v_z = u_z(z) \sin \vec{k} \cdot \vec{r} \quad , \quad r = (x, y) \tag{109}$$

$$\begin{bmatrix} v_x \\ \\ v_y \end{bmatrix} = \begin{bmatrix} u_x(z) \\ \\ u_y(z) \end{bmatrix} \cos \vec{k} \cdot \vec{r} \tag{110}$$

$$\begin{bmatrix} p_1 \\ \\ T_1 \end{bmatrix} = \begin{bmatrix} p(z) \\ \\ t(z) \end{bmatrix} \cos^2 \vec{k} \cdot \vec{r} \tag{111}$$

Substitution of Eqs. (109) through (111) into Eqs. (106) through (108) gives

$$k_x u_x^2 + k_y u_x u_y - u_z \frac{du_x}{dz} + \frac{2k_x}{\rho_0} p = 0 \tag{112}$$

$$k_x u_x u_y + k_y u_y^2 - u_z \frac{du_y}{dz} + \frac{2k_y}{\rho_0} p = 0 \tag{113}$$

$$k_x u_x u_z + k_y u_y u_z + \frac{1}{\rho_0} \frac{dp}{dz} - g\beta t = 0 \tag{114}$$

$$k_x u_x + k_y u_y = \frac{1}{\rho_0} \frac{d}{dz} (\rho_0 u_z) \tag{115}$$

$$2t(k_x u_x + k_y u_y) = u_z \frac{dt}{dz} \tag{116}$$

Defining $w = \rho_0 u_z$, we find that Eqs. (114) and (115) yield

$$t = \pm(t_0/w_0^2)\,w^2 \tag{117}$$

where $t_0 = \max(|t|)$ and $w_0 = \max(w)$. Now Eqs. (112) through (116) can be decoupled to obtain a nonlinear differential equation for w

$$\pm\left(2k^2 g\beta \frac{t_0}{w_0^2}\rho_0^2\right) w^2 = -\frac{dw}{dz}\frac{d^2w}{dz^2} + w\left[\frac{d^3w}{dz^3} + \frac{2}{H_0}\frac{d^2w}{dz^2} + \left(\frac{1}{H_0^2} + 2k^2\right)\frac{dw}{dz}\right] \tag{118}$$

where $k^2 = k_x^2 + k_y^2$ as before. Similar to the determining equation (74), Eq. (118) is to be solved with boundary conditions $w(0) = w(h) = 0$. The coefficient of w^2 on the left-hand side shall be considered constant.

The general solution of Eq. (118) is very difficult because of the high degree of nonlinearity. In our case $k \ll 1/h$, hence the term $2k^2(dw/dz)$ can be ignored. On the other hand, if H_0 becomes large compared to $h/2$, the term $(1/H_0^2)(dw/dz)$ also becomes small compared to $(2/H_0)(d^2w/dz^2)$. Hence, if such asymptotic approximations hold, we have a simpler equation

$$\pm\left(2k^2 g\beta \frac{t_0}{w_0^2}\rho_0^2\right) w^2 = -\frac{dw}{dz}\frac{d^2w}{dz^2} + \frac{d^3w}{dz^3} + \frac{2w}{H_0}\frac{d^2w}{dz^2} \tag{119}$$

A particular solution of Eq. (119) satisfying $w(0) = w(h) = 0$ is, surprisingly,

$$w(z) = w_0 \sin m\pi z/h \quad ; \quad m = 1, 2, \cdots \tag{120}$$

where m satisfies the relation

$$m^2\pi^2 = \frac{k^2h^2 g\beta H_0 \rho_0^2 t_0}{w_0^2} \quad , \quad m = 1, 2, \cdots \tag{121}$$

Using w_0 = max $(\rho_0 u_z)$ and assuming ρ_0 to be approximately constant, we have from Eq. (121) for the lowest mode, m = 1,

$$\max(u_z) \approx \left(\frac{k^2h^2}{2} t_0 g\beta H_0\right)^{1/2} \approx \frac{kh}{\pi}\left(\frac{t_0}{T_0} gH_0\right)^{1/2} \tag{122}$$

From our previous sections, we had shown that $kh/\pi \ll 1$; hence $\max(uz) \ll c$ even in the case of fully developed instability when $t_0 \rightarrow T_0$ if we compare Eq. (122) with Eq. (105).

Next, from the equation of continuity (106), and Eq. (120) we obtain an estimate of the horizontal velocity component for m = 1

$$\max(u_{x,y}) \approx \left(\frac{t_0}{T_0} gH_0\right)^{1/2} \tag{123}$$

Thus we see that our horizontal wind speed components approach the speed of sound when t_0/T_0 approaches ν. In such a case, T_1 is no longer small compared to T_0. Nevertheless, $\max(u_{x,y})$ can be a substantial fraction of the sound speed.

Finally, it is clear from Eqs. (109) and (120) that a solution of the convective type does exist for the highly nonlinear, high wind speed case. Although we have only shown that the solution exists in the asymptotic limit of $H_0 \gg h/2$, the full equation (118), together with the consistency condition $w_0 = \max(w)$ can be solved numerically to obtain w(z) and w_0. Further, Eq. (123) shows that our solution is valid for cases when the wind speed is a substantial fraction of the speed of sound.

REFERENCES

1. M. Nakamura, Postflight Ephemeris for Vehicle 4838, TOR-0158(3110-01)-15, The Aerospace Corporation, El Segundo, California (15 February 1968).

2. L. Schusterman, Vehicle 4838 Density Reduction and Post Flight Ephemeris, TM 55-31-0M-006, Lockheed Missiles and Space Company, Sunnyvale, California (13 October 1967).

3. J. H. Kainer, Estimated Variation of Aerodynamic Coefficients with Altitude for an Agena Configuration, TOR-0158(3110-01)-14, The Aerospace Corporation, El Segundo, California (January 1968).

4. L. H. Sentman, Free Molecule Flow Theory and its Application to the Determination of Aerodynamic Forces, LMSC-448514, Lockheed Missiles and Space Company, Sunnyvale, California (1 October 1961).

5. L. G. Jacchia, "Static Diffusion Models of the Upper Atmosphere with Empirical Temperature Profiles," Smithsonian Contr. to Astrophys., vol. 8, no. 9, pp 215-257 (1965).

6. R. W. Bruce, An Atmospheric Density Model Recommended for Analysis of Low Altitude Satellite Orbits, TOR-1001(2110-01)-8, The Aerospace Corporation, El Segundo, California (30 August 1966).

7. R. Schamberg, On Concave Bodies in Free Molecule Flow, AD 621-958, The RAND Corporation, Santa Monica, California (May 1965).

8. R. L. Jacobs, "Atmospheric Density Derived from the Drag of Eleven Low-Altitude Satellites," J. Geophys. Res., vol. 72, pp. 1571-1581 (1967).

9. R. L. Jacobs, Lockheed Atmospheric Density Model (1967), Tracking Note #87, Lockheed Missiles and Space Company, Sunnyvale, California (20 February 1967).

10. L. G. Jacchia and J. W. Slowey, Diurnal and Seasonal-Latitudinal Variations in the Upper Atmosphere, Smithsonian Astrophys. Obs. Special Report 242 (6 June 1967).

11. R. L. Jacobs, private communication, Lockheed Missiles and Space Company, Sunnyvale, California (August 1967).

12. N. C. Maynard and L. J. Cahill, Jr., "Measurement of the Equatorial Electrojet Over India," J. Geophys. Res., vol. 70, pp. 4395-4398 (1965).

13. P. O. Ogbuehi and A. Onwumechilli, "Seasonal Studies of the Equatorial Electrojet during Low Solar Activity," J. Geophys. Res., vol. 70, pp. 4909-4919 (1965).

14. Committee on Space Research (COSPAR), CIRA 1965, North-Holland Publishing Company, Amsterdam (1965).

15. United States Committe on Extension to the Standard Atmosphere (COESA), U.S. Standard Atmosphere Supplements, 1966, U.S. Government Printing Office, Washington, D. C. (1967).

16. A. B. Prag, private communication, The Aerospace Corporation, El Segundo, California (November 1967).

17. G. E. Thomas and B. K. Ching, Dynamical Response of the Thermosphere to Impulsive Heating, TR-0158(3260-10)-5, The Aerospace Corporation, El Segundo, California (January 1968).

18. L. L. DeVries, E. W. Friday, and L. C. Jones, "Analysis of Density Data Reduced from Low-Altitude, High Resolution Satellite Tracking Data," Space Research VII, ed. by R. L. Smith-Rose, et al., pp. 1173-1182, North-Holland Publishing Co., Amsterdam (1967).

19. L. G. Jacchia, J. Slowey, and F. Verniani, "Geomagnetic Perturbations and Upper-Atmosphere Heating," J. Geophys. Res., vol. 72, pp. 1423-1434 (1967).

20. K. S. W. Champion, Variations with Season and Latitude of Density, Temperature and Composition in the Lower Thermosphere, presented at the COSPAR 7th International Space Science Symposium, Vienna (May 1966).

21. K. S. W. Champion, F. Marcos, and J. Slowey, New Model Atmospheres Giving Latitudinal and Seasonal Variations in the Thermosphere, presented at the COSPAR 7th International Space Science Symposium, Vienna (May 1966).

22. Committee on the Extension of the Standard Atmosphere, U. S. Standard Atmosphere, 1962, U. S. Government Printing Office, Washington, D. C. (December 1962).

23. A. B. Prag, Geophysical Phenomena Observed Between 21 and 27 May 1967, TOR-0158(3110-01)-24, The Aerospace Corporation, El Segundo, California, (May 1968)

24. K. D. Cole, "Joule Heating of the Upper Atmosphere," Australian J. Phys. 15, 223-235 (1962).

25. A. B. Prag, F. A. Morse, and R. J. McNeal, "Nightglow Excitation and Maintenance of the Nighttime Ionosphere by Low Energy Protons," J. Geophys. Res. 71, 3141-3154 (1966).

26. T. N. Davis and R. Parthasarathy, "The Relationship between Polar Magnetic Activity DP and Growth of the Geomagnetic Ring Current," J. Geophys. Res. 72, 5825-5836 (1967).

27. Classified reference.

28. COSPAR International Reference Atmosphere 1965, North-Holland Publishing Company, Amsterdam (1965).

29. D. Krankowsky, W. T. Kasprzak, and A. O. Nier, "Mass Spectrometric Studies of the Composition of the Lower Thermosphere during Summer 1967," J. Geophys. Res. 73, 7291-7306 (1968)

30. W. T. Kasprzak, D. Krankowsky, and A. O. Nier, "A Study of Day-Night Variations in the Neutral Composition of the Lower Thermosphere," J. Geophys. Res. 73, 6765-6782 (1968)

31. G. E. Thomas and B. K. Ching, A Study of Atmospheric Heating Applied to the Phenomenon of Geomagnetic Heating, Report No. TR-0158(3110-01)-5, The Aerospace Corporation, El Segundo, California (June 1968).

32. H. E. Hinteregger and L. A. Hall, quoted in Handbook of Geophysics and Space Environments, S. L. Valley, ed., McGraw-Hill Book Co., Inc., pp 16-16, 16-17, New York (1965).

33. R. E. Bourdeau, S. Chandra, and W. M. Neupert, "Time Correlation of Extreme Ultraviolet Radiation and Thermospheric Temperature," J. Geophys. Res. 69, pp. 4531-4535 (1964).

34. H. E. Hinteregger and L. A. Hall, "Solar Extreme Ultraviolet Emissions in the Range 260 - 1300 Å Observed from OSO-III," Solar Physics. 6, 175-182 (1969)

35. J. H. Neally, M. J. Rademacher, and W. F. Rearick, The Modularized Vehicle Simulation (MVS) System, TOR-0158(3307-02)-2, The Aerospace Corporation, El Segundo, California (February 1968).

36. C. O. Hines, "Internal Gravity Waves at Ionospheric Heights," Can. J. Phys. 38, 1441 (1960).

37. H. Volland, "Heat Conduction Waves in the Upper Atmosphere," J. Geophys. Res. 72, 2831 (1967).

38. L. B. Smith, "An Observation of Strong Thermospheric Winds During a Geomagnetic Storm," J. Geophys. Res. 73, 4959 (1968).

39. J. E. Geisler, "Atmosphere Winds in the Middle Latitude F-Region," J. Atmospheric Terrest. Phys. 28, 702 (1966).

40. L. G. Jacchia, "Density Variations in the Heterosphere," Ann. Geophys. 22, 75 (1966).

41. A. J. Dessler, "Ionospheric Heating by Hydromagnetic Waves," J. Geophys. Res. 63, 405 (1958).

42. Lord Rayleigh, "On Convection Currents in a Horizontal Layer of Fluid When the Higher Temperature is on the Under Side," Phil. Mag. 32, 529 (1916).

43. A. Pellew and R. V. Southwell, "On Maintained Convective Motion in a Fluid Heated From Below," Proc. Roy. Soc. A176, 312 (1940).

44. S. Chandrasekhar, "The Instability of a Layer of Fluid Heated Below and Subject to Coriolis Forces," Proc. Roy. Soc. A217, 306 (1953).

45. E. A. Spiegel, "Convective Instability in a Compressible Atmosphere," Astrophys. J. 141, 1068 (1965).

46. G. E. Thomas and B. K. Ching, "Upper Atmosphere Response to Transient Heating," J. Geophys. Res. 74, 1796-1811 (1969)

47. K. W. Yeung and C. P. Yu, Convective Instability of a Polytropic Fluid Layer in a Magnetic Field, State University of New York (Buffalo) preprint (1968).

48. I. Harris and W. Priester, "Time Dependent Structure of the Upper Atmosphere," J. Atmospheric Sci. 19, 286 (1962).

49. H. Kohl and J. W. King, "Atmospheric Winds Between 100 and 700 km and Their Effects on the Ionosphere," J. Atmospheric Terrest. Phys. 29, 1045 (1967).

50. C. C. Lin, The Theory of Hydrodynamic Stability, Cambridge University Press, New York, London. (1955).

BIBLIOGRAPHY

Bruce, R. W., Upper Atmosphere Density Determined from a Low-G Accelerometer on Satellite 1967 50B, TOR-0158(3110-01)-16, The Aerospace Corporation, El Segundo, California (15 February 1968).

Chiu, Y. T., Thermospheric Convective Instability, TR-0066(9260-02)-3, The Aerospace Corporation, El Segundo, California (1 July 1969).

Feess, W. A., Reduced Data from the LOGACS Experiment, TOR-0158(3110-01)-17, The Aerospace Corporation, El Segundo, California (15 February 1968).

Feess, W. A., LOGACS Wind Analysis, TOR-0200(9990)-1, The Aerospace Corporation, El Segundo, California (August 1968).

Fotou, E. G., LOGACS - An Orbital Accelerometer Calibration Experiment, TOR-0158(3110-01)-21, The Aerospace Corporation, El Segundo, California (February 1968).

Pearson, J. A., Analysis of Atmosphere Density Obtained from Low-G Accelerometer Data on Satellite 1967 50B, TOR-0066(5306)-3, The Aerospace Corporation, El Segundo, California (7 July 1969).

Pearson, J. A., Predictability of Upper Atmosphere Density Based on LOGACS Data, ATM 69(4110-01)-60, The Aerospace Corporation, El Segundo, California (28 October 1968) (Internal correspondence only; not available outside The Aerospace Corporation).

Pearson, J. A., Computer Reduced Atmospheric Density Obtained from Low-G Accelerometer Data on Satellite 1967 50B, TOR-0200(9990)-2, The Aerospace Corporation, El Segundo, California (16 December 1968).

Prag, A. B., Alternate Formulation of the Midlatitutde Model of the Upper Atmosphere, TOR-0200(4110-01)-22, The Aerospace Corporation, El Segundo, California (11 March 1969).

Prag, A. B., Density Model of the Auroral and Polar Atmosphere Between 120 and 175 km, TOR-0066(5260-10)-1, The Aerospace Corporation, El Segundo, California (15 September 1969).

Prag, A. B., Density Model of the Midlatitude Atmosphere Between 120 and 220 km, TOR-0200(4110-01)-9, The Aerospace Corporation, El Segundo, California (26 December 1968).

Young, K. R., LOGACS Accelerometer Data, TOR-0200(4113-04)-1, The Aerospace Corporation, El Segundo, California (August 1968).

APPENDIX A

ACCELEROMETER DATA

The data for Revs. 5 through 67 are presented in Figs. A-1 through A-63, respectively. The actual data points are indicated by a cross and the dubbed points by triangles. The data in the plots have been converted to fps^2 by multiplying the instrument counts by $-g \times 10^{-7}$ ($g = 32.174\ fps^2$); the abcissa is TRG time in seconds.

The time tag on the accelerometer data was referenced to a clock on board the spacecraft, 0.0 sec being some time after launch. In order to adjust the data time on the abcissa of the plots (TRG time) to universal time, a time bias of 67,507.0 sec must be applied to the data. Referenced to 0.0 hr of the launch date 22 May 1967, the universal time is

$$t_{universal} = TRG + 67{,}507.0 \text{ sec}$$

The data shown in this report are available on cards and on magnetic tape in various forms. One of the forms available on magnetic tape is time-sequenced card images in a format which is readily convertible to computer systems other than the Aerospace system. The tape was written at 556 bits per inch in the Binary Coded Decimal (BCD) mode in one data file, and one physical record consists of 80 Binary Coded Integer (BCI) characters (240 bytes). The format for each record is as follows:

Columns	Contents
1 - 16	Blank
17 - 23	TRG time reference in seconds (integer right justified)

Columns	Contents
24 - 25	Blank
26 - 39	Accelerometer counts (variable of the form E 14.7)
40 - 79	Nonessential
80	1, 2, 3, or 4 (1, 2, 3 indicate actual data; 4 indicates dubbed data)

The accelerometer data on this tape have been processed according to the method outlined in Volume I of this report. Since the data appear as instrument counts, they must be multiplied by $-g \times 10^{-7}$ to convert to fps^2.

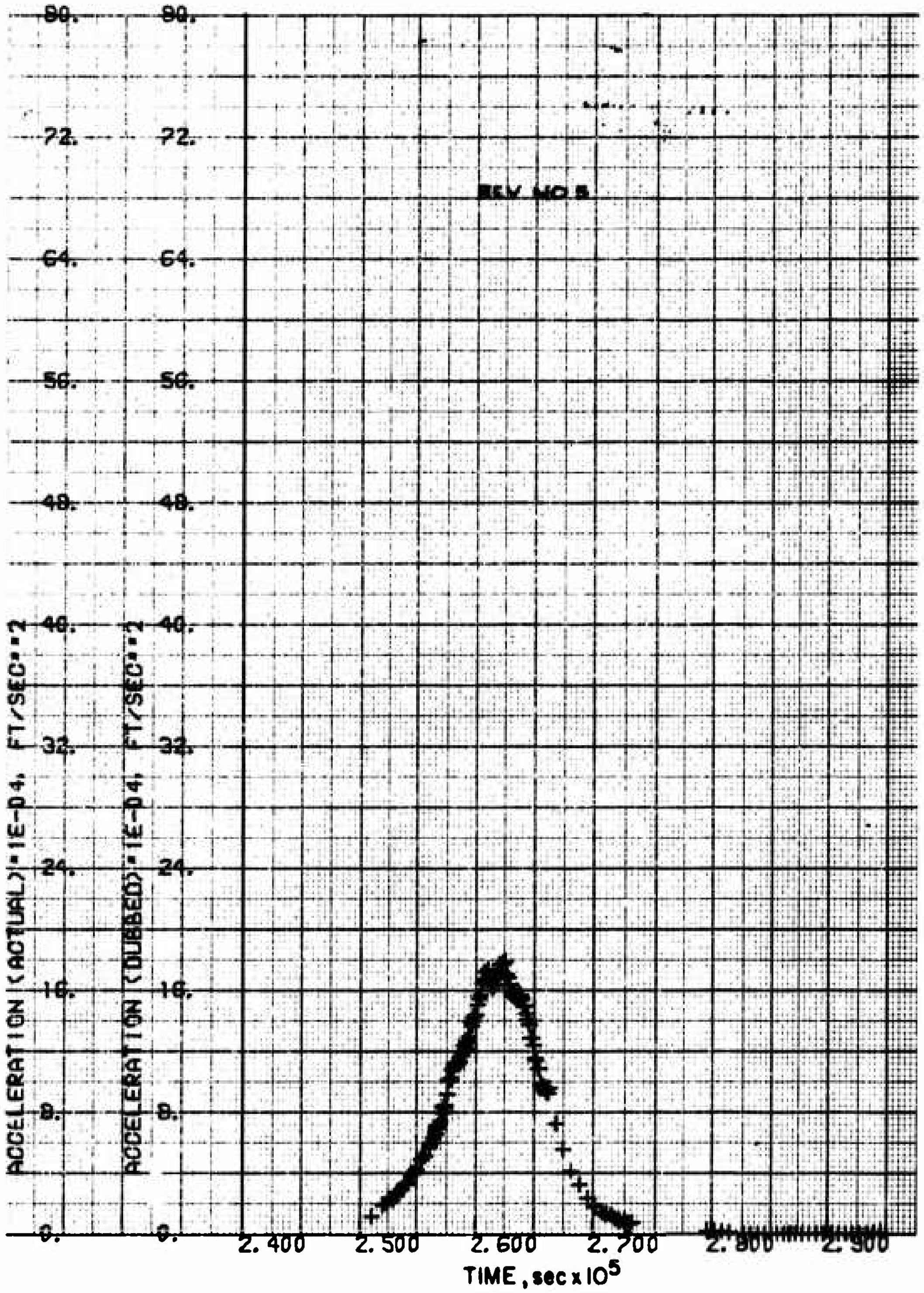

Fig. A-1. LOGACS Accelerometer Data for Rev. 5

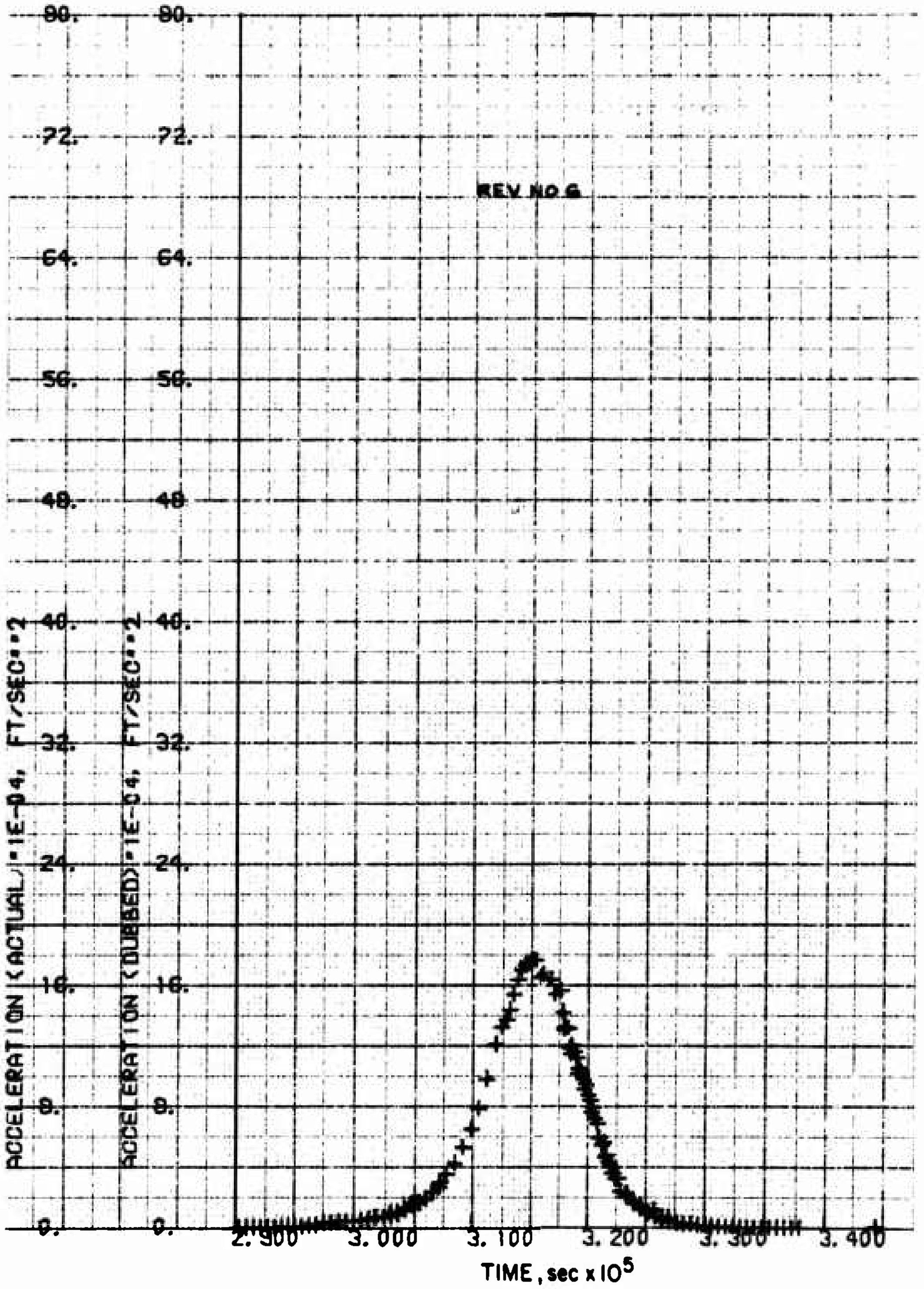

Fig. A-2. LOGACS Accelerometer Data for Rev. 6

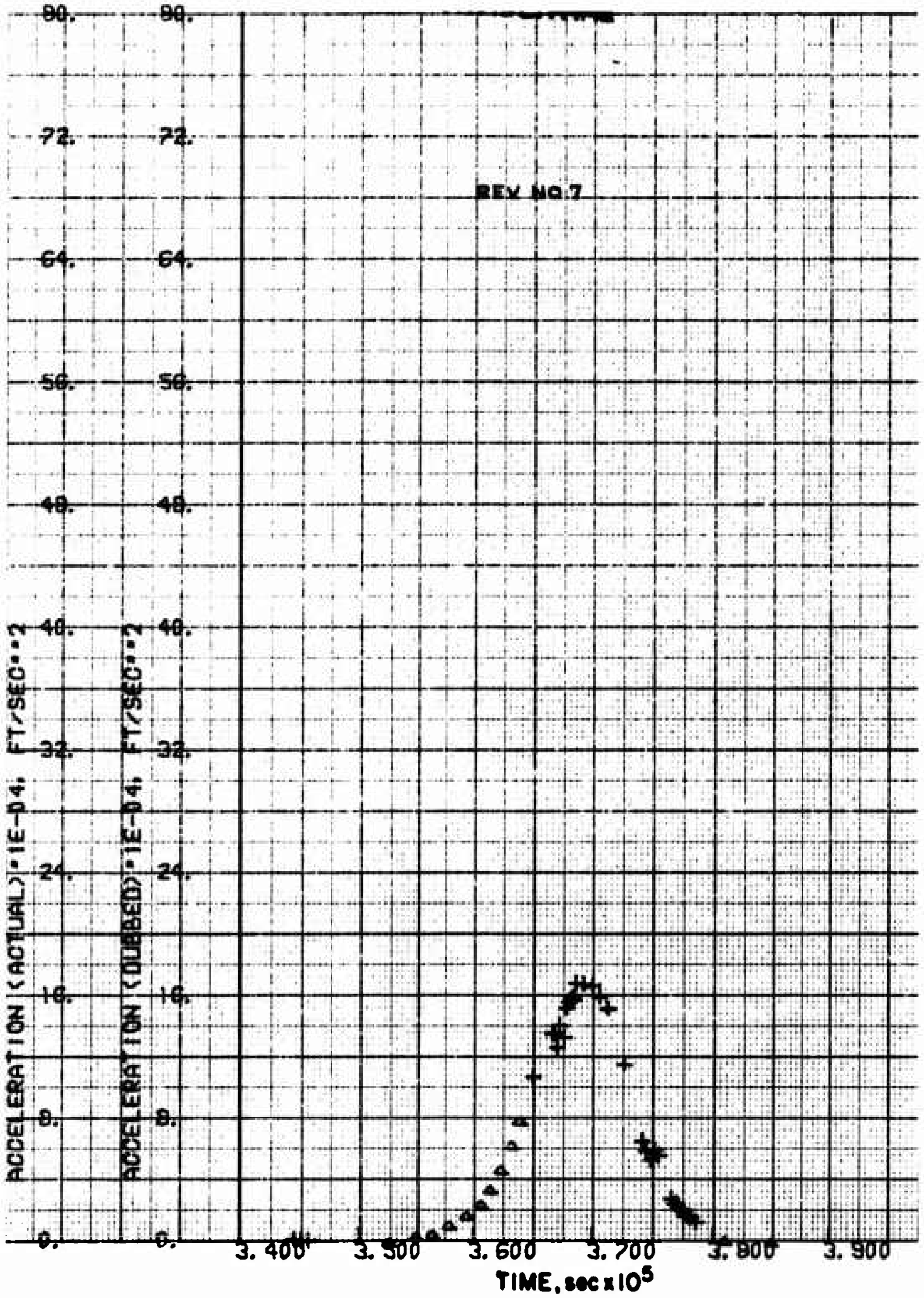

Fig. A-3. LOGACS Accelerometer Data for Rev. 7

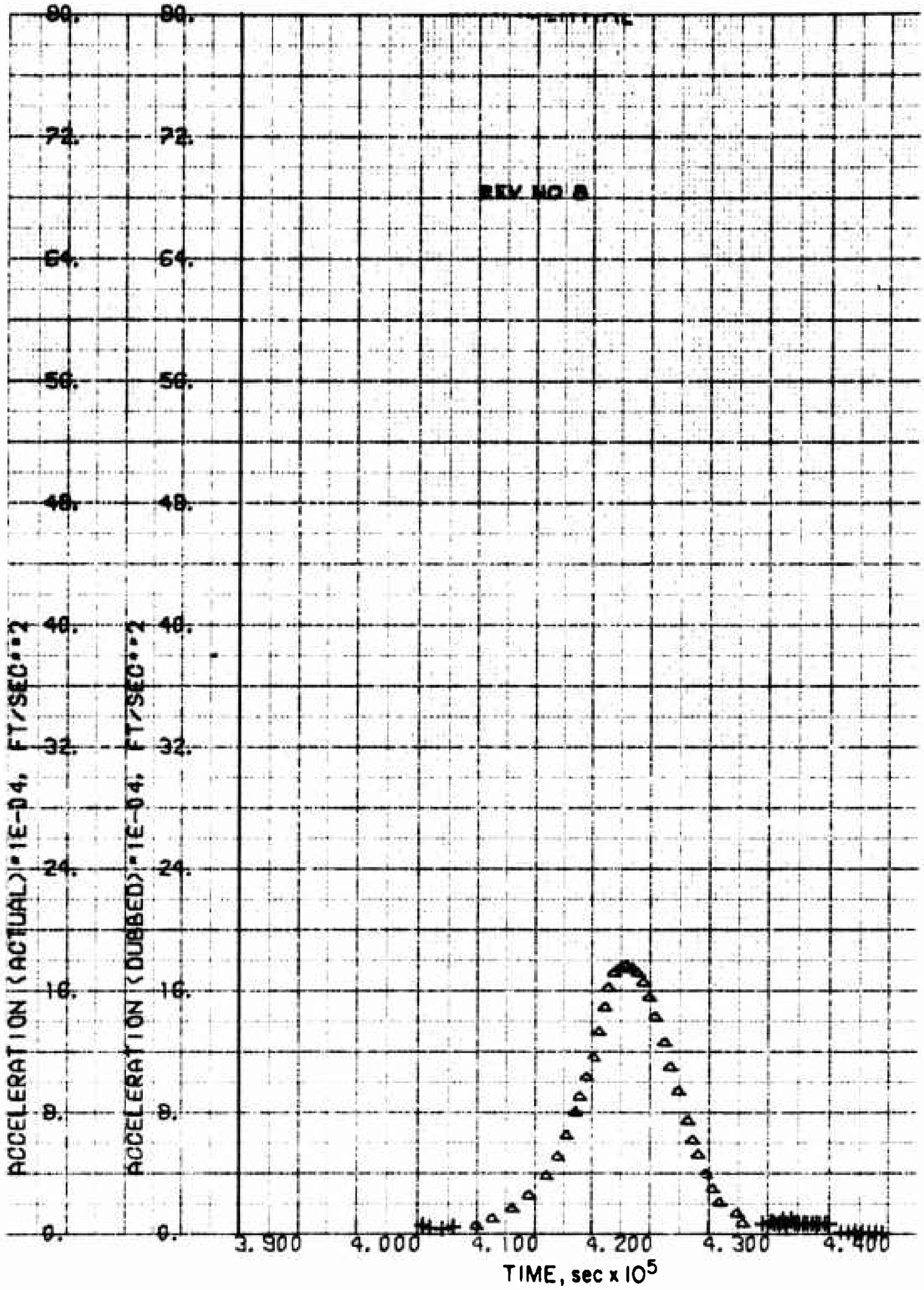

Fig. A-4. LOGACS Accelerometer Data for Rev. 8

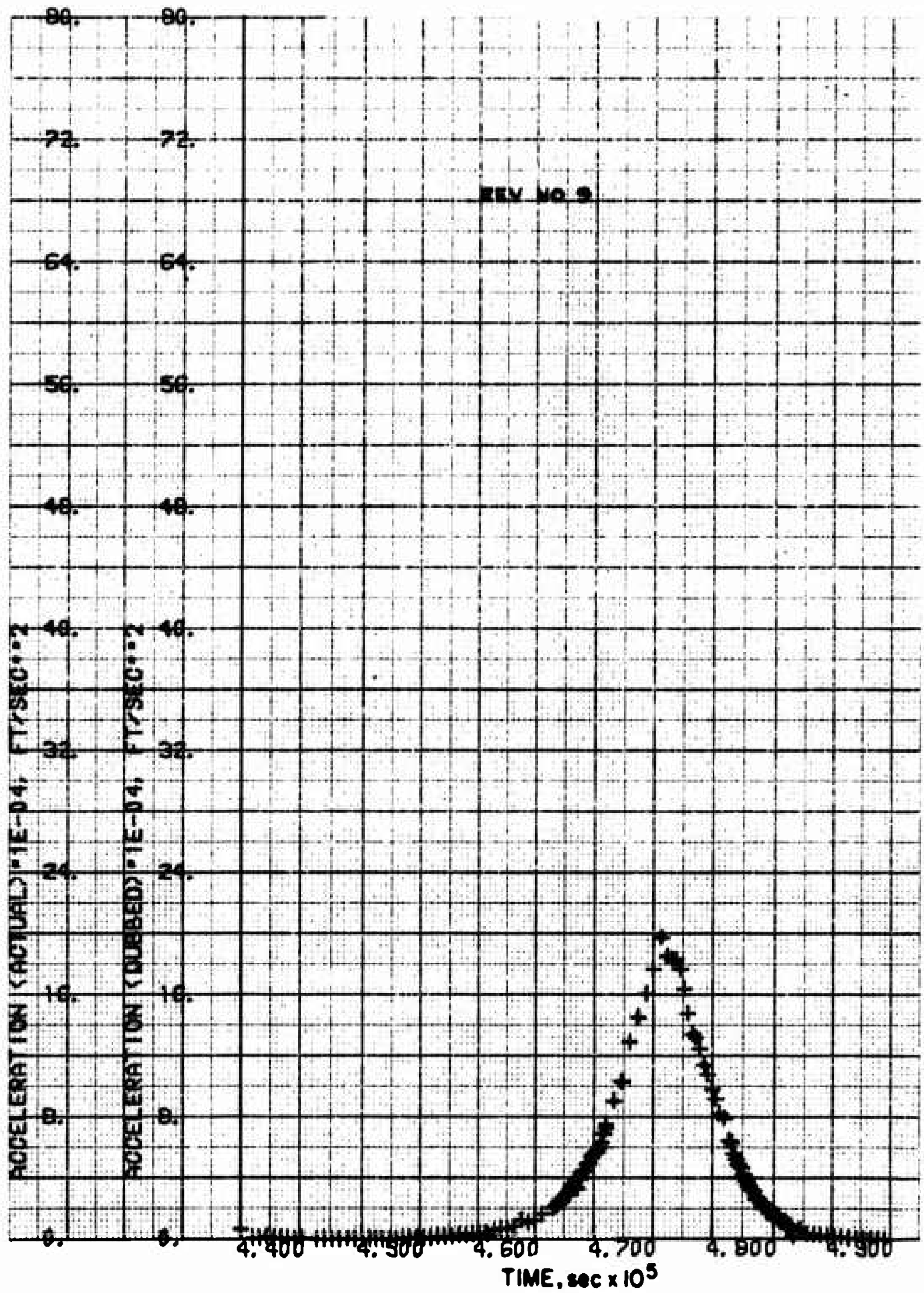

Fig. A-5. LOGACS Accelerometer Data for Rev. 9

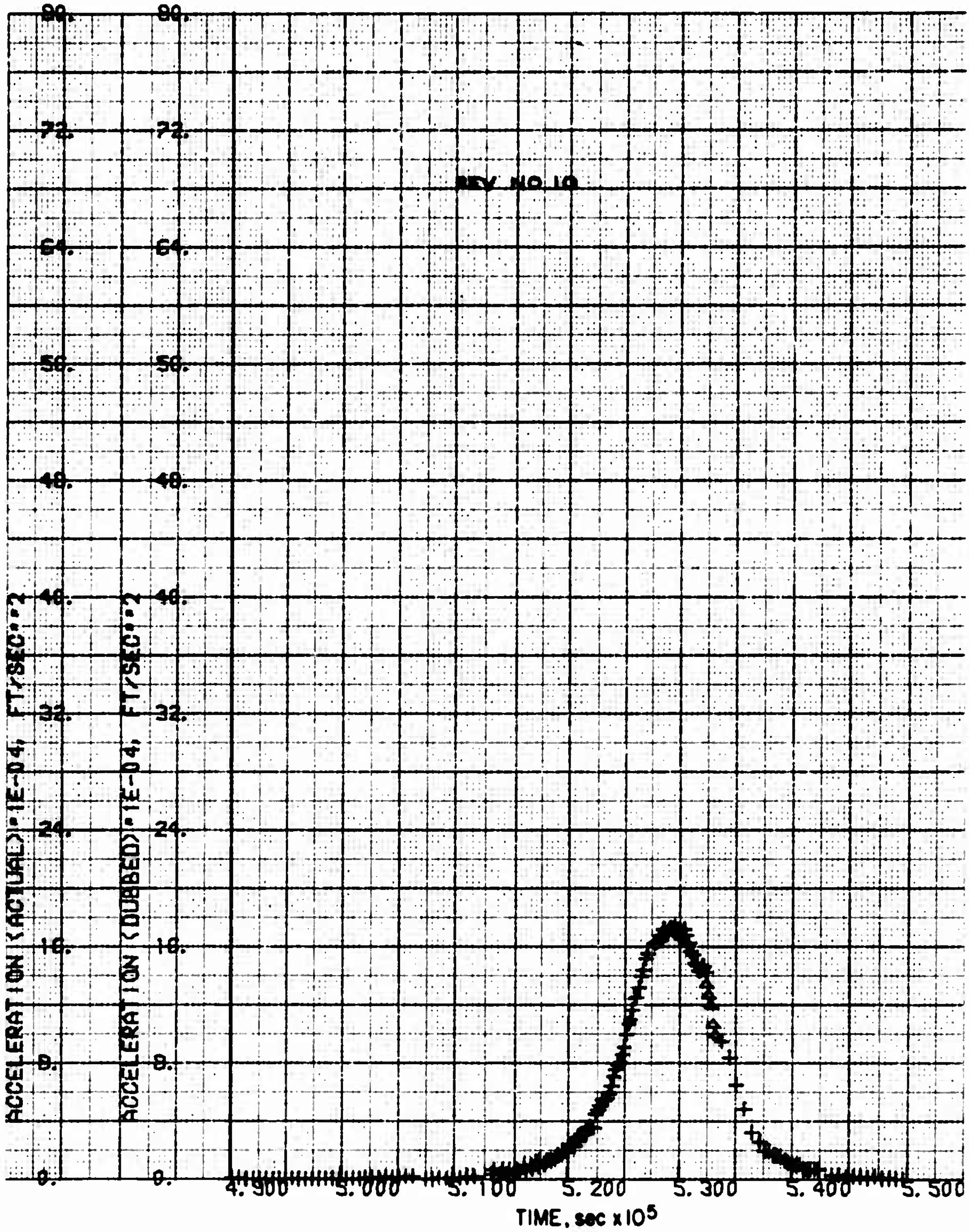

Fig. A-6. LOGACS Accelerometer Data for Rev. 10

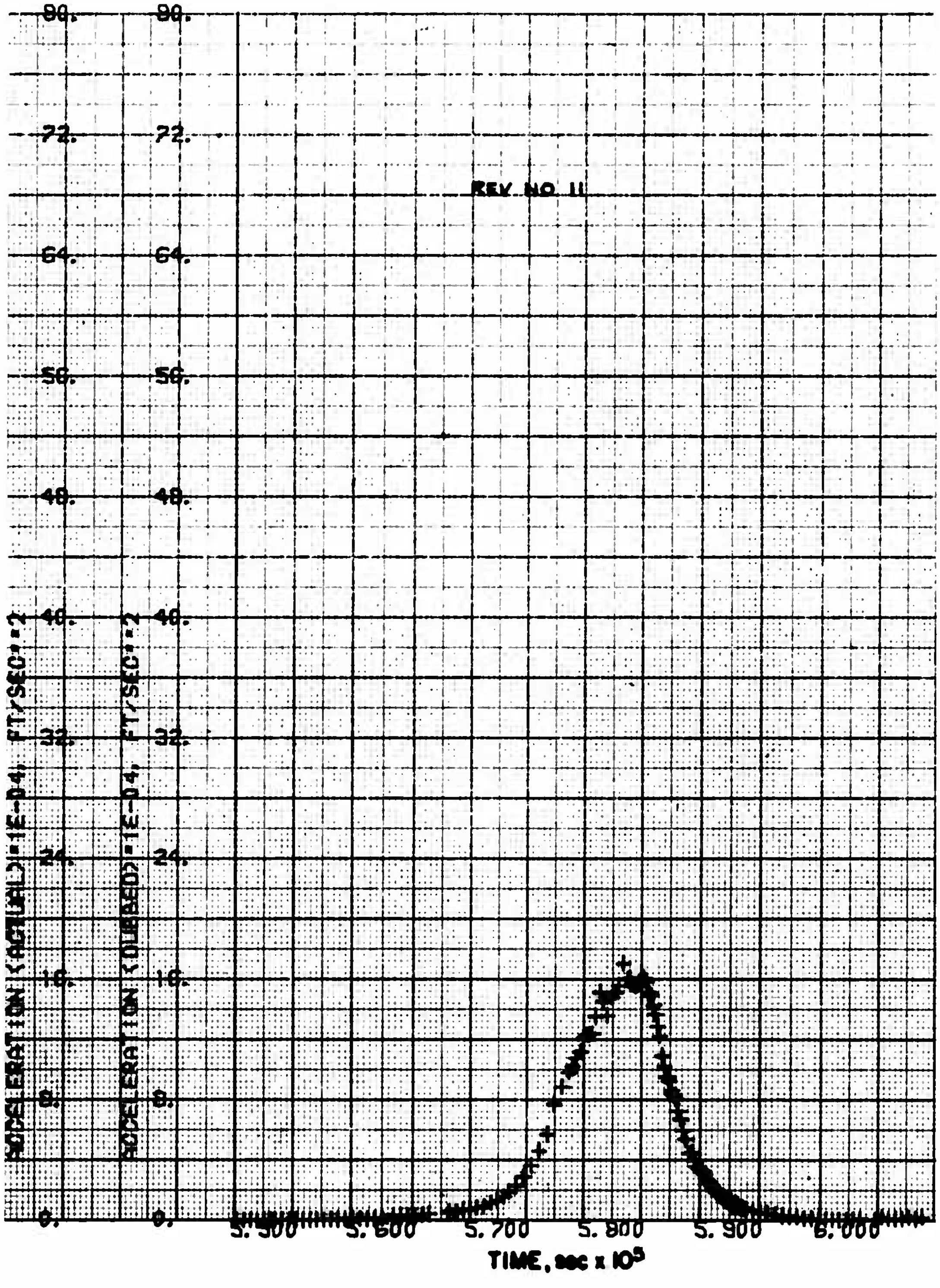

Fig. A-7. LOGACS Accelerometer Data for Rev. 11

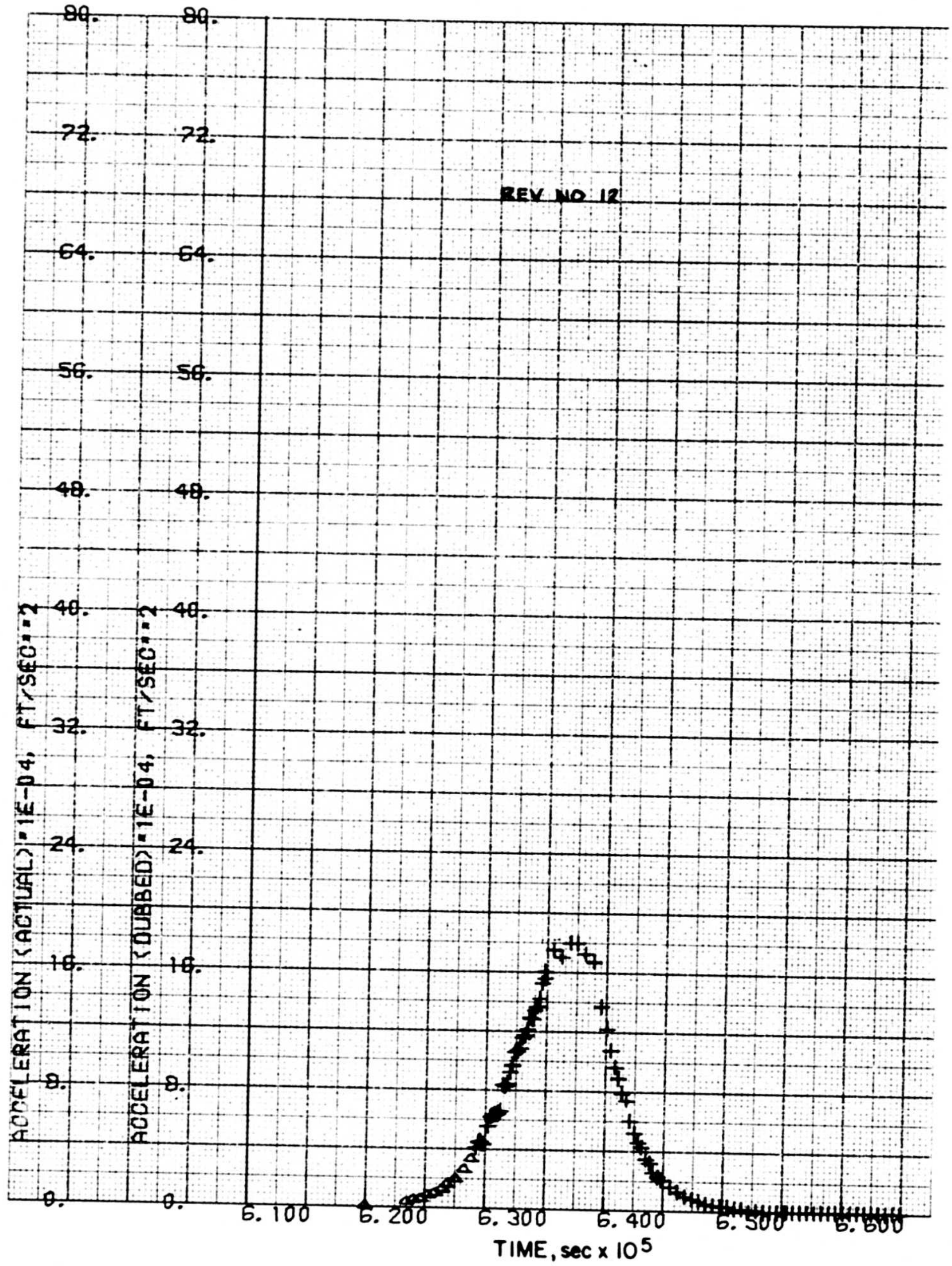

Fig. A-8. LOGACS Accelerometer Data for Rev. 12

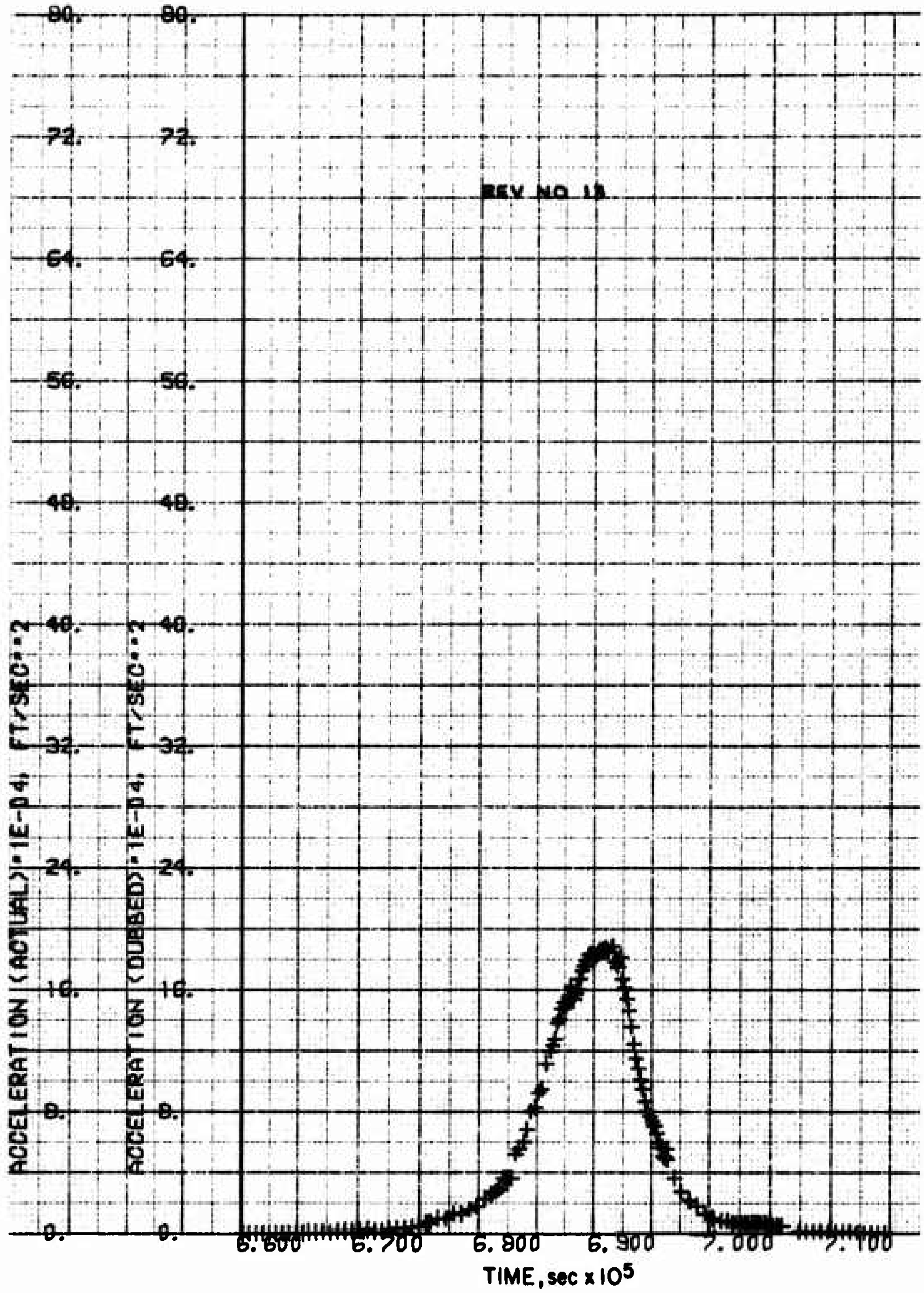

Fig. A-9. LOGACS Accelerometer Data for Rev. 13

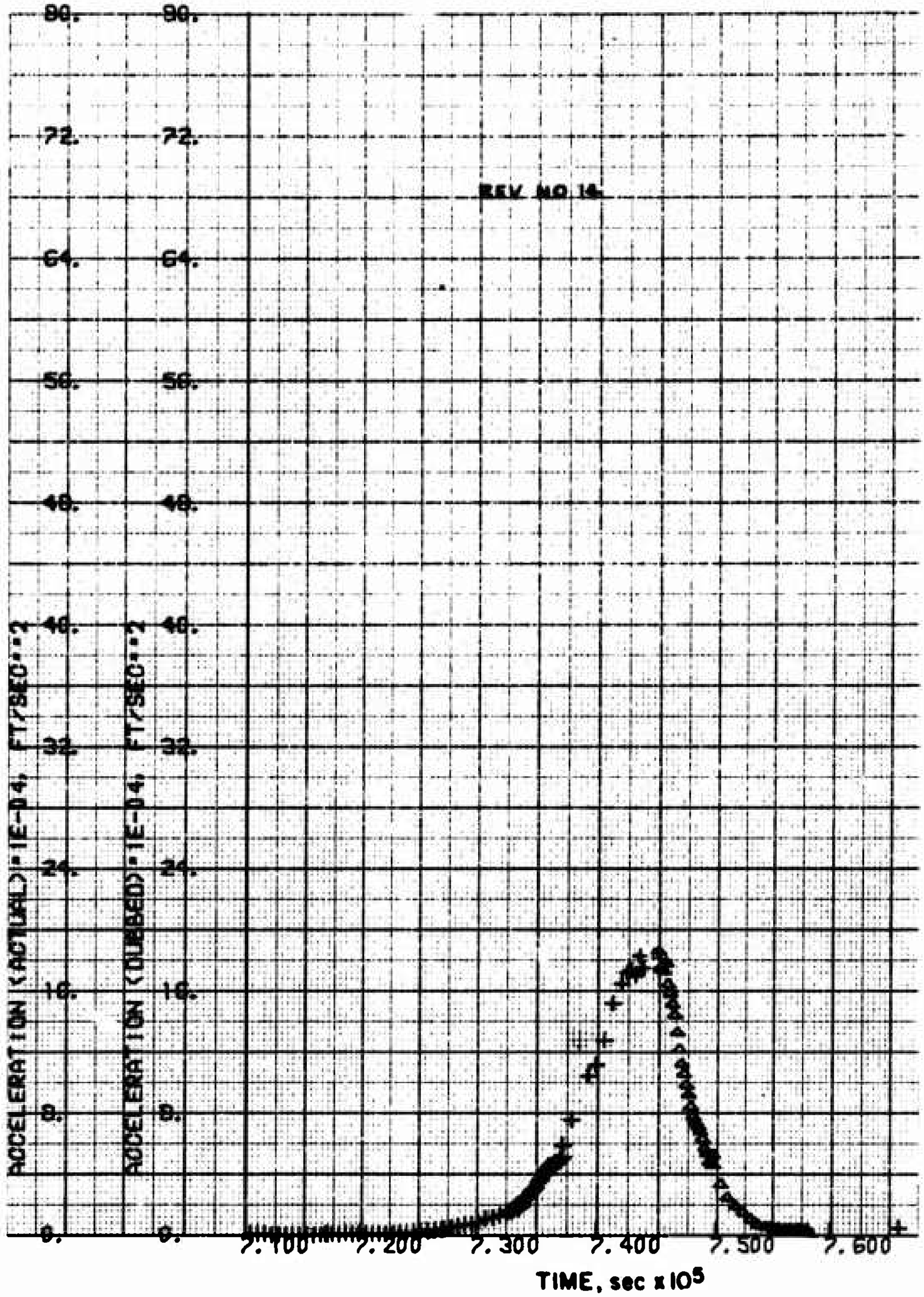

Fig. A-10. LOGACS Accelerometer Data for Rev. 14

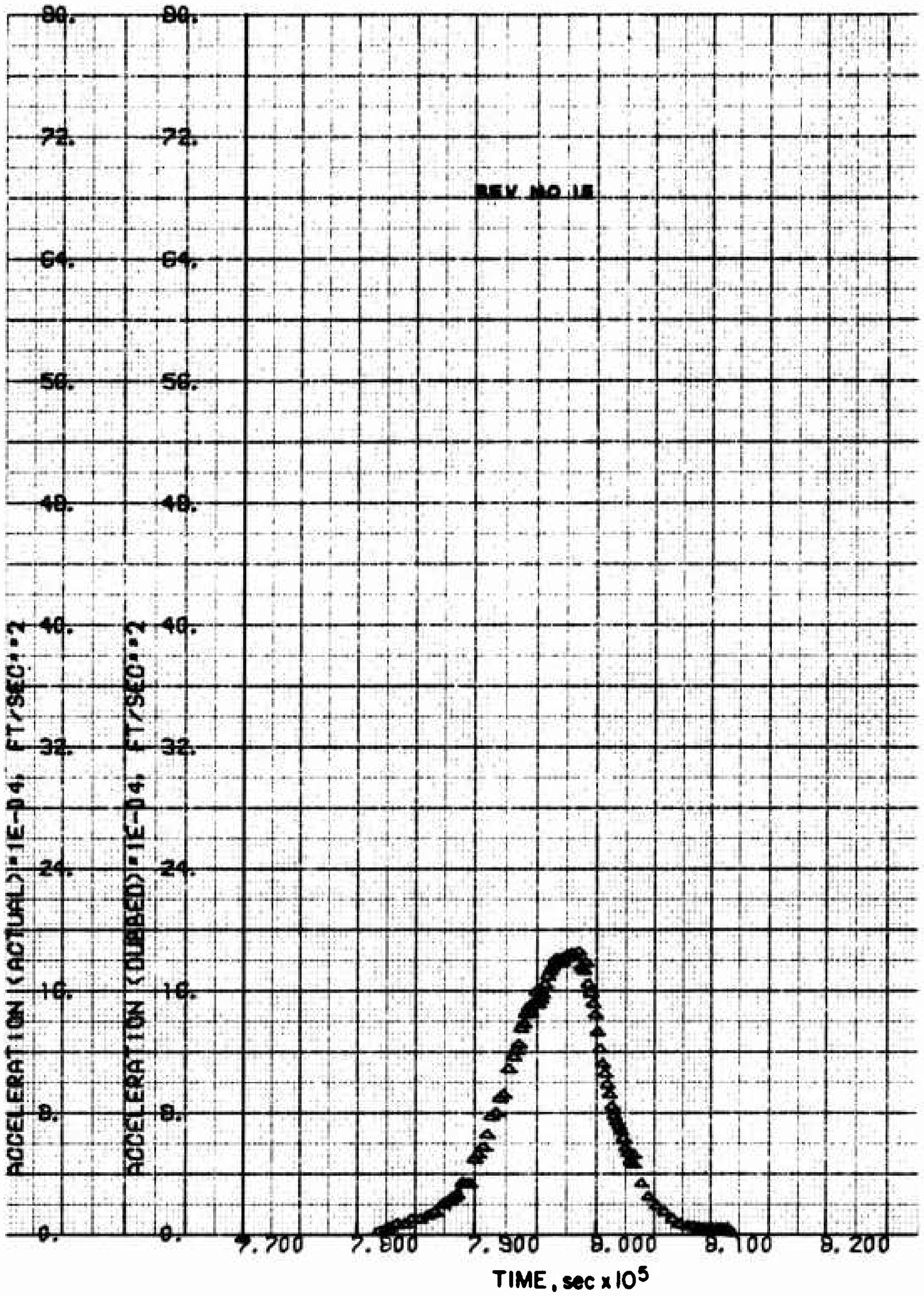

Fig. A-11. LOGACS Accelerometer Data for Rev. 15

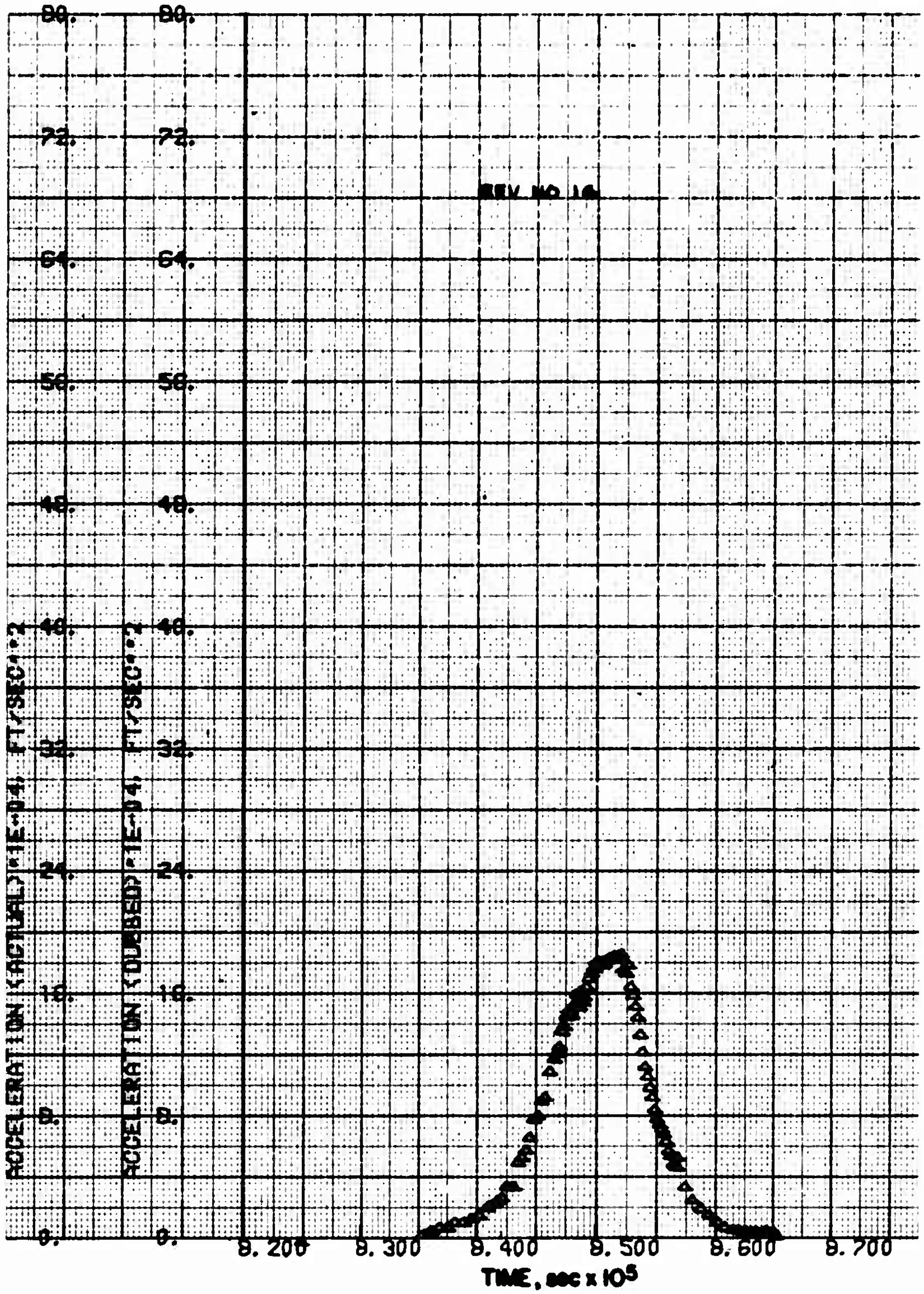

Fig. A-12. LOGACS Accelerometer Data for Rev. 16

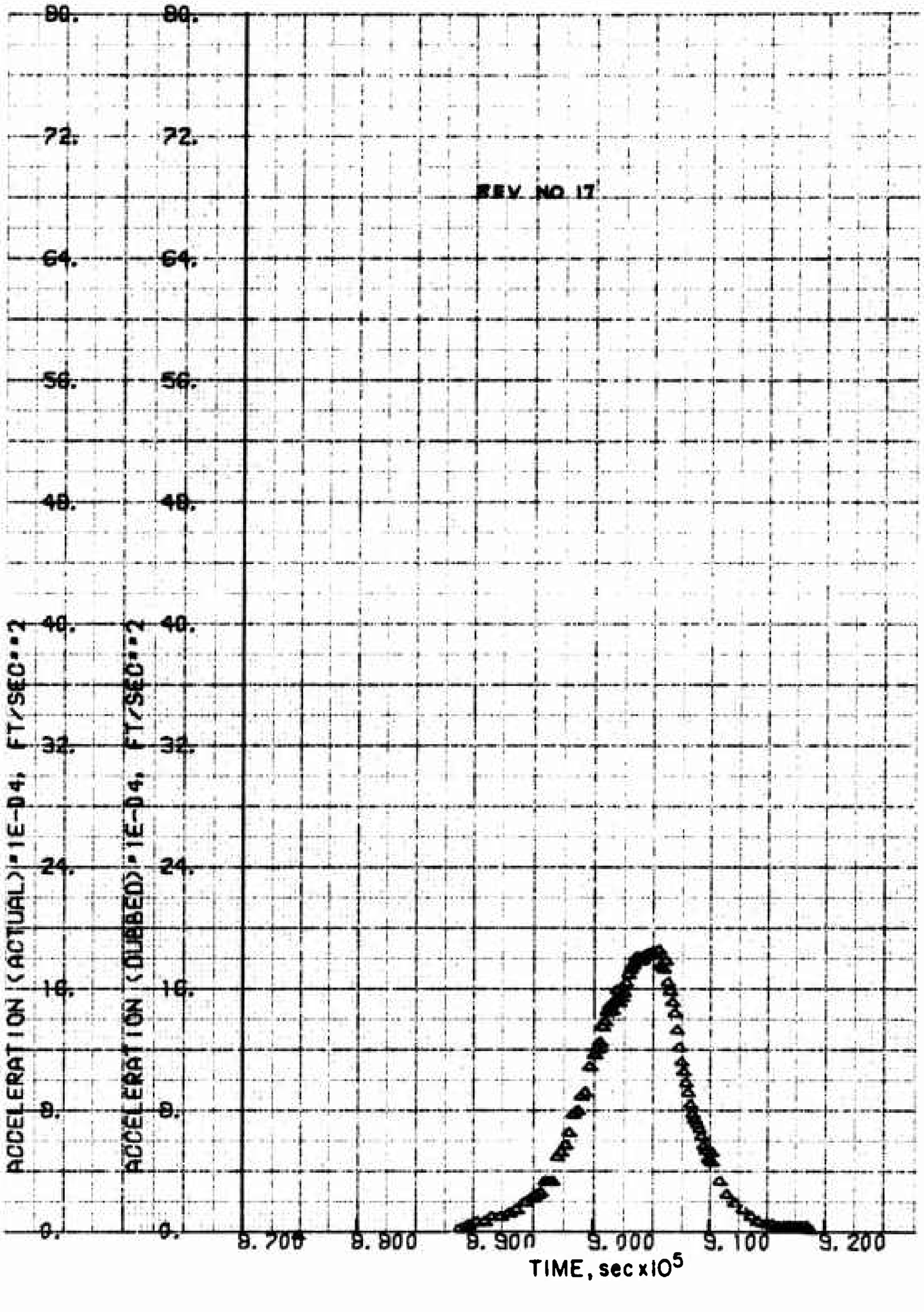

Fig. A-13. LOGACS Accelerometer Data for Rev. 17

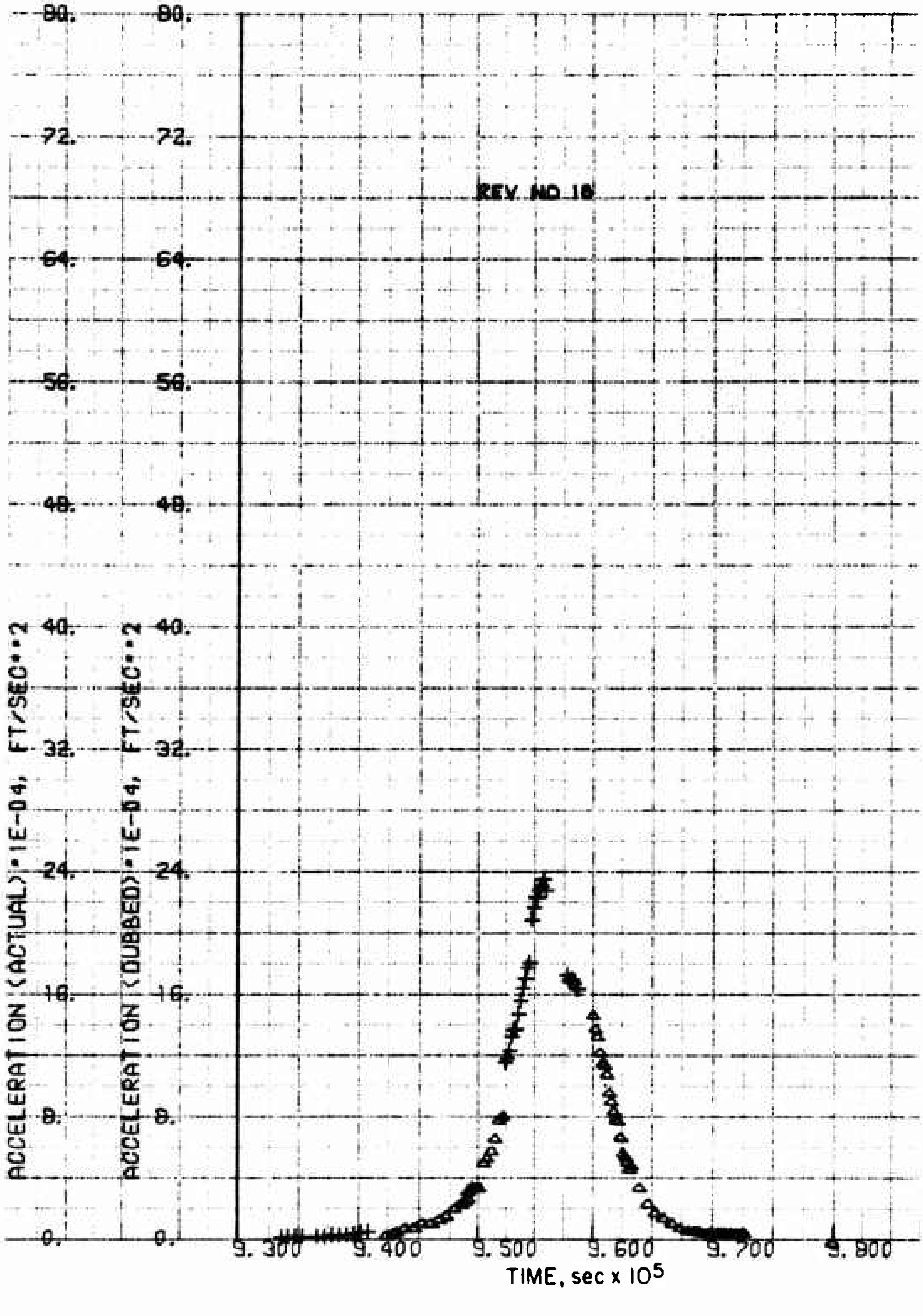

Fig. A-14. LOGACS Accelerometer Data for Rev. 18

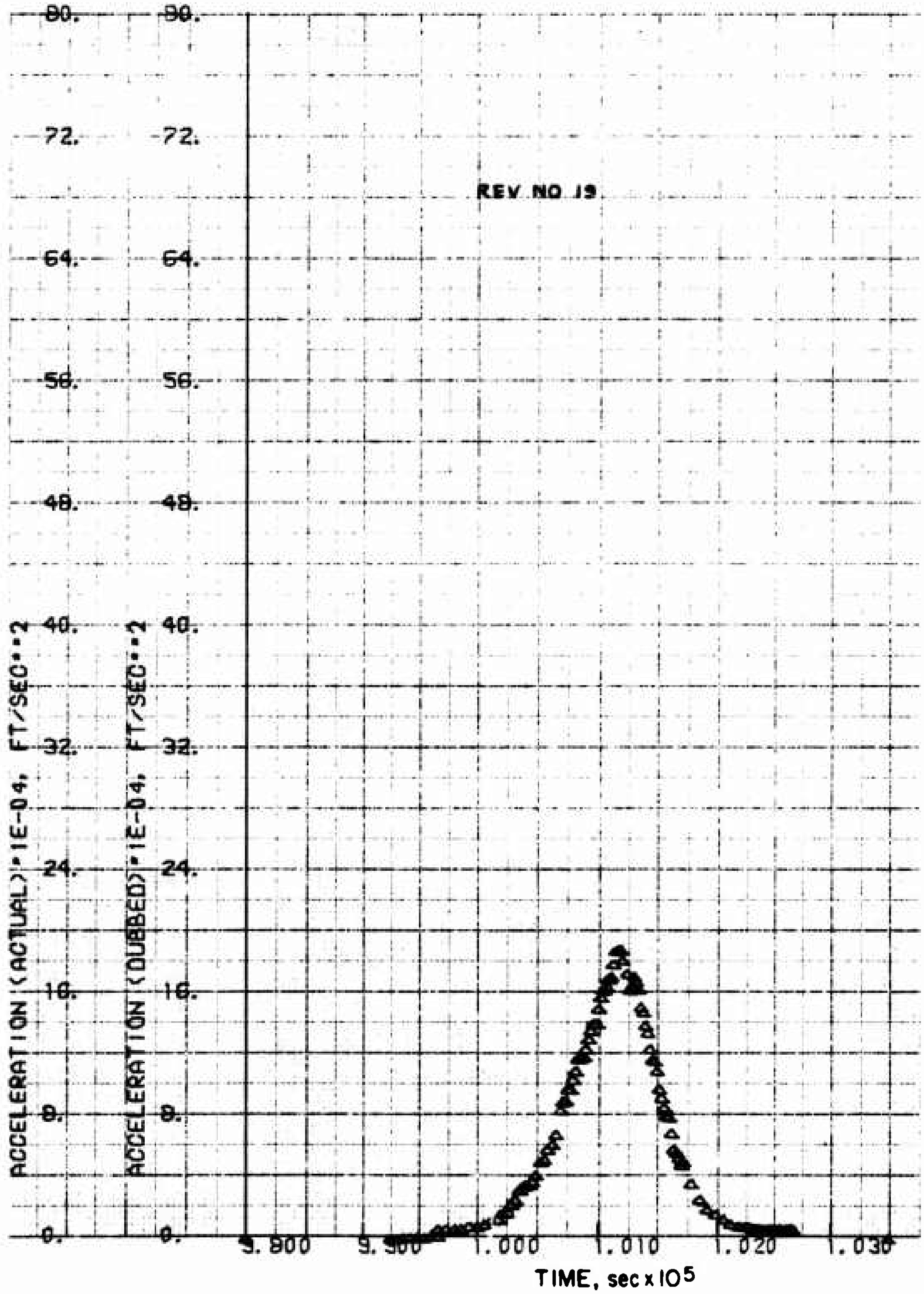

Fig. A-15. LOGACS Accelerometer Data for Rev. 19

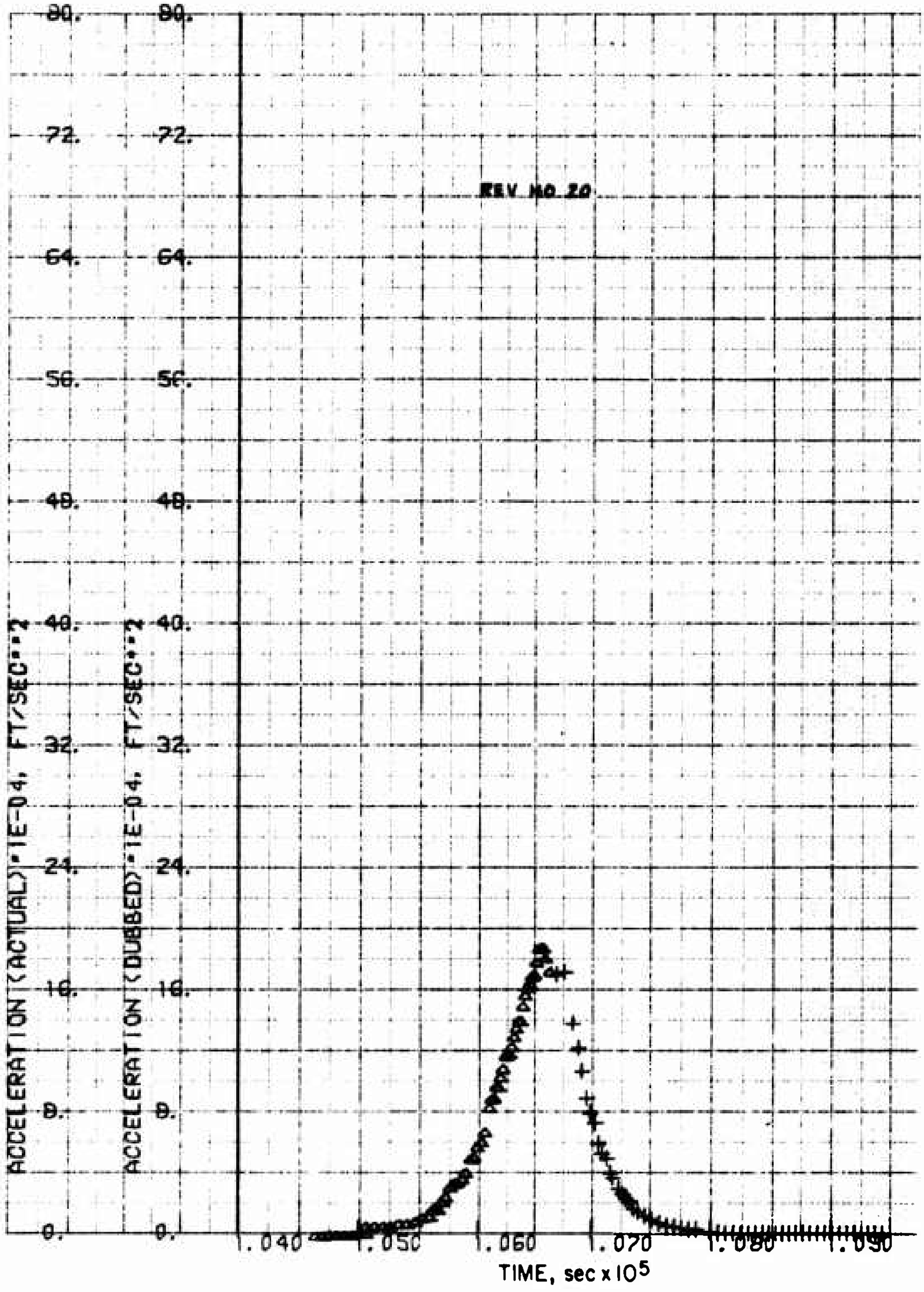

Fig. A-16. LOGACS Accelerometer Data for Rev. 20

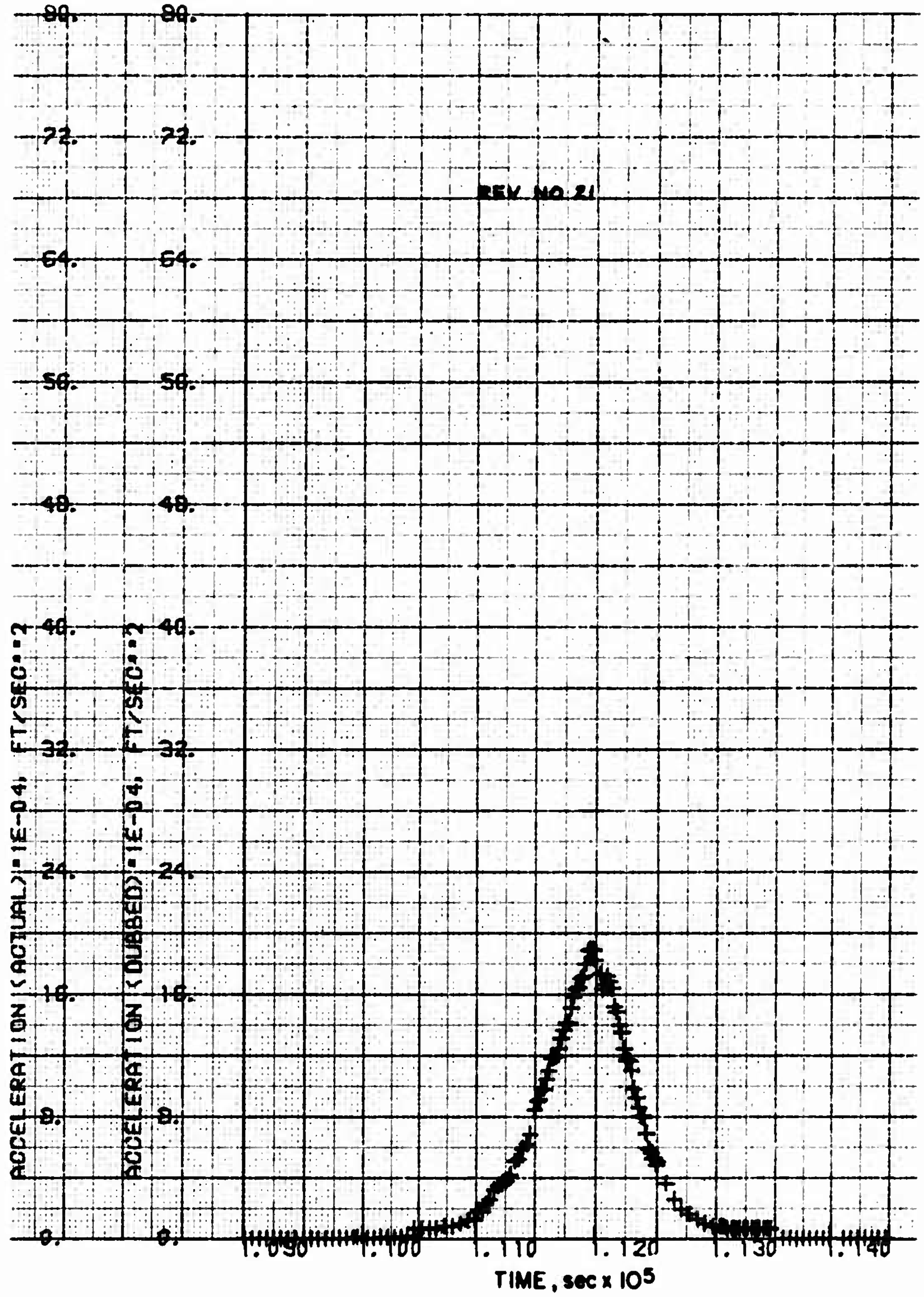

Fig. A-17. LOGACS Accelerometer Data for Rev. 21

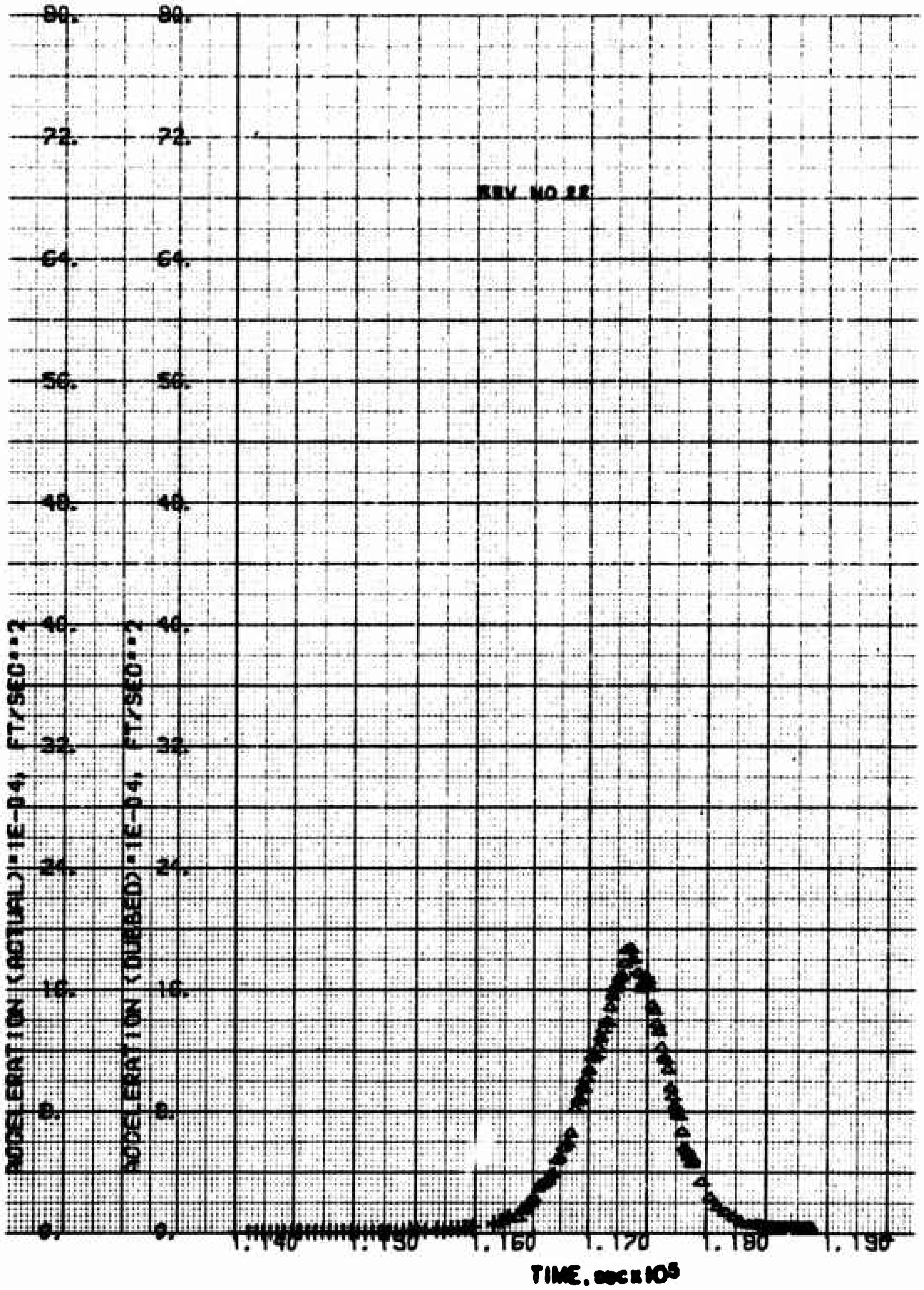

Fig. A-18. LOGACS Accelerometer Data for Rev. 22

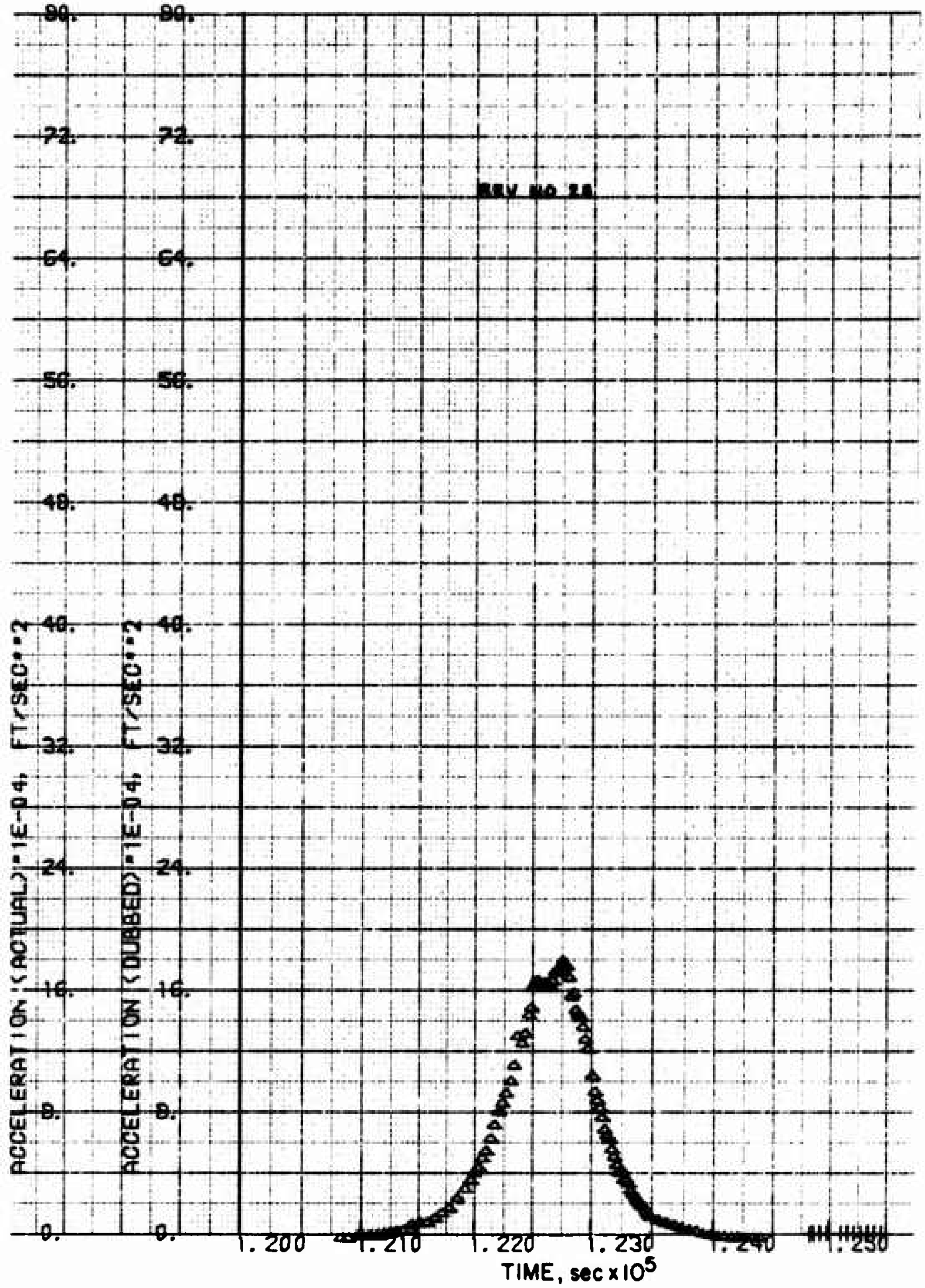

Fig. A-19. LOGACS Accelerometer Data for Rev. 23

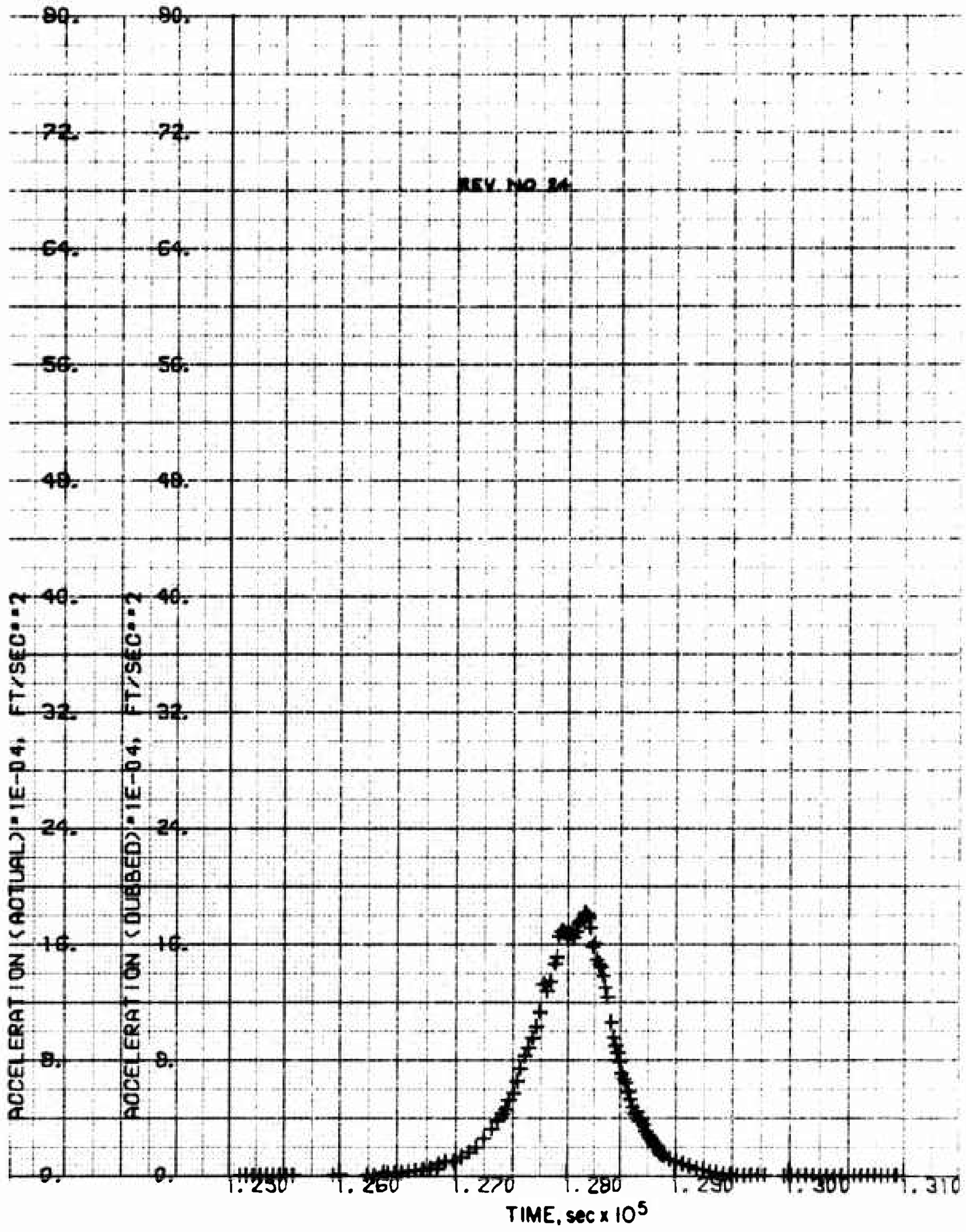

Fig. A-20. LOGACS Accelerometer Data for Rev. 24

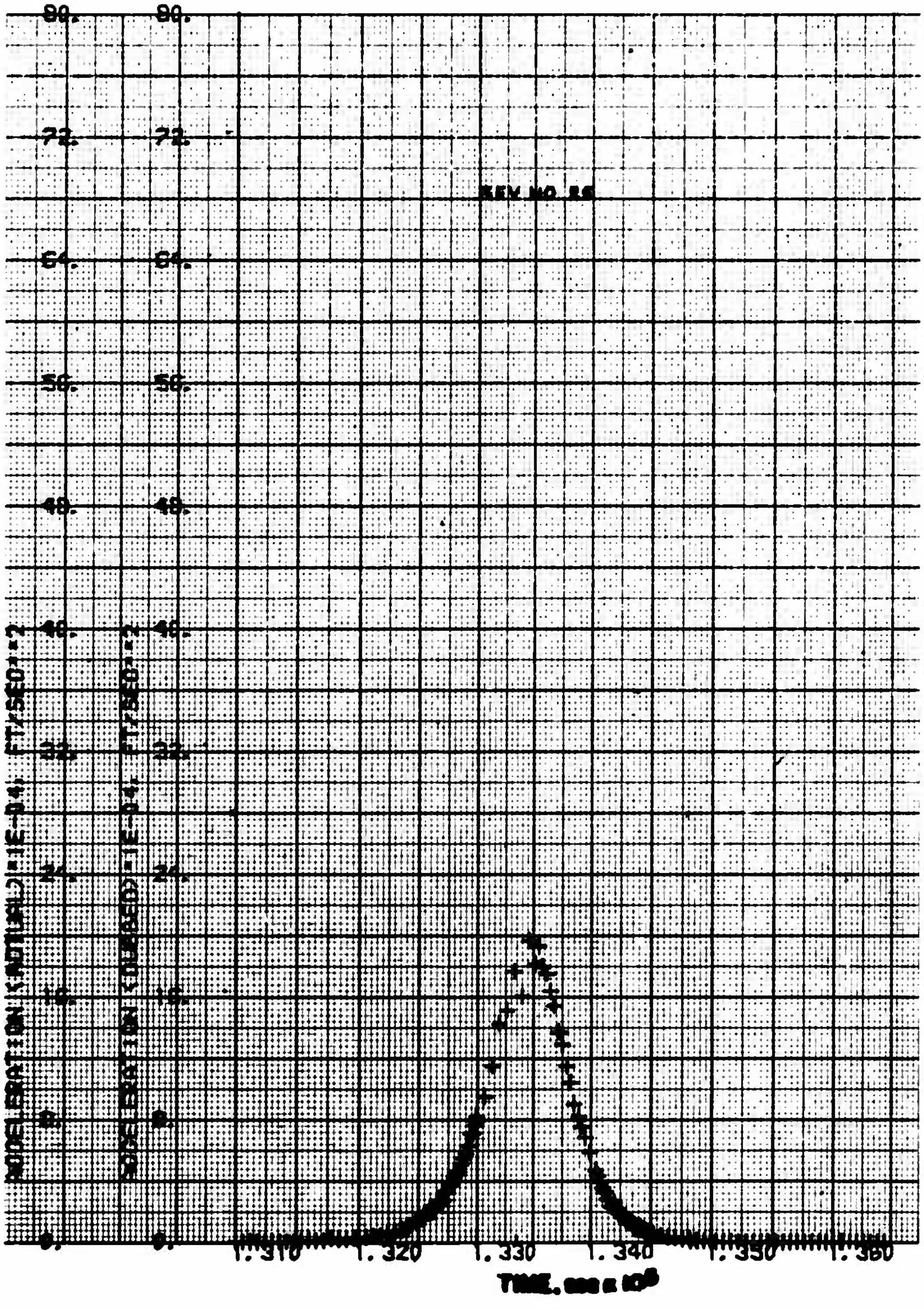

Fig. A-21. LOGACS Accelerometer Data for Rev. 25

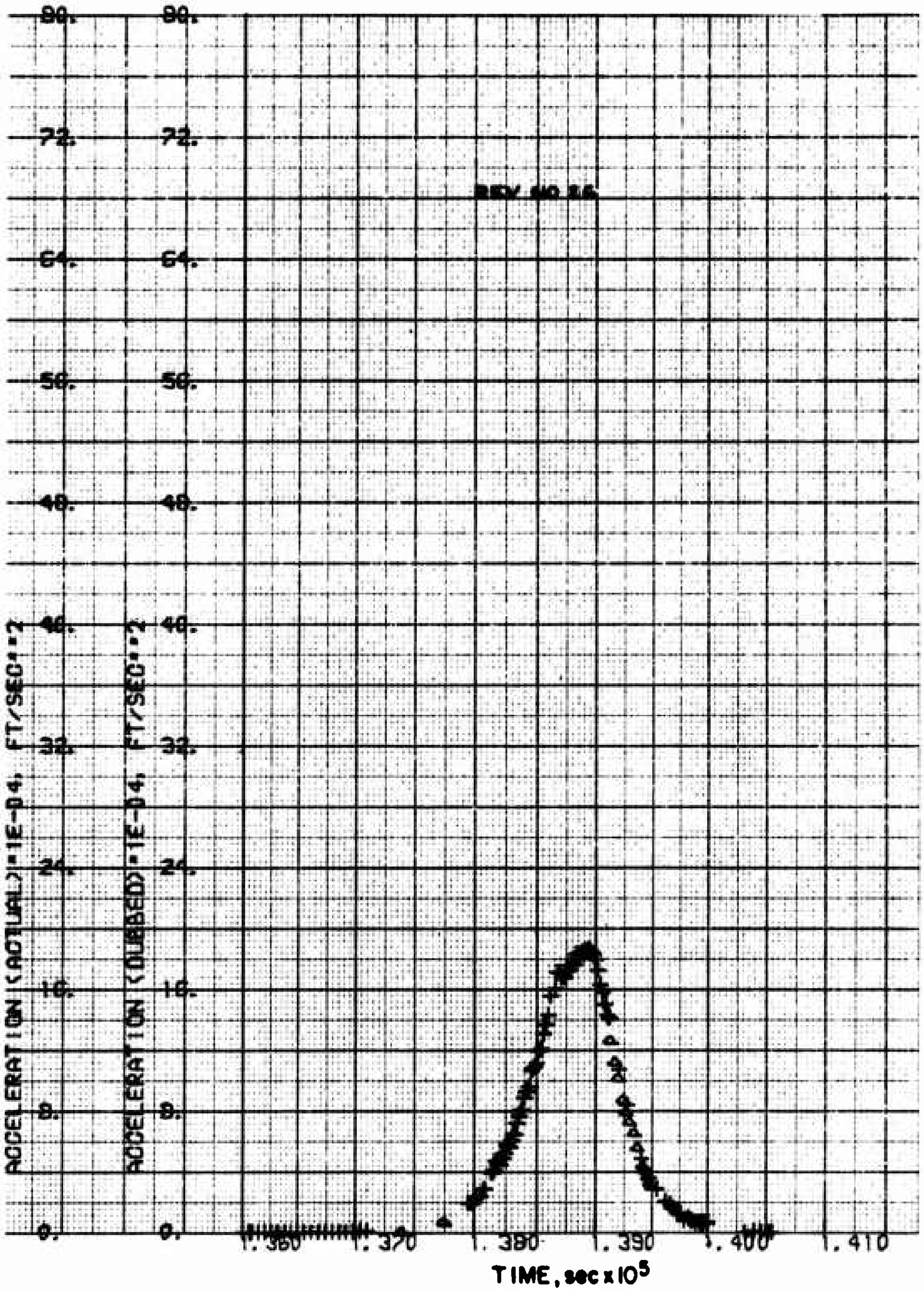

Fig. A-22. LOGACS Accelerometer Data for Rev. 26

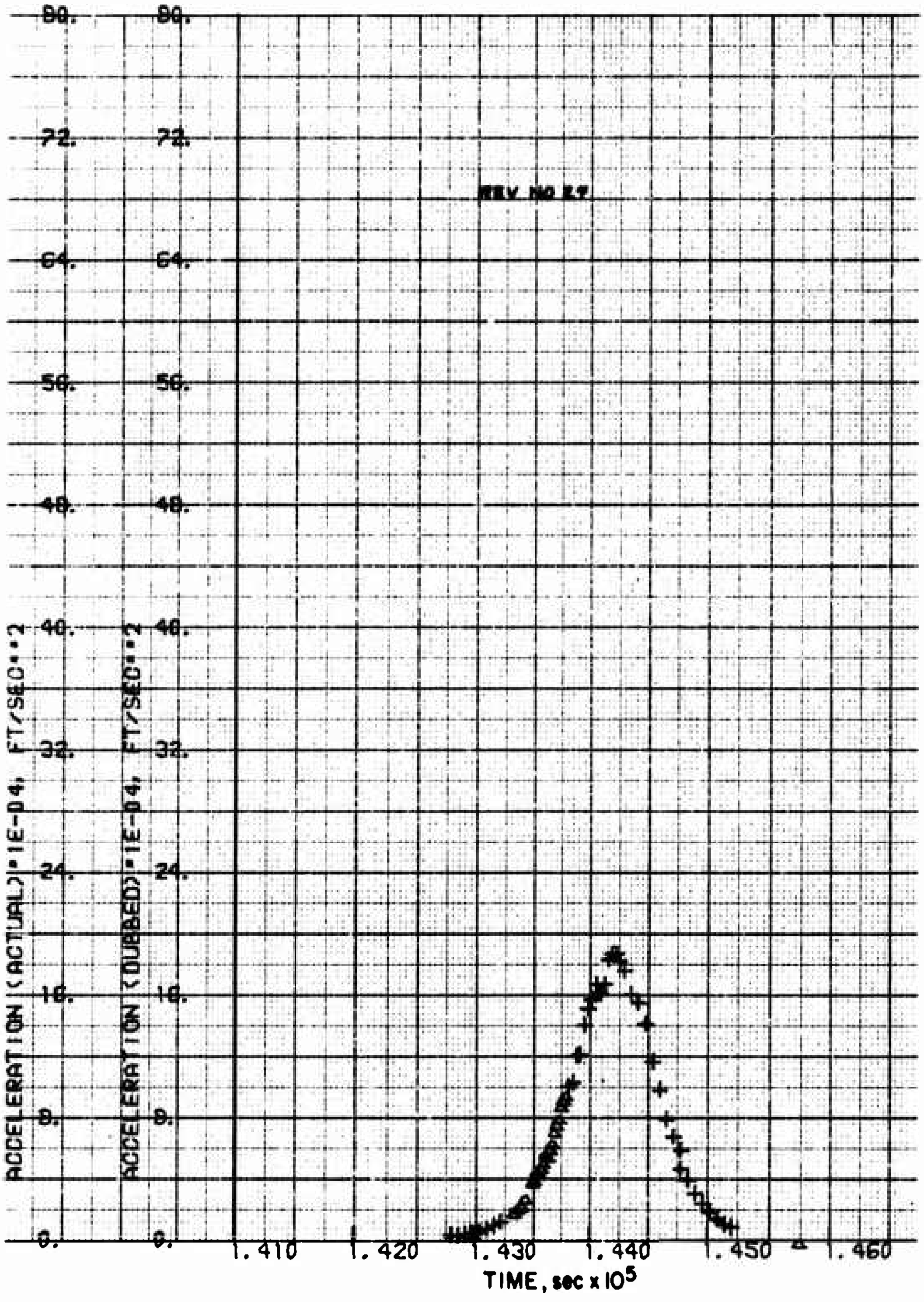

Fig. A-23. LOGACS Accelerometer Data for Rev. 27

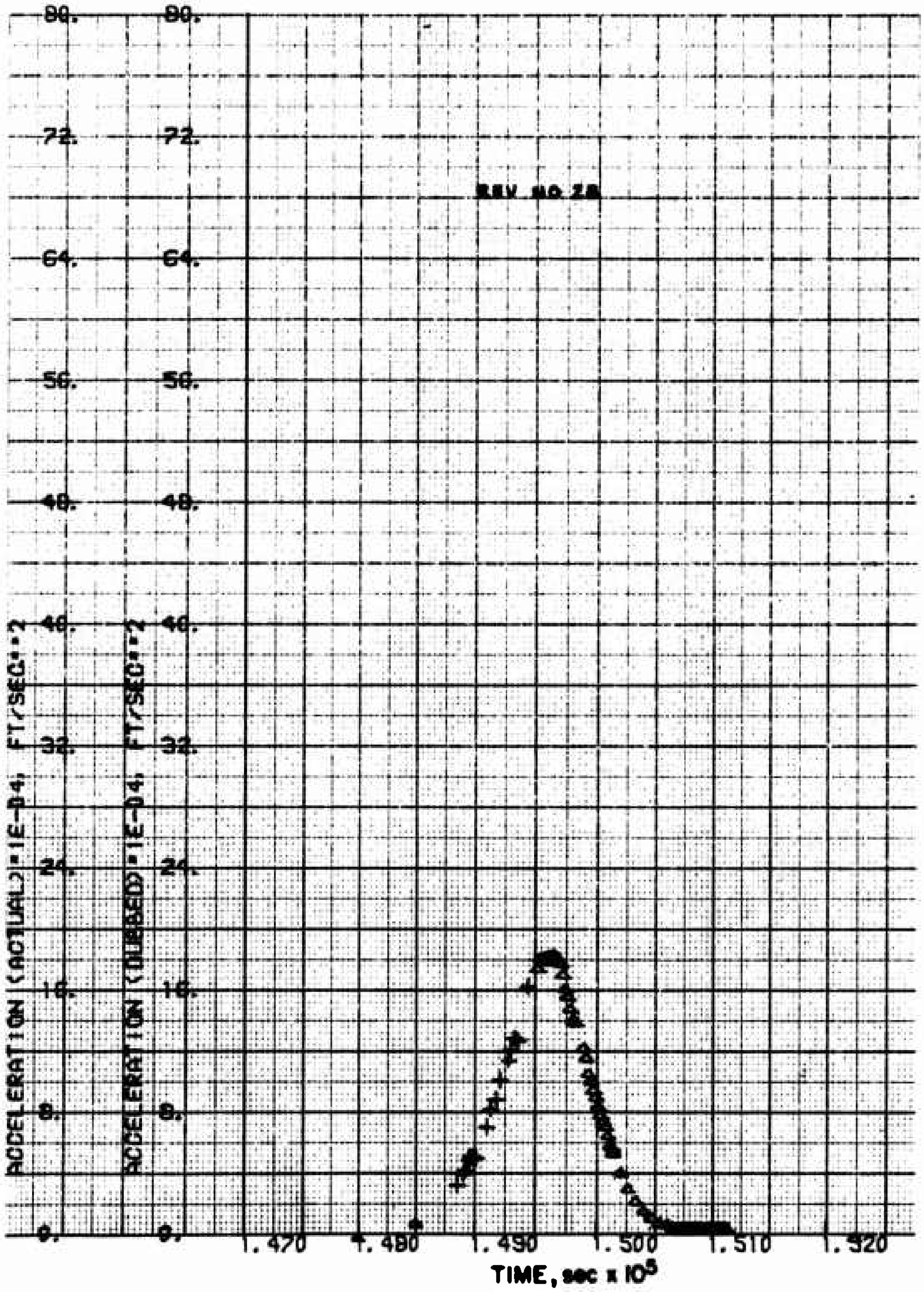

Fig. A-24. LOGACS Accelerometer Data for Rev. 28

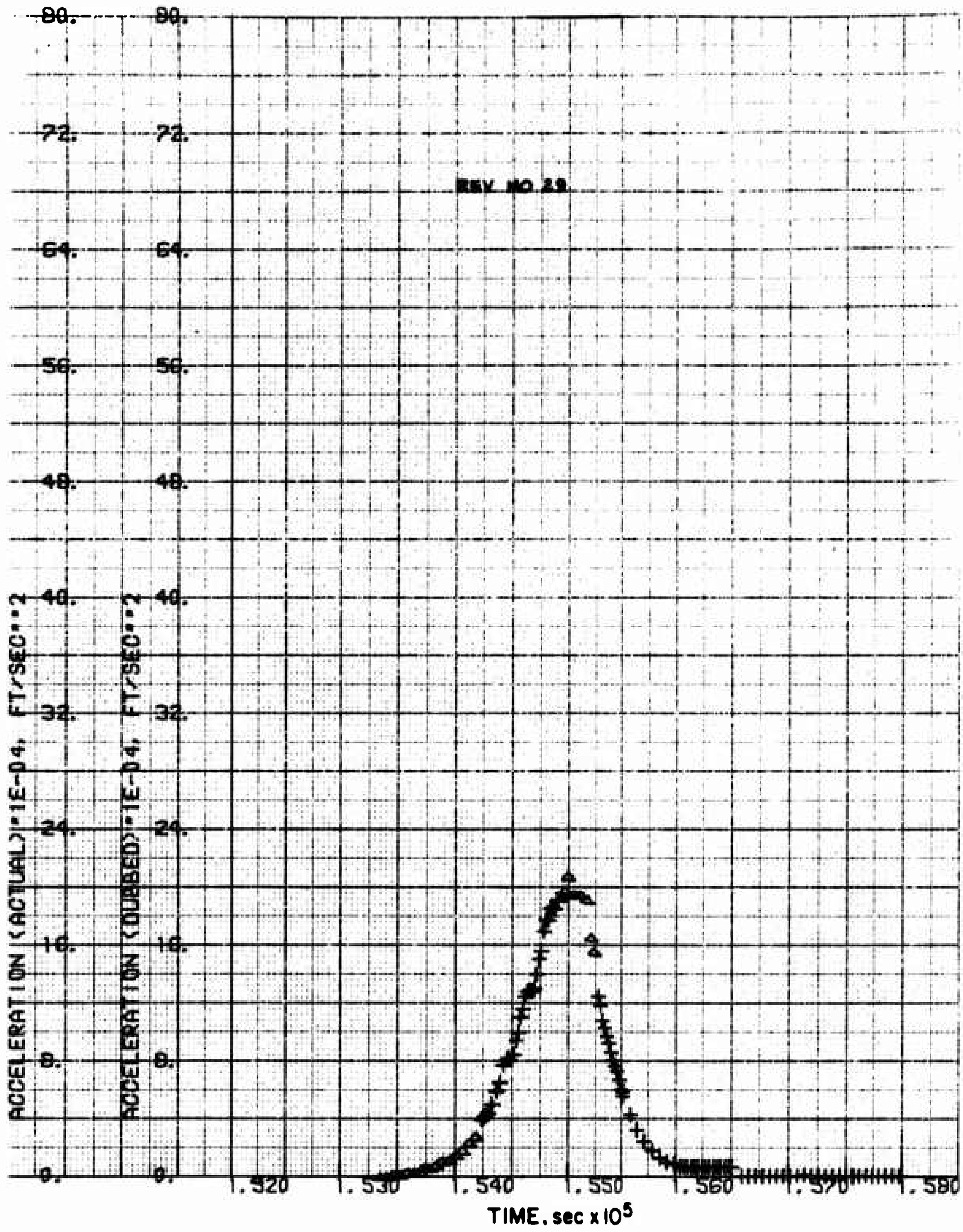

Fig. A-25. LOGACS Accelerometer Data for Rev. 29

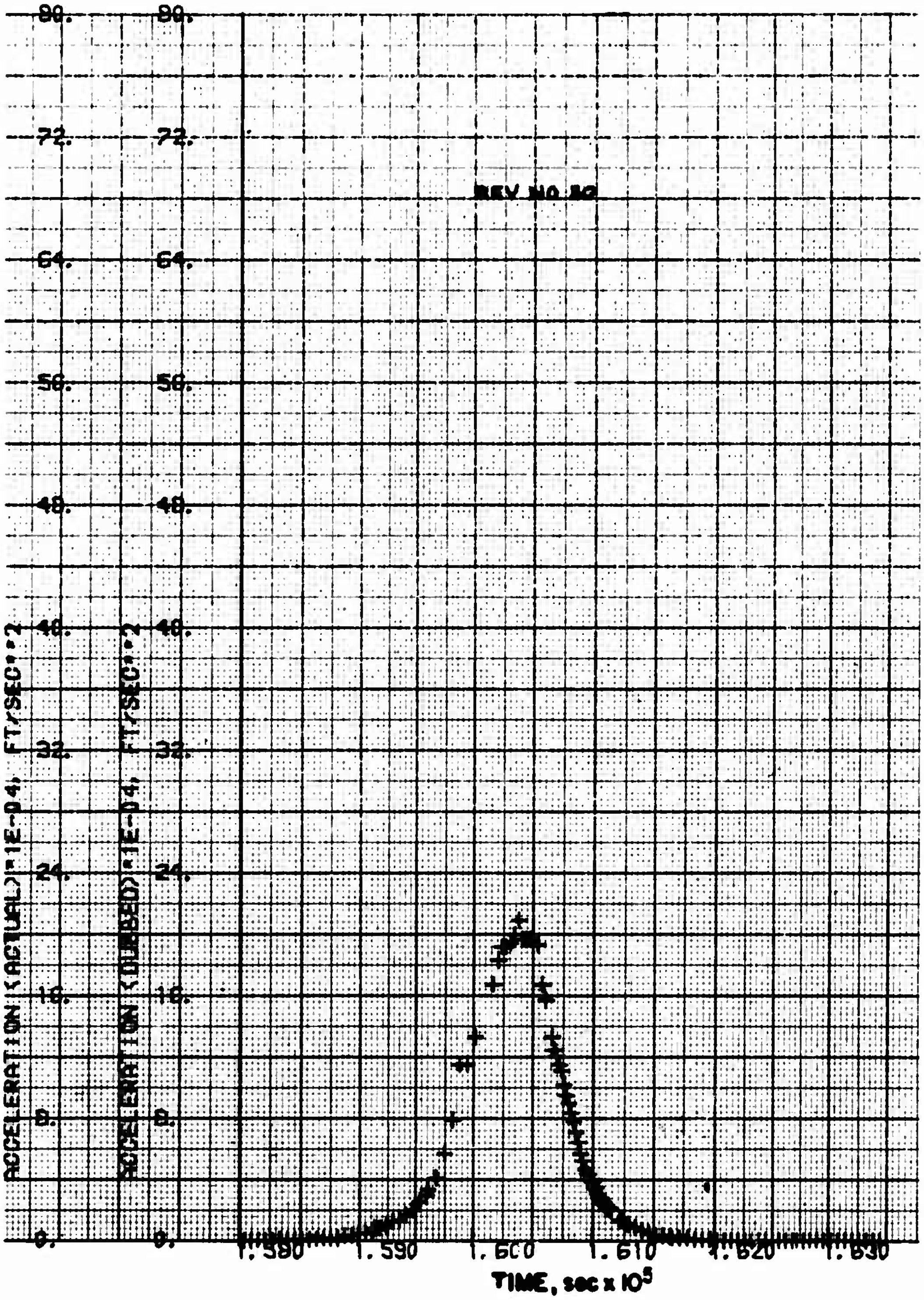

Fig. A-26. LOGACS Accelerometer Data for Rev. 30

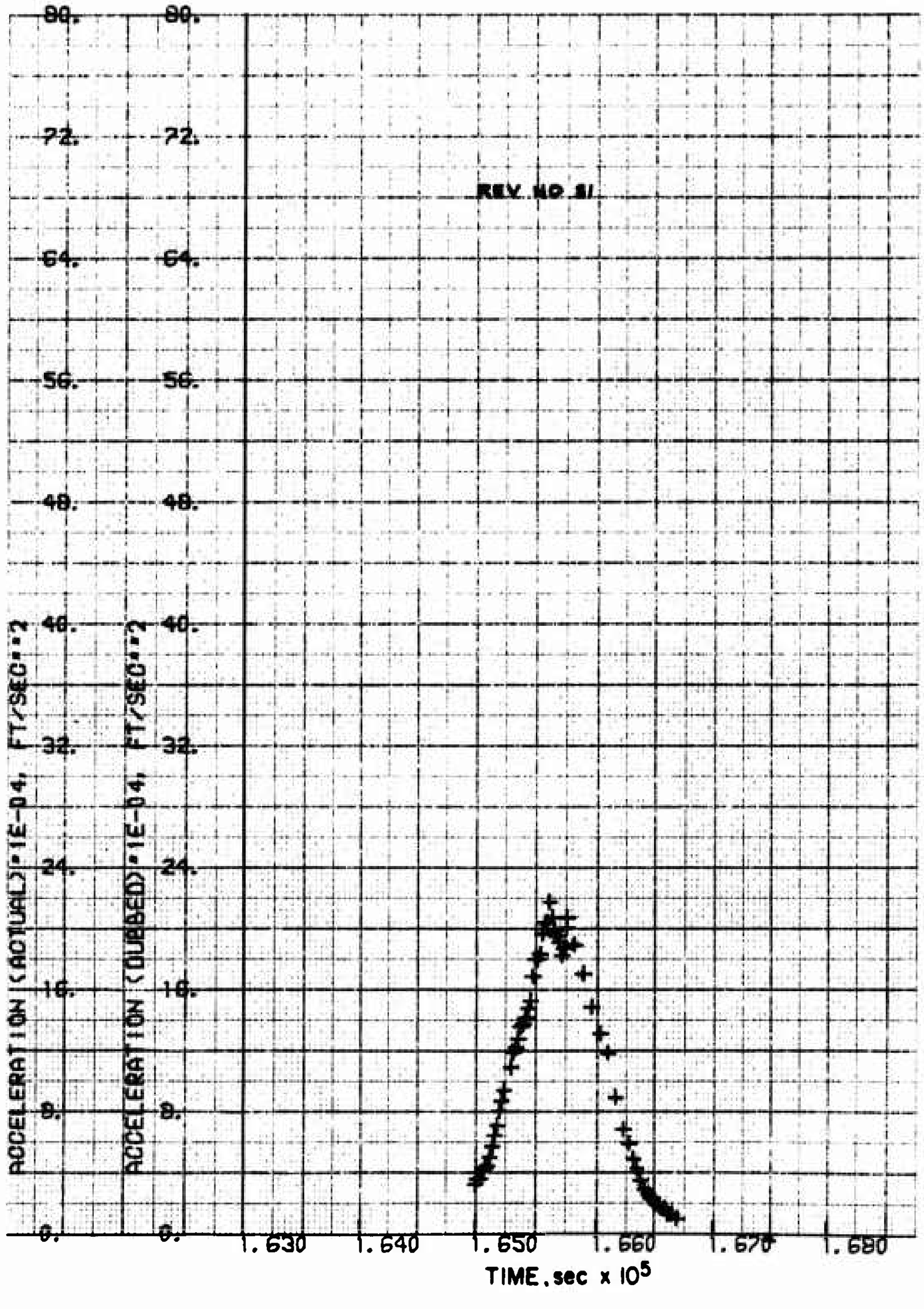

Fig. A-27. LOGACS Accelerometer Data for Rev. 31

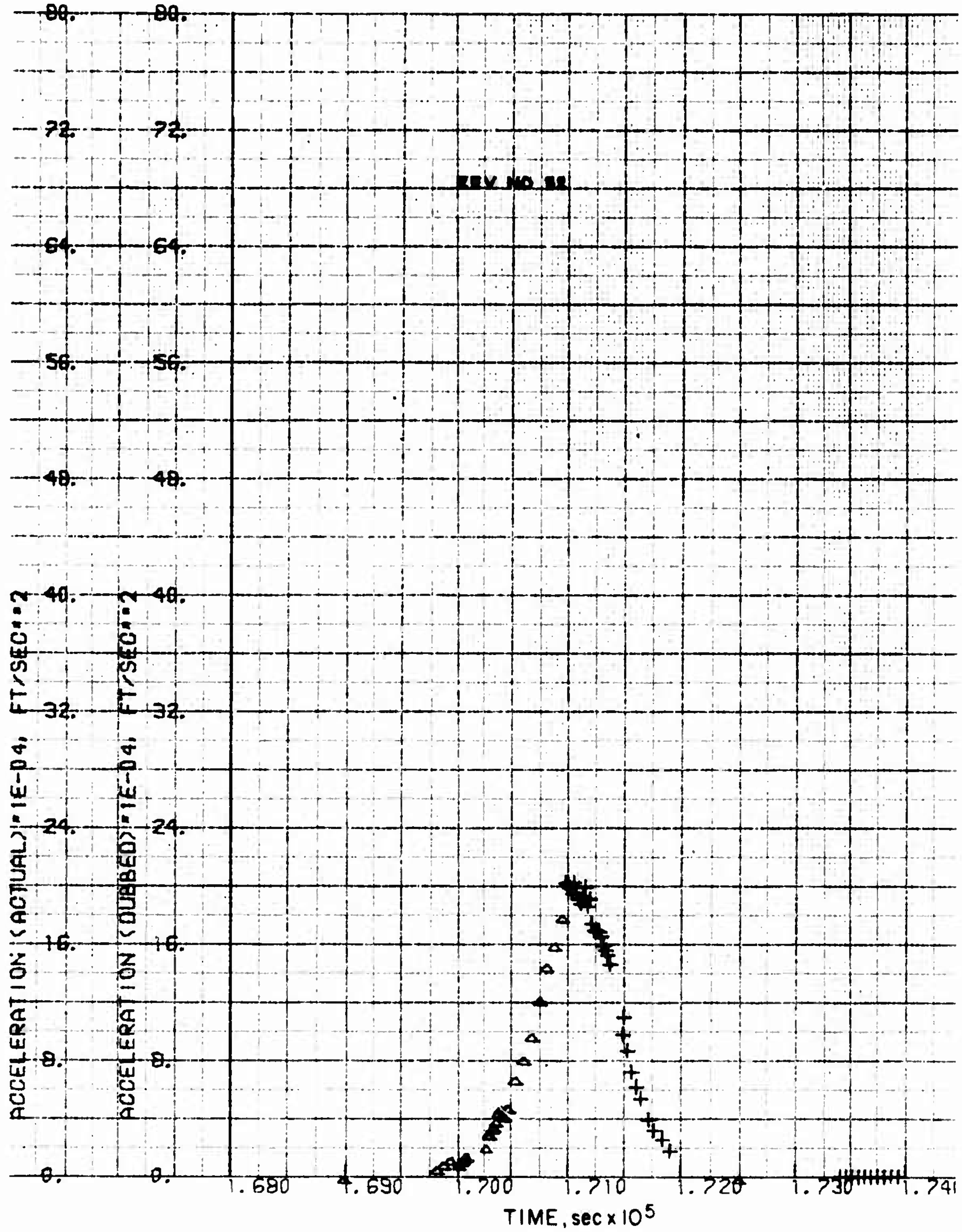

Fig. A-28. LOGACS Accelerometer Data for Rev. 32

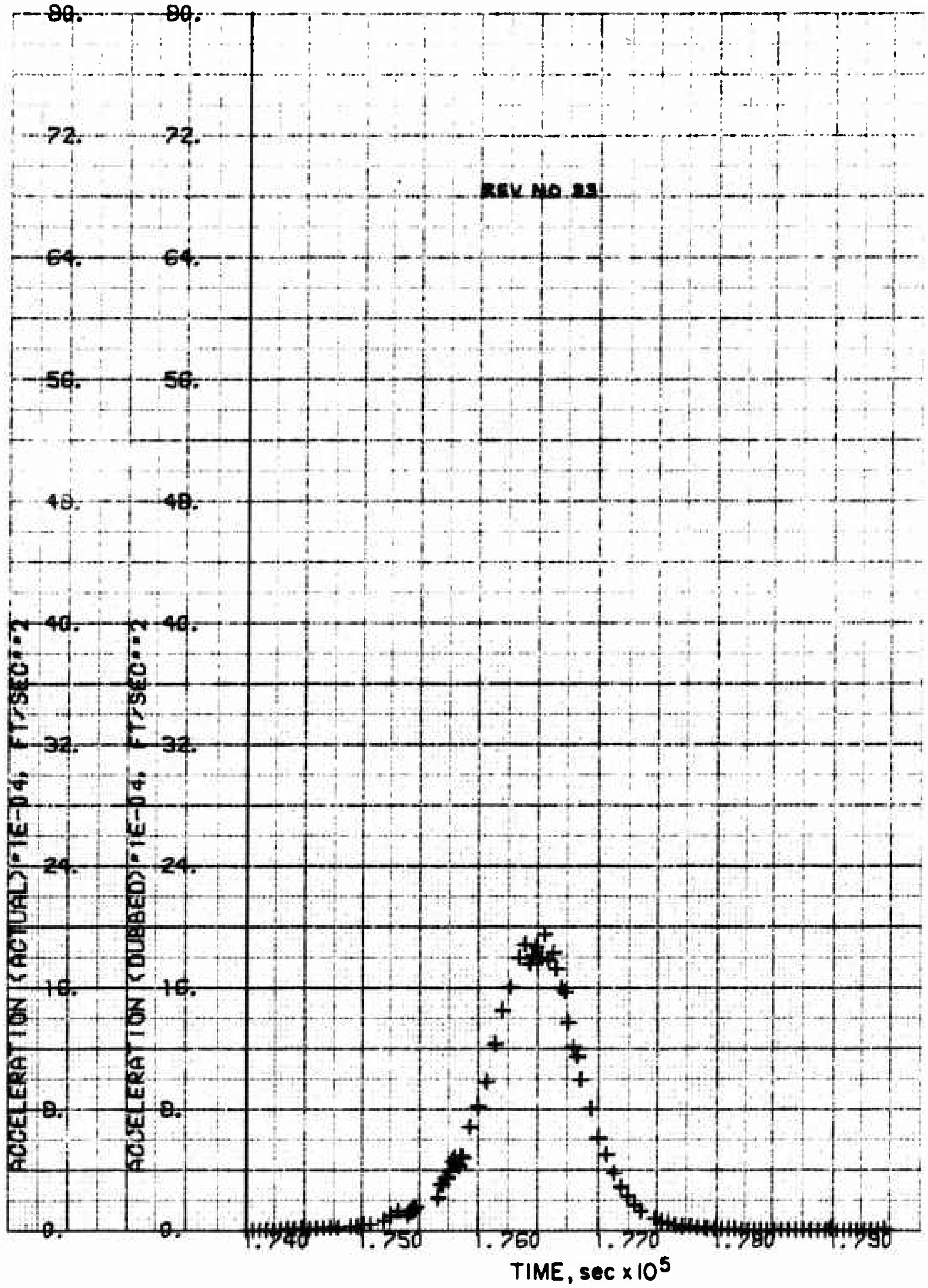

Fig. A-29. LOGACS Accelerometer Data for Rev. 33

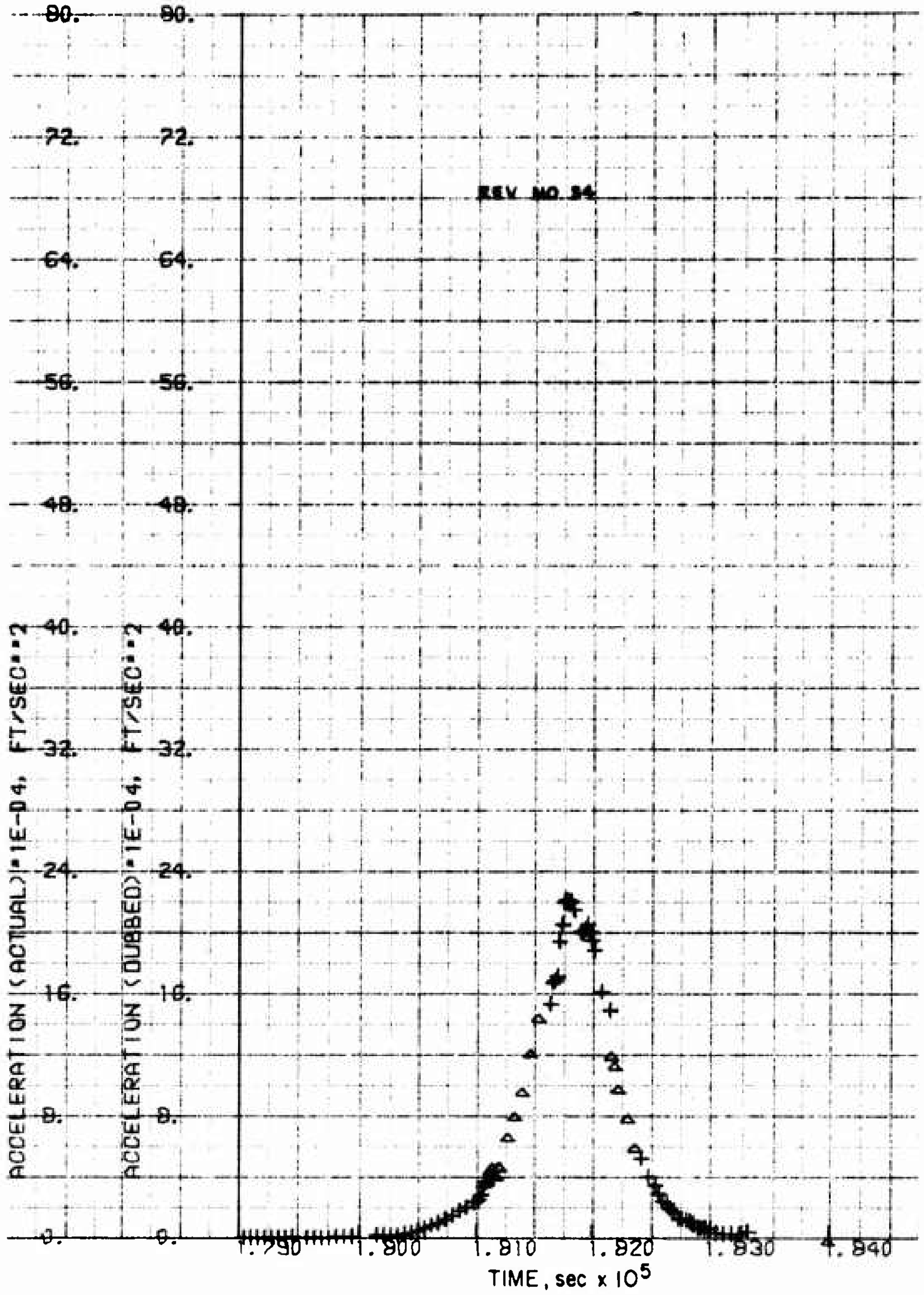

Fig. A-30. LOGACS Accelerometer Data for Rev. 34

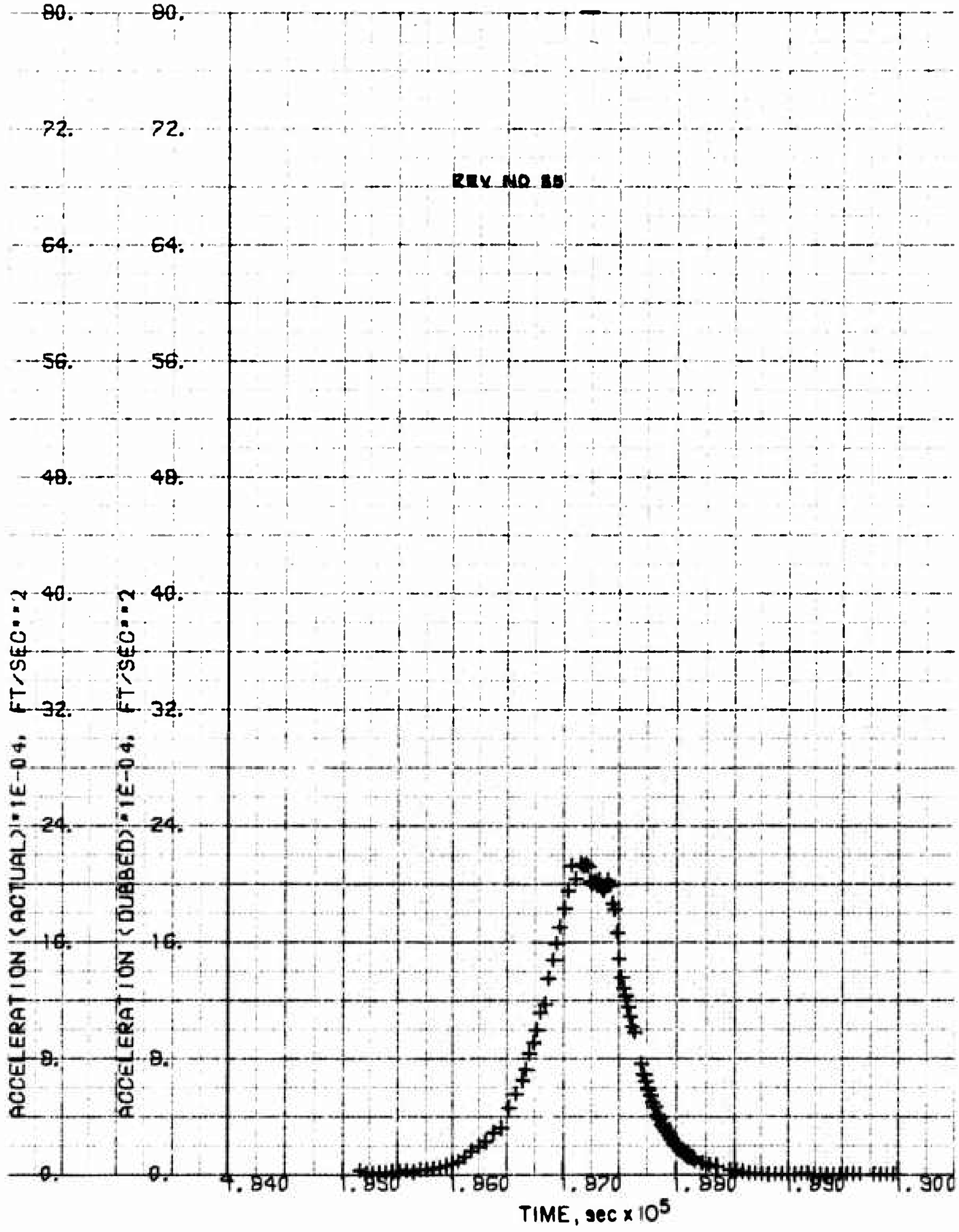

Fig. A-31. LOGACS Accelerometer Data for Rev. 35

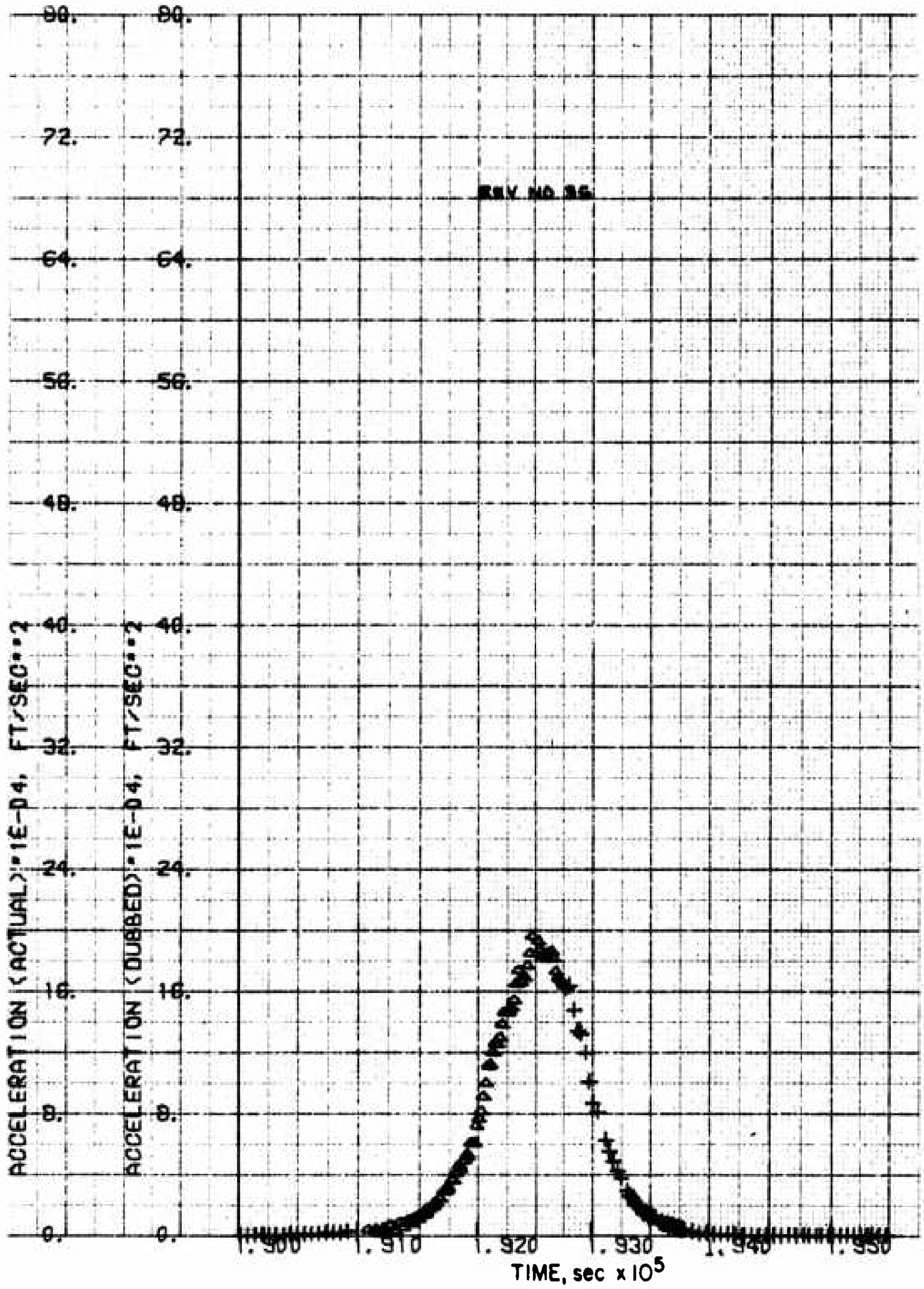

Fig. A-32. LOGACS Accelerometer Data for Rev. 36

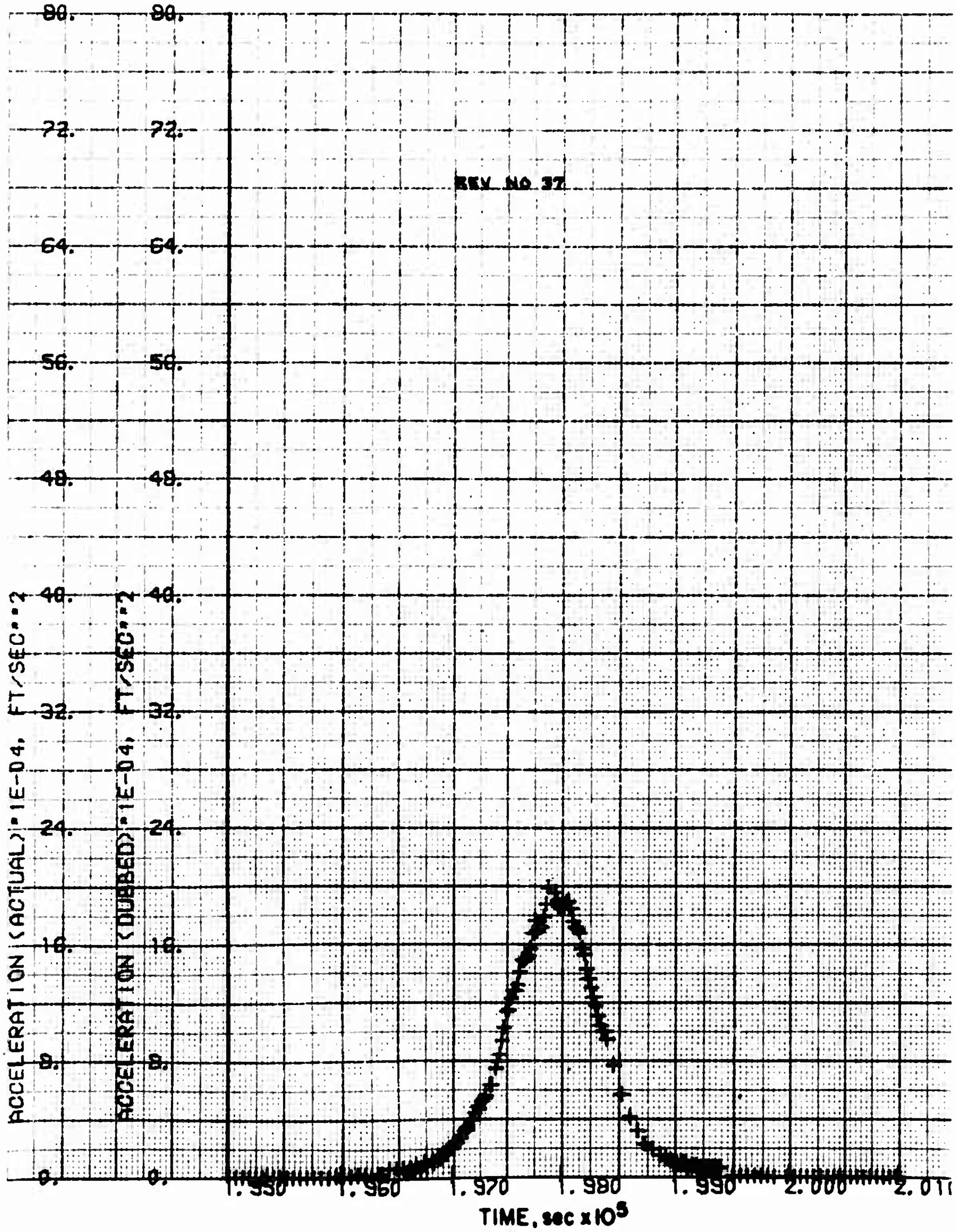

Fig. A-33. LOGACS Accelerometer Data for Rev. 37

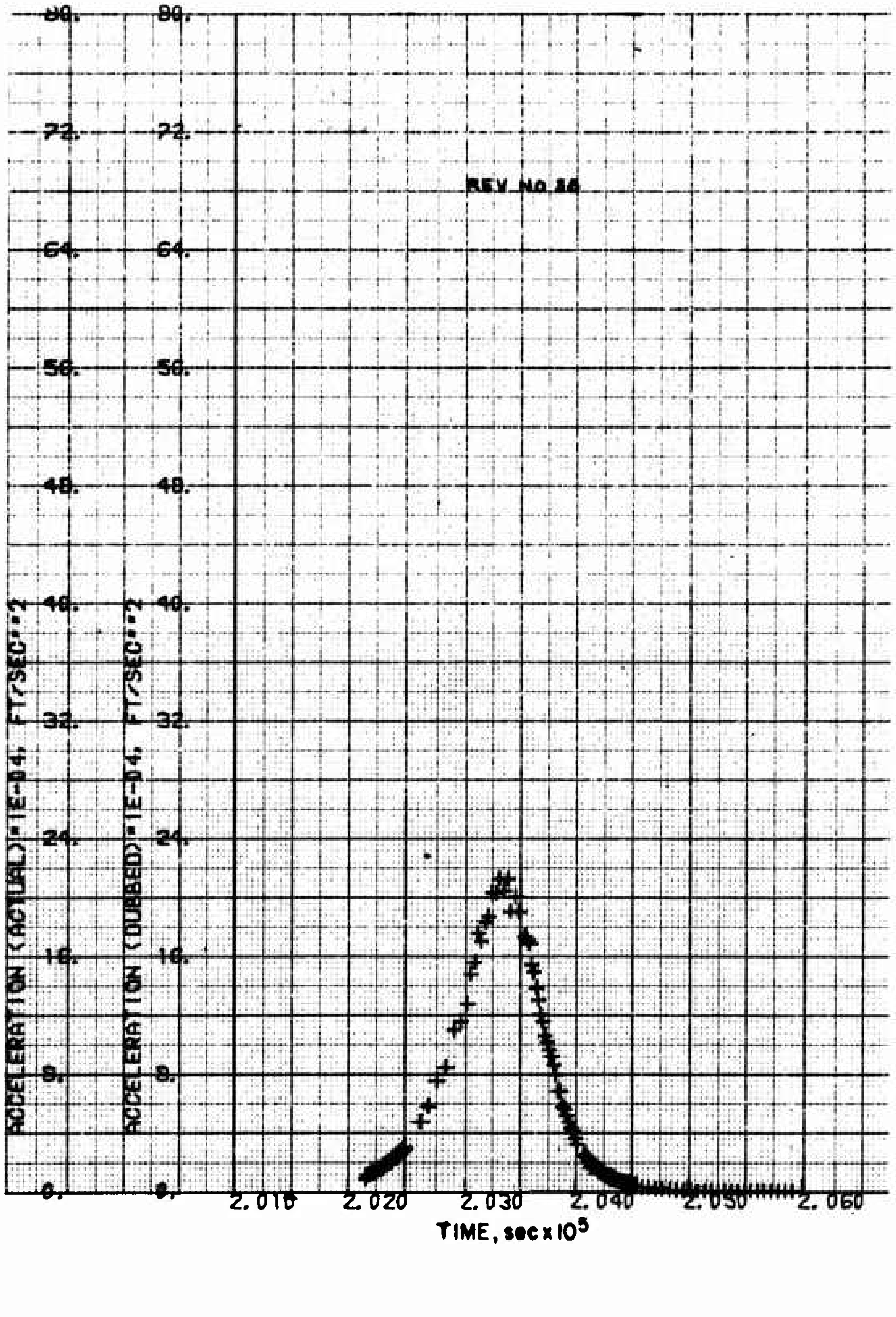

Fig. A-34. LOGACS Accelerometer Data for Rev. 38

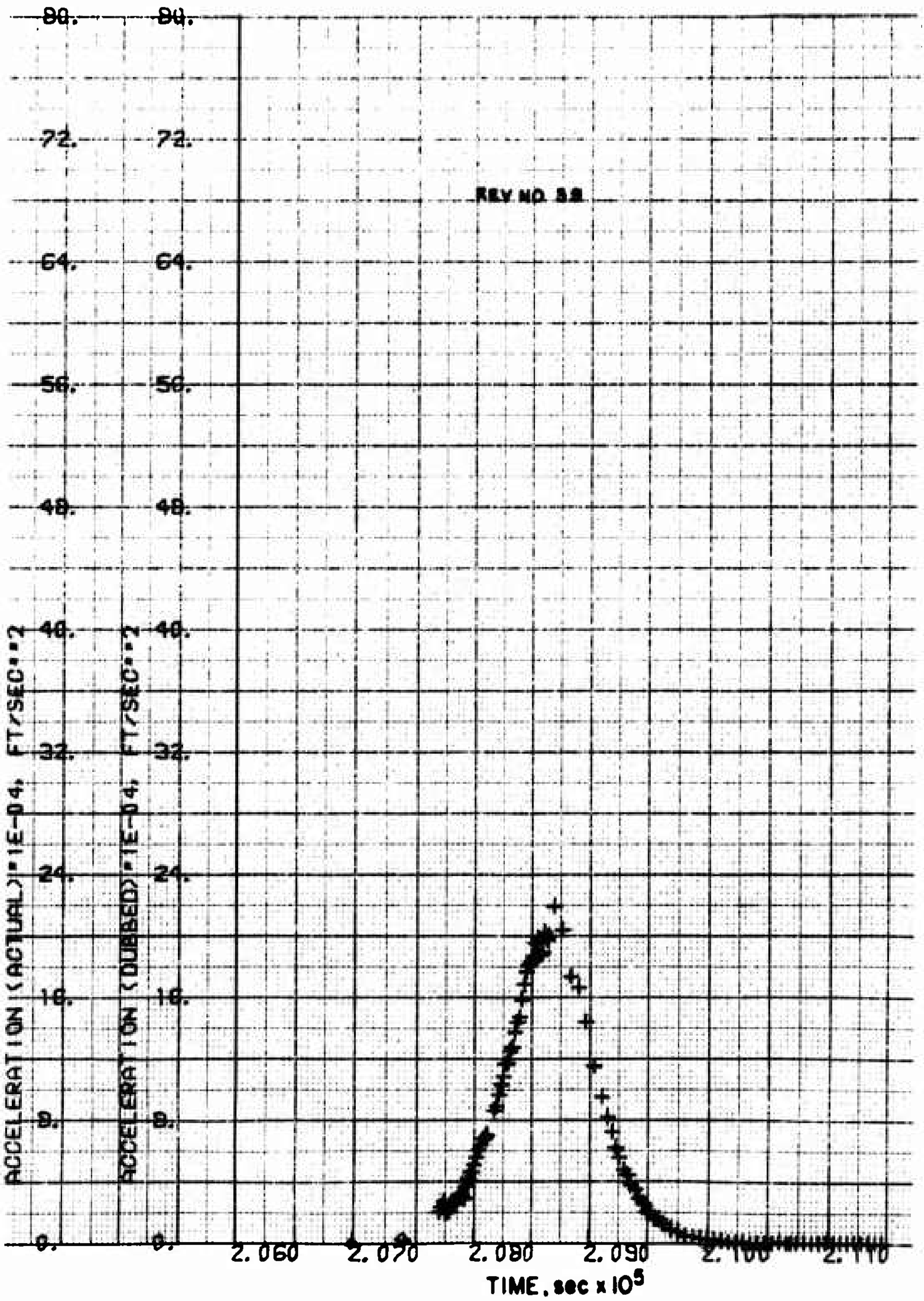

Fig. A-35. LOGACS Accelerometer Data for Rev. 39

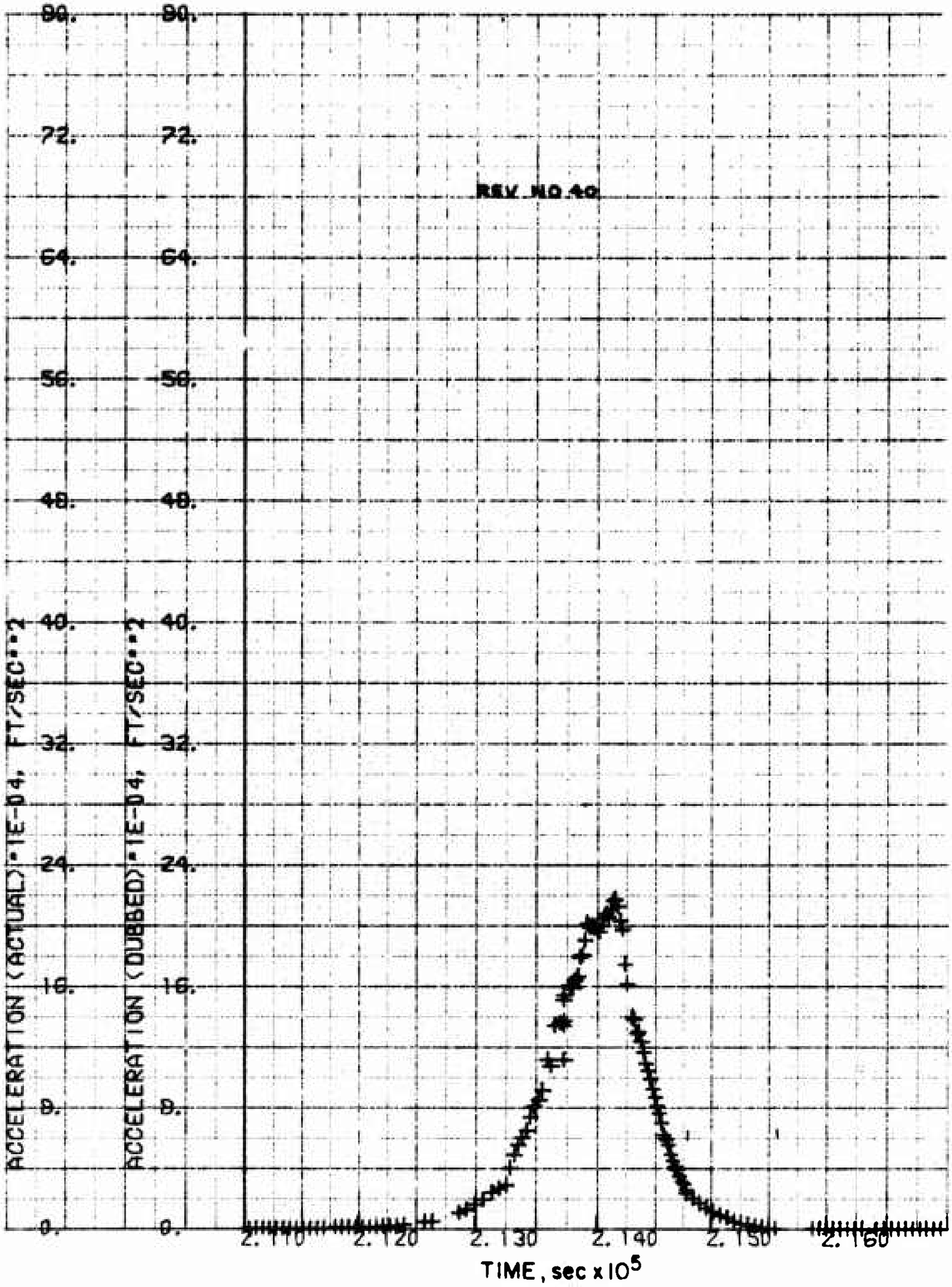

Fig. A-36. LOGACS Accelerometer Data for Rev. 40

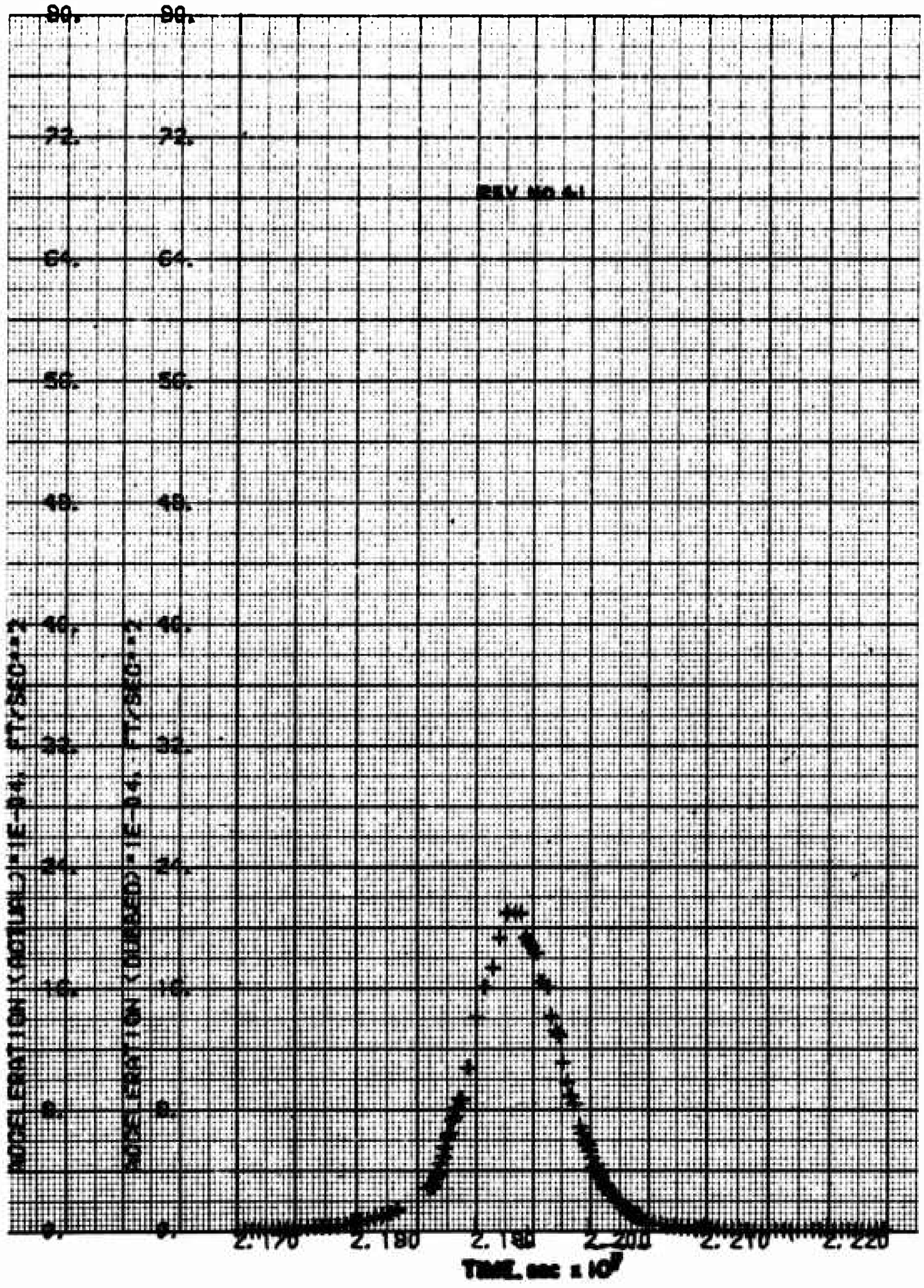

Fig. A-37. LOGACS Accelerometer Data for Rev. 41

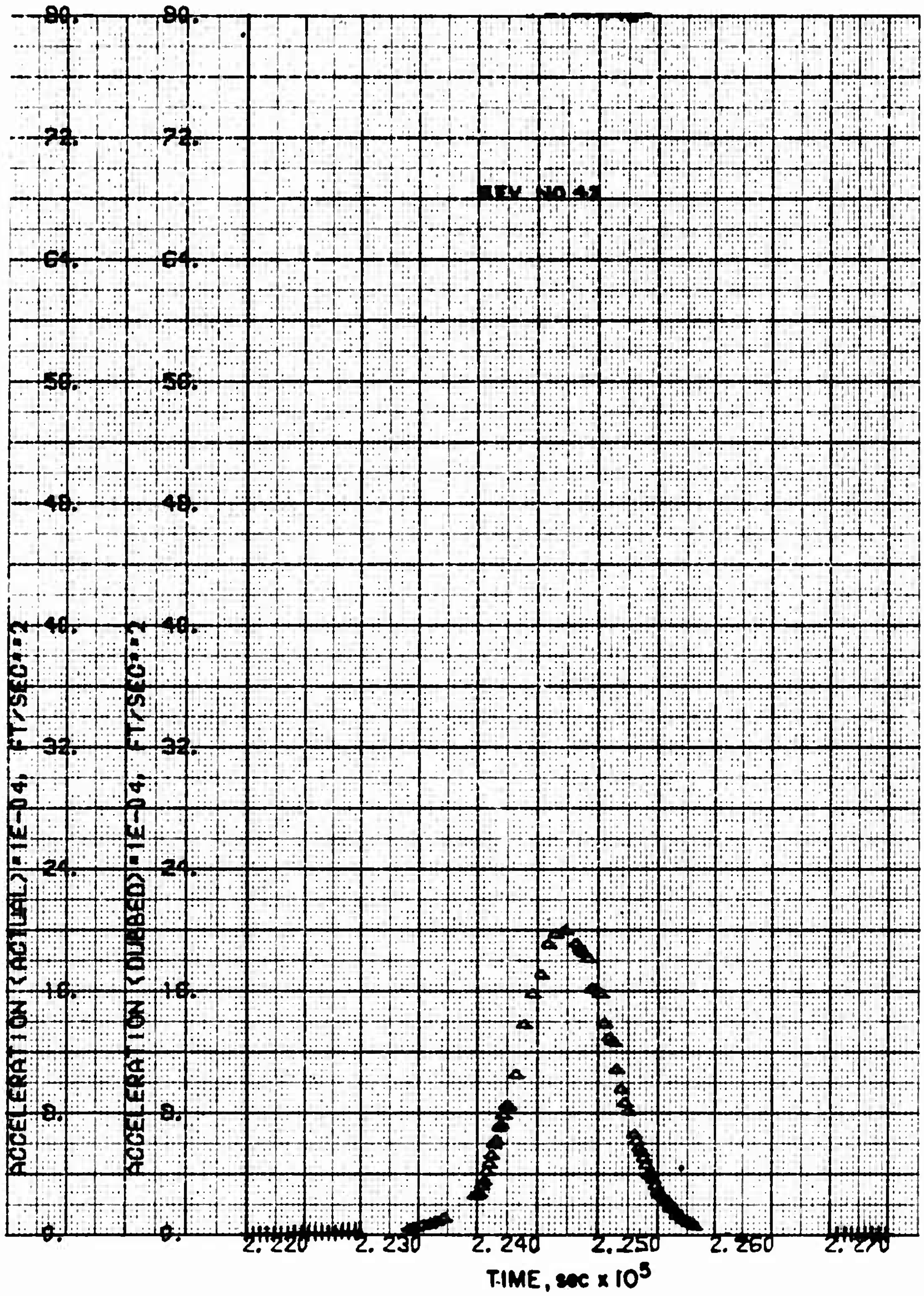

Fig. A-38. LOGACS Accelerometer Data for Rev. 42

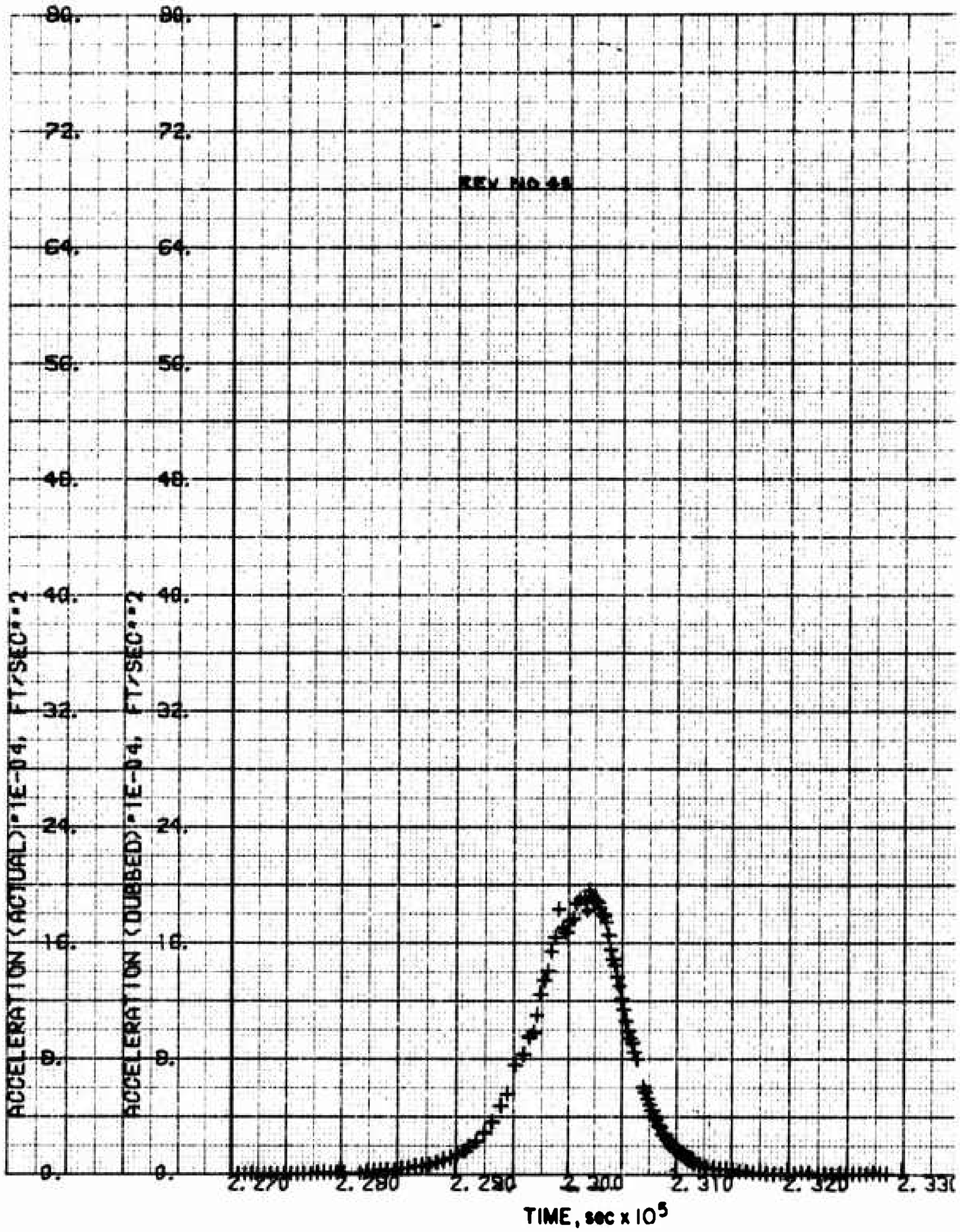

Fig. A-39. LOGACS Accelerometer Data for Rev. 43

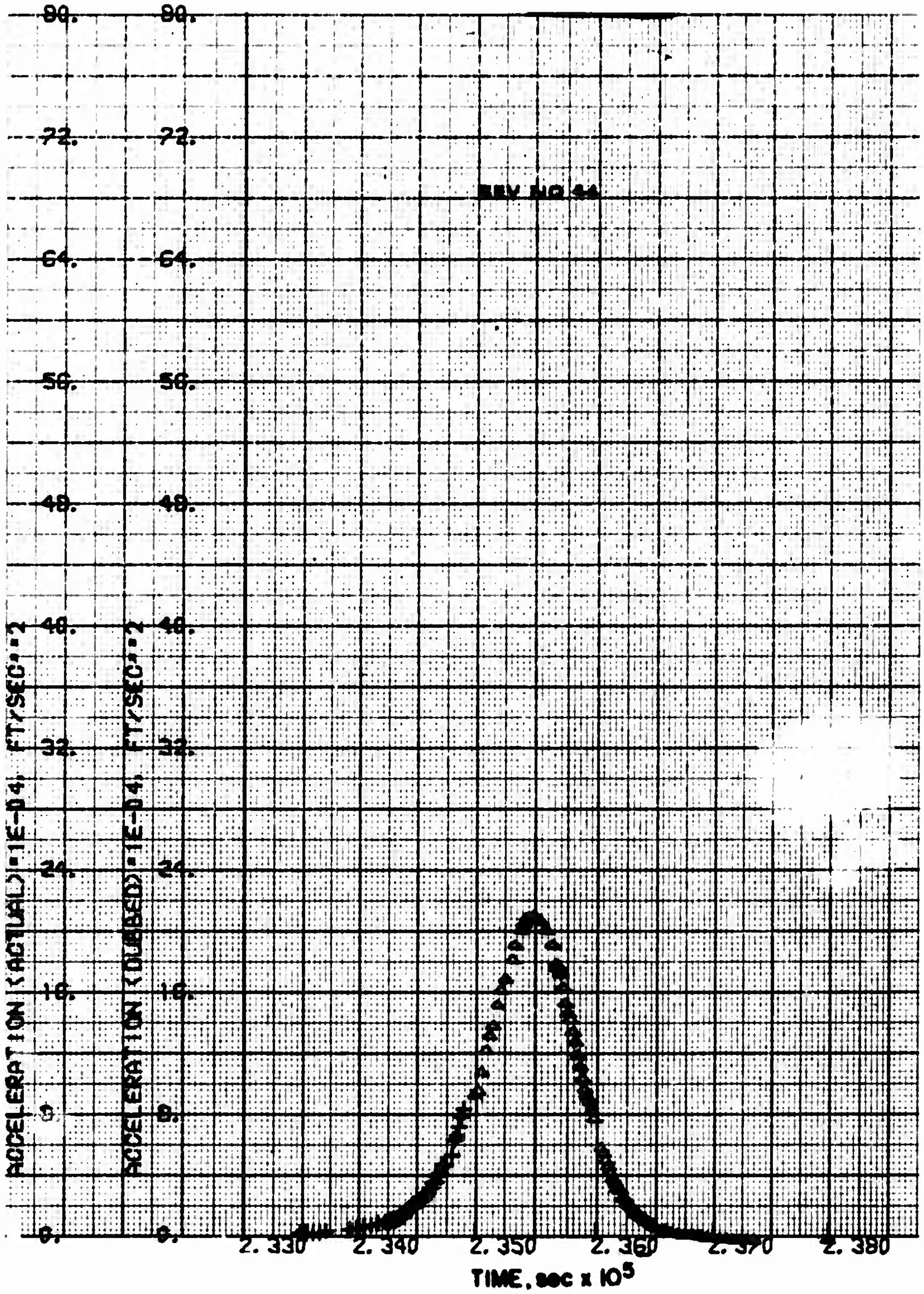

Fig. A-40. LOGACS Accelerometer Data for Rev. 44

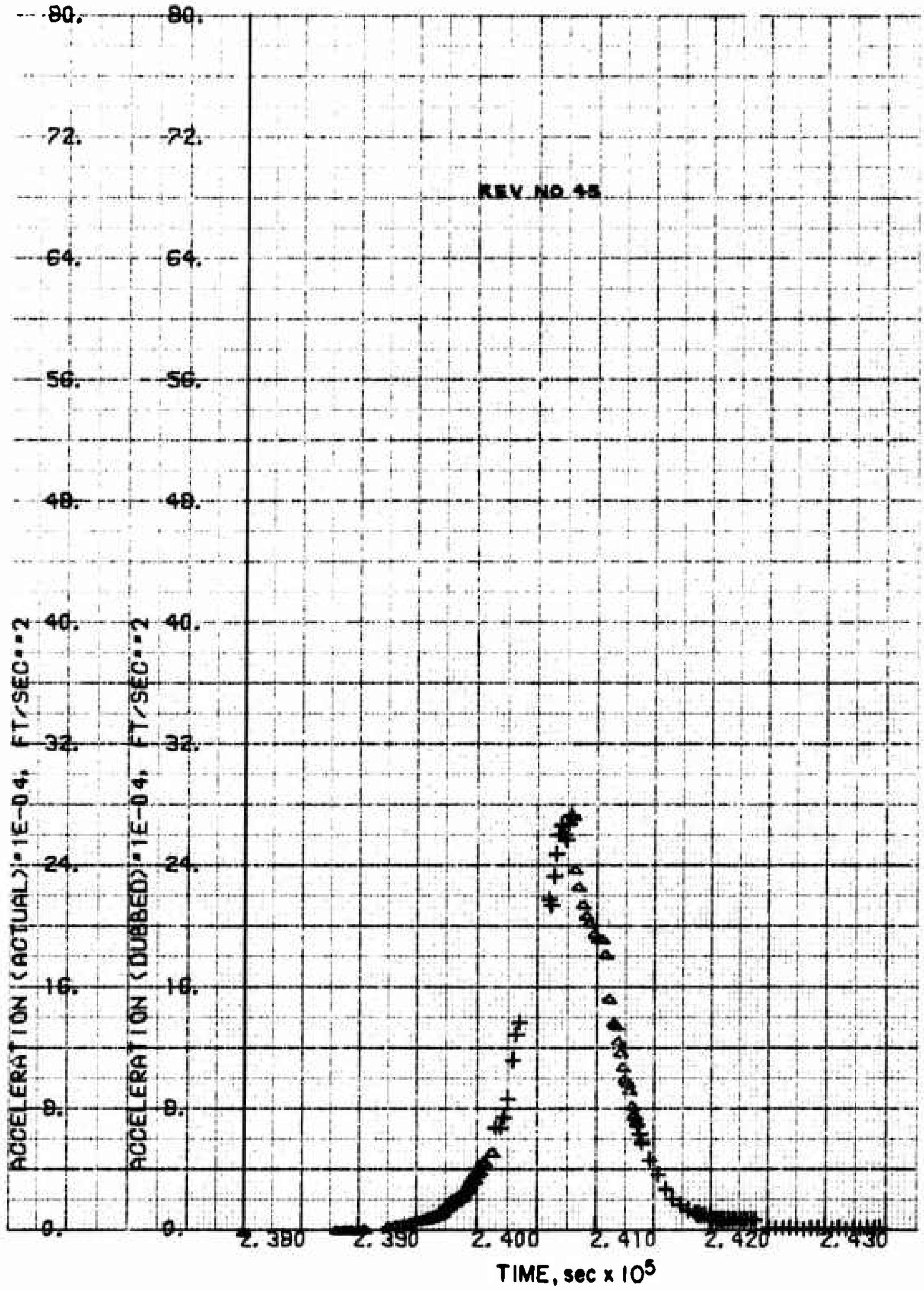

Fig A-41. LOGACS Accelerometer Data for Rev. 45

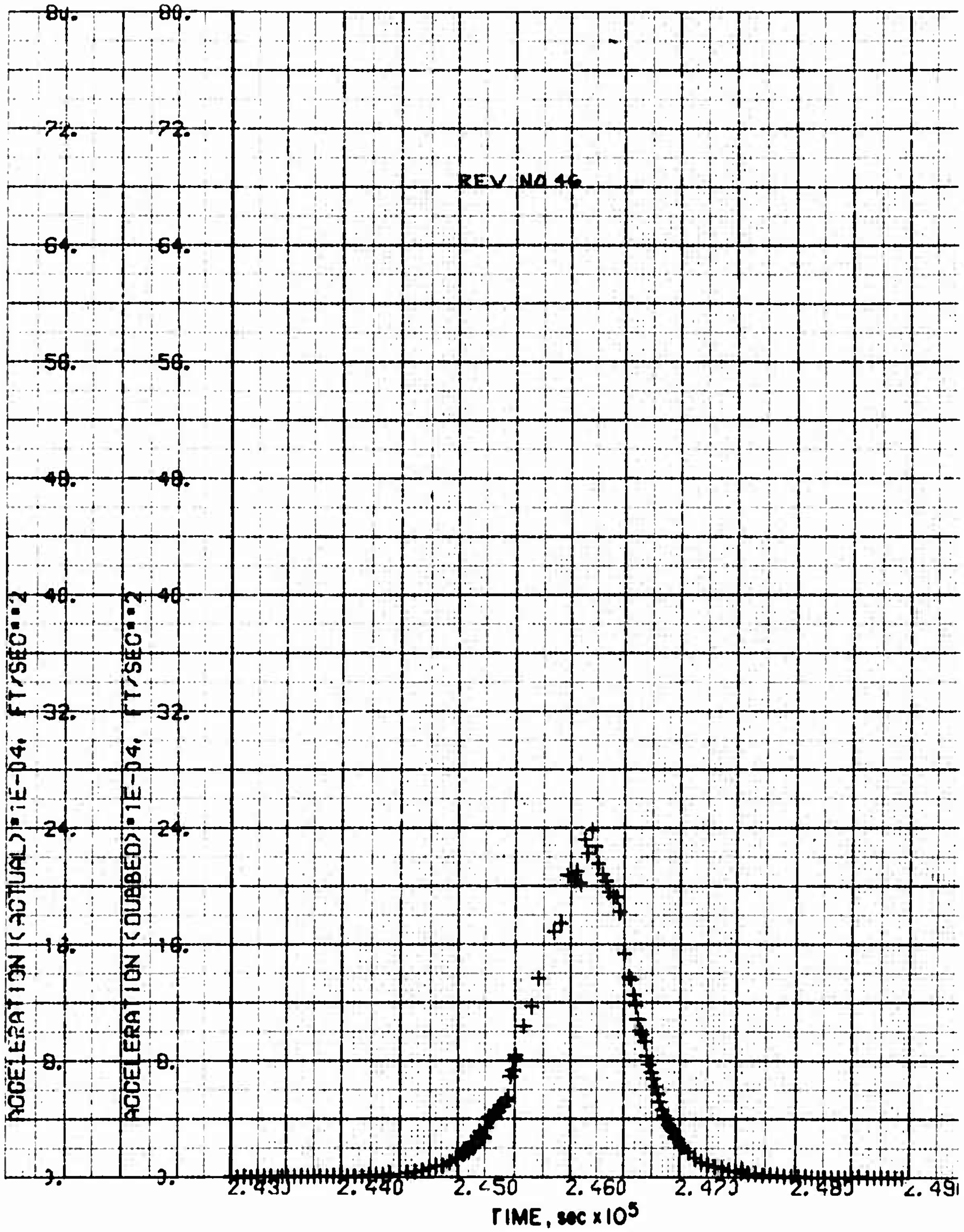

Fig. A-42. LOGACS Accelerometer Data for Rev. 46

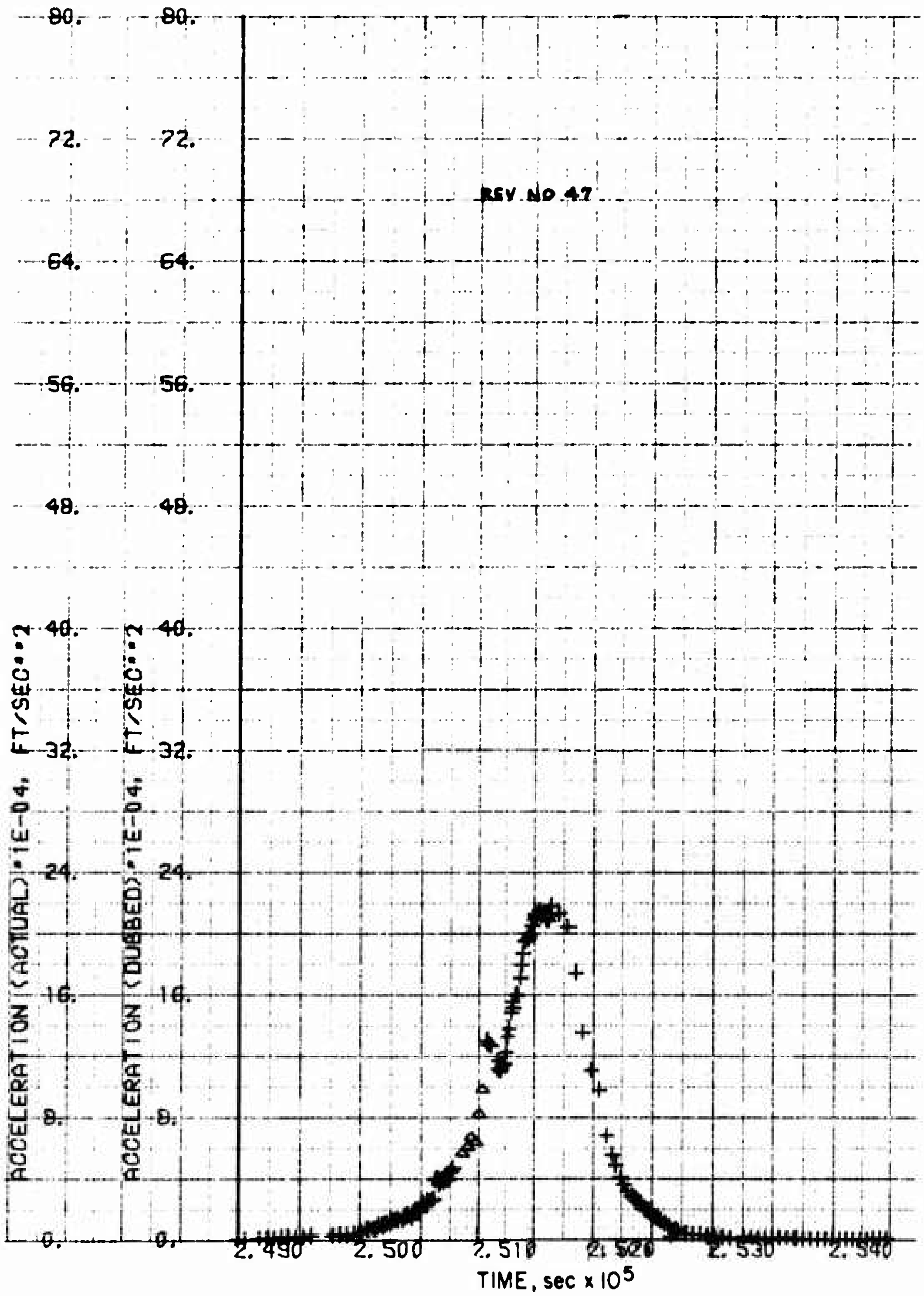

Fig. A-43. LOGACS Accelerometer Data for Rev. 47

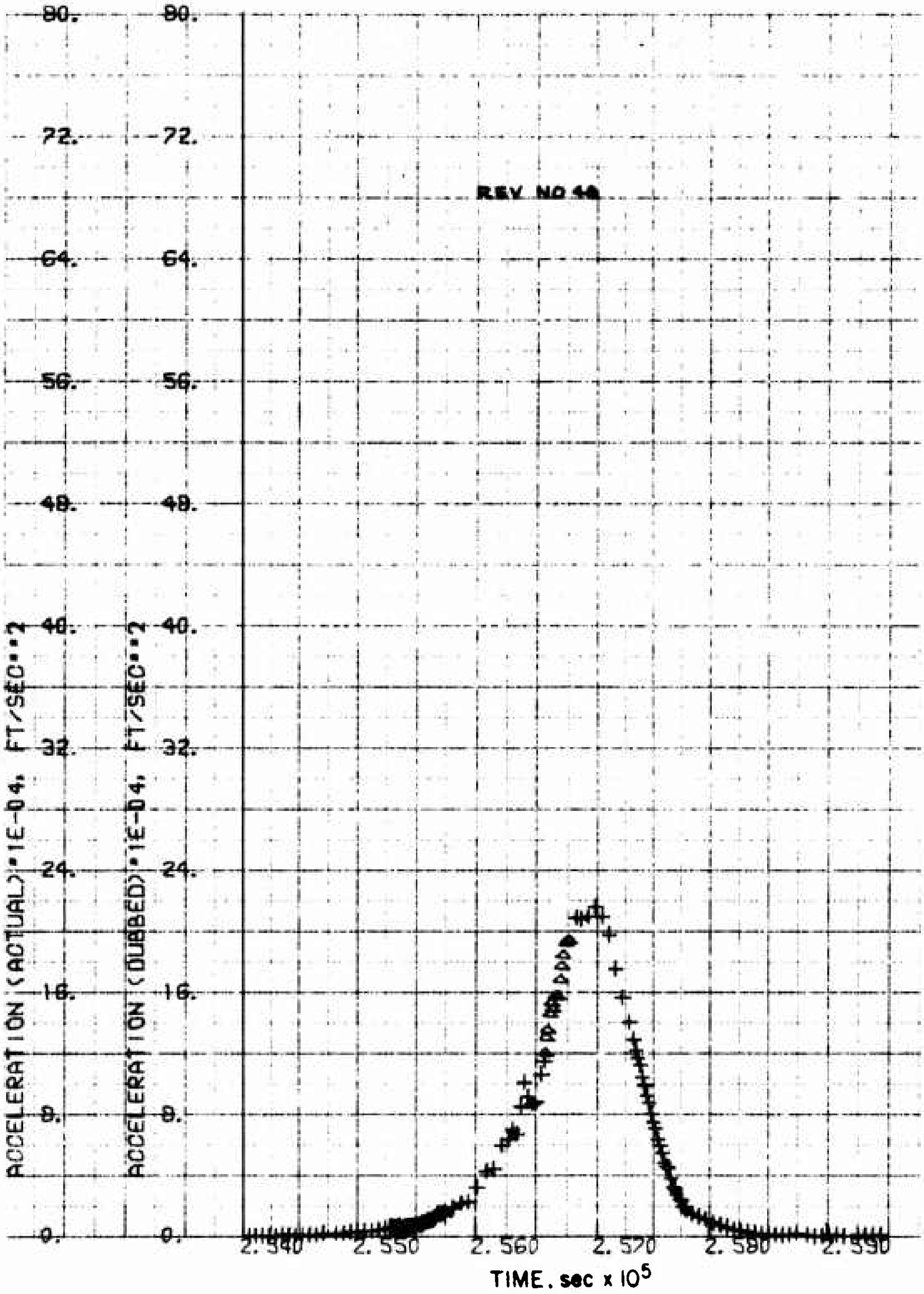

Fig. A-44. LOGACS Accelerometer Data for Rev. 48

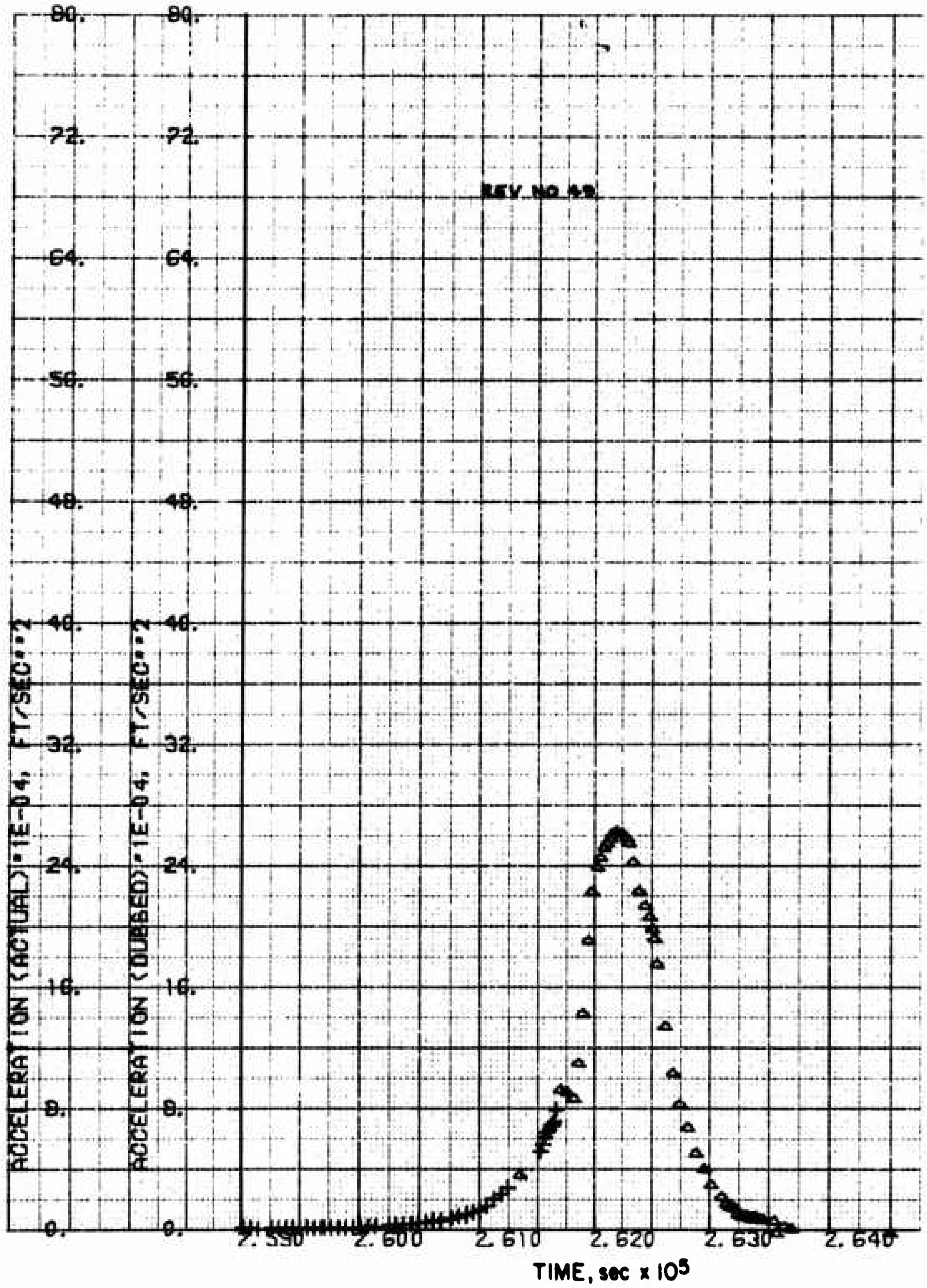

Fig. A-45. LOGACS Accelerometer Data for Rev. 49

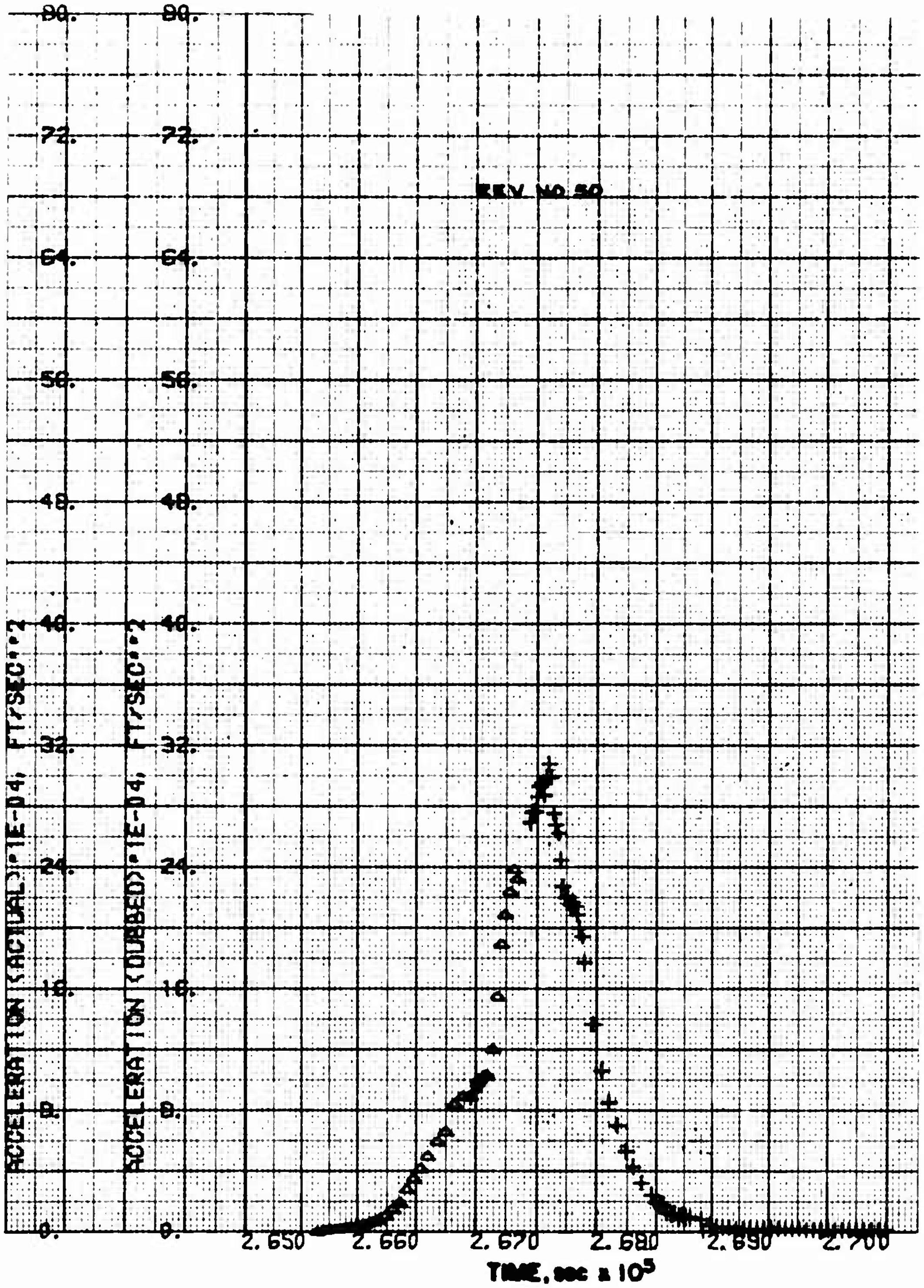

Fig. A-46 LOGACS Accelerometer Data for Rev. 50

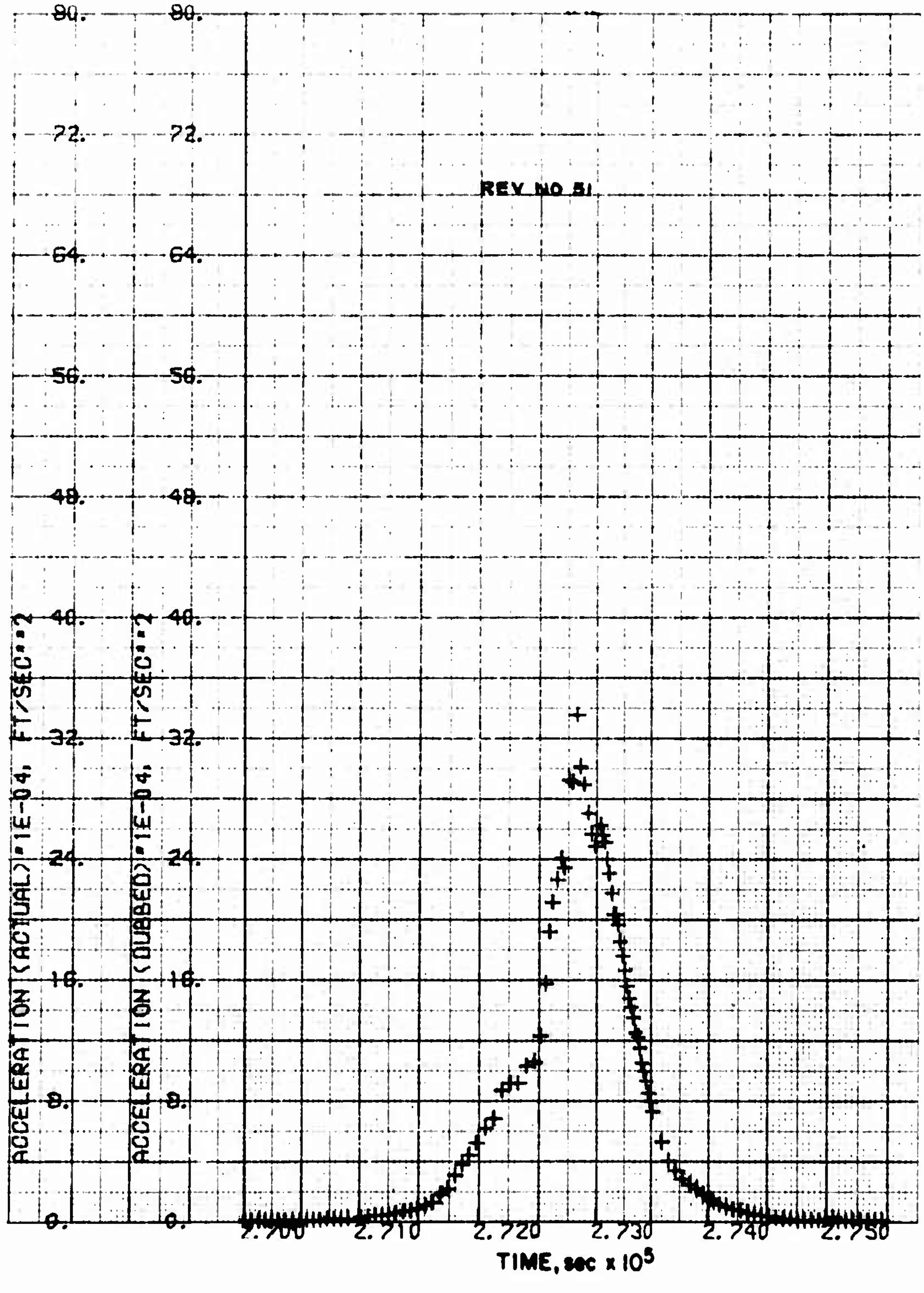

Fig. A-47. LOGACS Accelerometer Data for Rev. 51

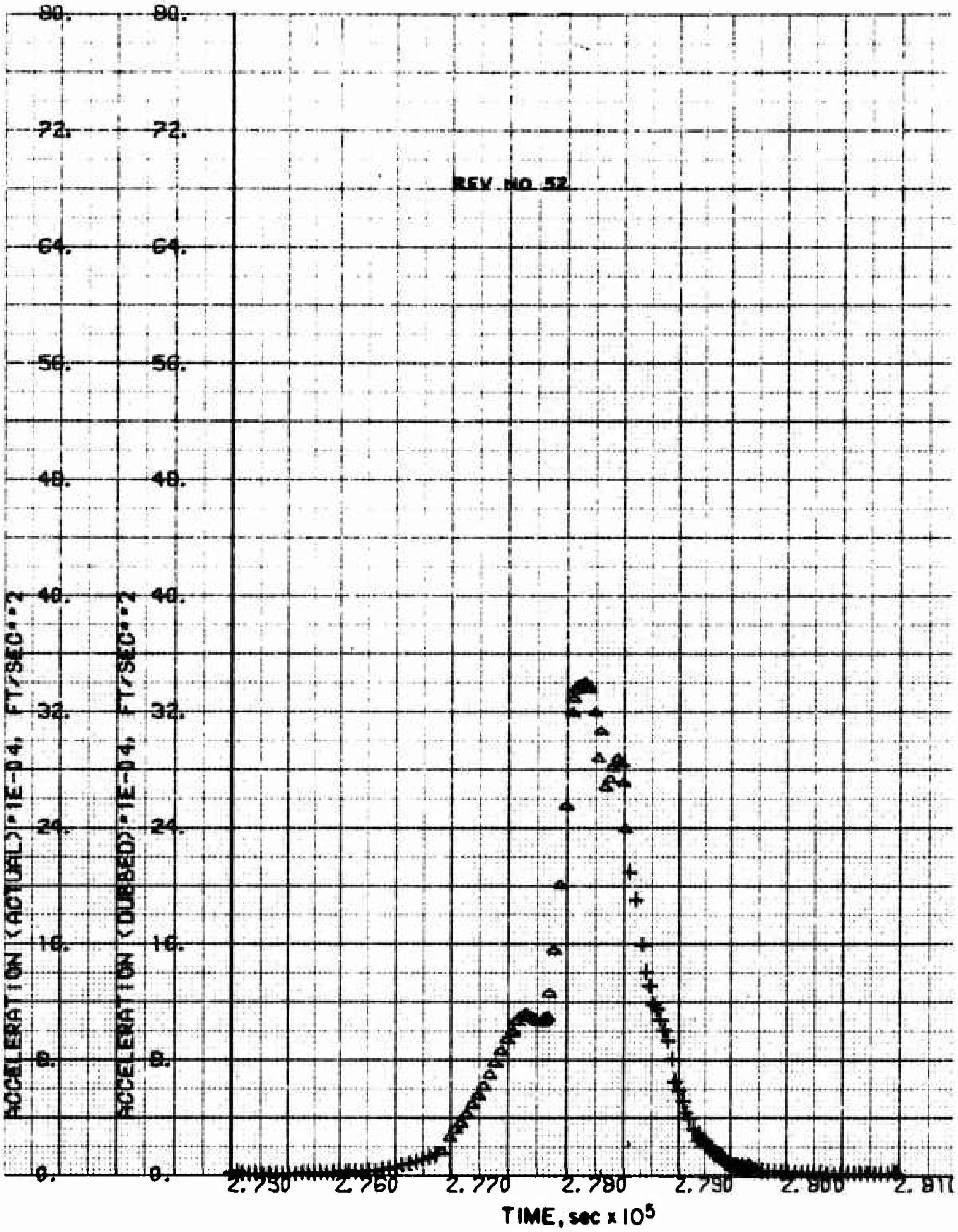

Fig. A-48. LOGACS Accelerometer Data for Rev. 52

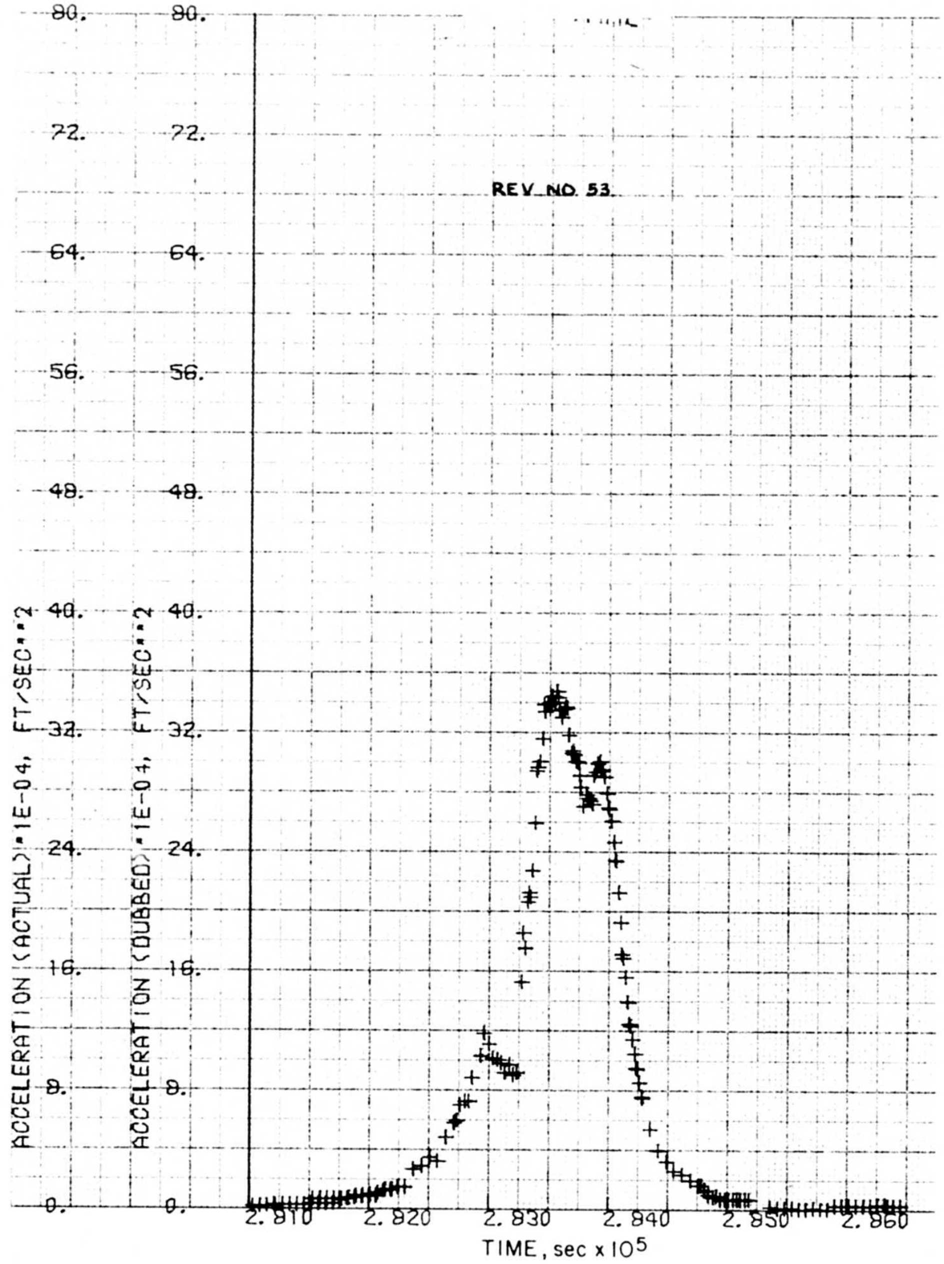

Fig. A-49. LOGACS Accelerometer Data for Rev. 53

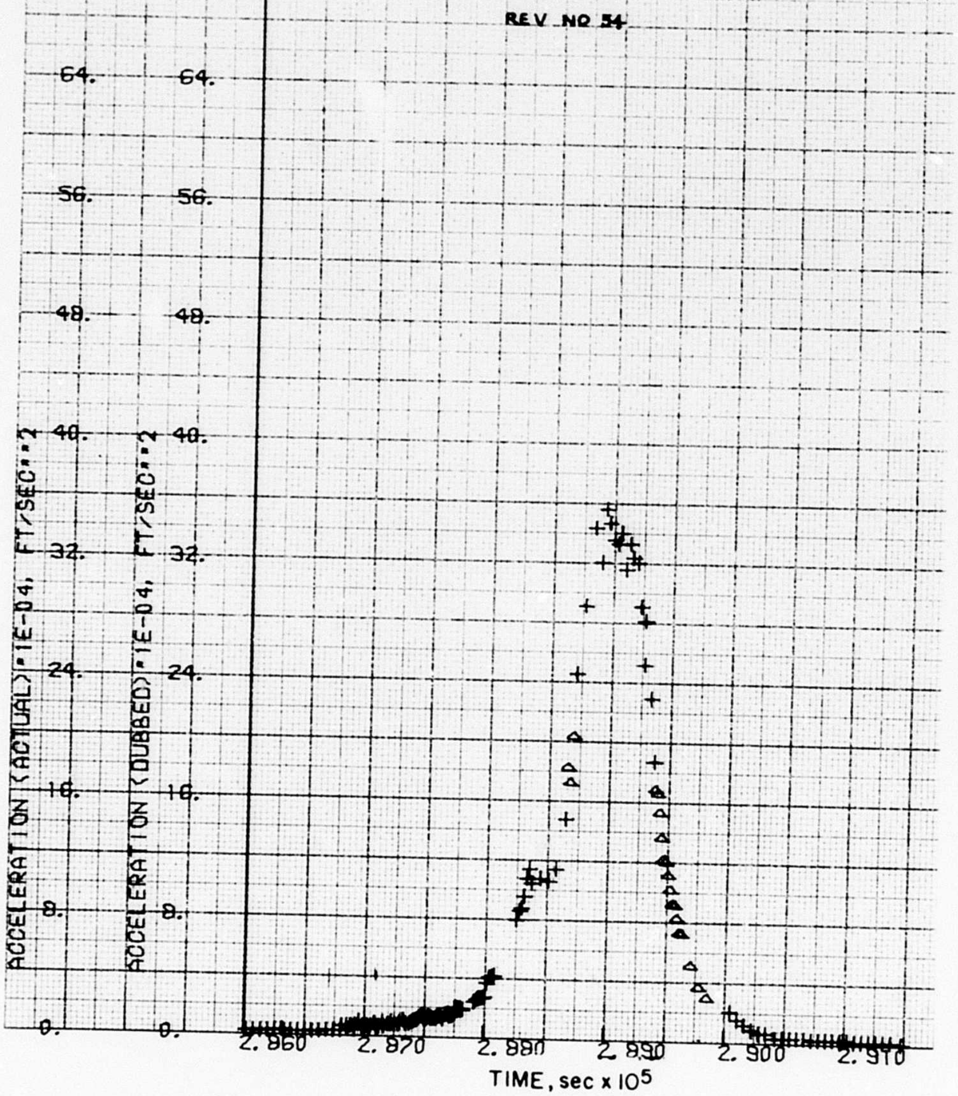

Fig. A-50. LOGACS Accelerometer Data for Rev. 54

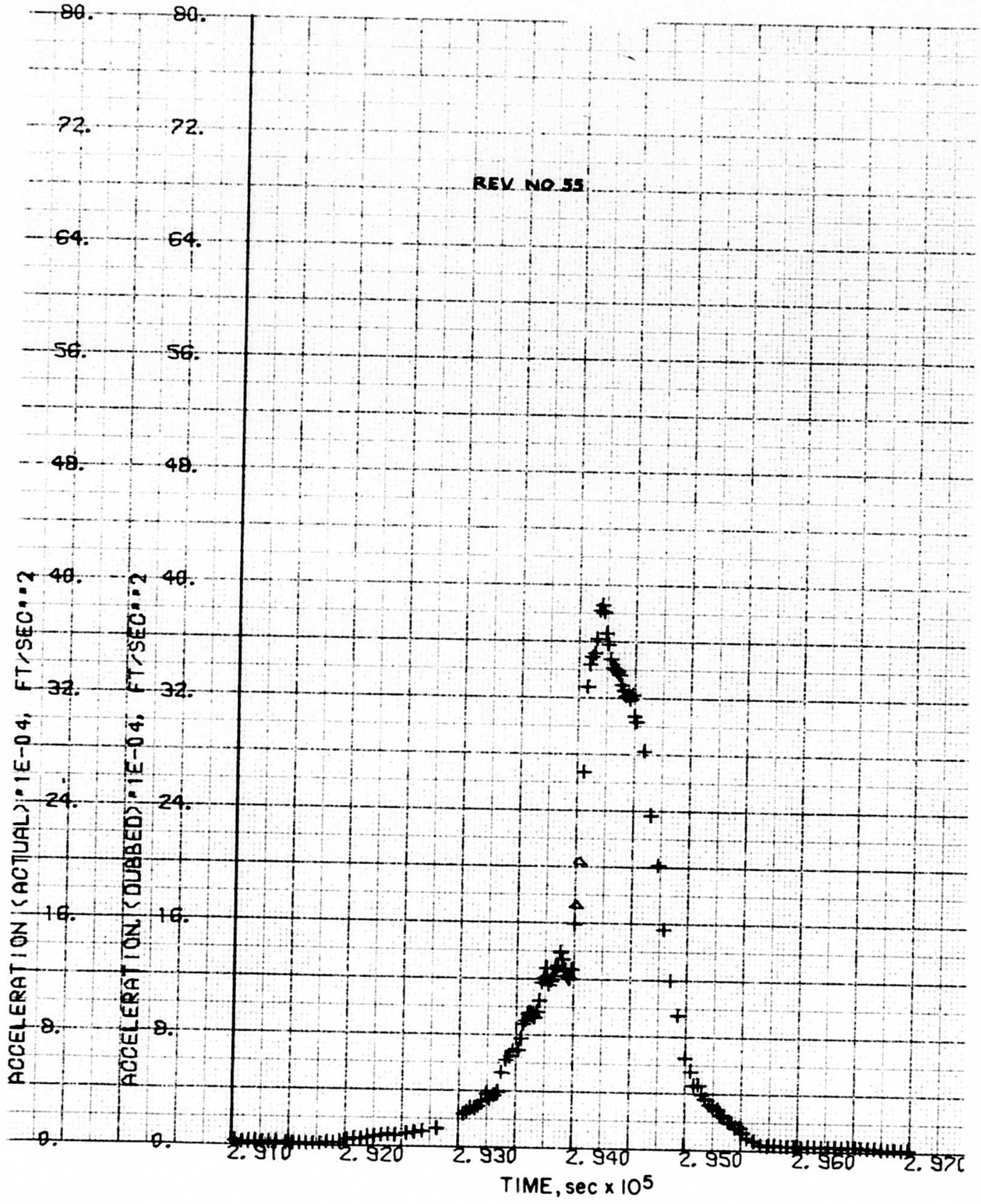

Fig. A-51. LOGACS Accelerometer Data for Rev. 55

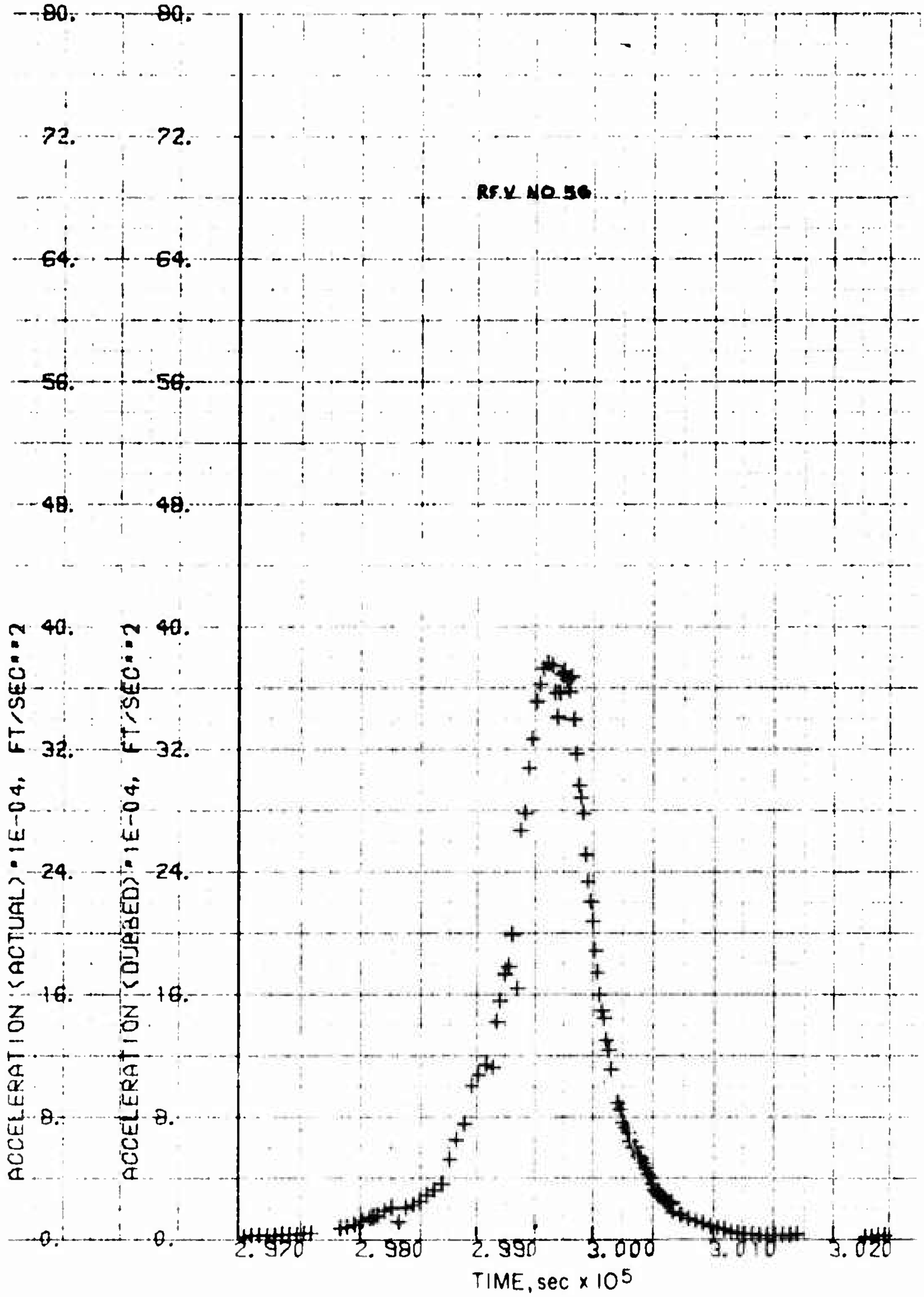

Fig. A-52. LOGACS Accelerometer Data for Rev. 56

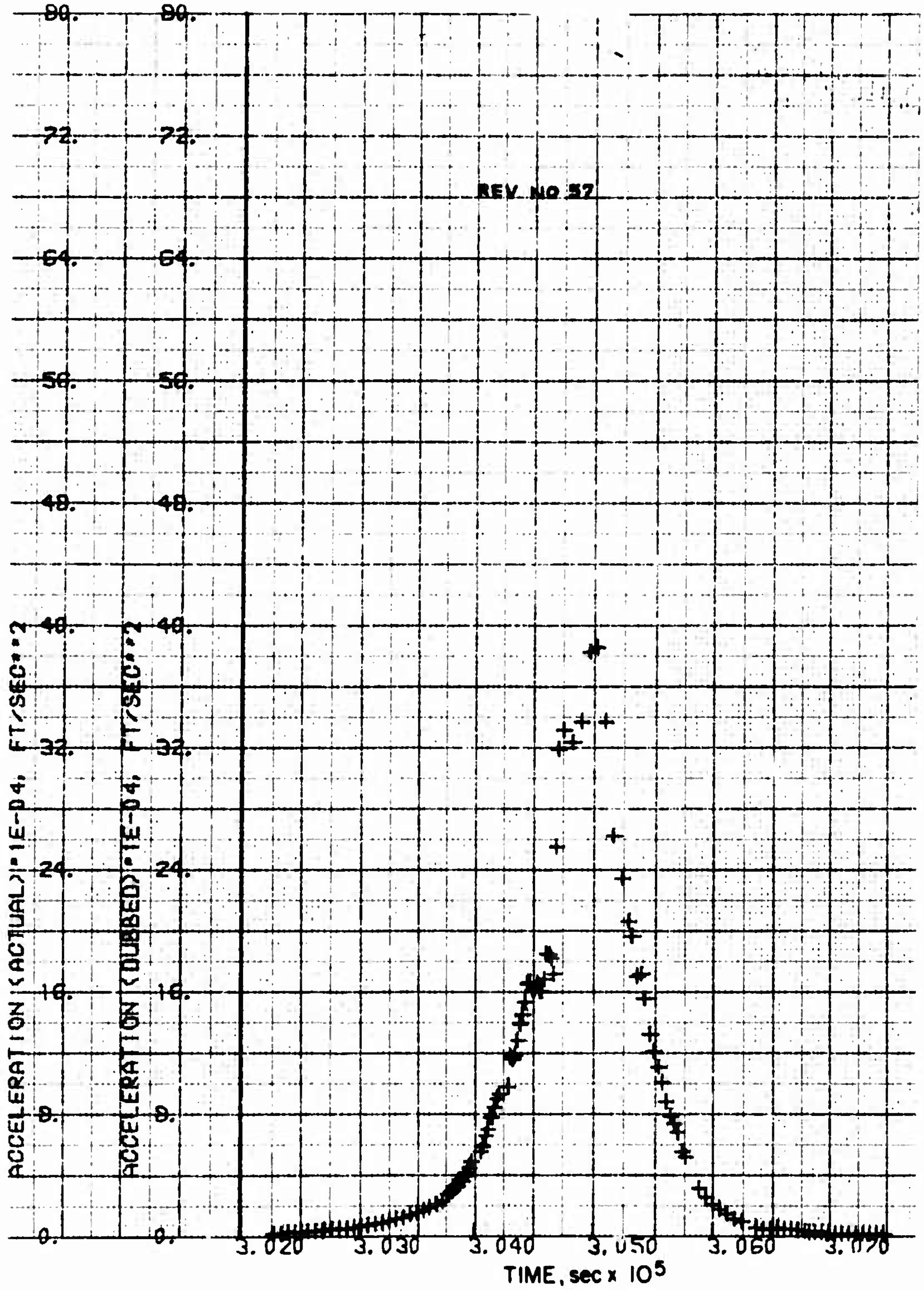

Fig. A-53. LOGACS Accelerometer Data for Rev. 57

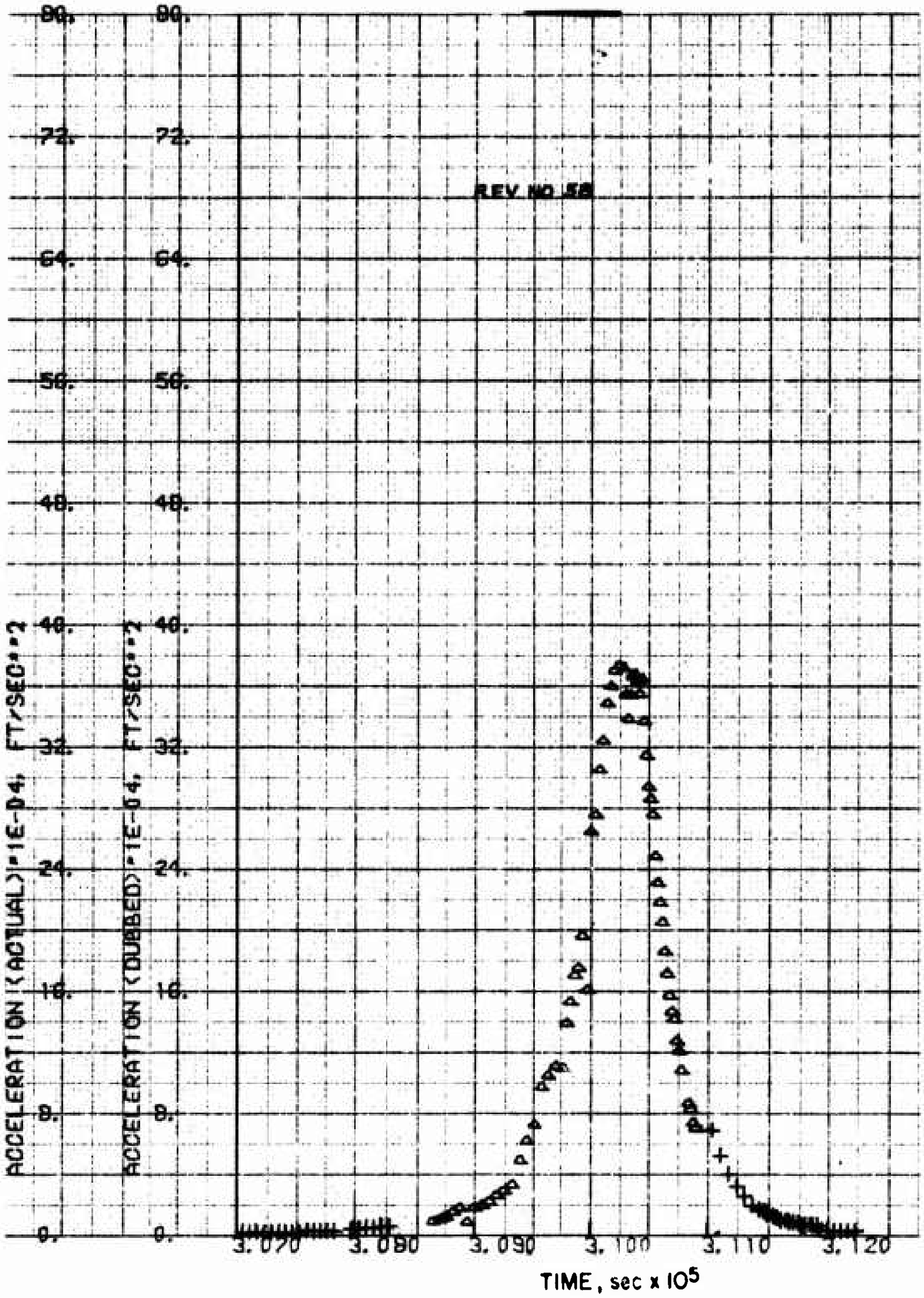

Fig. A-54. LOGACS Accelerometer Data for Rev. 58

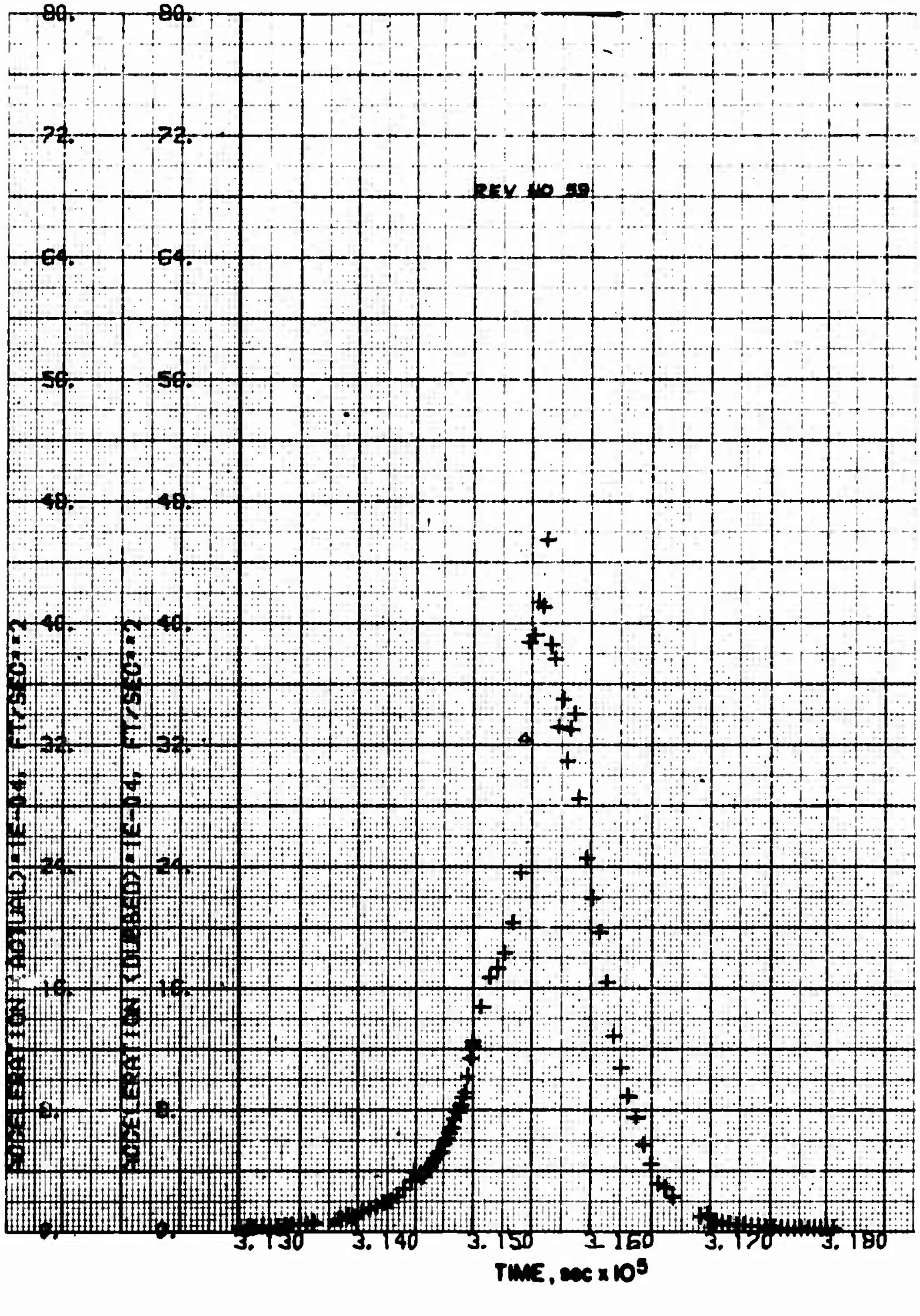

Fig. A-55. LOGACS Accelerometer Data for Rev. 59

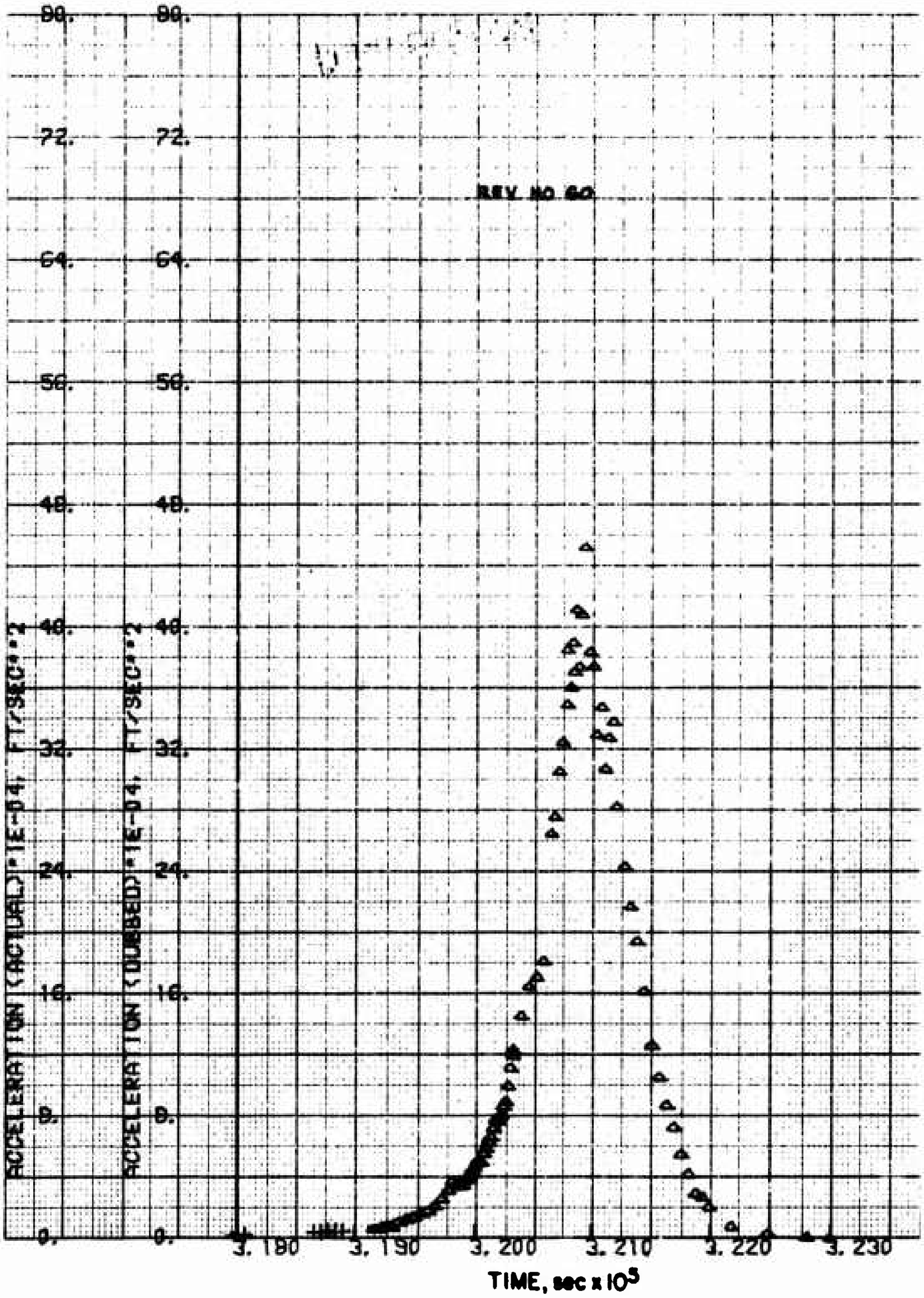

Fig. A-56. LOGACS Accelerometer Data for Rev. 60

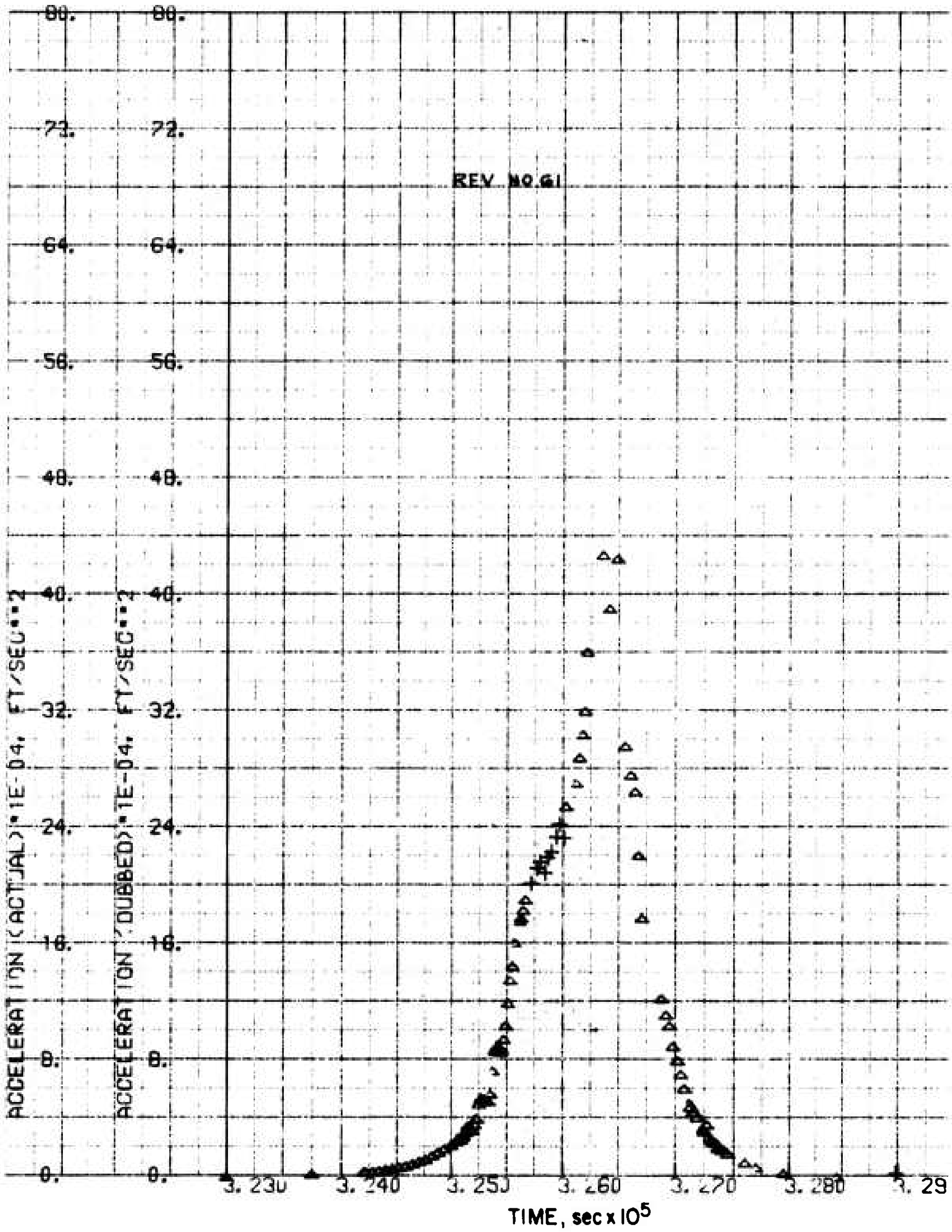

Fig. A-57. LOGACS Accelerometer Data for Rev. 61

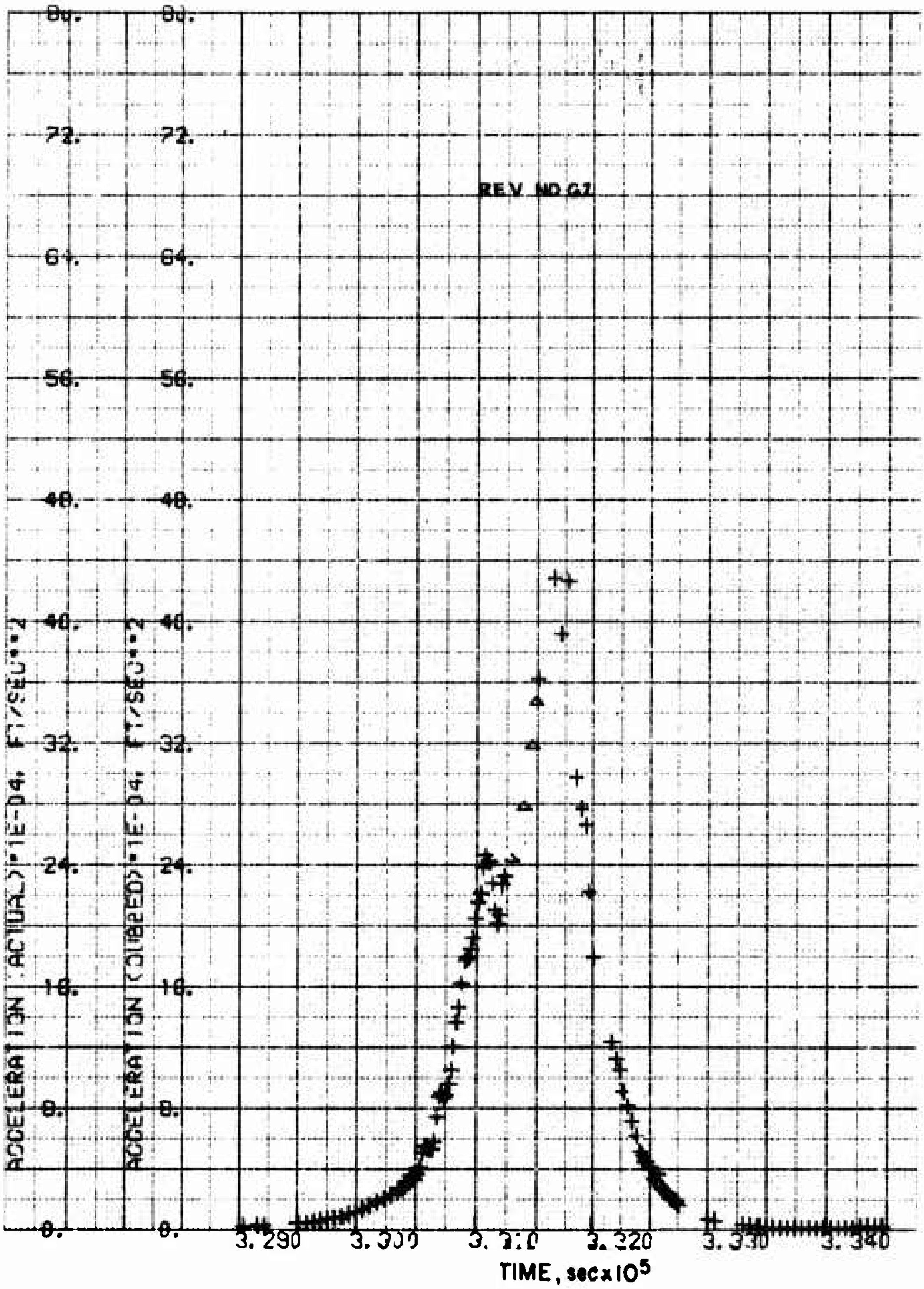

Fig. A-58. LOGACS Accelerometer Data for Rev. 62

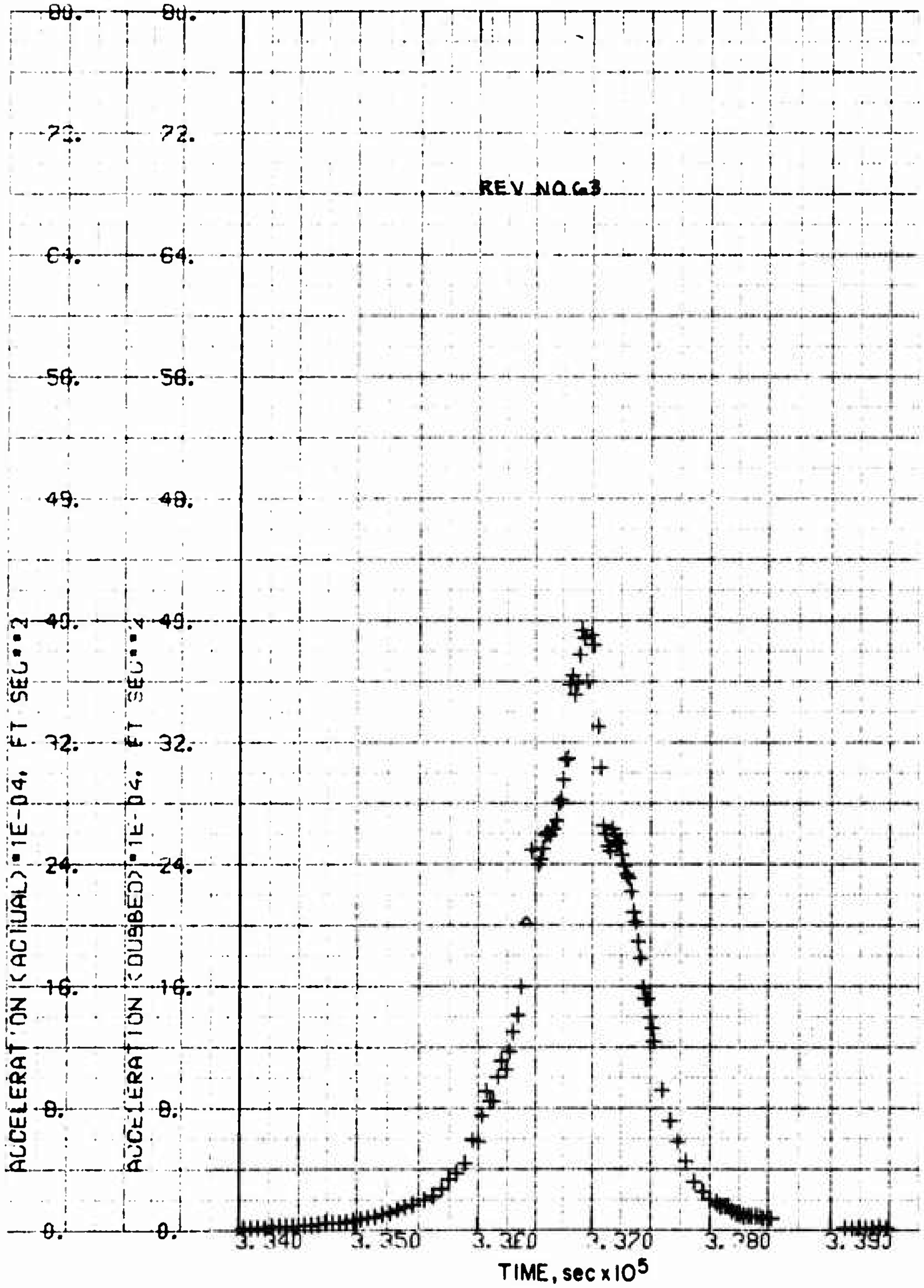

Fig. A-59. LOGACS Accelerometer Data for Rev. 63

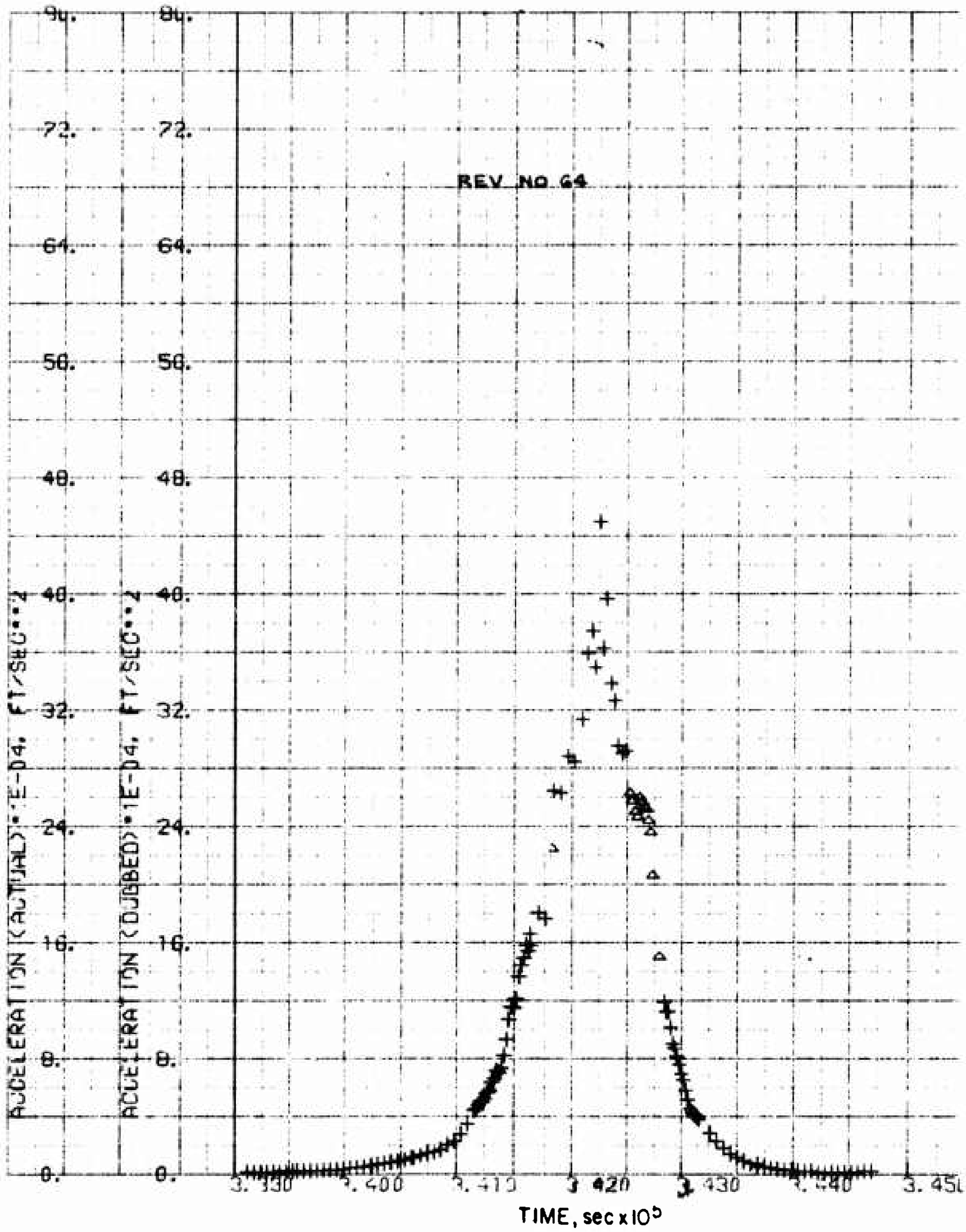

Fig. A-60. LOGACS Accelerometer Data for Rev. 64

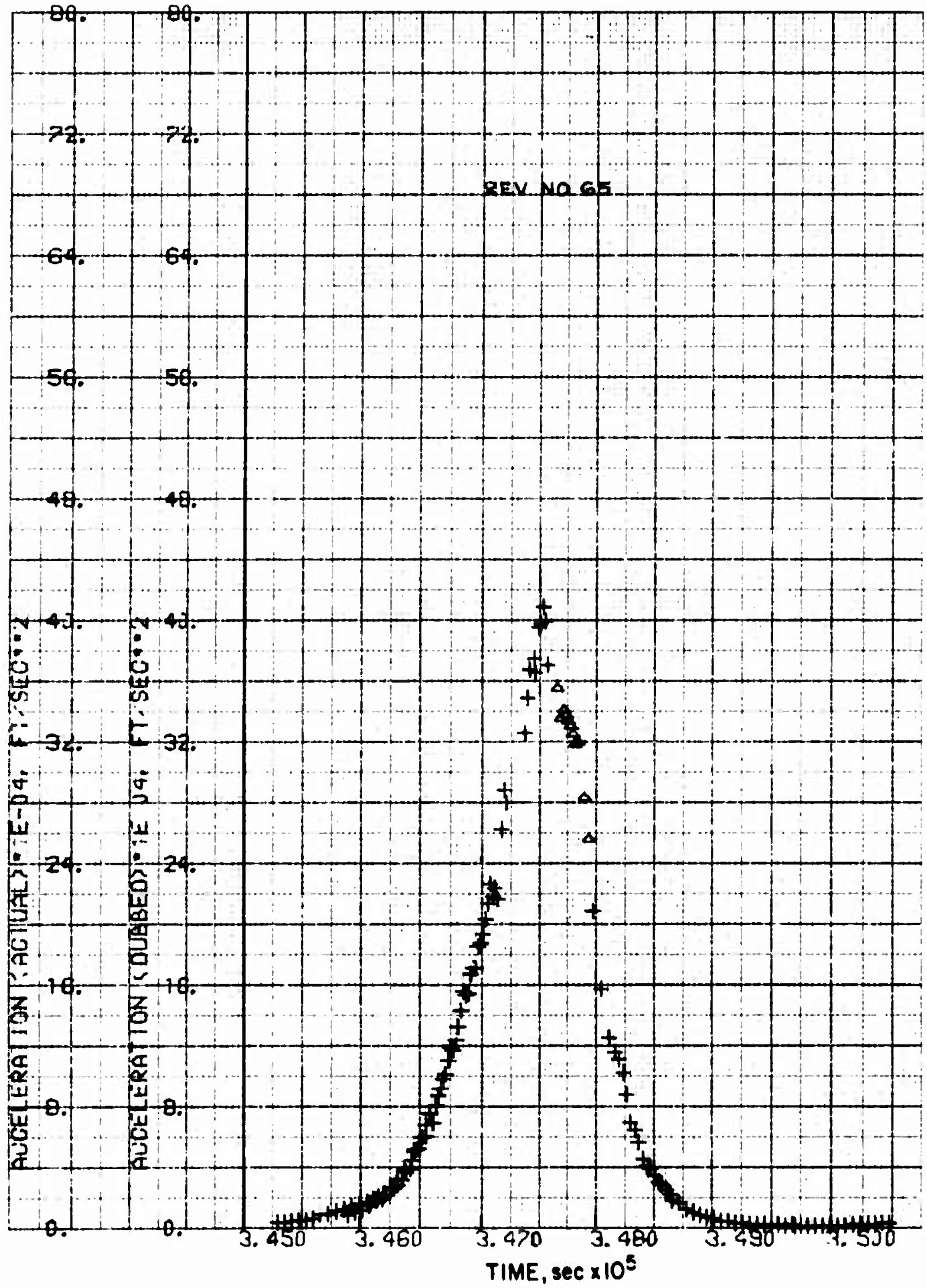

Fig. A-61. LOGACS Accelerometer Data for Rev. 65

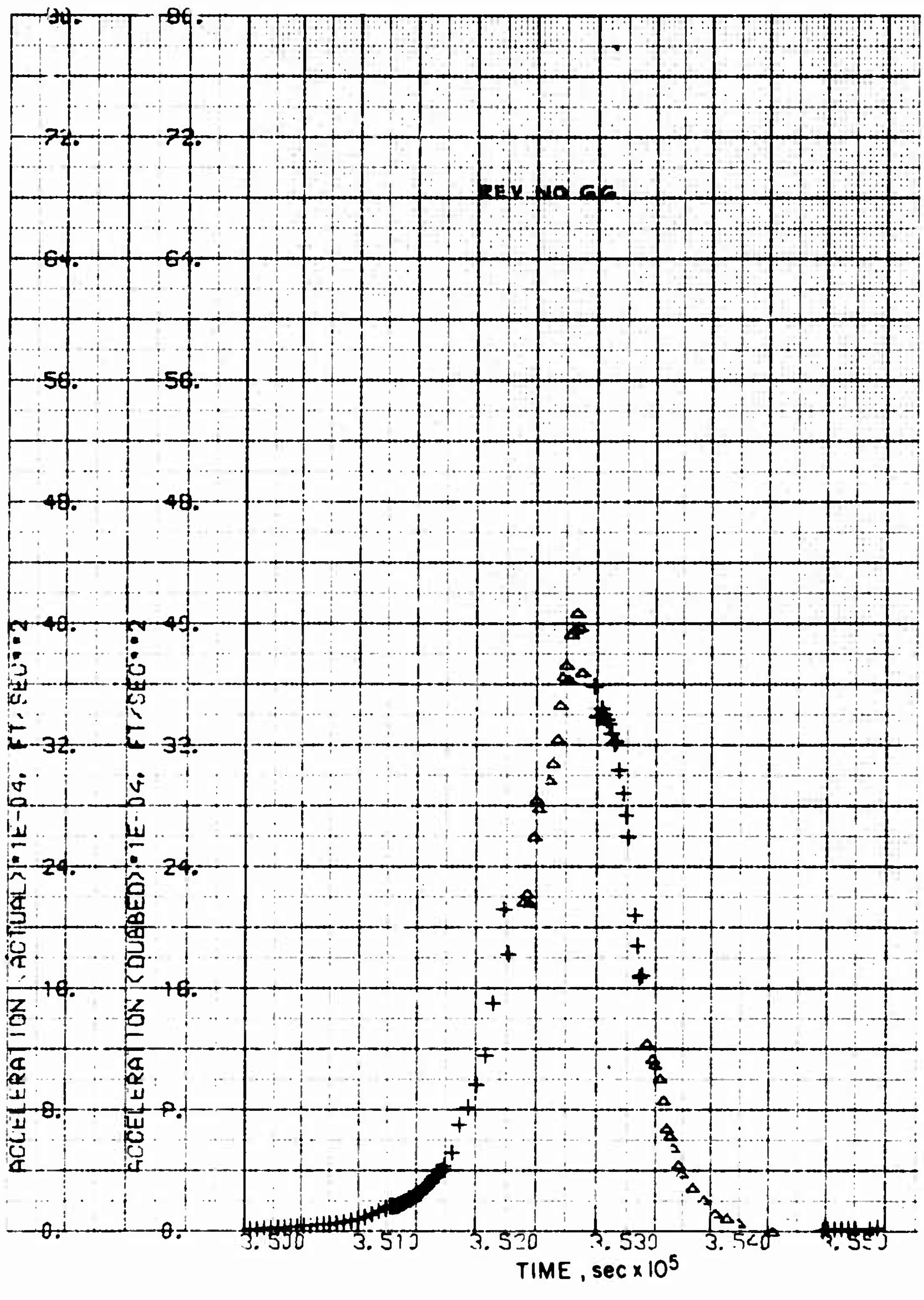

Fig. A-62. LOGACS Accelerometer Data for Rev. 66

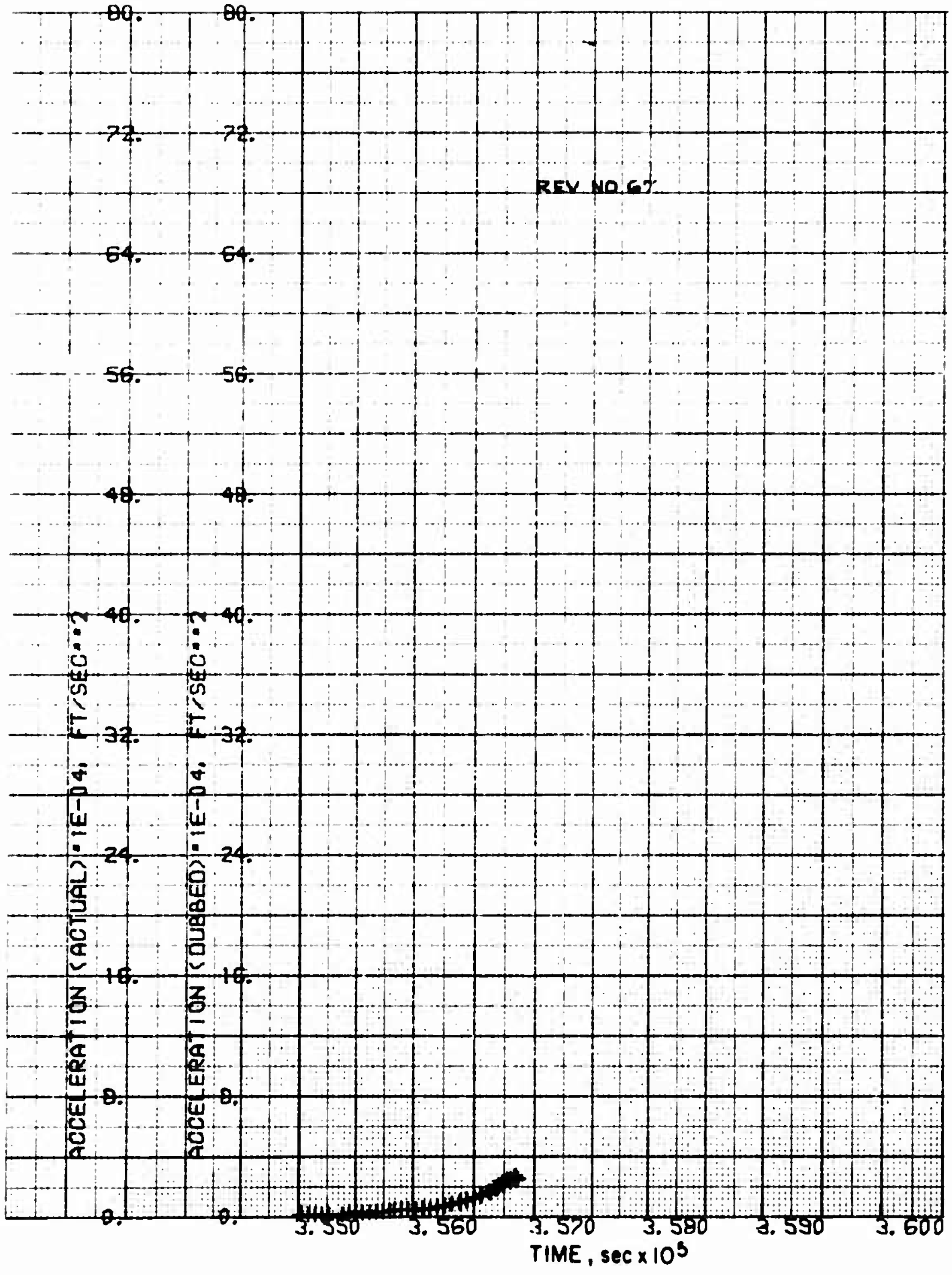

Fig. A-63. LOGACS Accelerometer Data for Rev. 67

APPENDIX B

DENSITY DATA

Densities reduced from the LOGACS data were processed through The Aerospace Corporation Computer Printout of Densities (CPD) program, to interpolate for density values at preselected values of time, altitude, density, and other parameters. CPD accepts as input the accelerometer data (fps^2) and an ephemeris, outputs the density derived from these two quantities, computes the values of solar and geomagnetic indices from tabular input, and compares LOGACS densities with densities from selected model atmospheres.

To study the behavior of the lower altitude portions of the LOGACS density data, we prepared semi-logarithmic plots of density versus altitude. These plots cover an altitude range from approximately 140 to 250 km. The data were arranged in files so that two plots per rev. were obtained: one toward perigee (250 to 140 km) and one away from perigee (140 to 250 km). The data for Revs. 5 through 67 (both toward perigee and away from perigee) are presented in Figs. B-1 through B-98, respectively.

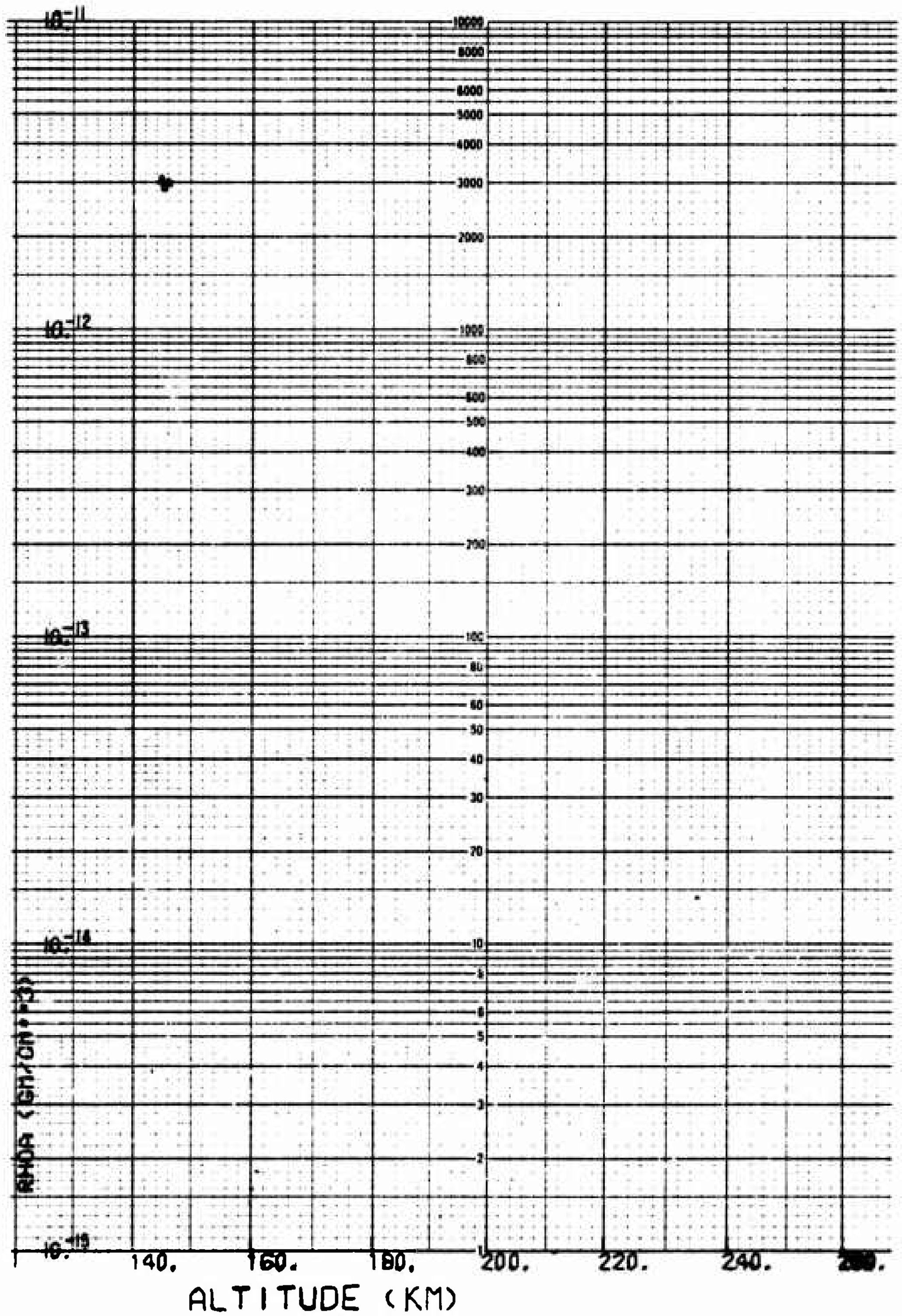

Fig. B-1. LOGACS Density Data for Rev. 5, Toward Perigee

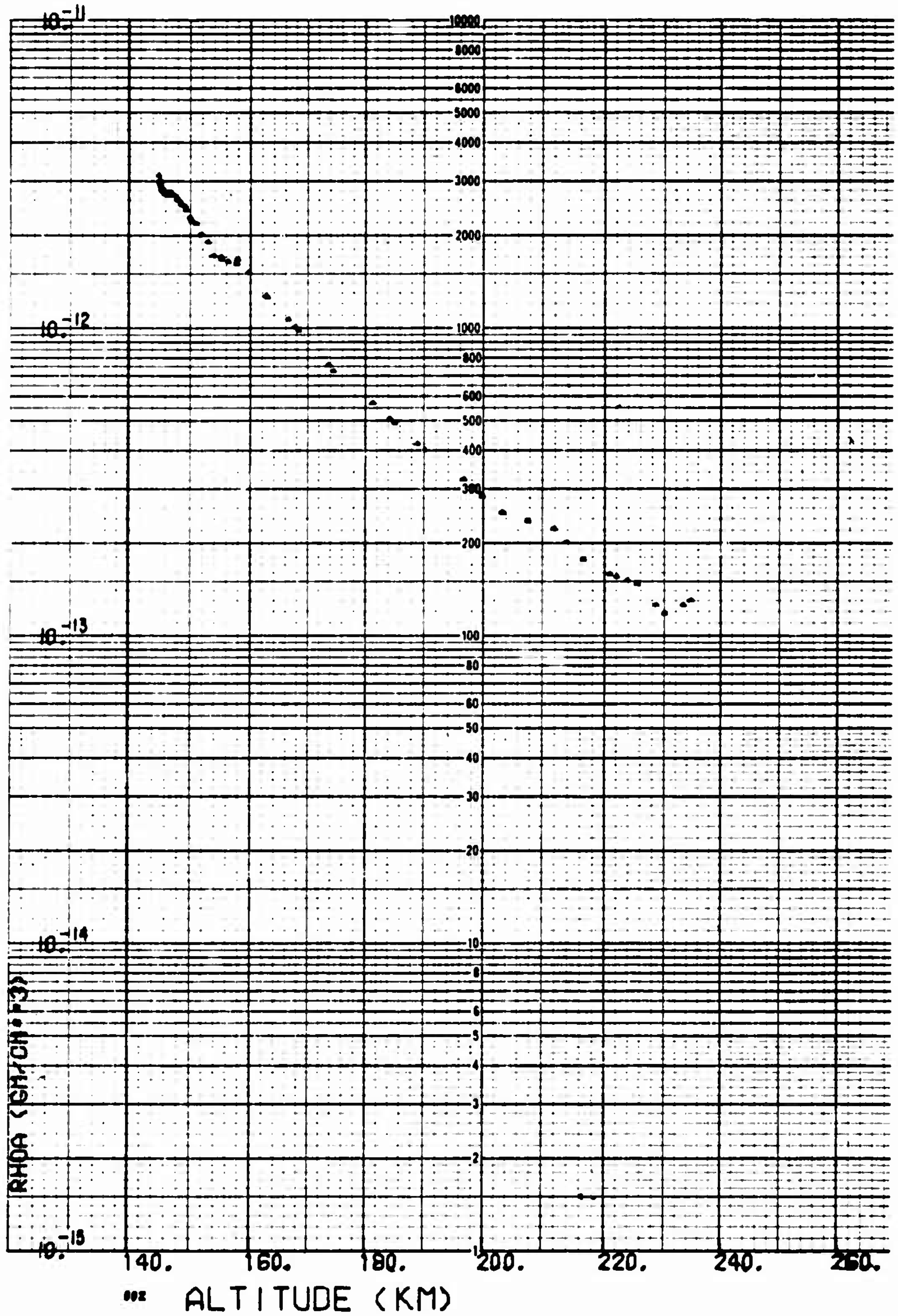

Fig. B-2. LOGACS Density Data for Rev. 5, Away from Perigee

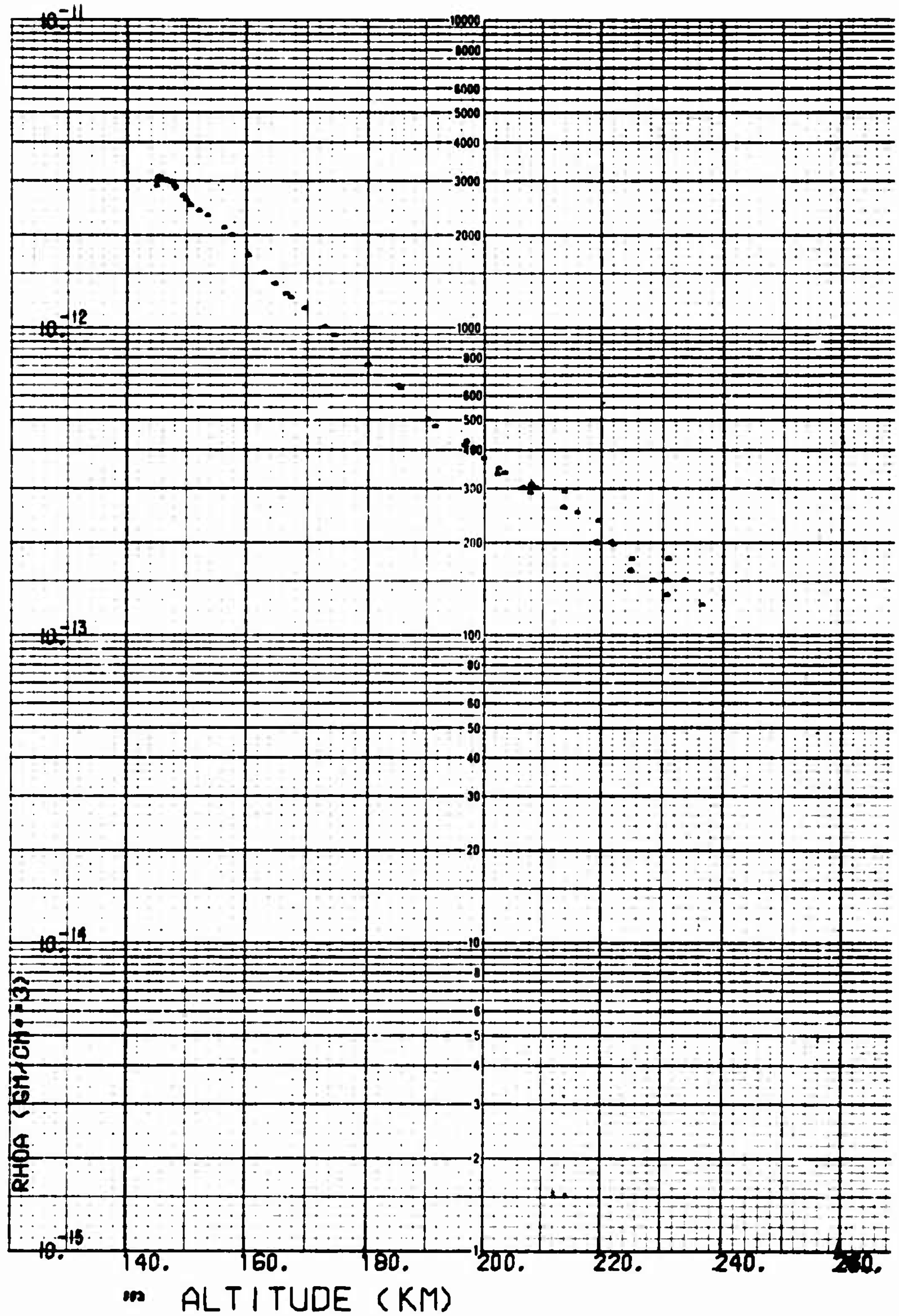

Fig. B-3. LOGACS Density Data for Rev. 6, Toward Perigee

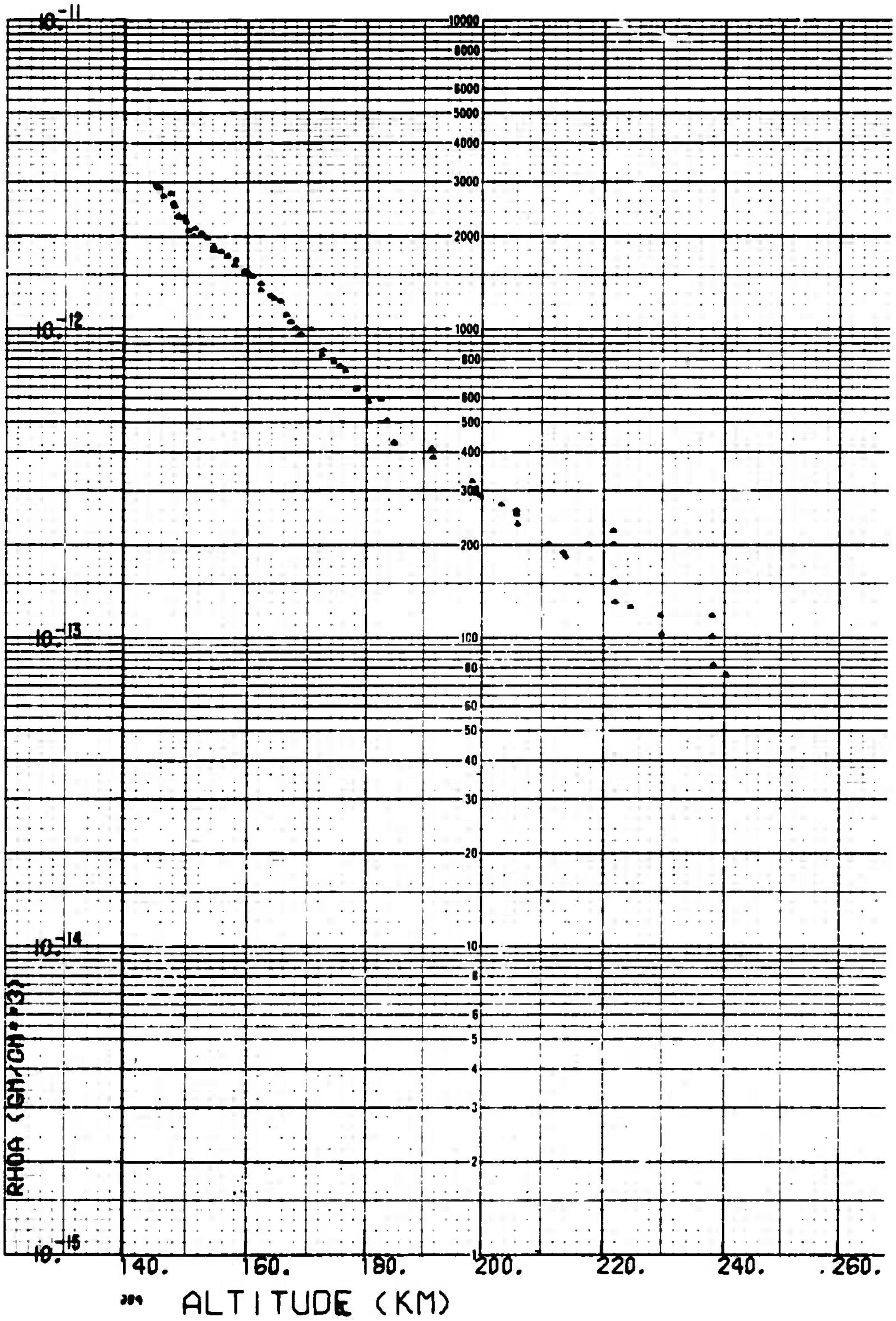

Fig. B-4. LOGACS Density Data for Rev. 6, Away from Perigee

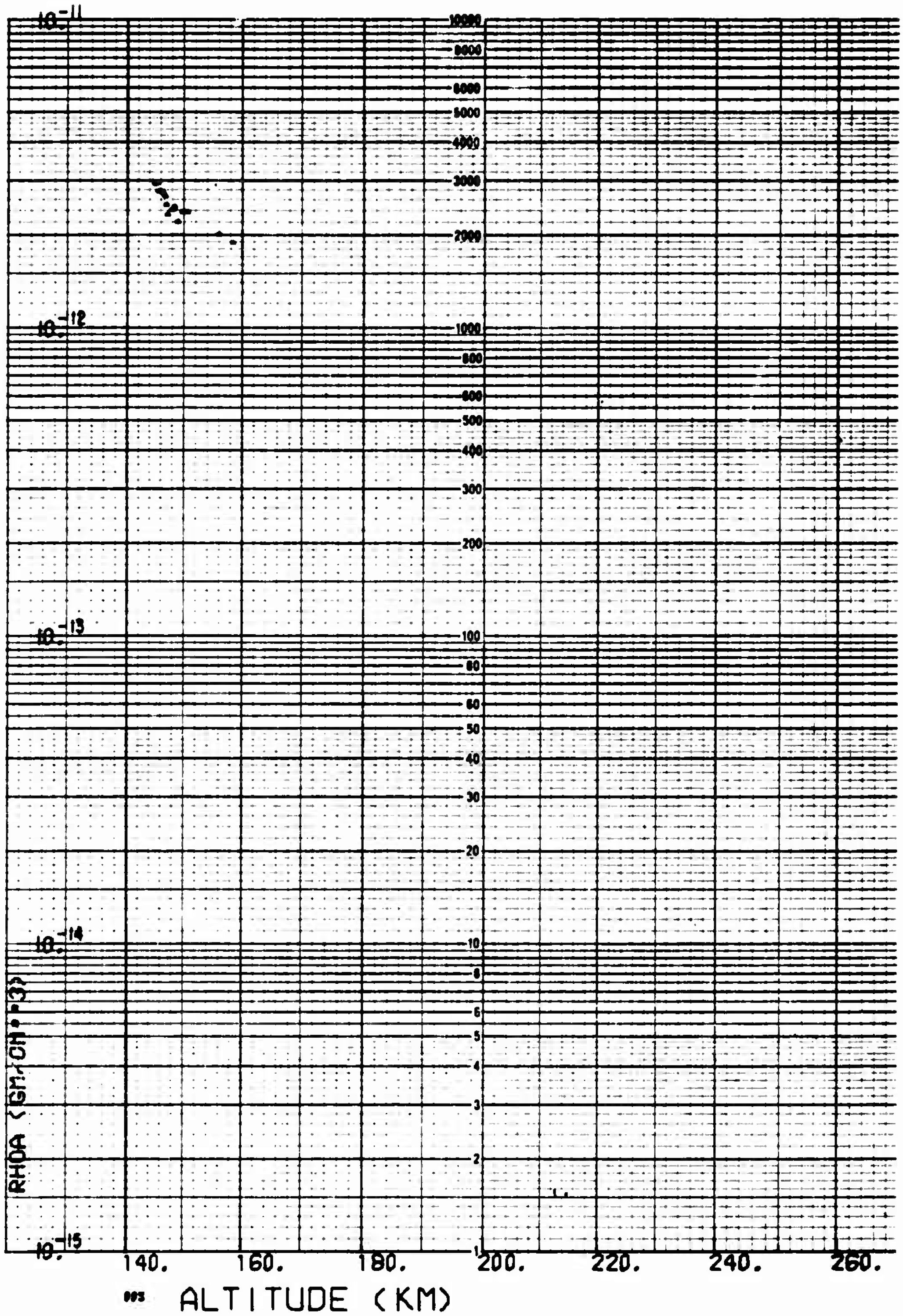

Fig. B-5. LOGACS Density Data for Rev. 7, Toward Perigee

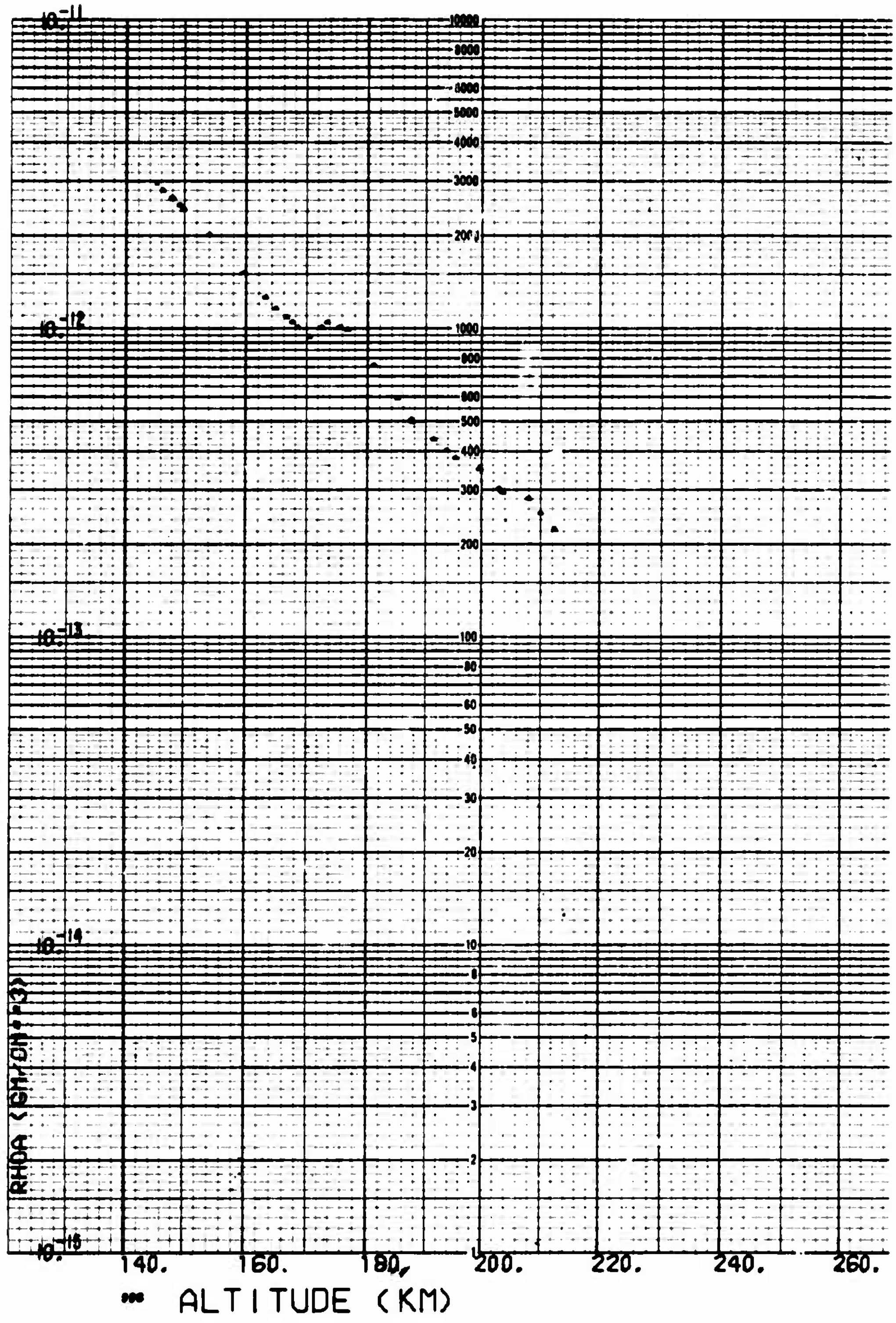

Fig. B-6. LOGACS Density Data for Rev. 7, Away from Perigee

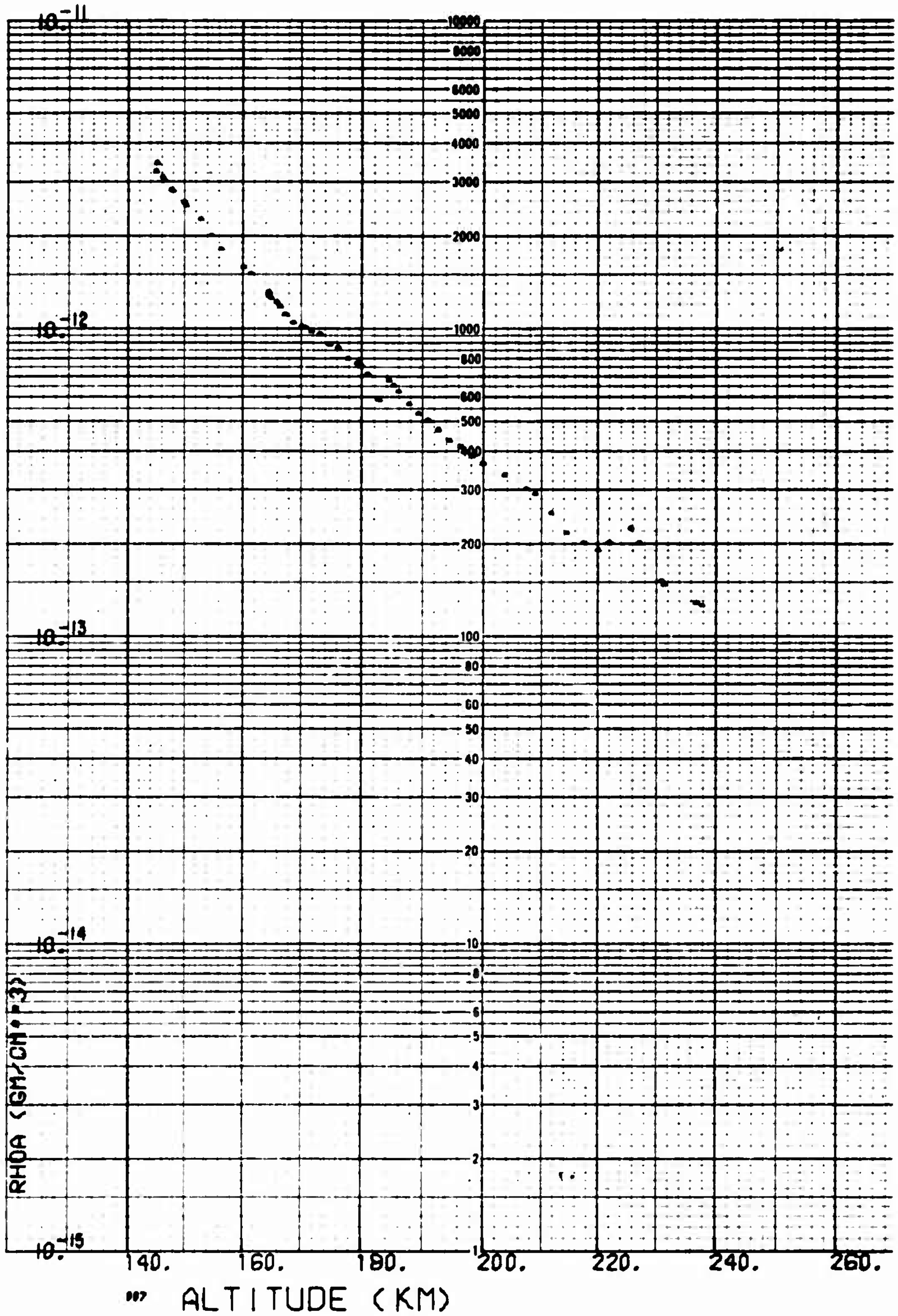

Fig. B-7. LOGACS Density Data for Rev. 9, Toward Perigee

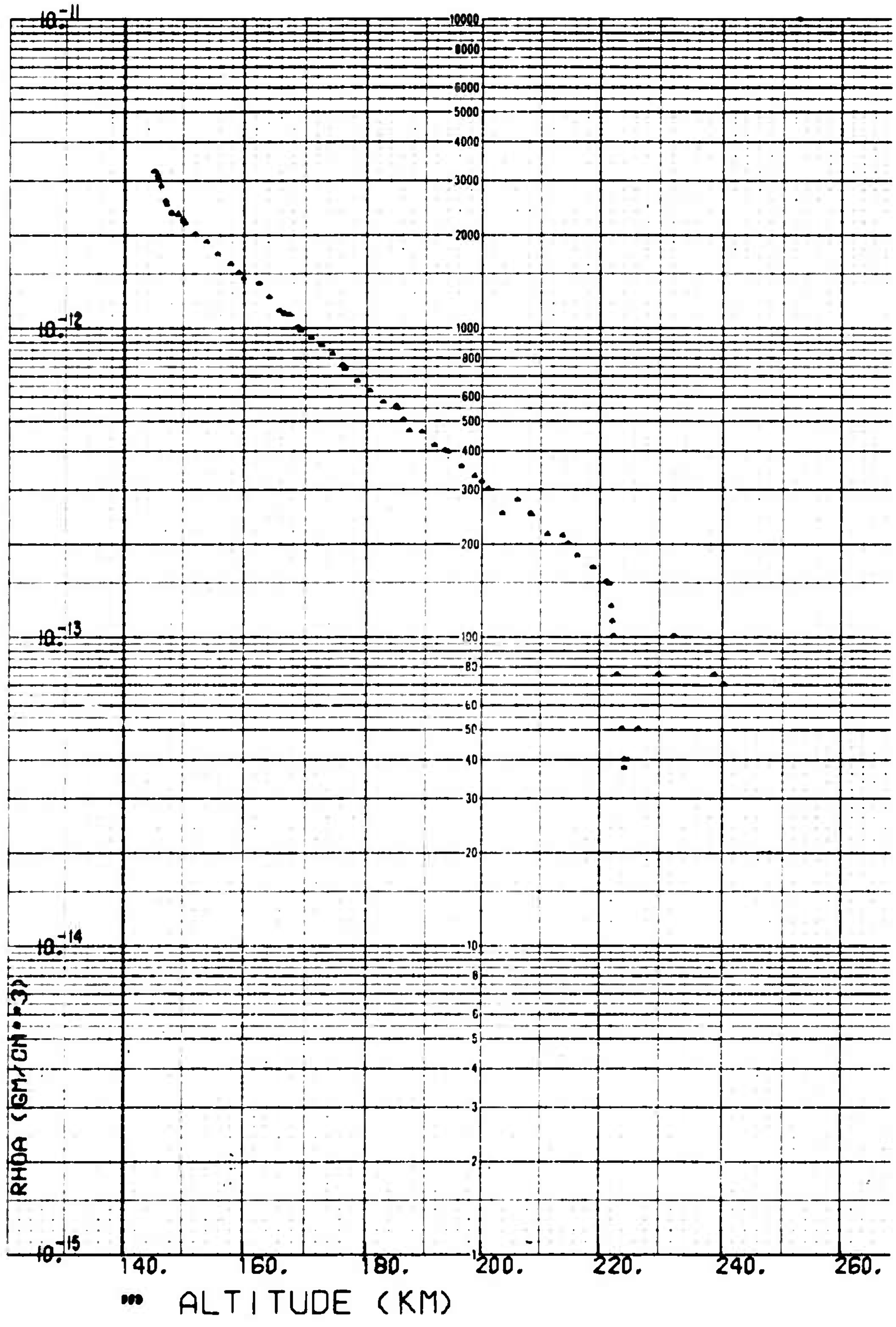

Fig. B-8. LOGACS Density Data for Rev. 9, Away from Perigee

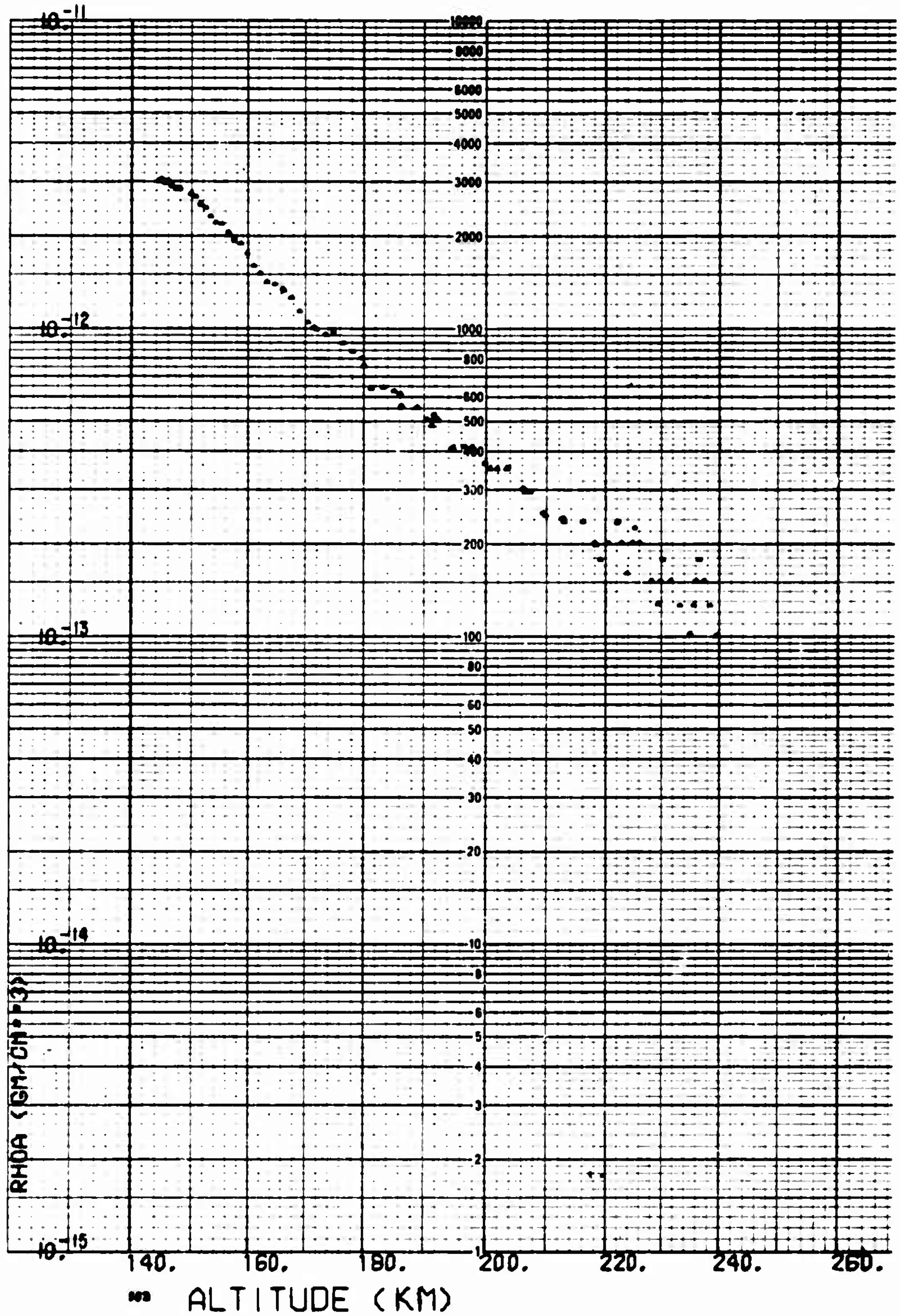

Fig. B-9. LOGACS Density Data for Rev. 10, Toward Perigee

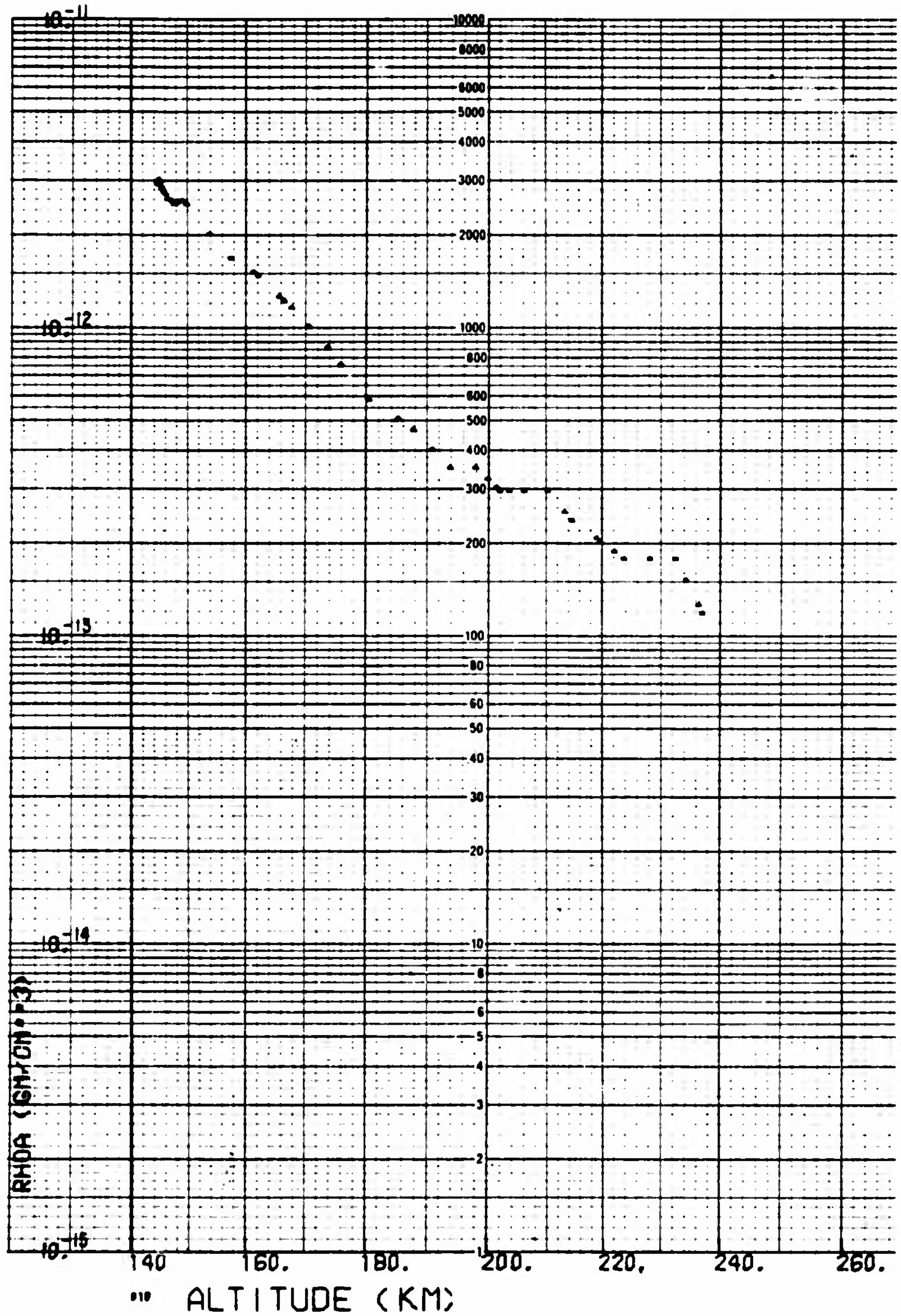

Fig. B-10. LOGACS Density Data for Rev. 10, Away from Perigee

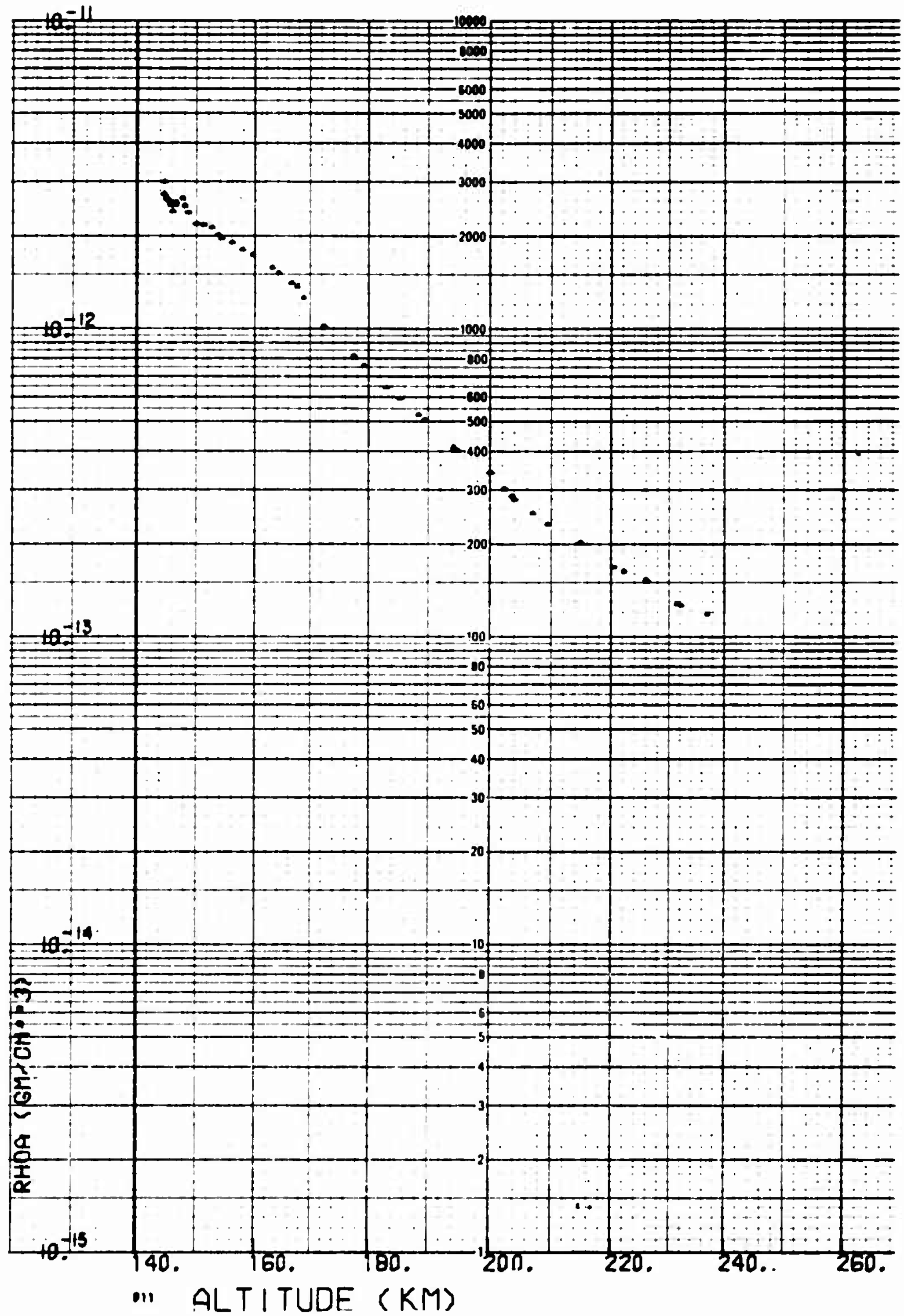

Fig. B-11. LOGACS Density Data for Rev. 11, Toward Perigee

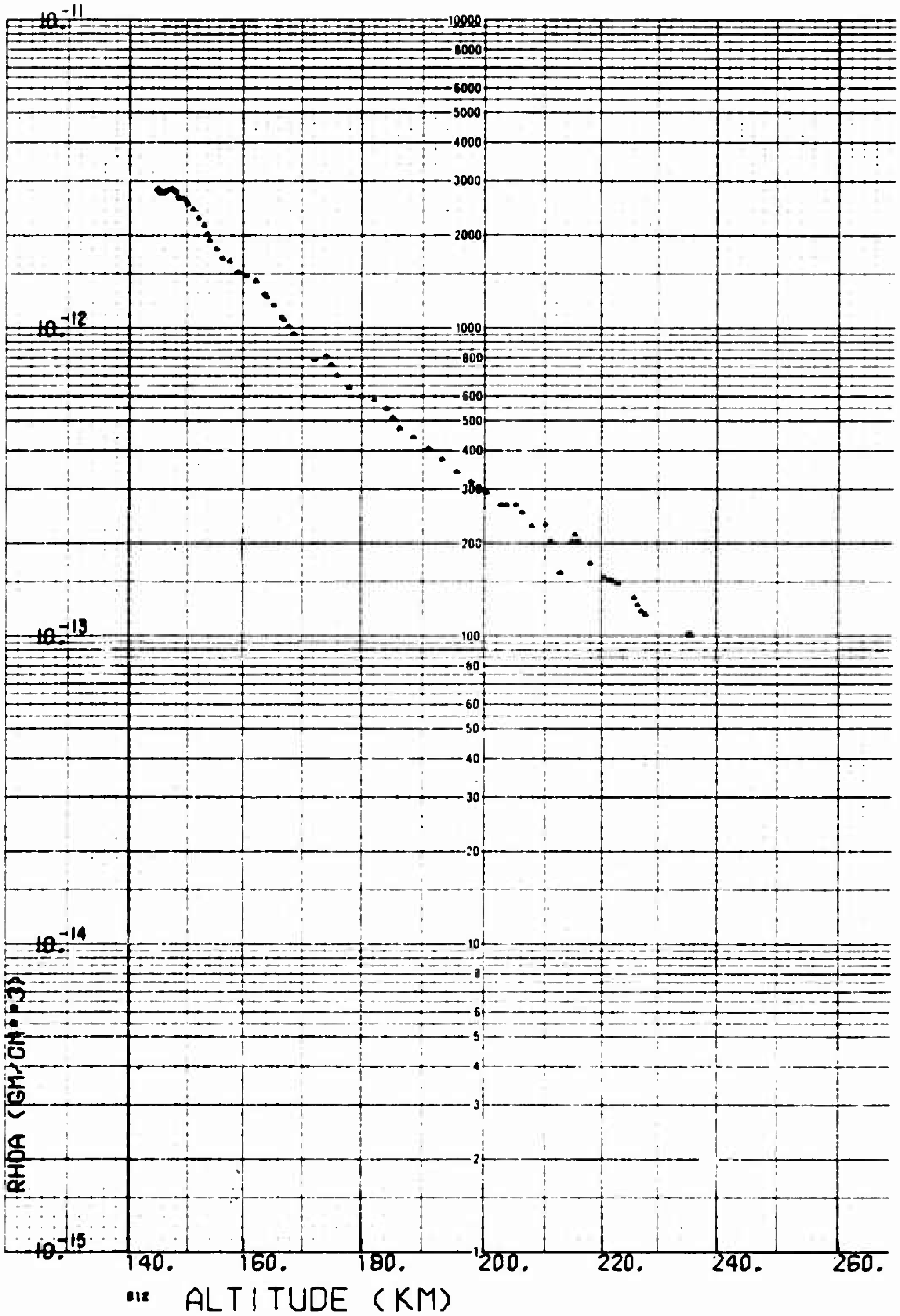

Fig. B-12. LOGACS Density Data for Rev. 11, Away from Perigee

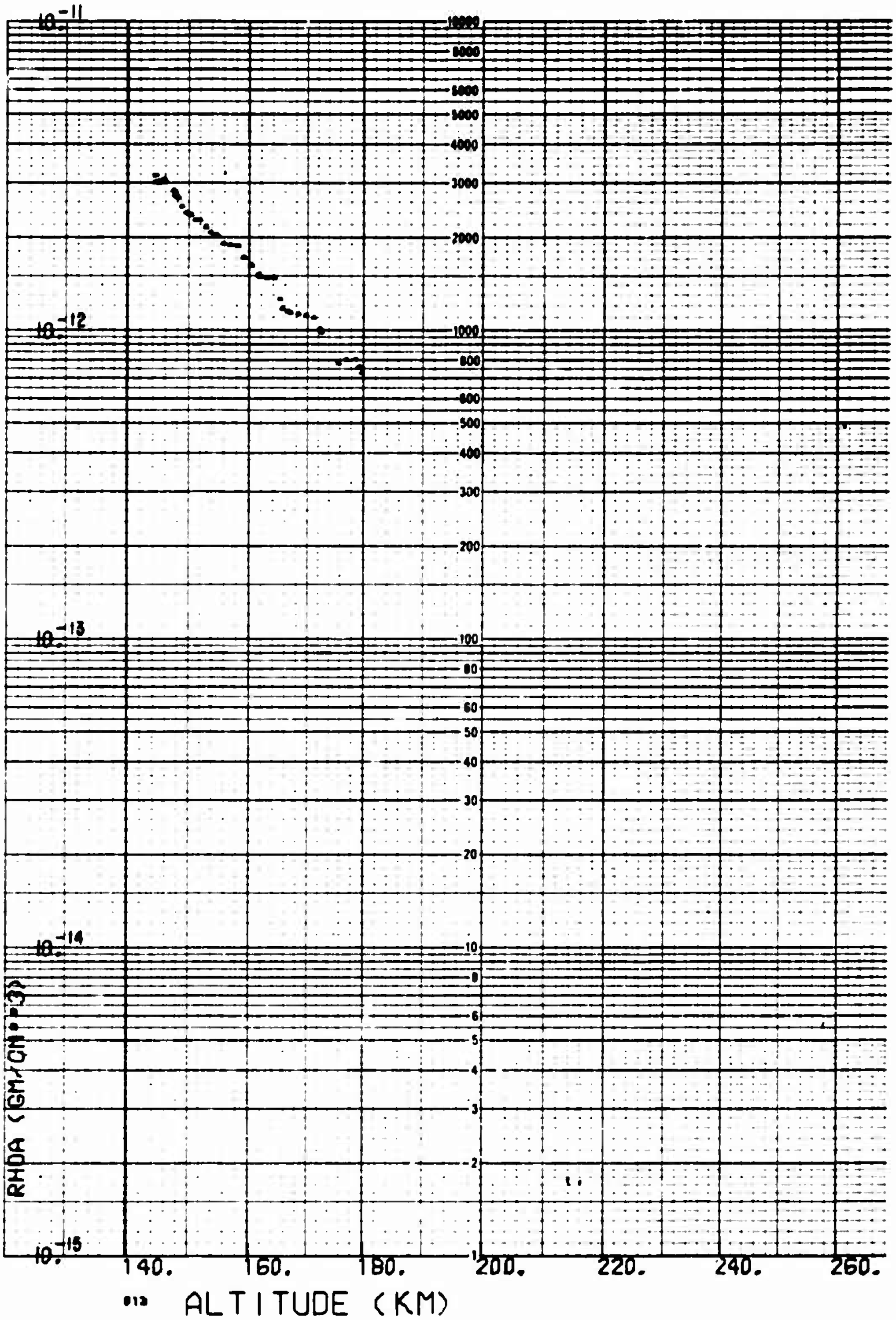

Fig. B-13. LOGACS Density Data for Rev. 12, Toward Perigee

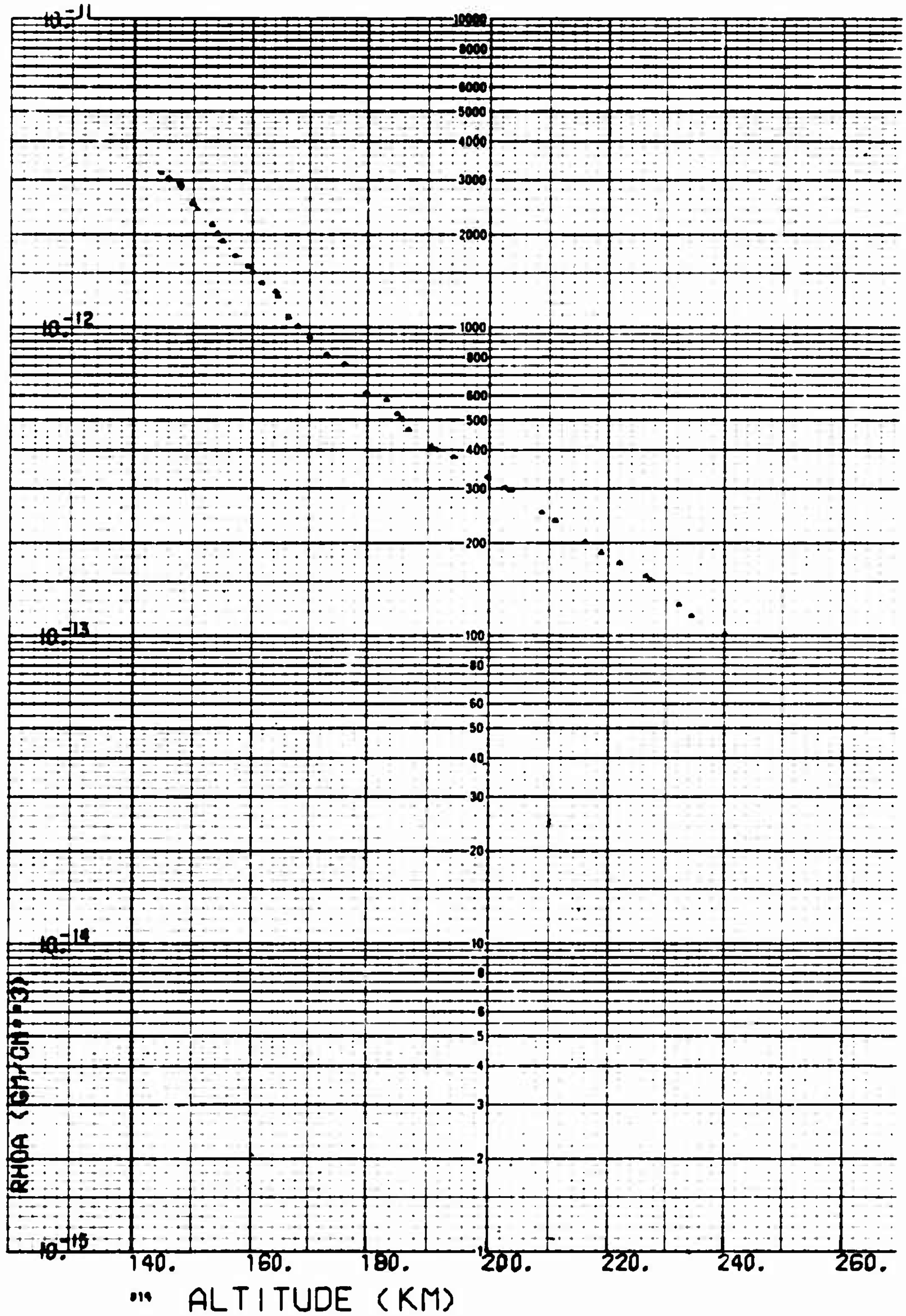

Fig. B-14. LOGACS Density Data for Rev. 12, Away from Perigee

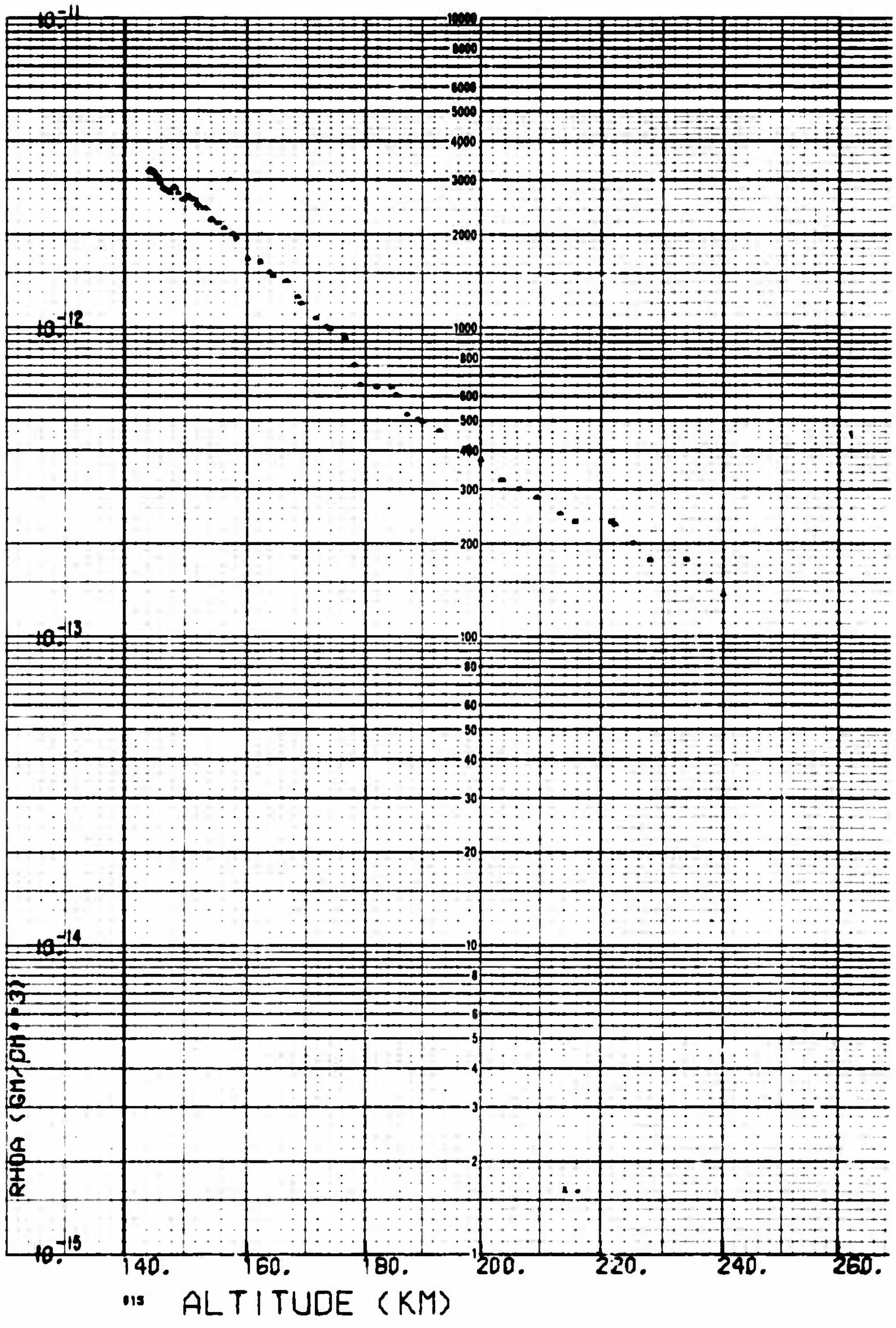

Fig. B-15. LOGACS Density Data for Rev. 13, Toward Perigee

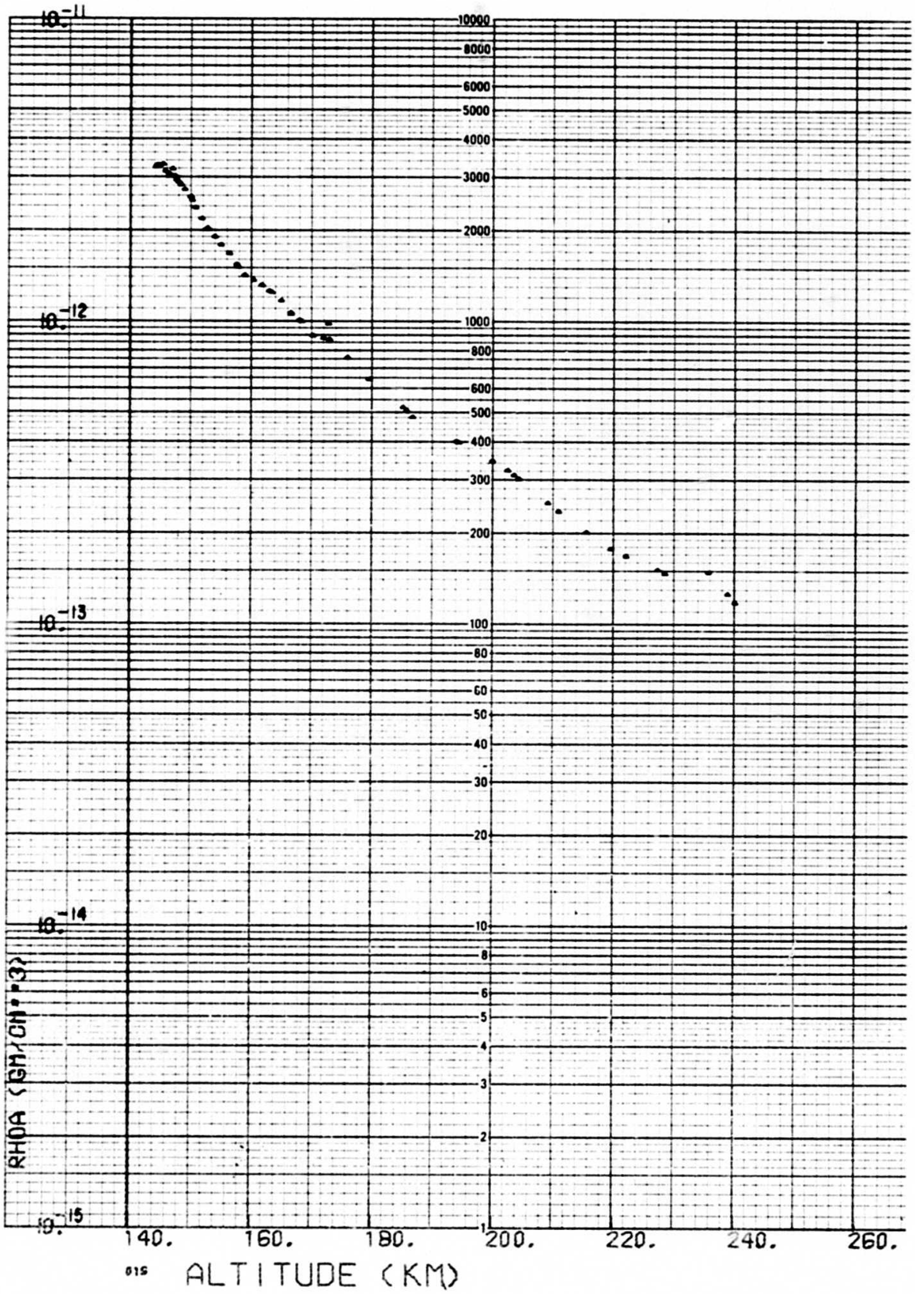

Fig. B-16. LOGACS Density Data for Rev. 13, Away from Perigee

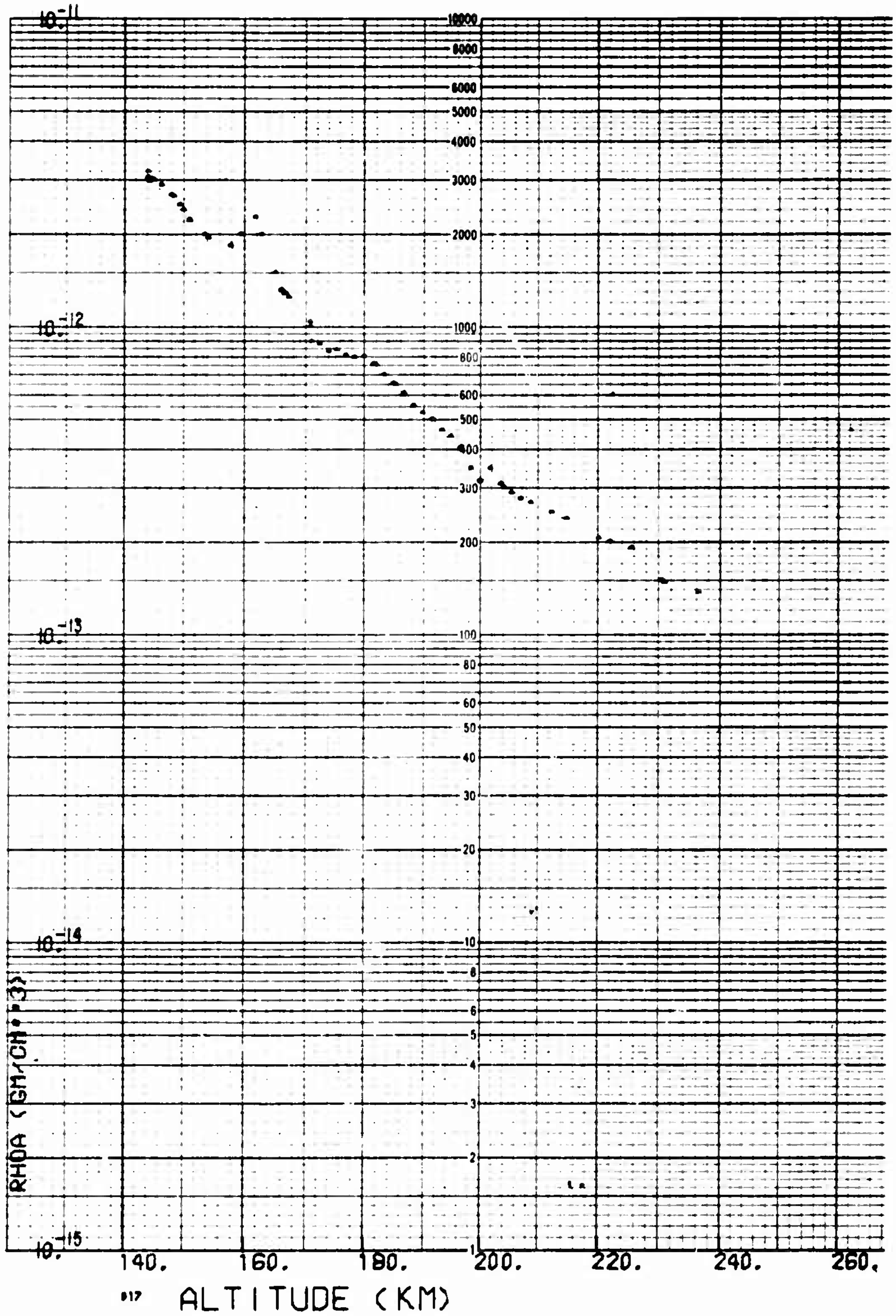

Fig. B-17. LOGACS Density Data for Rev. 14, Away from Perigee

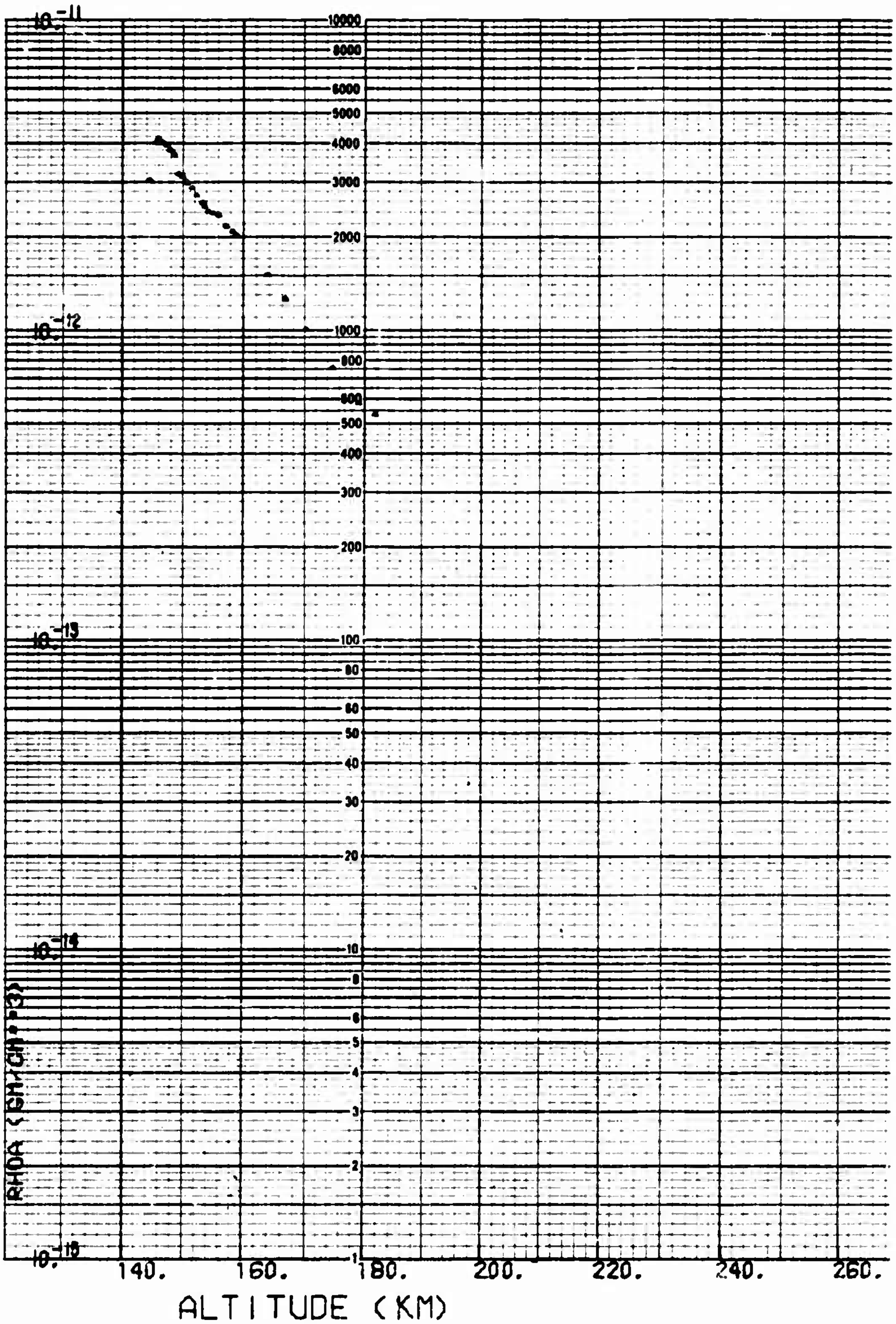

Fig. B-18. LOGACS Density Data for Rev. 18. Toward Perigee

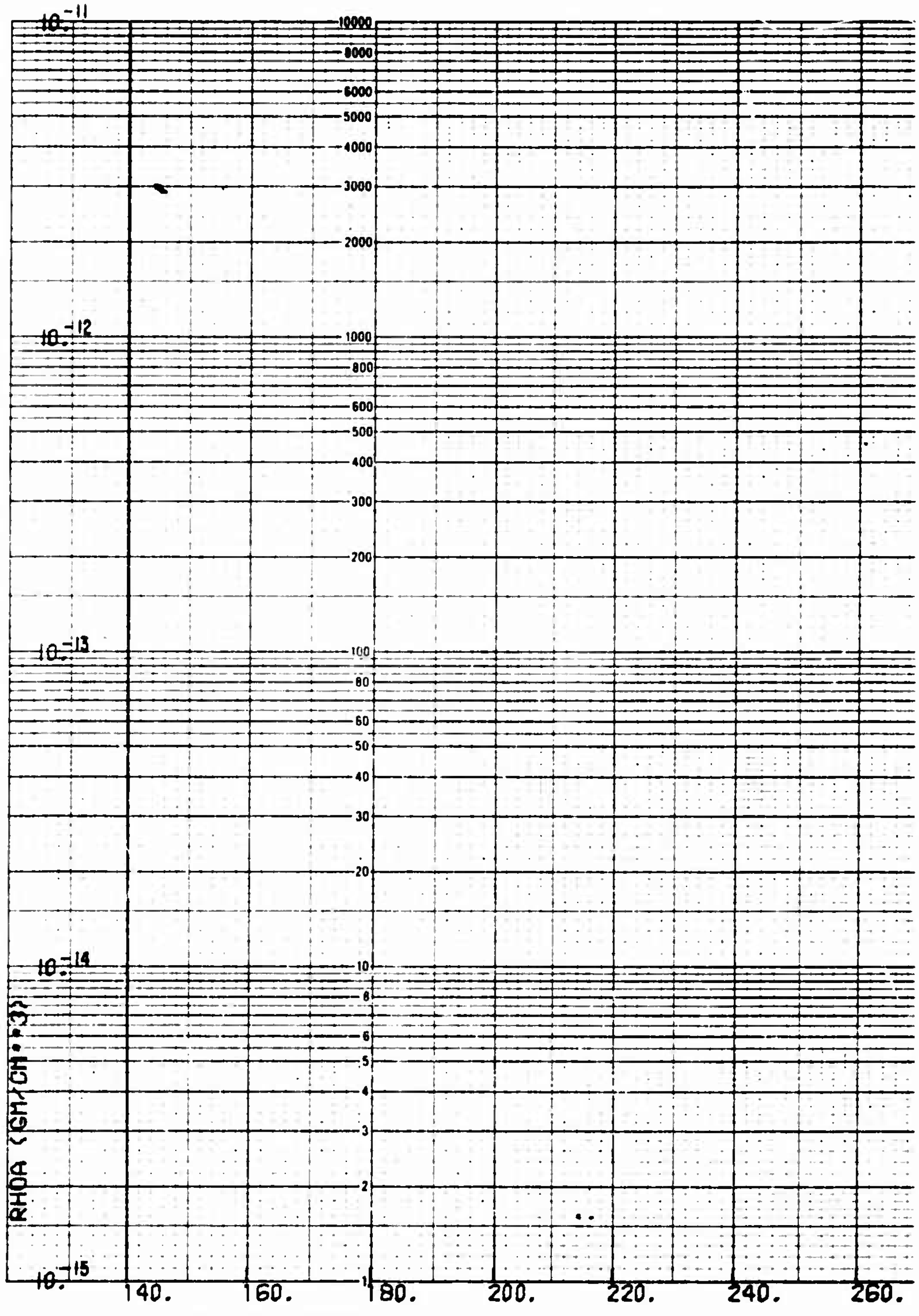

Fig. B-19. LOGACS Density Data for Rev. 18, Away from Perigee

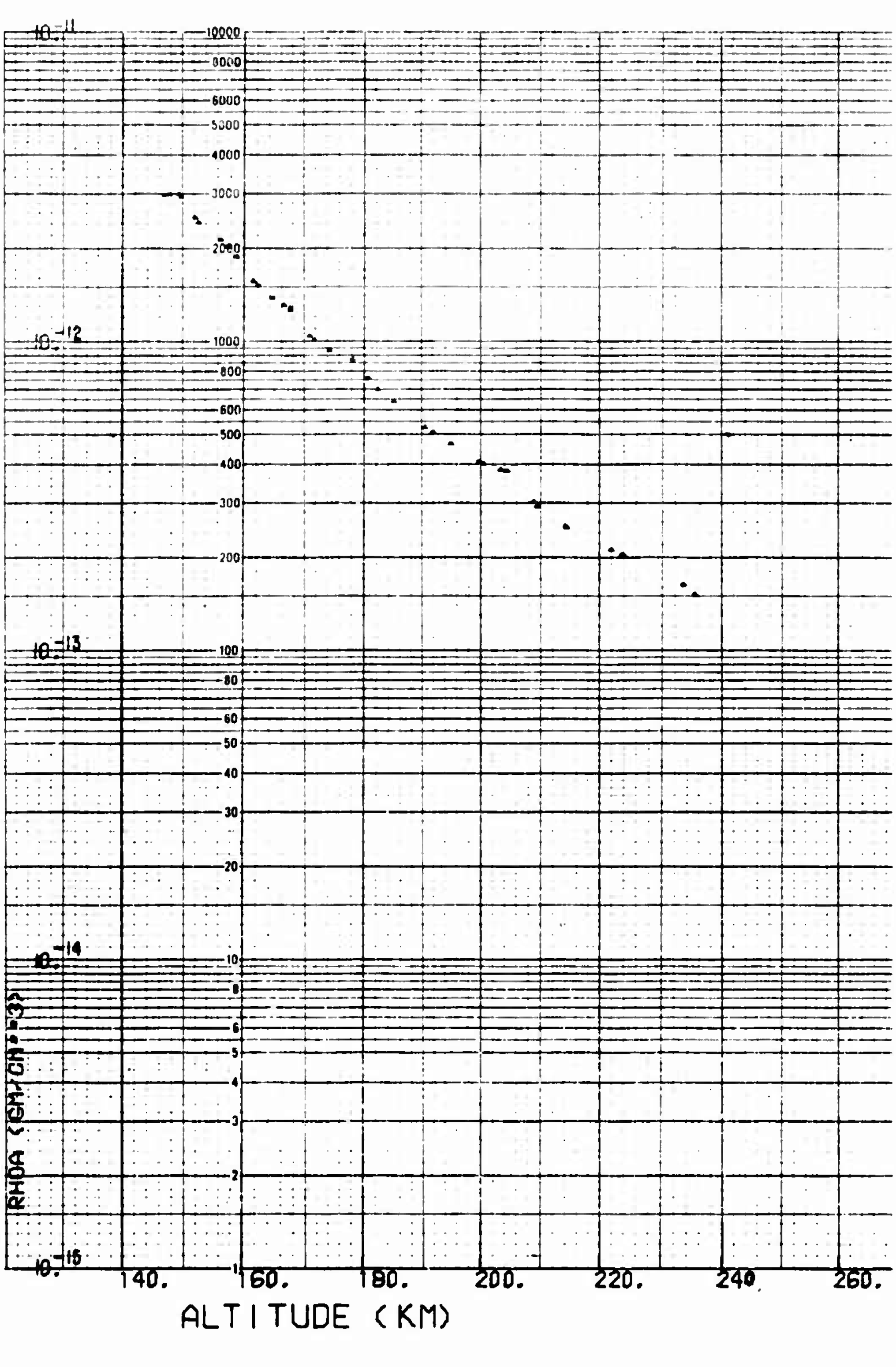

Fig. B-20. LOGACS Density Data for Rev. 20, Away from Perigee

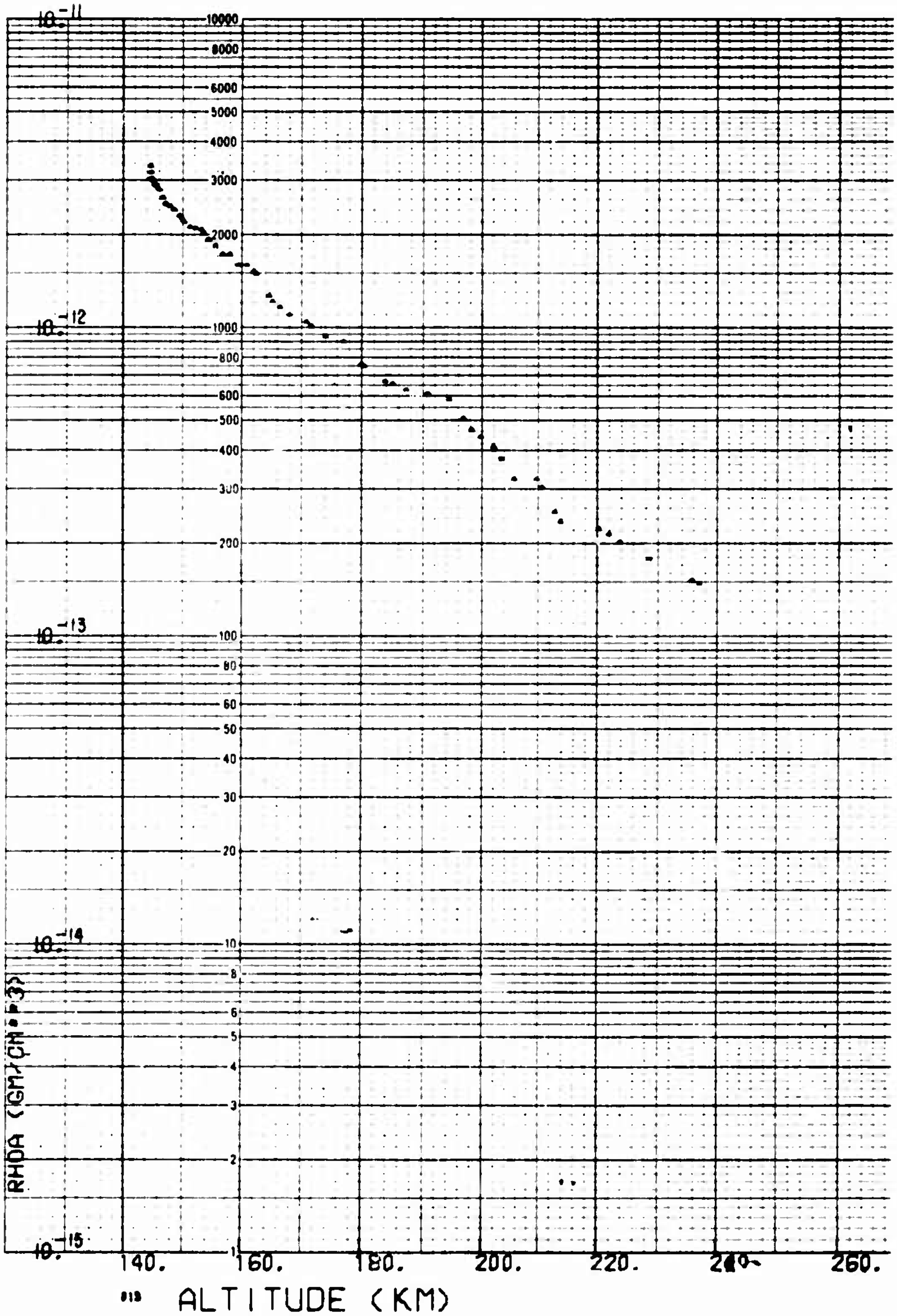

Fig. B-21. LOGACS Density Data for Rev. 21, Toward Perigee

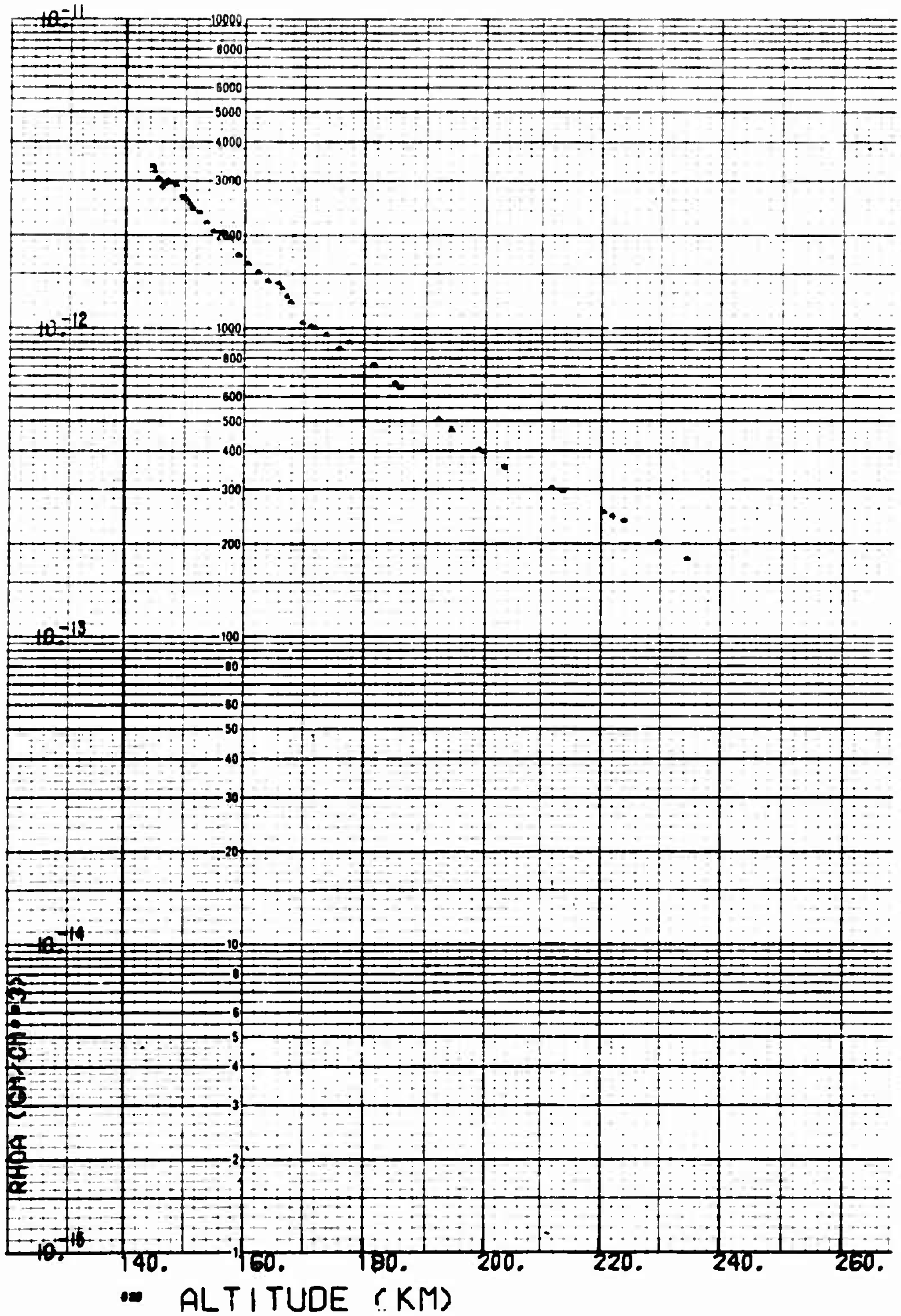

Fig. B-22. LOGACS Density Data for Rev. 21, Away from Perigee

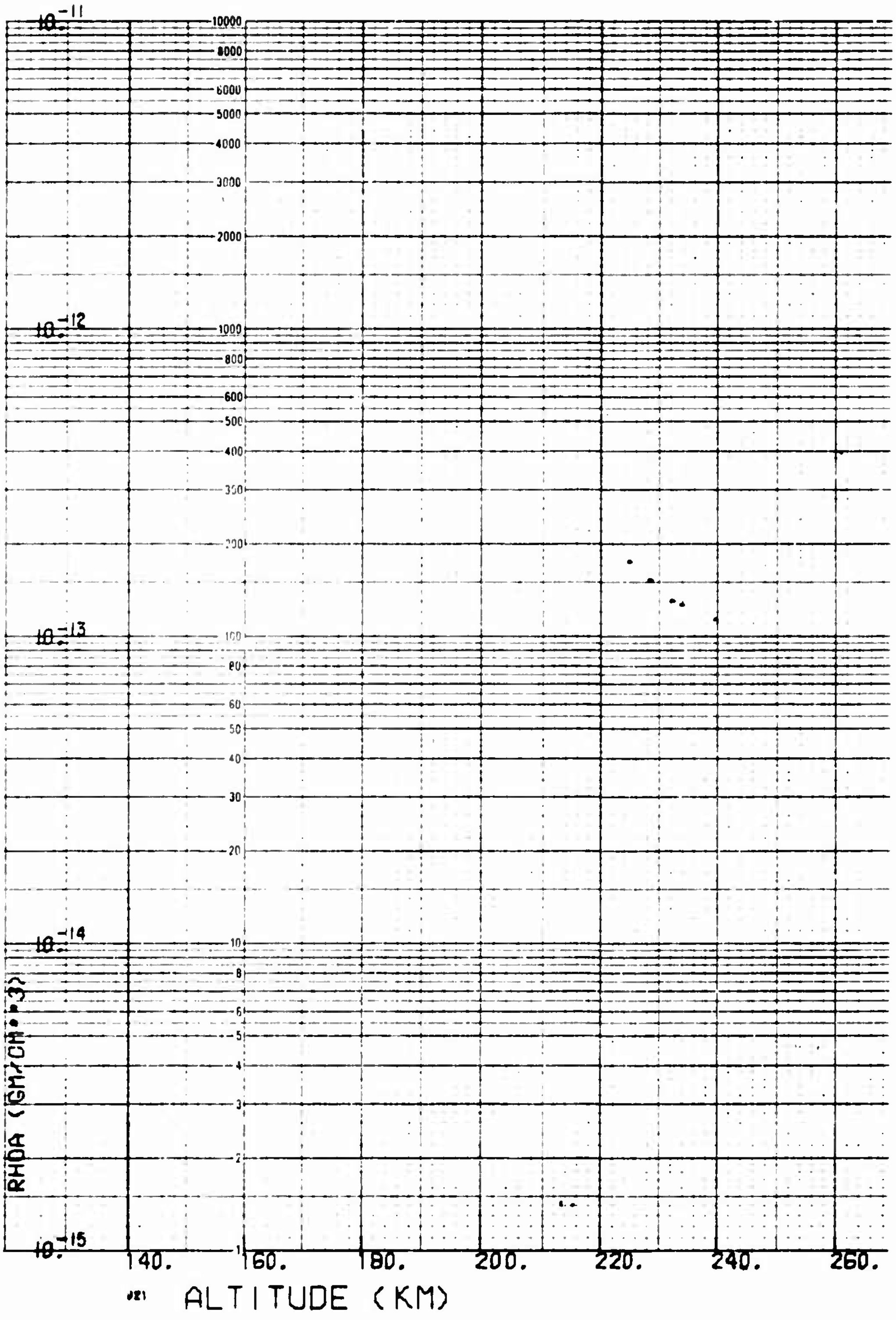

Fig. B-23. LOGACS Density Data for Rev. 22, Toward Perigee

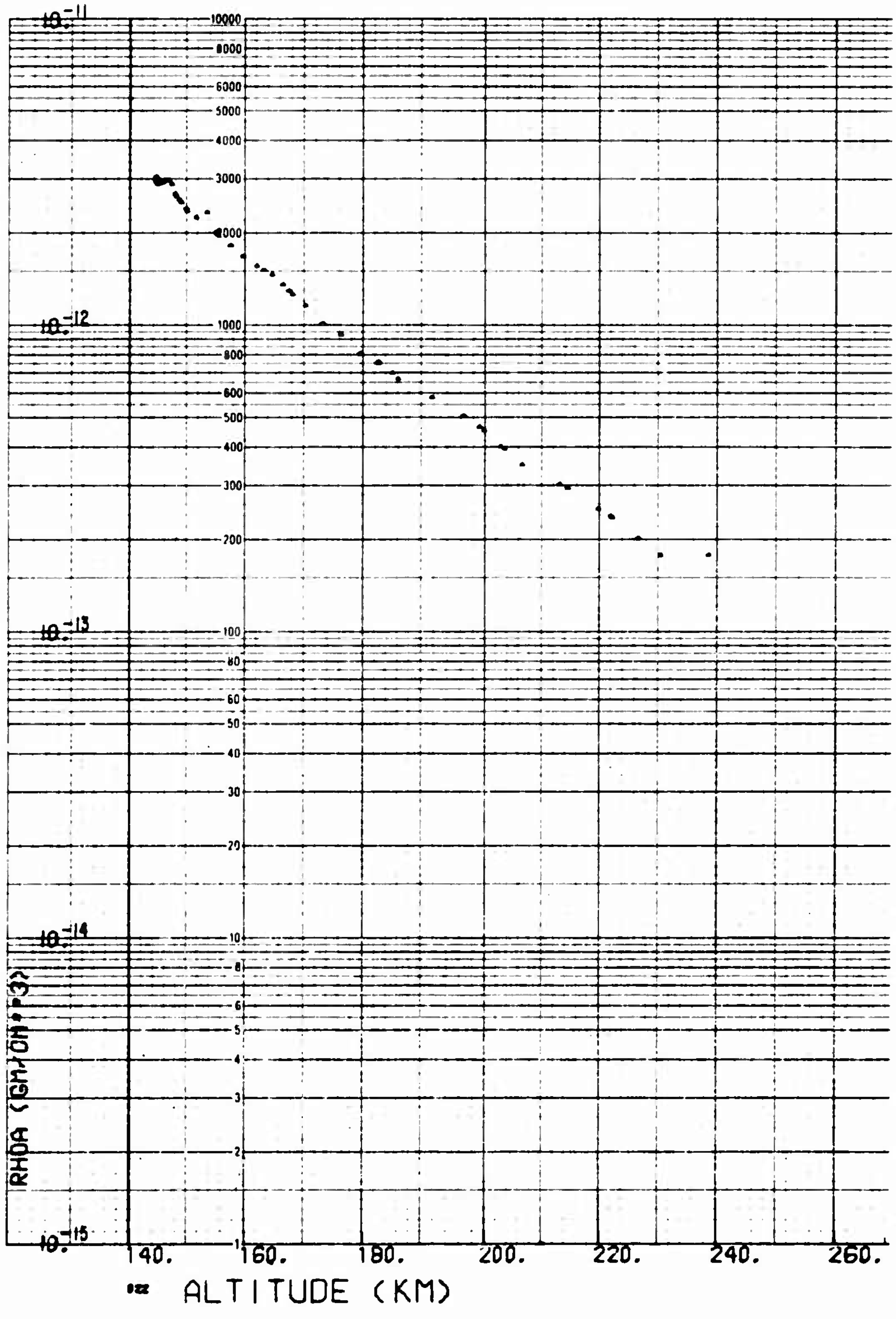

Fig. B-24. LOGACS Density Data for Rev. 24, Toward Perigee

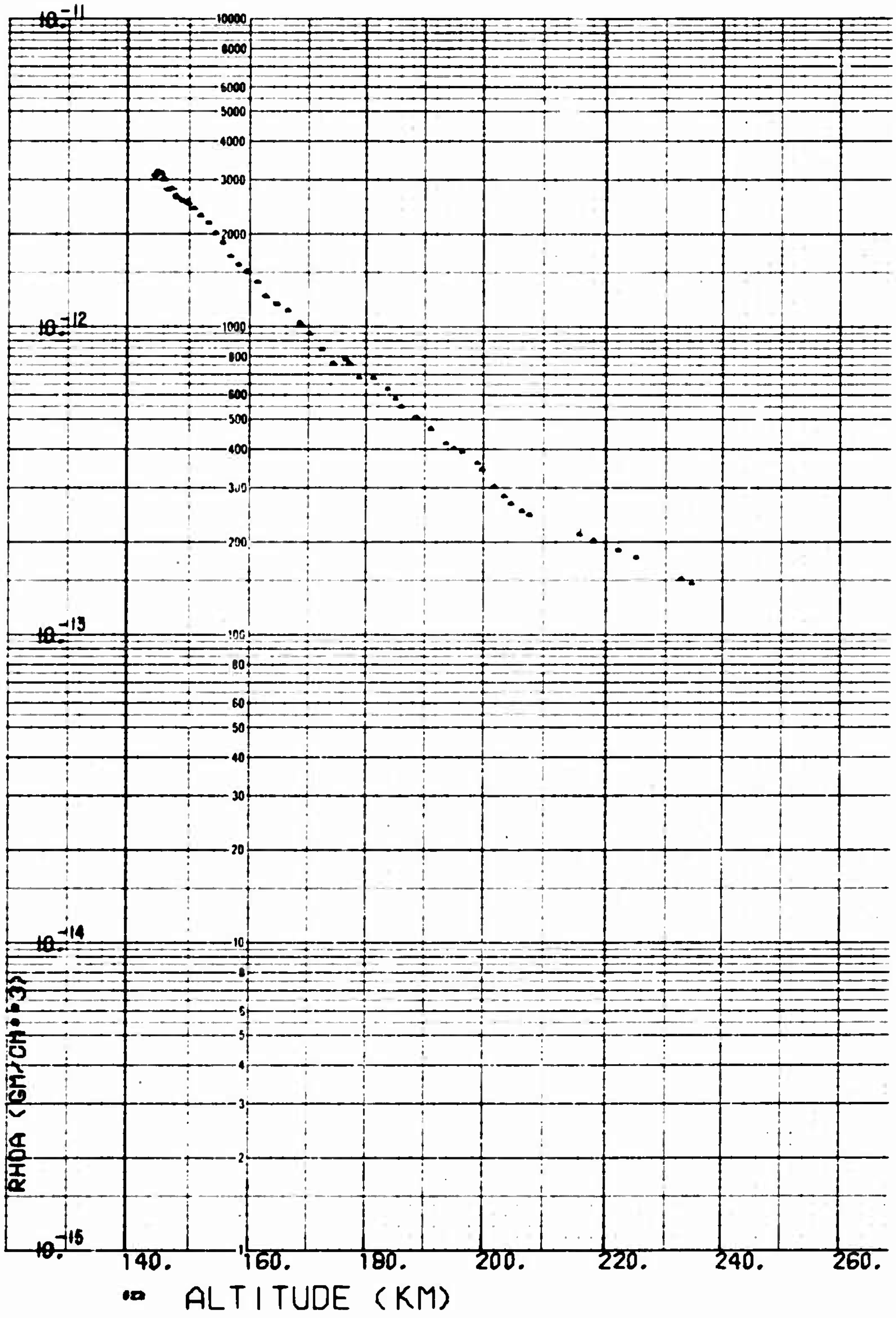

Fig. B-25. LOGACS Density Data for Rev. 24, Away from Perigee

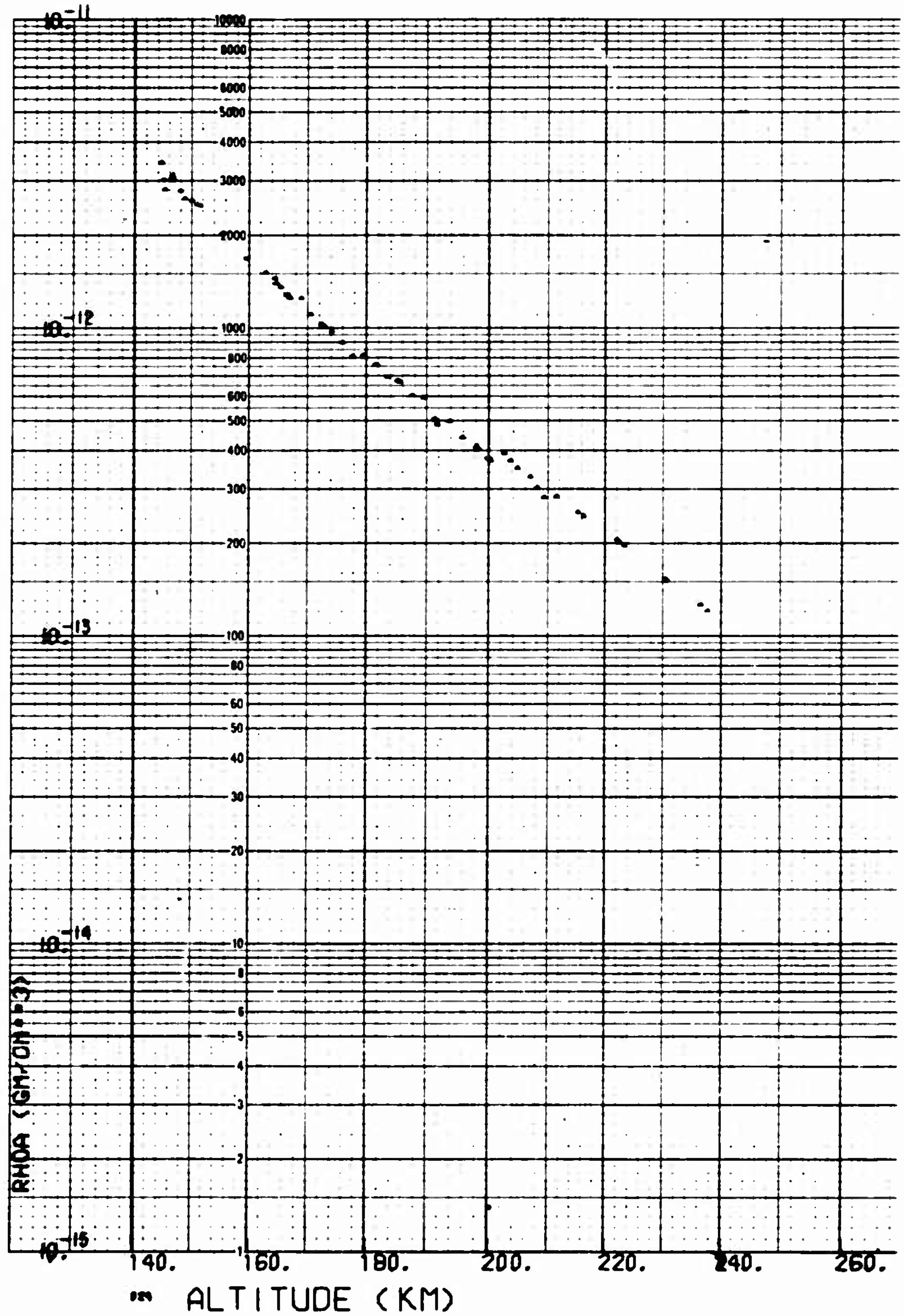

Fig. B-26. LOGACS Density Data for Rev. 25, Toward Perigee

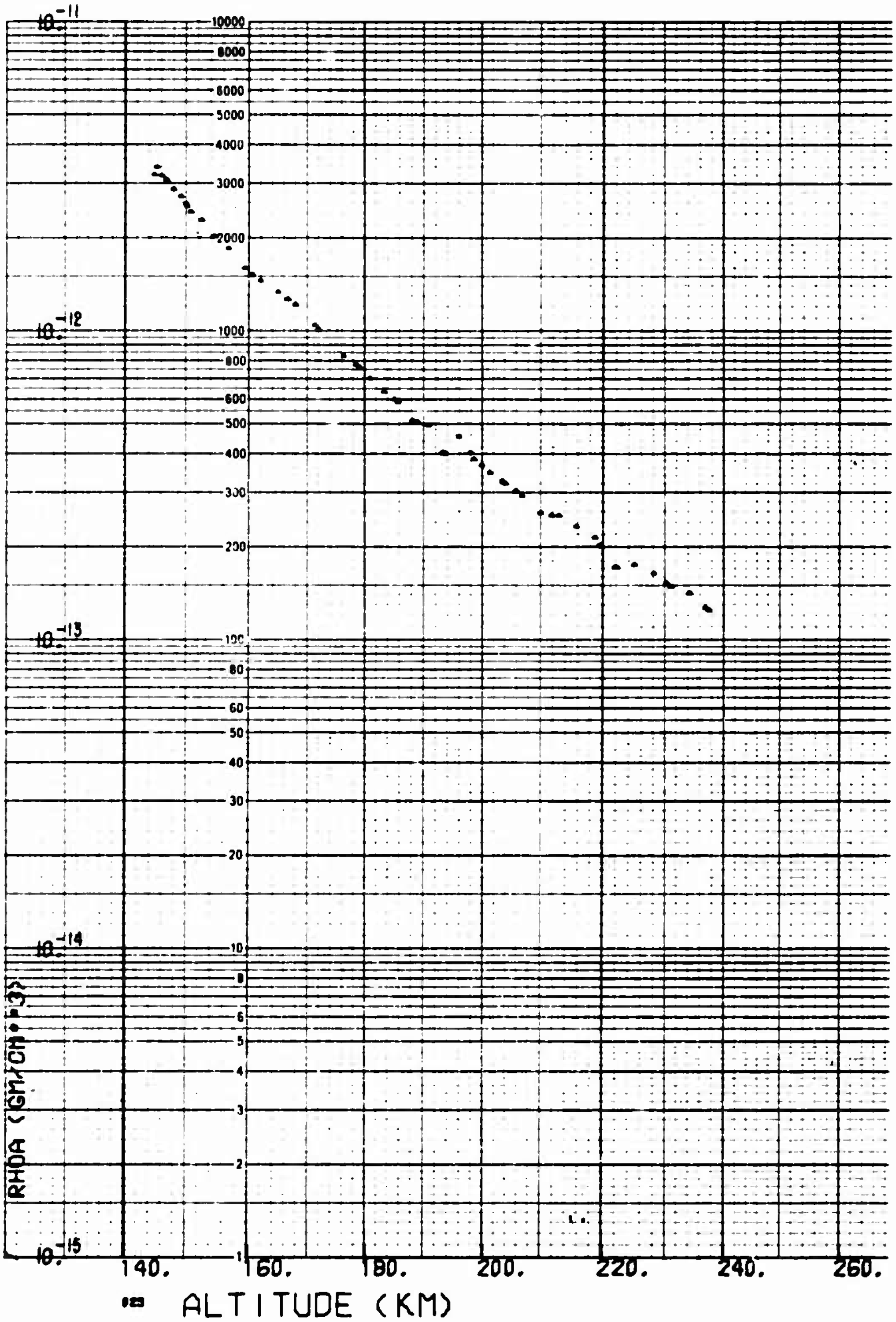

Fig. B-27. LOGACS Density Data for Rev. 25, Away from Perigee

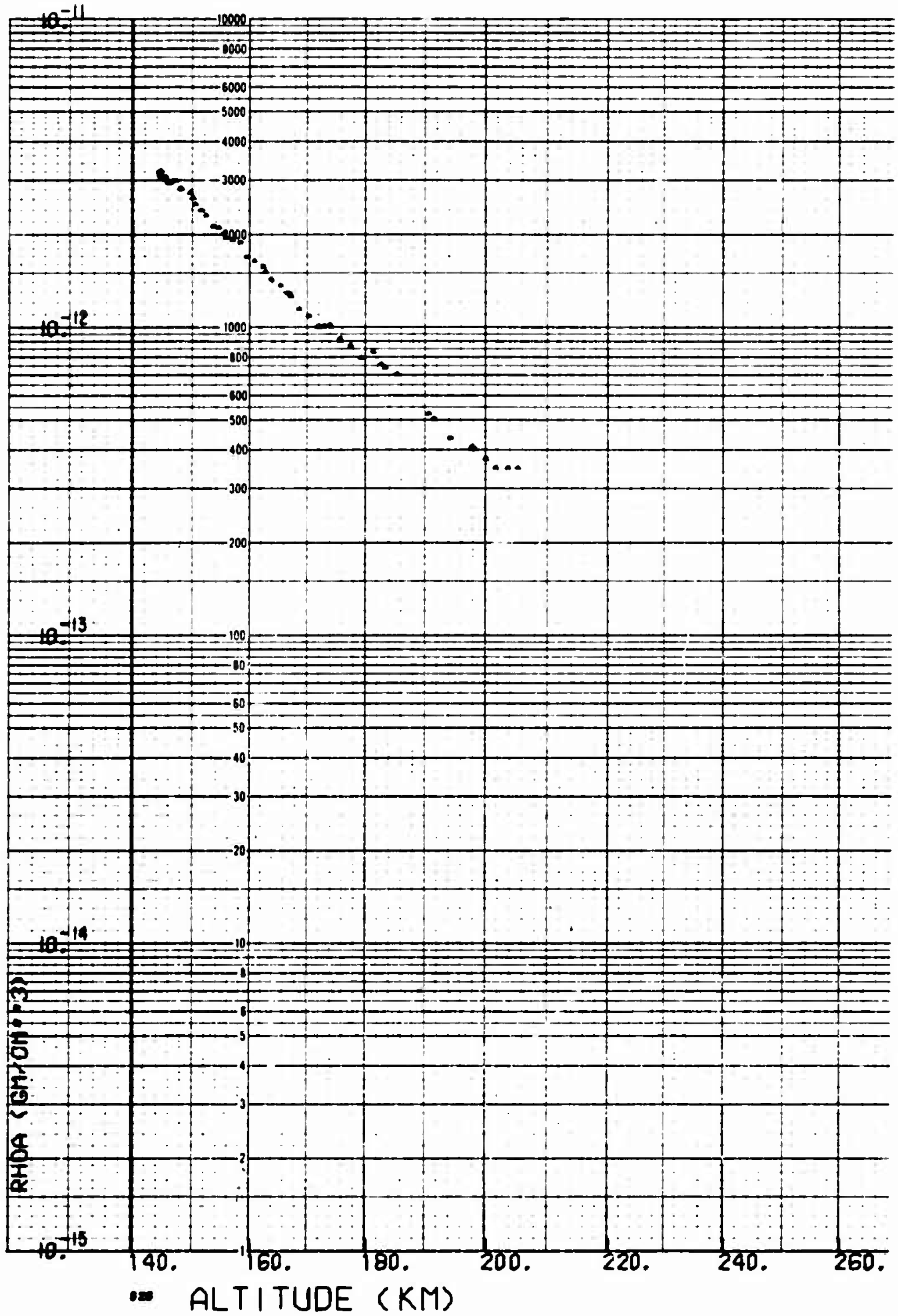

Fig. B-28. LOGACS Density Data for Rev. 26, Toward Perigee

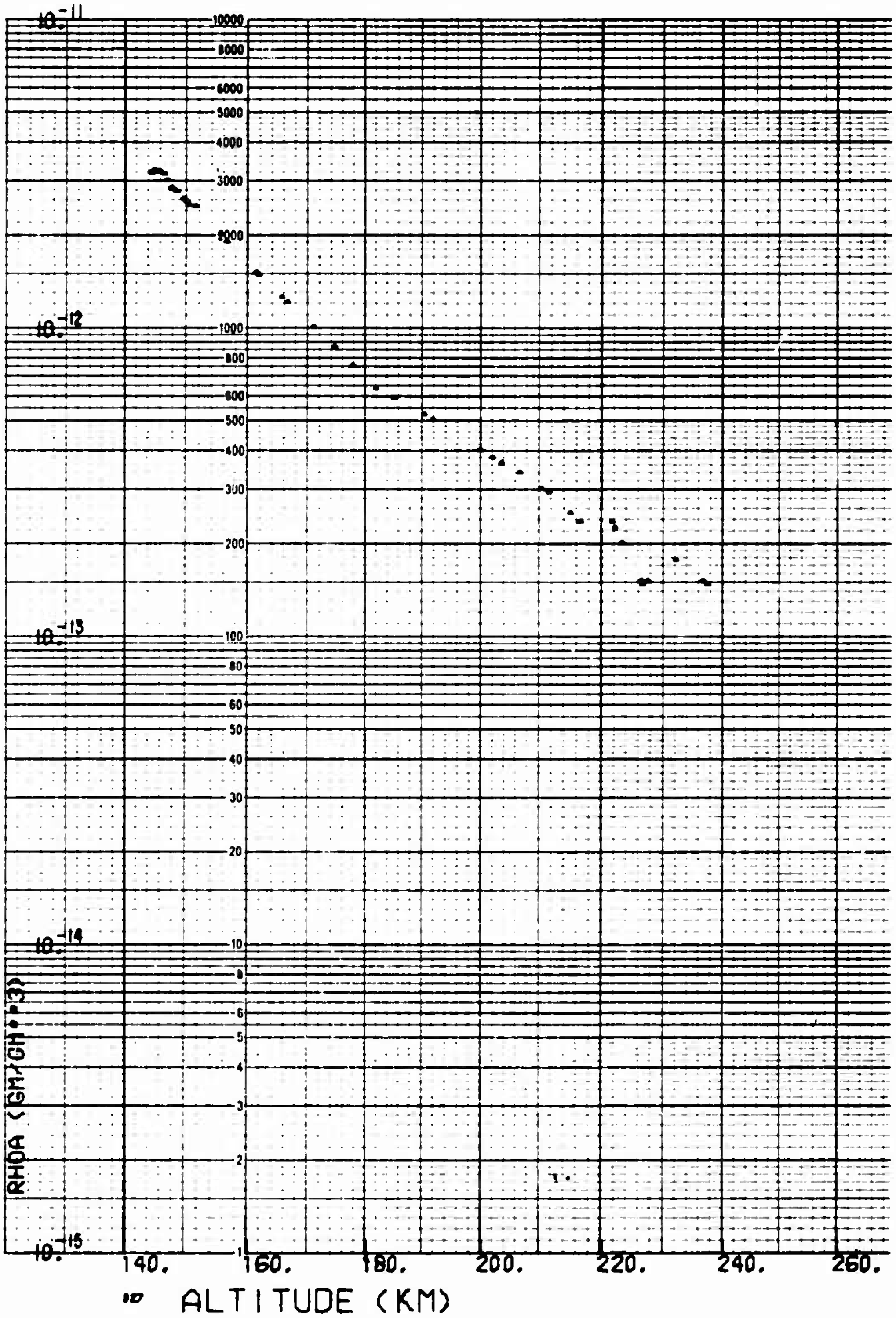

Fig. B-29. LOGACS Density Data for Rev. 26, Away from Perigee

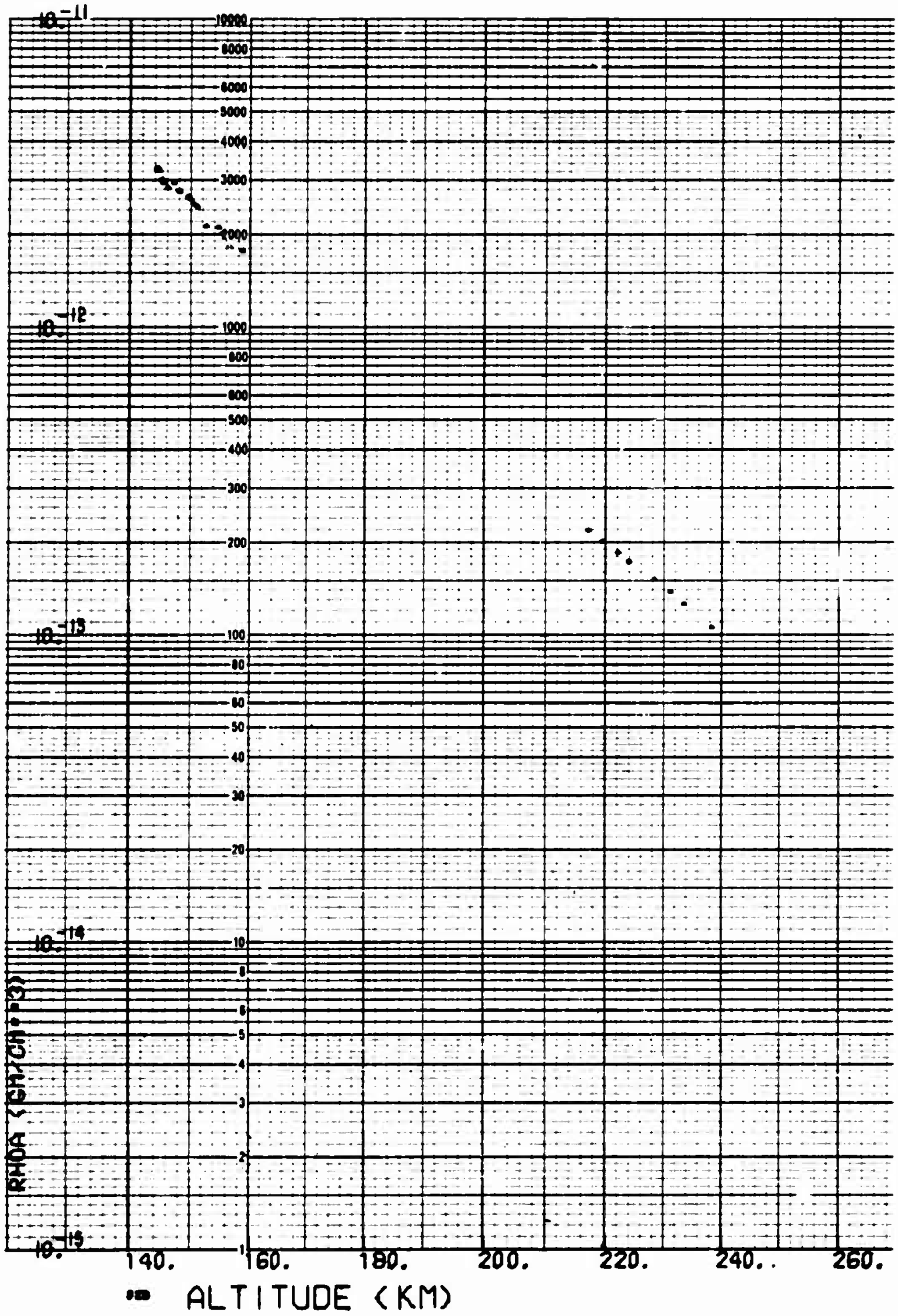

Fig. B-30. LOGACS Density Data for Rev. 27, Toward Perigee

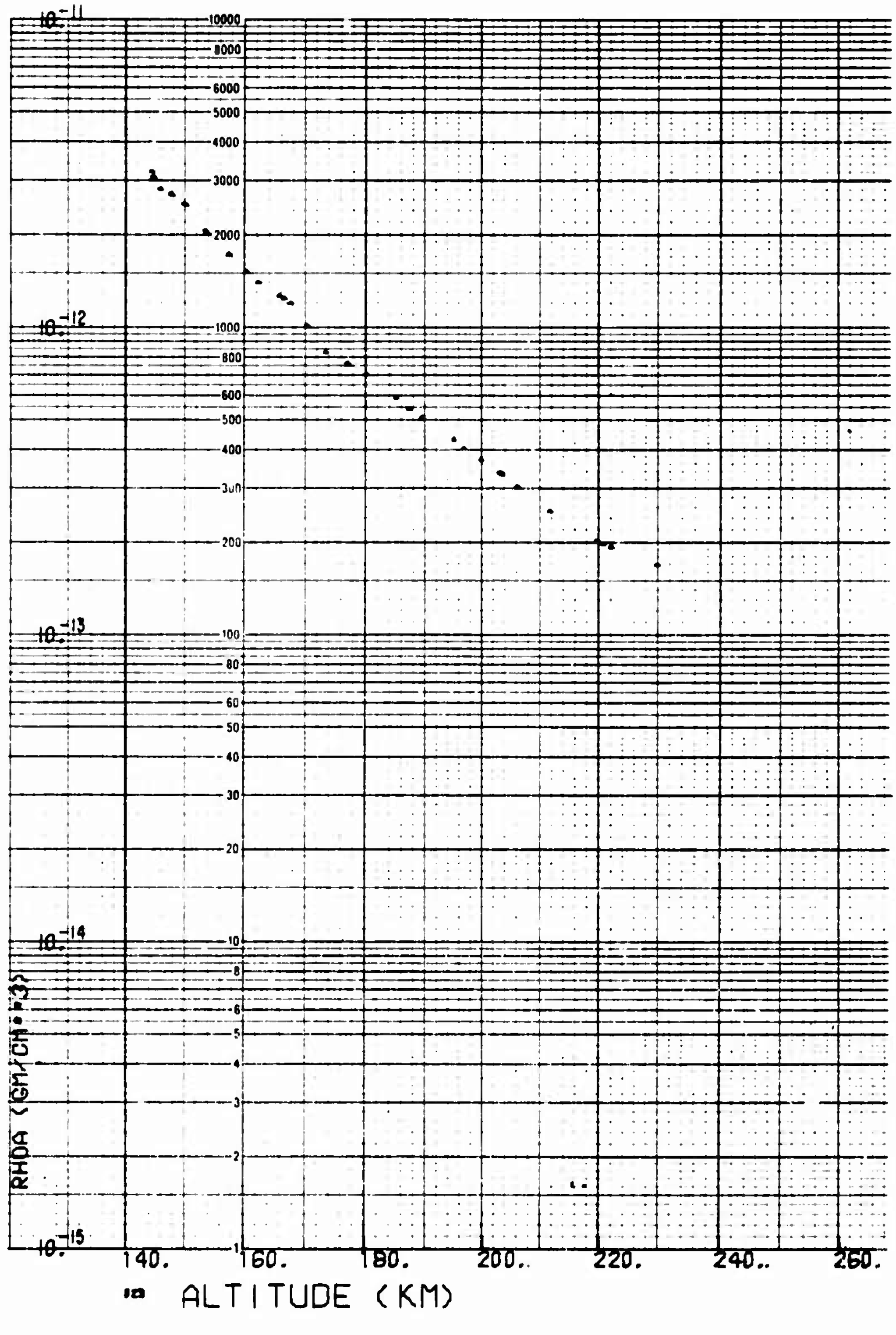

Fig. B-31. LOGACS Density Data for Rev. 27, Away from Perigee

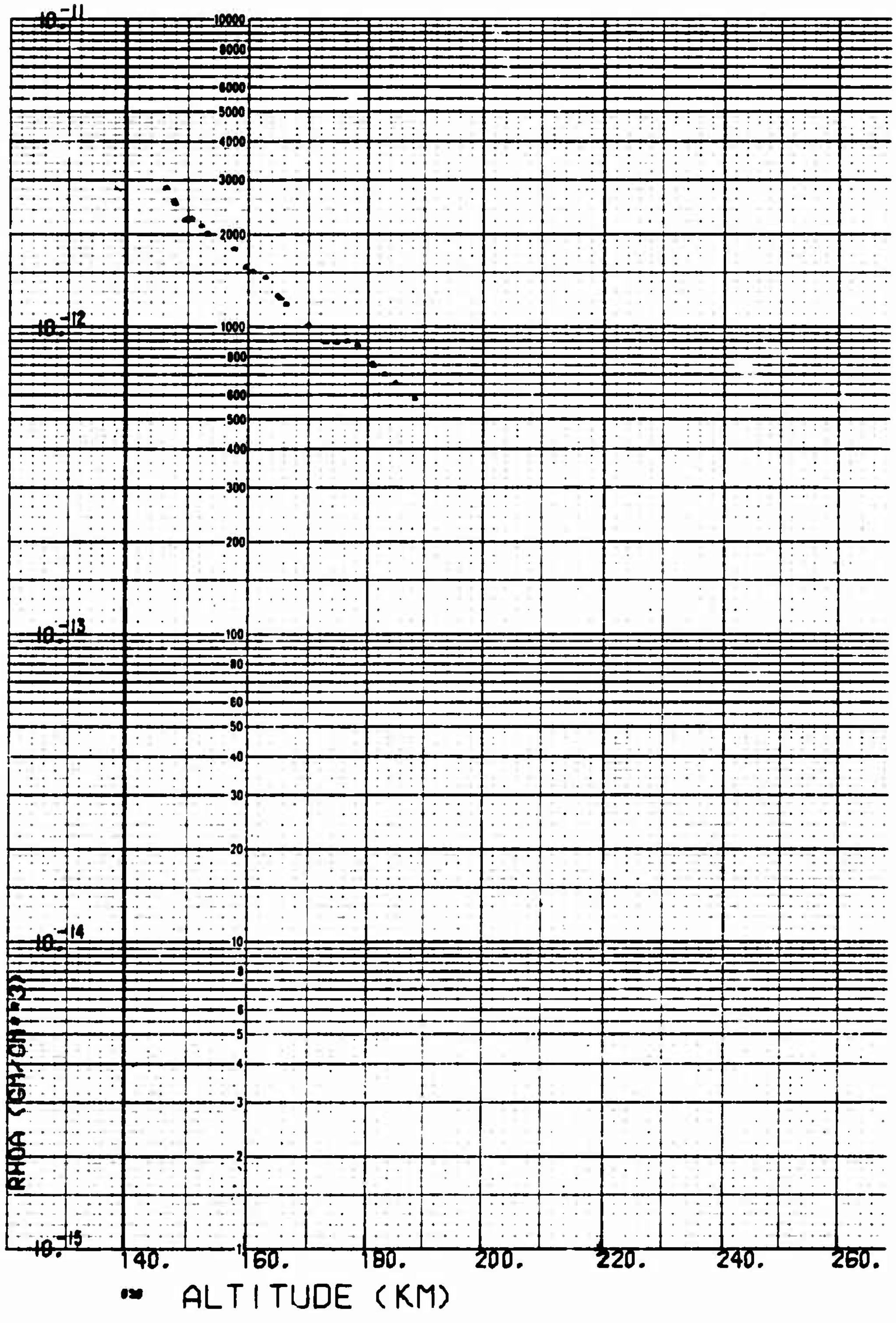

Fig. B-32. LOGACS Density Data for Rev. 28, Toward Perigee

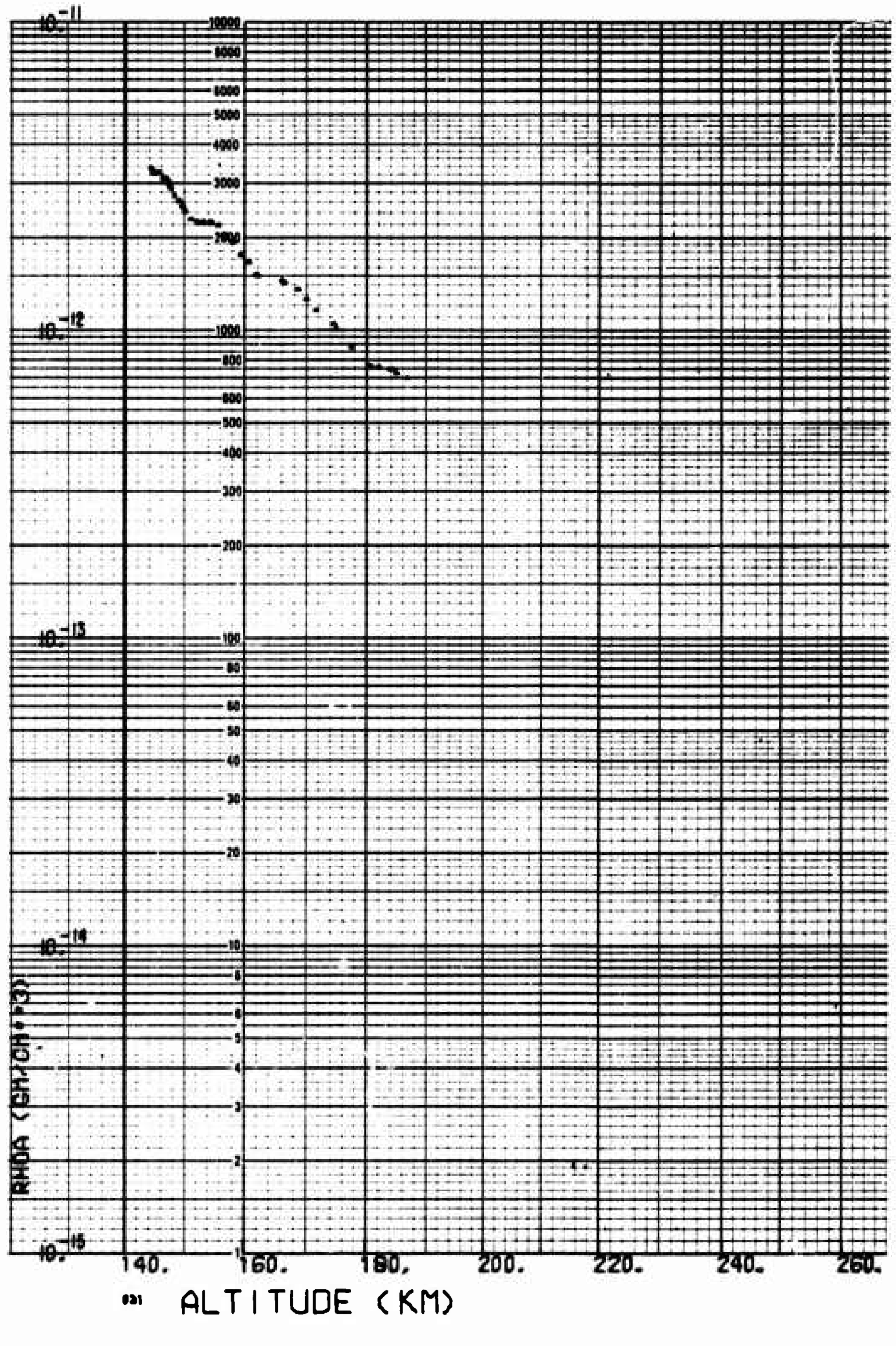

Fig. B-33. LOGACS Density Data for Rev. 29, Toward Perigee

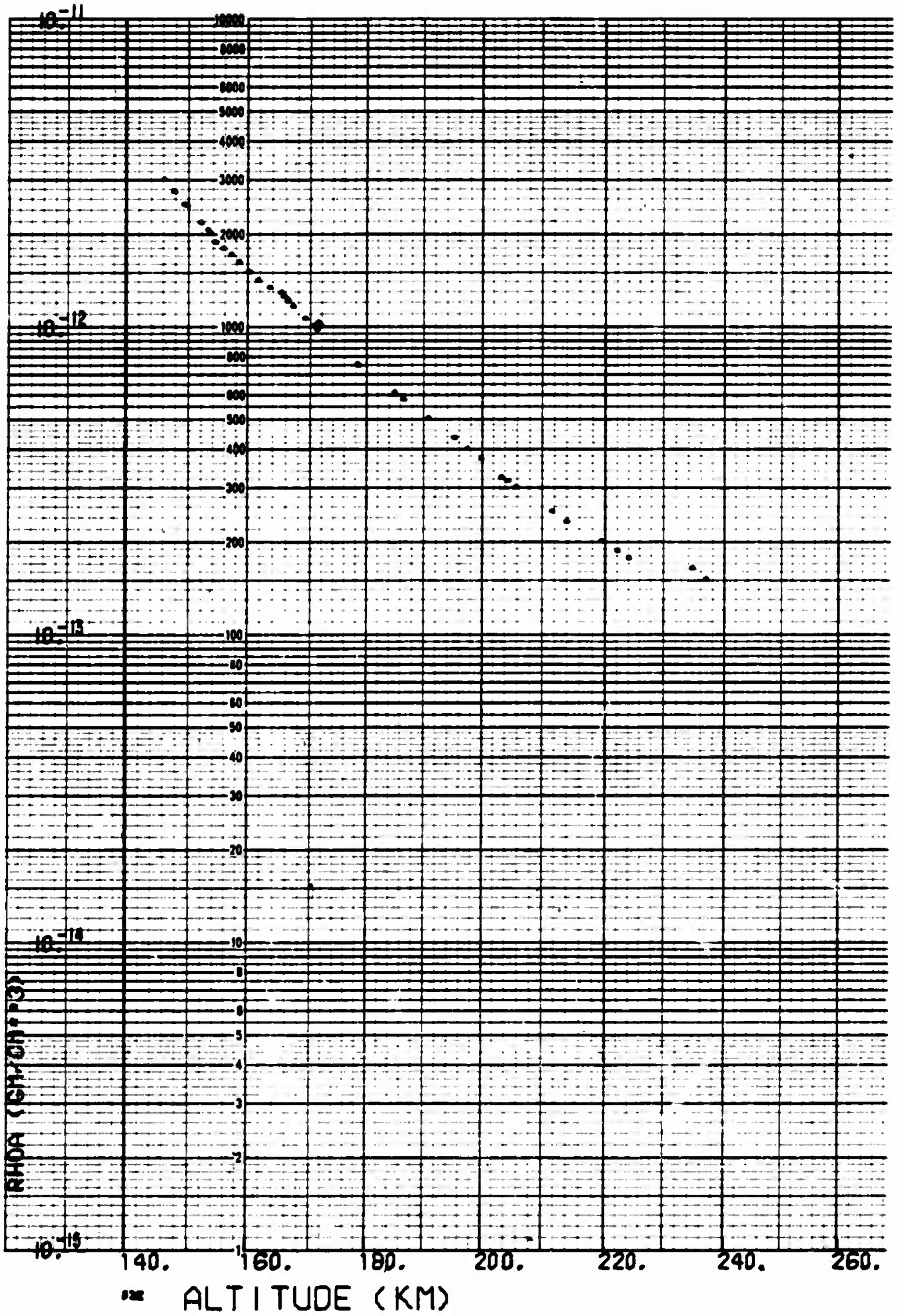

Fig. B-34. LOGACS Density Data for Rev. 29, Away from Perigee

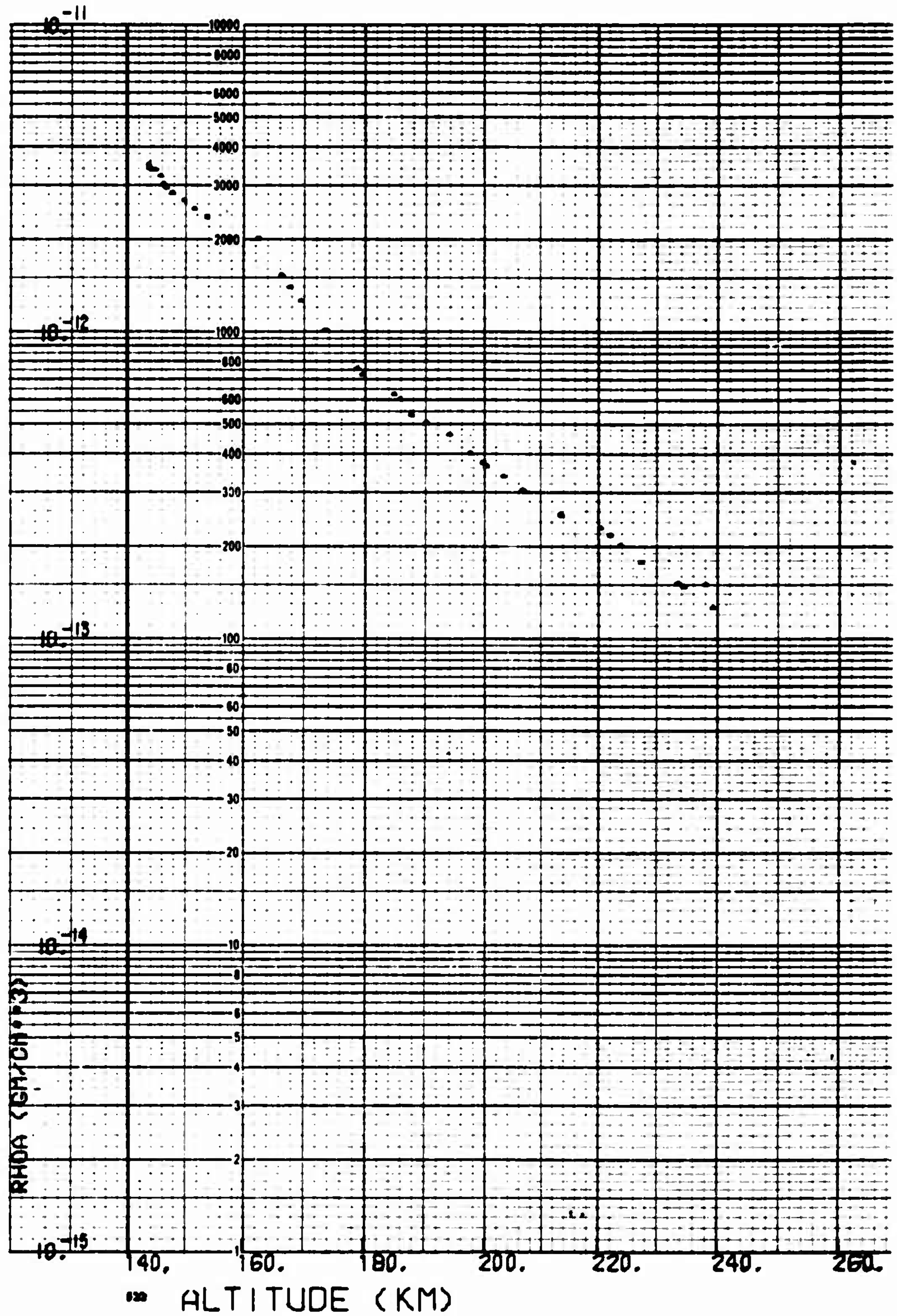

Fig. B-35. LOGACS Density Data for Rev. 30, Toward Perigee

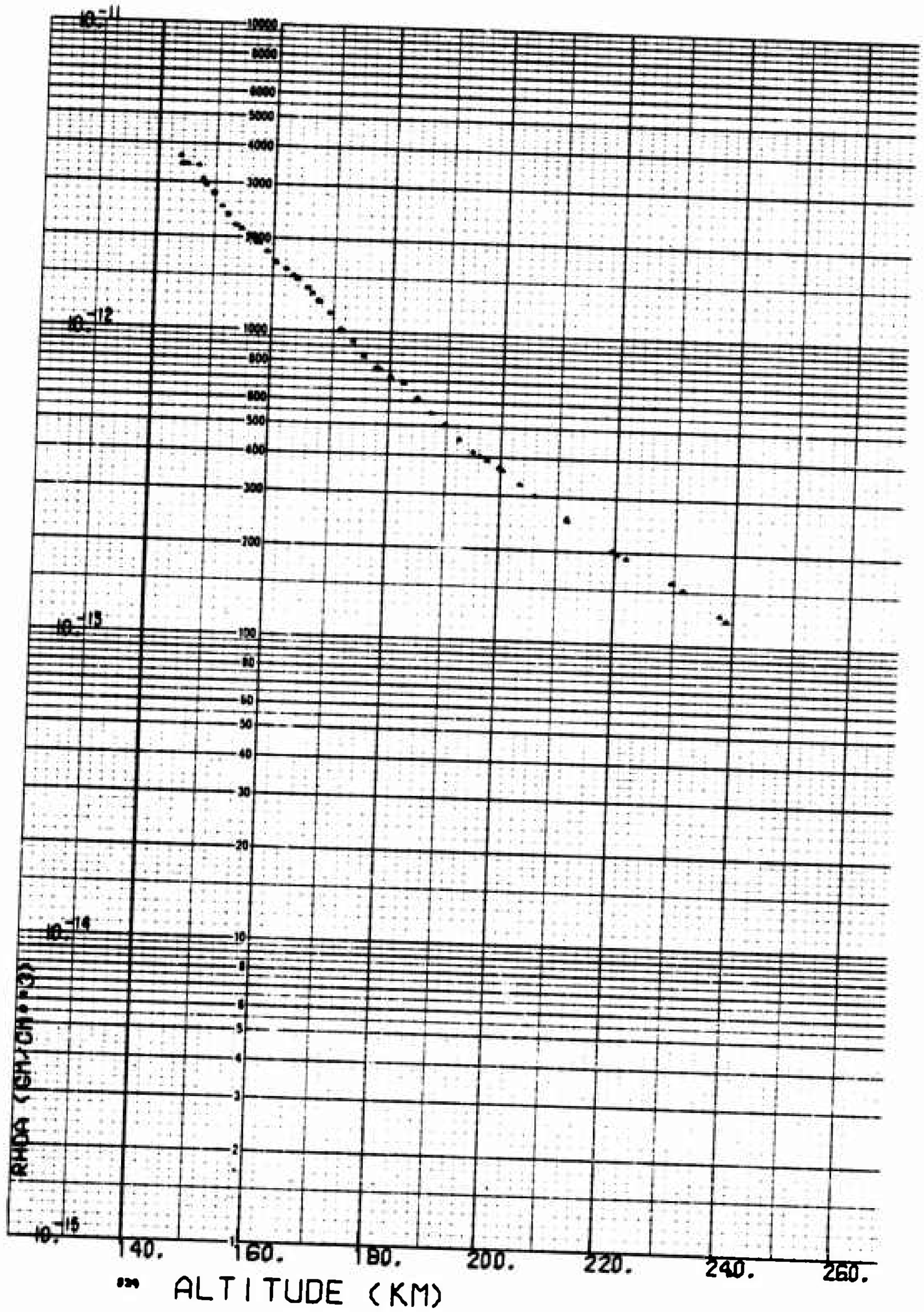

Fig. B-36. LOGACS Density Data for Rev. 30, Away from Perigee

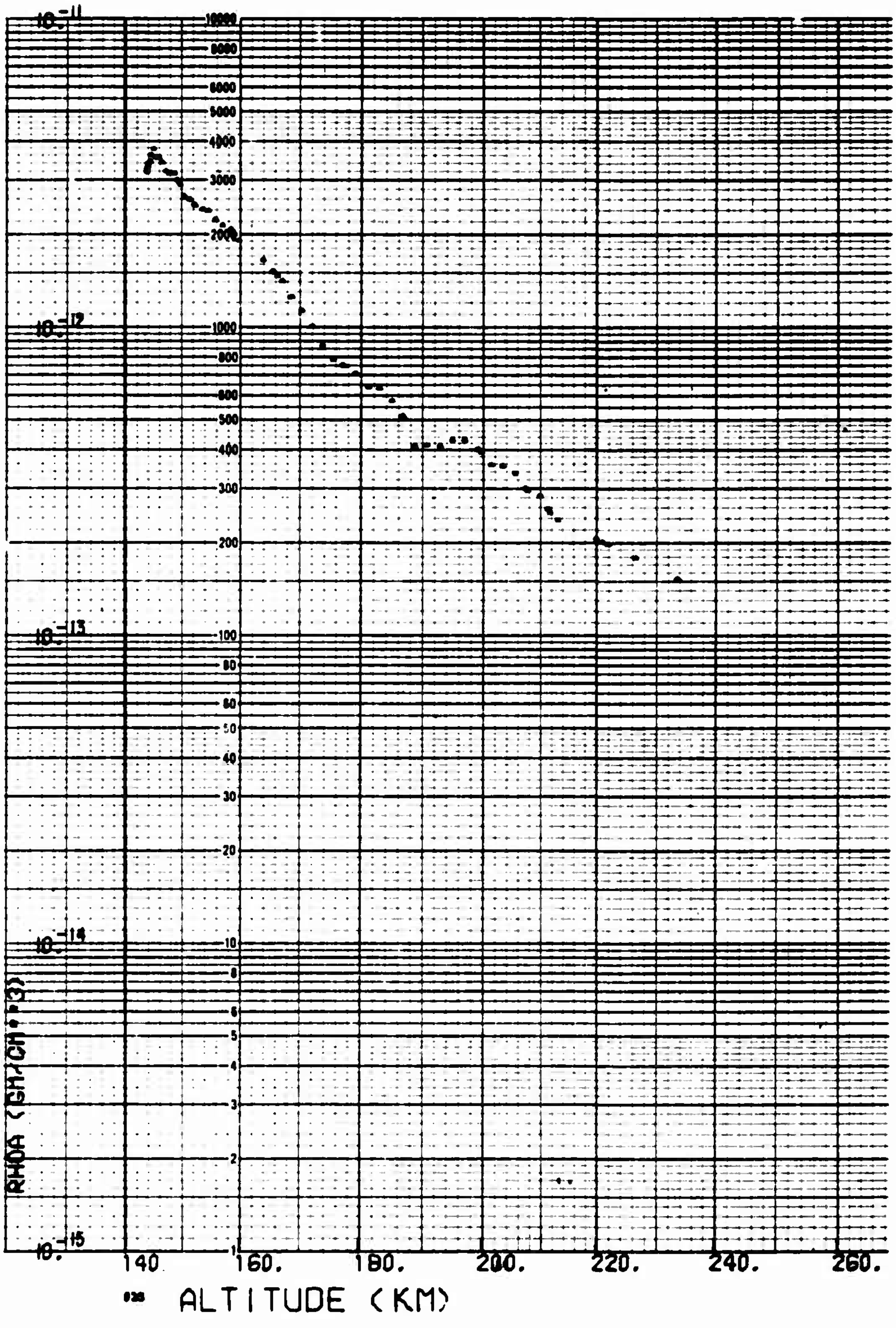

Fig. B-37. LOGACS Density Data for Rev. 31, Toward Perigee

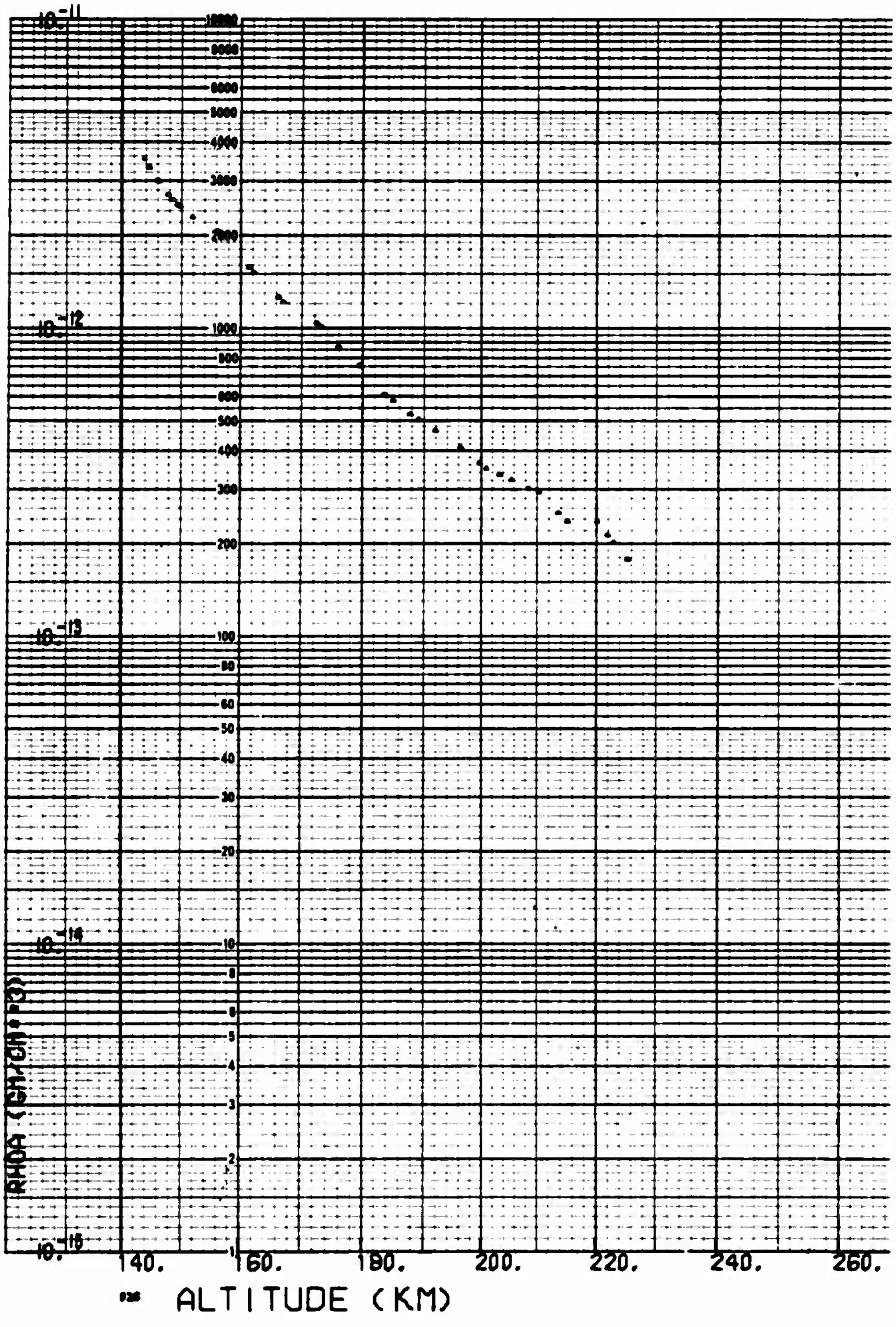

Fig. B-38. LOGACS Density Data for Rev. 31, Away from Perigee

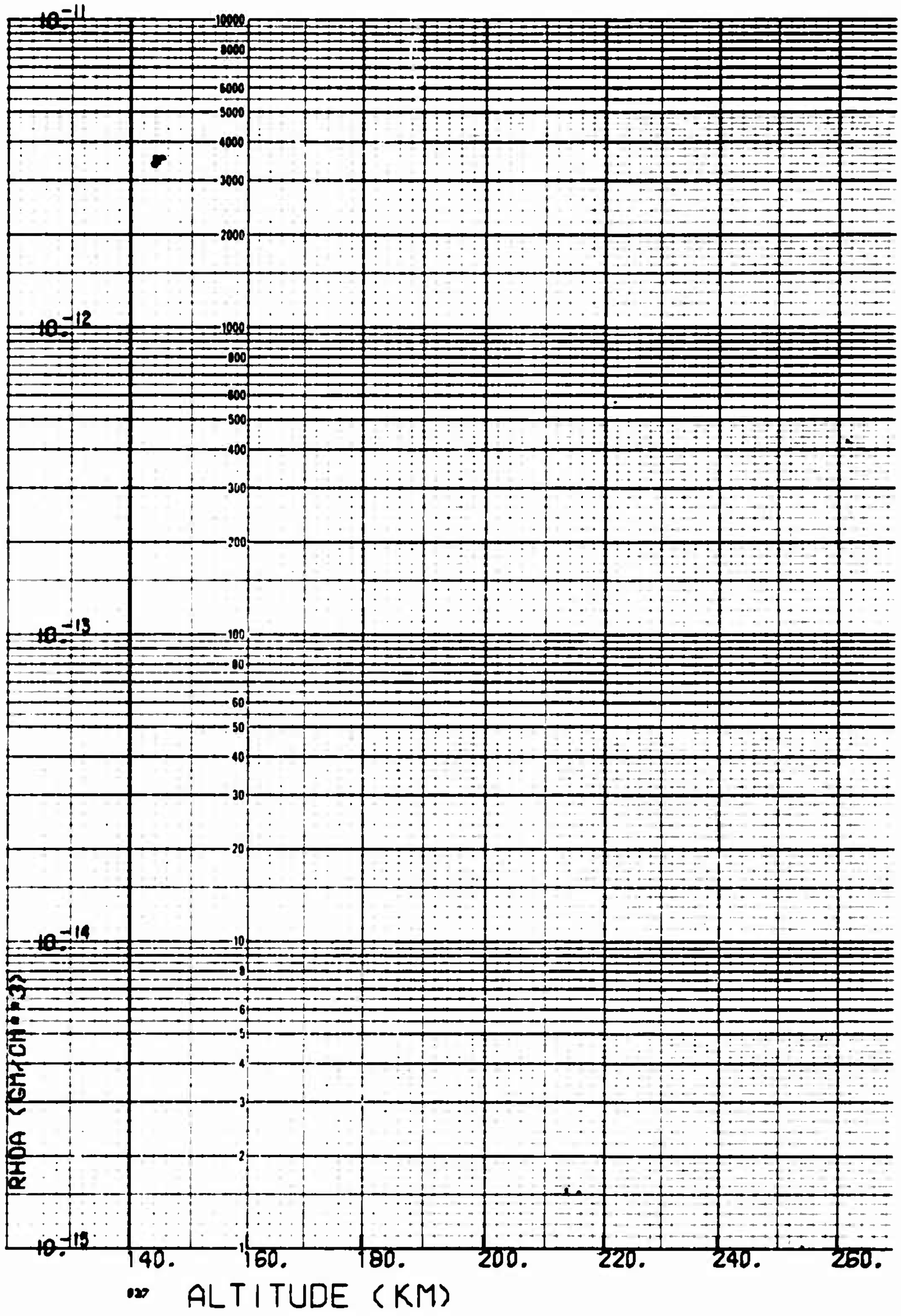

Fig. B-39. LOGACS Density Data for Rev. 32, Toward Perigee

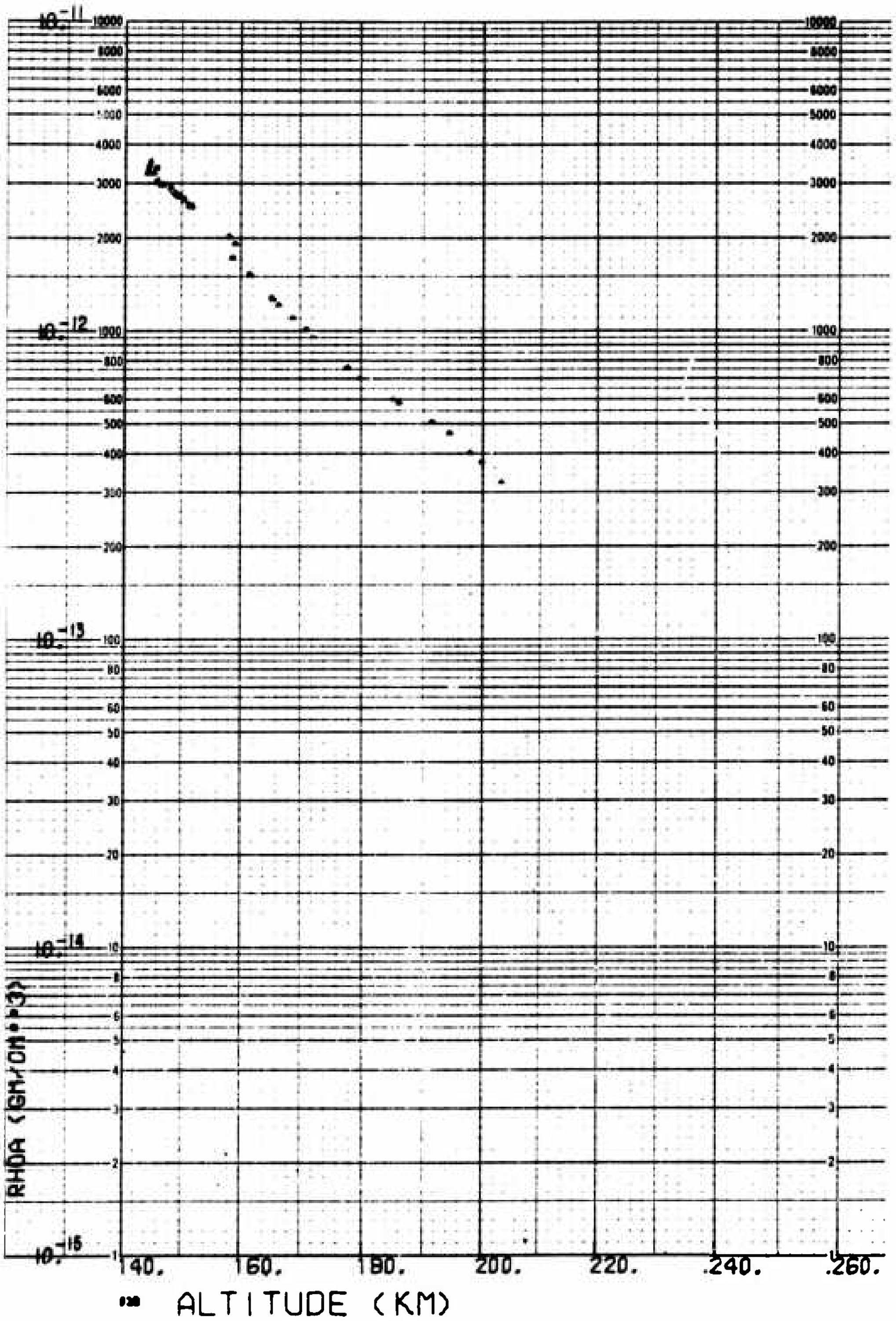

Fig. B-40. LOGACS Density Data for Rev. 32, Away from Perigee

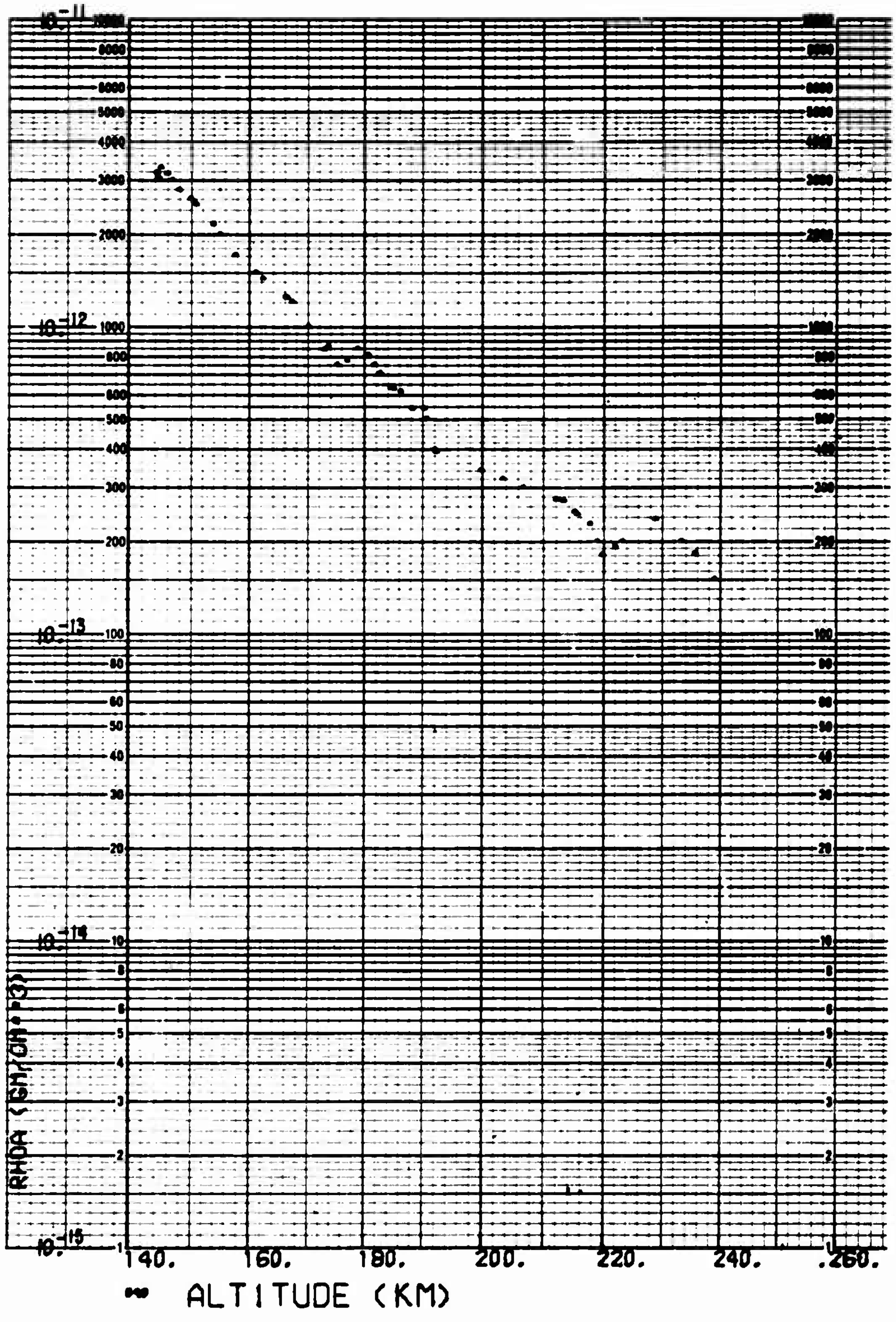

Fig. B-41. LOGACS Density Data for Rev. 33, Toward Perigee

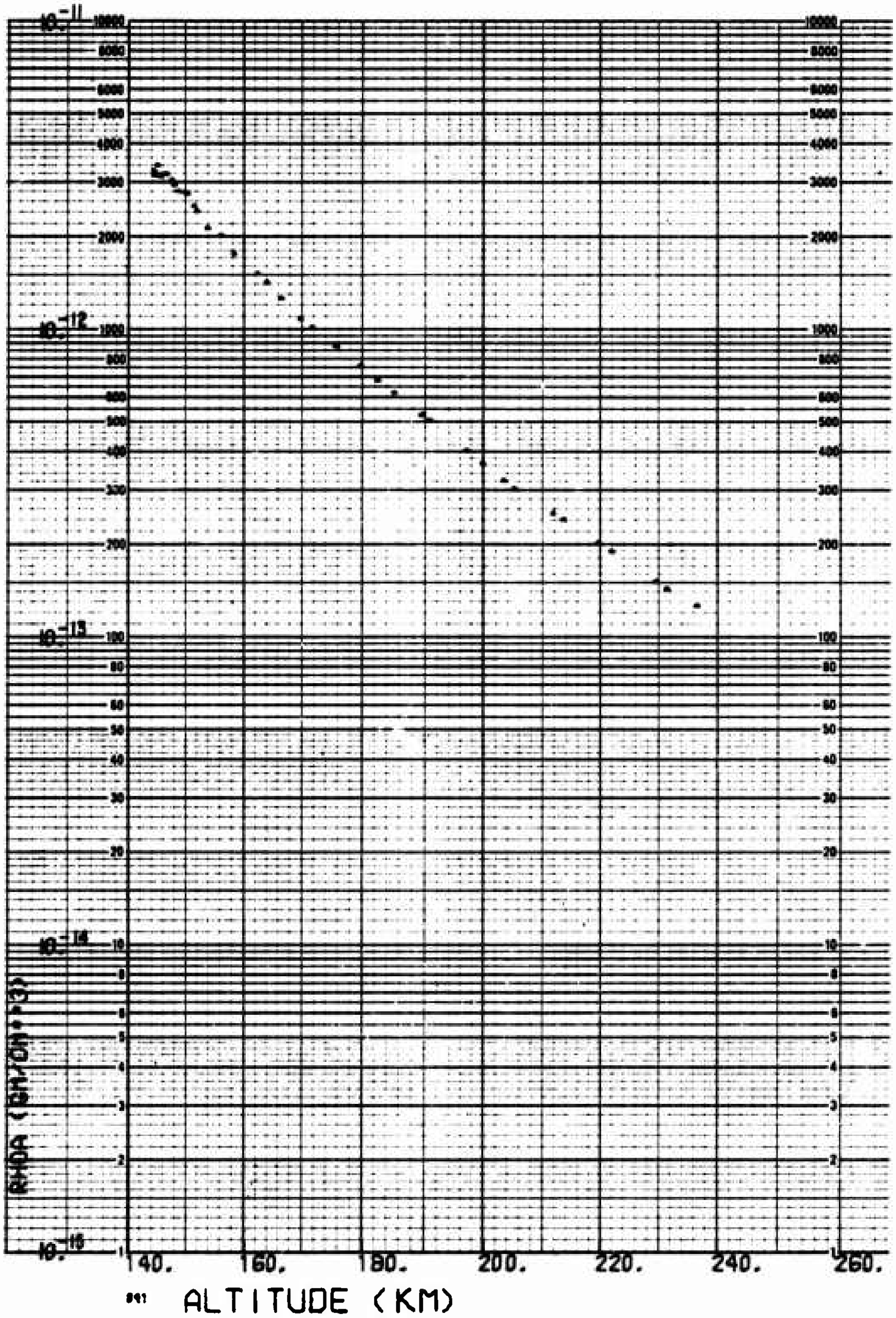

Fig. B-42. LOGACS Density Data for Rev. 33, Away from Perigee

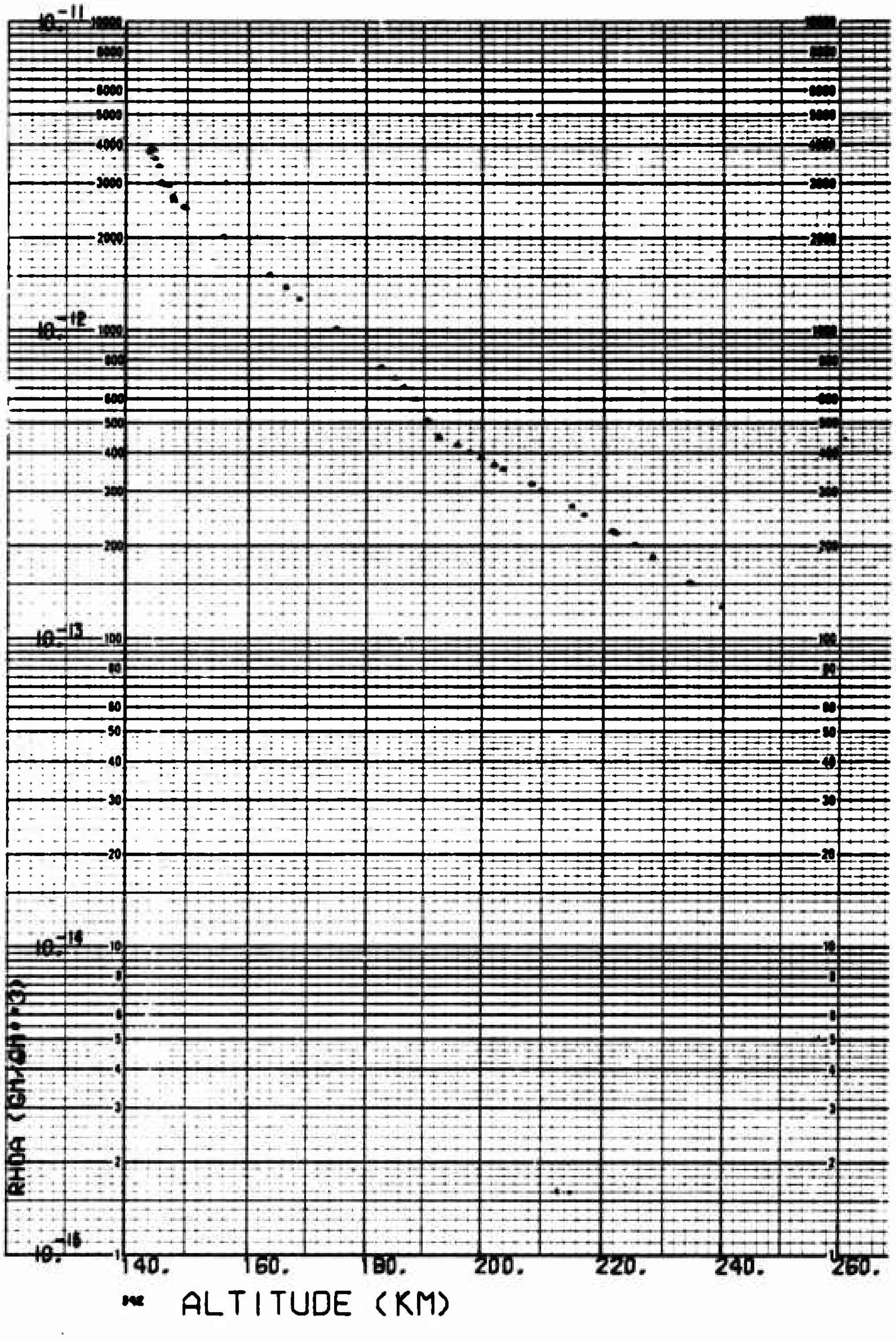

Fig. B-43. LOGACS Density Data for Rev. 34, Toward Perigee

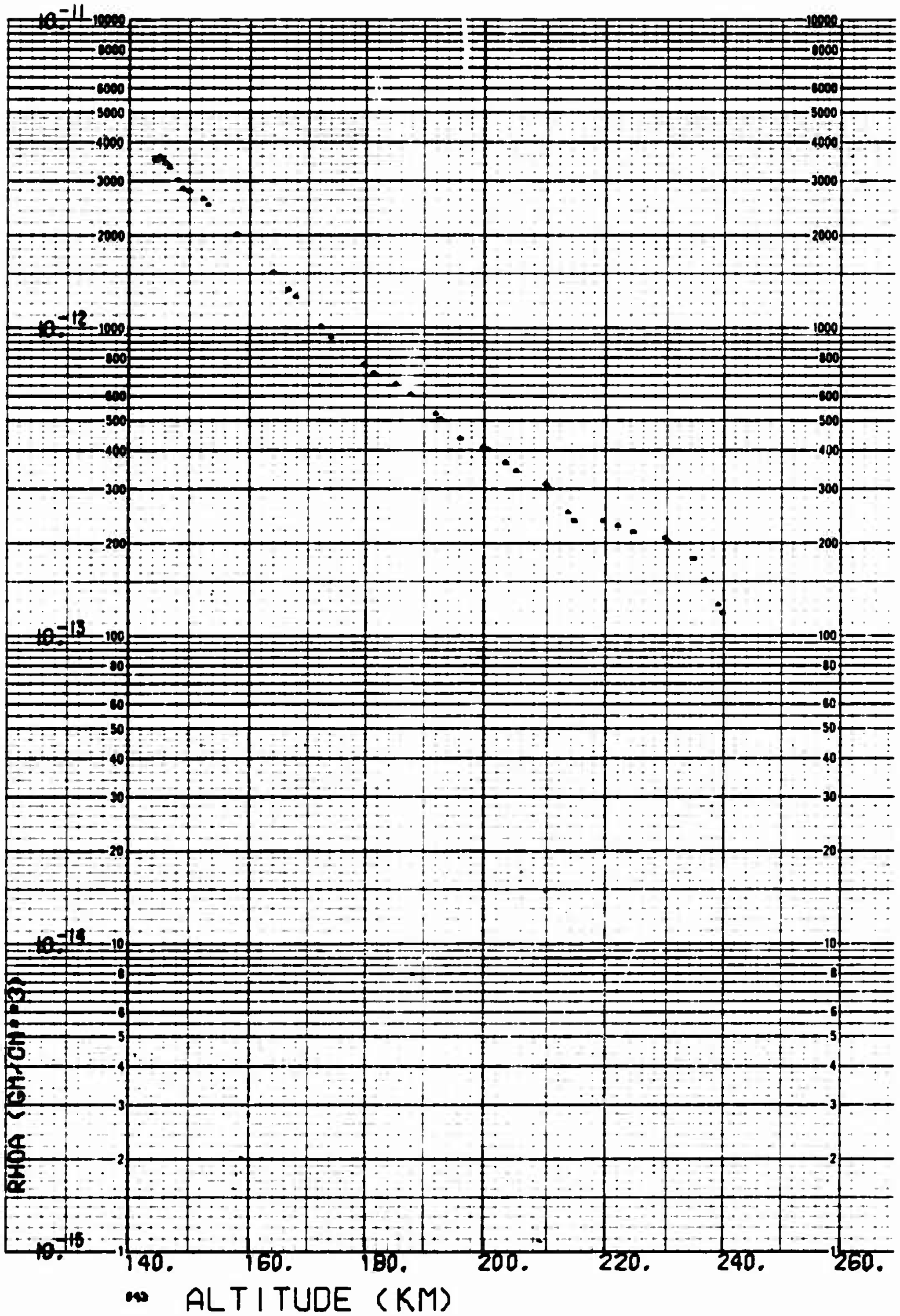

Fig. B-44. LOGACS Density Data for Rev. 34, Away from Perigee

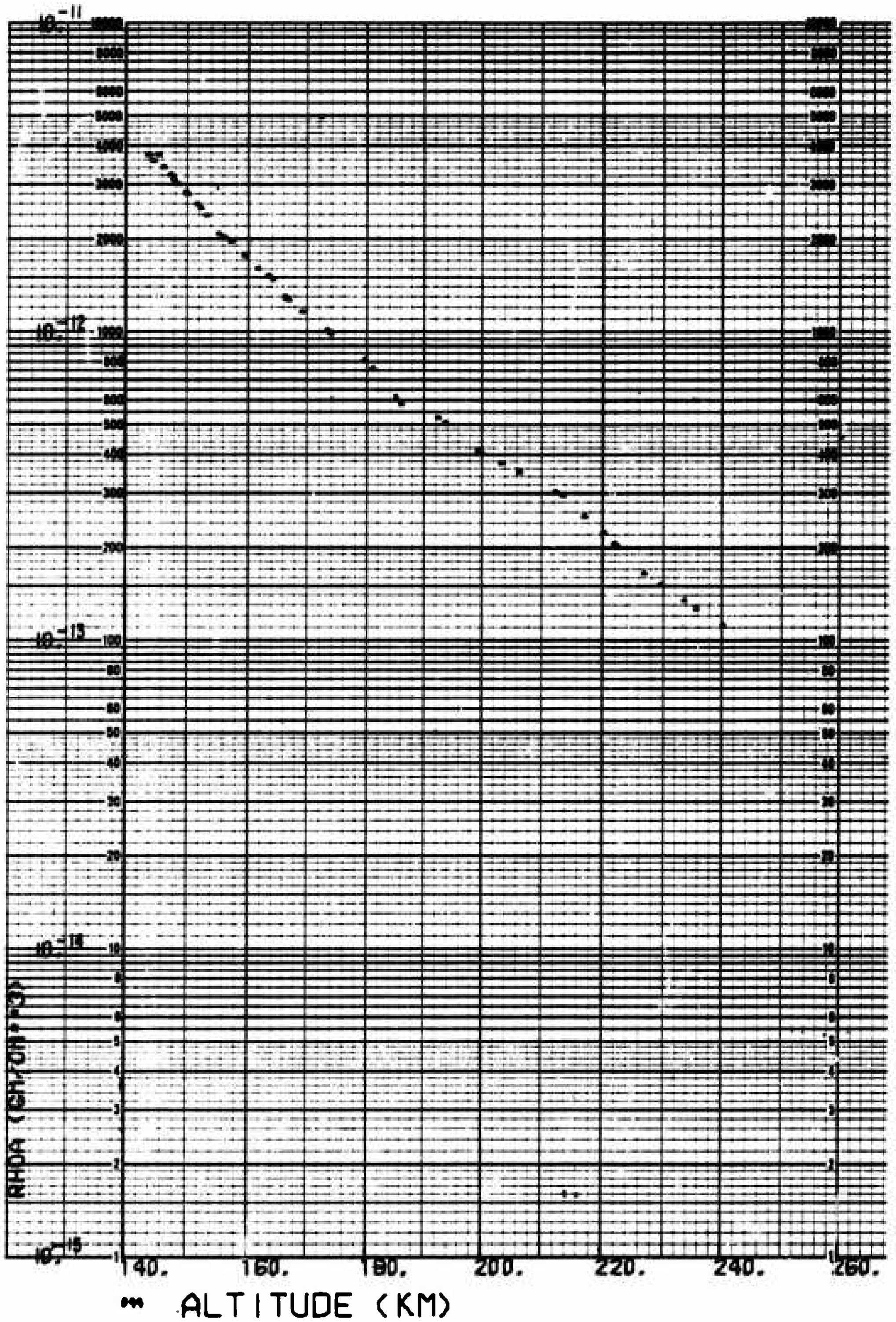

Fig. B-45. LOGACS Density Data for Rev. 35, Toward Perigee

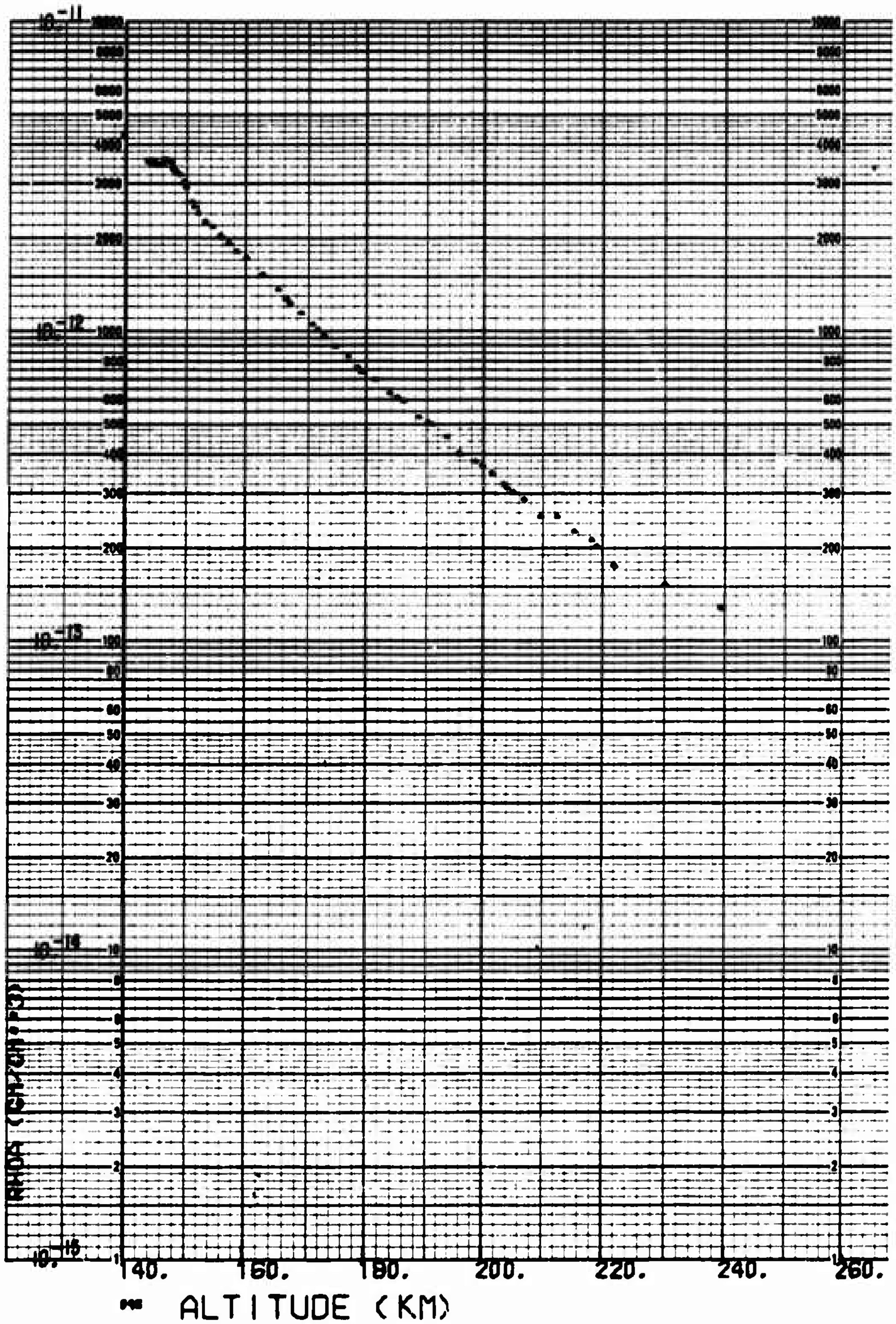

Fig. B-46. LOGACS Density Data for Rev. 35, Away from Perigee

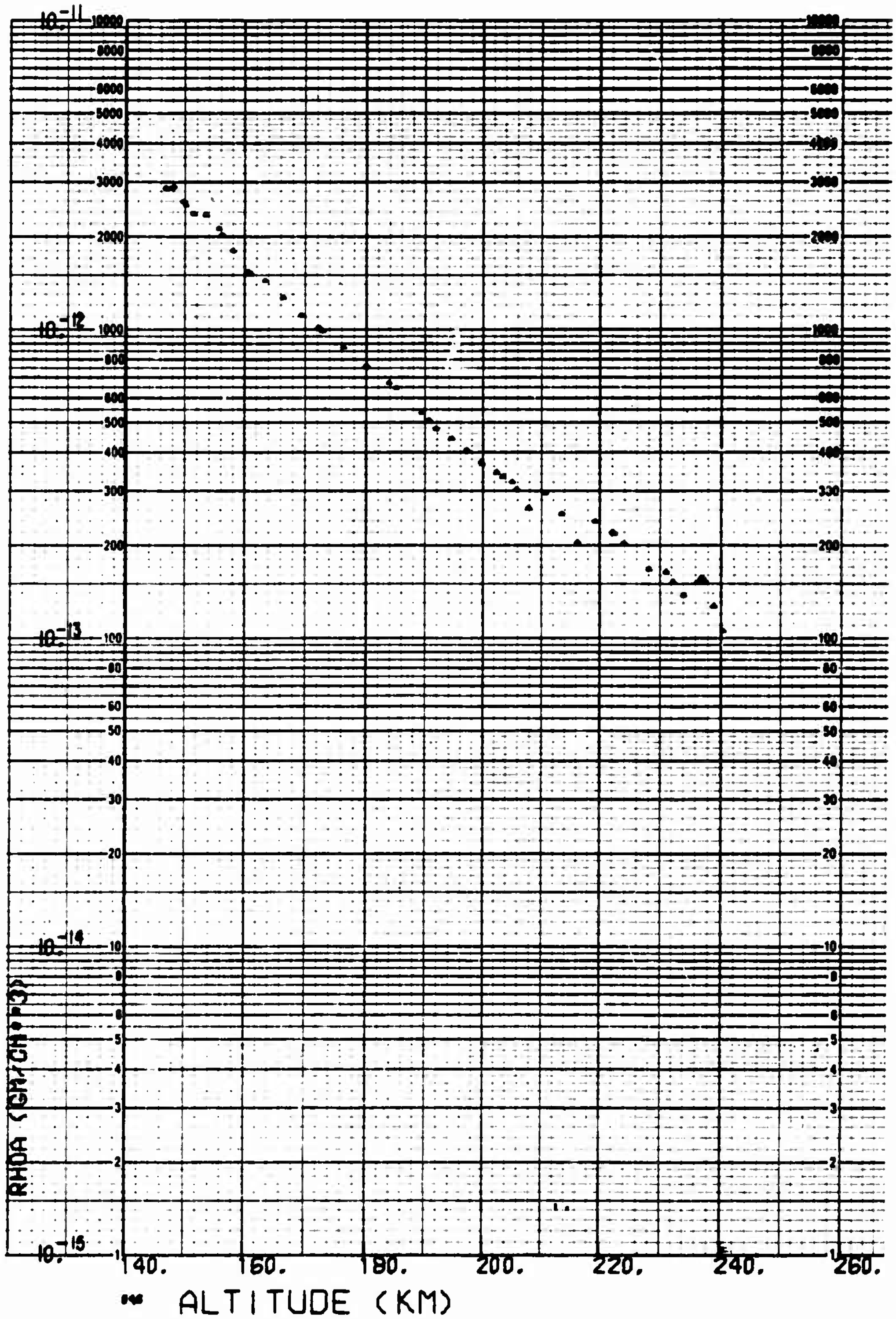

Fig. B-47. LOGACS Density Data for Rev. 36, Away from Perigee

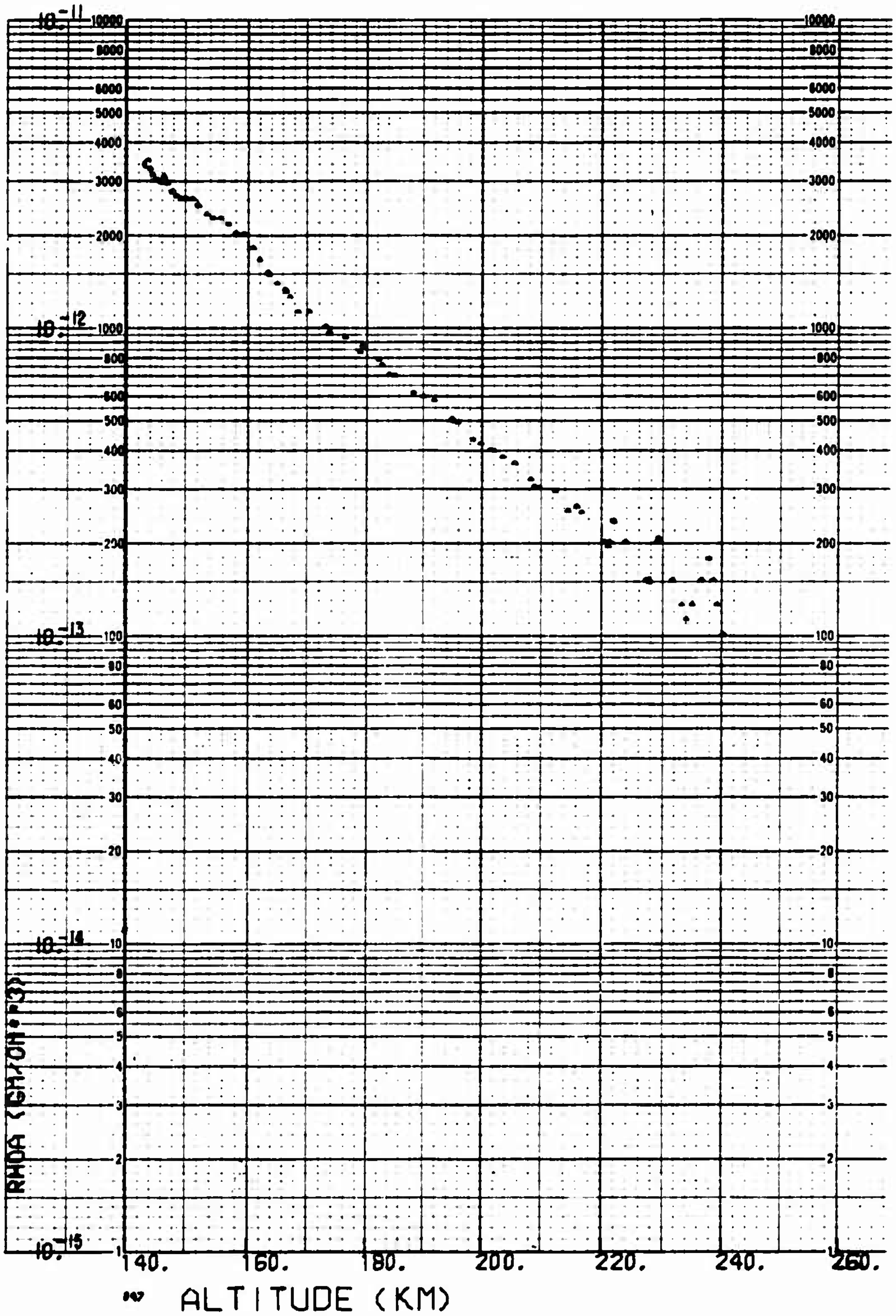

Fig. B-48. LOGACS Density Data for Rev. 37, Toward Perigee

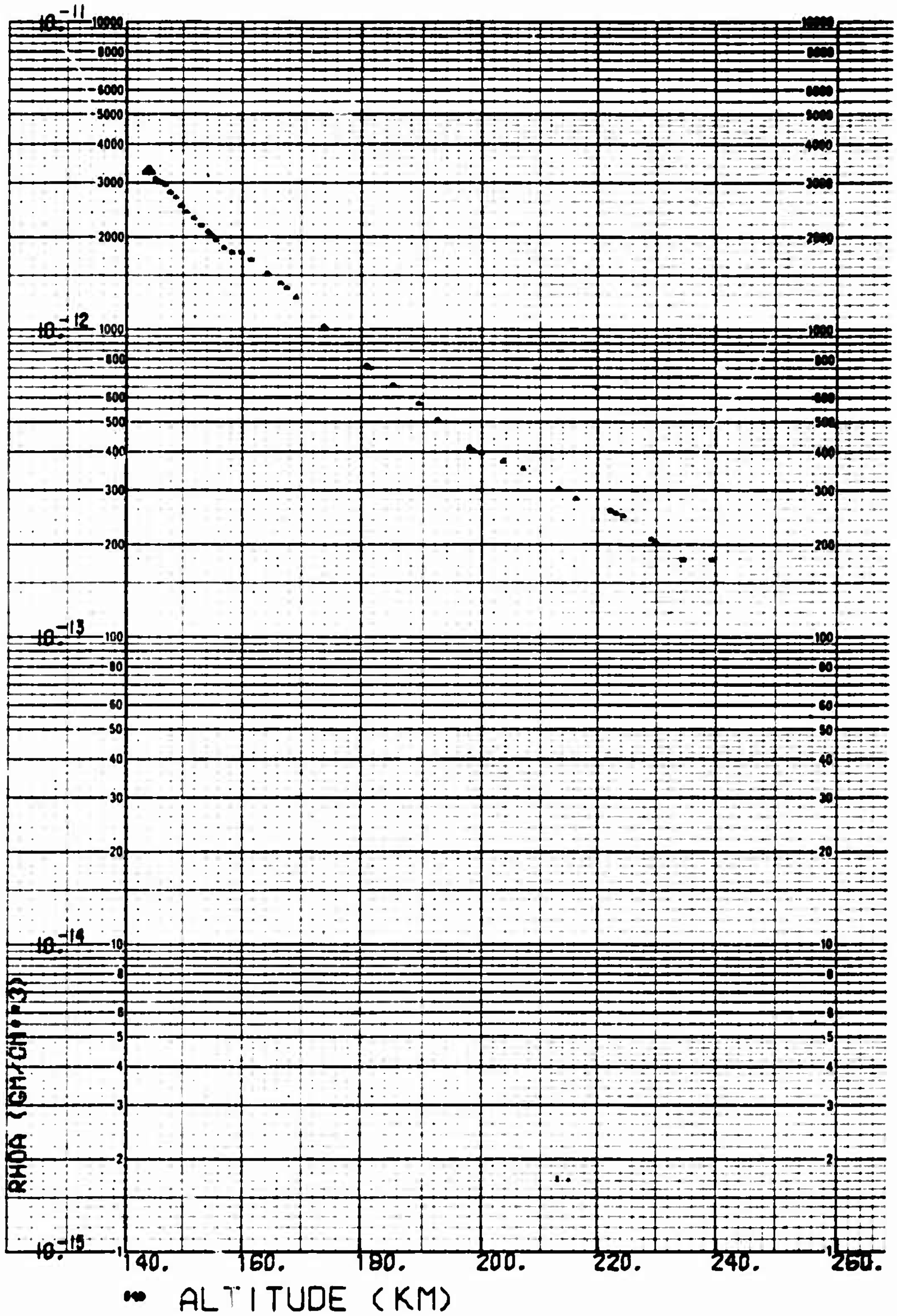

Fig. B-49. LOGACS Density Data for Rev. 37, Away from Perigee

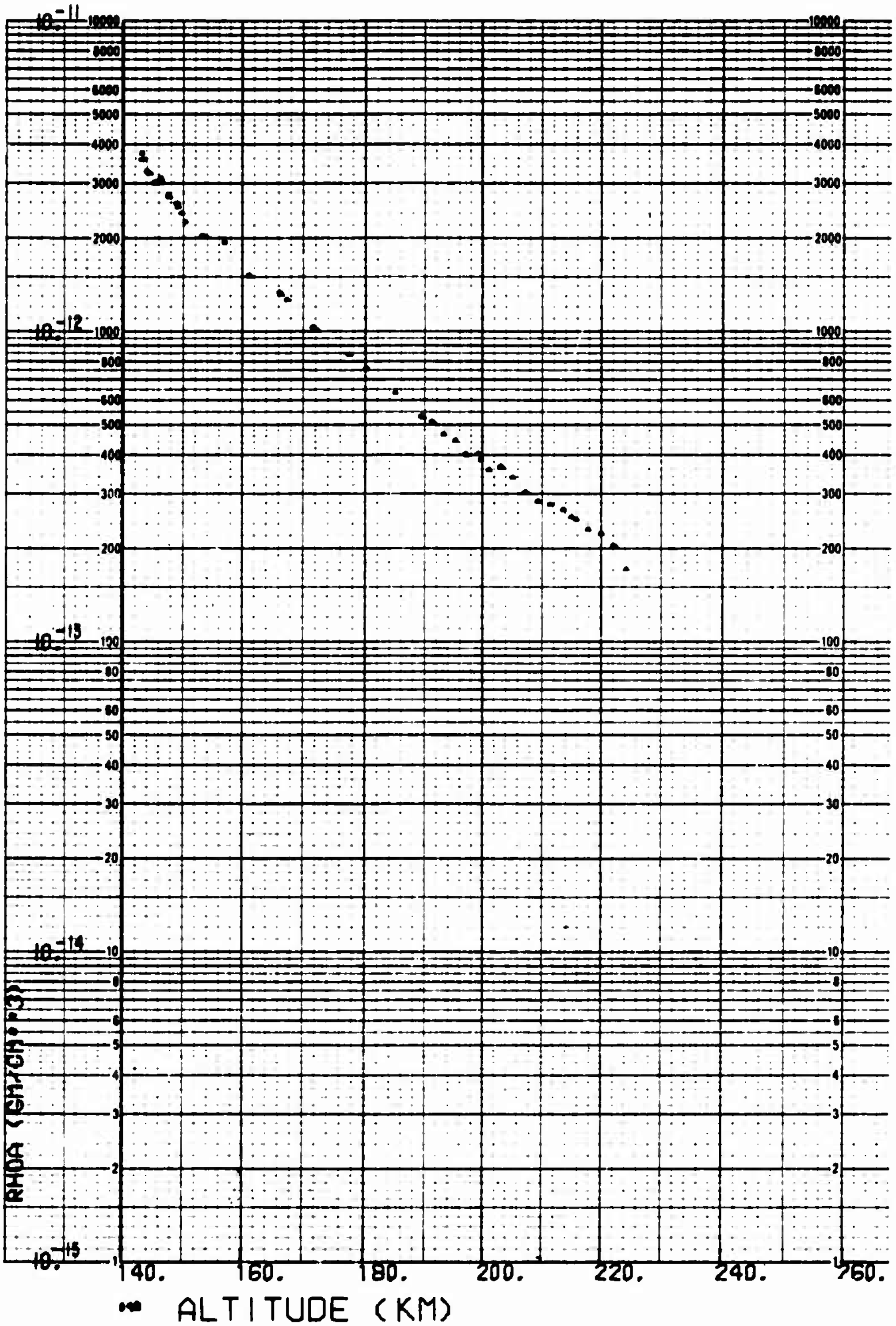

Fig. B-50. LOGACS Density Data for Rev. 38, Toward Perigee

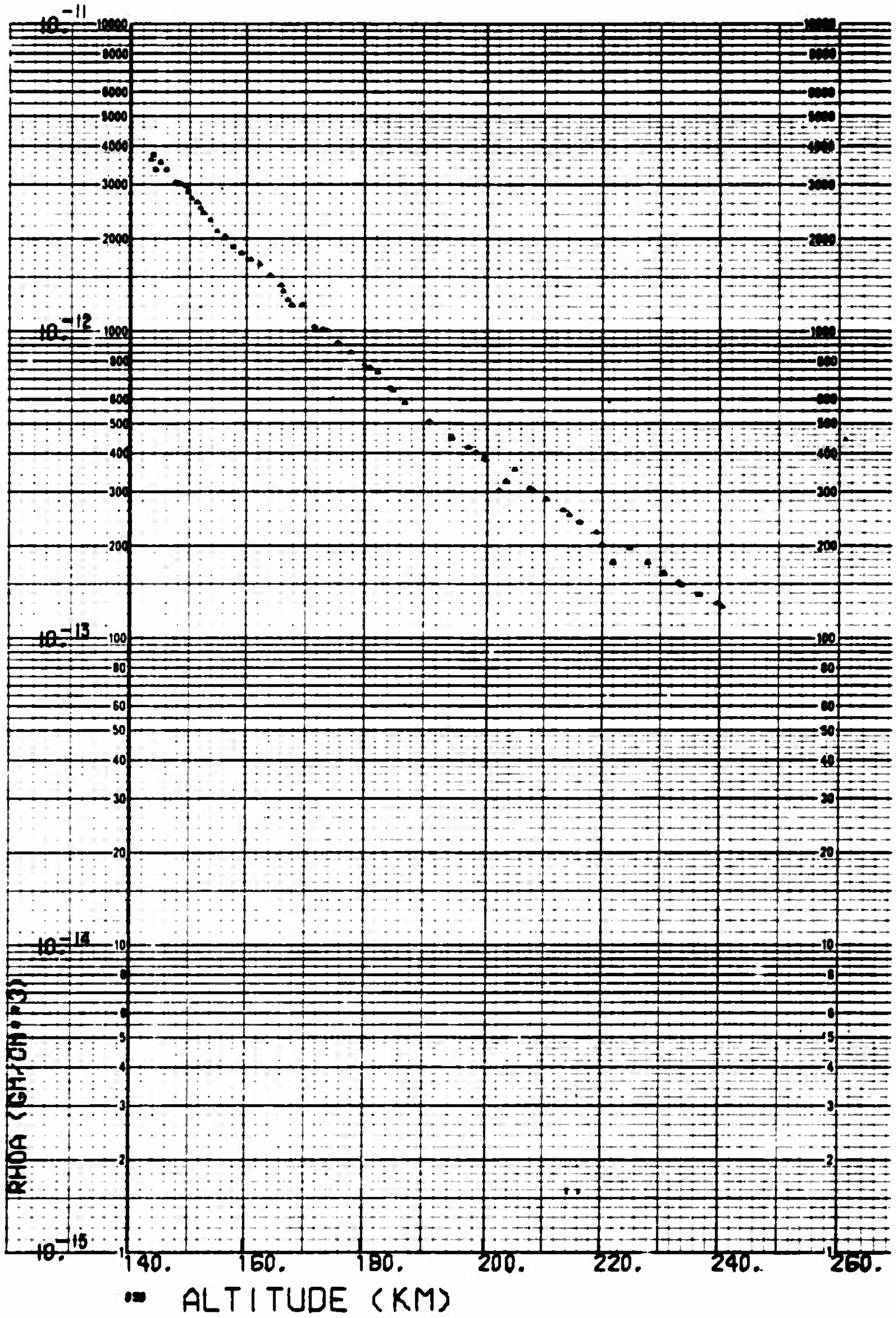

Fig. B-51. LOGACS Density Data for Rev. 38, Away from Perigee

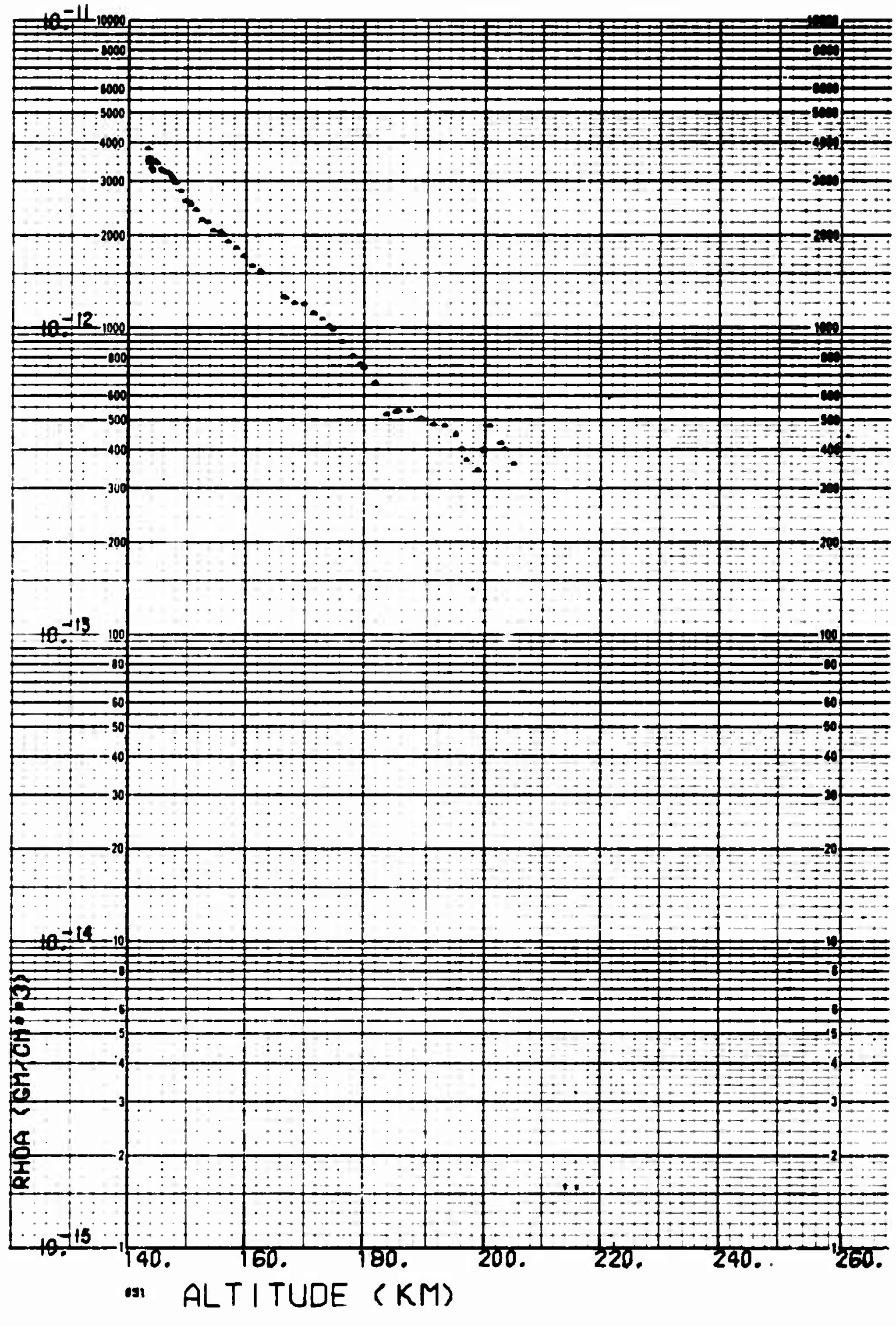

Fig. B-52. LOGACS Density Data for Rev. 39, Toward Perigee

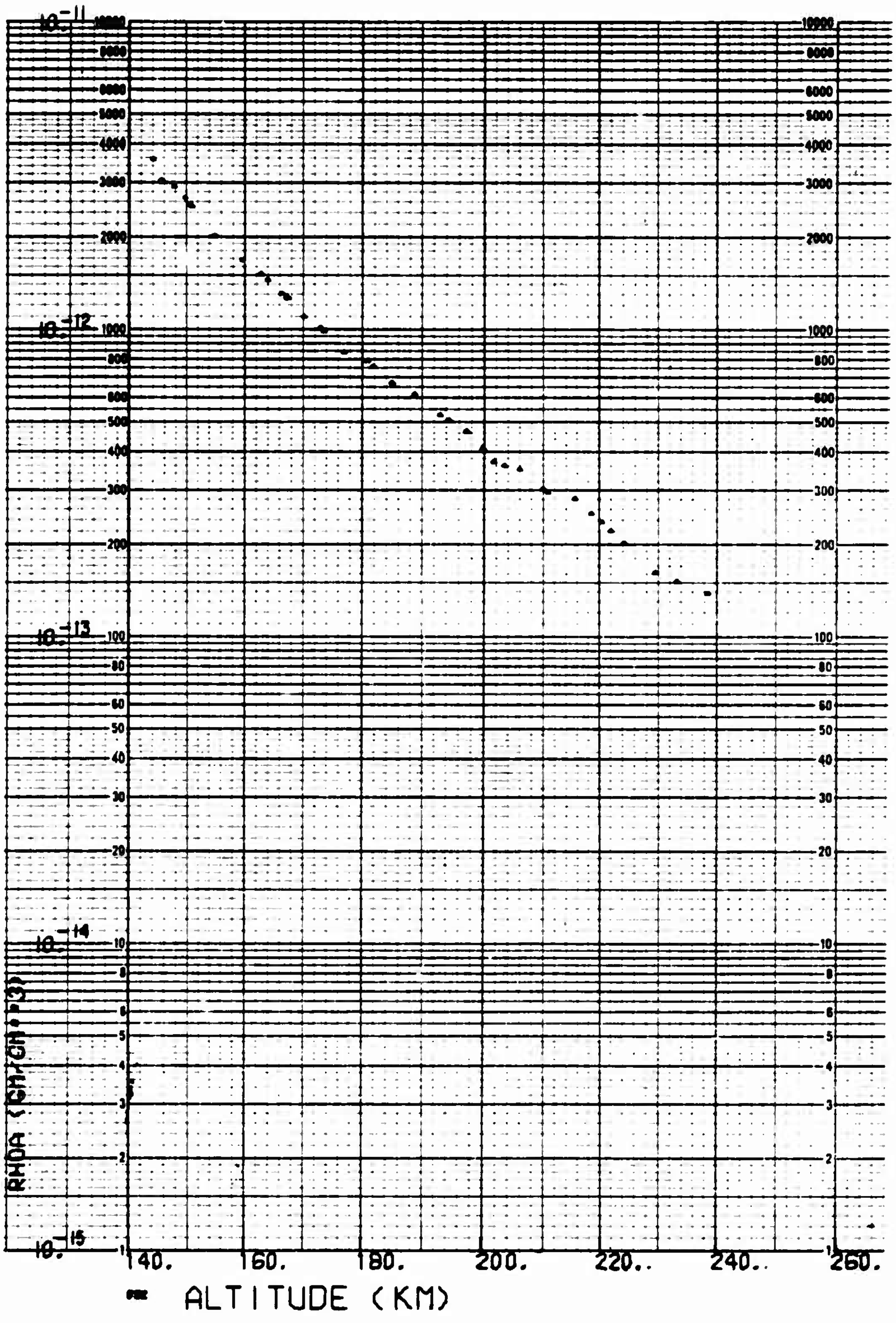

Fig. B-53. LOGACS Density Data for Rev. 39, Away from Perigee

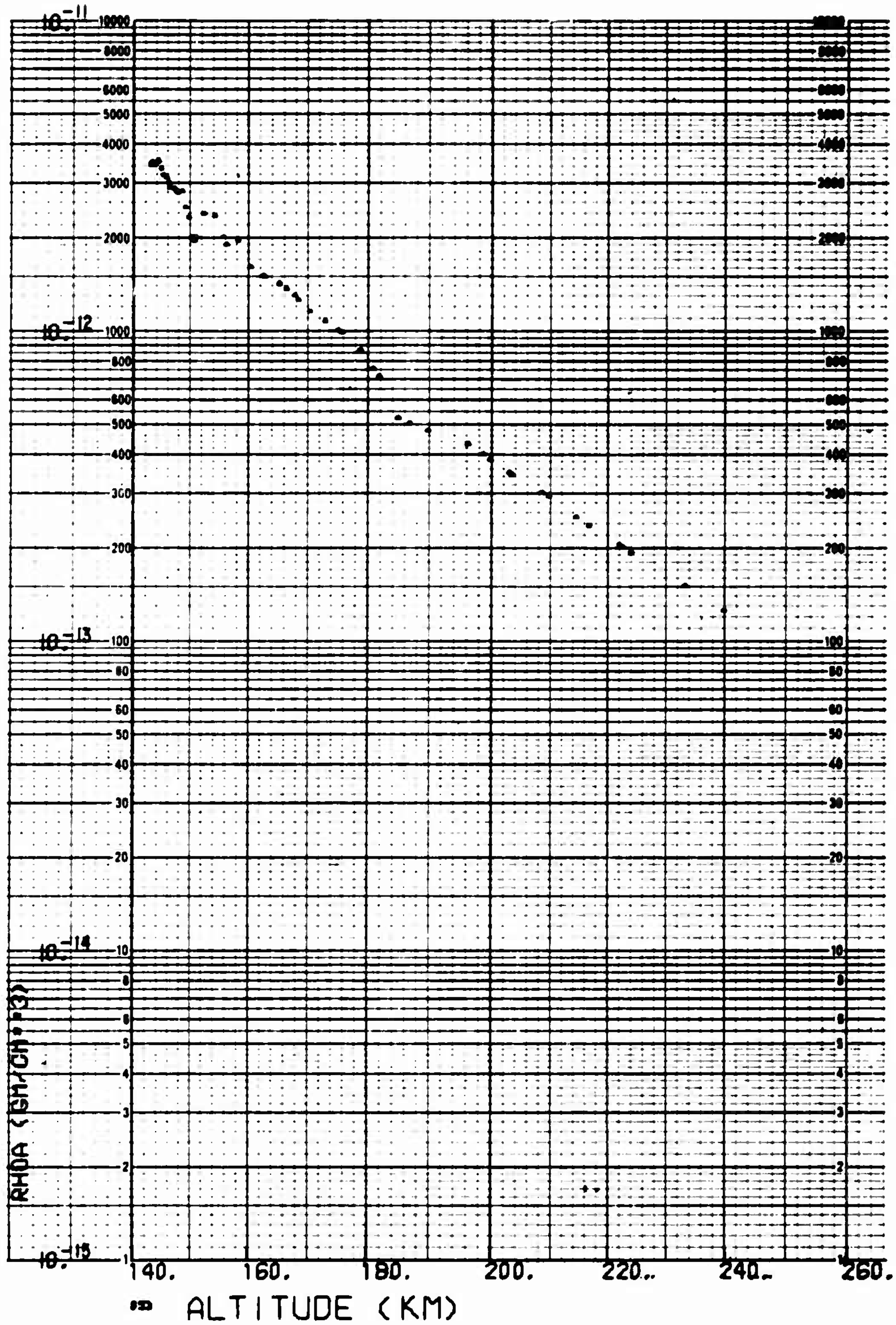

Fig. B-54. LOGACS Density Data for Rev. 40, Toward Perigee

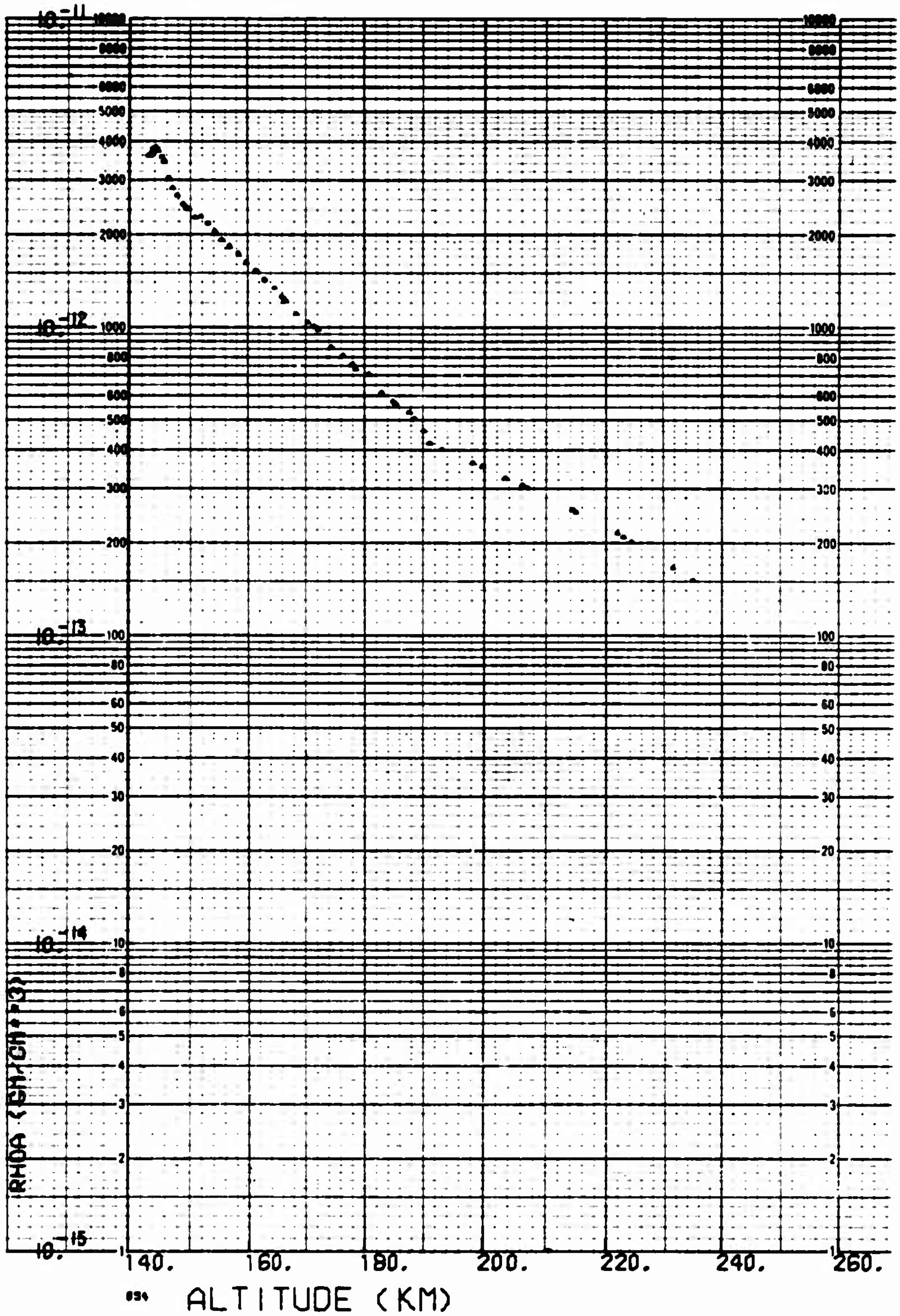

Fig. B-55. LOGACS Density Data for Rev. 40, Away from Perigee

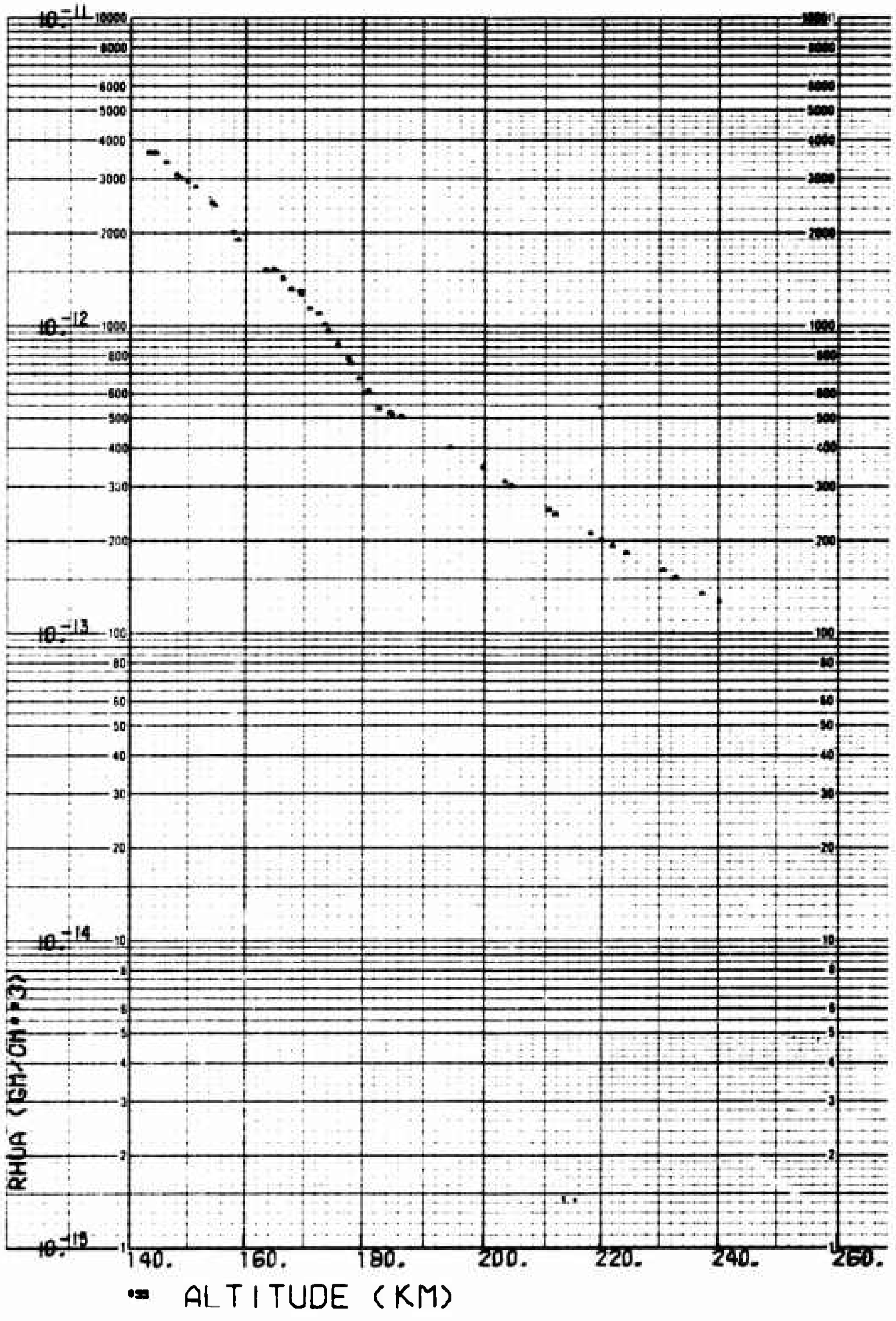

Fig. B-56. LOGACS Density Data for Rev. 41, Toward Perigee

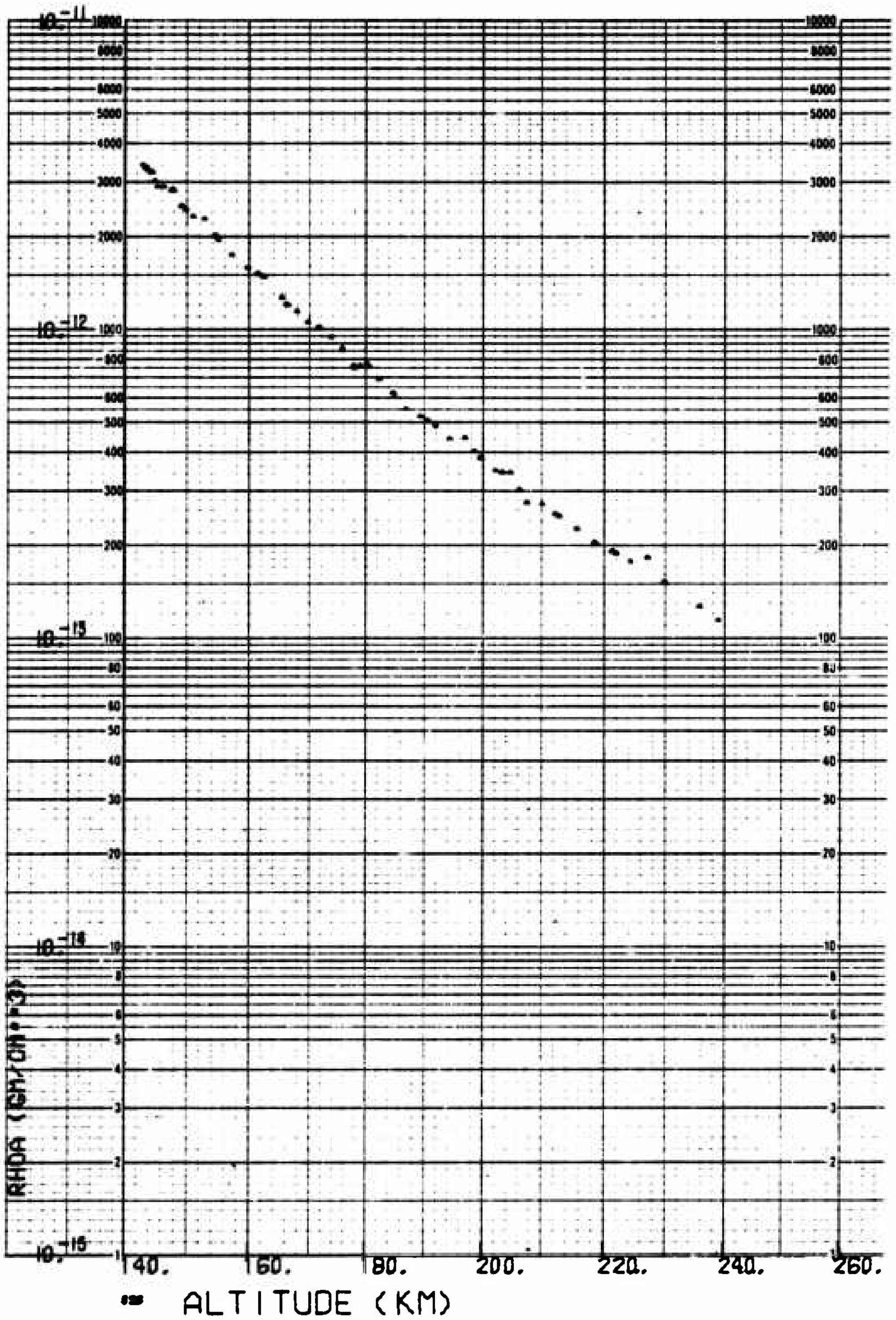

Fig. B-57. LOGACS Density Data for Rev. 41, Away from Perigee

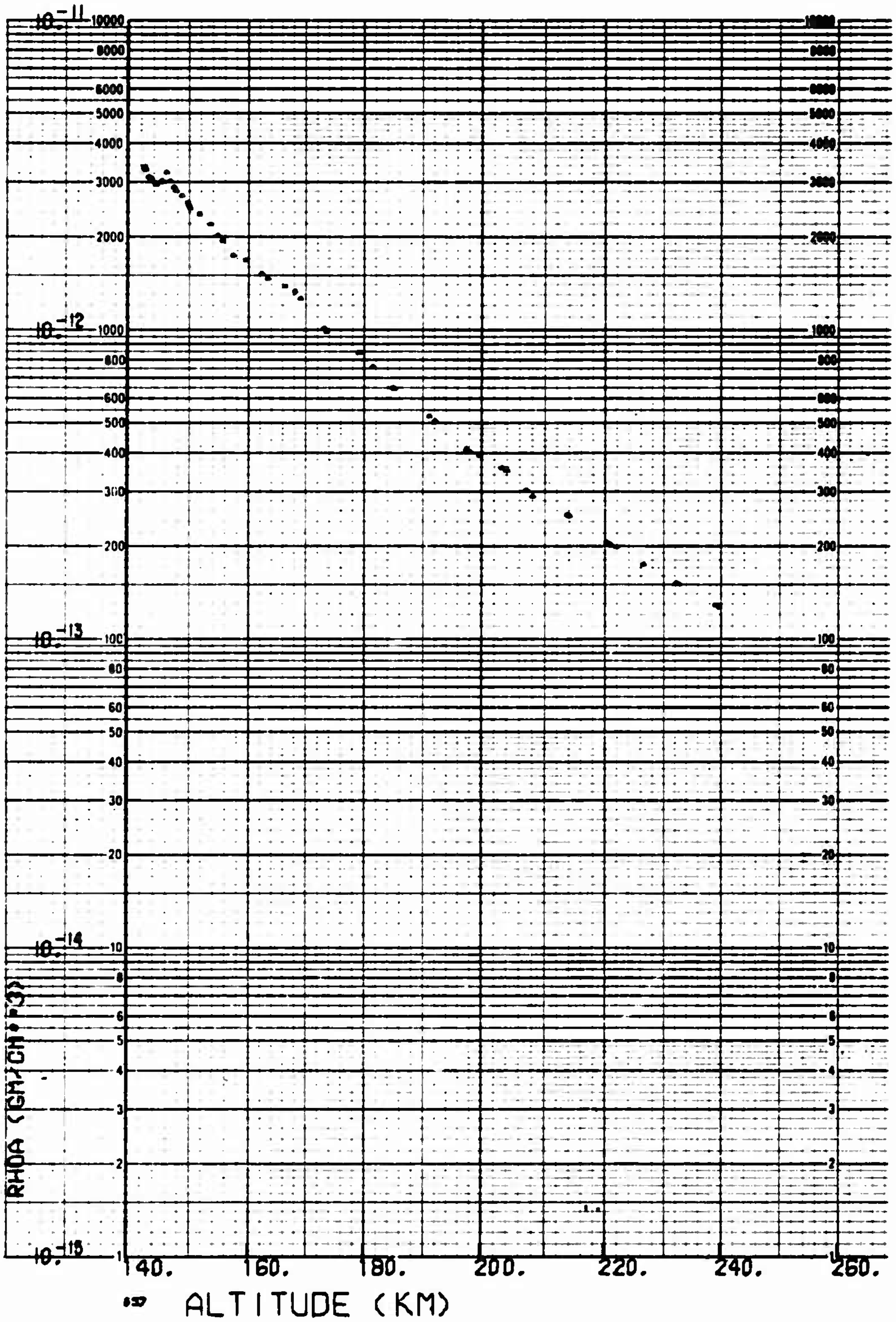

Fig. B-58. LOGACS Density Data for Rev. 43, Toward Perigee

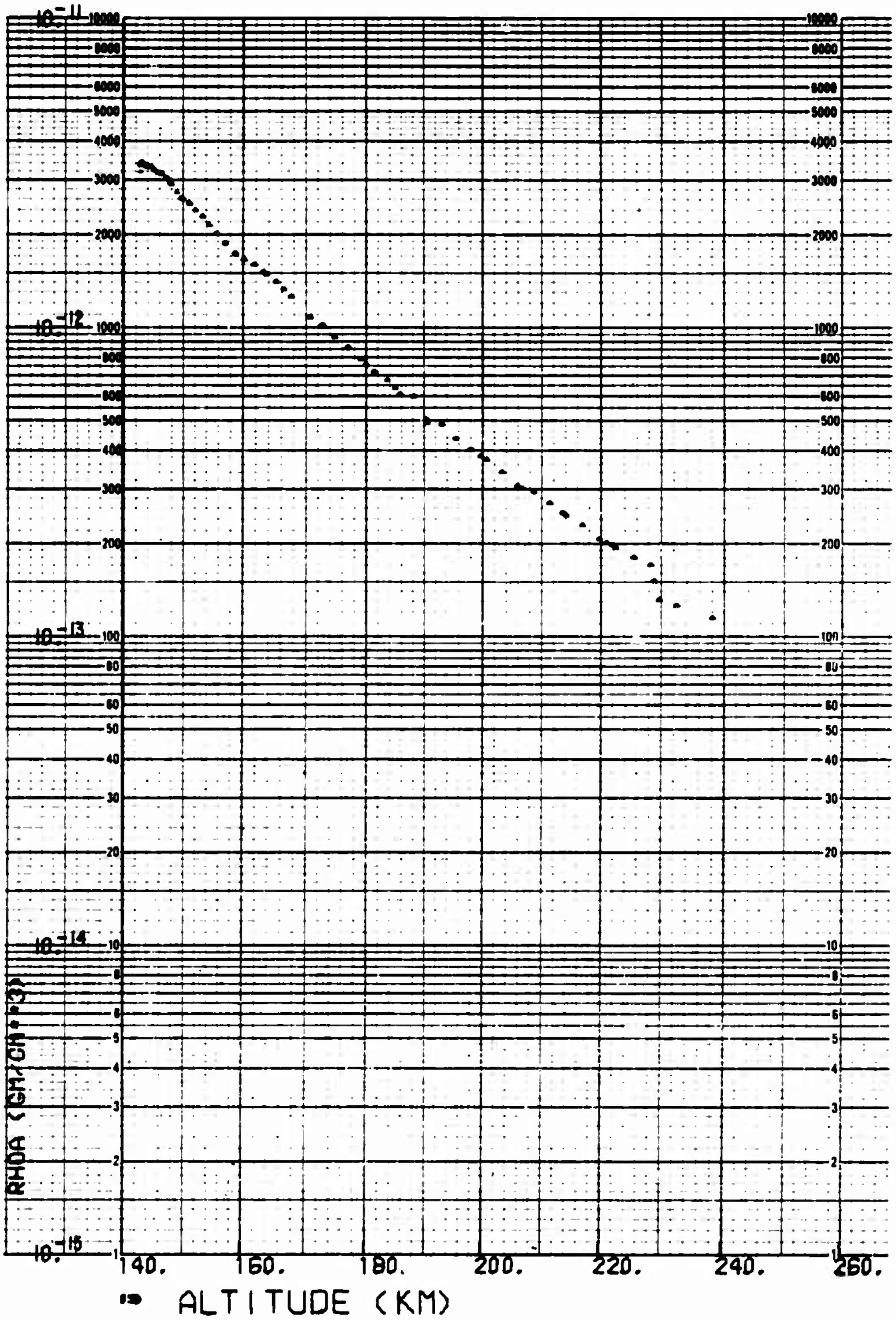

Fig. B-59. LOGACS Density Data for Rev. 43, Away from Perigee

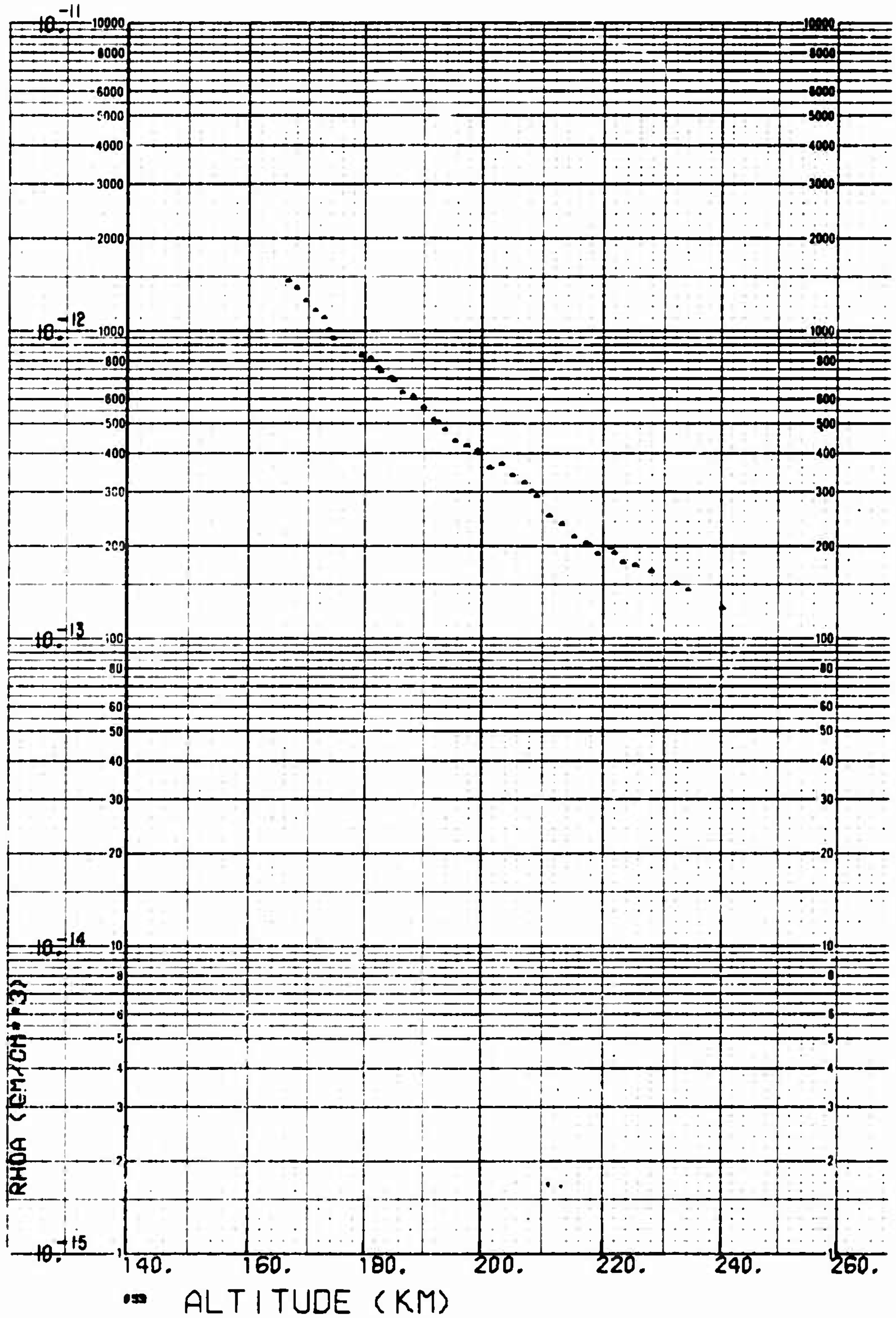

Fig. B-60. LOGACS Density Data for Rev. 44, Toward Perigee

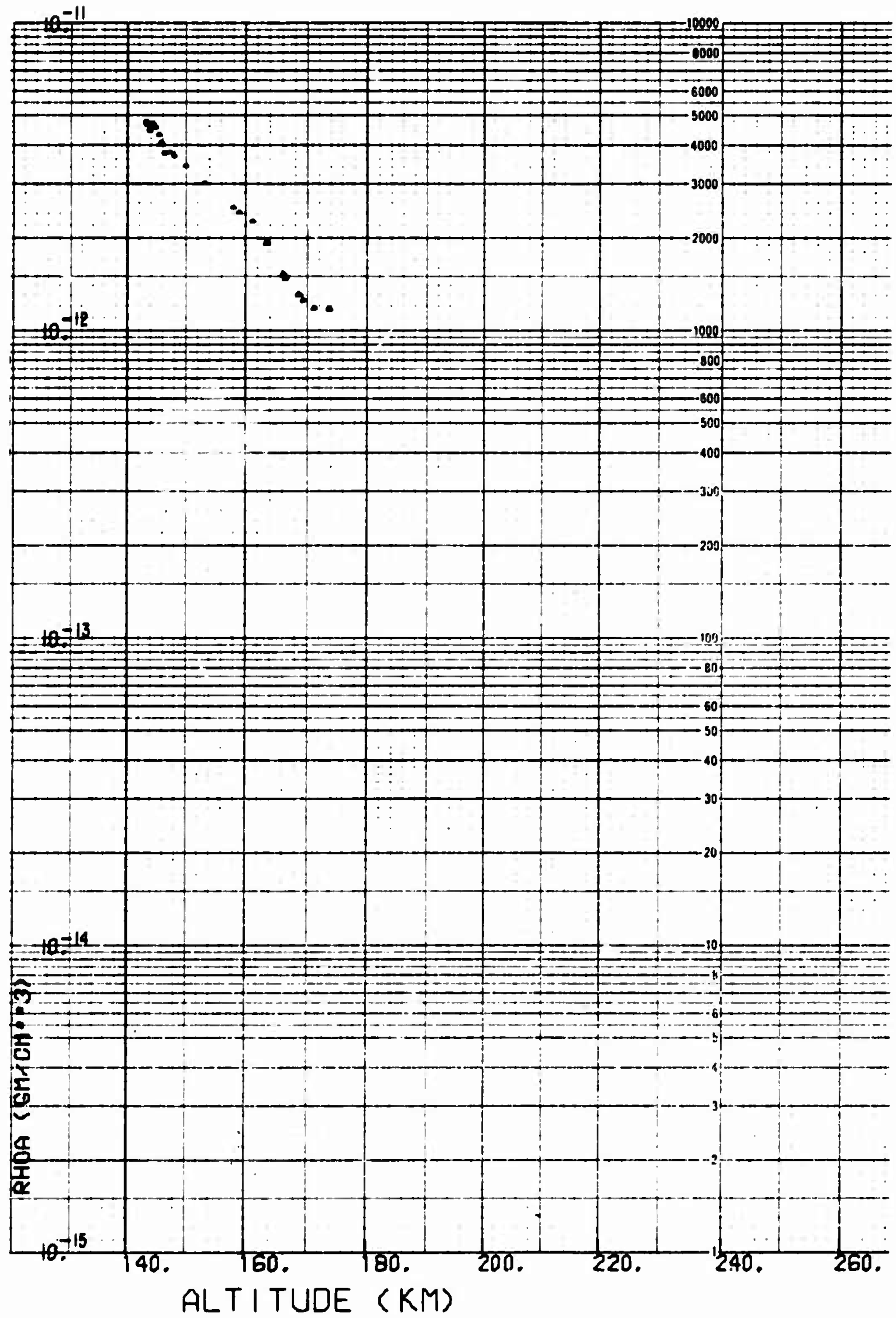

Fig. B-61. LOGACS Density Data for Rev. 45, Toward Perigee

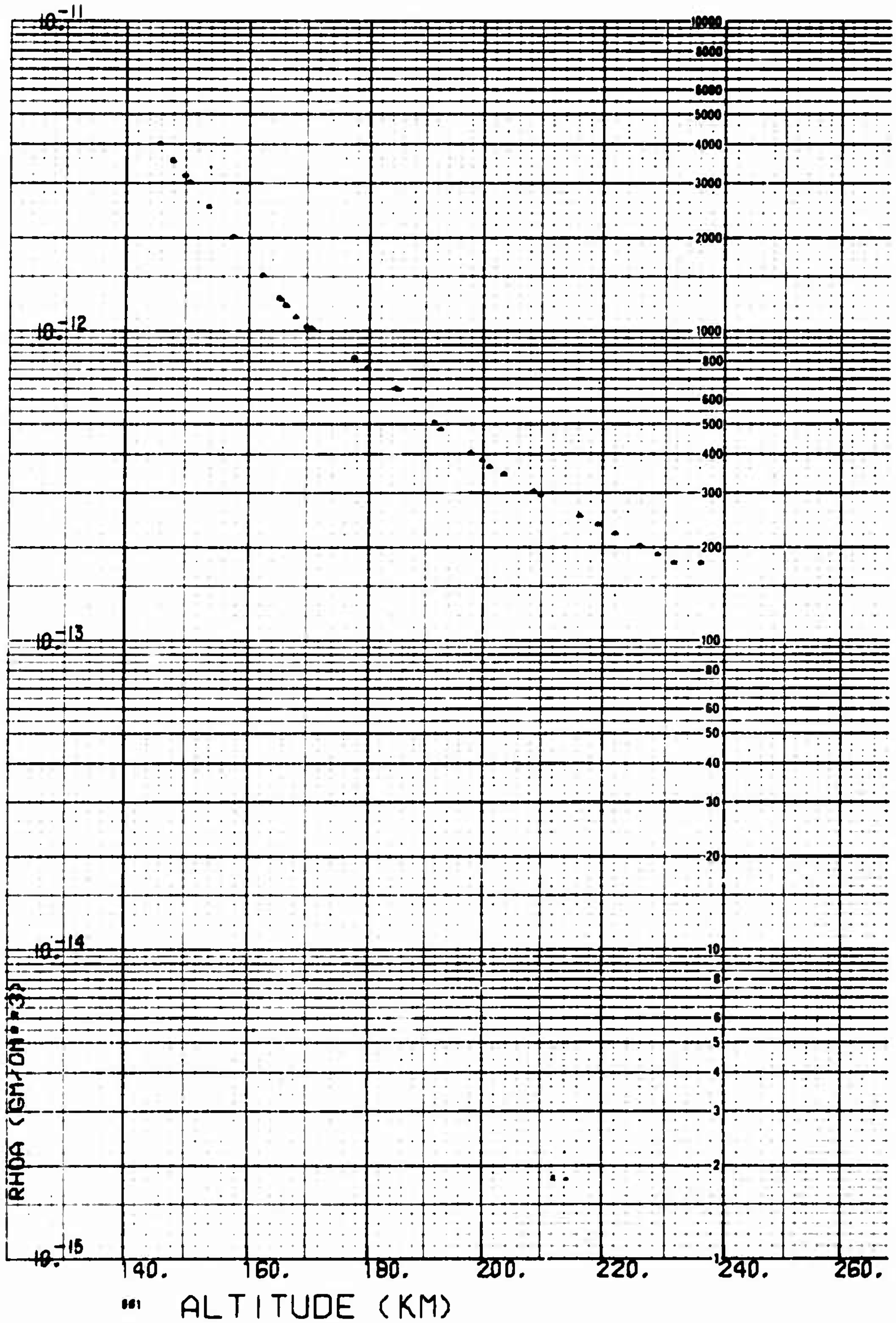

Fig. B-62. LOGACS Density Data for Rev. 45, Away from Perigee

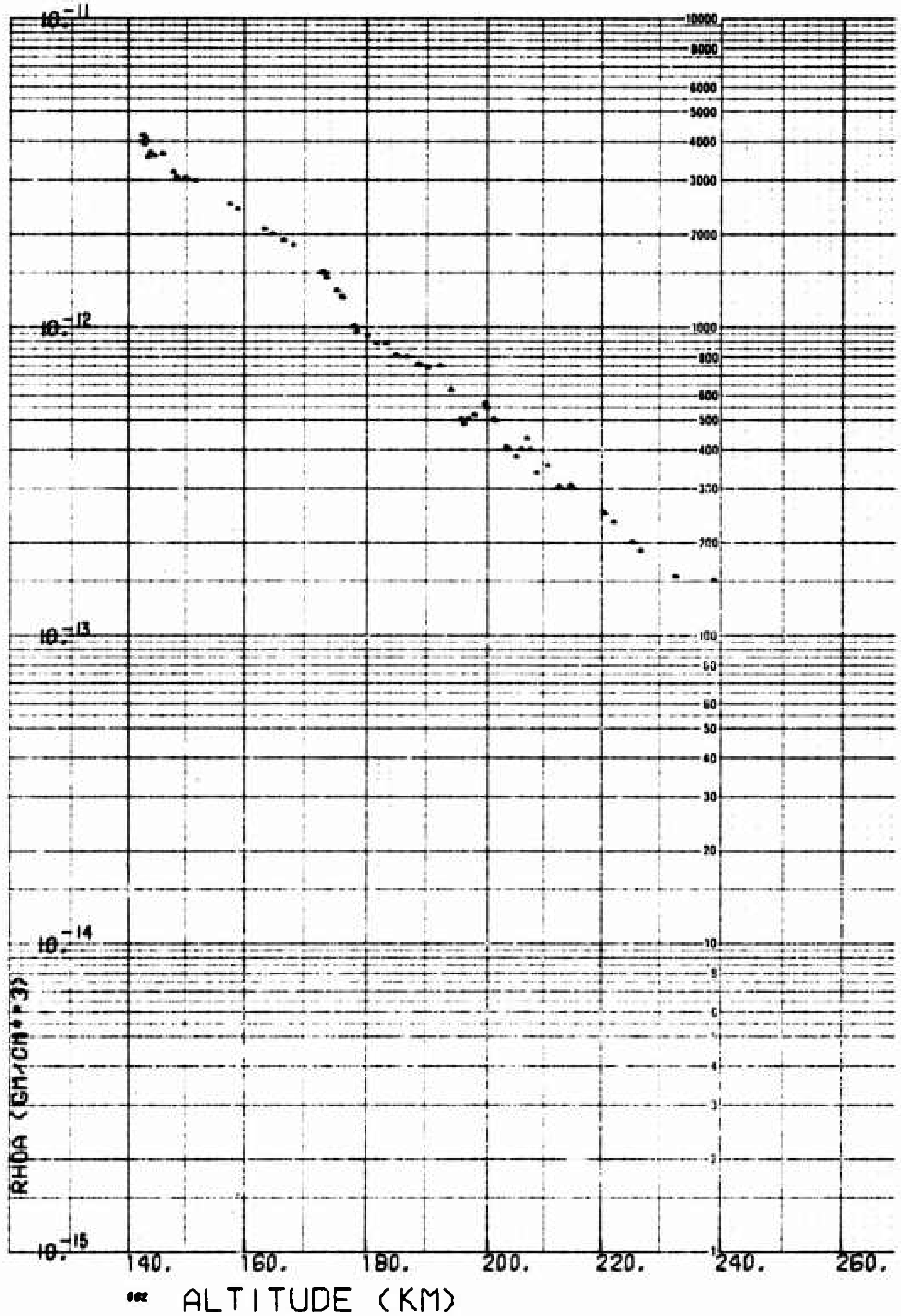

Fig. B-63. LOGACS Density Data for Rev. 46, Toward Perigee

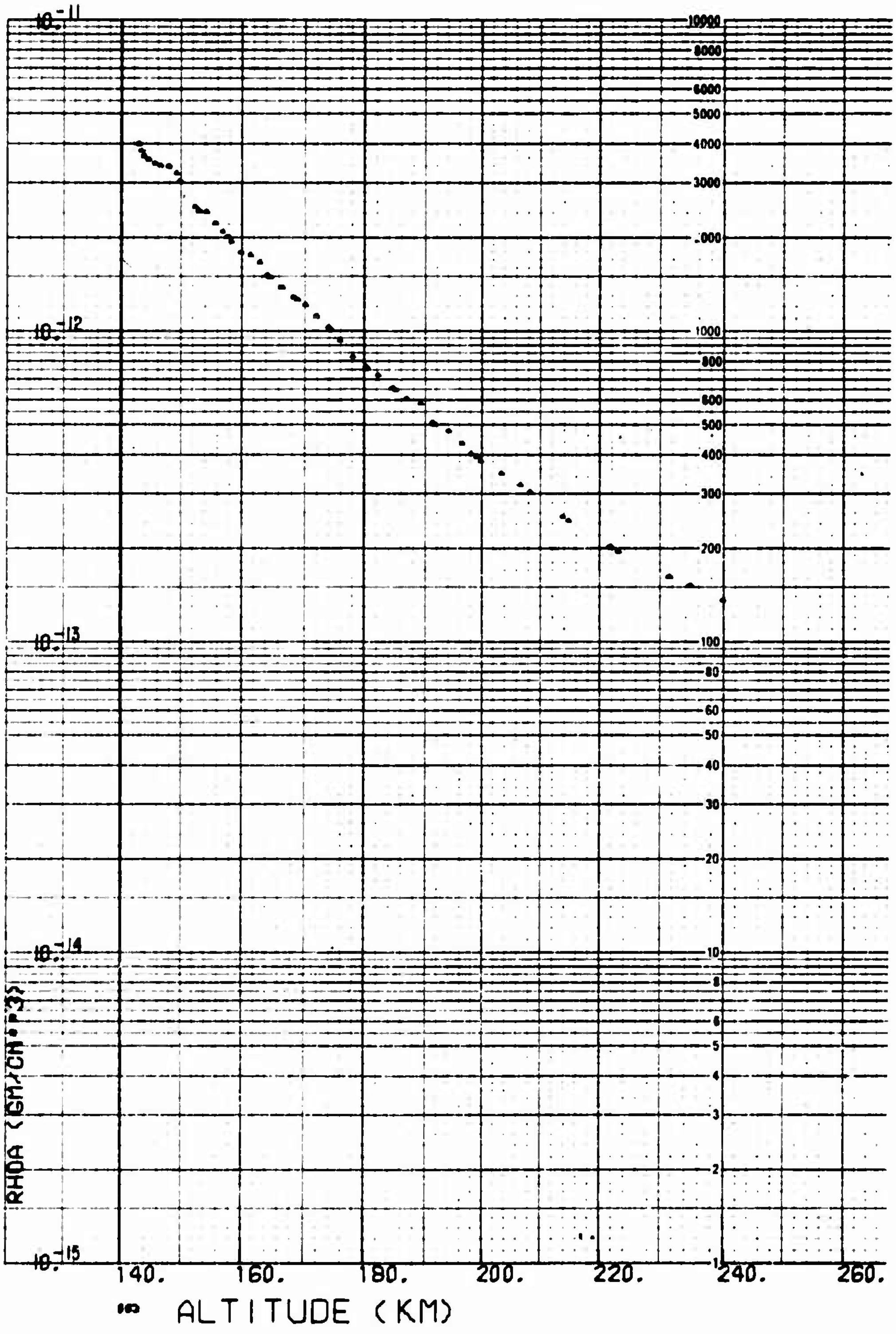

Fig. B-64. LOGACS Density Data for Rev. 46, Away from Perigee

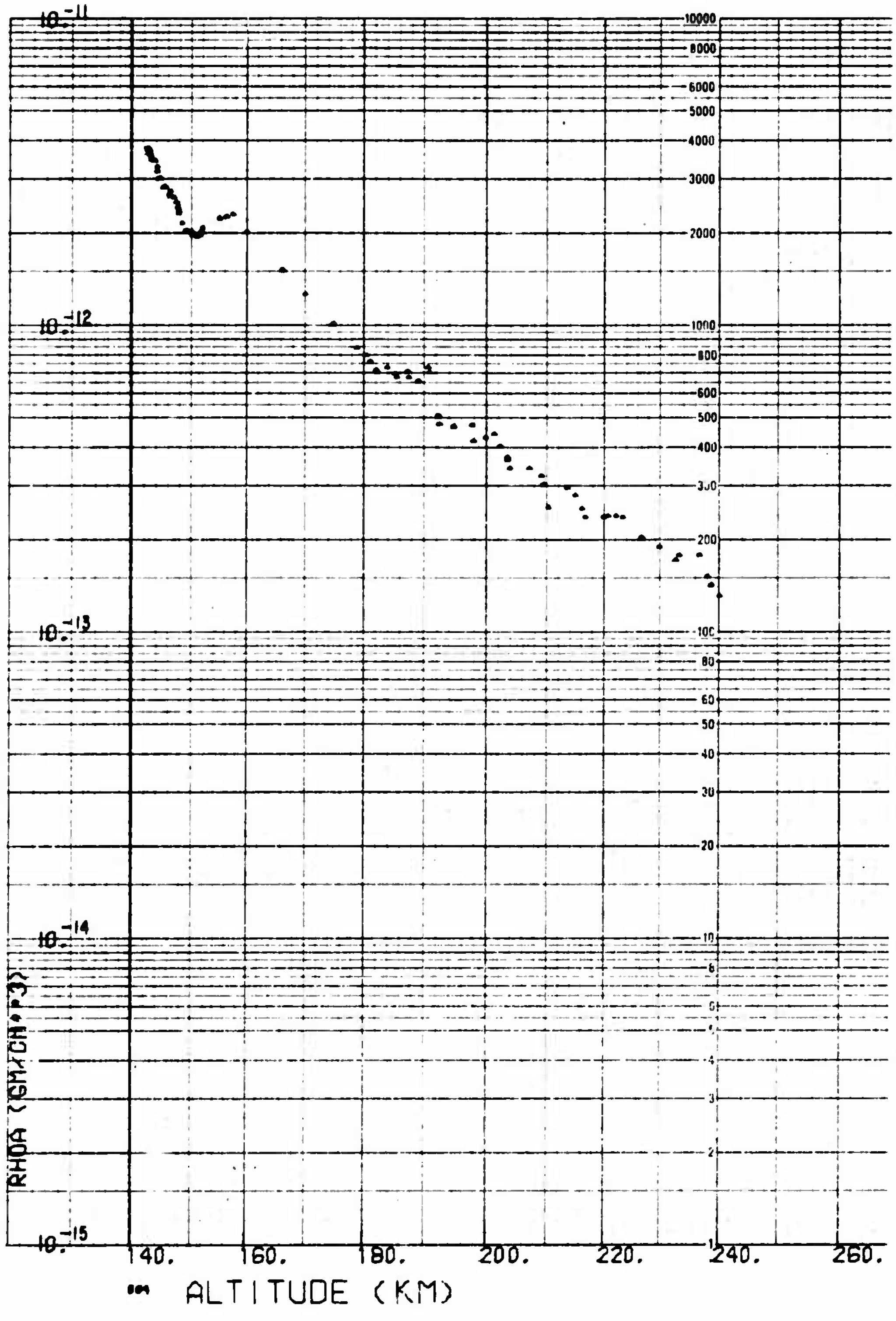

Fig. B-65. LOGACS Density Data for Rev. 47, Toward Perigee

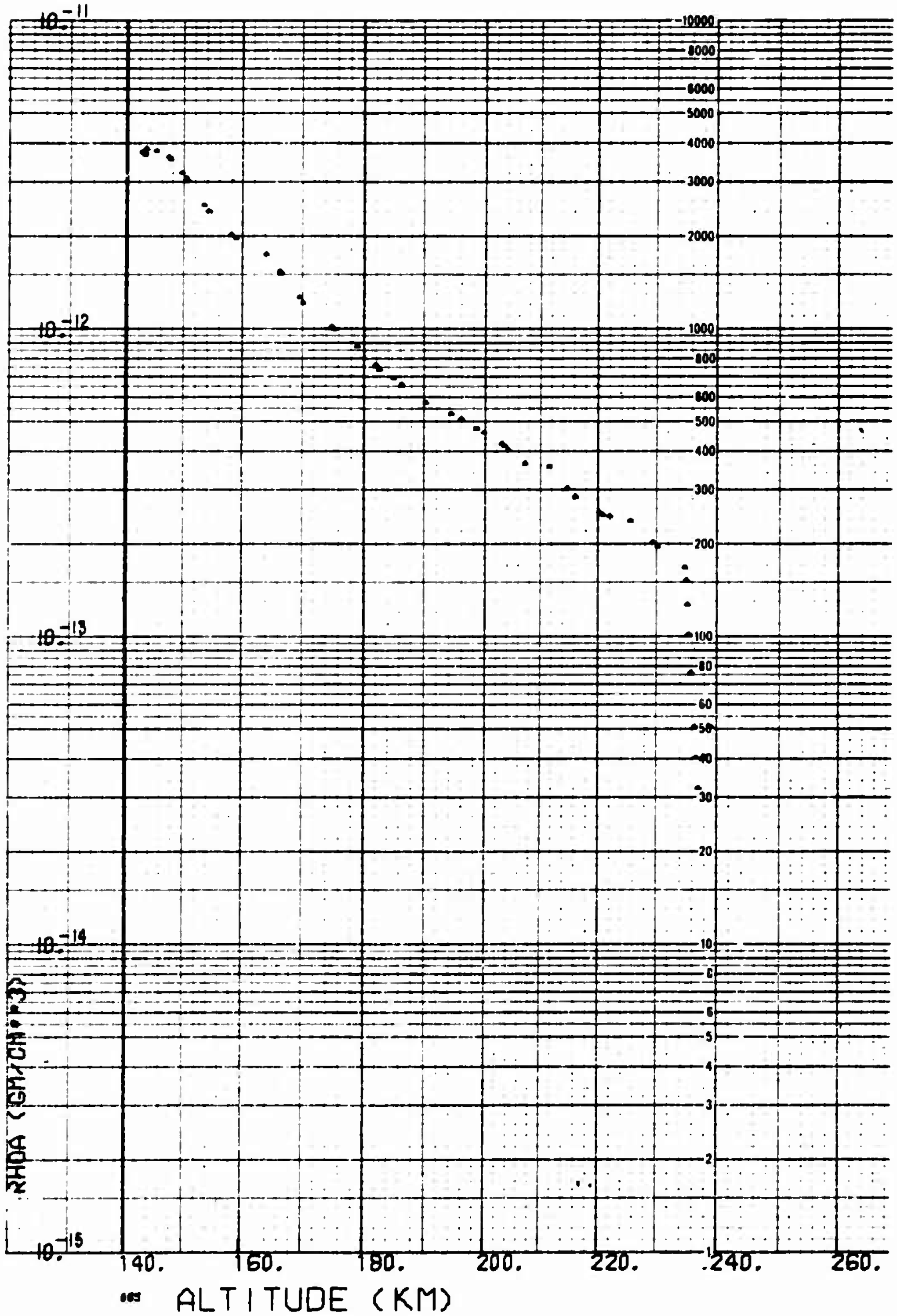

Fig. B-66. LOGACS Density Data for Rev. 47, Away from Perigee

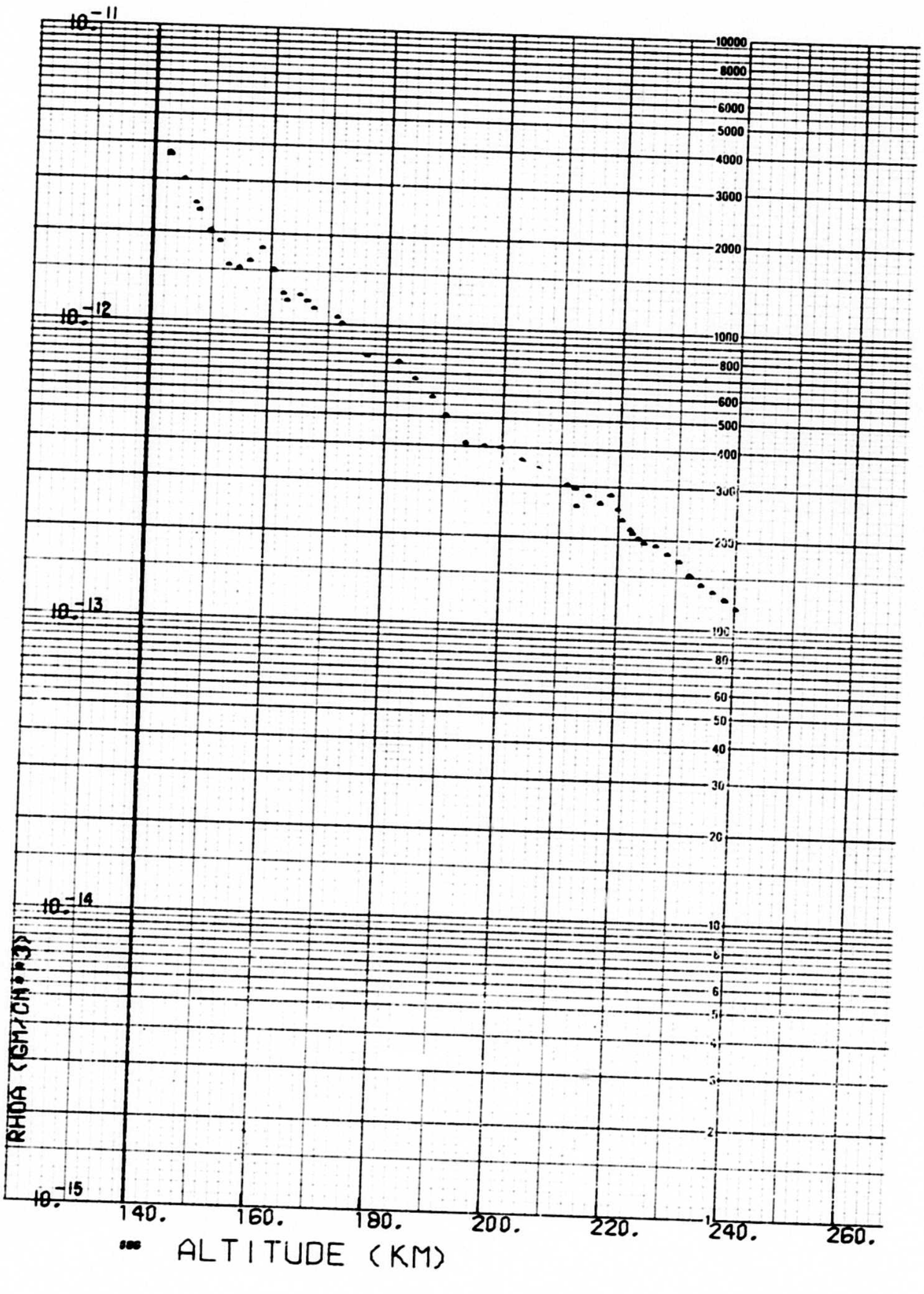

Fig. B-67. LOGACS Density Data for Rev. 48, Toward Perigee

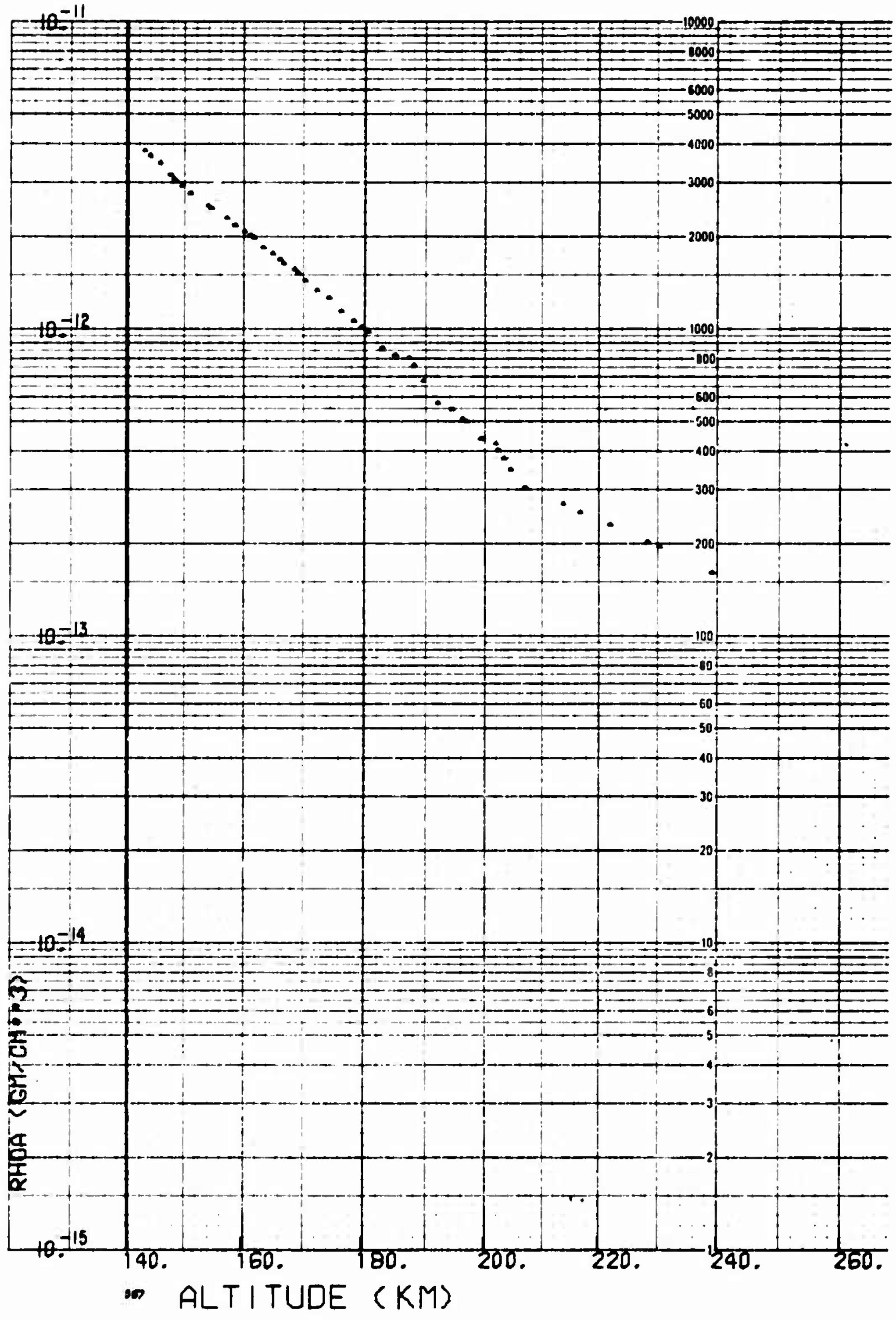

Fig. B-68. LOGACS Density Data for Rev. 48, Away from Perigee

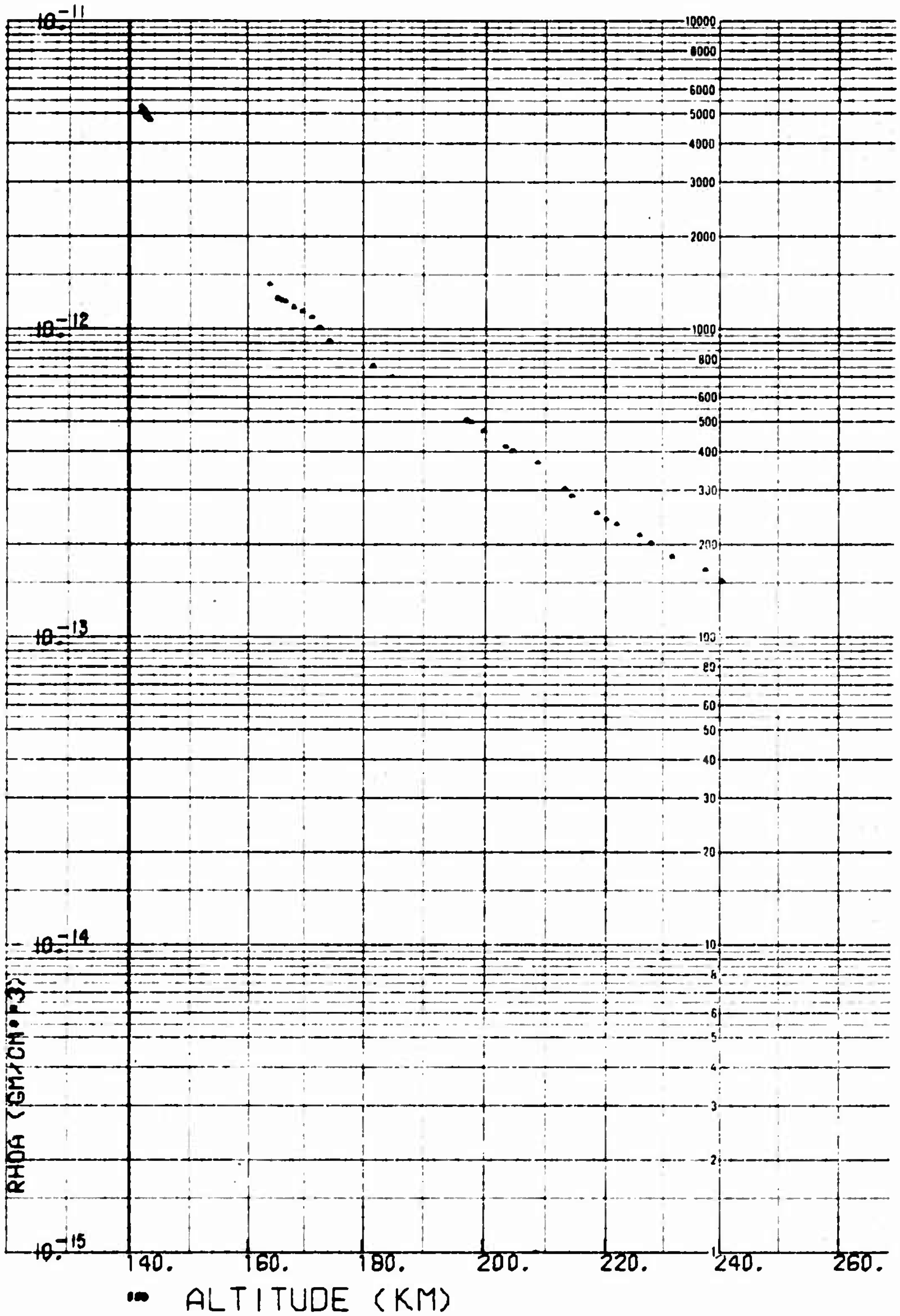

Fig. B-69. LOGACS Density Data for Rev. 49, Toward Perigee

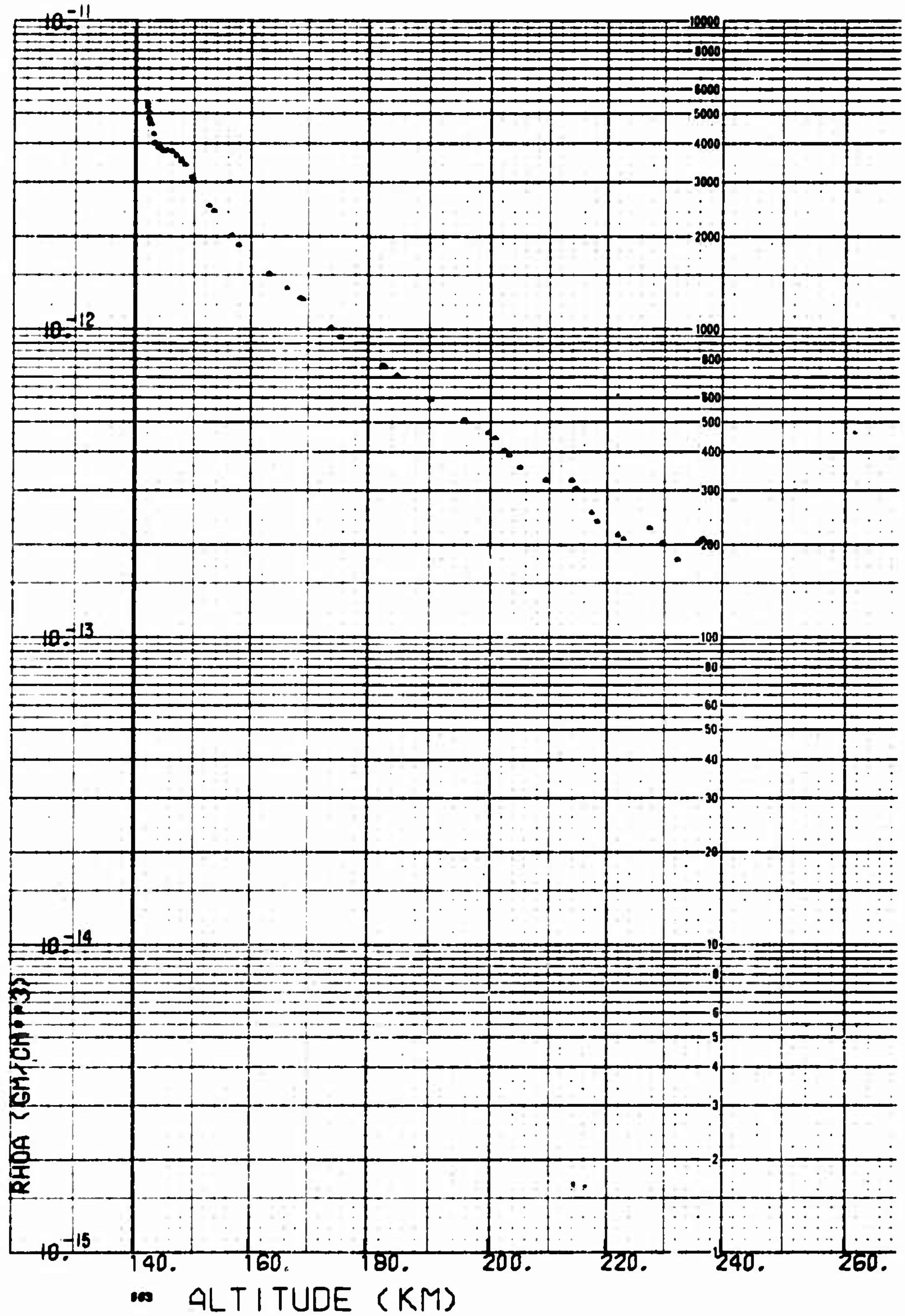

Fig. B-70. LOGACS Density Data for Rev. 50, Away from Perigee

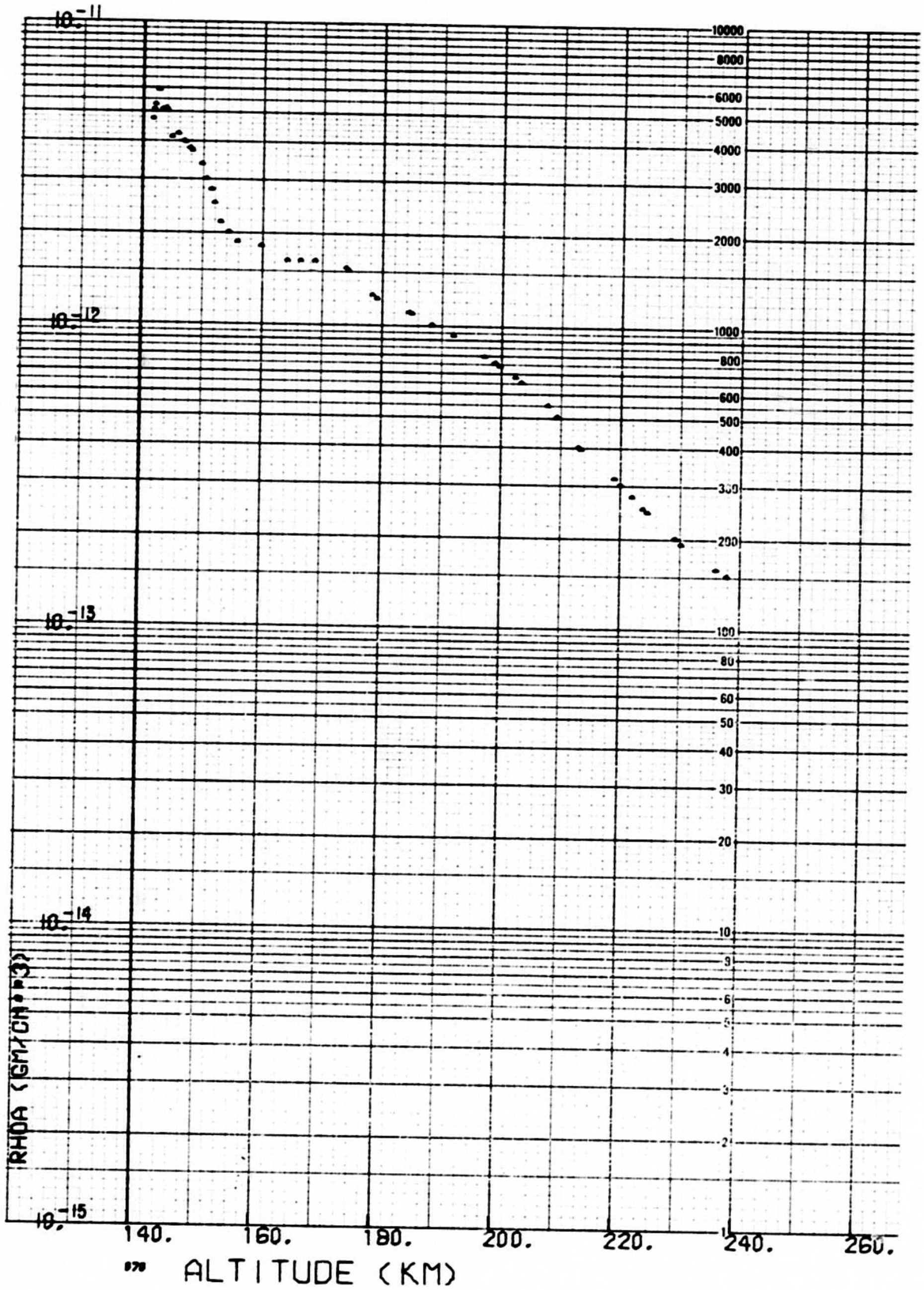

Fig. B-71. LOGACS Density Data for Rev. 51, Toward Perigee

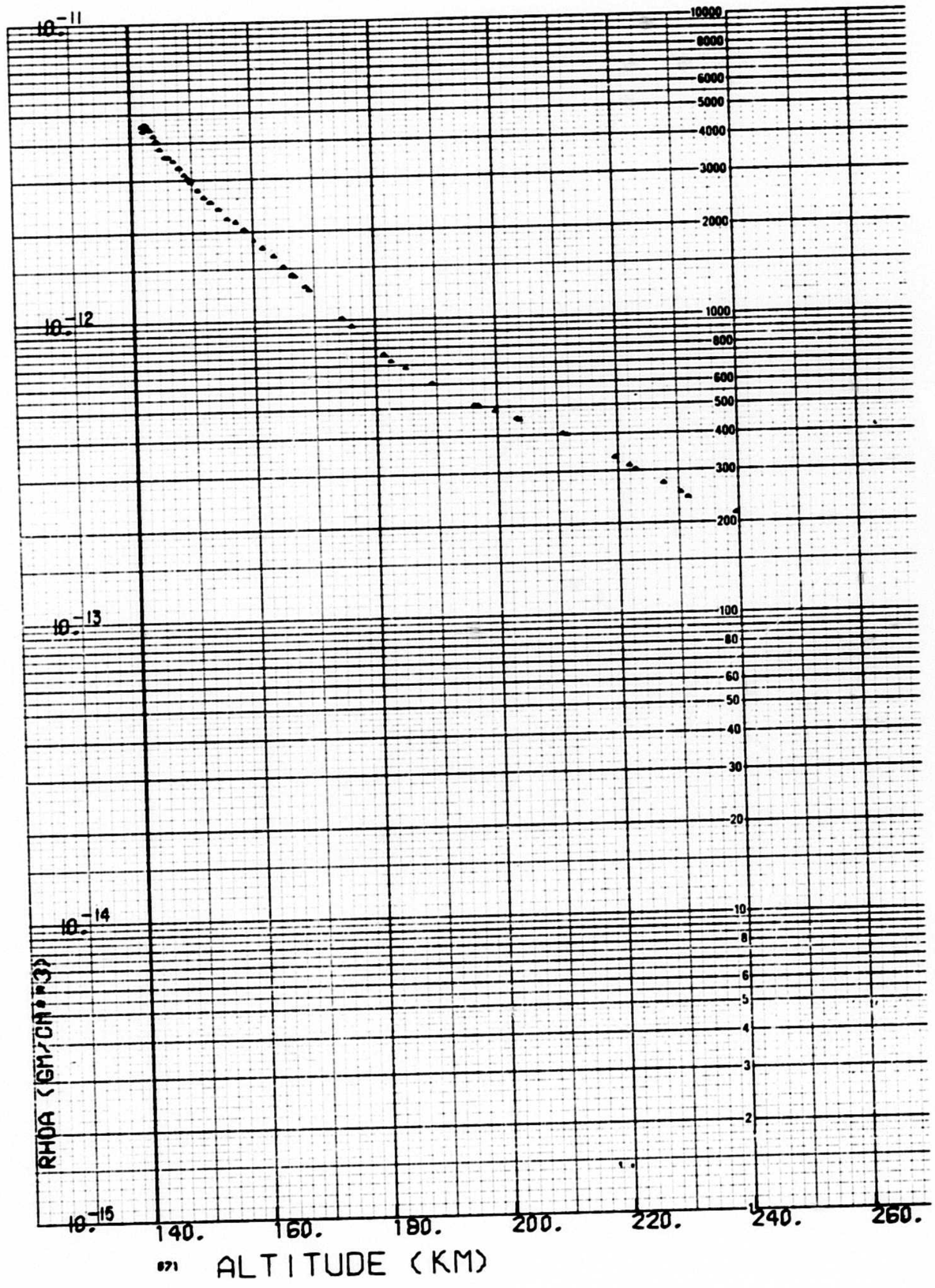

Fig. B-72. LOGACS Density Data for Rev. 51, Away from Perigee

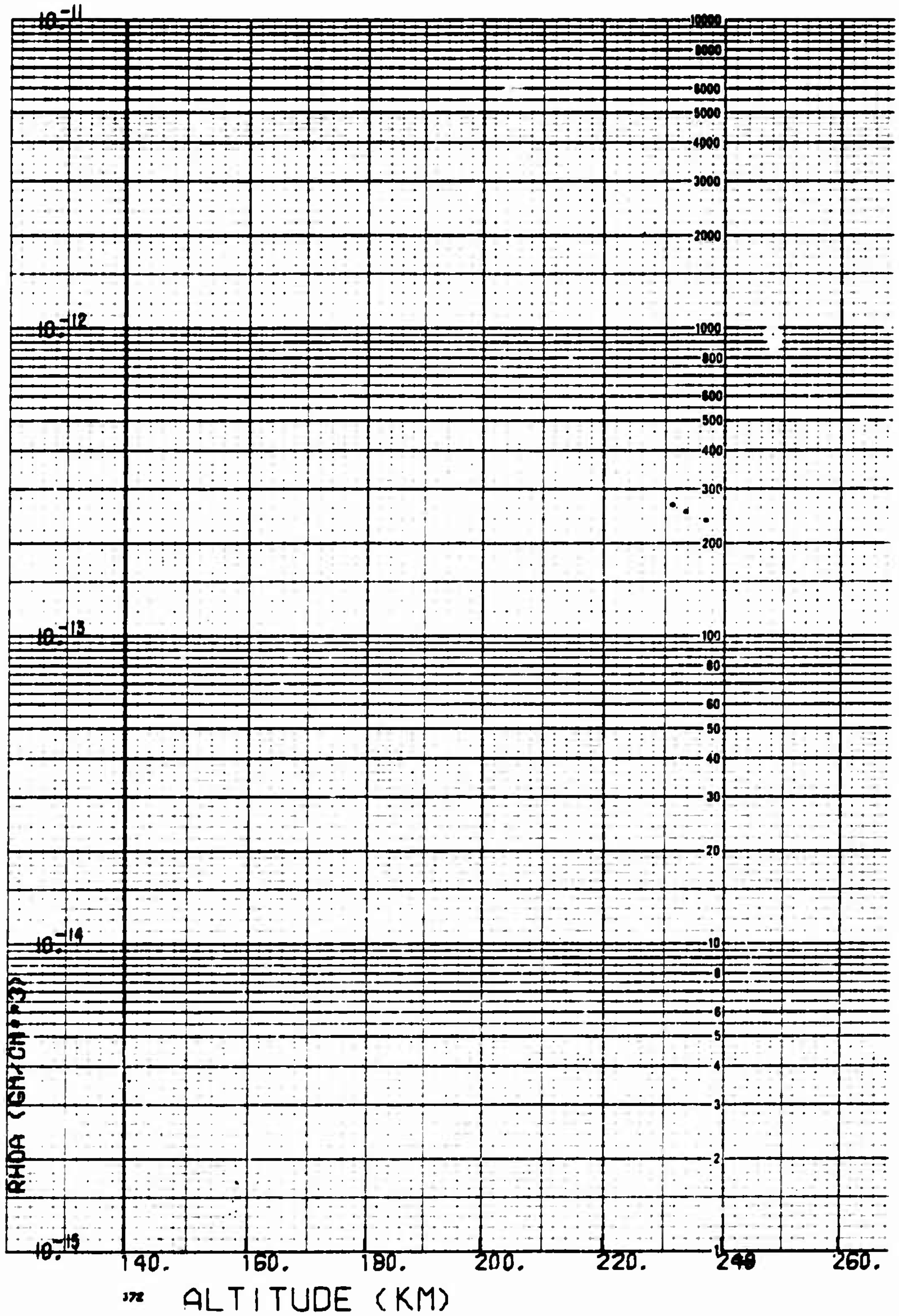

Fig. B-73. LOGACS Density Data for Rev. 52, Toward Perigee

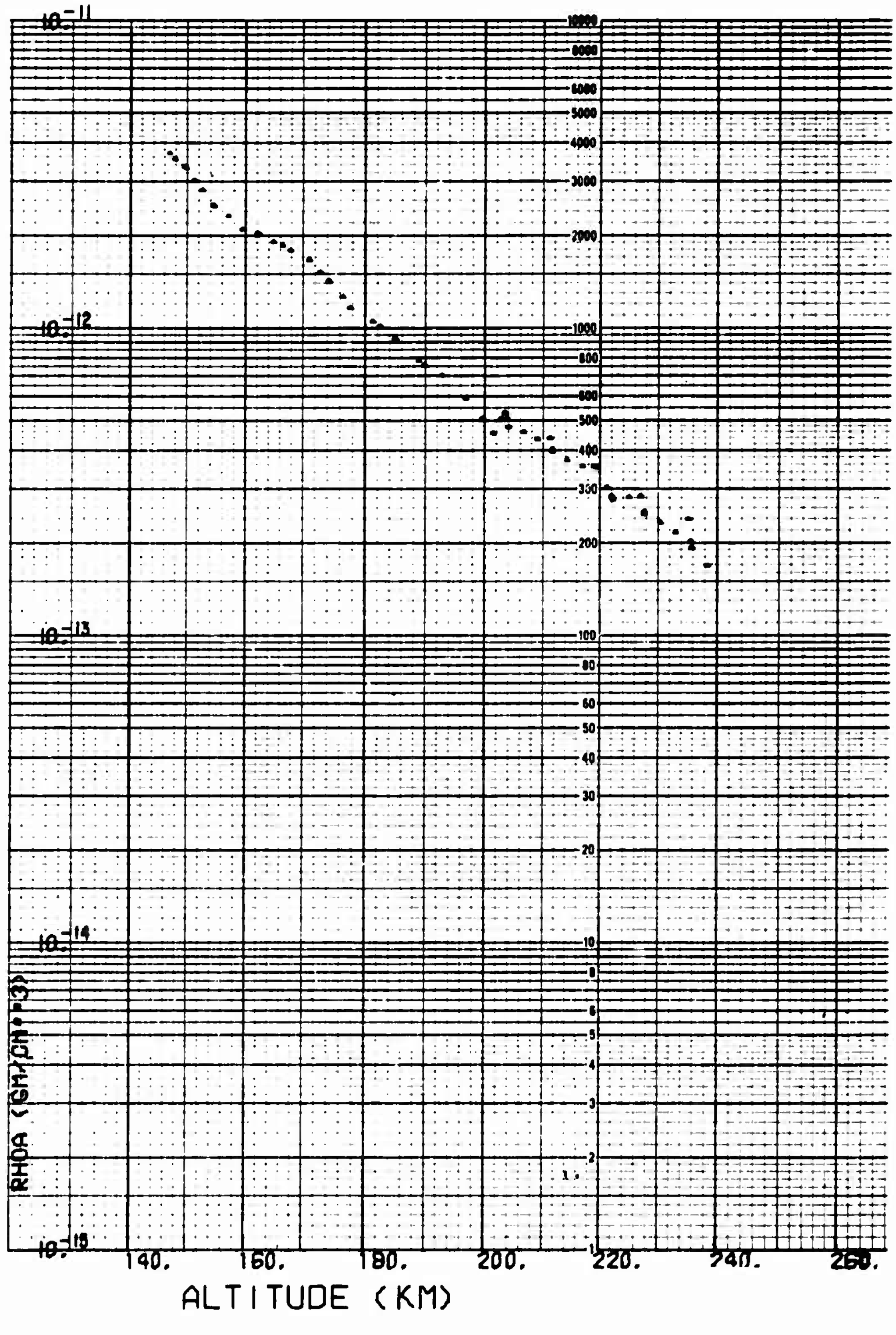

Fig. B-74. LOGACS Density Data for Rev. 52, Away from Perigee

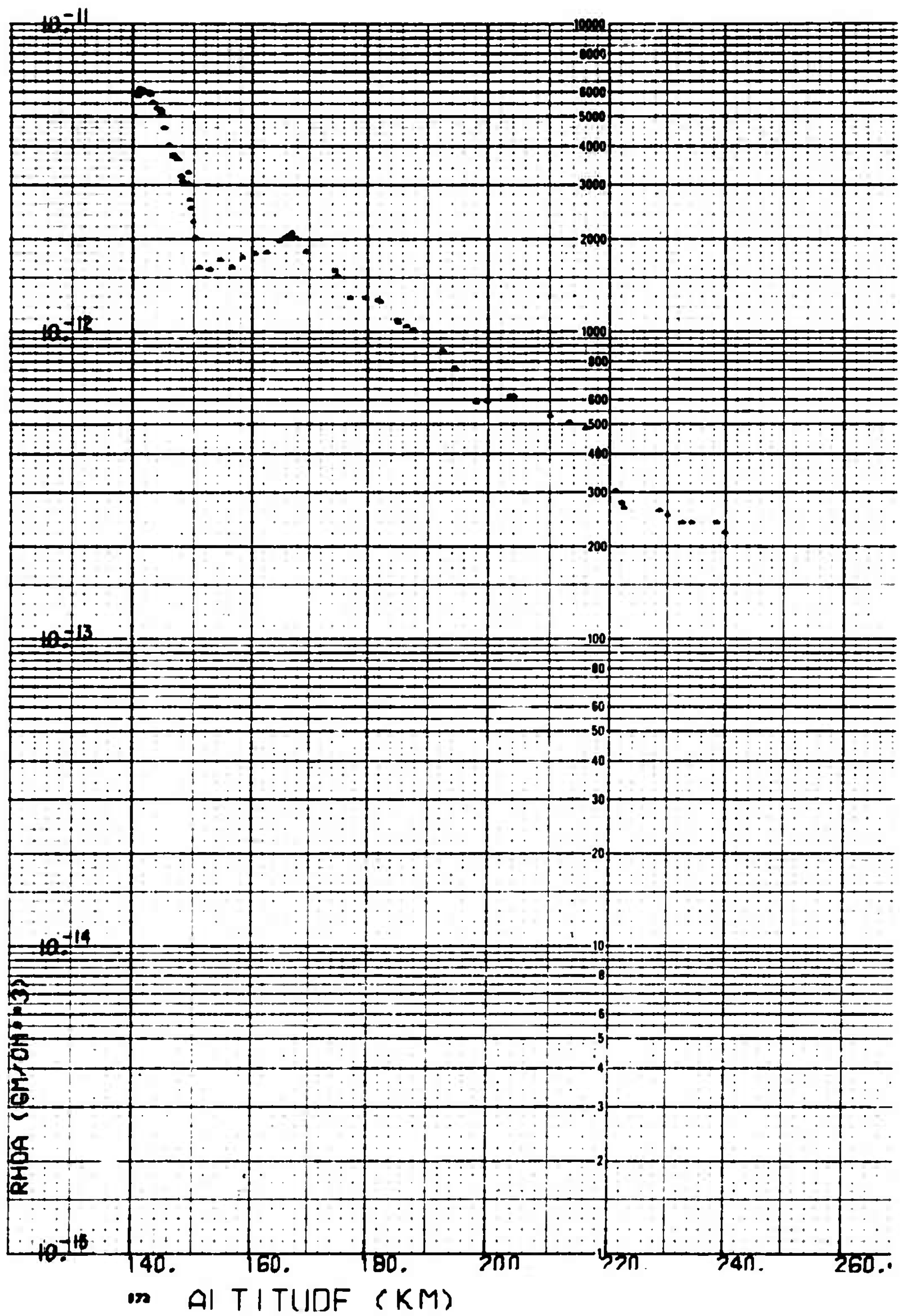

Fig. B-75. LOGACS Density Data for Rev. 53, Toward Perigee

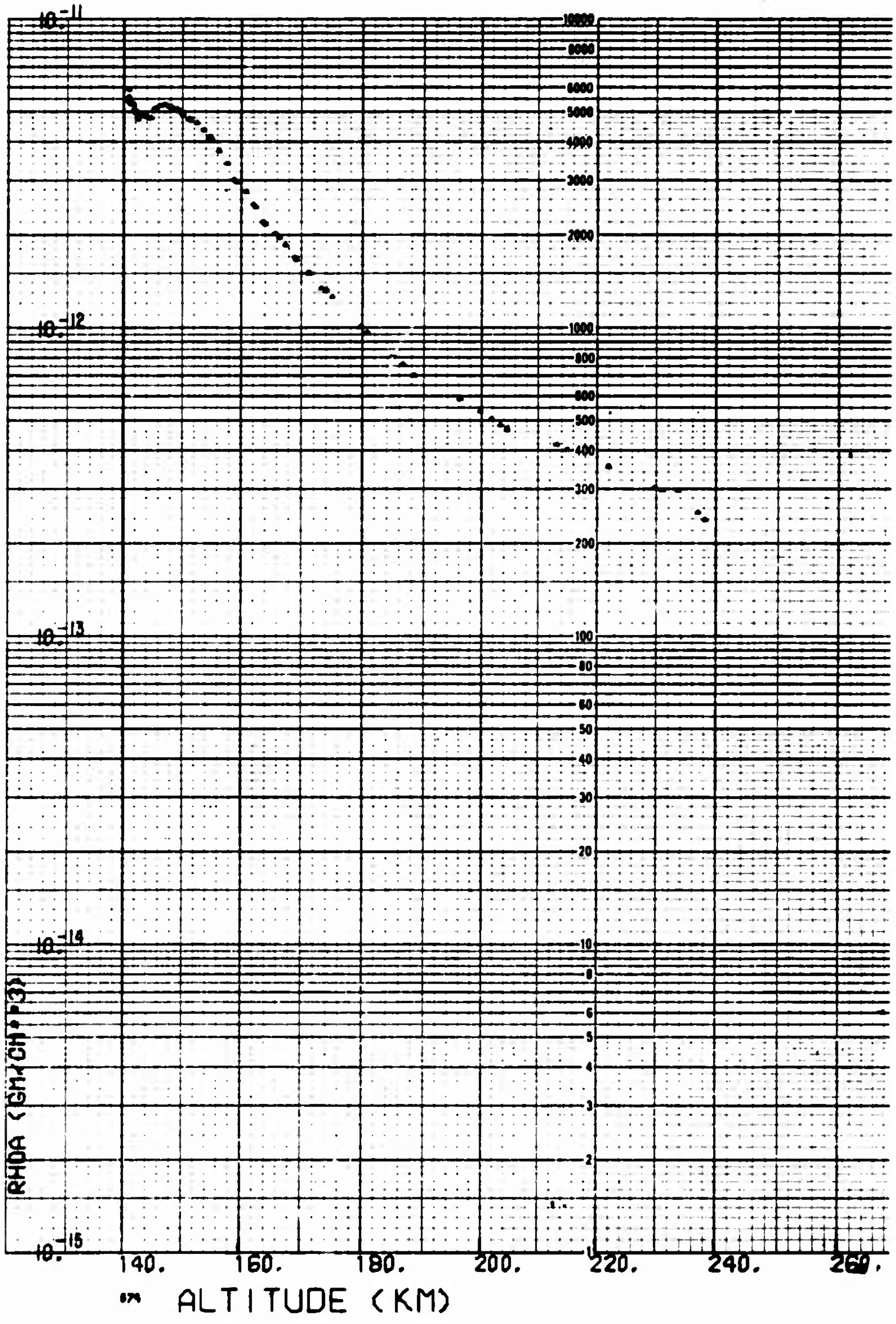

Fig. B-76. LOGACS Density Data for Rev. 53, Away from Perigee

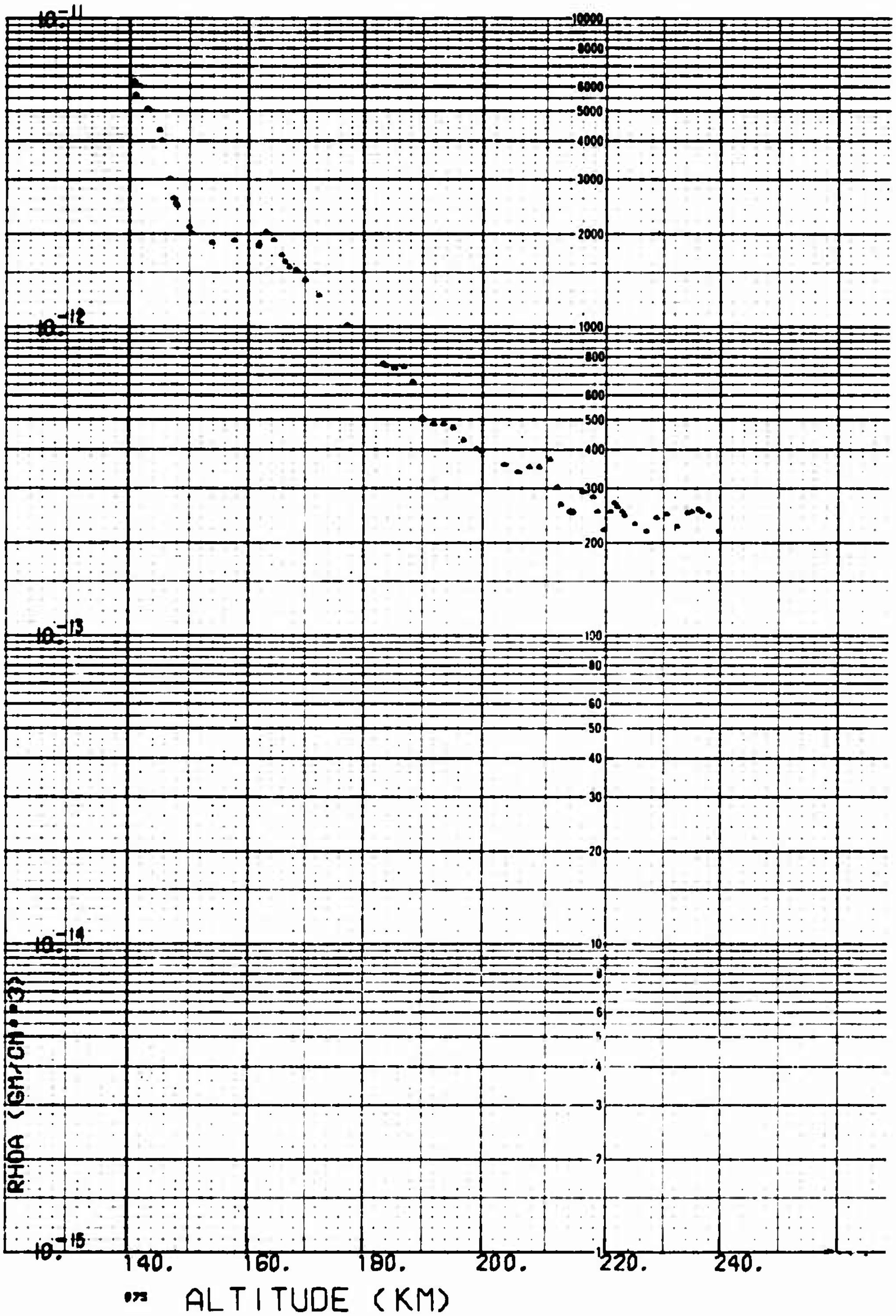

Fig. B-77. LOGACS Density Data for Rev. 54, Toward Perigee

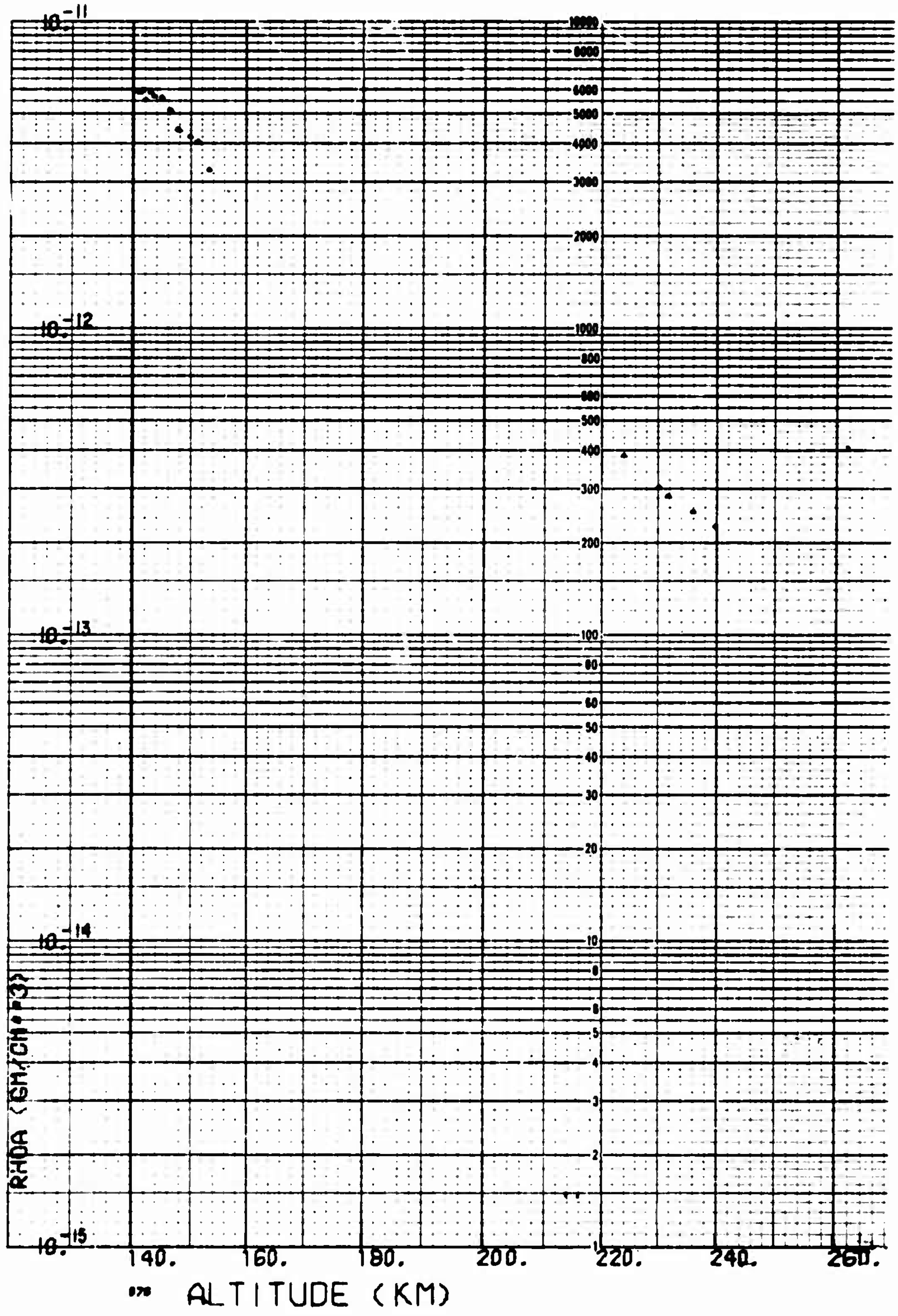

Fig. B-78. LOGACS Density Data for Rev. 54, Away from Perigee

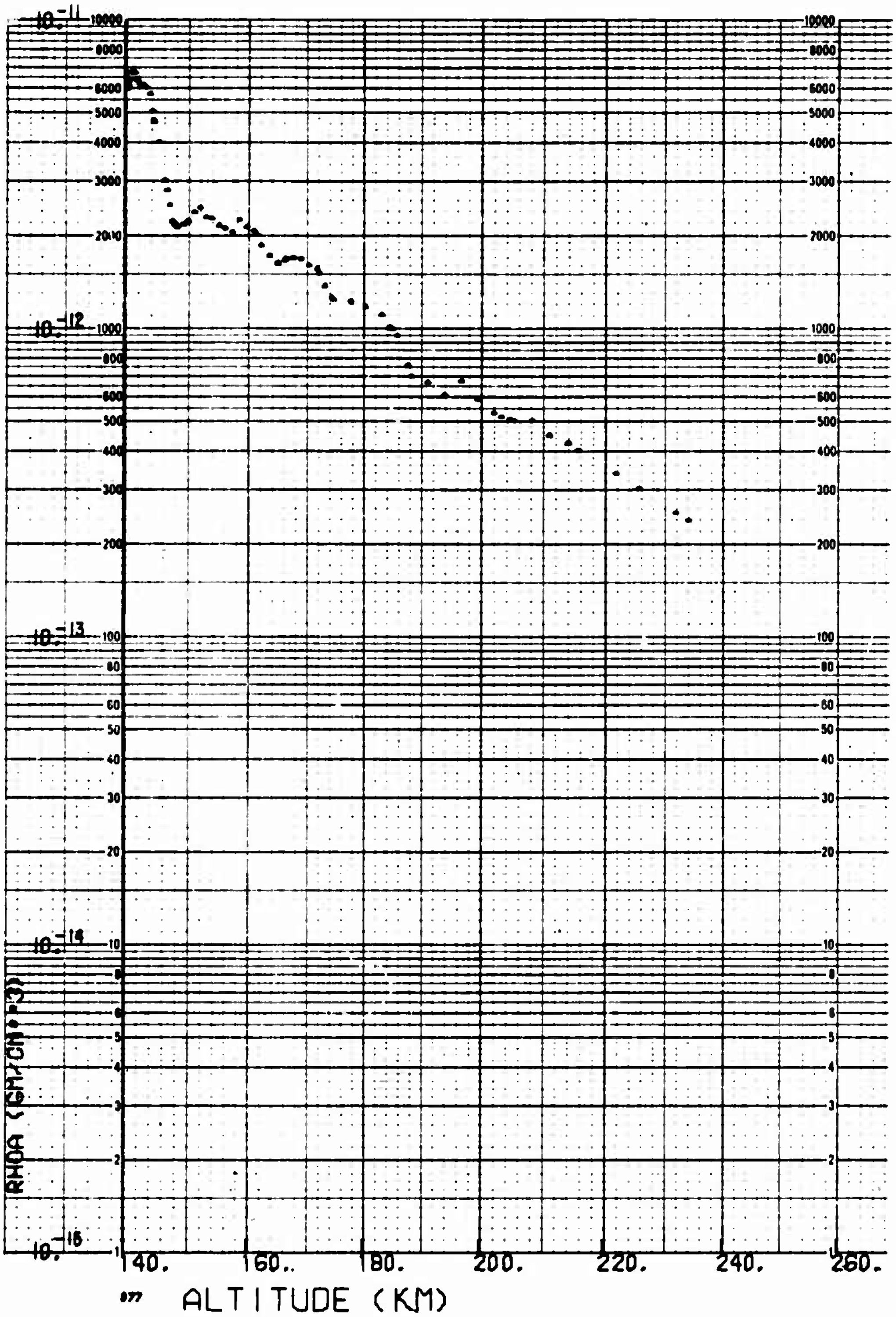

Fig. B-79. LOGACS Density Data for Rev. 55, Toward Perigee

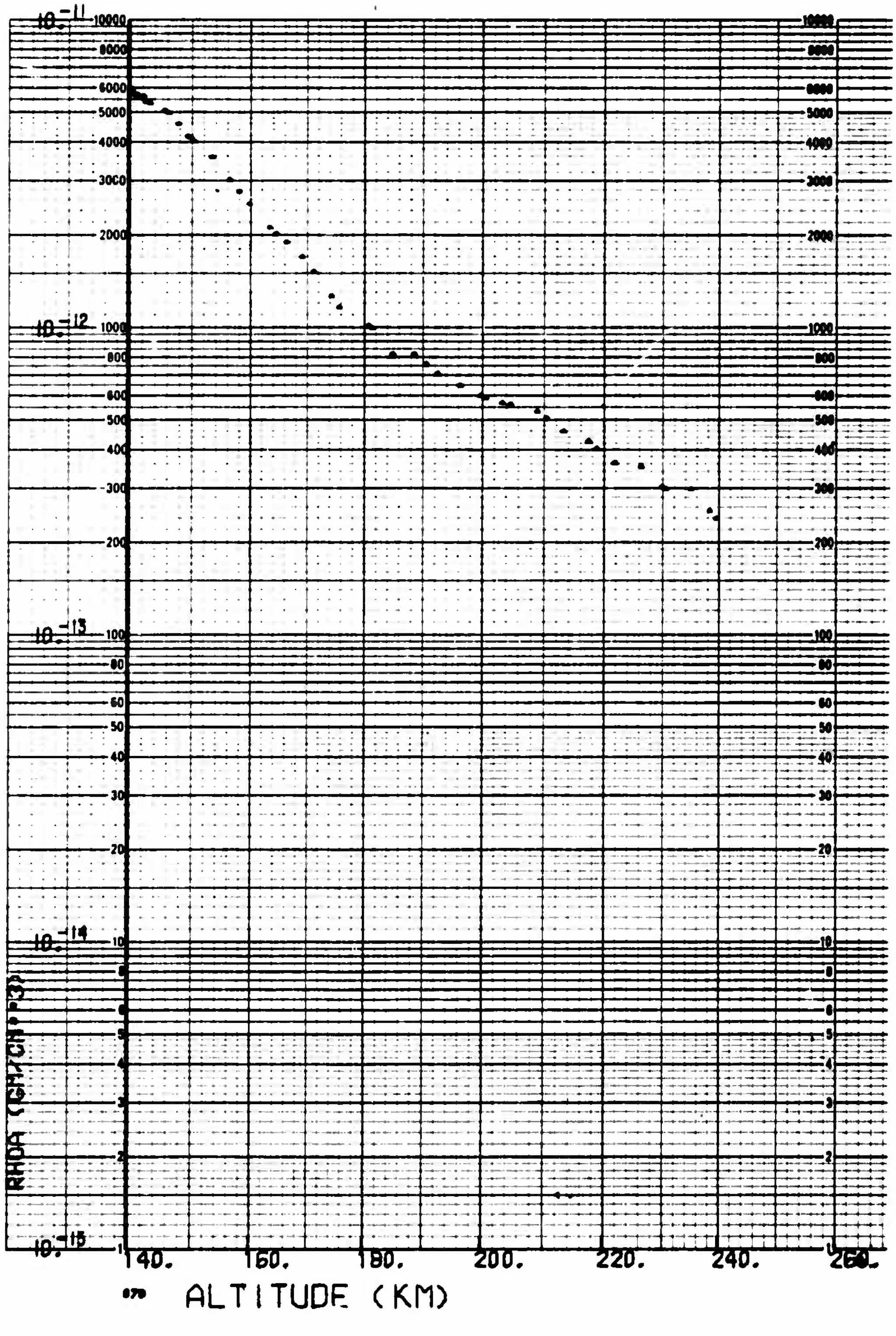

Fig. B-80. LOGACS Density Data for Rev. 55, Away from Perigee

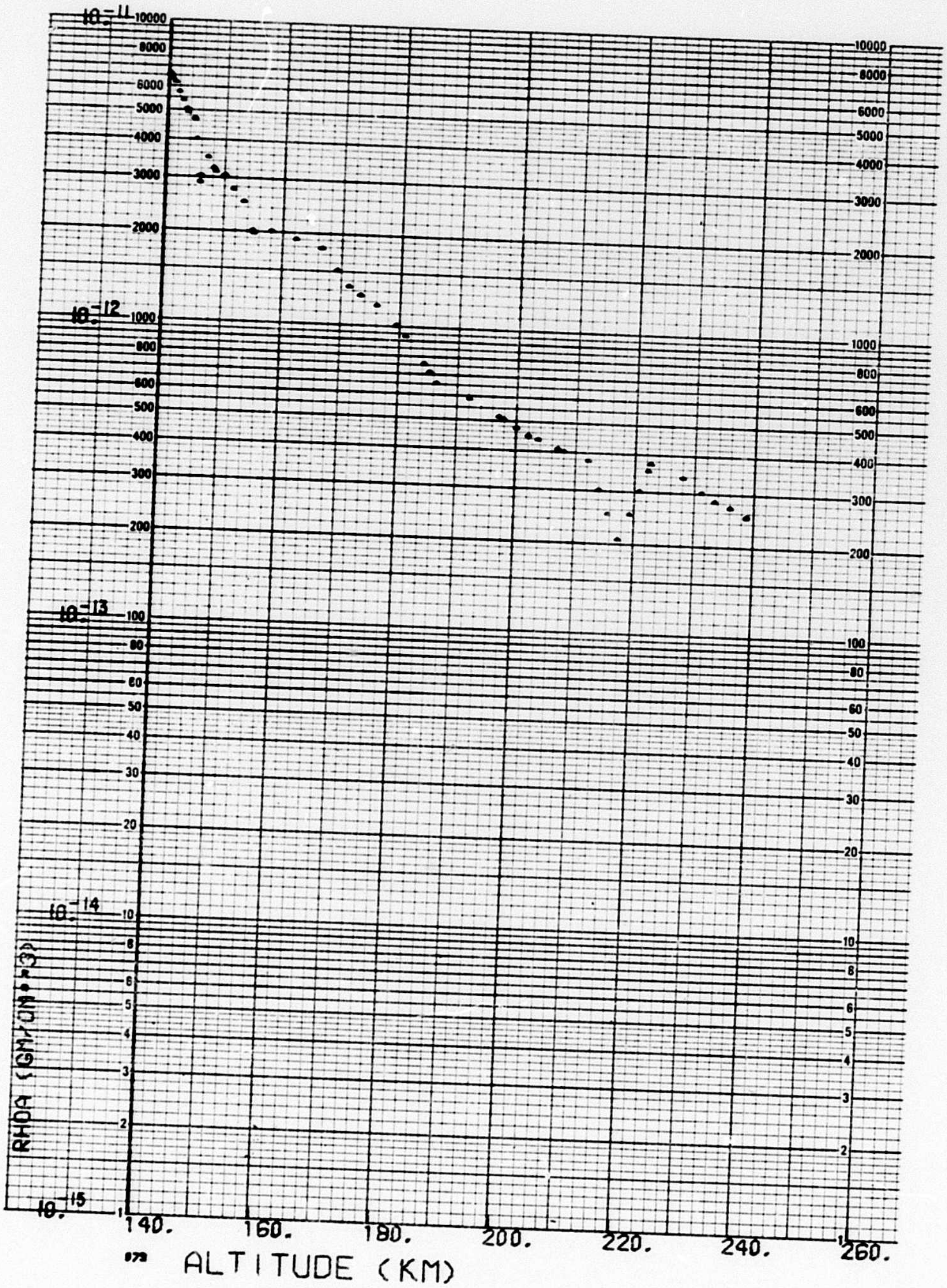

Fig. B-81. LOGACS Density Data for Rev. 56, Toward Perigee

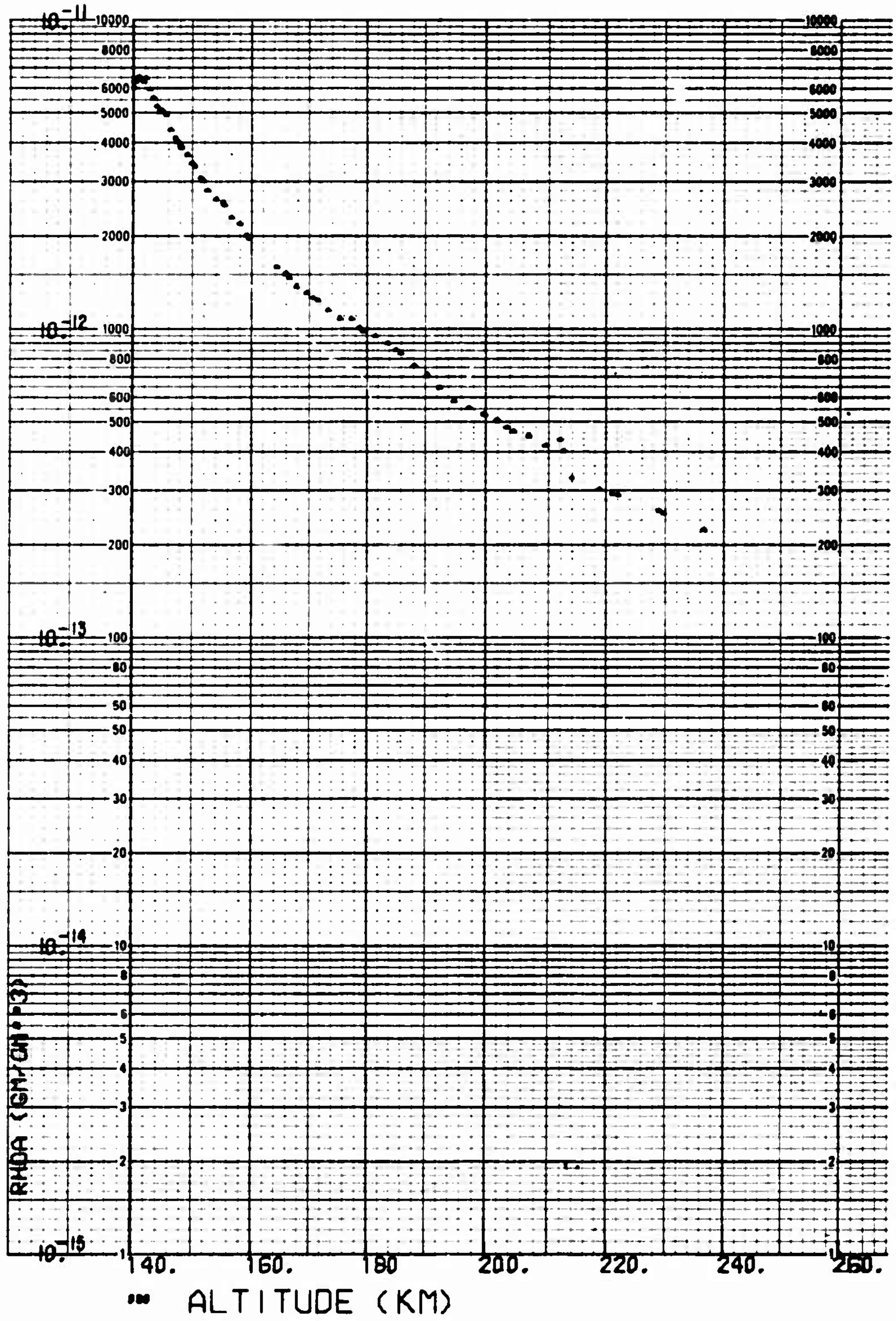

Fig. B-82. LOGACS Density Data for Rev. 56, Away from Perigee

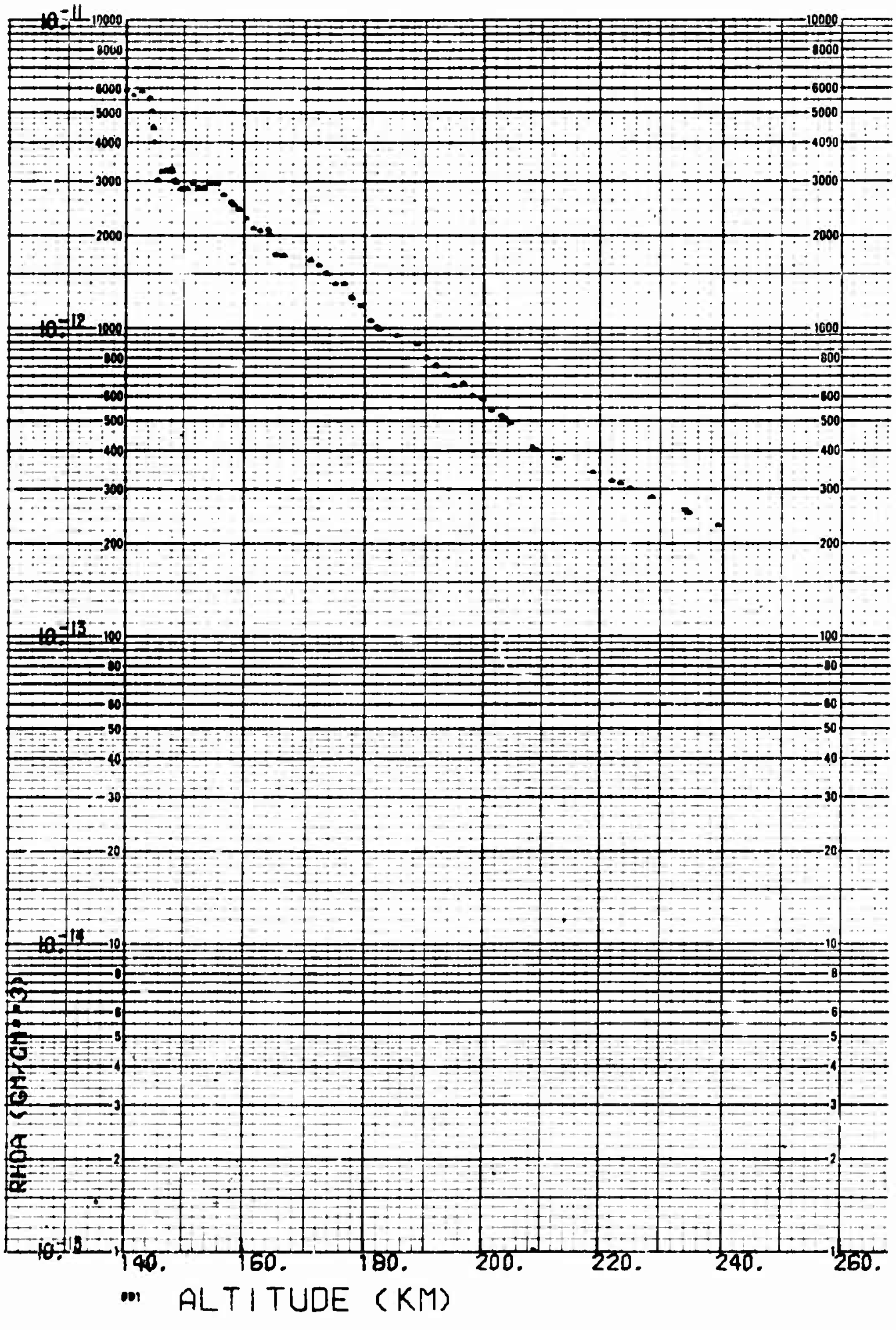

Fig. B-83. LOGACS Density Data for Rev. 57, Toward Perigee

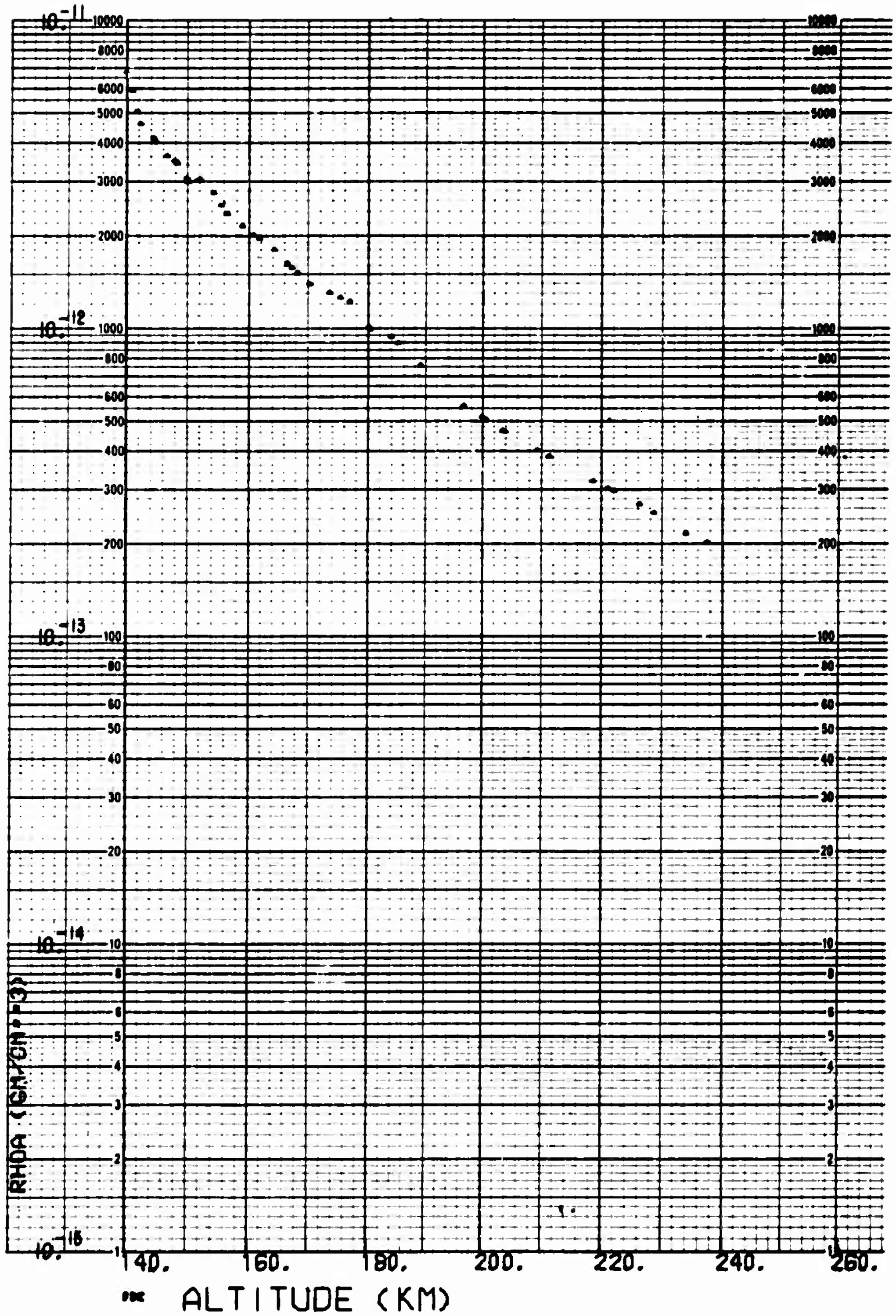

Fig. B-84. LOGACS Density Data for Rev. 57, Away from Perigee

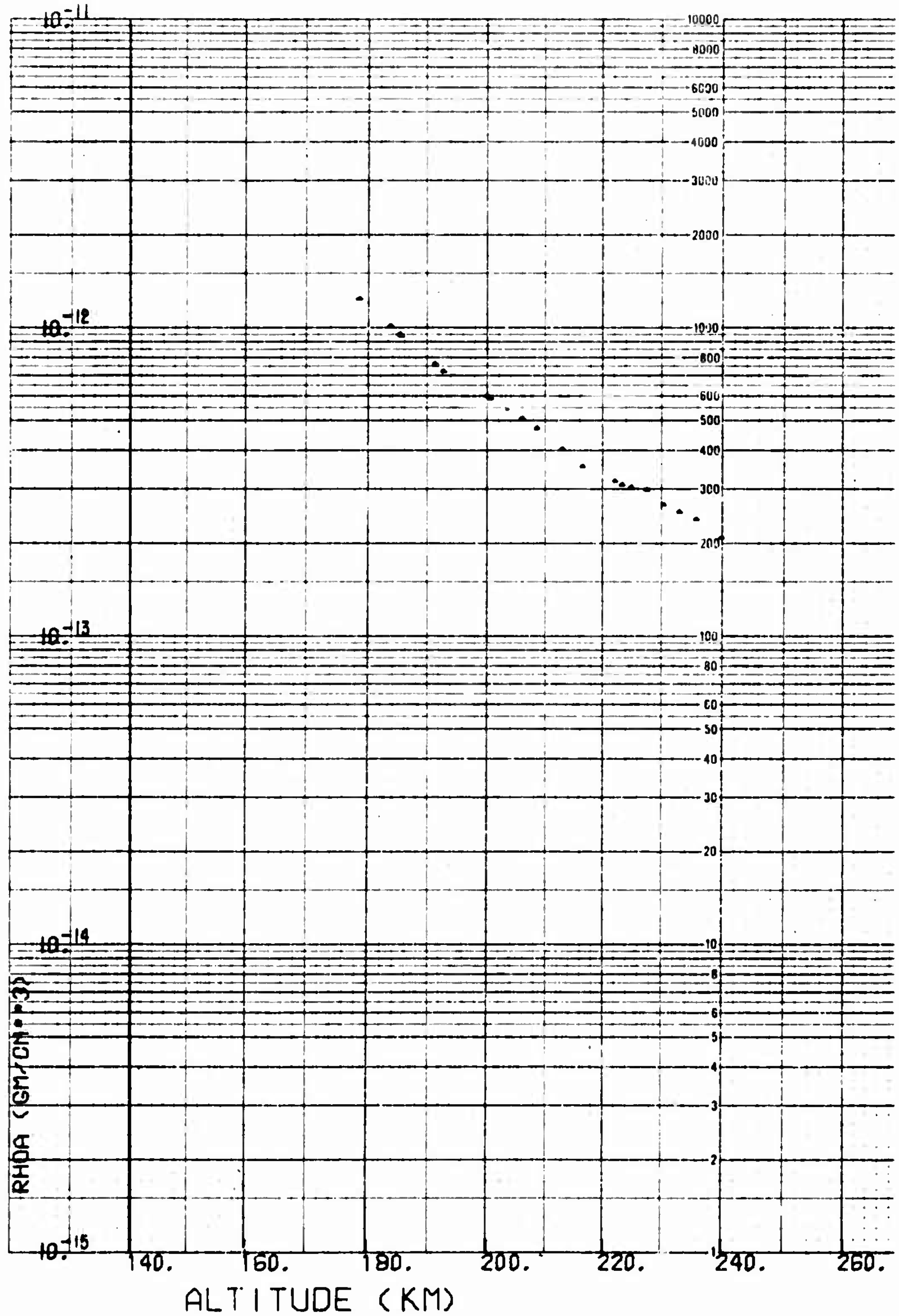

Fig. B-85. LOGACS Density Data for Rev. 58, Away from Perigee

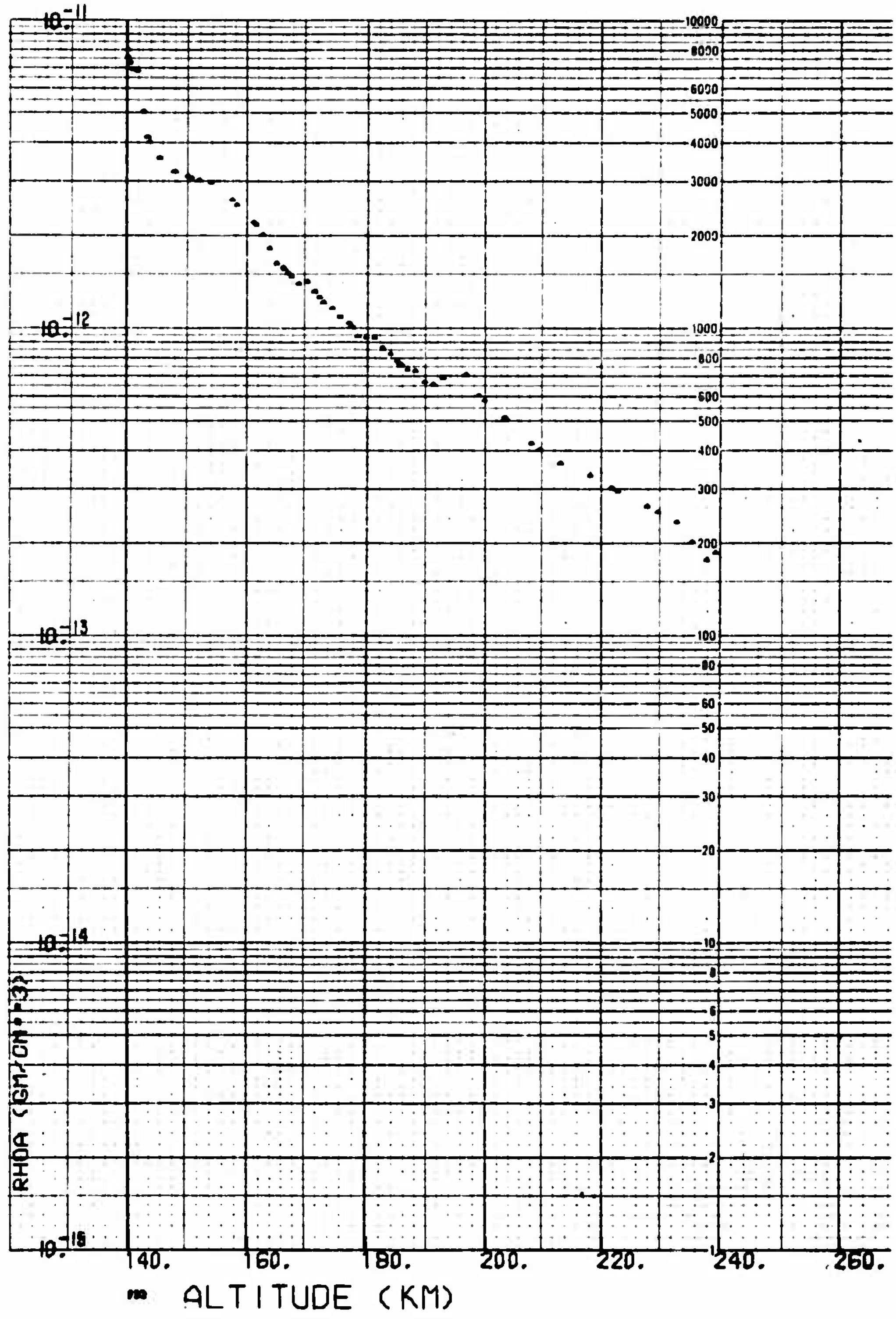

Fig. B-86. LOGACS Density Data for Rev. 59, Toward Perigee

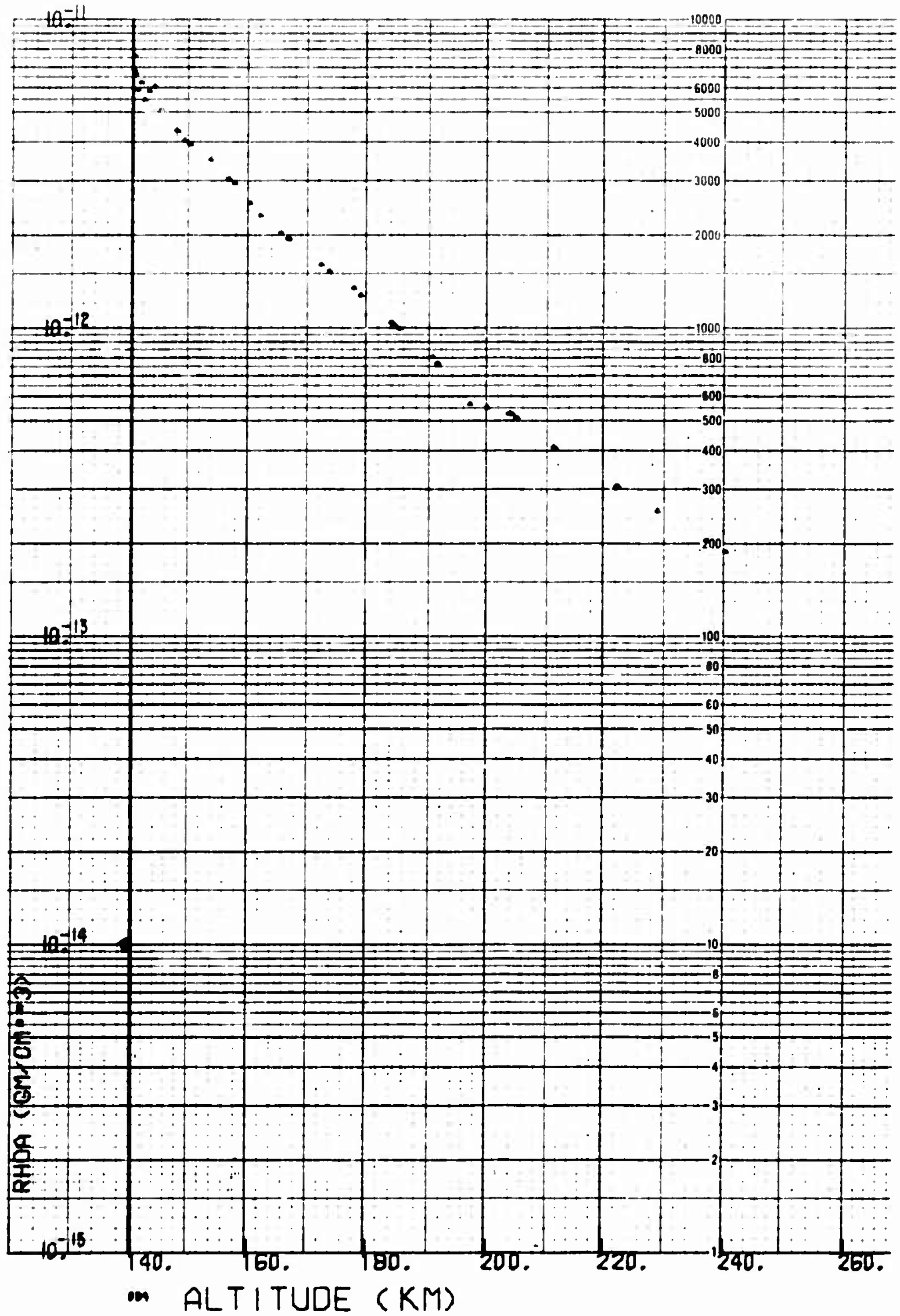

Fig. B-87. LOGACS Density Data for Rev. 59, Away from Perigee

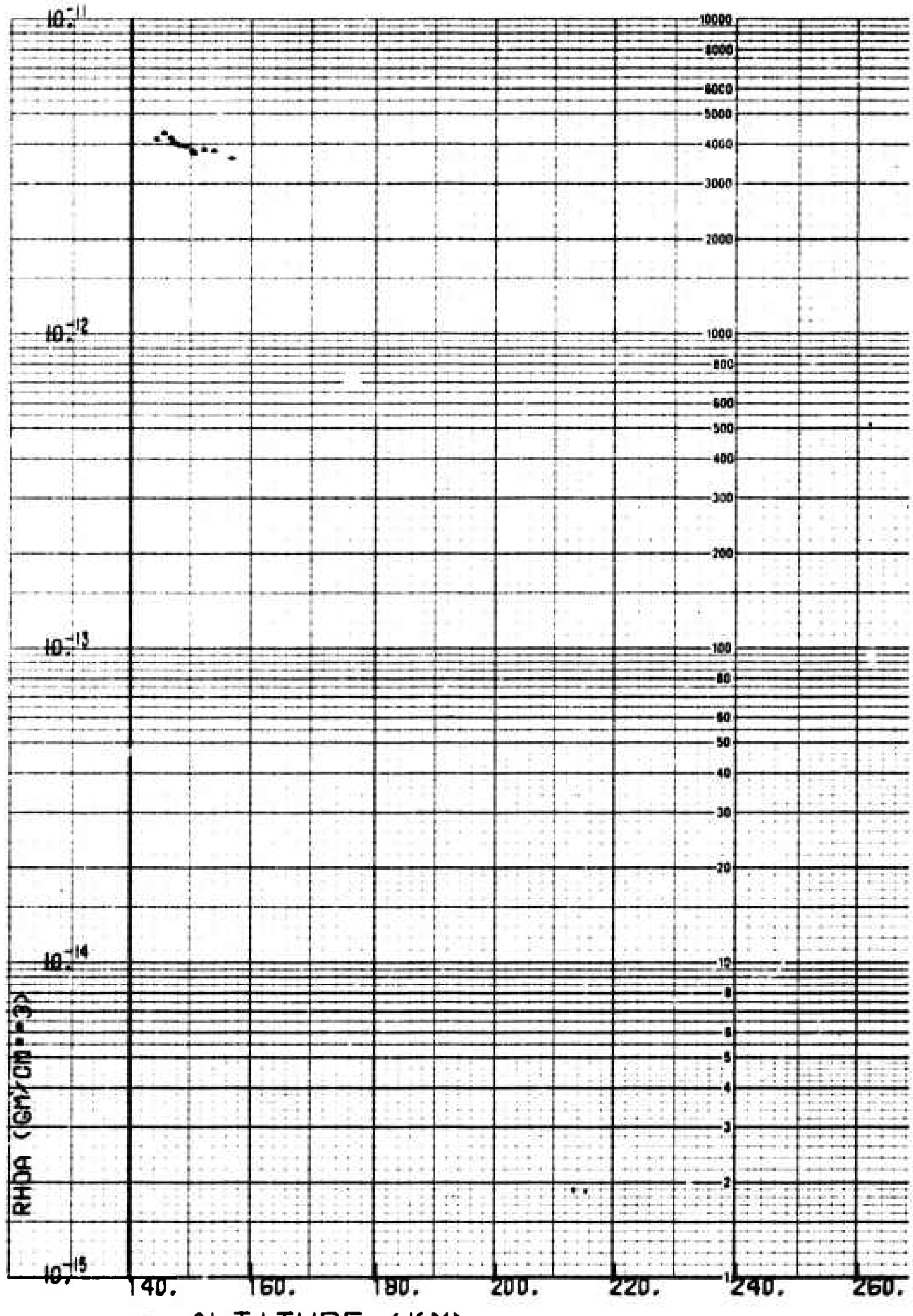

Fig. B-88. LOGACS Density Data for Rev. 61, Away from Perigee

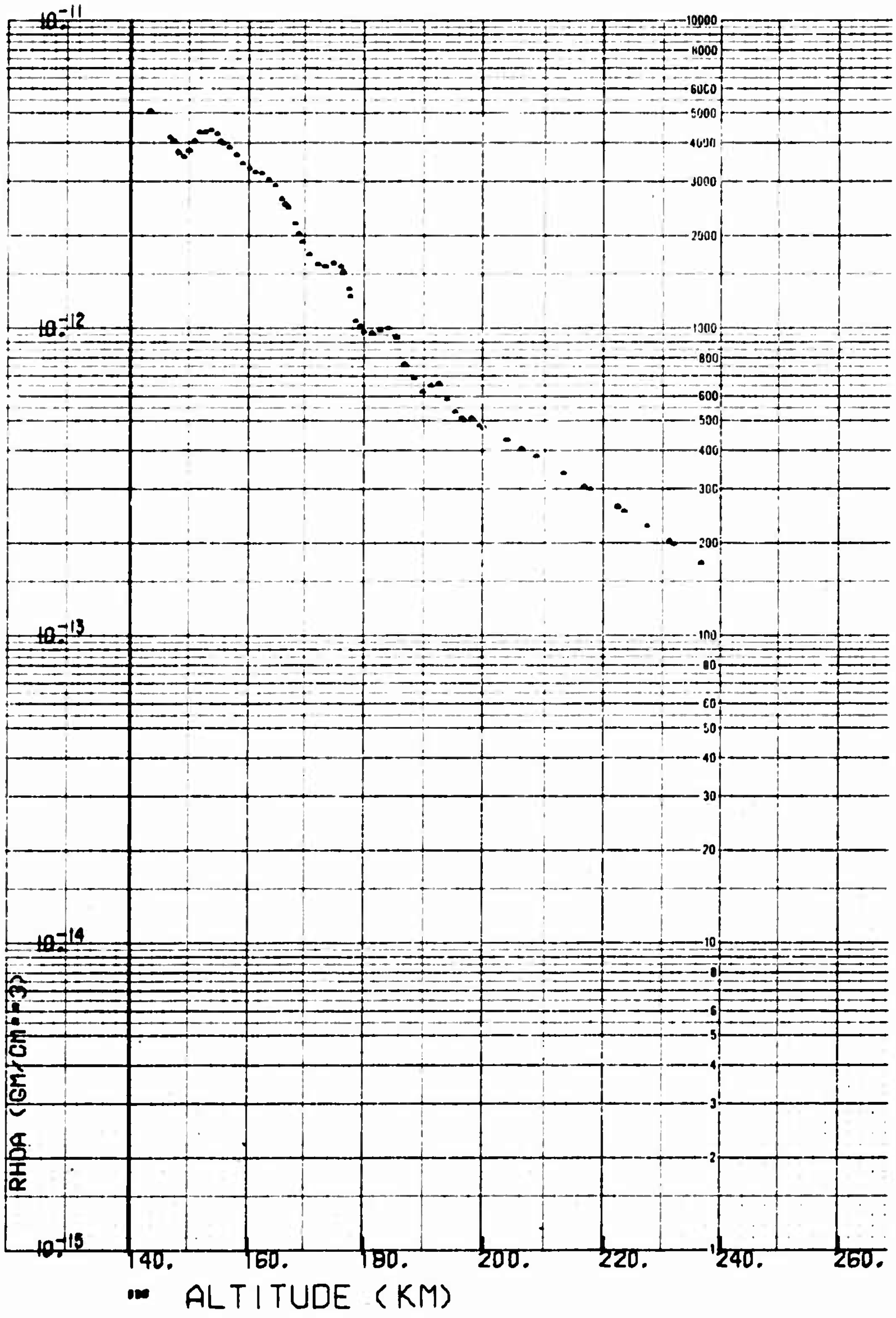

Fig. B-89. LOGACS Density Data for Rev. 62, Toward Perigee

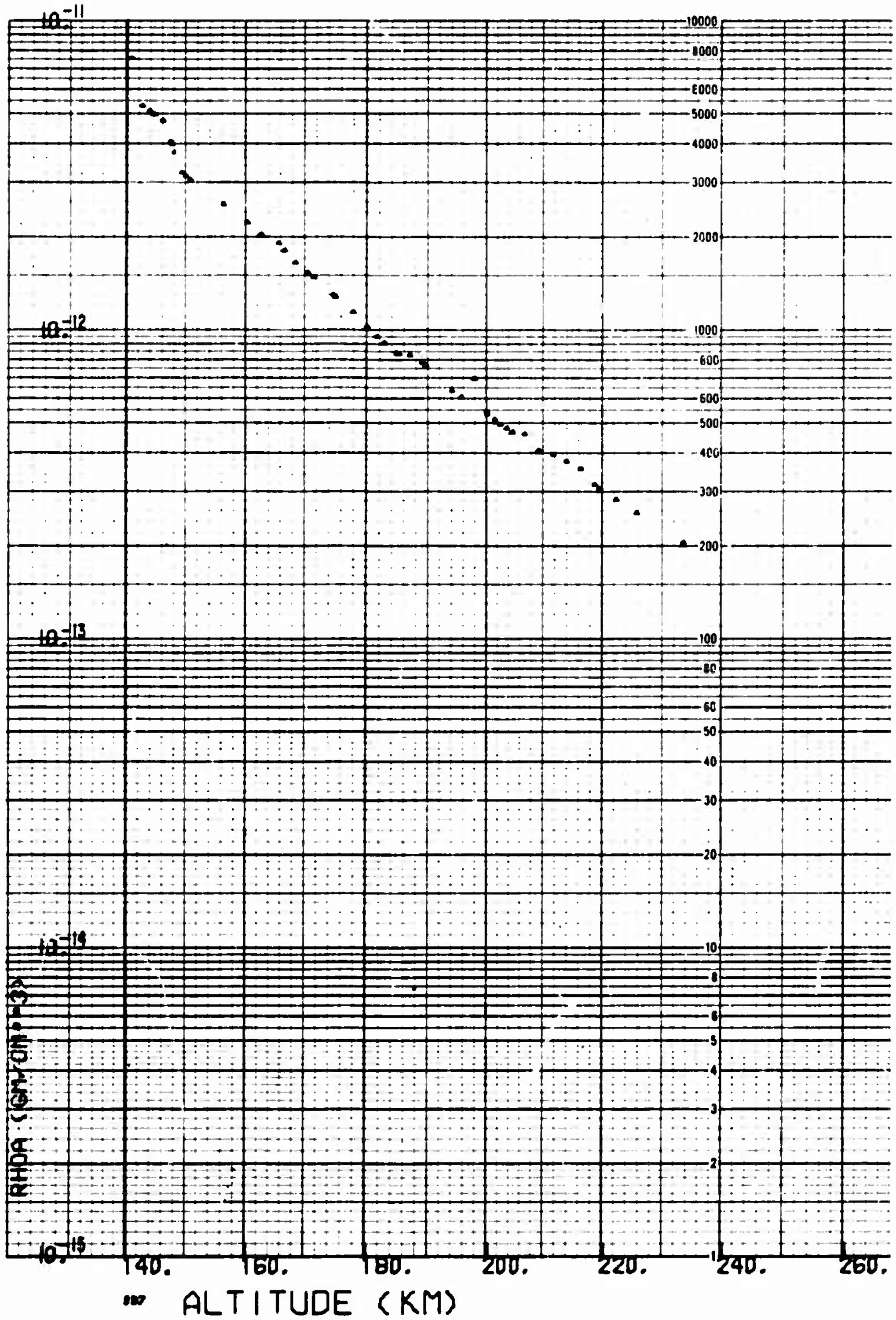

Fig. B-90. LOGACS Density Data for Rev. 62, Away from Perigee

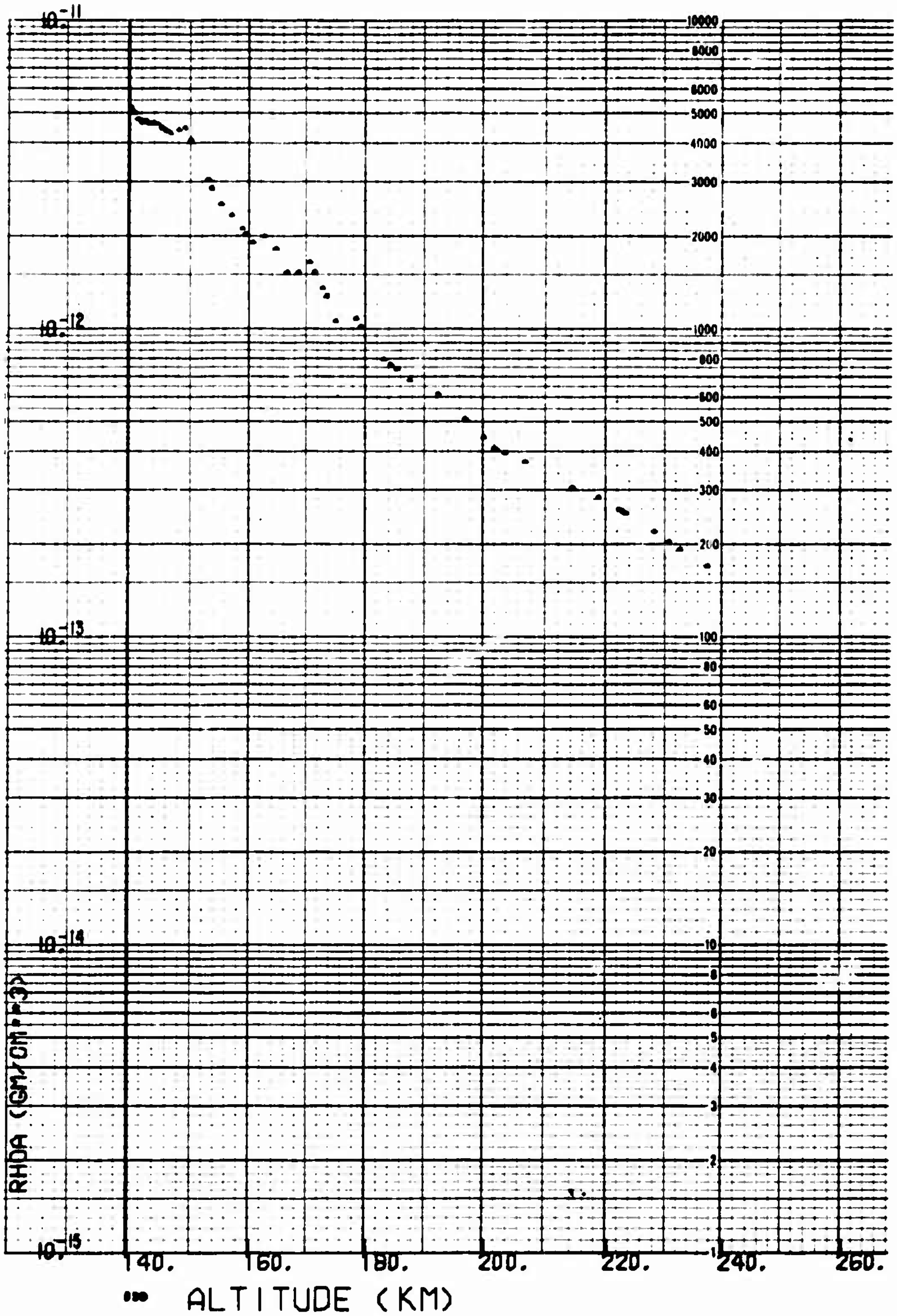

Fig. B-91. LOGACS Density Data for Rev. 63, Toward Perigee

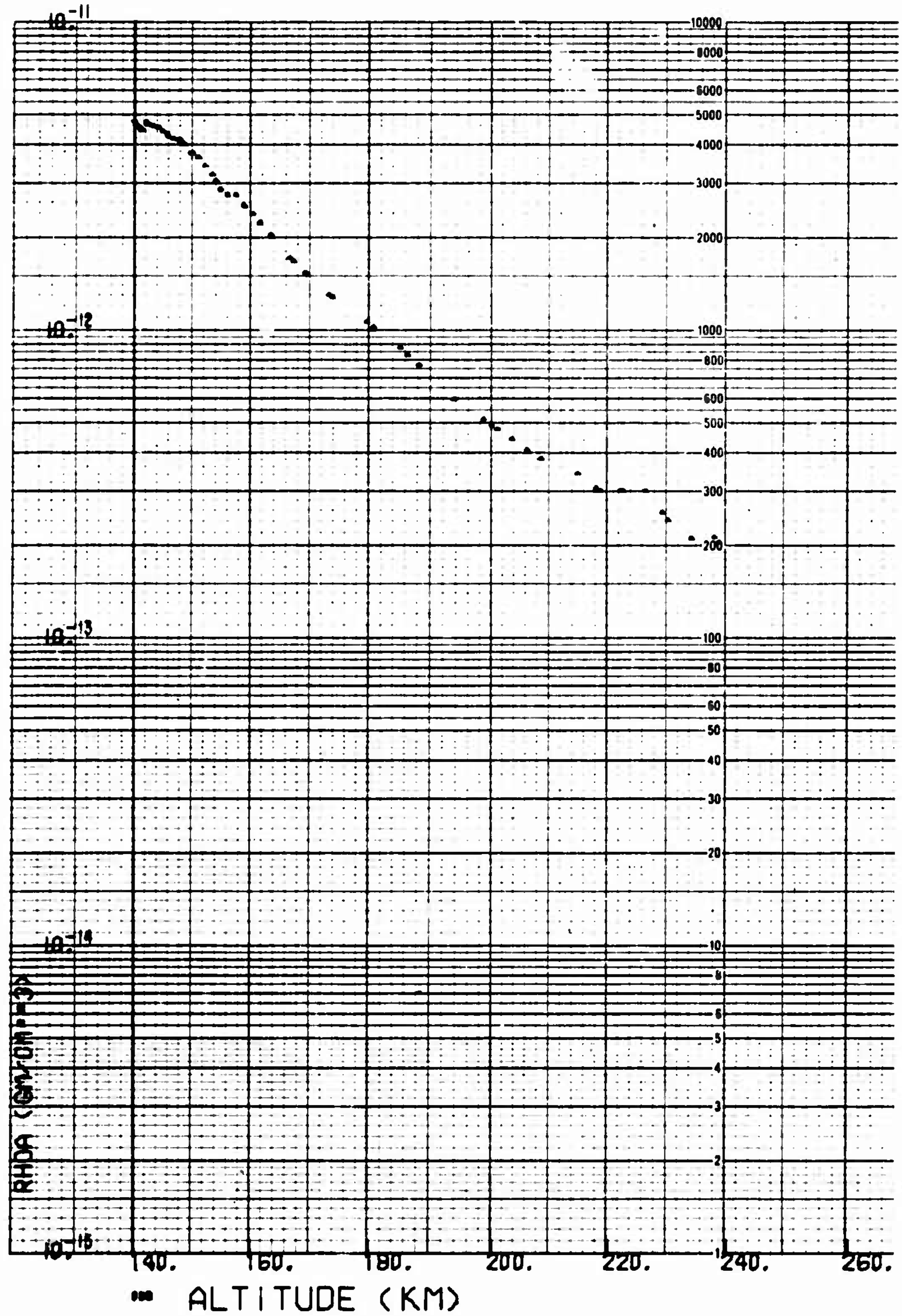

Fig. B-92. LOGACS Density Data for Rev. 63, Away from Perigee

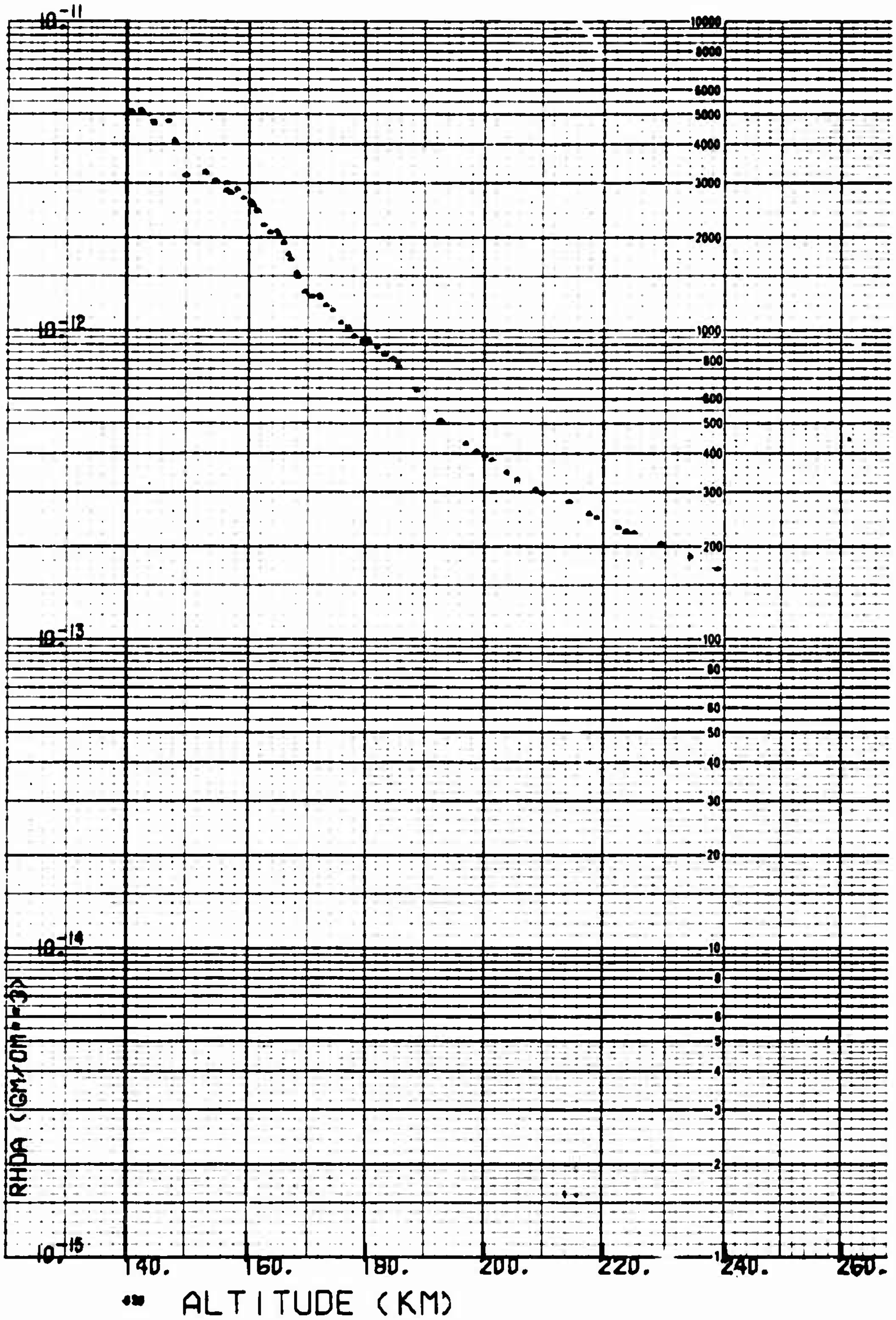

Fig. B-93. LOGACS Density Data for Rev. 64, Toward Perigee

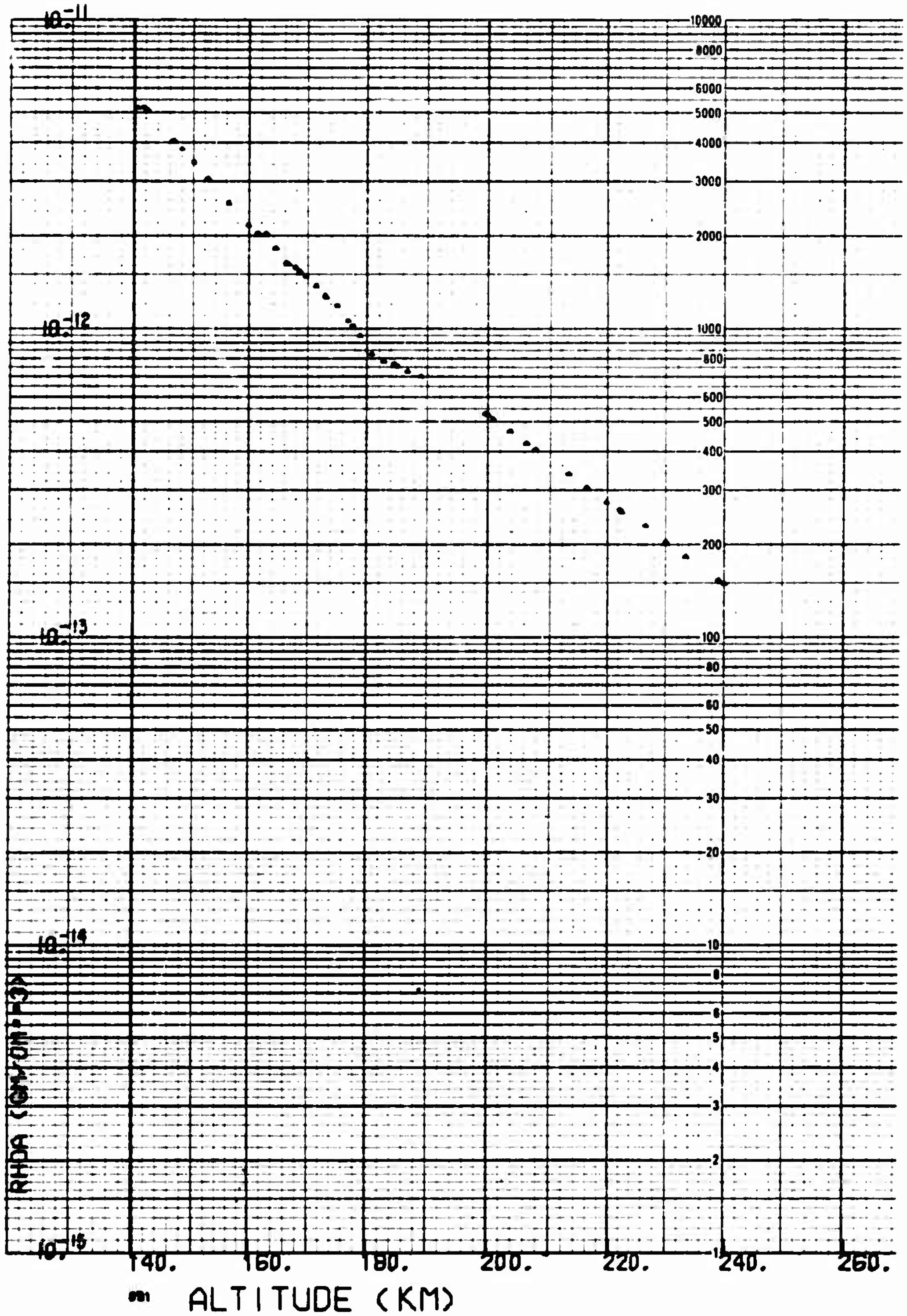

Fig. B-94. LOGACS Density Data for Rev. 64, Away from Perigee

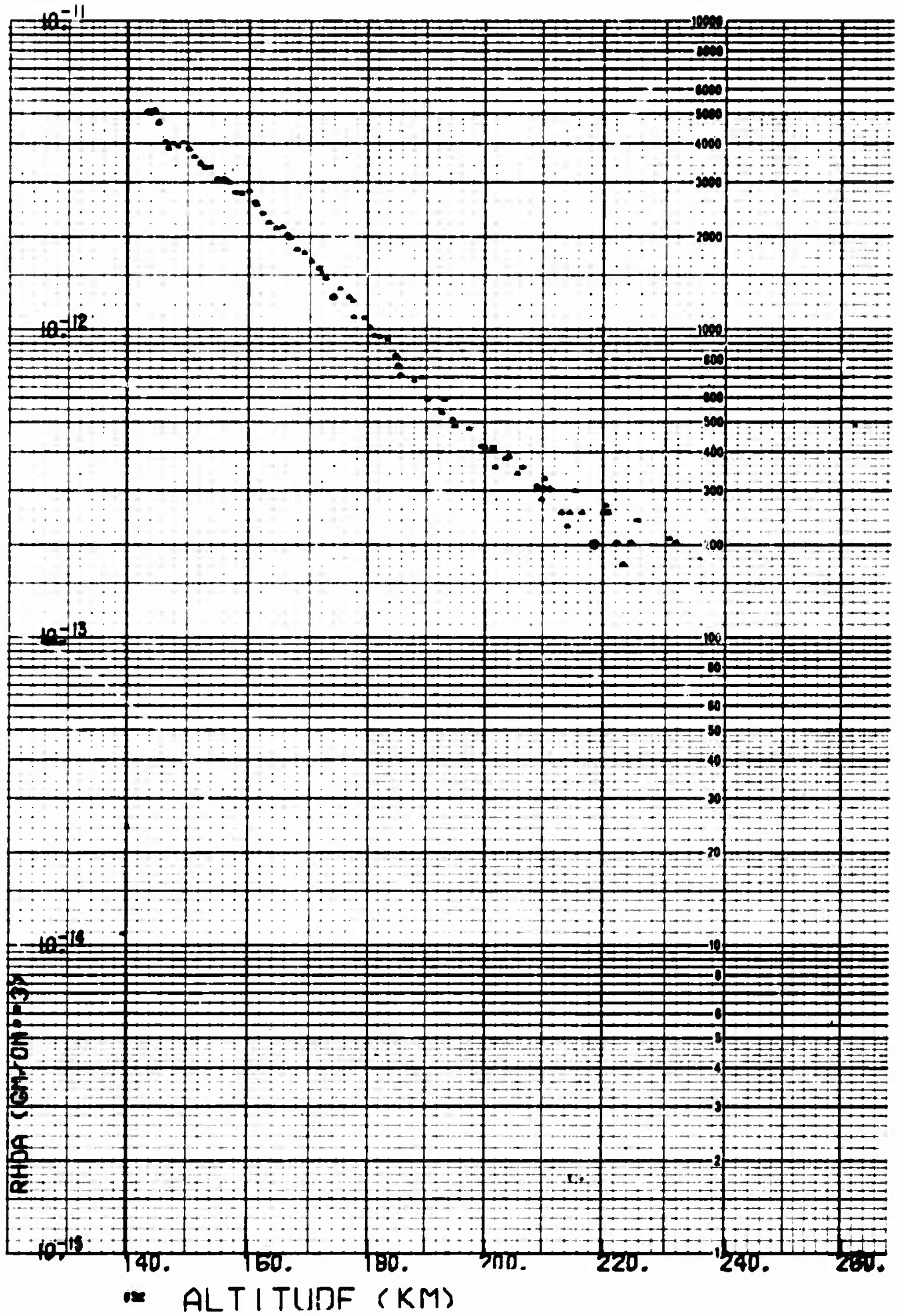

Fig. B-95. LOGACS Density Data for Rev. 65, Toward Perigee

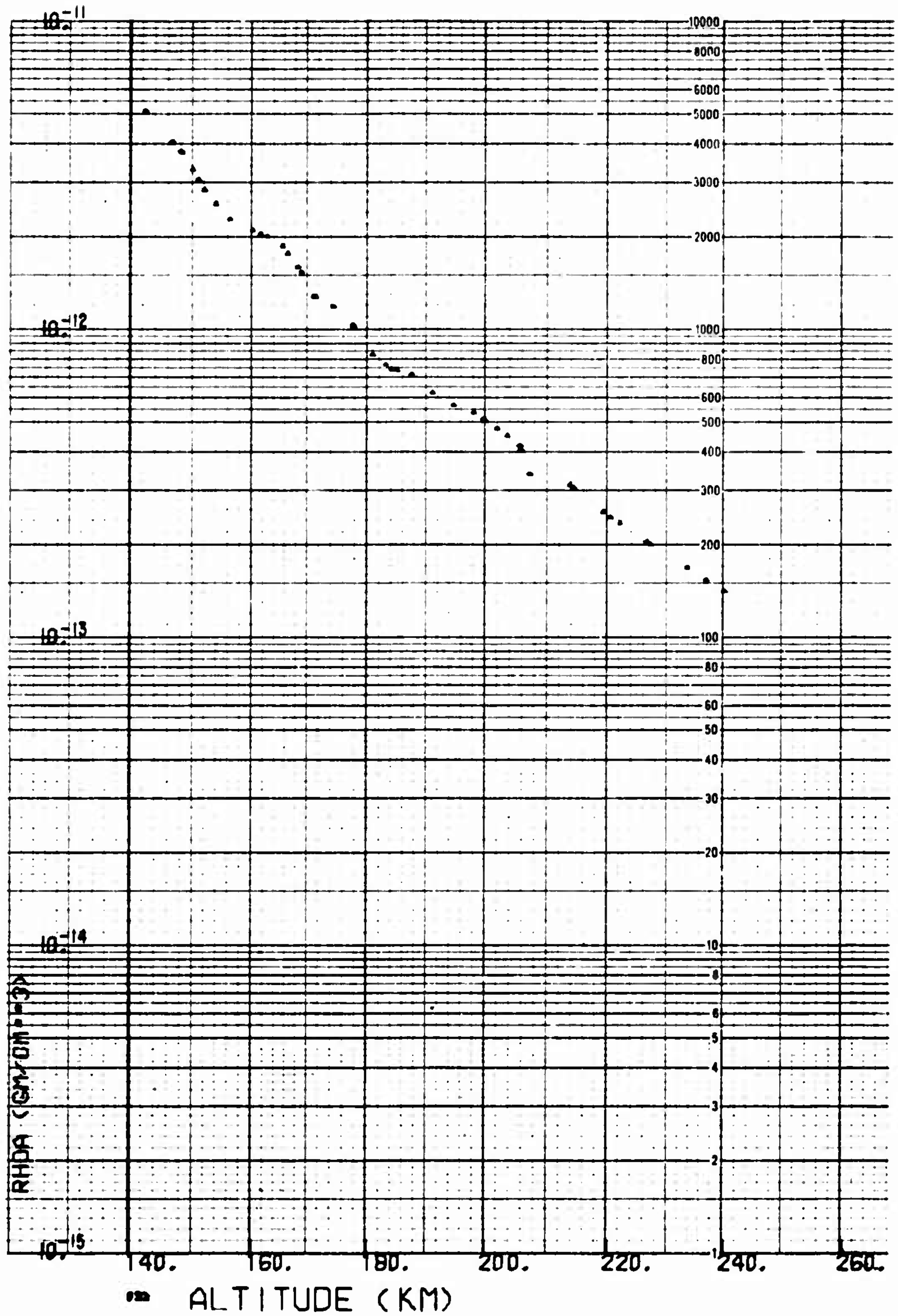

Fig. B-96. LOGACS Density Data for Rev. 65, Away from Perigee

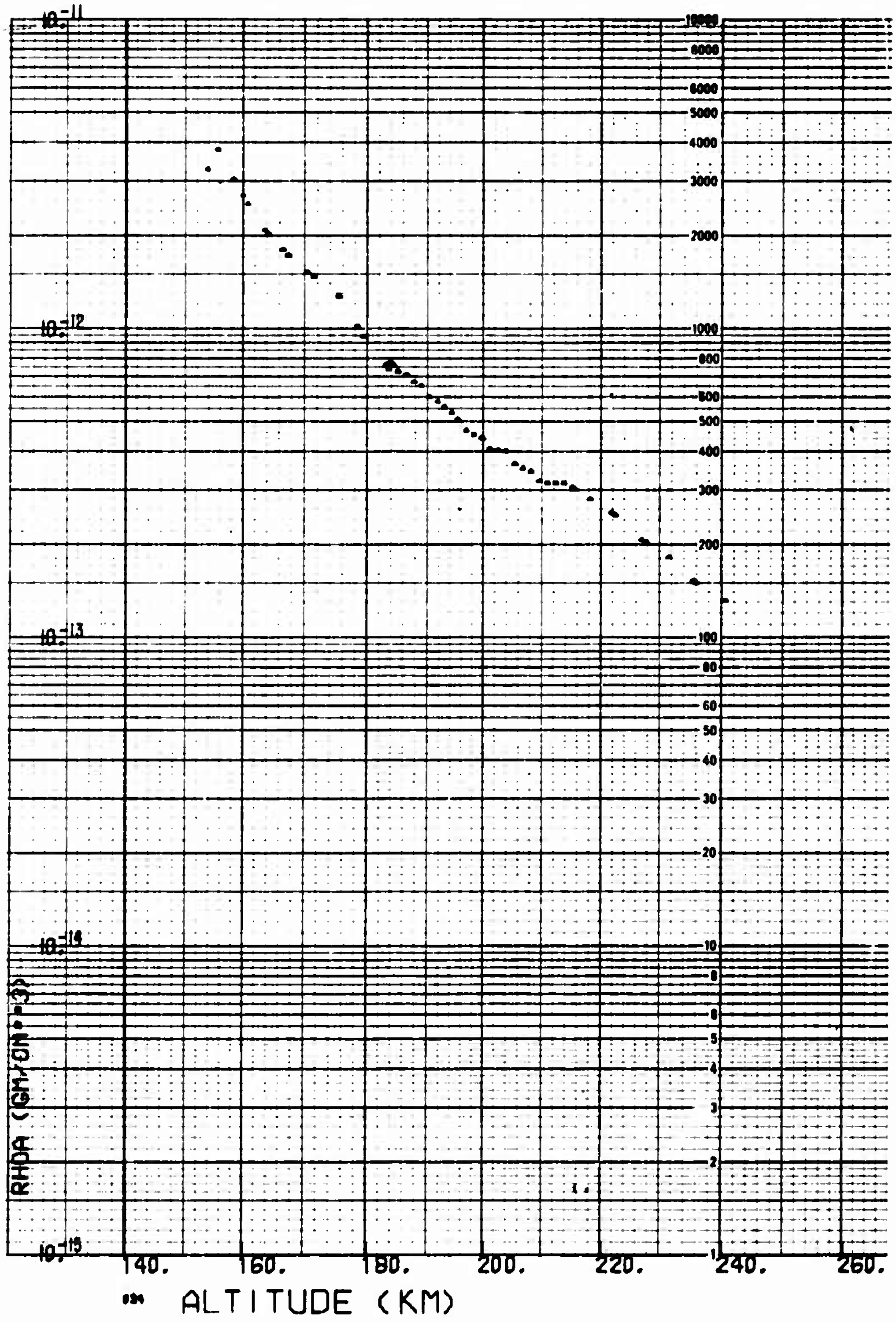

Fig. B-97. LOGACS Density Data for Rev. 66, Toward Perigee

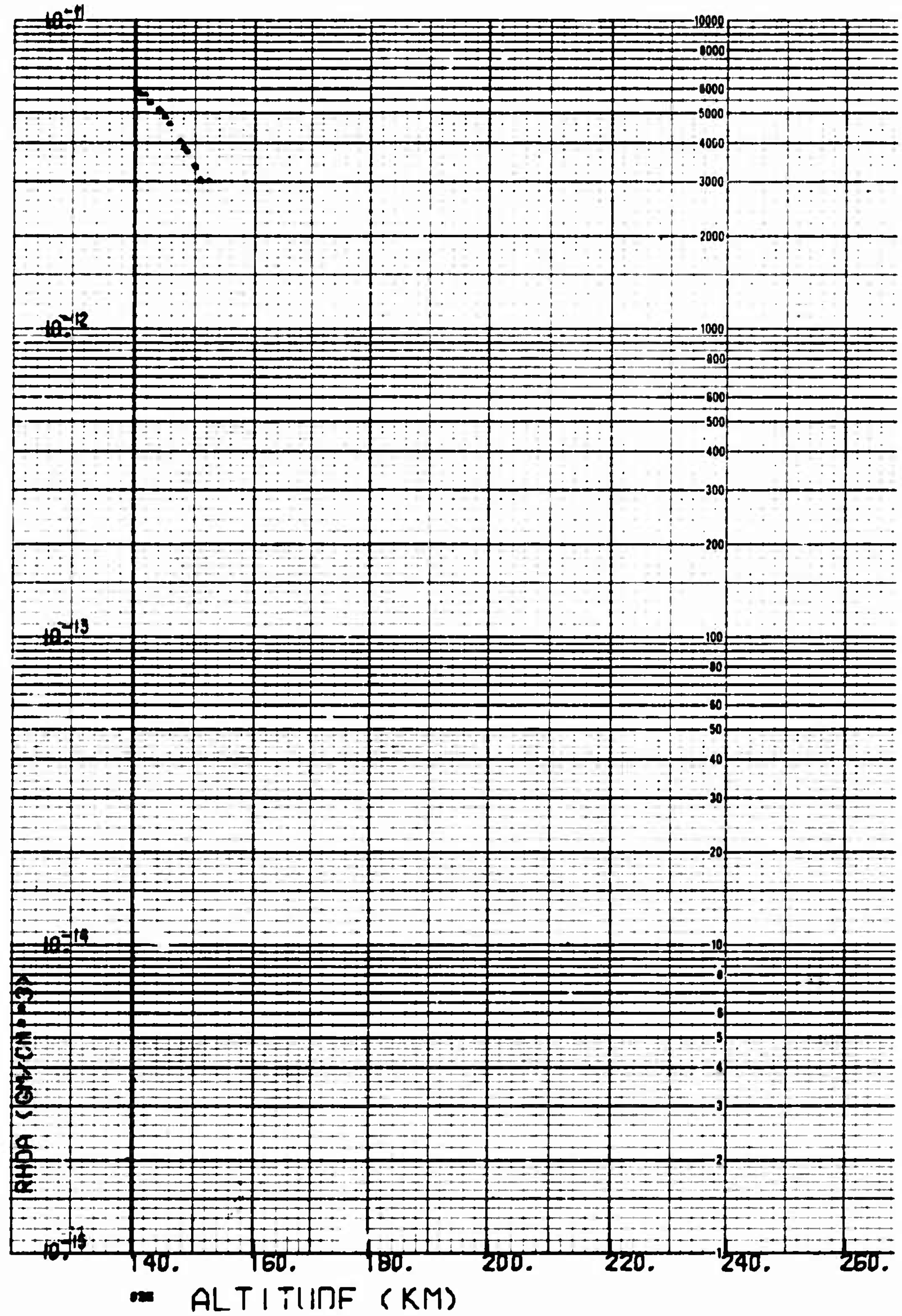

Fig. B-98. LOGACS Density Data for Rev. 66, Away from Perigee

(This page intentionally blank)

APPENDIX C

LOGACS WIND DATA

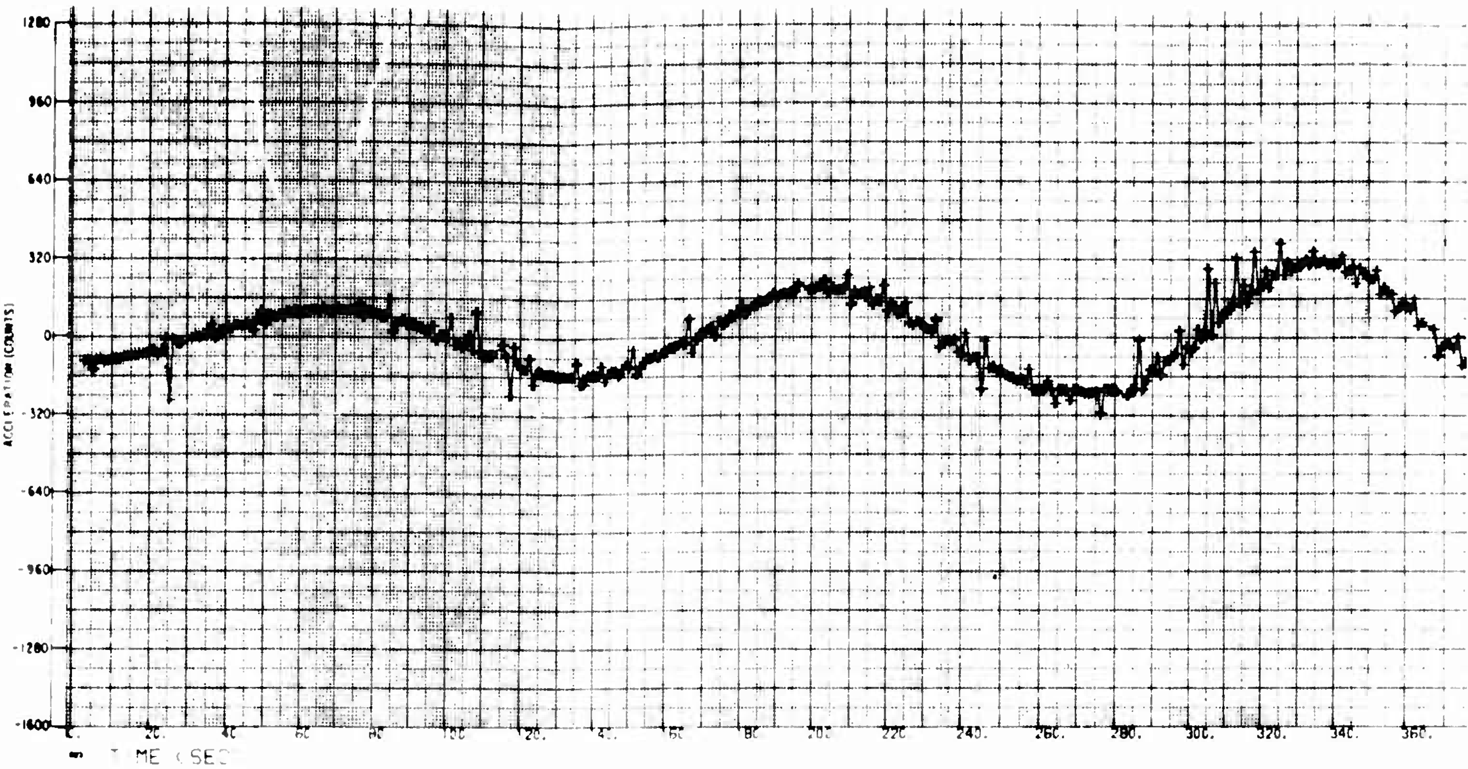

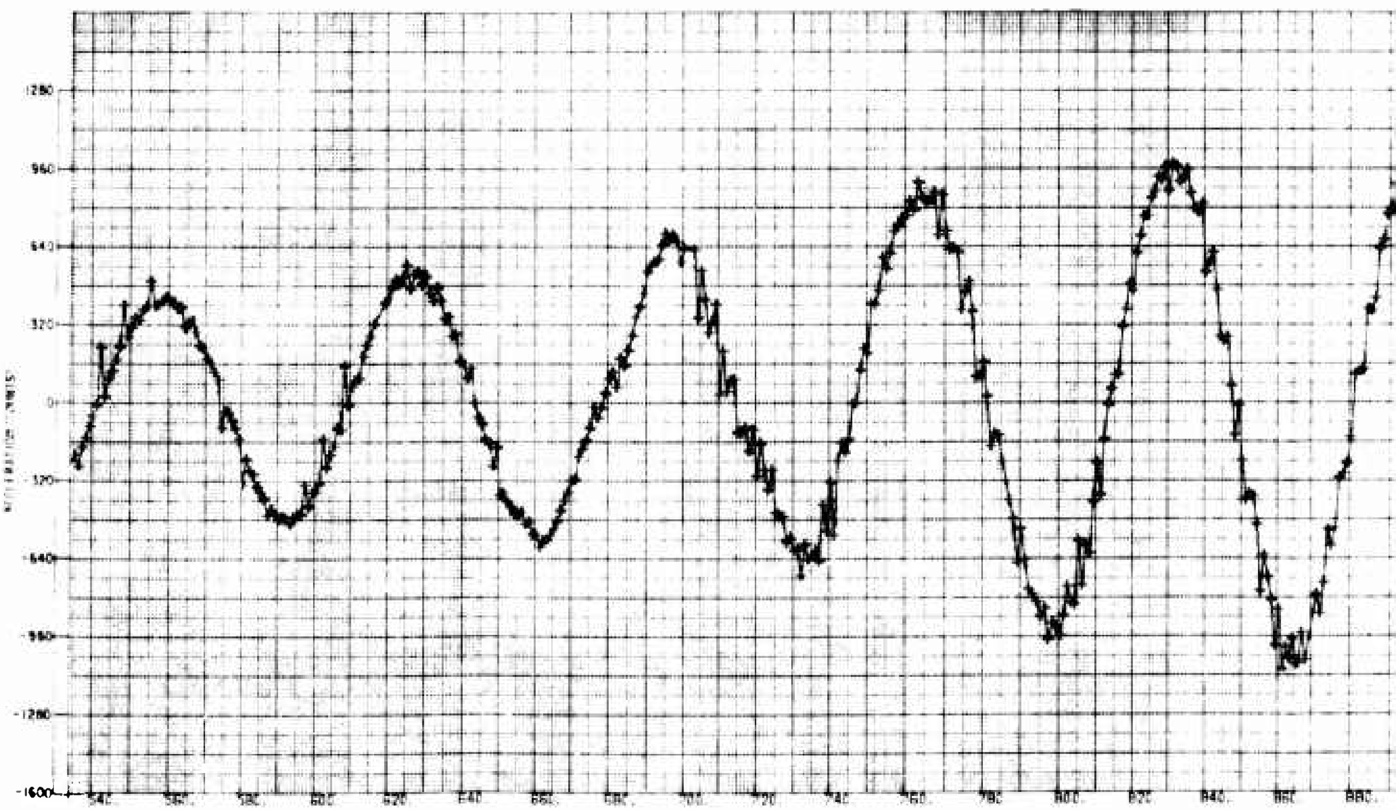

Fig. C-

A

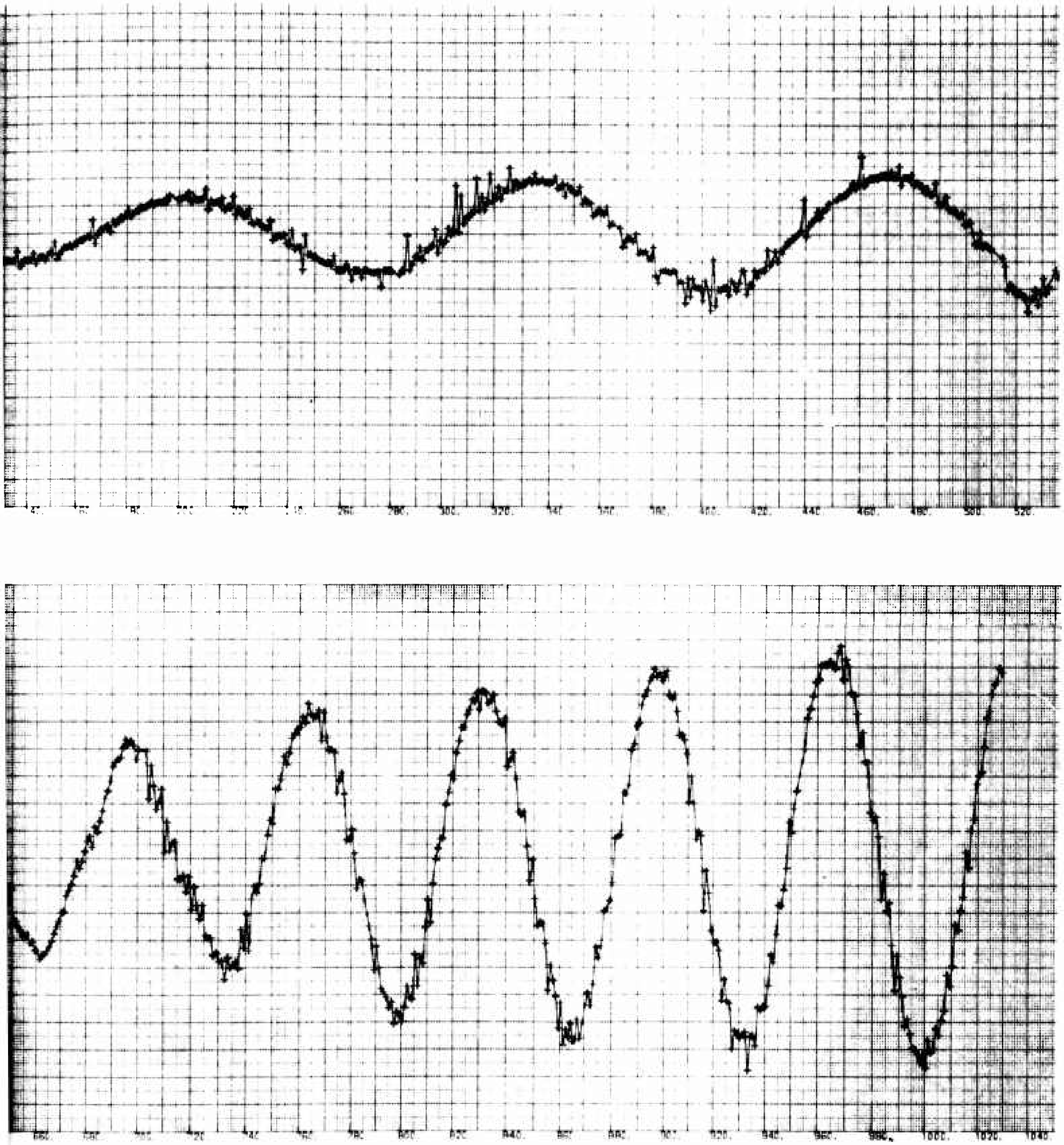

Fig. C-1. Revolution 56, Corrected Data

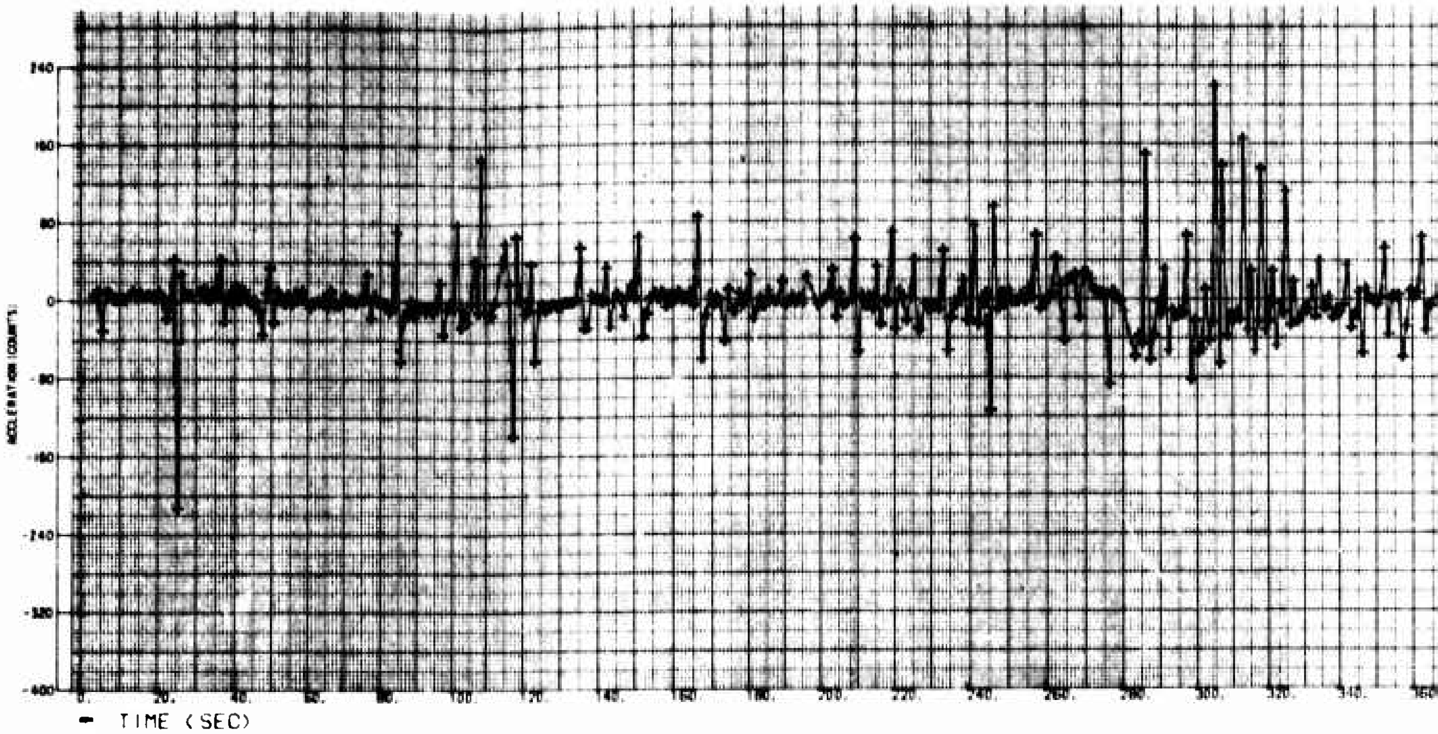

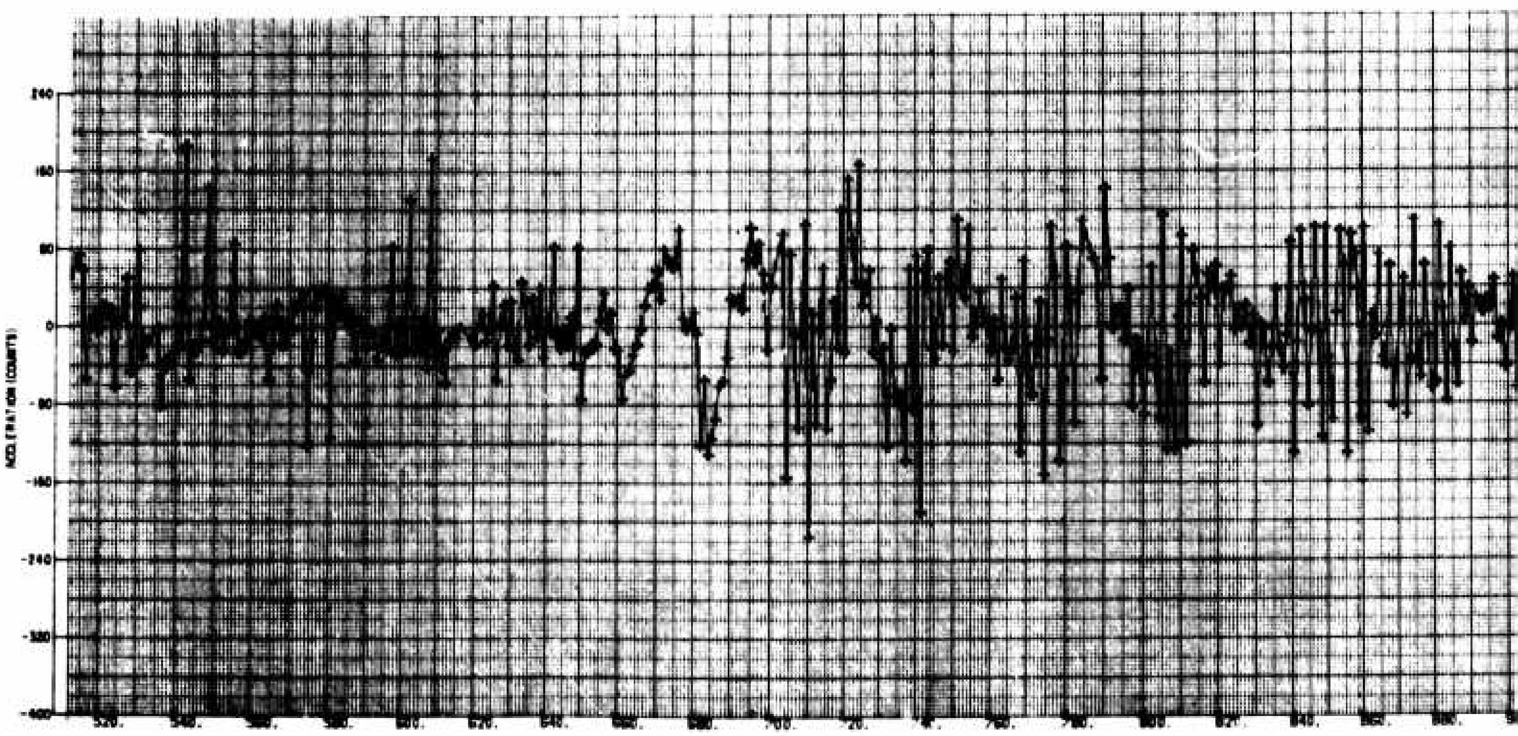

Fig.

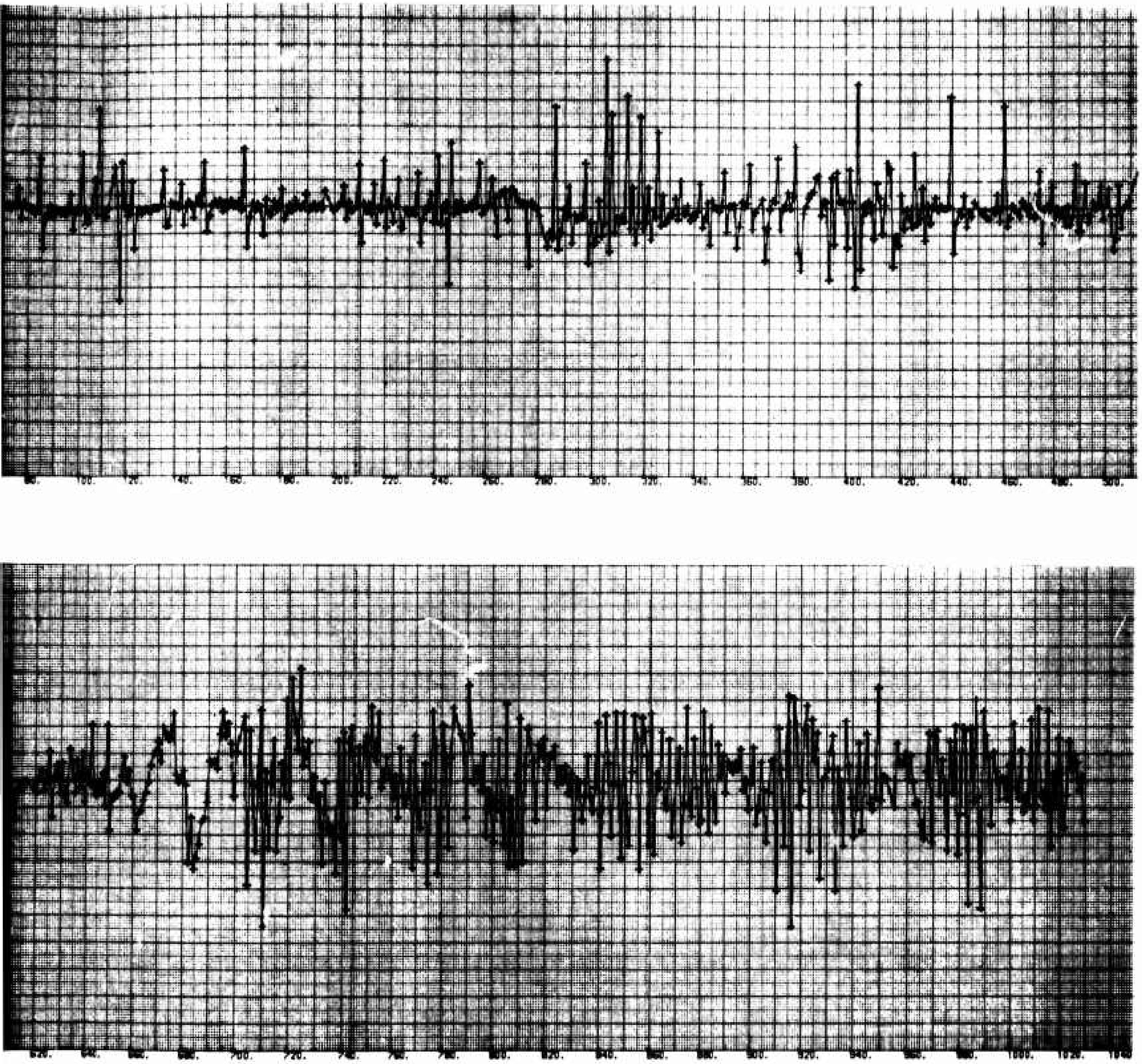

Fig. C-2. Revolution 56, Residuals

B

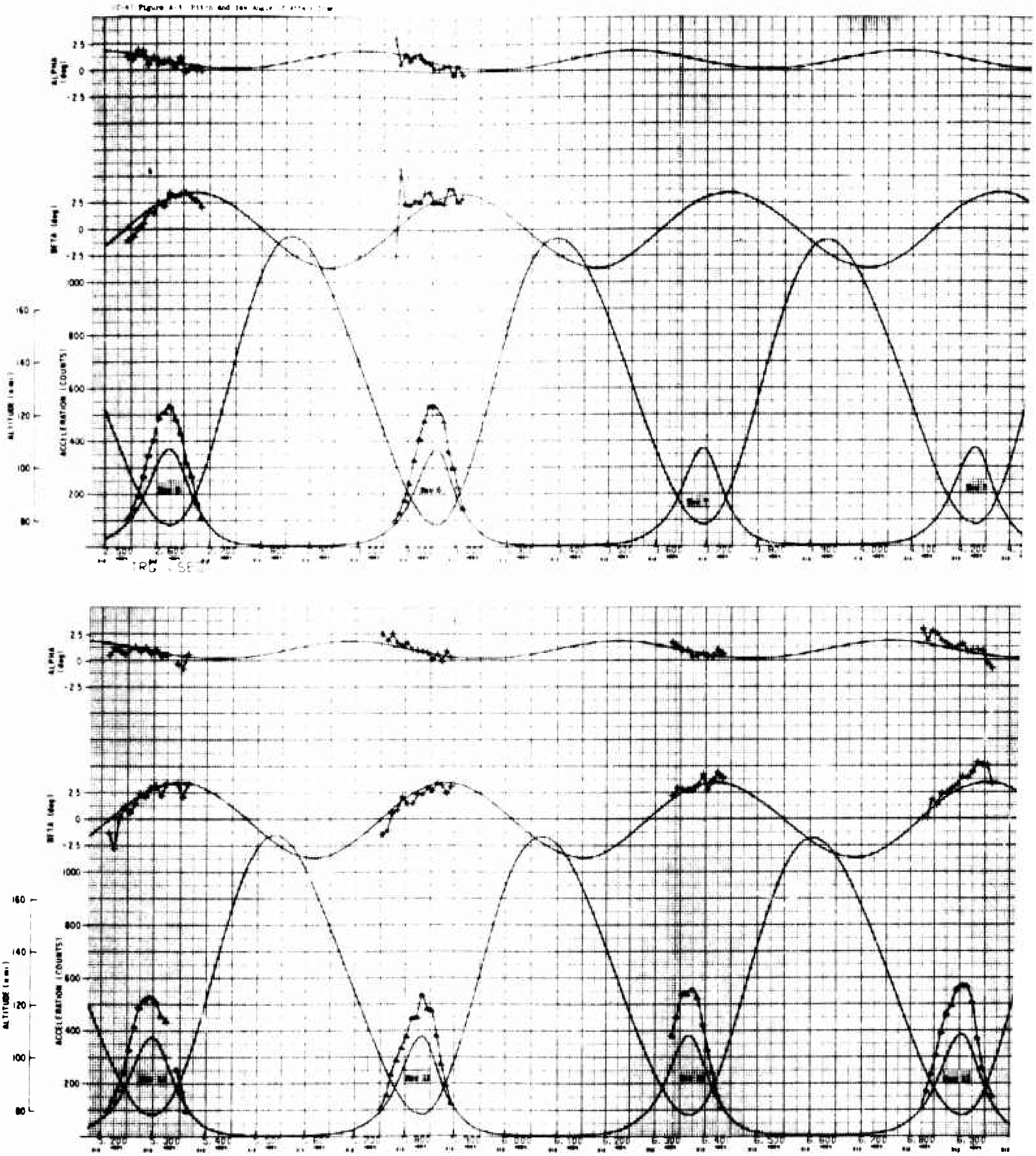

Fig. C-3. Pitch ar

A

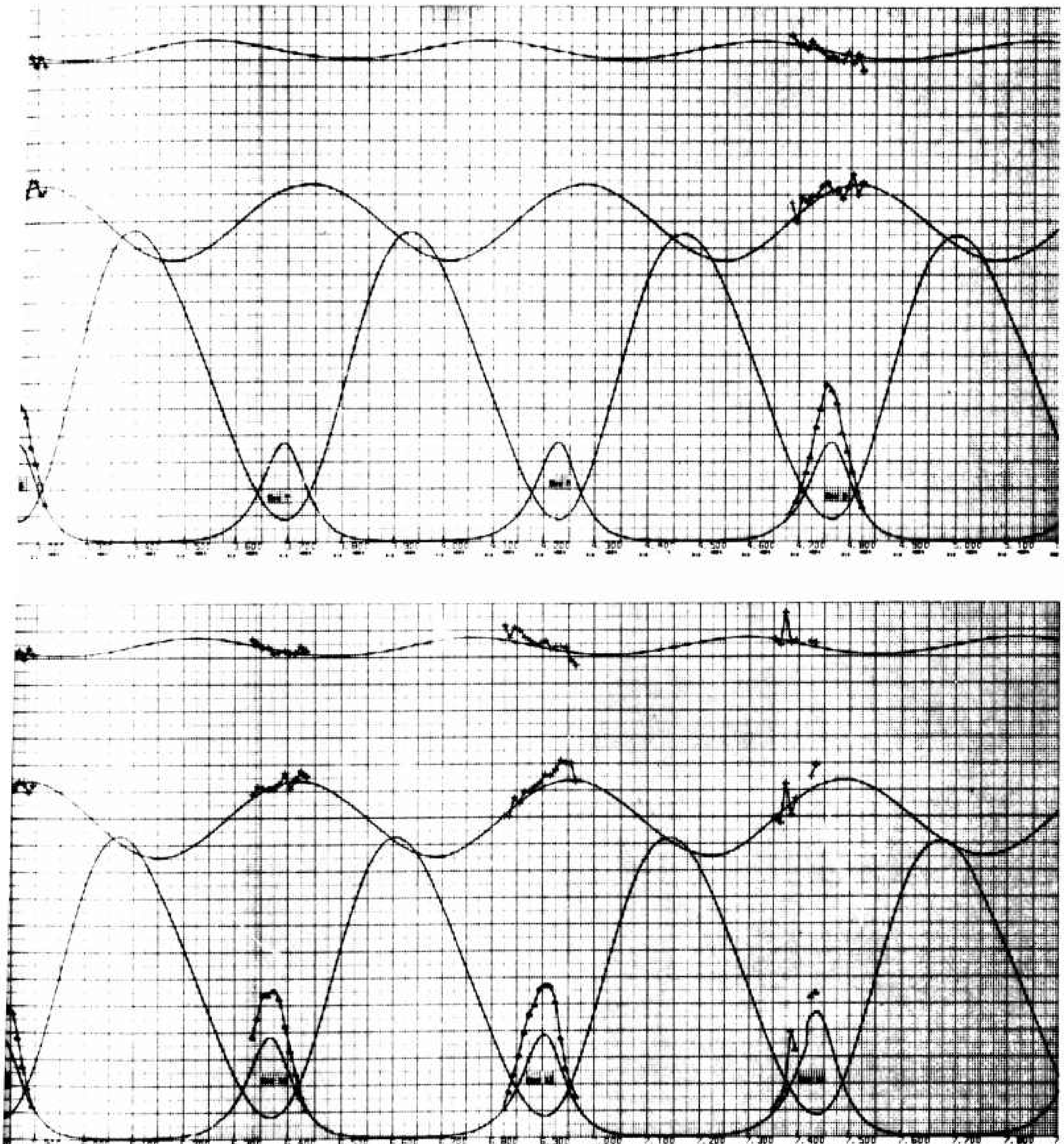

Fig. C-3. Pitch and Yaw Angle-of-Attack Time Histories

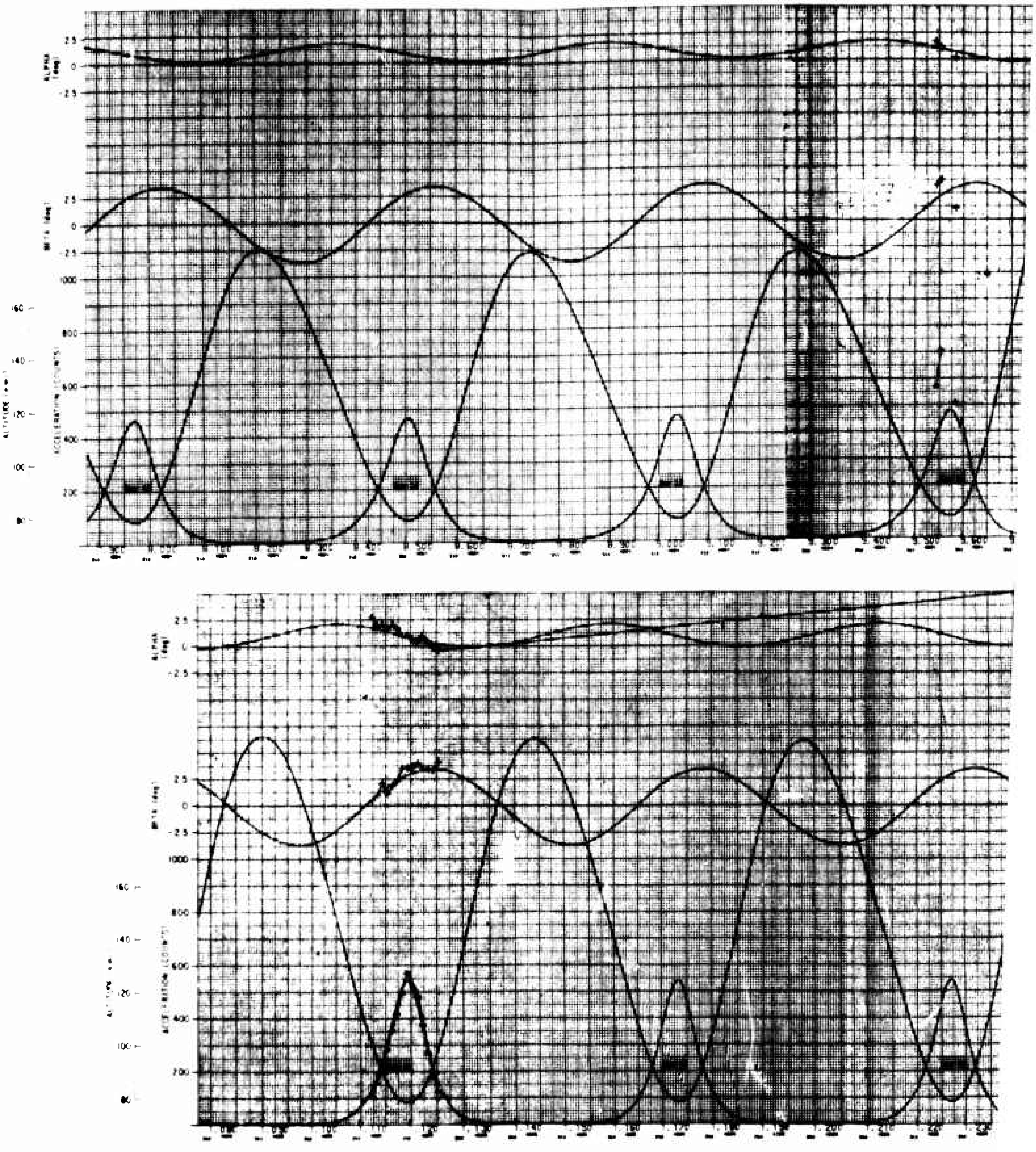

Fig. C-3. Pitch and

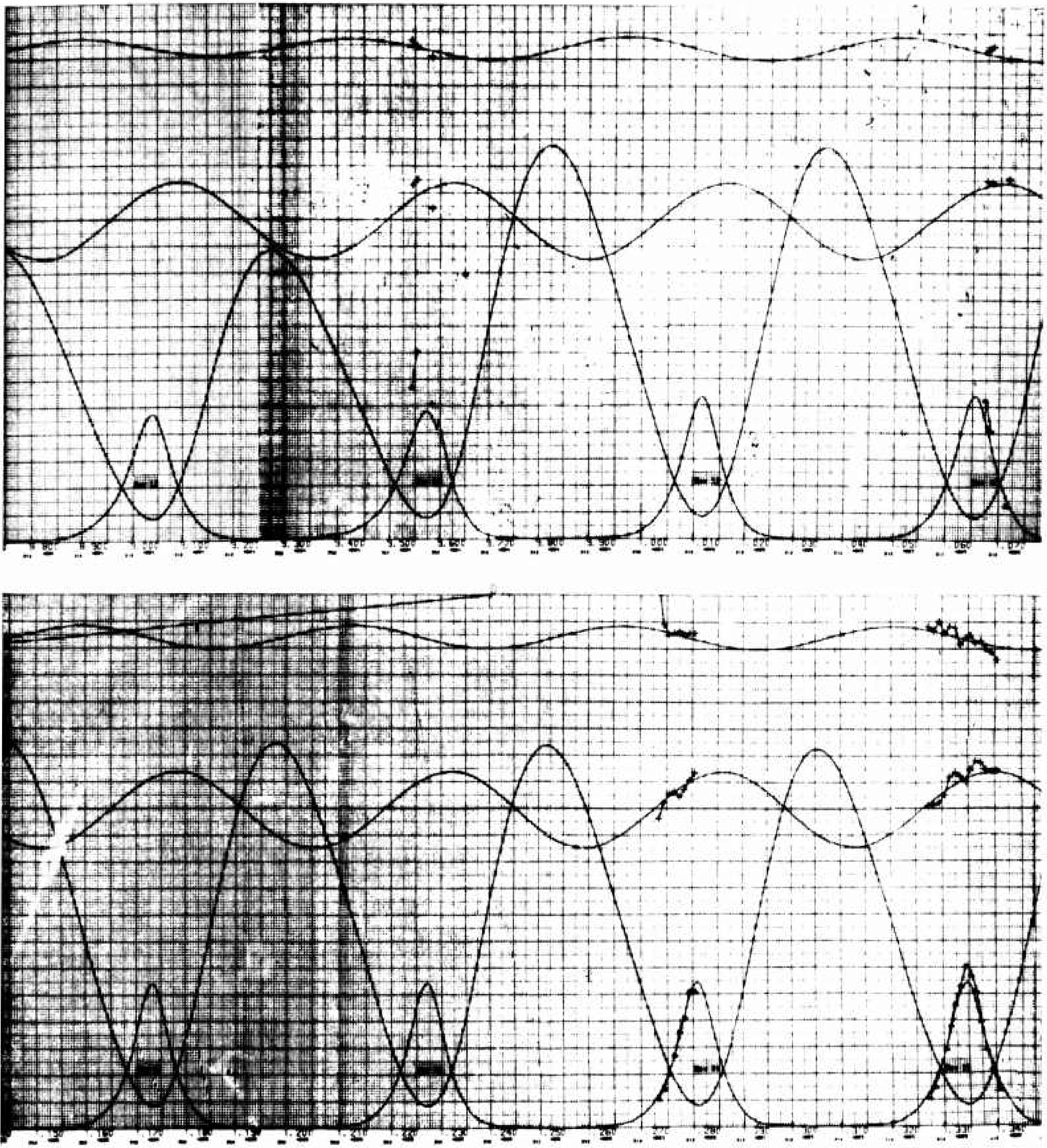

Fig. C-3. Pitch and Yaw Angle-of-Attack Time Histories (Continued)

B

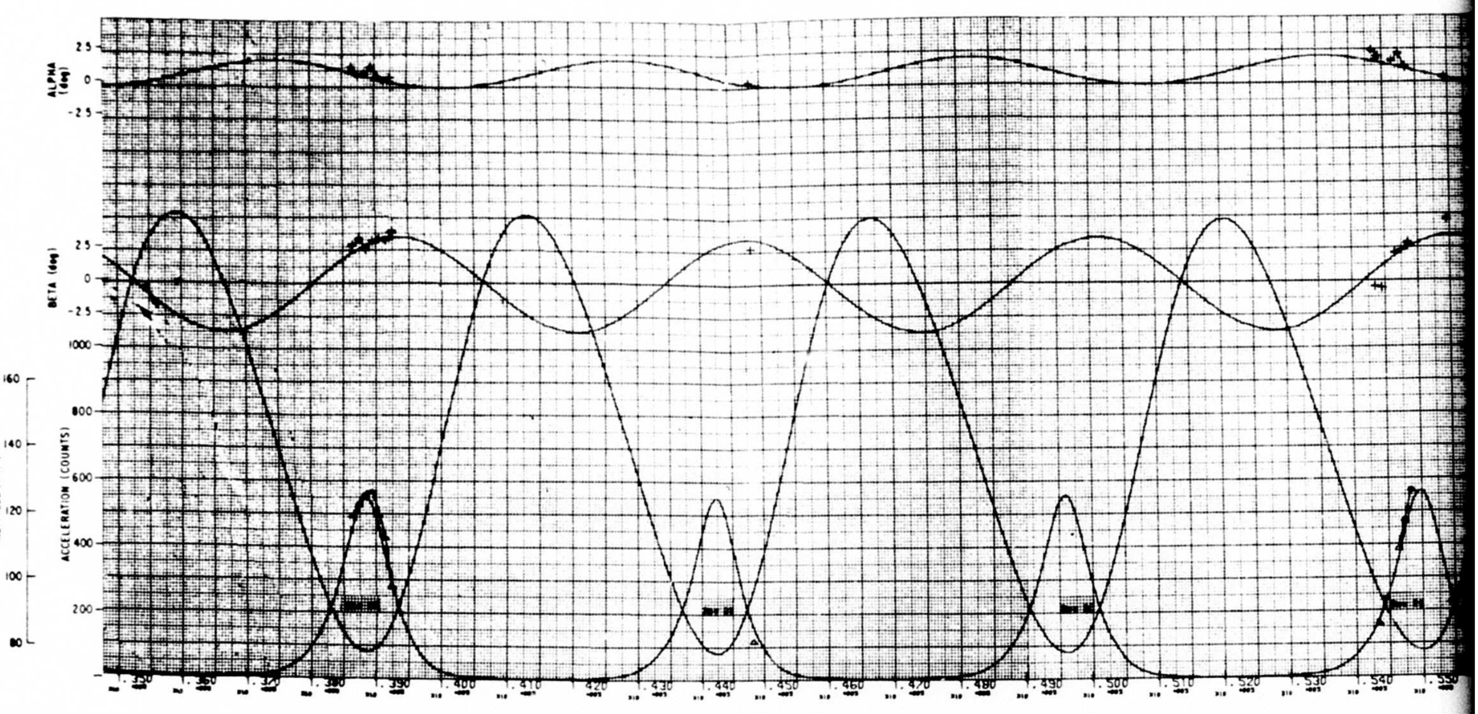

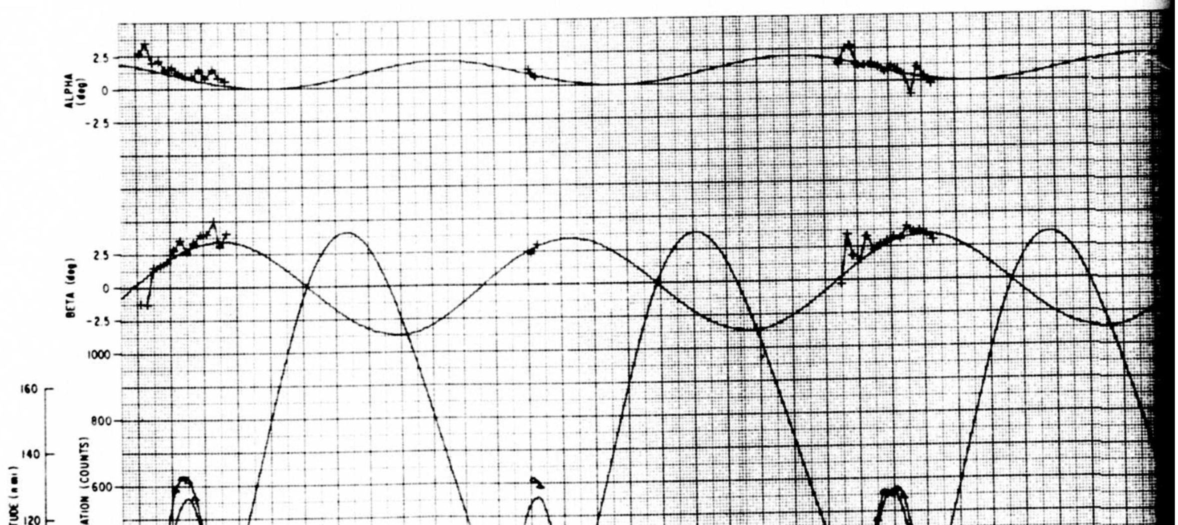

Fig. C-3. Pitch and Yaw An

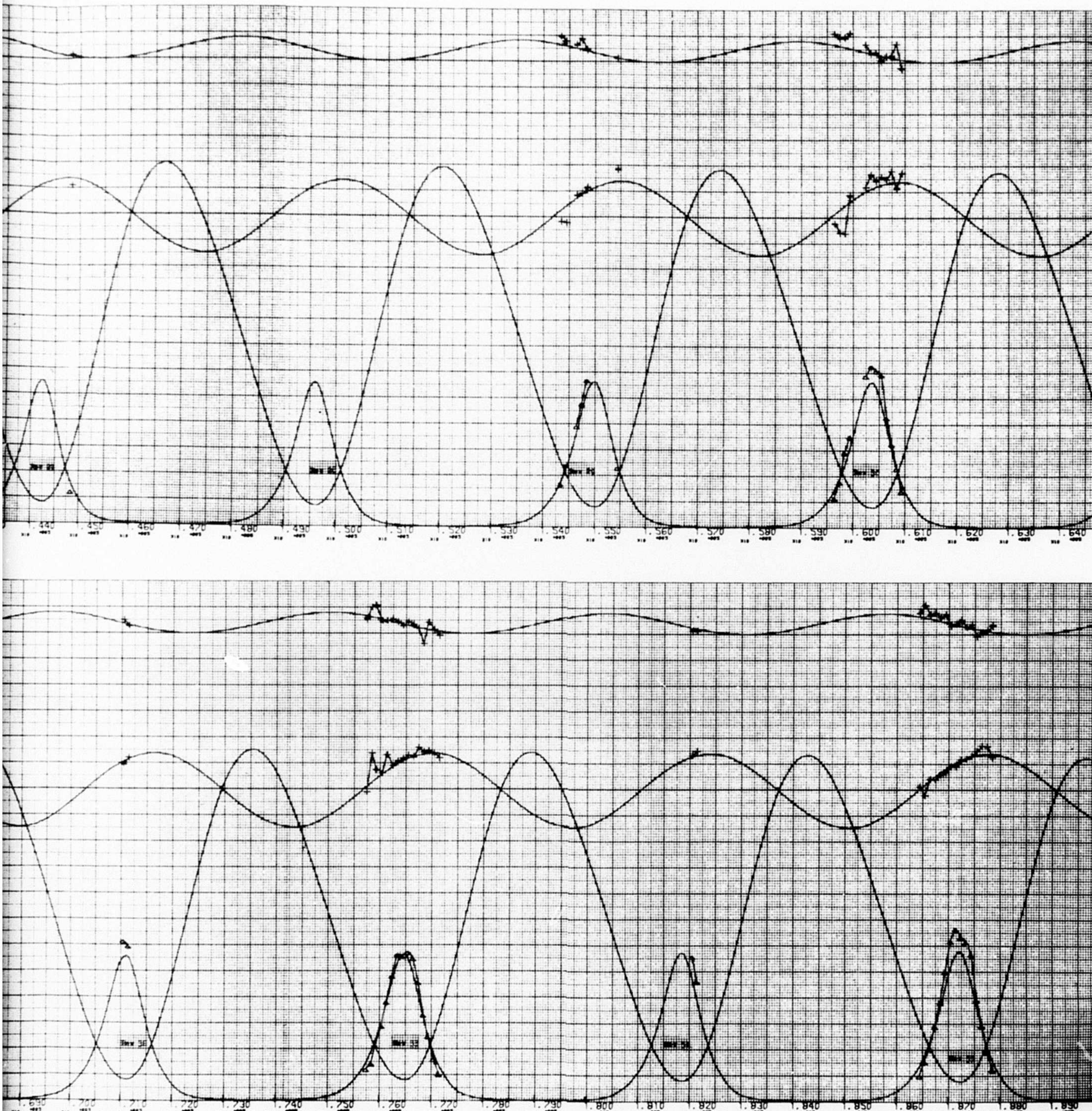

Fig. C-3. Pitch and Yaw Angle-of-Attack Time Histories (Continued)

B

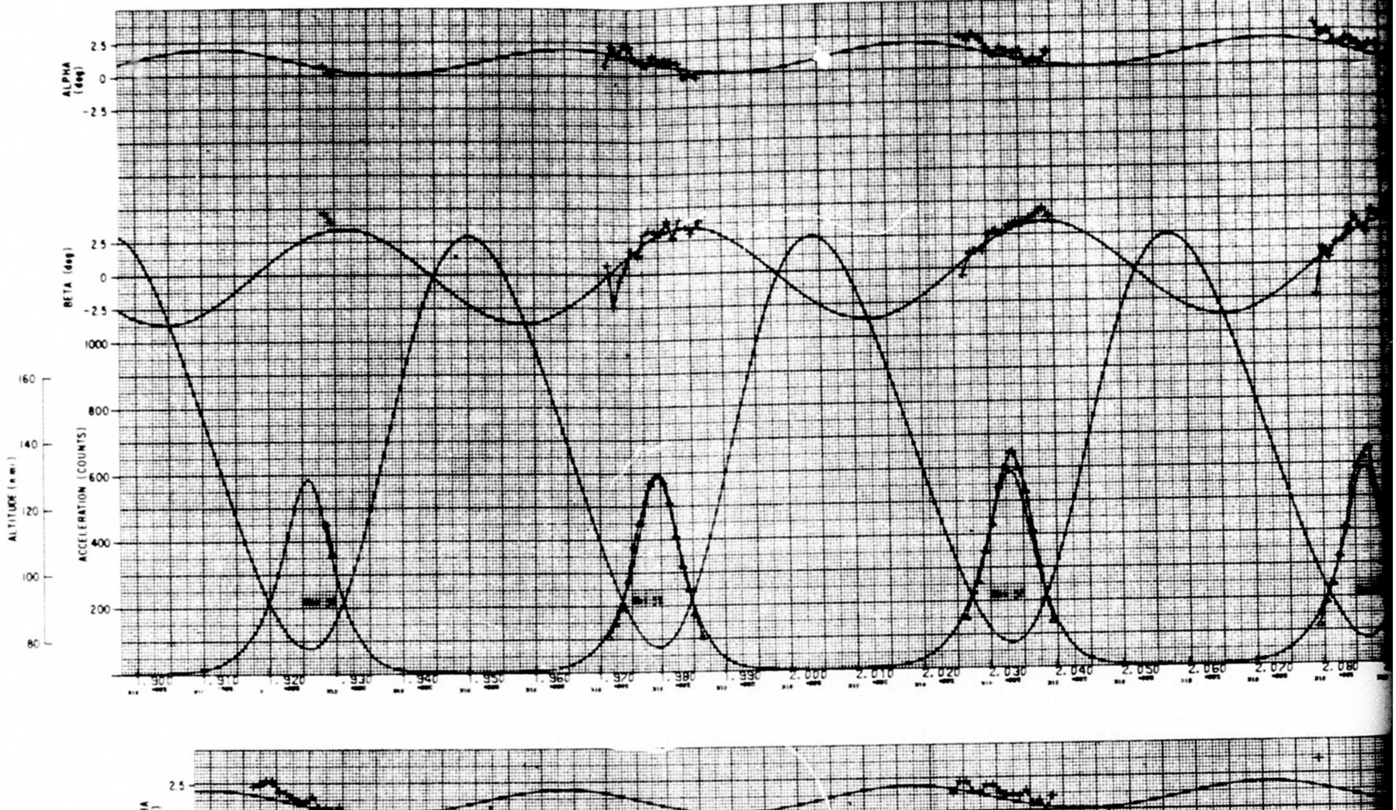

Fig. C-3. Pitch and Yaw Ang

A

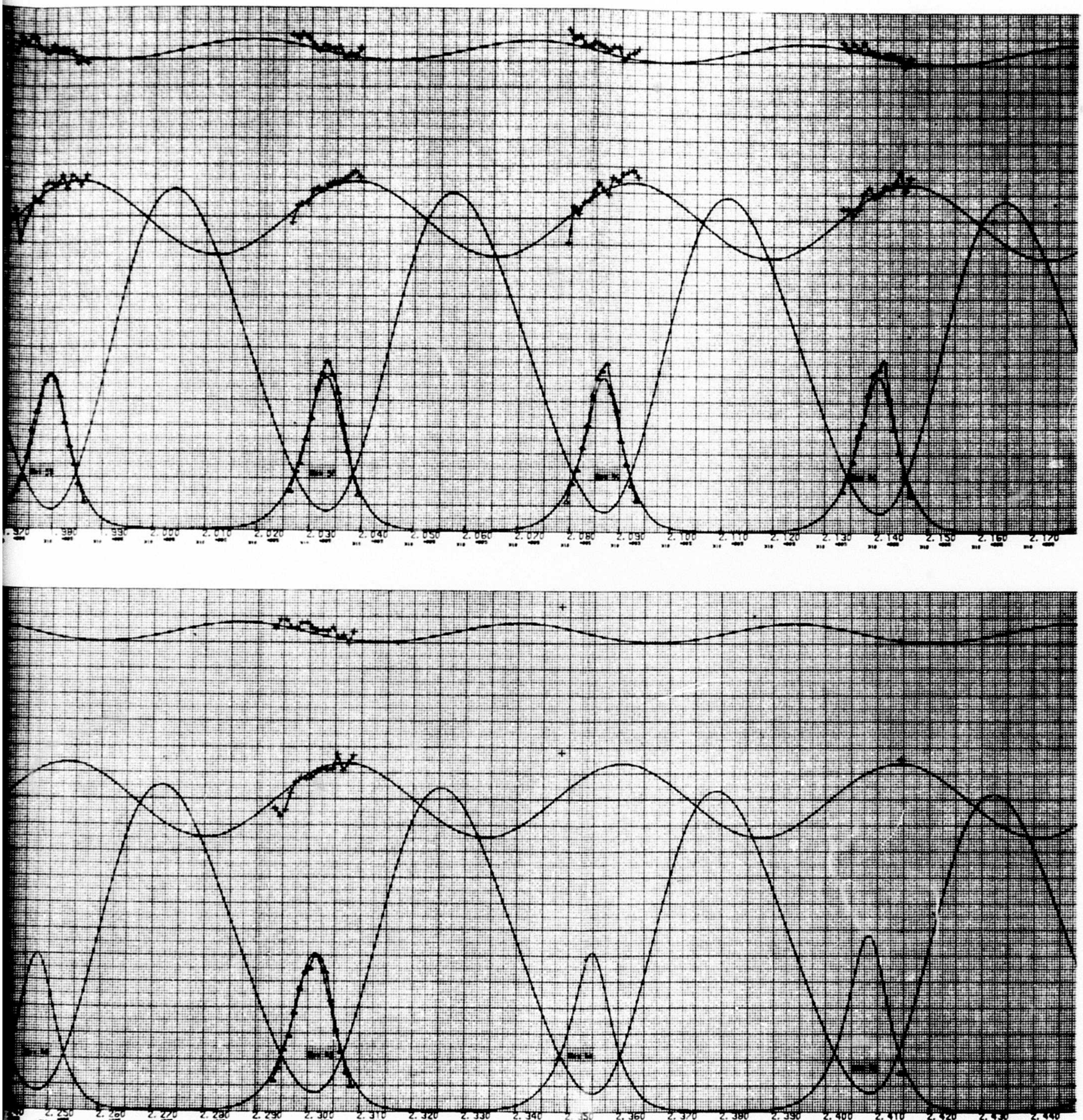

Fig. C-3. Pitch and Yaw Angle-of-Attack Time Histories (Continued)

B

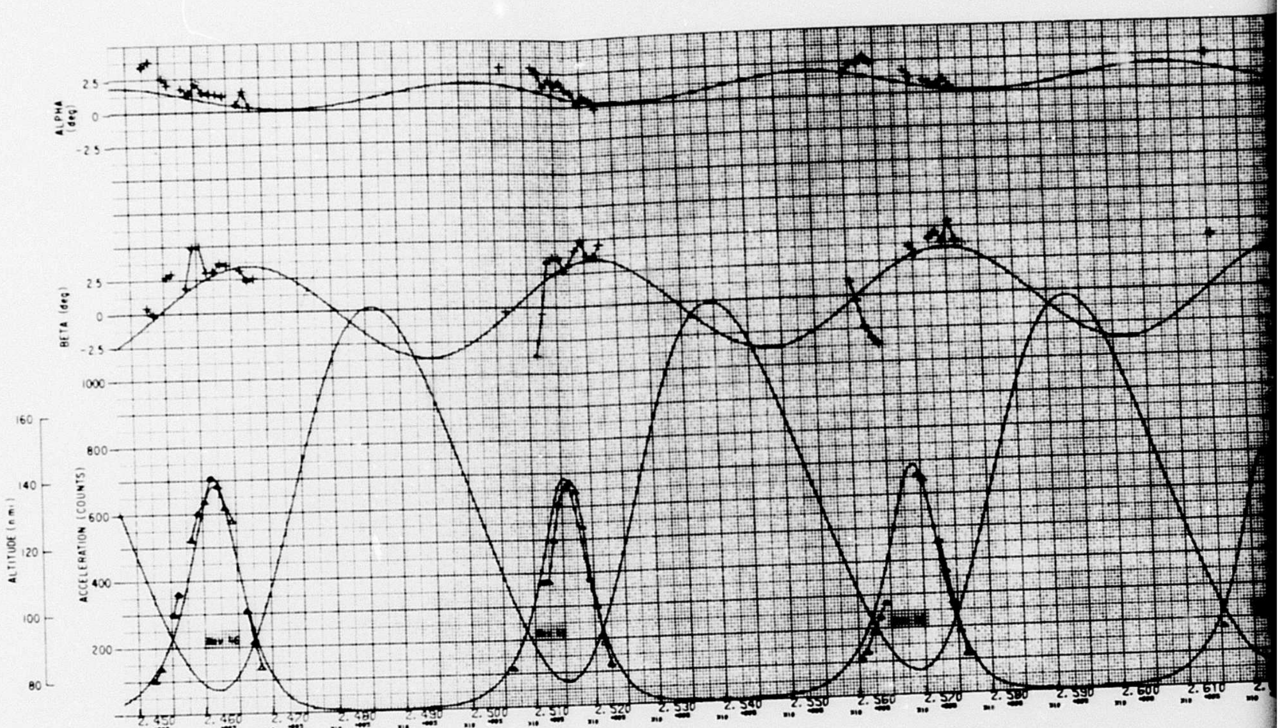

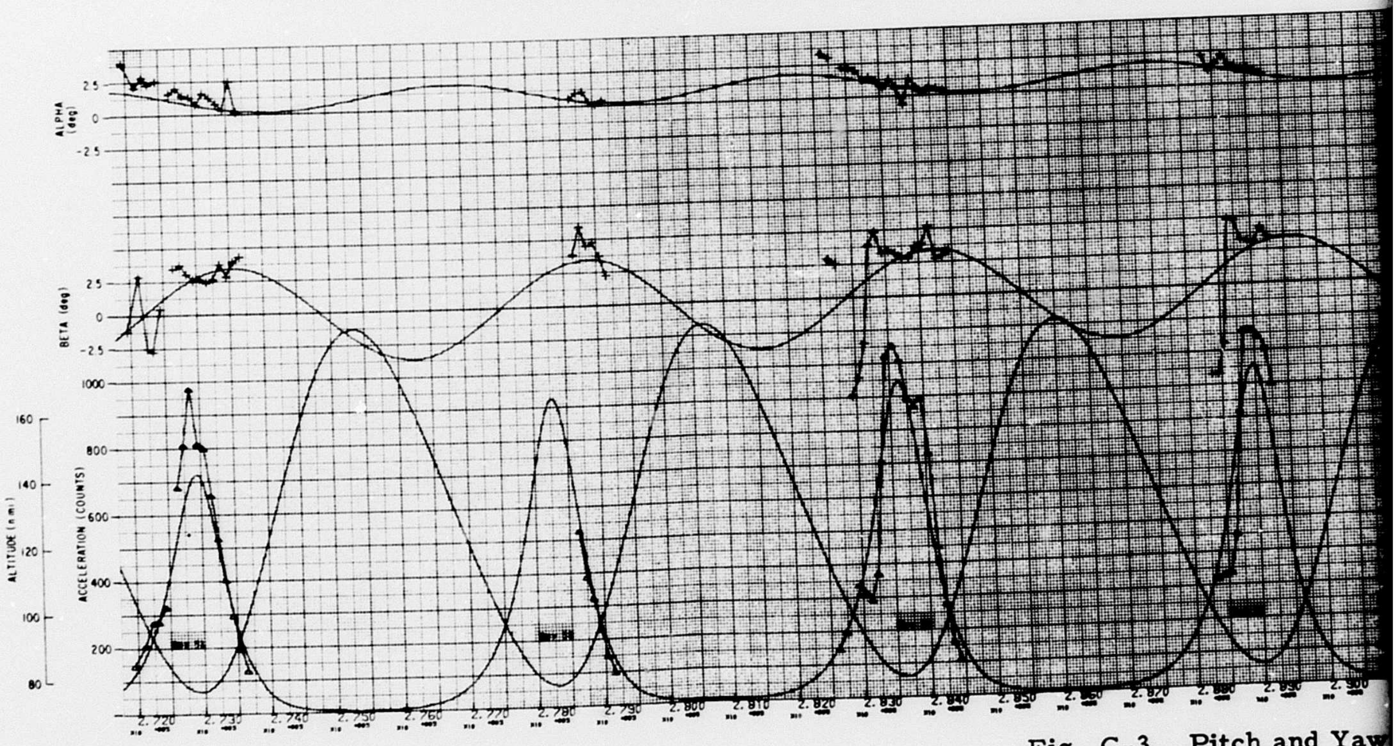

Fig. C-3. Pitch and Yaw

A

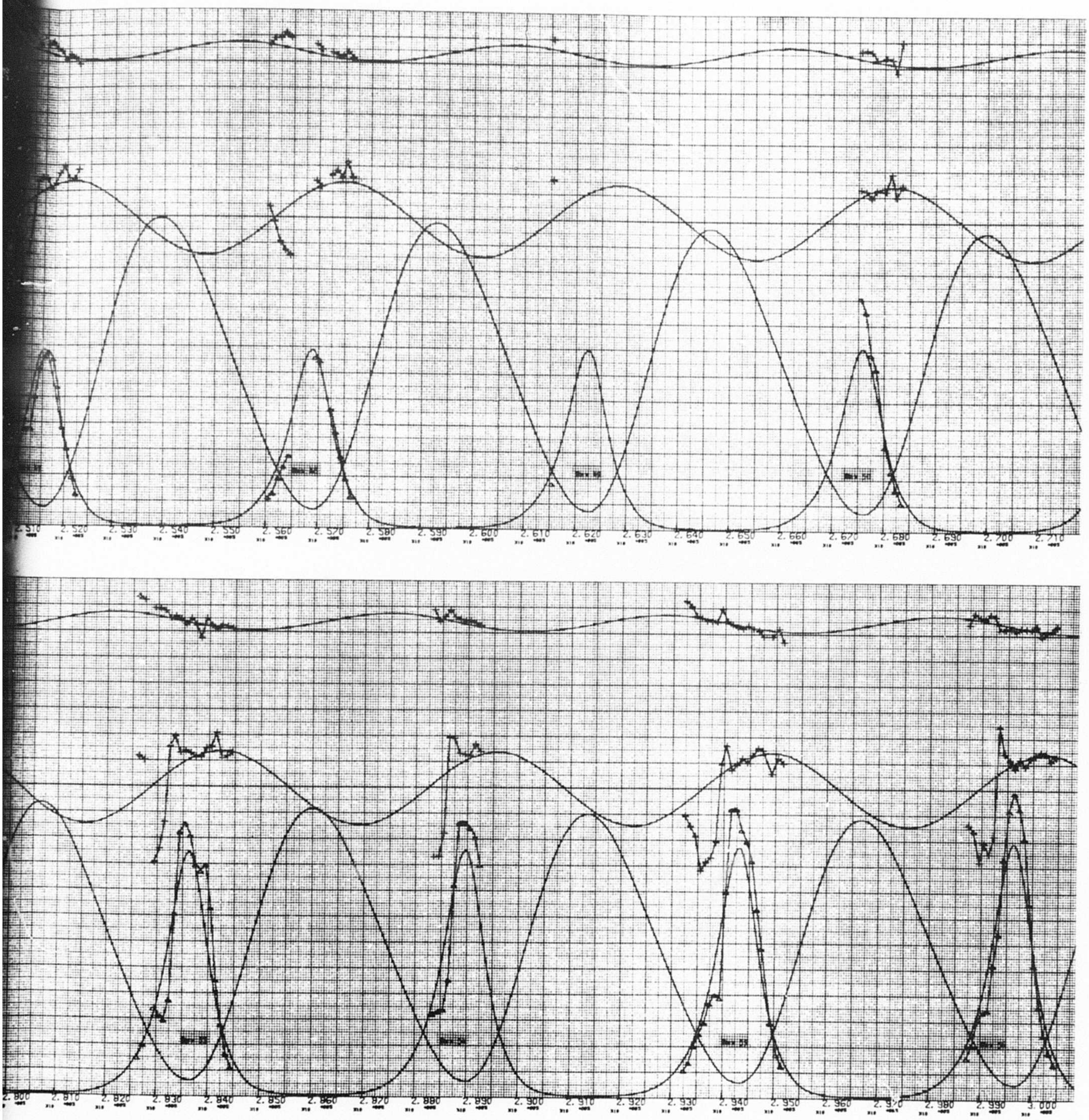

Fig. C-3. Pitch and Yaw Angle-of-Attack Time Histories (Continued)

13

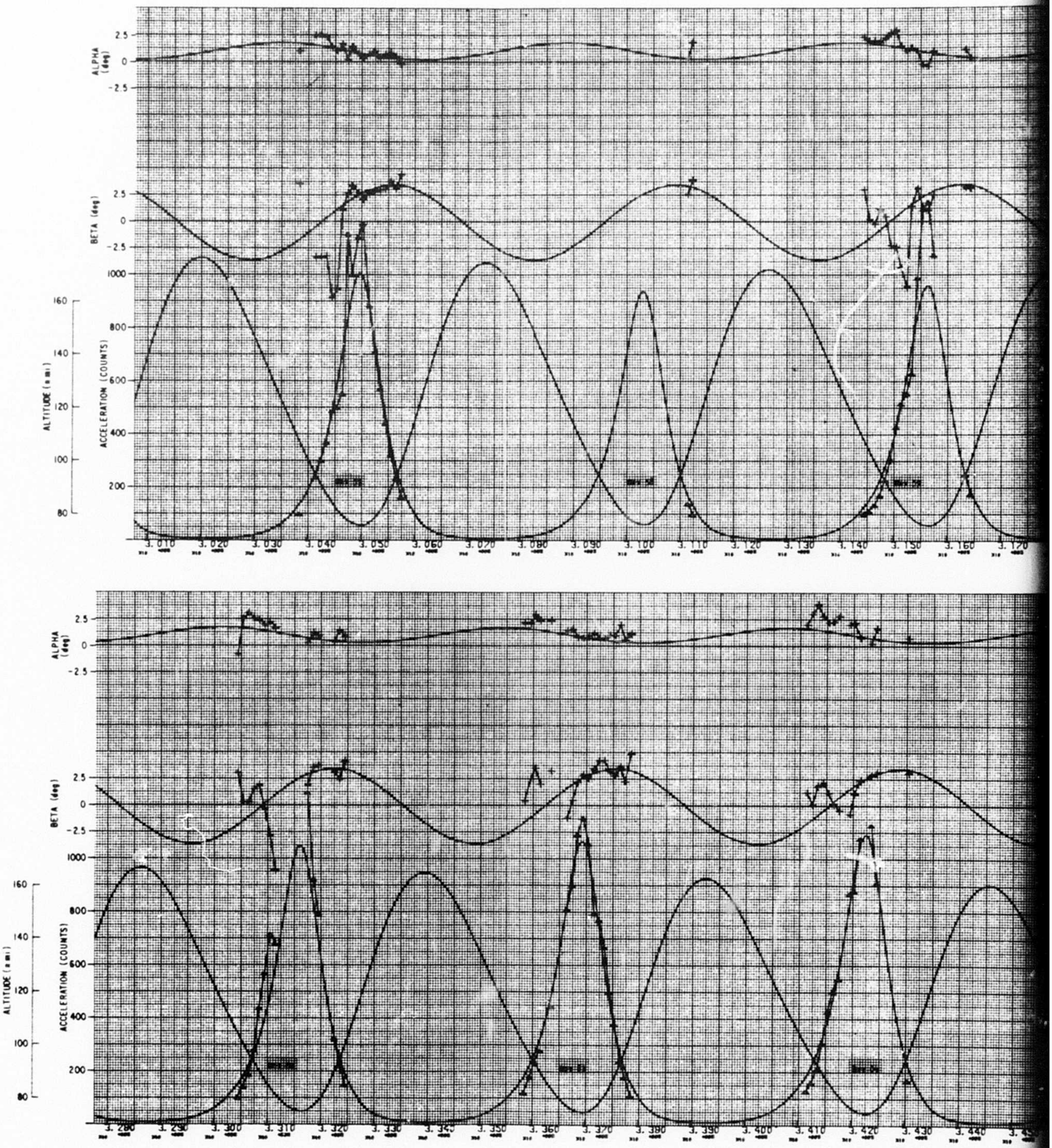

Fig. C-3. Pitch and Yaw

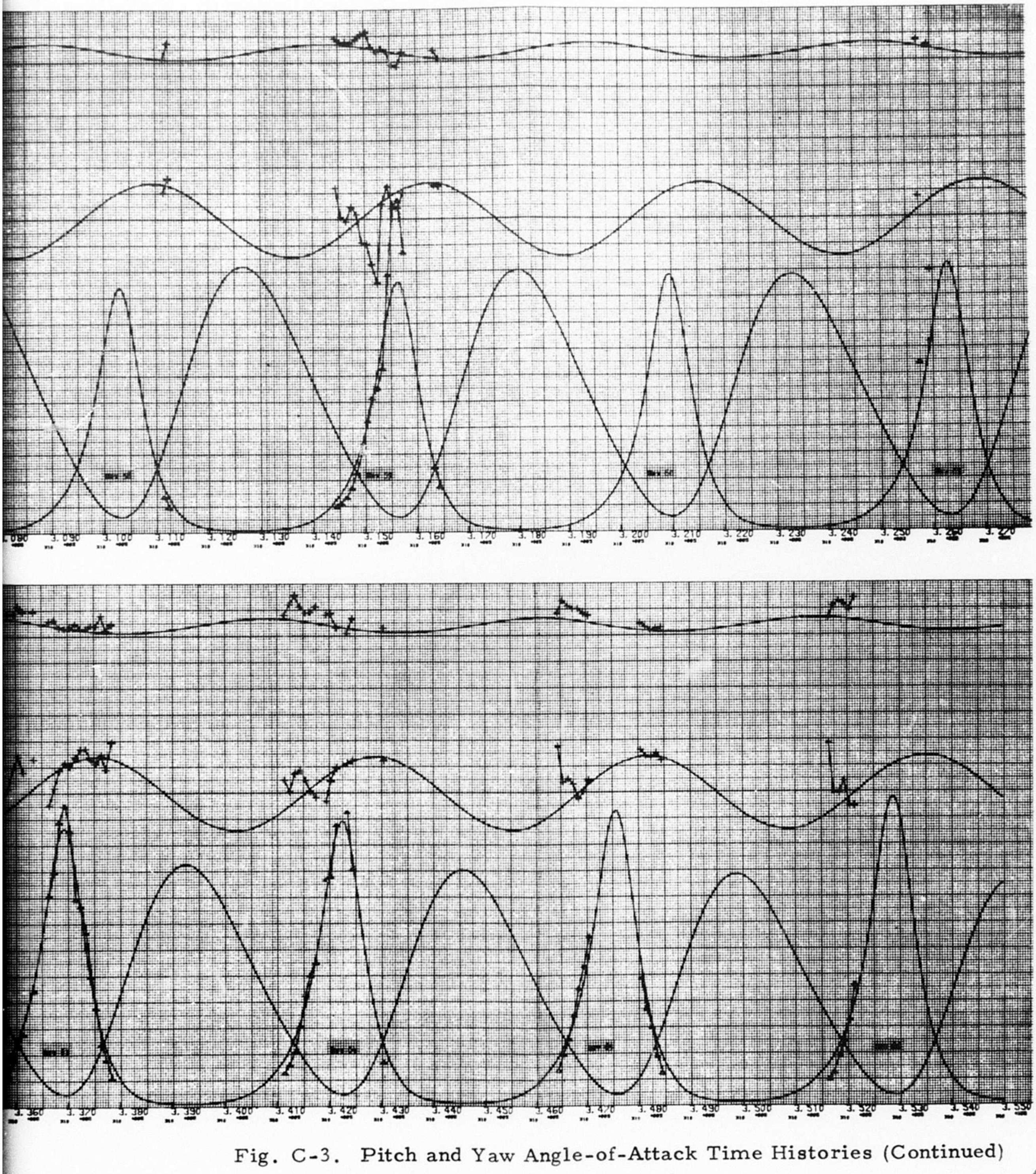

Fig. C-3. Pitch and Yaw Angle-of-Attack Time Histories (Continued)

B